(NASA-CR-170942) RESEARCH REPORTS: 1983 NASA/ASEE SUMMER FACULTY FELLOWSHIP PROGRAM (Alabama Univ., Huntsville.) 891 p HC A99/MF A01 CSCL 05I G3/80

N84-16022 THRU N84-16057 Unclas 18021

NASA CONTRACTOR REPORT

NASA CR-170942

RESEARCH REPORTS - 1983 NASA/ASEE SUMMER FACULTY FELLOWSHIP PROGRAM

University of Alabama in Huntsville
Huntsville, Alabama

December 1983

Prepared for

NASA-GEORGE C. MARSHALL SPACE FLIGHT CENTER
Marshall Space Flight Center, Alabama 35812

RESEARCH REPORTS

1983 NASA/ASEE SUMMER FACULTY FELLOWSHIP PROGRAM

George C. Marshall Space Flight Center
The University of Alabama in Huntsville
and
The University of Alabama

EDITORS:

Dr. Gerald R. Karr
Associate Professor of Mechanical Engineering
The University of Alabama in Huntsville

Dr. James B. Dozier
Director, Research and Technology Office
Marshall Space Flight Center

Mr. Leroy Osborn
Office of University and Congressional Affairs
Marshall Space Flight Center

Dr. Michael Freeman
Professor of Aerospace Engineering
The University of Alabama

TECHNICAL REPORT STANDARD TITLE PAGE

1. REPORT NO.	2. GOVERNMENT ACCESSION NO.	3. RECIPIENT'S CATALOG NO.
NASA CR-170942		

4. TITLE AND SUBTITLE	5. REPORT DATE
Research Reports - 1983 NASA/ASEE Summer Faculty Fellowship Program	December 1983
	6. PERFORMING ORGANIZATION CODE
7. AUTHOR(S) Edited by Dr. Gerald R. Karr, Dr. James B. Dozier, Mr. Leroy Osborn, and Dr. Michael Freeman	8. PERFORMING ORGANIZATION REPORT #
9. PERFORMING ORGANIZATION NAME AND ADDRESS University of Alabama in Huntsville Huntsville, Alabama	10. WORK UNIT NO.
	11. CONTRACT OR GRANT NO. NGT 01-005-021
	13. TYPE OF REPORT & PERIOD COVERED Contractor Report
12. SPONSORING AGENCY NAME AND ADDRESS National Aeronautics and Space Administration Washington, D. C. 20546	14. SPONSORING AGENCY CODE

15. SUPPLEMENTARY NOTES

Technical manager: Leroy Osborn, George C. Marshall Space Flight Center

16. ABSTRACT

This document is a compilation of 35 technical reports on research conducted by participants in the 1983 NASA/ASEE Summer Faculty Fellowship Program at Marshall Space Flight Center (MSFC) with one participant performing research at Kennedy Space Center (KSC). Six participants performed research in the Information and Electronics Systems Laboratory on logic simulation, lightning emissions, frequency-modulated continuous wave radar ranging, teleoperator maneuvering system, seven degree of freedom manipulation arm, and an orbital maneuvering vehicle. Eight participants performed research in the Materials and Processes Laboratory on thermal insulating foam, composite materials, silicon carbide-nitride fibers, atomic oxygen effects, techroll seal material, siloxane polymers, robot welding, and spectrometer automation. In the Space Science Laboratory, nine participants performed research on reflectance measurements, an Echelle spectrograph, accretion in impact sources, nuclear activation, superfluid helium, self-replicating systems, alloy solidification models, solid solution crystals, and electrophoresis systems. The Structures and Propulsion Laboratory had one participant performing laser propulsion research. Eight participants in the Systems Dynamics Laboratory performed research on Euler-Macheroni constants, numerical simulation of solidification, arc cloud complex, rotordynamics, statistical analysis, multiple vortex phenomenon, graphite-epoxy shells, finite element analysis. One participant performed research at the Test Laboratory on X-ray source monitor. One participant working in Program Development studied a satellite de-spin system. The one researcher at KSC studied the ecology of the canal and basin area at KSC.

17. KEY WORDS	18. DISTRIBUTION STATEMENT
Logic simulation, lightning emissions, teleoperator, composite materials, silicon carbide nitride fibers, atomic oxygen effects, robot welding, spectrometer automation, self-replicating systems, electrophoresis, solid solution crystals, rotordynamics.	Unclassified-Unlimited W T Carey DEC 13 1983 W. T. CAREY Director, Executive Staff

19. SECURITY CLASSIF. (of this report)	20. SECURITY CLASSIF. (of this page)	21. NO. OF PAGES	22. PRICE
Unclassified	Unclassified	888	NITS

MSFC - Form 3292 (May 1969)

For sale by National Technical Information Service, Springfield, Virginia 22151

PREFACE

This document is a collection of technical reports on research conducted by the participants in the 1983 NASA/ASEE Summer Faculty Fellowship Program at Marshall Space Flight Center (MSFC) with one participant performing research at Kennedy Space Center (KSC). This was the nineteenth consecutive year the program has been conducted at MSFC. The 1983 program was administered by the University of Alabama in Huntsville (UAH) in cooperation with MSFC and the University of Alabama (UA), University, Alabama. The program was operated under the auspices of the American Society for Engineering Education (ASEE) with sponsorship and funding from the Office of External Relations, NASA Headquarters, Washington, D. C. The MSFC program was one of seven such Aeronautics and Space Research Programs funded by NASA Headquarters in 1983. Similar programs were conducted at six other NASA centers. The basic common objectives of the NASA/ASEE Summer Faculty Fellowship Program are:

a. To further the professional knowledge of qualified engineering and science faculty members;

b. To stimulate an exchange of ideas between participants and NASA;

c. To enrich and refresh the research and teaching activities of participants' institutions; and,

d. To contribute to the research objectives of the NASA centers.

The MSFC Faculty Fellows spent 10 weeks (June 6 through August 12, 1983) working with NASA scientists and engineers on research of mutual interest to the University faculty member and the NASA counterpart. The editors of this document were responsible for selecting appropriately qualified faculty to address some of the many problems of current interest to NASA/MSFC. For the 1983 program, many more urgent problems exist than there were research funds to support and many more highly qualified applicants sought to become NASA/ASEE Summer Faculty than could be accommodated. As a result, the research performed by the 1983 Fellows represents the most highly qualified of University faculty applicants working on the most urgent NASA research interests. A separate document (UAH Report No. 382, September 1983) reports on the administrative aspects of the 1983 program. This document contains the technical reports on research performed by the individual 1983 participants. The NASA/ASEE program is basically a two-year program to allow indepth research by the University faculty member. In some cases, a faculty member has developed a close working relationship with a particular NASA group that has provided funding beyond the two-year limit. The reports are arranged in alphabetical order with the first-year faculty reports identified with a single asterisk and the second and more-year faculty reports identified with two asterisks.

TABLE OF CONTENTS

**I. Agarwal, Ravendra K.: "Logic Simulator Program"

**II. Ainsworth, Richard: "The Generalized Euler-Mascheroni Constants"

**III. Antar, Basil N.: "Analytical and Numerical Solution for a Solidifying Liquid Alloy Slab"

**IV. Askew, Raymond F.: "Hydrogen Ignition for Laser Propulsion"

**V. Barnes, Grover D.: "A Preliminary Survey of Plankton and Periphyton in the Turn Barge Canal and Basin Area of Kennedy Space Center, FL"

**VI. Brown, Robert A.: "Reflectance Measurements, Part II"

**VII. Brundidge, Kenneth C.: "Investigation of the Arc Cloud Complex"

*VIII. Chou, Libby W.: "Partial Analysis of Insta-Foam"

*IX. Clinton, Raymond G. Jr.: "Mechanical Property Characterization of P-100/934 Graphite-Epoxy Composite Material"

*X. Croft, Walter L.: "Preliminary Designs for Modifications to the X-Ray Source and Beam Monitor of the Marshall Space Flight Center's X-Ray Calibration Facility"

*XI. Crouse, David J.: "Synthesis of N-Substituted Silaneamines: Monomeric Precursors of Silicon Carbide-Nitride Fibers"

*XII. Day, William B.: "Linear and Nonlinear Aspects of Rotordynamics"

**XIII. Flesch, Terry R.: "Interfacing a Two-Stage Image Intensifier Tube to an Echelle Spectrograph"

*XIV. Fromhold, Albert T.: "Atomic Oxygen Effects on Materials"

**XV. Hall, William B.: "An Evaluation of Techroll Seal Flexible Joint Material"

**XVI. Hardee, Philip E.: "A Study of Accretion in Compact Sources: Disk Precession and Jet Helicity"

**XVII. Jalali, Fereydoun: "Characteristics of RF Lightning Emissions at 2 GHz and 250 MHz"

*XVIII. Kadaba, Prasad K.: "A Feasibility Study of Electromagnetic De-Spin System for Earth Orbiting Satellites"

**XIX. Laird, Christopher E.: "Studies of Neutron and Proton Nuclear Activation in Low-Earth Orbit II"

**XX. Ludwick, Larry M.: "Ultrahigh Molecular Weight Aromatic Siloxane Polymers"

TABLE OF CONTENTS
(continued)

*XXI. Mason, F. Curtis: "A Report on Superfluid Helium Flow Through Porous Plugs for Space Science Applications"

**XXII. McCord, Richard L.: "Population Control of Self-Replacing Systems; Option C"

**XXIII. McDonald, Malcolm W.: "A FMCW Radar Ranging Device for the Teleoperator Maneuvering System"

**XXIV. Pujol, Alfonso, Jr.: "The Development of a Digital Processing System for Accurate Range Determinations"

*XXV. Sias, Fred R., Jr.: "Sensor Control of Robot Arc Welding"

**XXVI. Siegrist, Kyle: "Statistical Analysis of a Debugging Model"

**XXVII. Smith, David R.: "A Numerical Investigation of the Multiple Vortex Phenomenon: Vortex Number and Structure as A Function of Swirl Ratio"

**XXVIII. Smith, James E. Jr.: "Determination of Systems Suitable for Study As Monotectic Binary Metallic Alloy Solidification Models"

*XXIX. Stensby, John: "Computer Control of a Seven Degree of Freedom Manipulator Arm"

*XXX. Teoh, William: "Orbital Maneuvering Vehicle Simulation System On-Board Processing Logic"

*XXXI. Thompson, James M.: "Laboratory Automation of a Quadrupole Mass Spectrometer"

*XXXII. Tolbert, R. Noel: "Stiffness Properties for Dynamic Modeling of Composite Graphite-Epoxy Cylindrical Orthotropic Shells"

**XXXIII. Wang, Jai-Ching: "Compositional Segregation in Unidirectionally Solidified Solid Solution Crystals"

*XXXIV. Weeks, George E.: "Finite Element Analysis of A Deployable Space Structure"

**XXXV. Williams, George, Jr.: "Evaluation of the Separability of Monodisperse Polystyrene Latex Microspheres in a Continuous Flow Electrophoresis System"

N84 16023

1983 NASA/ASEE SUMMER FACULTY RESEARCH FELLOWSHIP PROGRAM
MARSHALL SPACE FLIGHT CENTER

THE UNIVERSITY OF ALABAMA IN HUNTSVILLE

LOGIC SIMULATOR PROGRAM

Preapred by: R. K. Agarwal

Academic Rank: Assistant Professor

University and Department: Alabama A&M University
Department of Engineering Technology

NASA/MSFC:

Laboratory: Information & Electronic Systems Laboratory

Division: Electrical Division

Branch: Electrical/Electronics Parts Branch

MSFC Counterpart: Teddy Edge

Date: August 12, 1983

Contract No. NASA-NGT-01-008-021
(Univeristy of Alabama in Huntsville)

LOGIC SIMULATOR PROGRAM

Ravendra K. Agarwal
Alabama A&M University
Huntsville, AL

ABSTRACT

As a part of the Summer Research Faculty effort, this task will provide a software simulator for discrete and combinatorial electronic components. The simulator will be implemented and test cases run to determine its capability. The choice of simulator is Spice Version II, and it will be converted to run on the EB Laboratory Sigma-V CP-V operating system. The simulator will be used to determine gate and fan-out delays, logic state conditions, and signal race conditions for transistor array elements and circuit logic to be patterened in the Semi-process, Inc. (SPI) 7010 CMOS silicon gate semicustom array. The simulator will be operable from the CP-V time-sharing terminals.

LIST OF FIGURES AND TABLES

Figure		Page
1.	MOS/LSI Circuit	I-7
2.	Simulated Output Waveform	I-8

Table		Page
1.	Simulation Results	I-9

INTRODUCTION

Over the past 15 to 20 years, several investigators have made significant progress in developing computer-oriented models for the different semiconductor technologies. These models incorporate improved representations of both electrical effects and radiation effects. The results are documented in many excellent technical reports which give detailed discussion and application procedures. Nevertheless, many of these reports are not easily available to those who wish to apply the models to a specific problem. Even if the analyst has access to some of these reports, the analyst is often confronted with a rather tedious task of wading through the derivation in order to sort out the application information of his model.

SPICE II is one of many such general-purpose circuit simulation programs for nonlinear transient and linear a.c. analysis. Circuits may contain resistors, capacitors, inductors, mutual inductors, independent voltage and current sources, four types of dependent sources, transmission lines, and four most common semiconductor devices: Diodes, BJT's, JFET's and MOSFET's.

Under the SPICE II, there are three different MOSFET models available to the user. The Level 1 model is the simple Shiehman-Hodges model described by a Square-Law I-V characteristic. The MOS II or Level 2 model is an analytical one-dimensional model which incorporates most of the second-order effects of the small size devices. The Level 3 model is a semi-empirical model described by a set of parameters which are defined by curve-fitting rather than physical background. It is important for the circuit designer to know the different equations governing the behavior of the MOS's and to know the influence of the different model parameters.

OBJECTIVE

This year's Summer Research Faculty effort is to provide a software simulation of discrete and combinational electronic components. The simulator to be used is SPICE Version II. The first effort is to convert the simulator to run on the EB Laboratory Sigma-V CP-V Operating System, then to use the SPICE II model to determine various circuit time delays, logic state condition and signal race conditions. These simulations are to be patterened for the Semi-Process, Inc., (SPI) 7010 CMOS Silicon Gate Semiconductor Arrays.

BACKGROUND

The accuracy of the model depends heavily on the values of the input parameters. The current-voltage characteristics based on the equations of the model must match very closely the measured characteristics. A data acquisition software designed for a certain model provides accurate input parameters only for that particular model. When the model is changed, the parameter extraction software has to be changed as well.

A test chip should have the following features for parameter extraction:

a. A short and a long channel MOSFET

b. Diffused resistance

c. A narrow and a wide channel device

d. Polysilicon resistance

e. A thin and a field oxide capacitor

f. A rectangular and a meander form junction capacitor

SIMULATION EXAMPLE

The circuit of figure 1 represents a short path of an MOS/LSI circuit.[2] The output signal CS generated from clock (CLK) can be measured at an output pad and compared with the simulated waveform. The measured circuit chips were located on the same wafer with the test patterns from which the parameter extraction had been performed. For an accurate simulation, all the parasitics of the layout must be included: R_1 represents the series resistance of the input pad protection while R_2 and R_3 represent crossunder diffusions. Each capacitor (c) includes all the capacitive effects associated with the node. Each of the gates has been modeled as a subcircuit. A load capacitance of 100 pF has been used; the rest is attributed to the probe and parasitics. Figure 2 shows a sample simulated output waveforms.

The result has been obtained by performing the simulation with and without sidewall capacitance and with and without scattering limited drift-velocity effects. The devices which had no parameter specified had a negligible sidewall compared to the area. The results of the different simulations and the measured values are given in Table I.[2] It shows that the above two effects contribute a 15 to 20% accuracy improvement and simulation results of this circuit containing 22 MOSFET's is within 5 to 10% of the results for the actual circuit.

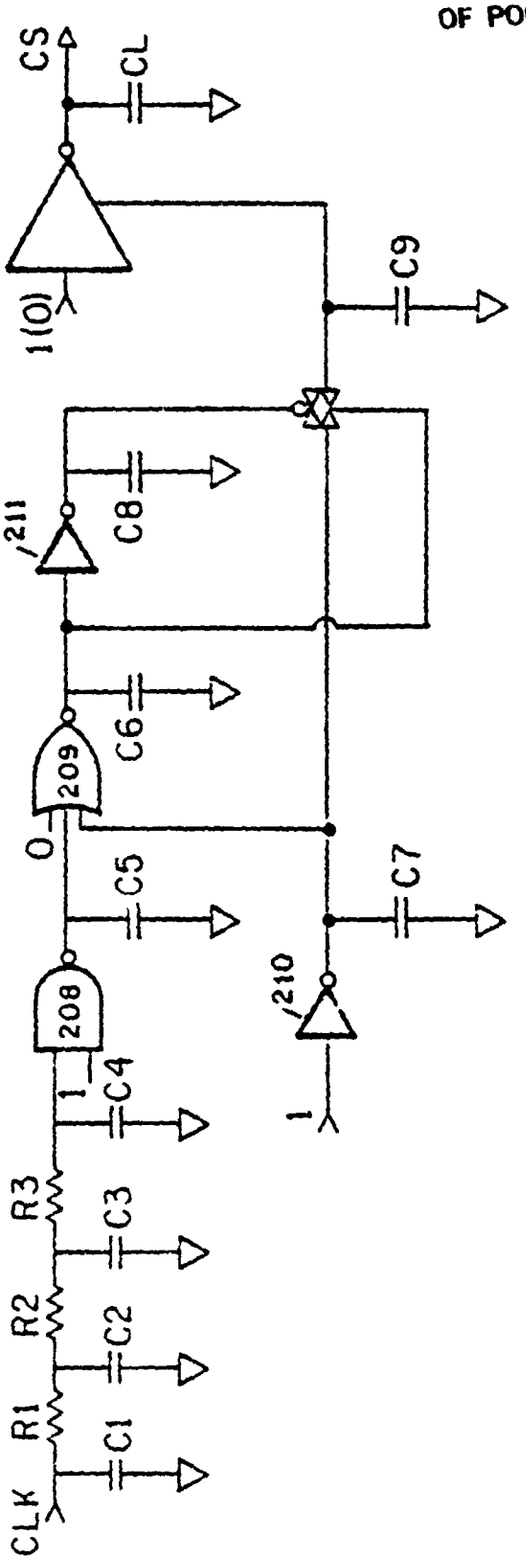

Figure 1

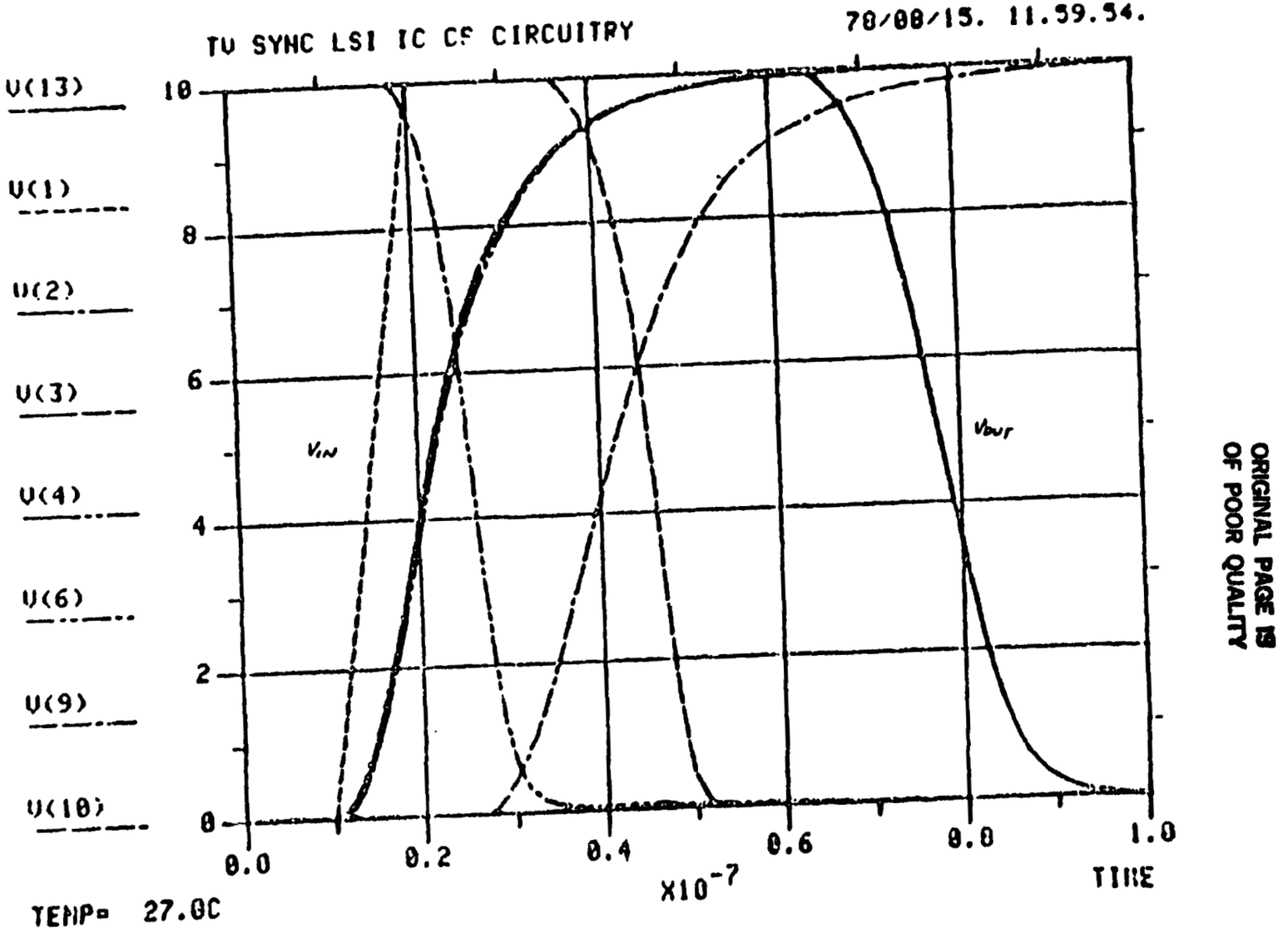

Figure 2

Table 1

PARAMETER		MEASURED	SIMULATED			
			W/O SIDEWALL		W/SIDEWALL	
			W/O V Max	W/ V Max	W/O V Max	W/ V Max
Delay	C_L = 20pF	64 - 75	49	51	60	62
T_D (N_S)	C_L = 120 pF	90 - 105	70	79	81	91
Fall Time	C_L = 20 pF	32 - 36	22	24	24	26
T_F (N_S)	C_L = 120 pF	85 - 120	90	100	94	102

CONCLUSIONS AND RECOMMENDATIONS

The SPICE Version II Simulator Program is written in FORTRAN, and the program source contains over 20,000 card images. The program came from the National Security Agency (NSA) through Mississippi State University. The program is large, and deblocking of the source code was required before the subroutines could be isolated and compiled. Also, incompatibilities between the UNIVAC 1180 FORTRAN and the Sigma-V CP-V FORTRAN IV had to be resolved. Due to this added effort and a delay in receiving the source tape, sample test runs have not been made at the time of this report. It is recommended that the included test case and a number of other sample simulation runs be made before attempting to use the program on the actual semicustom array data.

REFERENCES

1. R. Simon, D. R. Alexander, P. A. Young, and R. J. Antione, "Handbook of Modeling for Circuit Analysis Including Radiation Effects," AFWL-TR-79-83, May 1979.

2. Andrei Vladimirescu and Sally Liu, "The Simuation of MOS Integrated Circuits Using SPICE 2," Memorandum No. UCB/ERL M8017, February 1980.

3. R. S. Mullar and T. I. Kamins, "Device Electronics for Integrated Circuits," Wiley, NY, 1977.

1983

NASA/ASEE SUMMER FACULTY RESEARCH FELLOWSHIP PROGRAM

MARSHALL SPACE FLIGHT CENTER
THE UNIVERSITY OF ALABAMA

THE GENERALIZED EULER-MASCHERONI CONSTANTS

Prepared By: R. Ainsworth

Academic Rank: Professor

University and Department: University of Alabama
Department of Mathematics

NASA/MSFC:
Division:
Branch:

MSFC Counterpart: Henry Waites

Date: August 12, 1983

Contract No.: NGT 01-008-021
The University of Alabama in Hunstville

Co-Authored By: L.W. Howell, MSFC

To be submitted to American Math Society, Journal of Computation for publication.

THE GENERALIZED EULER-MASCHERONI CONSTANTS

BY

R. AINSWORTH (CO-AUTHORED BY L.W. HOWELL, MSFC)

Professor of Mathematics

University of Alabama

Tuscaloosa, AL

ABSTRACT

About $z = 1$ the function $f(z)$ has the Laurent expansion

$$\frac{1}{z-1} + \sum_{n=0}^{\infty} \frac{(-1)^n \gamma_n (z-1)^n}{n!}$$

Where

$$\gamma_n = \lim_{m \to \infty} \sum_{k=1}^{m} \frac{\ln^n k}{k} - \frac{\ln^{n+1} m}{n+1}.$$

The first 32 of these numbers are listed. Only the first four have been previously calculated.

THE GENERALIZED EULER-MASCHERONI CONSTANTS

INTRODUCTION

The generalized Euler-Mascheroni constants are defined by

$$\gamma_n = \lim_{M\to\infty} \sum_{k=1}^{M} \frac{\ln^n k}{k} - \frac{\ln^{n+1} M}{n+1} \quad , \quad n = 0, 1, 2, \ldots$$

and are the coefficients of the Laurent expansion of

$$\zeta(z) = \frac{1}{z-1} + \sum_{n=0}^{\infty} \frac{(-1)^n \gamma_n (z-1)^n}{n!} \quad .$$

They were first defined by Stieltjes in 1885, discussed by Stieltjes and Hermite [1], and have been periodically reinvented over the years [2,3,4].

The rate of convergence is painfully slow (Table 1) so one is forced to seek some method to speed up convergence, and of course the most common way is by employing the Euler-Maclaurin formula. Following a suggestion made by Edwards [5] in computing the Riemann Zeta function, the sum portion of γ_n is split into two sums so that the first (p -1) terms are directly summed and the p to M sum is approximated by the Euler-Maclaurin formula as M tends to infinity. Hence,

$$\gamma_n = \sum_{k=1}^{p-1} \frac{\ln^n k}{k} + \lim_{M\to\infty} \left\{ \int_p^M \frac{\ln^n x}{x}\,dx + 1/2 \left[\frac{\ln^n M}{M} + \frac{\ln^n p}{p} \right] + \sum_{k=1}^{j-1} \frac{B_{2k}}{(2k)!} \left[\left(\frac{\ln^n x}{x} \right)^{(2k-1)}_{x=M} - \left(\frac{\ln^n x}{x} \right)^{(2k-1)}_{x=p} \right] + \frac{B_{2j}}{(2j)!} \sum_{k=1}^{p} \left(\frac{\ln^n x}{x} \right)^{(2j)}_{x=p+k+\theta} - \left(\frac{\ln^n M}{n+1} \right) \right\} \qquad (1)$$

where $0 < \theta < 1$ and B_{2k} are the Bernoulli numbers. Letting $M \to \infty$, it follows that

$$\gamma_n = \sum_{k=1}^{p-1} \frac{\ln^n k}{k} - \frac{\ln^{n+1} p}{n+1} + \frac{1}{2}\frac{\ln^n p}{p} - \sum_{k=1}^{j-1} \frac{B_{2k}}{(2k)!}\left(\frac{\ln^{n+1} x}{x}\right)^{(2k-1)}_{x=p} + \frac{B_{2j}}{(2j)!}\sum_{k=0}^{p-1}\left(\frac{\ln^n x}{x}\right)^{(2j)}_{x=p+k+\theta} \quad . \tag{2}$$

The chief difficulty in using this formula is determining $(\ln^n x/x)^{(j)}$ in a usable form.

Lemma.

$$\frac{d^j}{dx^j}\left(\frac{\ln^n x}{x}\right) = \frac{\ln^{n-j} x}{x^{j+1}} \prod_{k=1}^{j} (y - k \ln x)$$

where, after expanding the product, put $y^k = n!/(n-k)!$.

Proof: Let

$$Q_m = \prod_{k=1}^{m} (y - k \ln x)$$

and set

$$\frac{d^m}{dx^m}\left[\frac{\ln^n x}{x}\right] = \frac{\ln^{n-m} x}{x^{m+1}} Q_m \tag{3}$$

and assume that, for some value of m,

$$D^{m+1}\left[\frac{\ln^n x}{x}\right] = D\left[\frac{\ln^{n-m} x}{x^{m+1}}\right] Q_m + \frac{\ln^{n-m} x}{x^{m+1}} Q'_m = \frac{\ln^{m-n-1} x}{x^{m+2}} \Big\{ [n-m-(m+1)\ln x]\, Q_m + x \ln x\, Q'_m \Big\} \tag{4}$$

and define

$$H_m = [n - m - (m+1)\ln x]\, Q_m + x \ln x\, Q'_m \quad .$$

Now

$$Q_m = \frac{n!}{(n-m)!} - \frac{p_1 n! \ln x}{(n-m+2)!} + \frac{p_2 n! \ln^2 x}{(n-m+1)!} + \ldots + (-1)^m p_m \ln^m x$$

$$= y_m - y^{m-1} p_1 \ln x + p_2 y^{m-2} \ln^2 x + \ldots + (-1)^m p_m \ln^m x \,. \qquad (5)$$

Since

$$(n-m)\frac{n!}{(n-m)!} = \frac{n!}{(n-m-1)!} = y^{m+1}$$

we obtain, upon substitution of (5) into (4):

$$H_m = y^{m+1} - y^m [p_1 + m + 1] \ln x + y^{m-1} [p_2 + (m+1) p_2] \ln^2 x + \ldots + (-1)^m (-1)(m+1) \ln^{m+1} x \,.$$

This is obviously

$$[y - (m+1)] Q_m = \prod_{k=1}^{m+1} (y - k \ln x) = Q_{m+1} \,.$$

Inserting this into (3) proves the theorem by induction. The last term in equation (2) is

$$\frac{B_{2j}}{(2j)!} \sum_{k=0}^{p-1} \left(\frac{\ln^n x}{x} \right)^{(2j)}_{x=p+k+\theta} \qquad (6)$$

and must now be given bounds. By the Cauchy integral formula,

$$\left[\frac{\ln^n (p+k)}{p+k} \right]^{(2j)} \leqslant \frac{(2j)!}{2\pi} \frac{2\pi R}{R^{2j+1}} \frac{\ln^n (p+k+Re^{\theta i})}{p+k+Re^{\theta i}} \leqslant \frac{(2j)!\, 2^{2j} \ln^n (k+p-2)}{p^{2j} \quad p}$$

where $R = p/2$,

$$| \ln^n (k+p+p/2\, e^{i\theta}) | \leqslant 2 \ln^n (k+2p)$$

and

$$\frac{1}{p} > \left| \frac{1}{p+k+p/2\, e^{i\theta}} \right|$$

Inserting this bound into (6) yields

$$\frac{B_{2j}(2j)!2^{2j}}{(2j)!p^{2j+1}} \sum_{k=1}^{p-1} \frac{\ln^n(2p+k)}{p} \leqslant \frac{B_{2j}2^{2j}}{p^{2j+2}} p\ln^n(3p+1) \leqslant \frac{2^{2j}\ln^n(3p+1)2\ (2j)!}{p^{2j+1}(2\pi)^{2j}(1-2^{1-2j})} \leqslant \frac{2(2j)!\ln^n(3p+1)}{(p\pi)^{2j}(1-2^{1-2j})} \tag{7}$$

COMPUTATION

The fourth term of equation (2) requires the construction of three matrices A, B, C and two vectors $\underline{u}$, $\underline{v}$. A is a (2j-3)X(2j-2) matrix whose first (L + 1) elements in the Lth row are given by the coefficients of

$$\prod_{k=1}^{L} (y - k \ln p)$$

and the remainder set equal to zero. B is a matrix of the same dimension whose Lth row is given by

$$\left(\frac{n!}{(n-L)!}, \frac{n!}{(n-L-1)!}, \ldots\right)$$

The elements are, of course, zero if L > n. C is a matrix defined by

$C = (a_{ij}b_{ij})$ for i = 1, 3, 5, 7 ..., and j = 1, 2, 3, 4...

Next define

$$\underline{u}^T = (1, \ln p, \ln^2 p, \ldots, \ln^{2j-2} p)$$

and

$$\underline{v}^T = \left(\frac{1}{2!}B_2, \frac{1}{4!}B_4, \ldots, \frac{1}{(2j-2)!}B_{2j-2}\right)$$

With these equations, (2) may be written as:

$$\gamma_n = \sum_{k=1}^{p} \frac{\ln^n k}{k} - \frac{\ln^{n+1} p}{p} + \frac{1}{2}\frac{\ln^n p}{n} - \underline{v}^T C \underline{u}$$

with an error bounded by (7). An APL computer program was written to evaluate γ_n (see Appendix).

It was observed that the minimum error in computing γ_n occurred in a neighborhood of p=j and a sensitivity study indicated that p=j=10 was an optimum choice. Table 2 contains the first 32 Euler-Mascheroni constants.

Table 3 shows that the Laurent expansion provides a very effective means of computing Riemann ζ function in a neighborhood of z = 1. However, the expansion is not a useful method for extending the list of zeros of $\zeta(z)$ known today.

The behavior of the Euler-Mascheroni constants themselves have been the subject of investigation Briggs [6] showed that infinitely many γ_n are negative and infinitely many are positive and Mitrovic extended this result by showing that each of these inequalities $\gamma_n < 0$, $\gamma_{2n-1} < 0$, $\gamma_n > 0$, $\gamma_{2n-1} > 0$ holds for infinitely many n [7].

Good [8] recently conjectured that the lengths of the runs of the same sign of $\Delta\gamma_n$ never decrease.

TABLE 1. γ_n VERSUS NUMBER OF TERMS COMPUTED (M)

	$M = 10^3$	$M = 10^4$	$M = 10^5$	$M = 10^6$
n = 0	0.57771558156810	0.57726566406712	0.57722066488224	0.57721616479093
n = 1	-0.06936246015836	-0.07235533352434	-0.07275828112056	-0.07280893950511
n = 2	0.01416535317172	-0.00544890007751	-0.0090276294304[illegible]	-0.00959495724544
n = 5	7.86463444728723	3.31473675482265	1.01213466958143	0.25241822958923

TABLE 2. GENERALIZED EULER-MASCHERONI CONSTANTS

n	γ_n
0	0.57721566490153
1	-0.07281584548368
2	-0.00969036319287
3	0.00205383442030
4	0.00232537006546
5	0.00079332381728
6	-0.0002387693455
7	-0.0005272895671
8	-0.0003521233539
9	-0.0000343947747
10	0.0C0205332814
11	0.000270184439
12	0.00016727291
13	-0.00002746381
14	-0.00020920927
15	-0.00028346867
16	-0.0001996969
17	0.0000262769
18	0.0003073682
19	0.000503605
20	0.000466342
21	0.0001044
22	-0.0005416
23	-0.0012439
24	-0.0015885
25	-0.0010746
26	0.000657
27	0.003477
28	0.006399
29	0.00737
30	0.003[illegible]
31	-0.0075[illegible]

TABLE 3.

x	iy	Reζ(z)	Imζ(z)
0.5	0	-1.46035450881	0.00000000000
0.01	0	-0.50929071404	0.00000000000
2	0	1.64493406685	0.00000000000
3	0	1.20205690316	0.00000000000
4	0	1.08232323371	0.00000000000
5	0	1.03692775514	0.00000000000
6	0	1.01734306198	0.00000000000
0.5	1	0.14393642708	-0.72209974353
0.5	3	0.53273667097	-0.07889651343
0.5	5	0.70181237117	0.23103800839

REFERENCES

1. Mitrović, Dragiša, Math. Reviews 29 (1965) No. 2232.

2. Kluyver, J. C.: On Certain Series of Mr. Hardy. Quart. J. of Pure and Applied Math., Vol. 50, 1927, pp. 185-192.

3. Briggs, W. E., and Chowla, S.: The Power Series Coefficients of $\zeta(s)$. Amer. Math. Monthly, Vol. 62, 1955, pp. 323-325.

4. Wilton, J. R.: A note on the Coefficients in the Expansion of $\zeta(s,x)$ in Powers of $s - 1$. Quart. J. of Pure and Applied Math., Vol. 50, 1927, pp. 329-332.

5. Edwards, H. M.: Riemann's Zeta Function. Academic Press, New York, 1974, pp. 114-118.

6. Briggs, W. E.: Some Constants Associated with the Riemann Zeta Function. Michigan Math. J., Vol. 3, 1955-56, pp. 117-121.

7. Mitrović, Dragiša: The Signs of Some Constants Associated with the Riemann Zeta Function. Mich. Math J., Vol. 9, 1962, pp. 395-397.

8. Good, I. J.: Dept. of Statistics, Virginia Polytechnic Institute and State Univ., Blacksburg, VA, Personal Communication, 1983.

APPENDIX

ORIGINAL PAGE IS
OF POOR QUALITY

```
      ∇EULER[⎕]∇
    ∇ R←NK EULER M;L;LM;Y;T;K;N
[1]   LM←(L←⊃⍴M)*¯1+⍳2×K←NK[2];N←NK[1]
[2]   Y←(+/((⊃⍳N)*N)÷⍳M)-((L*N+1)÷N+1)+0.5×(L*N)÷M
[3]   T←(÷M*1+⍳¯1+2×K)×(L*N-⍳¯1+2×K)×((GENN 2×K)×(2×K)GENN N)+.×LM
[4]   R←N,Y-+\(2÷BERNOULLI K+2)×T[K+¯1+2×⍳K]÷!2×⍳K
[5]   ⍝  NK[1] IS THE N'TH EULER CONSTANT
[6]   ⍝  NK[2] IS THE NUMBER OF TERMS IN THE BERNOULLI SUM
[7]   ⍝  M IS THE NUMBER OF TERMS IN THE FINITE SUM
    ∇

      ∇GENN[⎕]∇
    ∇ R←GENN K;V;I;T
[1]   R←((K-1),K)⍴0;I←2
[2]   V←(2,K)⍴(K⍴1),-⍳K
[3]   R[1;]←V[;1],(K-2)⍴0
[4]   L:T←V[;I]∘.×(R[I-1;]≠0)/R[I-1;]
[5]   T←(T[1;],0),[0.5]0,T[2;]
[6]   R[I;]←(+/T),(K-I+1)⍴0
[7]   →(K>I←I+1)/L
[8]   ⍝ GENERATES THE COEF. OF THE DERIVATIVE OF (LOG X)*N/X
    ∇

      ∇GENMV[⎕]∇
    ∇ R←K GENMV N;I
[1]   M←((K-1),K)⍴0;I←2
[2]   M[1;]←(N,1),(K-2)⍴0
[3]   L:M[I;]←(I ×R N),¯1+M[I-1;]
[4]   →(K>I←I+1)/L
[5]   ⍝  GENERATES MATRIX OF      N×(N-1)×...×(N-K+1)
[6]   ⍝  USED WITH FUNCTION EULER
    ∇
```

```
      ∇BERNOULLI[⎕]∇
    ∇ B←BERNOULLI N
[1]   →(N>22)/E
[2]   B←22⍴0
[3]   B[1]←1÷1
[4]   B[2]←¯1÷2
[5]   B[3]←1÷6
[6]   B[4]←¯1÷30
[7]   B[5]←1÷42
[8]   B[6]←¯1÷30
[9]   B[7]←5÷66
[10]  B[8]←¯691÷2730
[11]  B[9]←7÷6
[12]  B[10]←¯3617÷510
[13]  B[11]←43867÷798
[14]  B[12]←¯174611÷330
[15]  B[13]←854513÷138
[16]  B[14]←¯236364091÷2730
[17]  B[15]←8553103÷6
[18]  B[16]←¯2.374946E10÷870
[19]  B[17]←8.615841E12÷14322
[20]  B[18]←¯7.709321E12÷510
[21]  B[19]←2.577688E12÷6
[22]  B[20]←¯2.631527E19÷1919190
[23]  B[21]←2.929994E15÷6
[24]  B[22]←¯1.929658E16
[25]  →0;B←N↑B
[26]  L:'N MUST BE LESS THAN OR EQUAL TO 22'
[27]  ⍎  FIRST 22 BERNOULLI NUMBERS
    ∇
```

N84 16025

1983

NASA/ASEE SUMMER FACULTY RESEARCH FELLOWSHIP PROGRAM

MARSHALL SPACE FLIGHT CENTER
THE UNIVERSITY OF ALABAMA IN HUNTSVILLE

ANALYTICAL AND NUMERICAL SOLUTION FOR A SOLIDIFYING LIQUID ALLOY SLAB

Prepared By:	Basil N. Antar, Ph.D.
Academic Rank:	Associate Professor
University and Department:	University of Tennessee Space Institute Dept. of Engineering Science and Mechanics
NASA/MSFC: Division: Branch:	 Atmospheric Science Fluid Mechanics
MSFC Counterpart:	Charles Schafer
Date:	August 5, 1983
Contract No.:	NGT 01-008-021 The University of Alabama in Huntsville

Abstract

Analytical and Numerical Solution for a Solidifying

Liquid Alloy Slab

by

Basil N. Antar
Associate Professor
University of Tennessee Space Institute

Numerical and analytical solutions are presented for the temperature and concentration distributions during the solidification of a binary liquid alloy slab. The slab is taken to be of a finite depth but infinite in the horizontal direction. The solidification process is started by withdrawing a fixed amount of heat from the lower surface of the slab. The upper surface of the slab is subjected to both radiation and convective conditions. The solution gives the concentration and temperature profiles and the interface position as a function of time. Due to the smallness of the mass diffusion coefficient in the solid, the numerical solution method breaks down whenever the ratio of the diffusivities in the solid and the liquid falls below a certain value. An analytical method is developed which gives accurate solution for any value of the diffusivity ratio.

I. Introduction

The problem of solidification of materials, due to its analytical complexity and its physical relevance, have been, and still is receiving considerable attention. An essential feature of the solidification problem is the presence of a moving boundary between the two phases of the material and also the release of latent heat at that interface. The position of the interface as a function of time depends both on the two phases adjacent to it and the imposed boundary conditions and must be determined as part of the solution to the problem itself. This class of problems is generally known as the Stefan problem about which there is a great deal in the literature (e.g. [1] - [4]).

The simplest analytical problem in this area is the one dimensional solidification by conduction in a semi-infinite region. When the material is at a constant initial temperature and subject to another temperature at the surface, the temperature of both phases may be expressed by functions of a similarity variable. The position of the interface is found to be proportional to the square root of time. These are the classical solution which may be found in Carslaw and Yeager [1].- Recently Tao. [5] and [6], presented analytical exact solutions of the Stefan problem in a semi-infinite region with arbitrarily prescribed initial and boundary conditions. In these solutions the temperature was expressed in an infinite series of functions and polynomials in the error integral family and the time t, while the interface position was represented by a power series in $t^{\frac{1}{2}}$

When the freezing or melting material is an alloy, even a simple binary alloy, the Stefan problem is further complicated due to several reasons. First for an alloy the solidification temperature is a strong function of the concentration. The specific functional form of this temperature is given by the solidus curve in the appropriate phase diagram. This complication leads to the inclusion of an additional unknown in the mathematical formulation of the problem. Another complication arises as a consequence of the segregation process in the neighborhood of the interface which usually leads to strong concentration gradients. These gradients could set up a convective motion in the liquid which has to be accounted for in any realistic solidification process.

In addition to its relevance to obvious industrial processes, the problem of alloy solidification has recently found another important application. A great deal of interest has been generated recently in the possibility of processing materials in the reduced gravity environment of the forthcoming mission of Spacelab. The range of possibilities extend from producing large crystals of uniform properties to manufacturing materials with unique properties. Most of those processes involve the solidification

of alloys from the liquid state. Due to the nature of these experiments there exists few data on the solidifications process in these environments. Thus, a greater reliance is being made on accurate analyses to aide in the preparation for the solidification in the low gravity environments.

As outlined above the mathematical description of the solidification of a binary alloy is more elaborate and complex than the classical Stefan problem. A known exact solution of the problem exists, [2]. This solution is for a binary alloy in a semi-infinite region with constant initial and boundary conditions. Recently Tao, [7] and [8], had tackled the solidification problems of a binary alloy in a semi-infinite region with arbitrarily prescribed initial and boundary conditions. He presented exact analytical solution for the constant temperature boundary conditions [7] and the prescribed heat flux problem [8]. Both of these solutions are not necessarily restricted to a dilute alloy.

When the region of interest is of finite dimensions, say a slab, the similarity analysis cannot be used in general and there does not exist a known exact solution for this problem. Boly [9] presented a solution for the coupled Stefan problem for a slab of a binary mixture which is valid for a short time only. The problem of a slab is characterised by a solution which is strongly time dependent and thus is best resolved through numerical approximation techniques. In this paper, we present the solution to the solidification of a binary mixture fluid slab. We present two methods of solution one is purely numerical and another which is an analytical-numerical solutions. We see these solutions as an extension of the numerical technique of Meyer [10].

2. Statement of the Problem

We consider a slab of a binary liquid alloy of thickness, d, which is infinite in the horizontal direction. The slab is initially maintained at a uniform liquid temperature T_{Lo} and a uniform liquid concentration of solute C_{Lo}. The field equations governing both the temperature and solute concentrations distributions are given by:

$$\frac{\partial T_\ell}{\partial t} - (\frac{\rho_s}{\rho_\ell} - 1)\frac{dS}{dt}\frac{\partial T_\ell}{\partial z} = \kappa_\ell \frac{\partial^2 T_\ell}{\partial z^2} \qquad (1-a)$$

$$\frac{\partial C_\ell}{\partial t} - (\frac{\rho_s}{\rho_\ell} - 1)\frac{dS}{dt}\frac{\partial C_\ell}{\partial z} = D_\ell \frac{\partial^2 C_\ell}{\partial z^2} \qquad (1-b)$$

$$\frac{\partial T_s}{\partial t} = \kappa_s \frac{\partial^2 T_s}{\partial z^2} \qquad (1-c)$$

$$\frac{\partial C_s}{\partial t} = D_s \frac{\partial^2 C_s}{\partial z^2} \qquad (1-d)$$

where C and T denote solute concentration and temperature respectively. S(t) is the interface position and ρ, κ and D are the density, thermal diffusivity and solute diffusivity repectively. Note, that in the system (1) we have allowed for the density difference between the solid and the liquid phases. The subscripts s and ℓ denote the solid and the liquid respectively. These equations are to be solved subject to both interface and boundary conditions. At the interface the conservation of mass and energy equations imply that

$$k_s \frac{\partial T_\ell}{\partial z} - k_\ell \frac{\partial T_\ell}{\partial_z} = \rho_s \ell \frac{dS}{dt} \qquad (2-a)$$

$$D_s \frac{\partial C_s}{\partial z} - D_\ell \frac{\partial C_\ell}{\partial z} = -(1-\tilde{k}) C_\ell \frac{dS}{dt} \qquad (2-b)$$

$$T_\ell = T_s = T_i - mC_\ell \qquad (2-c)$$

$$C_s = \tilde{k} C_\ell \qquad (2-d)$$

where k, $\tilde{k}$, ℓ and m are the thermal conductivity, the partition coefficient, the latent heat and the gradient of the solidus line in the phase diagram respectively. Note that condition (2-c) implies that the freezing temperature of the alloy is a linear function of concentration which is a gross simplifications of the solidus-liquidus curves in the phase diagram. The method of solution employed here, however, does not depend on the equations of the solidus liquids curves and a more complicated equation may be used. However, there is no loss of generality in using the simple linear relationship described in $(2-c)$. The boundary conditions are the following

$$k \frac{\partial T}{\partial z} = h(T - T_1), \qquad (3-a)$$

$$\frac{\partial C}{\partial z} = 0, \qquad (3-b)$$

at $z = 0$, and

$$-k_\ell \frac{\partial T_\ell}{\partial t} = h_2(T - T_2) \qquad (4-a)$$

$$\frac{\partial C}{\partial z} = 0 \qquad (4-b)$$

at $z = d - (\frac{\rho_s}{\rho_\ell} - 1)S$

As for the initial conditions, as indicated earlier, the liquid slab will be taken at a homogeneous initial temperature and concentration. Then conditions $(3a)$ and $(4a)$ will be applied until the

temperature at the lower surface, $z = 0$, reaches the solidification temperature at the initial concentration. After which time equations (1) and (2) will be applicable. This initial condition will be discussed further in more detail in the next section.

Before discussing the method of solution it is best to nondimensionalize the equations and the boundary conditions. The governing equations and boundary conditions will take the following non-dimensional form:

$$\frac{\partial \theta_\ell}{\partial \tau} - (R-1)\frac{dS}{d\tau}\frac{\partial \theta_\ell}{\partial z} = \frac{\partial^2 \theta_\ell}{\partial z^2} \qquad (4-a)$$

$$\frac{\partial C_\ell}{\partial \tau} - (R-1)\frac{dS}{d\tau}\frac{\partial C_\ell}{\partial z} = P_\ell \frac{\partial^2 C_\ell}{\partial z^2} \qquad (4-b)$$

$$\frac{\partial \theta_s}{\partial \tau} = \kappa \frac{\partial^2 \theta_s}{\partial z^2} \qquad (4-d)$$

$$\frac{\partial C_s}{\partial \tau} = P_s \kappa \frac{\partial^2 C_s}{\partial z^2} \qquad (4-d)$$

$$K\frac{\partial \theta_s}{\partial z} - \frac{\partial \theta_s}{\partial z} = RL\frac{dS}{d\tau} \qquad (5-a)$$

$$RD\frac{\partial C_s}{\partial z} - \frac{\partial C_\ell}{\partial z} = \frac{(1-\tilde{k})}{P_\ell}(C_\ell - 1)\frac{dS}{d\tau} \qquad (5-b)$$

$$C_s = \tilde{k} C_\ell \qquad (5-c)$$

$$\theta_m = \theta_i - MC_\ell = \theta_\ell = \theta_s \qquad (5-d)$$

$$\frac{\partial \theta_s}{\partial z} = \frac{B_1}{K}(\theta_s - 1) \qquad (6-a)$$

and $z = 0$, and

$$\frac{\partial C_\ell}{\partial z} = 0 \qquad (6-b)$$

$$\frac{\partial \theta_\ell}{\partial t} = -B_2(\theta_\ell + \Psi) \qquad (6-c)$$

$$\frac{\partial C_\ell}{\partial z} = 0 \qquad (6-d)$$

at $z = 1-(R-1)\,S$. Where we have used in the above $(T - T_o)$, C_o, d_o, do^2/κ_s, for the temperature, concentration, length and the time scales respectively.

The rest of the nondimensional numbers are defined by:

$$R = \rho_s/\rho_\ell$$

$$\kappa = \kappa_s/\kappa_\ell$$

$$P_\ell = D_\ell/\kappa_\ell$$

$$P_g = D_g/\kappa_g$$

$$k = k_g/k_\ell$$

$$L = \frac{\ell}{C_{p\ell}(T_1 - T_0)}$$

$$D = D_g/D_\ell = \frac{P_g}{p_\ell}\kappa$$

$$B_i = h_i d_o/k_\ell$$

$$M = -\frac{\partial\theta_\ell}{\partial C_\ell}$$

3. The Solution Technique

In this section we will outline the method of solution to the one-dimensional coupled Stefan problem described by equations (4) — (6). The basic approach is a modification of the method of Meyer [10] to the binary system under consideration. Briefly, this technique first discretizes the time operator through an implicit finite difference approximation. This discretization will then yield a set of ordinary differential equations at any time level n, which forms a boundary value problem in the space variable. Since there are interface conditions which need to be satisfied at the location of the interface, which itself is an unknown of the problem, Meyer used the invariant imbedding technique to transform the bondary values into appropriate initial value problems. In the discussion below we will illustrate how Meyer's technique can be extended to solve for both the temperature and the concentration fields.

Let $N>0$, be an integer and define a time step $\Delta\tau$. If a_i^n, etc. denotes $a_i(n\Delta\tau, x)$ etc., for $n = 0, \ldots, N$, then an implicit one level approximation of the equations given by (4) yield:

$$\frac{d^2\theta_\ell^n}{dz^2} + (R-1)\frac{(S^n - S^{n-1})}{\Delta\tau}\frac{d\theta_\ell^n}{dz} - \frac{1}{\Delta\tau}\theta_\ell^n = -\frac{\theta_\ell^{n-1}}{\Delta\tau} \qquad (7-a)$$

$$\frac{d^2C_\ell^n}{dz^2} + (R-1)\frac{(S^n - S^{n-1})}{P_\ell\Delta\tau}\frac{dC_\ell^n}{dz} - \frac{1}{P_\ell\Delta\tau} = -\frac{1}{P_\ell\Delta\tau}C_\ell^{n-1} \qquad (7-b)$$

$$\frac{d^2\theta_g^n}{dz^2} - \frac{1}{\kappa\Delta\tau}\theta_g^n = -\frac{1}{\kappa\Delta\tau}\theta_S^{n-1} \qquad (7-c)$$

$$\frac{d^2C_s^n}{dz^2} - \frac{C_s^{n-1}}{\Delta P P_s \kappa} = -\frac{1}{P_s \Delta\tau \kappa} C_s^{n-1} \qquad (7-d)$$

Similarly the interface conditions after discretization will become:

$$K\frac{d\theta_s^n}{dz} - \frac{d\theta_\ell^n}{dz} - \frac{RL}{\Delta\tau}(S^n - S^{n-1}) = 0 \qquad (8-a)$$

$$RD\frac{dC_s^n}{dz} - \frac{dC_\ell^n}{dz} + \frac{(1-\tilde{k})}{P_\ell \Delta\tau}(C_\ell^n - 1)(S^n - S_{n-1}) = 0 \qquad (8-b)$$

$$C_s^n = \tilde{k} C_\ell^n \qquad (8-c)$$

$$\theta_\ell^n(S^n) = \theta_s^n = \theta_* - MC_\ell^n(S^n) \qquad (8-d)$$

While the boundary conditions may be written as:

$$\frac{d\theta_s^n}{dz} - B_1\theta_s^n = 0 \qquad (9-a)$$

$$\frac{dC_s^n}{dz} = 0 \qquad (9-b)$$

$$\frac{d\theta_\ell^n}{dz} + B_2(\theta_\ell^n + \Psi) = 0 \qquad (9-c)$$

$$\frac{dC_\ell^n}{dz} = 0 \qquad (9-d)$$

First it is convenient to split the second order operators in (7) into first order differential equations in the folloiwng manner:

$$\frac{d\theta_\ell^n}{dz} = T_\ell^n$$

$$\frac{dT_\ell^n}{dz} + \frac{(R-1)}{\Delta\tau}(S^n - S^{n-1})T_\ell^n - \frac{1}{\Delta\tau}\theta_\ell^n = -\frac{1}{\Delta\tau}\theta_\ell^{n-1}$$

$$\frac{dC_\ell^n}{dz} = G_\ell^n$$

$$\frac{dG_\ell^n}{dz} + \frac{(R-1)}{P_\ell\Delta\tau}(S^n - S^{n-1})G_\ell^n - \frac{1}{P_\ell\Delta\tau}C_\ell^n = \frac{1}{P_\ell\Delta\tau}C_\ell^{n-1}$$

$$\frac{d\theta_s^n}{dz} = T_s^n$$

$$\frac{dT_s^n}{dz} - \frac{1}{\kappa\Delta\tau}\theta_s^n = -\frac{1}{\kappa\Delta\tau}\theta_s^{n-1}$$

$$\frac{dC_s^n}{dz} = G_s^n$$

$$\frac{dG_s^n}{dz} - \frac{1}{\kappa P_s\Delta\tau}G_s^n = -\frac{1}{\kappa P_s\Delta\tau}C_s^{n-1}$$

Now since the external boundary conditions (9) are given in a derviative form (Neumann conditions), following Meyer, [10] we choose for the solution of T_s^n, T_ℓ^n, G_s^n, G_ℓ^n the functional forms given below:

$$T_s^n(z) = Y_s^n(z)\beta_s^n + X_s^n(z)$$

$$T_\ell^n(z) = Y_\ell^n(z)\beta_\ell^n + X_\ell^n(z)$$

$$G_\ell^n(z) = U_\ell^n(z)\gamma_\ell^n + V_\ell^n(z)$$

$$G_s^n(z) = U_s^n(z)\gamma_s^n + V_s^n(z)$$

where $Y_{s\ell}$, $U_{s,\ell}$, $X_{s,\ell}$ and $V_{s,\ell}$ are themselves solutions to suitable (respective initial value problems which are detailed in the Appendix.

Due to the fact that the interface conditions are written in terms of spatial derivative of both the temperature and concentration we implement the following solution algorithm. We initially start with suitable guesses for both the interface position S^n and the interface concentration C_ℓ^n (S^n). Then the initial value problems for $Y_{s,\ell}^n$, $X_{s,\ell}^n$, $U_{s,\ell}^n$ and $V_{s,\ell}^n$ are integrated to determine $T_{s,\ell}^n$ and $G_{s,\ell}^n$ from (14). These values for the temperature and concentration gradients are then substituted into the interface conditions (8). Since the original guesses on S^n and C_ℓ^n (S^n) are not exact, conditions (8) will lead to an error, which may be used to obtain a better guess on S^n and C_ℓ^n (S^n). This process is repeated several times untill the error in (8) falls below a certain tolerance value. At this point the process is stopped and the converged values of the temperature and concentration gradients and the values for S^n and C_ℓ^n (S^n) are used to calculate the concentration and temperature profiles, at the time step, by solving the following initial value problems:

$$\frac{d\theta_{\ell,s}^n}{dz} = Y_{\ell,s}^n\theta_{\ell,s}^n + X_{\ell,s}^n \qquad (15-a)$$

$$\frac{dC_{\ell,s}^n}{dz} = U_{\ell,s}^n C_{\ell,s}^n + V_{\ell,s}^n \qquad (15-b)$$

with the following initial conditions applied at the interface:

$$\theta_s^n(S^n) = \theta_\ell^n(S^n) = \theta_i - MC_\ell^n(S^n) \qquad (15-c)$$

$$C_\ell^n(S^n) = kC_\ell^n(S^n) \qquad (15-d)$$

To continue the solution process to the next time step, new initial guesses for S^{n+1} and C_ℓ^{n+1} (S^{n+1}) are chosen and the process described above is repeated. This process is repeated several times untill the liquid slab is solidified completely.

3A - Numerical Solution

The solution algorithm described above can be implemented in a straight forward manner through numerical approximation. Thus, for the initial value problems described in the Appendix a fixed step Runge - Kutta - Fehlberg integrator was used. Approximately 50 equal steps were used throughout the z-range and whenever necessary, a linear interpolations scheme was used to determine the variable values within each integration step. To achieve convergence on the interface position, S^n, and concentration, $C_\ell^n(S^n)$, a Neton-Raphson integration process was used. It was found that if the values of the converged previous time step were used as the initial guess convergence was achieved within three to four iterations. The final temperature and concentrations profiles were obtained by integrating the initial value problem (15) again using a Runge - Kutta - Fehlberg integrator.

3B - Analytical Solution

The above described numerical solution algorithm was found to work adequately as long as P_s, was above 10^{-5}. However when the values P_s dropped below 10^{-5} the numerical integration process failed. The fact may be easily understood upon inspecting equation (7-d). This equation is a second order linear differential equation which is inhomogeneous. The homogeneous solution to this equation comprise of two linearly independent functions of the form $\exp(-(P_s\Delta\tau\kappa)^{\frac{1}{2}}$ and $\exp(P_s\Delta\tau\kappa)^{\frac{1}{2}}$. However when z is of the order 1, the growing part of the solution fa. dominates the decaying part as long as P_s is very small. This problem is usually encountered with stiff linear differential equations.

In order to overcome the difficulty discussed above, the solution to the initial value problems given in the Appendix were produced analytically in a closed form. These solutions are given in the Appendix.

Appendix

In here we will derive both the equations which are needed for the descriptions of the temperature and concentrations gradients and their solutions. The various functions that make up the gradients are $Y_{s,\ell}$ $X_{s,\ell}$, $U_{s,\ell}$ and $V_{s,\ell}$ where we have dropped the superscript n for convenience here. These functions are solutions to the following initial value problems.

$$\frac{dY_\ell}{dz} = \frac{\cdot}{\Delta\tau} - (R-1)\left(\frac{S^n - S^{n-1}}{\Delta\tau}\right)Y_\ell - Y_\ell^2$$

$$Y_\ell(1-(R-1)S^n) = -B_2 \qquad (A-1)$$

$$\frac{dX_\ell}{dz} = -\left[(R-1)\left(\frac{S^n - S^{n-1}}{\Delta\tau}\right) + Y_\ell\right]X_\ell - \frac{\theta_\ell^{n-1}}{\Delta\tau}$$

$$X_1(1-(R-1)S^n) = -B_2\Psi \qquad (A-2)$$

$$\frac{dU_\ell}{dz} = -\frac{1}{P_\ell\Delta\tau} - (R-1)\left(\frac{S^n - S^{n-1}}{P_\ell\Delta\tau}\right)U_\ell - U_\ell^2$$

$$U_\ell(1-(R-1)S^n) = 0 \qquad (A-3)$$

$$\frac{dV_\ell}{dz} = -\left[(R-1)\left(\frac{S^n - S^{n-1}}{P_\ell\Delta\tau} + U_\ell\right]V_\ell - \frac{C_\ell^{n-1}}{P_\ell\Delta\tau}\right.$$

$$V_\ell(1-(R-1)S^n) = 0 \qquad (A-4)$$

$$\frac{dY_s}{dz} = \frac{1}{\kappa\Delta\tau} - Y_s^2$$

$$Y_s(0) = B_1/K \qquad (A-5)$$

$$\frac{dX_s}{dz} = -Y_sX_s - \frac{\theta_s^{n-1}}{\kappa\Delta\tau}$$

$$X_s(0) = -B_1/K \qquad (A-6)$$

$$\frac{dU_s}{dz} = \frac{1}{\kappa P_s\Delta\tau} - U_s^2$$

$$U_s(0) = 0 \qquad (A-7)$$

$$\frac{dV_s}{dz} = -U_sV_s - \frac{C_s^{n-1}}{\kappa P_s\Delta\tau}$$

$$V_s(0) = 0 \qquad (A-8)$$

Equations (A-1) - (A-8) were initially solved numerically using a Runge-Kutta initial value integrator. However, some difficulties were encountered whenever the value of P_s fell below say, $P_s = 10^{-4}$. It is possible, however, tc integrate these equations in an analytical closed form. Using

the variation of parameters technique, the solutions to these equations are the following:

$$Y_\ell = (r_1 exp(r_1 z) + C_1 r_2 exp(r_2 z))(exp(r_1 z) + C_1 exp(r_2 z))^{-1}$$

$$U_\ell = (r_3 exp(r_3 z) + C_3 r_4 exp(r_4 z))(exp(r_3 z) + C_3 exp(r_4 z))^{-1}$$

where

$$2r_{1,2} = -FR \pm (FR^2 + 4/\Delta\tau)^{\frac{1}{2}}$$

$$2Pr_{3,4} = -FR \pm (FR^2 + 4P_\ell/\Delta\tau)^{\frac{1}{2}}$$

$$C_1 = -(r_1 + B_2)(r_2 + B_2)^{-1} exp[(r_1 - r_2)z_f]$$

$$C_3 = -r_3 exp[(r_3 - r_4)z_f]/r_4$$

$$FR = (R-1)(\frac{S^n - S^{n-1}}{\Delta\tau})$$

$$z_f = 1 - (R-1)S^n$$

$$X_\ell = exp[\int_z^{z_f} (FR + Y_\ell)dz](C_2 + \int_z^{z_f} \frac{\theta_\ell^{n-1}}{\Delta\tau} exp[-\int_{zl}^{z_f} (FR + Y_\ell)dz]dzl)$$

$$V_\ell = exp[\int_z^{z_f} (\frac{FR}{P_\ell} + U_\ell)dz] \int_z^{z_f} \frac{C_\ell^{n-1}}{P_\ell \Delta\tau} exp[-\int_Z^{Z_F} (\frac{FR}{P_\ell} + U_\ell)dz]dzl$$

$$C_2 = -B_2\Phi$$

$$Y_s = \frac{1}{\lambda}[exp(z/\lambda) - C_5 exp(z/\lambda)][exp(z/\lambda) + C_5 exp(-z/\lambda)]^{-1}$$

$$\lambda = (\kappa\Delta\tau)^{\frac{1}{2}}$$

$$X_s = exp[-\int_0^z Y_s dz](C_6 - \int \frac{\theta_s^{n-1}}{\Delta\tau} exp[\int_0^{zl} Y_s dz]dzl)$$

$$C_5 = (\lambda^{-1} - B_1/K)(\lambda^{-1} + B_1/K)^{-1}$$

$$C_6 = -B_1/\kappa$$

$$U_s = \frac{1}{\varsigma} tanh(z/\varsigma)$$

$$V_s = -\frac{1}{cosh(z/\varsigma)} \int_0^z \frac{C_s^{n-1}}{\varsigma^2} cosh(z/\varsigma)dz$$

$$\varsigma = \lambda P_s^{\frac{1}{2}}$$

References

1. Carslaw, H. S. and Jaeger, J. C., Conduction of Heat in Solids, Clarendon Press, Oxford, 1959.

2. Rubenstein, L. I., The Stefan Problem, Trans. Math. Monographs, 27, Am. Math. Soc., 1971.

3. Ockendon, J. R. and Hodgkins, W. R., Moving Boundary Problems in Heat Flow and Diffusion, Oxford University Press, 1975.

4. Wilson, D. G., Solomon, A. D. and Bogs, P. T., Moving Boundary Problems, Academic Press, New York, 1978.

5. Tao, L. N., The Stefan Problem with Arbritary Initial and Boundary Conditions, Quart Appl. Math, 36, 1978.

6. Tao, L. N., The Analyticity of Solutions of the Stefan Problem, Arch. Rat. Mech. Anal., 72, 1980.

7. Tao, L. N., On Solidification of a Binary Alloy, Q. J. App. Math. Mech., 53, 1980.

8. Tao, L. N., Solidification of a Binary Mixture with Arbitrary Heat Flux and Initial Conditions, Arch. Rat. Mech. Anal. 76, 1981.

9. Boley, B. A., Time Dependent Solidification of Binary Mixtures, Int. J. Heat Mass Transfer, 21, 1978.

10. Meyer, G. H., A Numerical Method for Two-Phase Stefan Problems, S.I.A.M. J. Numer. Anal., 8, 1971.

1983

NASA/ASEE SUMMER FACULTY RESEARCH
FELLOWSHIP PROGRAM

MARSHALL SPACE FLIGHT CENTER
THE UNIVERSITY OF ALABAMA IN HUNTSVILLE

HYDROGEN IGNITION FOR LASER PROPULSION

Prepared by:	Raymond F. Askew
Academic Rank:	Professor
University and Department:	Auburn University Physics Department
NASA/MSFC: Laboratory: Division: Branch:	 Structures & Propulsion Propulsion Auxiliary Propulsion
MSFC Counterpart:	T. Dwayne McCay
Date:	September 2, 1983
Contract No.:	NGT 01-008-021 The University of Alabama in Huntsville

HYDROGEN IGNITION FOR LASER PROPULSION

by

Raymond F. Askew
Professor of Physics
Auburn University
Auburn, Alabama

ABSTRACT

Experimental studies of the breakdown of hydrogen by pulsed CO_2 laser radiation, first begun in the summer of 1982, have been concluded. These studies, intended to determine if reliable ignition of hydrogen could be achieved in the pressure range of 0.5 to 3.0 atmospheres, were carried out using a nominal 100 nanosecond, 6 joule CO_2 TEA laser pulse. Streak and framing photography, together with spectroscopic techniques and energy measuring devices, were used to determine spatial and temporal behavior of the plasma size, shape, velocity, temperature, electron density and absorption. Reliable ignition has been achieved with reproducible plasma behavior.

ACKNOWLEDGEMENTS

The author wishes to express his appreciation to the National Aeronautics and Space Administration for support received through the Research Fellows program. Technical assistance and cooperation from support groups, particularly the Test Laboratory, were most helpful. To my counterpart, Dr. Dwayne McCay, my appreciation for the opportunity to continue to interact and develop my own understanding of the research area. To David VanZandt, my thanks for keeping the pace so the results could be obtained. To Charles Smith, much appreciation for his constant effort to facilitate the work of myself and others. And to the several other individuals upon whom I depended for help, guidance, and assistance throughout the summer, my heartfelt thanks, one and all.

LIST OF FIGURES

Figure No.	Title	Page
1.	Block Diagram of Experimental System	7
2.	Photon Drag Detector Response to Laser Beam Pulse	8
3.	Frame and Streak Photographs of Laser Produced Plasmas at 0.5 Atmosphere in Hydrogen	10
4.	Frame and Streak Photographs of Laser Produced Plasmas at 1.0 Atmosphere in Hydrogen	11
5.	Frame and Streak Photographs of Laser Produced Plasmas at 2.0 Atmospheres in Hydrogen	12
6.	Frame and Streak Photographs of Laser Produced Plasmas at 3.0 Atmospheres in Hydrogen	13
7.	Threshold Power Density for Pulsed Laser Breakdown of Hydrogen	15
8.	Laser Energy Transmission Through the Focal Volume of Hydrogen as a Function of Average Power Density	17
9a.	Laser Energy Transmission Through the Focal Volume as a Function of Time for Power Density Input Just Above Threshold in 3.0 Atmospheres of Hydrogen	18
9b.	Laser Energy Transmission Through the Focal Volume as a Function of Time for Power Density Input Well Above Threshold in 3.0 Atmospheres of Hydrogen	18
10.	Relative Linewidth of H-Alpha and H-Beta at 3.0 Atmospheres Scanned at Three Spatial Locations Within the Plasma. Comparison is Shown to a Center Scan of Each Line at 0.5 Atmosphere Pressure	20

INTRODUCTION

Laser propulsion, as a concept whereby energy would be directed from a remote station by means of a laser to a space vehicle, was early described by Kantrowitz (1). One system proposed to utilize this concept involves the absorption of the beam energy by a relatively stable plasma onboard the space vehicle. This requires the remote initiation of the plasma and its stabilization. Such initiation can be accomplished using a focused laser pulse (2), (3) provided the power density exceeds some critical limit. However, the plasma so formed has been observed to move immediately toward the laser source (4), (5). This motion has recently been studied in considerable detail for air (6), yielding early time behavior of the plasma.

OBJECTIVE

Previous work (6) on the early time behavior of the plasma produced in air by a focused pulsed laser resulted in a reliable system for the initiation of a reproducible plasma. Streak and framing photographs of the early time development provided detailed information on the general structure and propagation speeds of the radiating front in air. The current work has expanded the diagnostics of the previously-developed system to permit early time measurements of the temporal and spatial behavior of the plasma temperature by spectroscopic means, the measurement of threshold power density for creating a plasma, and the absorption of the laser beam power by the plasma.

The objective of this work was to apply the system described above to the study of laser-induced plasmas in pure hydrogen over a range of pressures applicable to the laser propulsion concept. The results would be used to determine those conditions of operation which should lead to a stable steady-state plasma in the laser propulsion configuration.

EXPERIMENTAL ARRANGEMENT

A block diagram of the experimental system is shown in Figure 1. A Lumonics Model 203 Transverse Excited Atmospheric (TEA) carbon dioxide pulsed laser having a beam divergence of 0.6 milliradian half-angle was used as the energy source. Figure 2 shows the time dependence of a typical pulse from the TEA laser when operated at 40 KV as recorded by a Rolfin Model 7410 photon drag detector. Mode locking is clearly evident in the pulse shape. The overall pulse duration is approximately 100 nanoseconds with a rise time to the maximum of the envelope defined by the mode locking peaks of approximately 30 nanoseconds. Total energy in the laser pulse was measured using a Scientech Model 364 calorimeter and was determined to be, on average, 5.8 joules.

The plasma to be studied was created within the aluminum test chamber shown. The chamber was evacuated then backfilled with high purity hydrogen to the desired pressure. The TEA laser was fired with the beam traversing the path indicated in Figure 1. To control the total energy reaching the chamber, calibrated attenuators were inserted in the beam path. A sodium chloride flat was inserted as a beam splitter to sample the beam by use of the lower photon drag detector. The remaining beam was then focused to a point within the test chamber located at the level of the quartz viewing windows. A second lens was placed beyond the chamber to collect that portion of the laser beam which was transmitted through the chamber and to focus it onto a second photon drag detector.

The viewing windows were 6 millimeter (mm) thick quartz flats, each having a five centimeter (cm) diameter viewing aperture. The NaCl windows were 3.8 cm thick. The focusing lens for the main beam into the chamber had a focal length of 30 cm. The lens used to focus the transmitted beam onto the upper photon drag detector had a focal length of 25 cm. The lens used to focus the input beam sample onto the first photon drag detector had a focal length of 10 cm.

Polyethylene was used for attenuation, both for primary beam energy control, and to insure non-saturation of the photon drag detectors. Experiments were performed to directly measure the effect of the polyethylene attenuators on the beam pattern. No effect was found.

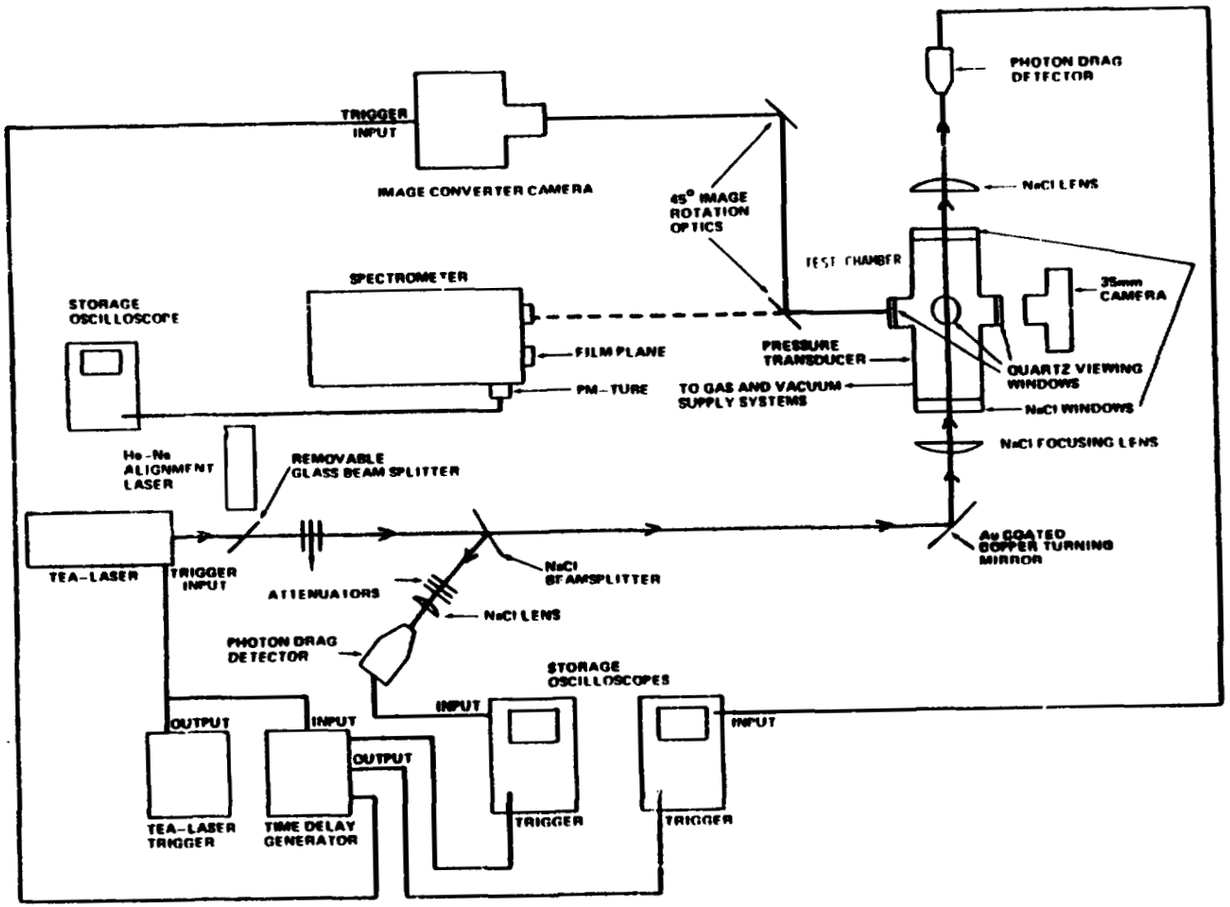

Figure 1. Block Diagram of Experimental System.

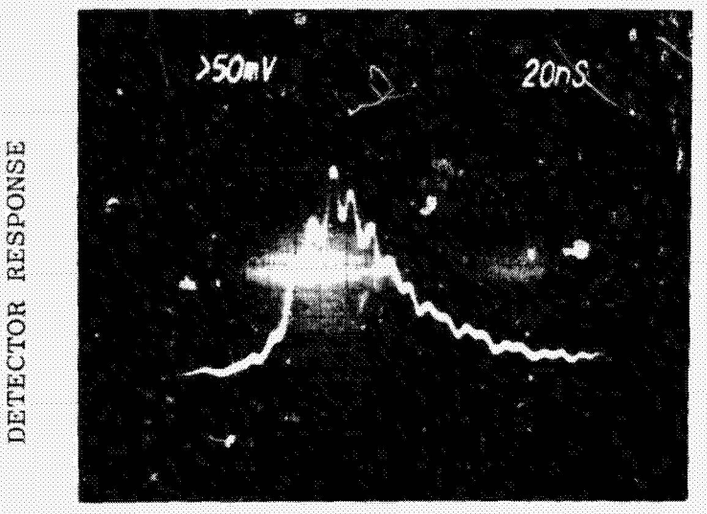

Figure 2. Photon Drag Detector Response to Laser Beam Pulse.

In addition to the photon drag detectors which were used to determine beam power and energy and plasma absorption, a 1.25 meter Spex Model 1269 f/9 scanning spectrometer with both photographic and photomultiplier detection was used to record spectra from the plasma. This provided both the rapid response necessary for time dependent measurements and line width measurements for use in temperature determinations.

The remaining diagnostic for the plasma was an STL Model 1D1 image converter camera, operated in both the streak and framing modes.

All diagnostics were triggered by a signal from the laser spark gap, with variable time delays determined from previous work (6).

The reliability and reproducibility of the previously developed system permitted recording times sufficiently short to detect detailed time dependent structure in the plasma.

RESULTS

The results are divided into four separate categories as follows: (i) spatial and temporal development of plasmoids, (ii) laser power density required to achieve hydrogen breakdown (threshold) as a function of pressure, (iii) absorption of laser energy by hydrogen as a function of pressure and beam power density, and (iv) spatial and temporal temperature measurements.

Previous work (6) has reported in considerable detail laser initiated plasmoid development and motion at one atmosphere pressure in air. Figures 3, 4, 5, and 6 show streak and framing photographs of plasma development in hydrogen at 0.5, 1.0, 2.0, and 3.0 atmospheres pressure. Each of the framing photographs represent a sequence of three exposures, reading in time from top to bottom. The exposure of each frame is for 20 ns with an innerframe delay of 50 ns. For these photographs, the focal point is to the left with the laser source being located to the right. For the streak photographs, time increases from top to bottom with a full streak time of 200 ns. The focal point is located to the left with the laser source at the right. The spatial dimensions shown are approximately twice the actual lengths, thus the total length of plasma observed is approximately one cm.

It is clear from Figure 3 that the plasmoids developed at 0.5 atmosphere move only slightly from their original locations. All plasmoids appear within a 70 ns period and have radiated away most of their energy within 70 ns. There appears to be no radiation coupling between distinct plasmoids.

Figure 4 shows a streak photograph very similar to those previously reported for air at one atmosphere pressure. Plasmoids are clearly seen in the framing pictures and these are seen to be fully formed within 70 ns, with most of the energy dissipated within 100 ns. The plasmoids move upbeam at a maximum speed of approximately 50,000 m/s.

Exposure: 20 ns Interframe Delay: 50 ns

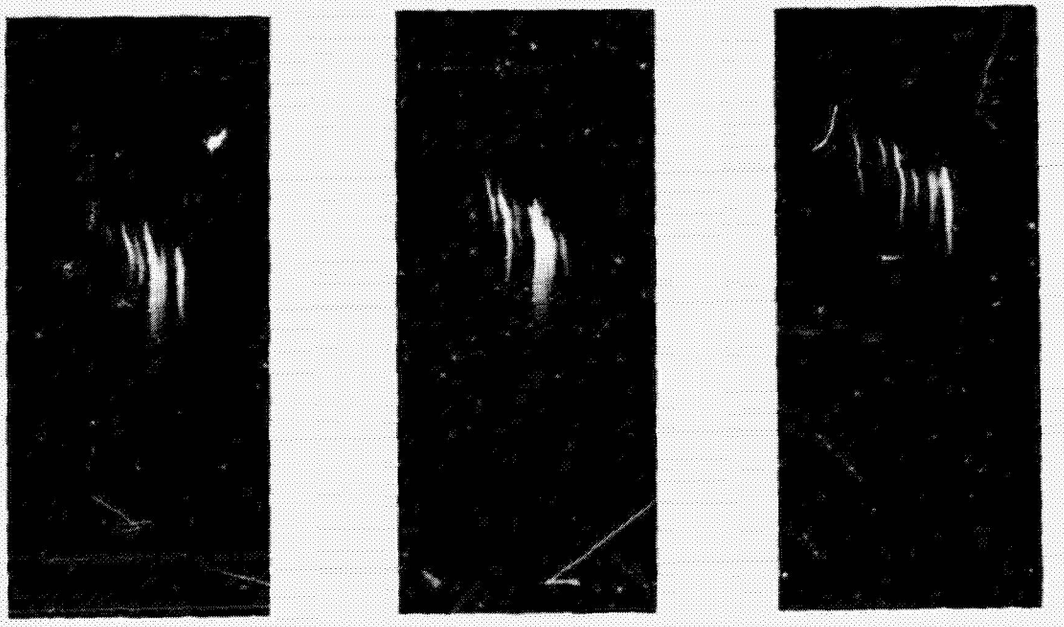

Streak Duration: 200 ns

Figure 3. Frame and Streak Photographs of Laser Produced Plasmas at 0.5 Atmosphere in Hydrogen.

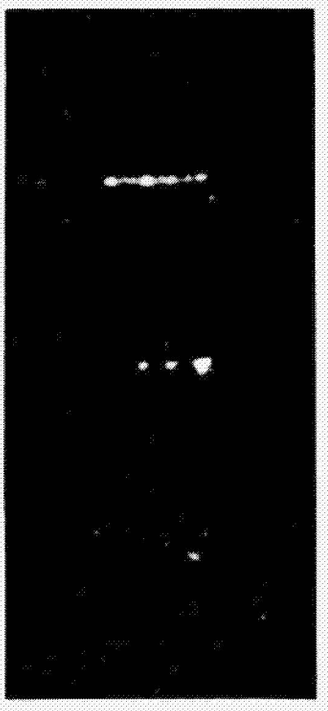

Exposure: 20 ns
Interframe Delay: 50 ns

Streak Duration: 200 ns

Figure 4. Frame and Streak Photographs of Laser Produced Plasmas at 1.0 Atmosphere in Hydrogen.

Exposure: 20 ns Interframe Delay: 50 ns

Streak Duration: 200 ns

Figure 5. Frame and Streak Photographs of Laser Produced Plasmas at 2.0 Atmospheres in Hydrogen.

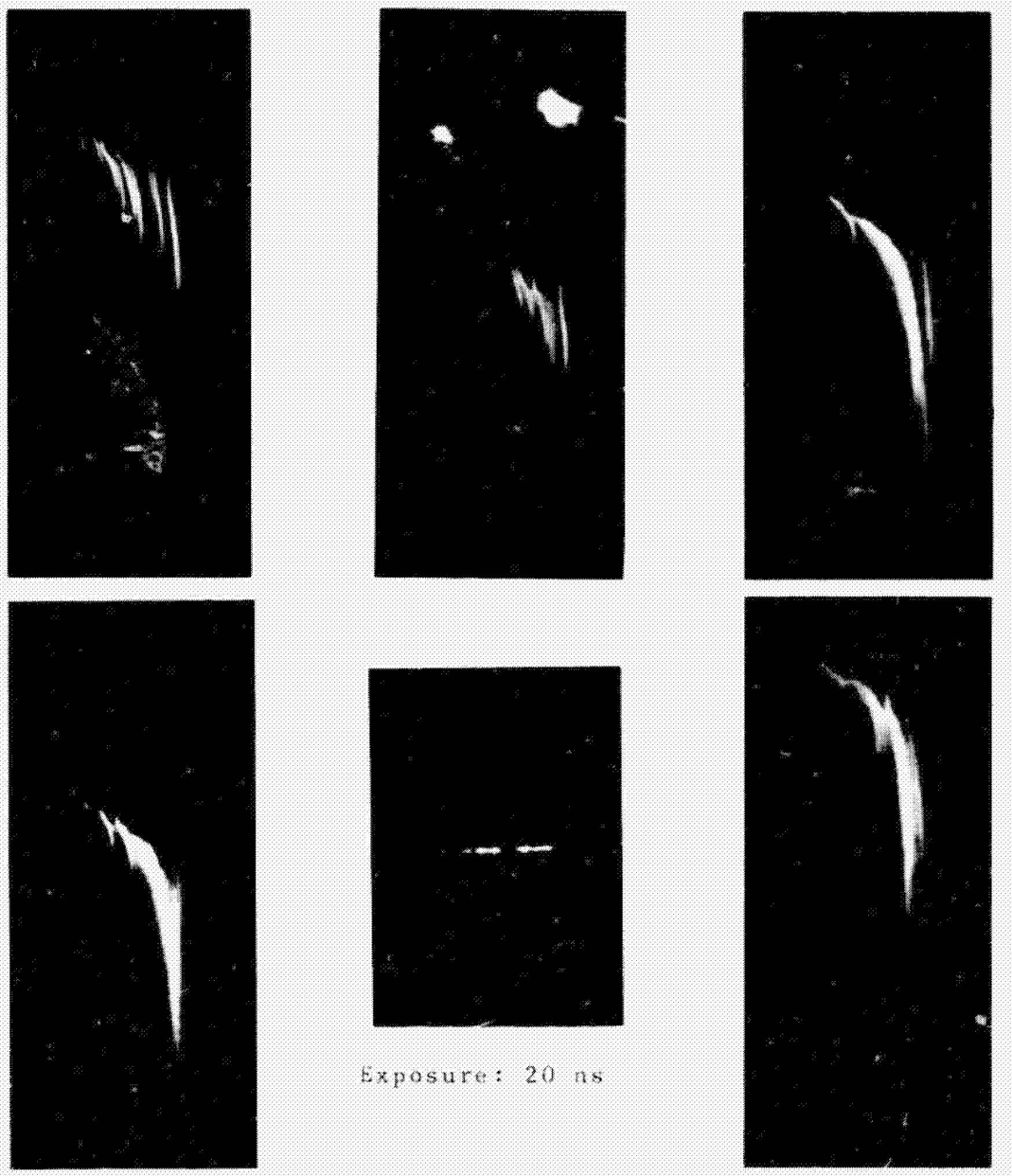

Figure 6. Frame and Streak Photographs of Laser Produced Plasmas at 3.0 Atmospheres in Hydrogen.

Figure 5 provides streak and framing photographs having considerable structures. Plasmoids appear to be created separately at times, each moving with its own speed upbeam. In other cases, there is strong radiative interaction between plasmoids. Again, onset of the initial spark to full development of the total plasma occurs in less than 70 ns. Also speeds of individual plasmoids are relatively slow, with the upper limit being approximately 75,000 m/s.

The images shown in Figure 6 appear to be more often like those at 0.5 atmosphere than any other shown above. Individual plasmoids appear to dominate the plasma development. However, these plasmoids do appear to move quite rapidly shortly after creation for a distance of about one to two millimeters, then quickly come to rest while radiating away their energy.

In order to determine the power density required to achieve threshold (breakdown of the gas with the formation of a radiating plasma), a determination of the focal spot size was required. This was calculated to be the diffraction limit assuming the beam intensity to be uniform across the beam area. Although burn patterns on thermally sensitive film show this not to be precisely the case, it is reasonably close. The calculated focal area was found to be 3.97×10^{-4} cm^2. In addition to some spatial structure, the laser pulse used in this study shows considerable temporal structure, this being due to mode locking as earlier shown in Figure 2.

As a first approach to establishing a threshold for hydrogen, the power density over the focal area was taken to be the total energy incident from the laser during the pulse divided by the period of the laser pulse, distributed uniformly over the focal area. Using the previously noted laser pulse period of 100 ns and the energy from photon drag detector measurements, data were analyzed and Figure 7 shows a plot of threshold power density as a function of hydrogen pressure for three separate measurements at each pressure. Some scatter is noted in these results, particularly at the lowest pressure. Even so, the general result at 0.5 atmosphere deviates markedly from what one would expect solely from an electron cascade model of breakdown.

Absorption measurements were made by comparing the energy received by the upper photon drag detector (transmitted) to that measured by the lower photon drag detector (incident). Each measurement was corrected for attenuation and reflections. A ratio was taken of the power density passing through the focal volume to that incident upon the focal volume. This was done for each of the four pressures previously indicated. These results are plotted in Figure 8. It is clear that the transition between breakdown of the hydrogen into a plasma and no breakdown is reasonably well defined for each pressure. These power densities are indicated by the dotted line on each graph. For incident power densities below breakdown, transmission is always high since all losses are due to regular path length attenuation due primarily to scattering. Once threshold is reached, more of the incident energy is removed due to the presence of the ionized species and free electrons. As the power density increases, the number of charge carriers increases, thus producing more absorption.

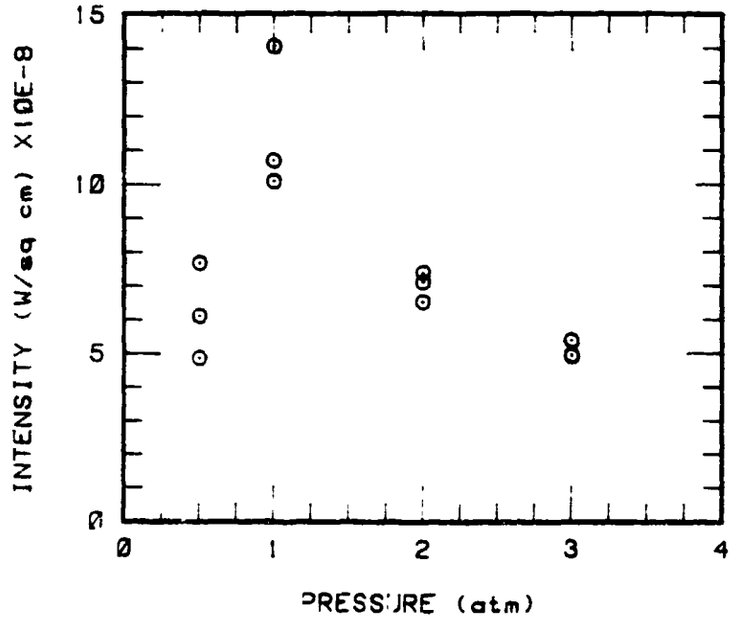

Figure 7. Threshold Power Density for Pulsed Laser Breakdown of Hydrogen

The results obtained above were further supported by measuring the relative transmission as a function of time for a single laser pulse for two separate cases at the same pressure where breakdown occurred in each case. Figure 9a shows the transmission when the power density is only slightly above threshold. Figure 9b shows the response for a power density considerably above threshold.

These figures show that the early time mode spike produces low transmission for the case near threshold, where maximum energy is absorbed in forming the first plasmoid at the focal volume. As the first spike diminishes, the power density level momentarily falls below threshold and transmission is increased. This pattern repeats.

For the case shown in Figure 9b, the initial mode spike behaves in much the same manner as for Figure 9a. However, as the plasma is formed and sustained by the excess energy required for breakdown, the absorption becomes more nearly constant. Smith (7) has reported no effects on breakdown or transmission due to the shape of the laser pulse. It would appear the above results in Figure 9b are consistent with that finding. However, for power densities near threshold, mode spiking is a significant factor in the absorption.

Spectroscopic data acquired using photographic plates were taken by imaging a longitudinal portion of the plasma onto the 2 mm high slit opening. Total light intensity was insufficient to permit plate recording of the spectrum for a single shot. Therefore, 100 exposures were accumulated on each plate. Although such a process will necessarily produce some spatial averaging due to shot-to-shot variations in structure, examination of framing and streak photographs of hundreds of shots under the same conditions show general shot-to-shot spatial reproducibility.

The resulting spectrum was then scanned photometrically from top to bottom to determine the variation of total time integrated light output from the plasma as a function of axial position.

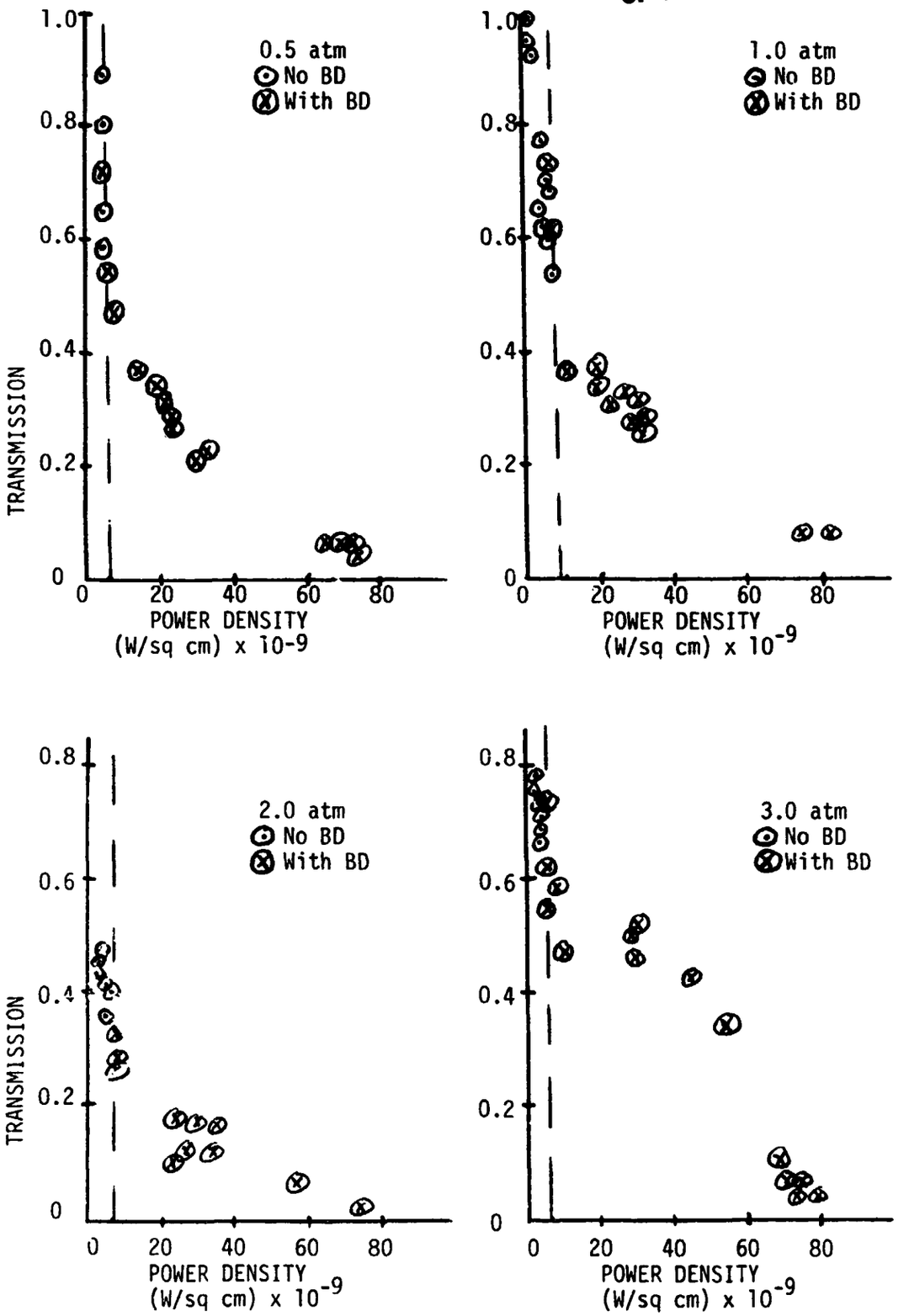

Figure 8. Laser Energy Transmission Through the Focal Volume of Hydrogen as a Function of Average Power Density.

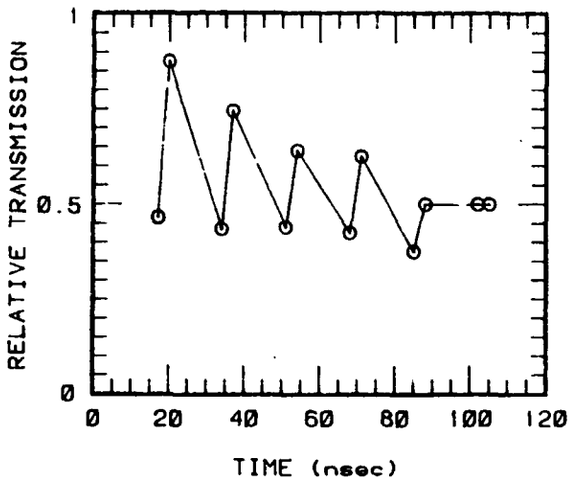

Figure 9a. Laser Energy Transmission Through the Focal Volume as a Function of Time for Power Density Input Just Above Threshold in 3.0 Atmospheres of Hydrogen.

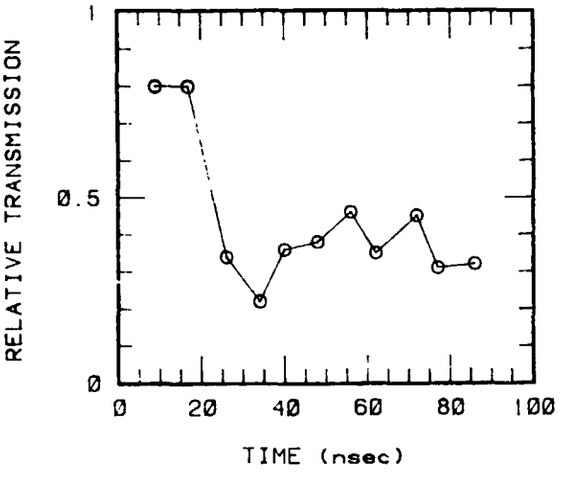

Figure 9b. Laser Energy Transmission Through the Focal Volume as a Function of Time for Power Density Input Well Above Threshold in 3.0 Atmospheres of Hydrogen.

Figure 10a shows this result at 3.0 atmospheres for H-alpha while Figure 10b shows the same representation at 3.0 atmospheres for H-beta. Only slight spatial variations are seen for a given pressure. However, the results show the effect of line broadening as pressure is increased as can be seen from the corresponding line at 0.5 atmosphere.

The line profiles obtained for H-alpha, beta, gamma, and delta were used together with the continuum level of radiation at these wavelengths to calculate the plasma temperature by taking the line-to-continuum ratio. For H-alpha, the calculated temperature was 18,000K, while for each higher frequency, the ratios predicted successively higher temperatures. This indicates thermal equilibrium has not been achieved.

The photomultiplier data from the spectrograph for each wavelength examined showed an initial rise in light output to a maximum over a period of approximately 200 ns, followed by a decay to approximately 30% of this peak in another 200 ns. This radiation level was sustained for approximately one microsecond, followed by an exponential decay to zero in approximately one microsecond.

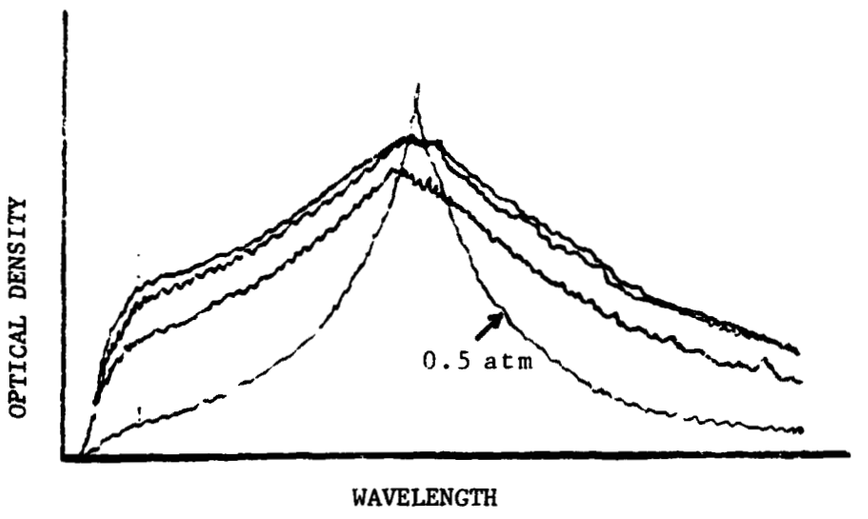

(a)

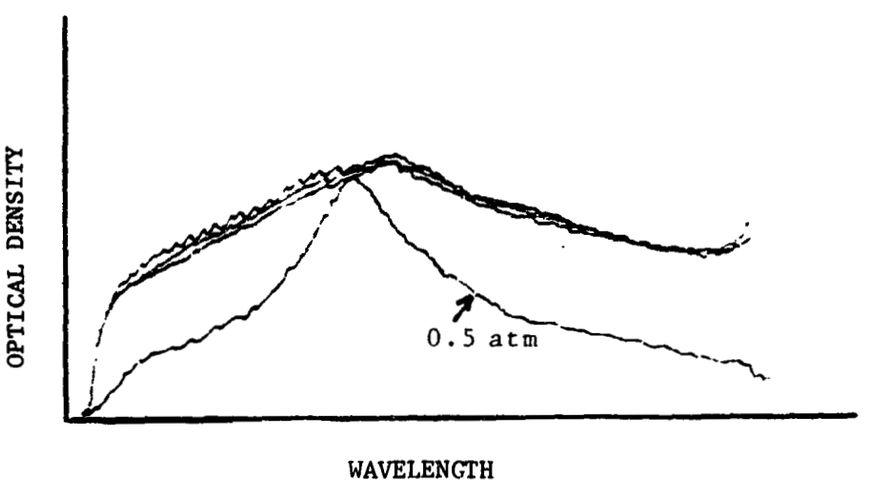

(b)

Figure 10. Relative Linewidth of H-Alpha (a) and H-Beta (b) at 3.0 Atmospheres Scanned at Three Spatial Locations Within the Plasma. Comparison is Shown to a Center Scan of Each Line at 0.5 Atmosphere Pressure.

CONCLUSIONS AND RECOMMENDATIONS

Although the object of defining the early time development of a laser spark plasma in hydrogen has been accomplished, the marked differences between hydrogen and air were unexpected. The processes involved in stabilizing these plasmoids are not yet understood and additional detailed experimental studies and analyses are required before a fundamental explanation will be obtained.

Laser spark thresholds in hydrogen as a function of pressure behaved as would be expected for an electron cascade process except for the anomaly at 0.5 atmosphere. Although the values obtained were calculated as time averages for specific assumptions, the results are directly usable for the specified system. For other systems, particularly for non-mode locked lasers and for lasers with different beam patterns, the reported numbers may not be usable. In addition, detailed attention should be given to the temporal structure of the laser pulse to ascertain which parameter or parameters control breakdown: temporal average power density, spatial average power density, or peak power density.

Absorption data seem conclusive in that a higher percentage of incident power is absorbed as the incident power level is increased. There appears to be no significant pressure dependence up to three atmospheres. This effect was observed not only for total pulse energy, but also for the mode spikes of the laser.

The spectroscopic results indicate only that the early time plasma is not in local thermal equilibrium, even within local plasmoids.

REFERENCES

1. A. R. Kantrowitz, J. of Astronautics and Aeronautics, 9, 34 (1971).

2. D. C. Smith, J. App. Phys., 41, 4501 (1970).

3. N. A. Generalov, V. P. Zimakow, V. A. Masyukov, and Yu. P. Raizer, Sov. Phys. JETP Lett. 11, 223 (1970).

4. Yu. P. Raizer, Sov. Phys. Usp. 23, 789 (1980).

5. G. I. Kozlov, Sov. Phys. Tech. Phys. 24, 37 (1979).

6. Askew, Raymond F., "Plasma Ignition for Laser Propulsion," Final Report. Contract NASA CR-162051, Section V, August 1982.

7. D. C. Smith, Applied Physics Letters 19(405), 1971.

1983

NASA/ASEE SUMMER FACULTY RESEARCH FELLOWHIP PROGRAM

KENNEDY SPACE CENTER

THE UNIVERSITY OF ALABAMA

A PRELIMINARY SURVEY OF PLANKTON AND PERIPHYTON IN THE TURN BARGE CANAL AND BASIN AREA OF KENNEDY SPACE CENTER, FLA.

Prepared By:	Grover D. Barnes, Ph.D.
Academic Rank:	Professor
University and Department:	Jackson State University Department of Biology
NASA/KSC:	
(Directorate)	Biomedical
(Branch)	Environmental Sciences
KSC Counterpart:	Dr. William Knott, Ph.D.
Date:	August 12, 1983
Contract No.:	NGT-01-008-021 (University of Alabama in Huntsville)

ABSTRACT

A PRELIMINARY SURVEY OF PLANKTON AND PERIPHYTON IN THE TURN BARGE CANAL AND BASIN AREA OF KENNEDY SPACE CENTER, FLA.

by
Grover D. Barnes
1983 ASEE/NASA Summer Faculty Fellow
with
C. Ross Hinkle
and
Carlton Hall
BIO-2
BIONETICS
Kennedy Space Center, Fla 32899

This project is a preliminary survey of plankton and periphyton in the Turn Barge Canal and Basin area of Kennedy Space Center, Fla. 32899,during the summer of 1983. The study initiates a long range monitoring program for the Kennedy Space Center.

Various steps are necessary to implement the plankton and periphyton study. Intervisitation with members of Bionetics is necessary to initiate the sampling program. Collection and identification of supplies and equipment are collected and identified for the study. Harbor Branch Consortium and the Department of Environmental Engineering, Brevard County Courthouse, will be visited to identify past plankton and periphyton projects on the Kennedy Space Center. A computer search in Oceanic and Water Resources Abstracts is made to determine prior investigations in the area included in this project. A statistical design will be selected to analyze data from the research project. Three sampling stations are to be identified for collecting plankton samples and samples will be collected biweekly from 22 June 1983 to 4 August 1983. An assessment will be made of plankton groups from the sampling stations.

ACKNOWLEDGEMENTS

I appreciate Dr. William Knott, my counterpart at KSC, making the arrangements for the fellowship. Special thanks is given to Dr. Ross Hinkle and Mr. Carlton Hall for the fine support given to this participant and to other members of the Environmental Staff of Bionetics for their help (especially Mark Provancha for drawing the map).

LIST OF FIGURES

Figure No.	Title	Page
1	Stations in the Turn Parge Canal and Turning Basin Area at KSC During the Present Study.	V-9

LIST OF TABLES

Table No.		Page
I	Surface Physical Data for the Five Stations	V-13
II	Phytoplankton, Bacteria and Zooplankton Species in Periphyton and Plankton	V-16
III	Periphyton and Bacterial Density (x 10^2 per mm^2) on 22 July 1983 at the Five Stations with Replicates (R) at KSC	V-20
IV	Percent Composition of Total Bacteria and Periphyton Numbers on 22 July 1983 on Glass Slides at the Five Stations.	V-23

INTRODUCTION

The Role of Kennedy Space Center

The primary role of Kennedy Space Center (KSC) includes the launching of vehicles into outer space using chemically fueled rockets from Launch Pads 39A and 39B. The total land area for KSC is slightly more than 56,500 hectares.

Descriptions of Previous Algal Studies

With the exception of studies conducted by Harbor Branch Consortium, Ft. Pierce, Florida, in the Indian River (1973-1975) and the Florida Department of Natural Resources at Hutchinson Island, Florida (1971-1974), no comprehensive algal surveys have been conducted in shallow nearshore waters of the Atlantic Ocean between KSC and St. Lucie Inlet, Florida. Conger (1954), stated in his historical review of diatom studies of the Gulf of Mexico that, "the few studies made have been of somewhat casual, quite limited, and localized nature leaving almost the entire shoreline and open water areas of the Gulf and Florida completely unexplored."

Proposed Polygeneration Site and Assessment

A feasibility study is being done on a polygeneration facility (PF) on the Kennedy Space Center (KSC) in Brevard County, Florida. KSC borders the Indian and Banana Rivers, important estuarine ecosystems.

Extensive surveys for the proposed PF were conducted. Three potential sites have been selected.

The design of the PF facility will utilize a combined cycle coal gasification system to produce 12 tons of liquid hydrogen/day. Best available control technology will be utilized to limit environmental pollution.

The source of make-up matter is groundwater from the Florida aquifer or a mixture of groundwater and treated sewage effluent from KSC. If any available technology (Luthy, 1981) is economically feasible, no discharge to surface waters will occur. If wastewater is eliminated, the effluent will be discharged into the Turning Basin or Turn Barge Canal which empties into the Banana River, a Class III Outstanding Florida Water Stream. Available technology within economic restraints will be utilized to control air pollution with emissions including the removal of sulfur, nitrogen, and particulates.

Long Term Monitoring Program

The Long Term Monitoring Program for phytoplankton communities in the waters of KSC is designed to allow for the assessment of major trends in community productivity and dynamics through time with the ultimate goal of developing a numerical model for KSC waters. This program is based on a progression of evaluation (systems approach) which will address both long term trends and site specific or project specific data needs as required for future environmental impact assessments. Estimates of productivity (chlorophyll and biomass) will be made in conjunction with ongoing long term water quality surveys. Microcosm studies conducted at both selected long term and short term project specific stations will be utilized to assess phytoplankton community structure, dynamics and diversity within the various aquatic systems present at KSC. Similarly, periphyton studies will be incorporated as needed to assess potential environmental impacts associated with STS operations and specific construction activities such as the proposed Polygeneration Project. By integrating these various tasks during the early years of the long term program, the maximum utility of data can be achieved for the identification of unique, common or otherwise interesting community types and distributions at KSC. Because little is currently known about phytoplankton in the KSC region, these data will be instrumental in developthe initial conceptual models of the area and in determining methods and techniques for future long term monitoring.

Climatology

Both tropical and meteorological phenomena influence the weather at KSC. The warm Florida current affects conditions in this area even where the Florida peninsula moves northwest from this current.

From May to October, the predominant wind direction is southeast around the Bermuda Anticyclone. Almost daily thunderstorms occur and approximately 70 per cent of the average rainfall occurs during this period or wet season. The average monthly precipitation is 10 cm.

Temperatures during the wet season average 26°C and rarely exceed 32°C. During the present experiment (22 June 1983 to August 1983), temperatures frequently exceeded the upper average temperature.

Topography

The general topography of the present study is influenced by a marine terrace system formed during the Pleistocene Epoch. A North-to-South barrier beach and dune systems are evident. Plains or flatlands are formed between the dunes and terraces evolve from the plains. The Banana and Indian Rivers are submerged terraces inundated by brackish water. The KSC area is part of a barrier beach system which is bordered by the Silver Bluff marine terrace on the Northeast and Pamlico marine terrace on the west. The Pamlico and Silver Bluff Terraces are 8 to 11 m and 0.9 to 2.4 m, respectively in elevation.

The present study included five stations: Station 1 (the mouth of the Turn Barge Canal on the Banana River), Station 2 (near the mid point of the Turn Barge Canal), Station 3 (the Turning Basin), Station 4 (a marsh swale with a predominate growth of saw grass - Cladium jamaicensis), and Station 5 (a marsh swale with bunch grass - Spartina bakeri) as the predominate grass (Figure 1). Station 1 is included in the Long Range Monitoring Program while Stations 2-5 are located near a proposed Polygeneration Site.

Geology

KSC was covered repeatedly by the sea during the Eocene Epoch. During these intrusions, limestone formations were exposed to erosion. A thick series of sand, silts and clay comprise the existing oligocene and lower Miocene deposits. The top strata influencing this project generally consists of loose to fairly compact fine sands and shelly sands. The texture of the silts and clays vary from moderately stiff to soft. The five general soil associations (Paola-Pomello-Astatula, Canaveral - Palm Beach - Welaka, Myakka - Eau Gallie - Immokalee, Copeland - Wabasso and Salt Water Marsh - Salt Water Swamp Associations) at KSC and Cape Canaveral Air Force Station (CCAFS) were conglomerates of shell, limestone and sand deposited in the Pleistocene and recent eras (Koller, 1978).

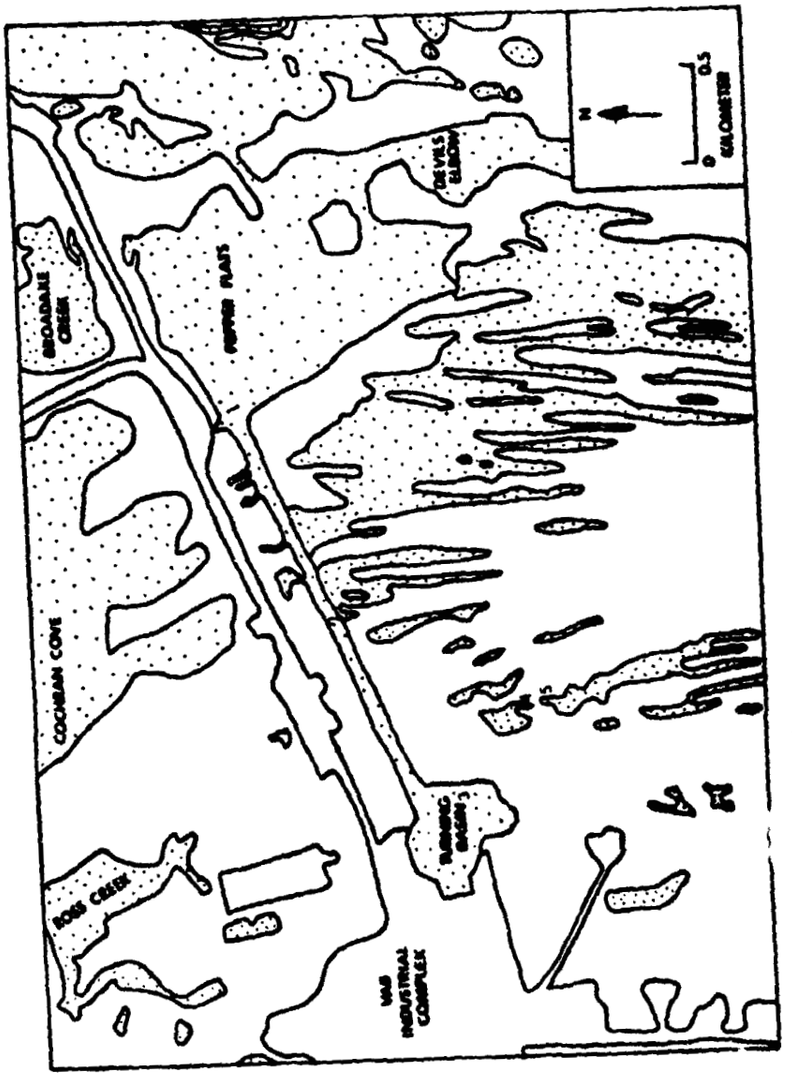

Figure 1. Stations in the Turn Barge Canal and Turning Basin Area at KSC During the Present Study.

Dr. Grover D. Barnes

Outline of the 1983 NASA/ASEE Summer Fellowship Program Objectives

I. Intervisitation with members of Bionetics to implement a phytoplankton sampling program in the Turn Barge Canal and Basin at Kennedy Space Center.

II. Collect and identify equipment and supplies necessary for the project.

III. Visit Harbor Branch Consortium and the Department of Environmental Engineering, Brevard County Courthouse, to identify past phytoplankton projects on the Banana River.

IV. Run a computer search in Oceanic and Water Resources Abstracts to determine prior investigations in phytoplankton research.

V. Select a statistical design to analyze data from the research project.

VI. Identify three sampling stations and collect phytoplankton samples biweekly after 22 June 1983.

VII. Identify phytoplankton groups found in the project sites.

BODY OF REPORT

Essentially all of the objectives of the 1983 NASS/ASEE Summer Fellowship Program were completed. Meetings were held with various members of the Environmental Branch (Drs. Ross Hinkle and Paul Schmalzer, David Breininger, Mark Provancha and Jane Provancha) to implement the phytoplankton sampling program in the Turn Barge Canal and Turning Basin area. Equipment and supplies were collected and ordered from various sources. Harbor Branch Consortium and the Department of Environmental Engineering, Brevard County Courthouse, were visited on 14 June 1983 and 8 June respectively. No organized studies were conducted in the Banana River to identify periphyton or plankton populations. A computer search in the Oceanic and Water Resources Abstracts showed no past periphyton or plankton experiments in the Banana River area. The rest of of the objectives are discussed in the Methods or Results and Discussion sections.

Methods

A Completely Randomized Block Design will be used to study analysis of variance and correlation of numbers of organisms and numbers of divisions of marsh and estuarine algae. Three samples were collected at each station for sampling replication with treatment levels (Stations) and blocks (time).

Periphyton samplers were placed at the stations on 7 July 1983. Periphyton samples were collected using a sampling devise similar to a Catherwood Diatometer (Weber, 1973 and EPA, 1978) at the five stations (Figure 1) initially on 22 July 1983. Periphyton from the Catherwood Diatometer was scraped from microscope slides and preserved in 12.5% methanol. Grass shrimp and a Goby were observed grazing on the slides at stations one and two respectively. The drop method (Prescott, 1942) and standard techniques (A.P.H.A., 1960) were used to count the organisms. Organisms were enumerated using an Olympus BH-2 Phase Contrast Microscope. Diatoms were incinerated for 1 hr at 1000° F in a Blue M Lab Heat Muffle Furnace and verified for secondary identification using 1000x magnification.

Physical parameters were collected at similar times throughout the present study (Table 1). Conductivity and salinity were higher at stations 1-3 (estuarine water) than stations 4-5 (freshwater marsh swales). Temperature was generally lower at stations four and five due to shading. Oxygen and pH were lower in the marsh swales due to a high organic content and decaying vegetation. It appeared that stations four and five could probably be classified as acid lakes. The color of the water was brown in the swales throughout the study. The depth of the stations were: Station one - 3 m, station two - 0.2 m, station three - 0.2 m, station four - 0.3 and station five - 0.2 m. From 7 July 1983 to 4 August 1983, water levels dropped approximately 0.6 m at station 4

TABLE I

SURFACE PHYSICAL DATA FOR THE FIVE STATIONS

Station	Conductivity (μmhos)	Salinity (mg l^{-1})	Temperature (°C)	Oxygen (mg l^{-1})	pH
22 June 1983					
1	28600	16.2	29.0	5.5	7.6
2	*	15.8	29.5	5.1	8.4
3	*	15.1	29.7	5.6	8.6
4	*	*	*	*	*
5	*	*	*	*	*
7 July 1983					
1	31000	16.0	34.0	7.1	8.8
2	31000	16.0	32.0	4.6	8.4
3	31000	16.5	33.0	7.1	8.4
4	*	*	26.0	1.6	5.2
5	*	*	*	*	*
22 July 1983					
1	34000	18.5	33.0	6.2	9.1
2	*	*	*	*	*
3	*	*	*	*	*
4	120	*	26.0	1.6	5.2
5	320	*	28.0	2.1	4.1
4 Aug 1983					
1	33800	18.2	33.0	8.1	9.0
2	34000	19.0	34.0	6.3	8.9
3	38000	18.5	32.0	6.1	8.9
4	120	0	27.0	1.6	4.1
5	335	1.2	30.1	4.0	2.8

* Data not collected

and 0.5 m at station five. On 22 July 1983, the periphyton samplers were moved 4 m south at station four and 20 m north at station five to maintain similar depths. Vegetation was the same as the previous location at both sites. A strong hydrogen sulfide odor was detectible at stations four and five on 22 July 1983 and at stations one, four and five on 4 August 1983.

Results and Discussion

Community Composition

Thirty-seven species of various groups of organisms were identified at the sampling stations: Cyanophyta (11 species), Chrysophyta (14), Chlorophyta (6), Thallophyta (2), Euglenophyta (1), Protozoa (1), Rotifera (1) and Decapoda (1), (Table II). The photosynthetic bacterium (Chlorobium sp.), a free swimming organism, was the predominate species at all stations, especially four and five. High levels of hydrogen sulfide were detected at stations four and five and this organism is species specific for hydrogen sulfide. Chlorobium sp. was reported in other studies (Czeczuga, 1965; Juday and Manning, 1941) and sewage oxidations ponds (Godniew and Winberg, 1951). Chromatium sp. is a red photosythetic bacterium and was observed at station one. Chromatium sp. apparently was not tolerant of hydrogen sulfide.

Species of algae have been classified according to their pollutional status by Whipple et al. (1948). Spirulina and Aphanotheca were listed as polysaprobic by Whipple and the former group was collected only in station one and the latter in station five. Species collected in the present study that were listed as mesosaprobic by Whipple were: Oscillatoria sp., Euglena sp. and Navicula radiosa. All three species were found only in station one, while Oscillatoria sp. was observed in station two as well. Groups collected in the present study that were

TABLE II

PHYTOPLANKTON, BACTERIA AND ZOOPLANKTON
SPECIES IN PERIPHYTON AND PLANKTON

Cyanophyta
- Anabaina subcylindrica Naegeli
- Aphanothece stagnina (Spreng) A. Braun
- Calothrix stagnalis Gomont
- Chaetoceros sp.
- Chrococcus pallidus Naegeli
- Cosmarium sp.
- Oscillatoria amoena Gomont
- Oscillatoria nigro-viridis Thwaites
- Phormidium fragile (Meneghini) Gomont
- Rhabdoderma lineare Schmidle & Lauterborn
- Spirulina subsalsa Oersted

Chrysophyta
- Asterionella gracillima Hassal
- Fragillaria crotonensis Kitton
- Grammatophora angulosa Ehrenberg
- Gyrosigma sp.
- Melosira moniliformis (Muller) Agardh
- Navicula radiosa Kuetzing
- Navicula sp.
- Nitzschia sp.
- Nitzschia linearis Agardh and W. Smith
- Pleurosigma sp.
- Rhizoselenia setigera Brightwell
- Rhopalodia gibba (Ehrenberg) O. Muller
- Stephanodiscus niagrae Ehrenberg
- Thalassiothrix frauenfeldii Cleve and Grunow

Chlorophyta
- Ankistrodesmus spiralis (Turner) Lemmerman
- Crucigenia tetrapedia (Kirchner) Wm. and G.S. West
- Gleocystis vesiculosa Naegeli
- Kirchneriella subsolitaria G.S. West
- Mongectia scalaris Hass
- Stigeoclonium subsecundum Kuetzing

Thallophyta
- Chlorobium sp.
- Chromatium sp.

TABLE II (Continued)

Euglenophyta
Euglena sp.
Protozoa
Paramecium sp.
Rotifera
Keratella cocclearis (Gosse)
Decapoda
Palaemonetes pugio Holthuis

classified as oligosaprobic were: Fragillaria crotonesis, Navicula hungaria and Rhopalodia gibba. These species were observed at station one.

Palmer (1962) listed genera of algae that are tolerant of organic pollution and clean water environments. Examples included Euglena, Navicula, Oscillatoria and Phormidium. These organisms were collected at station one.

Hutchinson (1967) gives a classification of lakes by phytoplankton types classified according to dominant species. Fragillaria crotonesis was listed as a eutrophic diatom plankter and was observed at stations one and three in the present study. Cosmarium was listed as a eutrophic desmid indicator. Cosmarium was found at station three.

The rotifers, especially Keratella cochlearis, were the most abundant zooplankters observed in the present study. Keratella cochlearis is perhaps the most common planktonic perennial rotifer od lakes in the temperate region (Hutchinson, 1967). This species was considered generally to be eutrophic by Pejler (1957). Keratella sp. and Polyarthra sp. were the predominant zooplankton species during the late spring in enriched ponds (Ewing and Dorris, 1970). Edmondson (1964) recorded higher reproductive rates for Keratella cochlearis about 15 C than for many other species. Hutchinson (1967) reported maximum density of Keratella cochlearis in the summer and rare winter occurrence in Lake Glan, Sweden. The mean daily temperature (26.5 C) of the present study probably favored this species. A trend in zooplankton could not be

observed in the present study since a homogenizer was used to separate algal clumps and many zooplankton were destroyed or mutilated beyond recognition.

Prescott (1962) reported species of algae that were specific in acid bog lakes (usually kettlehole Sphagnum bogs): Cyanophyta (Scytonema ocellatum, Hapalosiphon pumilus and Chrococcus Prescotti), Microspora (Chlorophyta), Batrachospermum and Oedogonium. None of these species or genera were found in the acid marsh swales of this study. Rhabderma lineare was found abundantly in the swales and other stations. Prescott reported this species to occur in acid lakes. Fresh water Cyanophyta were reported to adapt to brackish or marine environments within 6 hrs (Humm, 1981). A concentration of organic acids and decaying matter were observed in the marsh swales of the present study as was present in acid bogs.

Filamentous Chlorophyta (Prescott, 1962) were noted to be abundant in acid bogs. Stigeoclonium subsecundum (a filamentous Chlorophyta) was found in the marsh swales. This species was more abundant in the periphyton at station four. A visual observation (4 August 1983) noted that this species was 2-6 cm deep in the ditches at station five.

Variations in periphyton and bacterial density (x 10^2 per mm^2) were observed at all stations on 22 July 1983 (Table III). Thallophyta was generally the most abundant group (nannoplankton). Chlorobium and Chromatium sp. were the populations present in this group. Lively et.al.

TABLE III

PERIPHYTON AND BACTERIAL DENSITY (x 10^2 per mm^2) ON 22 JULY 1983
AT THE FIVE STATIONS WITH REPLICATES (R) AT KSC

Station	Organism	Replicate 1	Replicate 2	Replicate 3	$\bar{x}$
1	Cyanophyta coccoid	217	119	209	182
	Cyanophyta filamentous	0	19	12	11
	Chlorophyta coccoid	0	0	1	0
	Chlorophyta filamentous	0	0	0	0
	Chlorophyta flagellates	0	0	0	0
	Chrysophyta centric	3	1	0	1
	Chrysophyta pennate	38	110	322	100
	Thallophyta	229	100	152	160
2	Cyanophyta coccoid	213	47	350	203
	Cyanophyta filamentous	0	4	0	1
	Chlorophyta coccoid	0	0	0	0
	Chlorophyta filamentous	0	0	0	0
	Chlorophyta flagellates	4	8	0	0
	Chrysophyta centric	0	0	0	0
	Chrysophyta pennate	31	70	66	56
	Thallophyta	167	70	144	127
3	Cyanophyta coccoid	209	66	579	285
	Cyanophyta filamentous	1	1	42	15
	Chlorophyta coccoid	0	0	0	0
	Chlorolphyta filamentous	0	0	0	0
	Chlorophyta flagellates	0	0	4	1
	Chrysophyta centric	0	8	0	3
	Chrysophyta pennate	204	139	136	160
	Thallophyt	229	268	268	255
4	Cyanophyta coccoid	152	507	43	234
	Cyanophyta filamentous	1	1	74	25
	Chlorophyta coccoid	64	0	0	21
	Chlorphyta filamentous	0	42	16	20
	Chlorophyta flagellates	29	0	0	10
	Chrysophyta centric	8	2	0	3
	Chrysophyta pennate	15	4	0	6
	Thallophyta	480	222	311	338
5	Cyanophyta coccoid	48	38	79	55
	Cyanophyta filamentous	5	1	6	4
	Chlorophyta coccoid	0	0	0	0
	Chlorophyta filamentous	6	7	5	6
	[illegible]	0	0	0	0
	[illegible]	0	0	4	1
	[illegible]	13	0	1	5
	[illegible]	292	148	379	273

(1983) reported a recurrent dominance of small forms (Chlorophytes) in a barrier island estuary: Great South Bay, New York. Cassin (1978) and Weaver and Hirshfield (1976) reported a recurrent numerical dominance of Chlorophytes (photosynthetic organisms or bacteria) in a barrier island estuary (Fire Island Inlet, Long Island, N.Y.). Ralph Montgomery (personal communication) stated that the biomass and numerical enumeration of nannoplankton have been a neglected area of plankton and periphyton investigations. In the Great South Bay Study, 2-4 μm chlorophytes were numerically dominant, and contributed approximately half of the total phytoplankton biomass. Organisms from 2-6 μm were the dominant forms in this study.

The concentration of the Cyanophyta coccoids ranged from 38 to 507 organisms x 10^2 per mm. This group comprised the second highest density at all stations. This was probably due to the environmental adaptibility of this group. From 8/18/1967 to 11/24/1967, Weber (1973) found periphyton densities of 3 to 19 organisms x 10^2 per mm in the Ohio River near Cincinnati above a sewage outfall. Early in his experiment, filamentous Cyanophyta and pennate diatoms were the dominant groups and at the latter of the study, pennate and centric diatoms were the abundant forms. Densities in the Ohio River were lower than in this study. Pollution and colder temperatures probably caused lower density values in periphyton in the Ohio River.

Percent composition of total bacteria and periphyton numbers on 22 July 1983 on glass slides at the five stations at KSC followed the same

trends as density. (Table IV). In abundance, pennate chrysophyta were third among organisms in the present study. In Weber's study (1973), pennates were the second most abundant organism above a sewage outfall on the Ohio River in August. Pennates were more abundant at stations one and three. Pennate diatoms were larger at station one. This may have been due to increased nutrient (dissolved ortho-phosphate) and trace element (dissolved silicate) circulation in the Banana River. Walker and Steidinger (1979) stated that high counts of large or chain-forming net phytoplankton represent estuarine and coastal species suggesting a resident population from the Indian River at Hutchinson Island, Fla. Dinoflagellates were designated as indicators of oceanic influence in the Hutchinson Island Study.. No dinoflagellates were observed in this study. The species composition of the periphyton in this study probably indicate an estuarine habitat.

Skeletonema costatum is a recurrent dominant in many areas along the east coast - the Cape Fear estuary (Carpenter, 1971), the James River estuary (Marshall, 1967), Old Plantation Creek, Virginia (Marshall. 1980), Narragansett Bay (Pratt, 1959), Long Island Sound (Conover, 1956; Staker & Bruno, 1978), and Great Pond, Massachusetts (Hulburt, 1956). Previous studies in the Great South Bay (Weaver and Hirsch-field, 1976; Cassin, 1978; Weaver, 1979), Hutchinson Island, Fla. (Walker and Steidinger, 1979) and Indian River in Florida (Gibson, 1975) have found S. costatum to be seasonally dominant. Walker and Steidinger

TABLE IV

PERCENT COMPOSITION OF TOTAL BACTERIA AND PERIPHYTON NUMBERS ON 22 JULY 1983 ON GLASS SLIDES AT THE FIVE STATIONS

Station	Organism	Replicate 1	Replicate 2	Replicate 3	$\bar{x}$
1	Cyanophyta coccoid	36.8	33.9	30.2	34.0
	Cyanophyta filamentous	0	5.5	1.6	2.7
	Chlorophyta coccoid	0	0	1	0.3
	Chlorophyta filamentous	0	0	0	0
	Chlorophyta flagellates	0	0	0	0
	Chrysophyta centric	0.6	0.9	0	0.5
	Chrysophyta pennate	36.8	31.2	46.4	38.1
	Thallophyta	23.8	28.5	21.8	24.7
2	Cyanophyta coccoid	51.4	75.9	67.1	64.8
	Cyanophyta filamentous	0	4	0	1.3
	Chlorophyta coccoid	0	0	0	0
	Chlorophyta filamentous	0	0	0	0
	Chlorophyta flagellates	0.9	1.3	0	0.7
	Chrysophyta centric	0	0	0	0
	Chrysophyta pennate	7.5	11.4	5.2	7.8
	Thallophyta	40.2	11.4	27.7	26.4
3	Cyanophyta coccoid	31.5	10.5	56.2	32.7
	Cyanophyta filamentous	1.0	3.2	4.2	2.8
	Chlorophyta coccoid	0.3	0	0	0.1
	Chlorophyta filamentous	0	0	0	0
	Chlorophyta flagellates	0	0	0.4	0.1
	Chrysophyta centric	0	0	0	0
	Chrysophyta pennate	31.6	29.0	13.2	24.6
	Thallophyta	35.6	55.7	26.0	39.1
4	Cyanophyta coccoid	31.4	56.1	9.0	32.1
	Cyanophyta filamentous	1.0	4.1	16.3	7.1
	Chlorophyta coccoid	13.4	0	0	4.5
	Chlorophyta filamentous	0	0	3.0	1.0
	Chlorophyta flagellates	6.0	0	0	2.0
	Chrysophyta centric	0.4	0	0	0.1
	Chrysophyta pennate	3.2	13.2	3.0	6.1
	Thallophyta	44.6	26.4	68.7	46.6
5	Cyanophyta coccoid	13.2	19.5	16.7	16.5
	Cyanophyta filamentous	1.3	0.5	1.3	1.0
	Chlorophyta coccoid	0	0	0	0
	Chlorophyta filamentous	1.7	3.5	1.0	2.1
	Chlorophyta flagellates	0	0	0	0
	Chrysophyta centric	0	0	1.0	0.3
	Chrysophyta pennate	3.8	0	0.3	1.4
	Thallophyta	80.0	76.5	79.7	78.7

(1979) report this organism as the most common centric diatom world wide and list this species as neritic and estuarine. The absence of S. costatum in this study is surprising. Several factors (sampling times or limiting factors) may have prevented the observance of this organism in the present study.

Conclusions

Further sampling is needed to further enumerate and identify phytoplankton and periphyton at the five stations at KSC for the Long Term Monitoring Program and Assessment for a probable Polygeneration site. Thallophyta, Cyanophyta coccoid and Chrysophyta pennate were the dominant organisms in this study. Chlorobium sp. was the most abundant Thallophyta. Pennate diatoms were larger and more abundant at station one. The absence of Skeletonema costatum (a common centric diatom) was surprising. Stations four and five appear to be acid marsh swales. Rhabdoderma lineare, a Cyanophyta coccoid found in acid lakes, was abundant in stations four and five.

Literature Cited

American Public Health Association, 1960. Standard Methods for the Examination of Water and Wastewater. 11th edition. American Public Health Association. New York.

Carpenter, E. J. 1971. Annual phytoplankton cycle of the Cape Fear River Estuary, North Carolina. Chesapeake Science 12: 95-104.

Cassin, J. 1978. Phytoplankton floristics of a Long Island embayment. Bulletin of the Torrey Botanical Club 105: 205-213.

Conger, P.S. 1954. Present status of diatom studies in the Gulf of Mexico. Fish Bull. U.S., 89: 227-232.

Conover, S.A.M. 1956. Oceanography of Long Island Sound, 1952-1954. IV. Phytoplankton. Bulletin of the Bingham Oceanographic Collection 15: 62-112.

Edmondson, W. T. 1964. Reproduction rate of planktonic rotifers as related to food and temperature in nature. Ecol. Monogr. 35:61-71.

Ewing, M. S., and T.C. Dorris. 1970. Algal community structure in artificial ponds subjected to continuous organic enrichment. Amer. Midland Natur. 8:565-582.

Gibson, Robert A. 1975. Phytoplanktonic and hydrographic variations in the Indian River System including an inventory of pollution sources, pp. 14-45. In David K. Young, Indian River Coastal Study (Second Annual Report). Compass Publications, Arlington, Virginia.

Hulburt, E. M. 1956, The phytoplankton of Great Pond, Massachusetts. Biological Bulletin 110: 137-168.

Hutchinson, G. E. 1967. A treatise on limnology. Vol. 2. Introduction to Lake Biology and the Limnoplankton. John Wiley and Sons, New York. 1115 pp.

Koller, Albert M. Jr. 1979. Environmental Impact Statment For the Kennedy Space Center. National Aeronautics and Space Administration, Kennedy Space Center, Fla. 396 pp.

Webber, C. F. 1973. Recent Development in the measurement of the Response of Plankton and Periphyton to Changes in Their Environment, In: Bioassay Techniques and Environmental Chemistry. G. Glass. ed., Ann Arbor Science Publishers. Inc., Ann Arbor, pp. 119-138.

Whipple, G. C., G. M. Fair, and M.C. Whipple. 1948. The Microscopy of Drinking Water. John Wiley and Sons, New York. 586 pp.

U. S. Environmental Protection Agency. 1978. Basic Water Monitoring Program, U. S. Environmental Protection Agency, Washington, D. C.

1983
NASA/ASEE SUMMER FACULTY RESEARCH FELLOWSHIP PROGRAM

MARSHALL SPACE FLIGHT CENTER
THE UNIVERSITY OF ALABAMA IN HUNTSVILLE

REFLECTANCE MEASUREMENTS, PART II

Prepared By:	Robert A. Brown, Ph. D., P. E.
Academic Rank:	Professor of Industrial and Systems Engineering
University and Department:	The University of Alabama in Huntsville Department of Industrial and Systems Engineering
NASA/MSFC:	
Laboratory:	Space Science
Division:	Solar-Terrestrial Physics
Branch:	Atomic Physics
MSFC Counterpart:	Donald R Wilkes
Date:	August 12, 1983
Contract No.:	NGT-01-008-021 University of Alabama in Huntsville

C-2

REFLECTANCE MEASUREMENTS, PART II

by

Robert A. Brown, Ph. D., P. E.
Professor of Industrial and Systems Engineering
The University of Alabama in Huntsville
Huntsville, Alabama

ABSTRACT

This year's efforts are a continuation of the project started during the first year, viz., to improve the productivity of spectroreflectometer readings taken to monitor induced contamination of lenses, mirrors, and coatings in the space environment. The efforts were organized in two thrusts.

The first thrust has been to apply more sophisticated modelling techniques to the laboratory data collected last summer in order to produce a more accurate model of the nonlinearities and noise sources of the instrumentation. This would ultimately allow for correction of known anomalies by the digital computer, yielding an anticipated order of magnitude improvement in the accuracy of the reflectance measurements, while reducing the total measuring time.

The second thrust is the construction of and programming for a modernized version of the electronics used in Beckman DK-2 spectroreflectometers. This part of the project suffered because of a schedule lag in fabrication of a modified form of the carrier frequency pickoff built and tested last year. Separate development of the electronics and the computer programming therefore has been partially accomplished.

INTRODUCTION

In last year's report, the importance of measuring the reflectance of paints, lenses, and mirrors was noted. The growing commitment to a U. S. space station, with an in-orbit life of at least ten years, underscores the need to know the reflectance characteristics of thermal coatings, lenses, and mirrors, and their contamination over long periods of time.

In about six months, a Long Duration Exposure Facility will be launched into orbit, where it will remain for a year. One of the experiments on that flight will take reflectance measurements over the course of that year. Suppose that no detectable effects are observed. Does this mean that there are no effects? Not necessarily, of course. We may just not be able to detect the effects over the relatively short time period of the flight relative to the orbital life of a space station.

Similarly, accelerated tests on the ground in simulated space environments can use greater sensitivity of reflectance measurements to shorten the testing time. Typical repeatability of reflectance measurements using current state of the art is about one percent; absolute accuracy is two to three percent. Increased sensitivity and accuracy in reflectance measurements are highly desirable to support the development of long-duration satellites.

Efforts this year have been directed in two thrusts. The first thrust is to apply more sophisticated modelling techniques to the measurement of reflectance. As a trial these techniques, based upon multiple regression methods, have been applied with good results to the data collected last year and analysed by simple regression methods then.

The second thrust has been the systems analysis and development of software to use in the modified and rejuvenated Beckman DK-2 spectroreflectometer system, currently under construction by a contractor.

MULTIPLE REGRESSION METHOD

The results of last year's efforts at measuring the nonlinearities of the detector response are shown again in Table I. Recall that in preparing this table eight separate simple linear regressions were run, one for each of the source-detector-attenuator-gain combinations. Through the special estimating equation developed then, it was possible to remove the effects of a large high-level (instrumental) noise component in the data and provide estimates of the true reflectance with the noise contamination. This showed

Table I -- Simple Linear Regression Results

Source	Detect.	Atten.	Gain	# Pts.	N Est.	%R Est.	Coeff. of Determination
W (200nm.)	PbS	1/10	10	9	0.888mv.	89.2	0.999,991
			100	7	0.828	88.4	0.999,910
			1000	9	0.753	91.1	0.999,860
W (575nm.)	PMx 20	1/1000	1	9	1.194	104.3	0.997,279
			100	6	0.842	94.3	0.999,757
D (575nm.)	PMx 20	1/10	1	6	0.920	94.2	0.999,994
			10	4	0.959	95.7	0.999,992
			100	5	0.967	97.1	0.999,986

that there was either detector non-linearity or a low level (detector) noise component, or both, unaccounted for. One of last year's recommendations was that multiple regression techniques be used to try to extract this second factor from the data. This has now been accomplished.

For the multiple regression, data in each of the separate areas of Table I were lumped together, and an additional factor equal to the product of the Gain times the Attenuator setting was introduced in the prediction equation, as required by the following derivation.

It is assumed now that the total signal applied to the synchronous detection method is the result of three components: A difference signal between the sample and the reference, which it is desired to recover; noise associated with the operation of the detector, which will be amplified along with the signal in the electronics; and a high-level instrumentation noise resulting from phase and commutation errors in the synchronous detection process. (See last year's report for a more detailed discussion of these sources of noise.)

The sample-to-reference ratio, S/R, which we desire to estimate was derived as

$$S/R = [(S+N_T) - N_T]/[(R+N_T) + 1] \qquad \text{VI-1}$$

where we write N_T to represent the <u>total</u> noise corrupting the sample and reference measurements. The total noise is composed of two terms, one independent of and the other dependent upon the gain following the detector.

$$N_T = N_I + K_j * N_D \qquad \text{VI-2}$$

The two noise components are assumed to be stochastically independent and consequently uncorrelated.

Substituting Eq. VI-2 into Eq. VI-1 and rearranging in

the same manner as in the previous report, we arrive at a linear multiple regression model of the following form:

$$y_{i,j} = B(\emptyset) + B(1)*x_{1,i,j} + B(2)*x_{2,i,j} + E_{i,j} \qquad \text{VI-3}$$

where

$x_{1,i,j} = K_j$	The combined gain-attenuator setting.
$x_{2,i,j} = (R+N_T)_{i,j}+1$	The measured reference signal plus one.
$y_{i,j} = (S+N_T)_{i,j}$	The measured sample signal.
$B(\emptyset) = N_I$	The high-level noise.
$B(1) = N_D$	The low-level (gain-dependent) noise.
$B(2) = S/R$	The true reflectance.
$E_{i,j}$	The unique error associated with each observation.

In selecting data for the multiple regression test the data used for the construction of Table I were augmented by data collected last summer but not used for several reasons. First, a replication of the (W,1200nm.) set was not used because there was a suspicion that it was taken while there was a problem with the PbS detector bias supply. Second, some of the very low energy readings produced raw reflectances greater than one causing their rejection.

In choosing to use <u>all</u> the available data in the multiple regression analysis, it was reasoned that this would be a worst-case test; if it could tolerate the suspected bad data and still produce reasonable results, then there would be that much more confidence in the method. Thus it was that sample sizes of 35, 17, and 17 were used. The data used are shown in Appendix A, where

$X(1) = x_1$ above.

$X(2) = x_2$ above.

$X(3) = y$ above.

Appendix B shows the computer program used to implement the multiple regression of Eq. VI-3. The results appear in Table II.

Table II -- Multiple Regression Results

Tungsten Source, 1200nm., Lead Sulphide Detector	
COEFFICIENTS	
INSTRUMENTATION ERROR = B(0) =	-.4112026
DETECTOR ERROR = B(1) =	-6.2791116E-03
TRUE REFLECTANCE = B(2) =	.88571873
PREDICTION ERRORS.	
STANDARD ERROR OF THE ESTIMATE	.40806102
COEFFICIENT OF DETERMINATION	.9673858
(MULTIPLE) CORRELATION COEFFICIENT	.98355772

Deuterium Source, 575nm., Photomultiplier x20 Detector	
COEFFICIENTS	
INSTRUMENTATION ERROR = B(0) =	-1.5115794
DETECTOR ERROR = B(1) =	3.4859903E-02
TRUE REFLECTANCE = B(2) =	.97255672
PREDICTION ERRORS.	
STANDARD ERROR OF THE ESTIMATE	1.1428448
COEFFICIENT OF DETERMINATION	.8402463
(MULTIPLE) CORRELATION COEFFICIENT	.91664949

Tungsten Source, 575nm., Photomultiplier x20 Detector	
COEFFICIENTS	
INSTRUMENTATION ERROR = B(0) =	-1.3421217
DETECTOR ERROR = B(1) =	12.465887
TRUE REFLECTANCE = B(2) =	.94618434
PREDICTION ERRORS.	
STANDARD ERROR OF THE ESTIMATE	.6263425
COEFFICIENT OF DETERMINATION	.8874724
(MULTIPLE) CORRELATION COEFFICIENT	.94205753

Note that the results at 575nm. allow us to compare the technique under two quite different conditions due to the large difference in energy output of the deuterium and tungsten sources at that wavelength. The difference in the true reflectance as measured by the conditions is about 2.6%, well within the normal absolute accuracy for the machine using constant incident energy. Thus the wide variations in slit width and gain setting have been well tolerated by the regression method.

Additional runs were made with modifications to the program to test whether the detectors might have nonlinear response which could be pulled out of this data. Among the variations tried were:

Logarithms of all measurements
Squares of all measurements
Squares of all measurements except gain
Squares of variables with cross product.

The last of these was particularly directed toward pulling out a nonlinear term between gain and incident energy. None of these variations performed as well overall as the simple model described in Eq. VI-3. The results of these variations are shown in detail in Appendix C.

The objective of finding a better way to treat the observational data has been achieved with these results. Further demonstration of the advantages of the method of multiple linear regression now awaits the completion of the fully digital measurement and control system for the DK-2 spectroreflectometer.

FULLY DIGITAL MEASUREMENT AND CONTROL

To aid in the achievement of fully digital measurement and control of the DK-2, a systems analysis was performed, and the results are presented next. Activity analysis of what goes on during a measurement run is shown in Fig. 1.

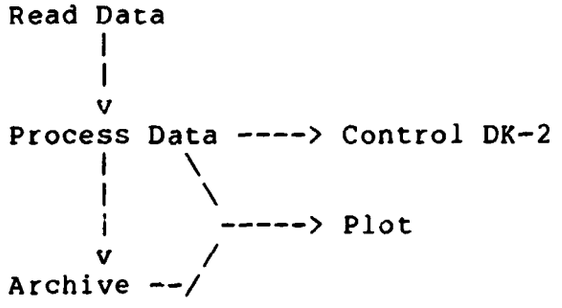

Figure 1 -- Activities during a run

Some data are read regarding the reference and sample values of reflected light. These are then processed, presumably by calculating an updated value of reflectance for the present wavelength. When an endpoint is reached, the machine is set for the next wavelength-slit combination and new data are read until the next endpoint is reached. When all wavelengths have finally been measured, the data are plotted and archived if the plot is found acceptable.

Fig. 1 represents the activities only during one data (or zero) run. To take a system view of the whole process, it would be desirable to also look at and set up for a sequence of runs. A sample time schedule of runs is shown in Fig. 2. This is illuminating because it shows the importance of a turn-on and turn-off sequence of events which digital control of the DK-2 should also handle. It

Turn on (power up).

Command mode -- Set sequence (schedule) of calibration and data runs.

Zero run -- Determine the no-light detector response (DC bias).

Calibration Run -- Find differences between sample and reference paths.

Data Run 1 -- Sample and Reference measurements for sample #1. Plot optional.

:

:

:

Data Run n -- Sample and Reference measurements for sample #n. Plot optional.

Zero run.

Calibration Run -- Same as above; comparison shows any drift. Can possibly interpolate drift corrections for each data run.

Plots (optional).

Turn off (power down).

Figure 2 -- Sample time schedule

also shows that other things beside data runs are important. The zero runs, for establishing the dark response of the detector(s), and the calibration runs, to establish differences between the sample and reference light paths, are essential for accurate work and must be provided for. An additional advantage of going to the all-digital machine is that these corrections can be applied automatically to all data taken within the same time period, increasing the potential for correcting for drift.

Control of the DK-2 can be broken down into two major subheadings. First, there is a requirement for supervisory control, by which is meant a high level of control directed toward the gross behavior of the machine. Examples of tasks to be performed under supervisory control are turning on and off and warming up the equipment, prompting the operator for the next manual step, and selecting a light source and detector combination.

Second, there is low level, feedback control. Such closed-loop control is used to maintain some characteristic of the machine or measurement process constant. In particular this type of control may be used to determine the endpoint (the point at which no further data are needed at a particular wavelength) for measurement.

Three different endpoint criteria can be easily identified:

> i. Constant energy -- Slit width set to maintain constant reference reading, insofar as possible. Number of readings at each wavelength fixed. This is the current mode of operation.
>
> ii. Constant resolution -- Slit width a function of wavelength to keep delta-lambda constant. Number of readings at each wavelength fixed.
>
> iii. Constant error -- Slit width as in (i.) or (ii.) above, but observation time (number of sample measurements averaged) varies to yield constant maximum error of the statistical estimators.

Many activities must be carried out in order to read data. An outline listing of these is contained in Appendix D.

All of the foregoing considerations result in a flow chart for digital reflectance measurement as shown in Fig. 3. It will be noted that there are two loops in the flow chart, an inner loop and an outer loop. The inner loop deals exclusively with the flow of computation during a single data run. It is traversed many times as the machine is directed through many different wavelength settings, and many datum readings for each wavelength in order to implement the desired endpoint criterion, as described above.

Each of the activities shown in the flowchart of Fig. 3 has been further analyzed. It was not possible to completely program any of them except one, for doing so will depend upon particular features of the hardware which is ultimately built. For now, the analysis has stopped with a detailed outline of each of the flowchart activities; these are presented in Appendix E. Finally, Appendix F shows the command mode program, in CB80 BASIC language, a compilable version of BASIC. All other activities will be programmed as subroutines called by this main program.

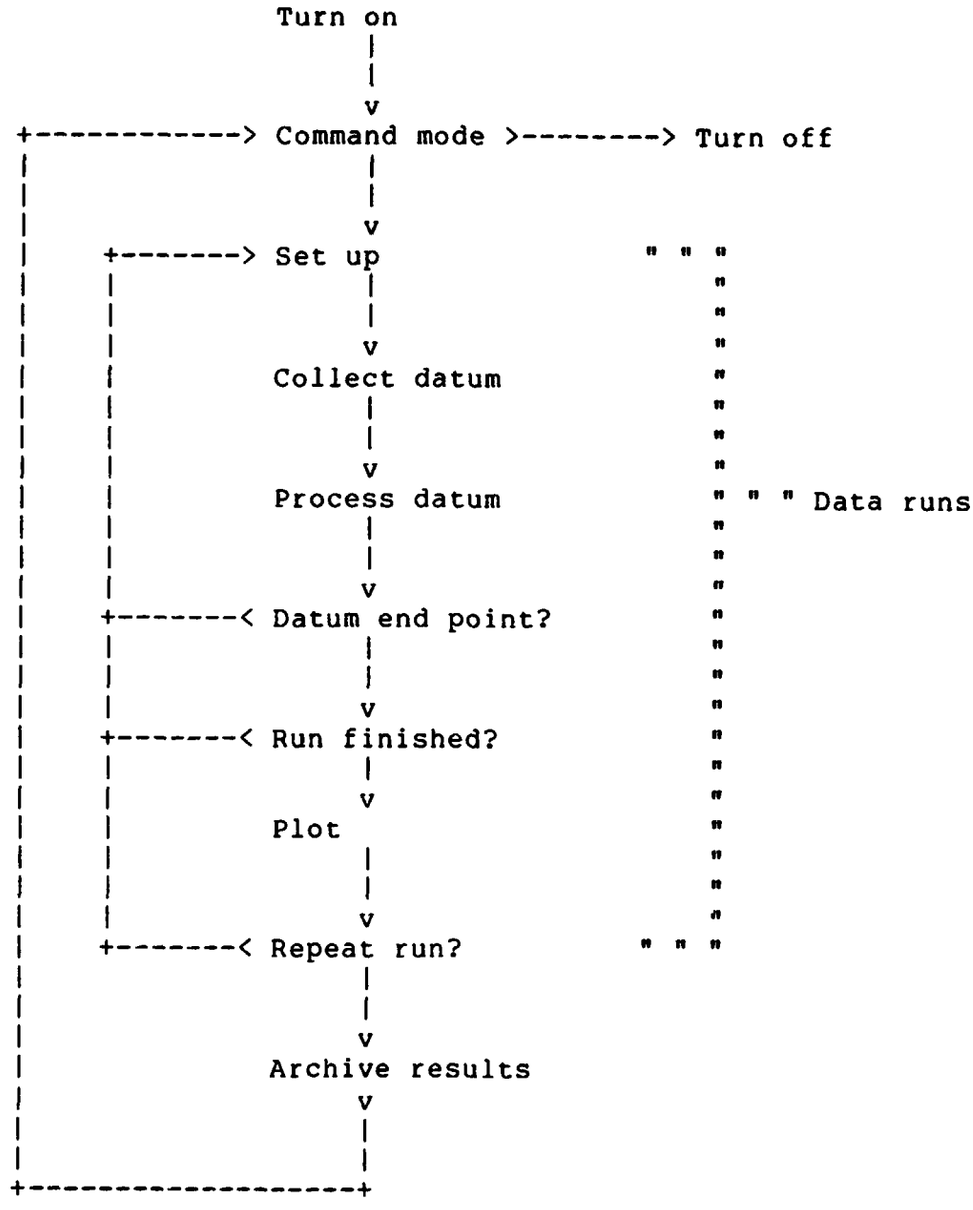

Figure 3 -- Flowchart for digital reflectance measurement

RESULTS AND CONCLUSIONS

The following results have been obtained:

1. An extension of the regression model for reducing reflectance measurement data has been developed.

2. The extended model has been used to analyse an augmented set of data collected last year, with good results.

3. Systems analysis has been done on the whole problem of digital reflectance measurement.

4. An outline of the logic to be implemented in the digital computer and a flowchart of this logic have been prepared.

The following conclusions have been reached:

1. Data reduction of reflectance data by means of multiple regression techniques is feasible.

2. On-line control of the measurement process, in order to increase productivity, repeatability, and accuracy, is feasible.

ACKNOWLEDGEMENTS

My grateful thanks for the opportunity to conduct these investigations go to Mr. Don R. Wilkes, my NASA counterpart and contact for the summer. I wish to thank Dr. G. Karr, ASEE, and NASA for providing the facilitating framework under which this work was performed.

APPENDIX A -- MULTIPLE REGRESSION DATA

TUNGSTEN SOURCE, 1200 nm.

NUMBER OF OBSERVATIONS = 35

X(1)	X(2)	X(3)	X(1)	X(2)	X(3)
100	1.77	1.77	10	1.31	1.26
100	2.04	2.05	10	1.79	1.62
100	2.33	2.29	10	2.73	2.44
100	2.68	2.56	10	3.35	3.01
100	3.01	2.88	10	4.51	4.03
100	3.44	3.30	10	7.03	6.29
100	3.99	3.79	10	9.75	8.67
100	5.26	4.95	10	1.29	1.17
100	7.66	7.14	1	1.45	1.30
100	1.75	1.74	1	1.81	1.62
100	1.98	1.90	1	2.26	2.02
100	2.22	2.17	1	2.76	2.46
100	2.53	2.44	1	3.82	3.46
100	2.88	2.71	1	5.10	4.56
100	3.21	3.06	1	6.52	5.84
100	3.75	3.51	1	8.11	7.23
100	4.88	4.62	1	9.90	8.84
100	7.17	6.54			

DEUTERIUM SOURCE, 575 nm.

NUMBER OF OBSERVATIONS = 17

X(1)	X(2)	X(3)	X(1)	X(2)	X(3)
.1	2.86	2.72	1	2.45	2.34
.1	2.46	2.34	10	6.42	6.24
.1	2.11	2.01	10	3.80	3.70
.1	1.77	1.69	10	2.35	2.28
.1	1.43	1.37	10	1.62	1.59
.1	1.12	1.08	10	1	.97
1	8.65	8.28	100	8.69	8.58
1	7.17	6.85	100	4.68	4.68
1	4.53	4.37			

TUNGSTEN SOURCE, 575 nm.

NUMBER OF OBSERVATIONS = 17

X(1)	X(2)	X(3)	X(1)	X(2)	X(3)
.001	2.81	2.80	.01	5.00	4.63
.001	2.79	2.78	.01	1.39	1.33
.001	2.77	2.76	.1	7.84	7.46
.001	2.73	2.70	.1	5.09	4.94
.001	2.62	2.58	.1	3.72	3.65
.001	2.33	2.22	.1	2.76	2.72
.001	2.03	1.93	.1	1.86	1.81
.001	1.71	1.61	.1	.90	.94
.001	1.08	1.02			

APPENDIX B -- MULTIPLE REGRESSION PROGRAM

```
100  REM  PROGRAM "FINDR2A.2" FOR FINDING REFLECTANCE IN NORTH STAR BASIC
110  REM  USES MULTIPLE REGRESSION TECHNIQUES TO PULL OUT DETECTOR AND
120  REM  INSTRUMENTATION RMS NOISE.
130  REM  COPYRIGHT 1983 BY ROBERT A. BROWN
140 P = 2 \ REM  # OF INDEPENDENT VARIABLES
150 INPUT "NUMBER OF OBSERVATIONS ", N
160 DIM X(P+1,N), S(P+1,P+1), B(P+1), E(N)
170 FOR J = 1 TO N
180     PRINT "OBS'N ", J,"  ENTER X1,...,XP,Y "
190     FOR I = 1 TO P+1
200          INPUT1 "  ", X(I,J)
210          IF I=2 THEN X(I,J)=X(I,J) + 1   \ REM  TRANSFORM X(2)
220     NEXT I
230     PRINT
240 NEXT J  \ REM  ALL DATA IN, NOW COMPUTE SUMS OF SQUARES
250 PRINT\PRINT\PRINT "CALCULATING SUMS"
260 FOR I = 1 TO P+1 \ REM FIND SUMS OF VARIABLES
270     FOR J = 1 TO N
280          X(I,0)=X(I,0) + X(I,J)
290     NEXT J
300 NEXT I
310 PRINT\PRINT\PRINT "CALCULATING MEANS"
320 FOR I = 1 TO P+1 \ REM  SUBTRACT OFF MEANS OF VAR'S.
330     X(I,0) = X(I,0)/N \ REM  CALCULATE MEAN OF I'TH IND. VAR.
340     FOR J = 1 TO N
350          X(I,J) = X(I,J) - X(I,0)
360     NEXT J
370 NEXT I
380 PRINT\PRINT\PRINT "CALCULATING SUMS OF SQUARES"
390 FOR I = 1 TO P+1  \ REM  FIND SUMS OF SQUARES
400     FOR I1 = 1 TO I
410          FOR J = 1 TO N
420               S(I,I1) = S(I,I1) + X(I,J)*X(I1,J)
430          NEXT J
440          IF I1<>I THEN S(I1,I) = S(I,I1)
450     NEXT I1
460 NEXT I
470 PRINT\PRINT\PRINT "CALCULATING COEFFICIENTS"
480 B(0) = X(P+1,0)
490 FOR I = 1 TO P
500     B(I) = S(I,P+1)/(S(I,I)+1E-64)  \ REM TO PREVENT DIVIDE BY ZERO ERROR
510     B(0) = B(0) - B(I)*X(I,0)
520 NEXT I
530 FOR I = 0 TO P  \ REM PRINTOUT
540     IF I=0 THEN PRINT "INSTRUMENTATION ERROR = ",
550     IF I=1 THEN PRINT "DETECTOR ERROR = ",
560     IF I=2 THEN PRINT "TRUE REFLECTANCE = ",
570     PRINT "B(",I,") = ", B(I)
580 NEXT I
590 PRINT\PRINT\PRINT "CALCULATING PREDICTION ERRORS."
```

```
600 FOR J = 1 TO N
610     E(J) = X(P+1,J)  \ REM  PUT IN Y VALUE
620     FOR I = 1 TO P
630          E(J) = E(J) - B(I)*X(I,J)
640     NEXT I
650     E(0) = E(0) + E(J)*E(J) \ REM  GET ERROR SUM OF SQUARES
660 NEXT J
670 C = E(0)/S(P+1,P+1)
690 C1 = 1-C
700 IF C1<=0 THEN C2=0 ELSE C2 = SQRT(C1)
710 IF P = 1 THEN C2 = C2*SGN(B(1))
720 E = SQRT(E(0)/(N-(P+1)))  \ REM STD. ERROR OF ESTIMATE
730 PRINT "STANDARD ERROR OF THE ESTIMATE", TAB(50),E
740 PRINT "COEFFICIENT OF DETERMINATION", TAB(50), C1
750 PRINT "(MULTIPLE) CORRELATION COEFFICIENT", TAB(50), C2
760 END
```

APPENDIX C -- OTHER RESULTS

FINDR2B.2 -- LOGS OF ALL MEASUREMENTS

W1200
CALCULATING COEFFICIENTS

INSTRUMENTATION ERROR = B(0) =	-.9471414
DETECTOR ERROR = B(1) =	-2.1879843E-02
TRUE REFLECTANCE = B(2) =	.97156212

CALCULATING PREDICTION ERRORS.

STANDARD ERROR OF THE ESTIMATE	7.6973973E-02
COEFFICIENT OF DETERMINATION	.983804
(MULTIPLE) CORRELATION COEFFICIENT	.99165538

D575
CALCULATING COEFFICIENTS

INSTRUMENTATION ERROR = B(0) =	-1.0936337
DETECTOR ERROR = B(1) =	.12120414
TRUE REFLECTANCE = B(2) =	1.0045559

CALCULATING PREDICTION ERRORS.

STANDARD ERROR OF THE ESTIMATE	.3084682
COEFFICIENT OF DETERMINATION	.8493336
(MULTIPLE) CORRELATION COEFFICIENT	.92159297

W575
CALCULATING COEFFICIENTS

INSTRUMENTATION ERROR = B(0) =	-.6770683
DETECTOR ERROR = B(1) =	6.4784281E-02
TRUE REFLECTANCE = B(2) =	.98647691

CALCULATING PREDICTION ERRORS.

STANDARD ERROR OF THE ESTIMATE	.14744318
COEFFICIENT OF DETERMINATION	.9440524
(MULTIPLE) CORRELATION COEFFICIENT	.97162359

FINDR2C.2 -- SQUARES OF ALL MEASUREMENTS

W1200
CALCULATING COEFFICIENTS

INSTRUMENTATION ERROR = B(0) =	4.094836
DETECTOR ERROR = B(1) =	-8.1754428E-04
TRUE REFLECTANCE = B(2) =	.79860265

CALCULATING PREDICTION ERRORS.

STANDARD ERROR OF THE ESTIMATE	4.987219
COEFFICIENT OF DETERMINATION	.9474212
(MULTIPLE) CORRELATION COEFFICIENT	.97335564

D575
CALCULATING COEFFICIENTS

INSTRUMENTATION ERROR = B(0) =	-4.94967
DETECTOR ERROR = B(1) =	3.284767E-03
TRUE REFLECTANCE = B(2) =	.94226116

CALCULATING PREDICTION ERRORS.

STANDARD ERROR OF THE ESTIMATE	10.871484
COEFFICIENT OF DETERMINATION	.8397751
(MULTIPLE) CORRELATION COEFFICIENT	.91639244

W575
CALCULATING COEFFICIENTS

INSTRUMENTATION ERROR = B(0) =	-4.46891
DETECTOR ERROR = B(1) =	1093.2991
TRUE REFLECTANCE = B(2) =	.90094516

CALCULATING PREDICTION ERRORS.

STANDARD ERROR OF THE ESTIMATE	5.6067258
COEFFICIENT OF DETERMINATION	.8656901
(MULTIPLE) CORRELATION COEFFICIENT	.93042469

FINDR2D.2 -- SQUARES OF ALL MEASUREMENTS EXCEPT GAIN

W1200
CALCULATING COEFFICIENTS

INSTRUMENTATION ERROR = B(Ø) =	4.592471
DETECTOR ERROR = B(1) =	-8.7473041E-02
TRUE REFLECTANCE = B(2) =	.79860265

CALCULATING PREDICTION ERRORS.

STANDARD ERROR OF THE ESTIMATE	5.073625
COEFFICIENT OF DETERMINATION	.9455835
(MULTIPLE) CORRELATION COEFFICIENT	.97241118

B575
CALCULATING COEFFICIENTS

INSTRUMENTATION ERROR = B(Ø) =	-5.940334
DETECTOR ERROR = B(1) =	.33068476
TRUE REFLECTANCE = B(2) =	.94226116

CALCULATING PREDICTION ERRORS.

STANDARD ERROR OF THE ESTIMATE	10.644372
COEFFICIENT OF DETERMINATION	.8463996
(MULTIPLE) CORRELATION COEFFICIENT	.91999978

W575
CALCULATING COEFFICIENTS

INSTRUMENTATION ERROR = B(Ø) =	-4.809397
DETECTOR ERROR = B(1) =	113.85488
TRUE REFLECTANCE = B(2) =	.90094516

CALCULATING PREDICTION ERRORS.

STANDARD ERROR OF THE ESTIMATE	5.7246838
COEFFICIENT OF DETERMINATION	.8599793
(MULTIPLE) CORRELATION COEFFICIENT	.92735069

FINDR3.2 -- SQUARES OF VARIABLES WITH CROSS PRODUCT

W1200
CALCULATING COEFFICIENTS

INSTRUMENTATION ERROR = B(0) =	.7425231
DETECTOR ERROR = B(1) =	-8.1754428E-04
TRUE REFLECTANCE = B(2) =	.79860265
CROSS-SQRS = B(3) =	4.0561396E-05

CALCULATING PREDICTION ERRORS.

STANDARD ERROR OF THE ESTIMATE	4.5835647
COEFFICIENT OF DETERMINATION	.9542869
(MULTIPLE) CORRELATION COEFFICIENT	.97687609

D575
CALCULATING COEFFICIENTS

INSTRUMENTATION ERROR = B(0) =	-9.2951087
DETECTOR ERROR = B(1) =	3.284767E-03
TRUE REFLECTANCE = B(2) =	.94226116
CROSS-SQRS = B(3) =	7.3774898E-05

CALCULATING PREDICTION ERRORS.

STANDARD ERROR OF THE ESTIMATE	25.887292
COEFFICIENT OF DETERMINATION	.0358762
(MULTIPLE) CORRELATION COEFFICIENT	.18941013

W575
CALCULATING COEFFICIENTS

INSTRUMENTATION ERROR = B(0) =	-9.8909567
DETECTOR ERROR = B(1) =	1093.2991
TRUE REFLECTANCE = B(2) =	.90094516
CROSS-SQRS = B(3) =	77.201779

CALCULATING PREDICTION ERRORS.

STANDARD ERROR OF THE ESTIMATE	17.848107
COEFFICIENT OF DETERMINATION	-.4443783
(MULTIPLE) CORRELATION COEFFICIENT	0

APPENDIX D -- READ DATA ACTIVITIES

A. Monochromator setting.
B. Slit setting.
C. Light source setting:
    1. Setting.
        a. Deuterium.
        b. Tungsten.
    2. Verifying.
D. Detector setting:
    1. Type setting.
        a. Lead sulphide (PbS).
        b. Photomultiplier x 1 (PM x 1).
        c. Photomultiplier x 20 (PM x 20).
    2. Gain setting (in electronics).
        a. x1 to x10,000
        b. x10 increments maximum (min. of four decades).
    3. Verifying.
E. Power on or off.
    1. Items.
        a. Electronics.
        b. Deuterium lamp.
        c. Photomultiplier tube high voltage.
        d. Lead sulphide detector bias.
    2. Verifying -- cf. C2 and D2 above.
F. Reference/sample mirror position.
    1. Reference.
    2. Sample.

APPENDIX E -- SUBROUTINE OUTLINES

I. TURN-ON FUNCTIONS

- A. Electronics.
  - 1. Power up.
  - 2. Calibrate gains.
- B. Deuterium lamp.
  - 1. Heaters
  - 2. Delay; may go on and come back to this.
  - 3. High voltage.
  - 4. Delay; ditto (2) above.
- C. PbS detector bias supply.
  - 1. Power up.
  - 2. Calibrate (?).
- D. Photomultiplier (PM) tube high voltage.
  - 1. Power up.
  - 2. Calibrate(?).
- E. Initialize Status Vector in COMMON area.

II. COMMAND MODE FUNCTIONS

- A. Prompt operator; get
  - 1. Description of next test series.
  - 2. Feedback control mode.
    - a. Constant energy.
    - b. Constant delta-lambda.
    - c. Constant error.
  - 3. Optional plot instructions.

B. Set up for (A.).

1. Batch-mode command list.

2. Set Status Vector.

C. Turn off Repeat Run Flag in Status Vector.

D. Provide overall abort capability.

E. Receive control from Archive Results: More to do?

1. Yes -- to (B.) above.

2. No -- to Turn Off.

III. STATUS VECTOR

A. Linear array.

1. Vector represents the current "state" of the process. "State" includes

a. Machine settings.

b. Decision variables for entering each of the possible next states.

2. Elements are integers.

3. Type of contents:

a. Flags -- 16 bits.

i. 0000H = False.

ii. 0FFFFH = True.

b. Numbers

i. If integer, then the number itself.

ii. If real, then the index to a linear array of real numbers.

B. Similar to a "stack".

1. A means of passing information from one program function to another.

2. Except,

a. No last-in-first-out rule.

b. Constant size (but not all items are necessarily meaningful at any given time).

C. Elements.

Ø. Next phase pointer.

1. Dicke mode on/off.

2. Detector code.

3. Source code.

4. Amplifier gain.

5. A/D converter value.

6. Mirror position code (Dicke mode off).

7. End point decision value.

8. Current decision value.

9. End-point decision mode.

1Ø. Repeat run flag.

11. Repeat measurement flag.

12. End of run range.

13. Abort flag.

IV. SET UP

A. Read and interpret Status Vector (repeat run?).

B. Prompt operator to insert sample or reference.

C. Make machine settings (and verify).

1. Monochromator.

2. Slits.

3. Detector.

4. Electronics gain.

5. Source.

D. N. B.: Order of taking data should be randomized.

1. Eliminate electronic drift.

2. Eliminate cumulative mechanical tolerance errors.

V. COLLECT DATUM (ONE READING)

A. Mirror position (if in Dicke mode).

1. Sample.

2. Reference.

3. Store (in Status Vector?).

B. A/D converter.

1. Read.

2. Store (in Status Vector?).

VI. PROCESS DATUM

A. Fetch datum from Status Vector.

B. Increment data counter.

C. Calculate statistic(s).

1. Mean

2. Error estimates, corrected reflectance.

D. Place decision statistics in Status Vector.

VII. END POINT DECISION

A. Fetch statistics form Status Vector.

1. Current value.

2. Decision value.

B. Fetch end-point decision mode code.

C. Fetch decision mode program.

D. Decide, alter repeat measurement flag.

1. Take more data at current machine settings (set).

2. Go on to next settings (reset).

E. Branch to Set Up. Implies

1. Resetting mechanical and switch settings.

a. Monochromator.

b. Slits.

c. Etc.

2. Ensures that setting errors will be included in error estimates.

VIII. RUN FINISHED DECISION

A. Fetch last monochromator setting.

B. Compare to end of run range.

C. Branch.

1. Repeat.

a. Set Repeat Run Flag in Status Vector.

b. Go to Set Up.

2. Go to Plot routine for visual inspection.

IX. REPEAT RUN DECISION

A. Prompt operator to:

1. Repeat run.

2. Archive results.

3. Abort.

B. Accept input and execute.

X. ARCHIVE RESULTS

A. Call up data base program.

B. Enter data from Status Vector.

C. Execute data base storage.

D. Return to Command Mode.

XI. TURN-OFF

A. Prompt operator to remove last sample.

B. Reverse Turn-On functions.

APPENDIX F -- EXAMPLE DIGITAL CONTROL PROGRAM

```
REM     COMMAND.BAS -- THE CENTRAL PROGRAM FOR INTERPRETING
REM     COMMANDS TO RUN THE BECKMAN DK2 SPECTROREFLECTOMETER.
REM     WRITTEN IN CB-80 BY ROBERT A. BROWN, 8/10/83


REM     DECLARATIONS

        COMMON STATUS(1)
        INTEGER FALSE, TRUE, STATUS
        STRING ALPHA
        N = 15
        DIM STATUS(N)
        DEF     TURN.ON          EXTERNAL
        FEND
        DEF     SET.UP           EXTERNAL
        FEND
        DEF     COLLECT.DATUM    EXTERNAL
        FEND
        DEF     PROCESS.DATUM    EXTERNAL
        FEND
        DEF     END.POINT        EXTERNAL
        FEND
        DEF     RUN.FINISHED     EXTERNAL
        FEND
        DEF     PLOT             EXTERNAL
        FEND
        DEF     REPEAT.RUN       EXTERNAL
        FEND
        DEF     ARCHIVE.RESULTS  EXTERNAL
        FEND
        DEF     TURN.OFF         EXTERNAL
        FEND


REM     DEFINE CONSTANTS

        FALSE = 0       :\DEFINE TRUE AND FALSE
        TRUE = 0FFFFH


REM     START OF PROGRAM

        FOR I=0 TO N
                STATUS(I) = 0    :\INITIALIZE STATUS VECTOR
        NEXT I

        CALL TURN.ON             :\TURN ON & WARM UP ALL EQUIPMENT
        GOTO DISPATCHER
1       CALL SET.UP              :\SET UP MACHINE
        GOTO DISPATCHER
2       CALL COLLECT.DATUM       :\GET THE DATUM FOR A WAVELENGTH
```

```
        GOTO DISPATCHER
3       CALL PROCESS.DATUM      :\DO THE DATA REDUCTION
        GOTO DISPATCHER
4       CALL END.POINT          :\ENOUGH DATA?
        GOTO DISPATCHER
5       CALL RUN.FINISHED       :\ALL WAVELENGTHS DONE?
        GOTO DISPATCHER
6       CALL PLOT               :\PLOT RESULTS FOR VALIDITY CHECK
        GOTO DISPATCHER
7       CALL REPEAT.RUN         :\DO IT OVER?
        GOTO DISPATCHER
8       CALL ARCHIVE.RESULTS    :\SAVE THE RUN
        GOTO DISPATCHER
9       CALL TURN.OFF           :\ALL DONE -- SECURE
        STOP

DISPATCHER:     :\THIS ROUTINE CONSULTS THE STATUS VECTOR AND
                :\DETERMINES THE NEXT ACTIVITY TO BE DONE.

        IF STATUS(13) THEN      \FIRST, CHECK THE ABORT FLAG
                PRINT "RUN ABORTED" :\
                GOTO 1

        ON STATUS(Ø) GOTO 1, 2, 3, 4, 5, 6, 7, 8, 9

        END
```

1983

NASA/ASEE SUMMER FACULTY RESEARCH PROGRAM

MARSHALL SPACE FIGHT CENTER
THE UNIVERSITY OF ALABAMA IN HUNTSVILLE

INVESTIGATION OF THE ARC CLOUD COMPLEX

Prepared By:	Kenneth C. Brundidge, Ph.D.
Academic Rank:	Professor
University and Department:	Texas A&M University Department of Meteorology
NASA/MSFC:	
Division:	Atmospheric Sciences
Branch:	Atmospheric Effects
MSFC Counterpart:	James E. Arnold, Ph.D.
Date:	August 12, 1983
Contract No.:	NGT 01-008-021 The University of Alabama in Huntsville

INVESTIGATION OF THE ARC CLOUD COMPLEX

BY

Kenneth C. Brundidge
Professor of Meteorology
Texas A&M University
College Station, Texas

ABSTRACT

Thunderstorm gust fronts, frequently identifiable as arc clouds, have come to be recognized as triggering mechanisms for new convective activity at points of intersections. Arc clouds are recognizable as such only by high resolution meteorological satellite observations and may take on several configurations, depending upon the circumstances. A situation in which an arc cloud is associated with a large convective area is called an arc cloud complex. A detailed analysis is presented of several arc cloud complex cases, based upon a combination of satellite, radar and conventional meteorological observations. Use also is made of the Man-Computer Interactive Data Access System (McIDAS) of the Atmospheric Sciences Division of the Systems Dynamics Laboratory, Marshall Space Flight Center. A discussion is presented describing the circumstances which led to the development of the arc clouds and their subsequent impact upon their environment.

Acknowledegements

My thanks are extended to all the members of the Atmospheric Science Division for their friendship and hospitality. In particular, I thank Dr. Jim Arnold for directing me toward this study of arc clouds and for our discussions of mesoscale systems. I also greatly appreciate his help and that of Gary Jedlovec and Dave Keller in guiding me thr ugh the idiosyncrasies of data procurement via McIDAS.

LIST OF FIGURES

Figure	Title	Page
1	Surface Temperature and Pressure Fields for 1200 GMT, 17 May 1982	VII-17
2	GOES-EAST Infrared Image at 1230 GMT	VII-18
3	GOES-EAST Visible Image at 1300 GMT	VII-19
4	RAOB Sounding at SEP for 1200 GMT, 17 May 1982	VII-20
5	Surface Divergence Field at 1700 GMT	VII-20
6	Arc Cloud Complex at 1930 GMT	VII-20
7	Surface Temperature and Pressure Fields for 2000 GMT	VII-21
8	GOES-EAST Visible Image at 2001 GMT	VII-22
9	GOES-EAST Infrared Image at 1100 GMT, 19 May 1982	VII-23
10	Surface Temperature and Pressure Fields for 1200 GMT, 19 May 1982	VII-24
11	GOES-EAST Visible Image at 1200 GMT	VII-24
12	Surface Divergence at 1200 GMT, 19 May 1982	VII-25
13	Visible Image and Temperature at 1600 GMT	VII-25
14	Visible Image and Temperature at 2200 GMT	VII-26
15	RAOB at OKC for 12 GMT, 19 May 1982	VII-26

Introduction

Over the past 10-15 years, the high-resolution meteorological satellite has been revealing atmospheric convective activity on a scale which is up to two orders of magnitude smaller than can be resolved by standard meteorological observations. This unique view of atmospheric events provided by the Geostationary Operational Environmental Satellite (GOES) also has shown that frequently convection is organized along lines and that where these lines intersect is a point where intense convection is likely to develop (Purdom, 1973, 1976).

Thunderstorm areas are the precursors of a line of low-level convective cells which Purdom (1973, 1976, 1979) has called collectively the "arc cloud." This line has been identified by Purdom as the boundary of the mesohigh which is created in the surface pressure field by the cold downdrafts from the thunderstorm cells (Byers and Braham, 1949; Fujita, 1963). The leading edge of the cold air spreads outward from the storm area like a gravity current. On the basis of measurements made on an instrumented tower, Charba (1974) and Goff (1976) have found that this leading surface has many of the properties of a cold front in that a gusty wind shift (called the gust front) occurs as it passes a given point and there is a sharp drop in temperature and dewpoint temperature.

As it undercuts and lifts the warmer, moister air ahead of it, the arc cloud is formed where conditions permit. A numerical model of gust fronts in good agreement with the tower observations has been developed by Mitchell and Hovermale (1977). Phenomena resembling the arc cloud gust front but occurring in the trade wind flow of the tropics have been described by Zipser (1969) and Black (1978).

Thunderstorm gust fronts, as delineated by their associated cloud pattern and observed by GOES, may have a variety of shapes and scales. Gurka (1976) has examined some 80 gust front situtations and found that he could classify them into four types, three of which were associated with thunderstorms. The greatest number of these (66) were called type 1 and found to be "generally formed by a shortwave trough embedded in northwesterly flow aloft or in the southwesterly flow ahead of a large-scale upper trough." With an eastward moving system, the gust front was found to be on the southern and eastern edges of the convective area.

Gurka distinguished between three versions of type 1 front situations. Type 1A represents a cluster of thundestorms with an oval-shaped leading edge and with the anvil cirrus blowing northward with anticyclonic curvature. An arc cloud as such is not apparent in the satellite imagery for this form. Type 1B has the general appearances of the type 1A storm mass except that a comma-shaped appendage appears on its south side. Extending westward from the appendage is a solid line of growing convective cells, i.e. and arc cloud; cirrus blow-off from the arc cloud appears in the otherwise clear area between the arc and the main cloud mass. Type 1C is a weaker version of

1B with the arc cloud broken into segments of low-level convection and with a clear area to the north side of the arc. Although not stated by Gurka, it appears that types 1B and 1C are stages in the dissipation of a type 1A storm.

Maddox (1980) has described a type of storm area which he has named a "mesoscale convective complex" (MCC). He states that the genesis of the MCC lies with a number of individual thunderstorms which develop in close proximity to form large storm complex. The growing storms entrain mid-tropospheric air which becomes involved in the storms as evaporationally-cooled downdrafts. The downdrafts produce mesohighs and cold outflow boundaries at the ground. A merging of the mesohighs produces a single large mesohigh and outflow boundary. Intense new convection is produced in the convergence zone at the outflow boundary and rain falls over a very large area.

In order to be called an MCC by Maddox, the storm area must show certain characteristics in the IR satellite imagery:

1. There must be a contiguous cloud shield with IR temperature less than -32°C over an area of at least $10^5 km^2$.
2. The interior of the cold cloud region must have an IR temperature no warmer than -52°C over an area greater than $5x10^4 km^2$.

Other requirements are that the size criteria be maintained for at least 6 hrs and that the cloud shield be nearly circular. These criteria result in a storm area looking very much like type 1A storms in Gurka's (1976) classification system. Gurka imposed no limitations on size or conditions on cloud-top temperature, however.

Maddox hypothesizes that a dissipation stage of the MCC is reached when "intense, convective elements no longer develop," which is indicated in the satellite imagery by a chaotic appearance of the clouds. One of the reasons he suggested for this demise is that 'the cold air dome beneath the system may become so intense that the surface convergence zone moves away from the region of mid-and upper-level subsidence." This outward movements of the outflow boundary while dissipation of the main storm area is occurring suggests that an arc cloud would appear in the satellite imagery and that the MCC takes on the appearance of a type 1B or 1C cloud pattern in Gurka's (1976) classification system.

The arc cloud cases to be discussed here bear a close resemblence to the MCC in their early stages, although perhaps not meeting all of the conditions demanded by Maddox. Because of this similarity and the similarity to the type 1 cloud patterns described by Gurka (1976), they will be referred to as "arc cloud complexes" (ACC).

The importance of the study of ACC's lies in the fact that the arc clouds associated with such systems may be maintained for many hours after the main storm area has begun to dissipate and that they can trigger new storm development of significant size hundreds of miles away from their origin. Thus, there can develop a sequence of storm events extending over several days. It should be noted that the scale of the ACC is meso-β to meso-α (Orlanski, 1975) while being composed of elements in the meso-γ range.

Thus as noted earlier, many of the features which are observable by satellite and radar measurements cannot be resolved by the synoptic observations, forcing one to draw conclusions based to a large degree on surmise.

Case 1 - 17 May, 1982

During the predawn hours of 17 May, 1982 an arc cloud appeared in north, central Texas. Over the next 10 hrs., it moved southward and outward from its source region at speeds which varied from about $3ms^{-1}$ on its east side to about $12ms^{-1}$ on its south side and about $6ms^{-1}$ on its western flank. In its late stages it marked a line of convective storms extending northward from the Gulf Coast of eastern Texas to another storm area in Missouri. It also appears to have been involved in storm development during the evening of 17 May in far west Texas.

The progenitor of this arc cloud was found from examination of the synoptic weather maps to have been a storm area that formed in Kansas and western Oklahoma on 16 May, 1982. This storm area was on the east side of a stationary front analyzed by the National Weather Service (NWS) to extend from South Dakota to the Texas Panhandle and beyond to the southeast corner of New Mexico. This was found to be a very shallow front and very difficult to justify south of Kansas on the basis of the temperature fields of the lower troposphere. The storm area expanded southward into the Texas panhandle during the night of 17 May and showed signs of becoming an ACC in the IR imagery of GOES-EAST about 1000 GMT.

To study the chain of events for this case hourly, sectional maps for the period 0900 GMT, 17 May through 0000 GMT, 18 May were analyzed for temperature and pressure. Temperature was analyzed at 2°F increments and altimeter sitting was analyzed at an increment of 0.03 inches of Hg which corresponds to a 1mb increment in pressure. For the most part the reported data were all accepted as valid and utilized and the analysis was subjective. However, features in the temperature and pressure fields were carefully checked for continuity. Also, the analyses were coordinated with the GOES-EAST imagery and the NWS Radar Summary maps. Other items used in the study were the NWS maps at the mandatory RAOB levels for 0000 GMT and 1200 GMT on 17 May; soundings from OKC, AMA, SEP, CGG, MAF, VCT and LCH; and analysis of divergence and vertical cross sections obtained through the Man-Computer Interactive Data Access System (McIDAS) of NASA's Marshall Space Flight Center.

Figure 1 shows the analysis of the surface reports at 1200 GMT, 17 May. The heavier lines represent the pressure analysis and the thin lines are isotherms. The light shading represents areas in which MDR level 1 reflectivity was reported according to the 1135 GMT Radar Summary. It is assumed that light rainfall was occuring in these areas. MDR levels 3 and 5 are shown by gradations in shading. The southern and eastern edges of the ACC are indicated by the squall line symbolism. The GOES-EAST IR imagery

10 hrs. earlier shows an MCC-like storm covering most of Kansas, three-fourths of Oklahoma and the eastern half of the Texas panhandle. The Radar Summary at the time showed a broad band of levels 3 and 5 cells extending from a point somewhere south of Lubbock, TX. (LBB) northeastward into southern Kansas. Tops of these thunderstorms ranged up to 59×10^3ft and hail was reported at one point in Kansas. From then until the time of Fig. 1, the axis of strongest convection slowly rotated clockwise, pivoting about the cell cluster between Lubbock and Abiline (ABI). Thus, the axis of levels 3 and 5 came into a position along the southern and eastern edges of the ACC shown in Fig. 1. During the period the cloud tops lowered and warmed.

The pressure analysis in Fig. 1 shows the ACC mesohigh and the temperature analysis shows a dominance of cold air along the high pressue axis. A sharp temperature gradient lies along the gust front under the strongest convection. In their Thunderstorm Project report, Byers and Braham (1949) remark that a pocket of colder temperature is usually left behind by the gust front of an individual moving thunderstorm. This remaining layer of cold air was observed to gradually undergo modification due to turbulent mixing. These observations match the conditions found in this ACC Case, making it appear that the ACC behaves as a single, huge thunderstorm.

One other feature that should be noted in Fig. 1 is the numerous reports of fog in eastern Texas and Louisiana. Warm (note isotherms), moist surface air in this area was a ready source of energy for storm development. The 1200 GMT sounding at Longview, TX (GGG) shows the layer from the ground to 850 mb was saturated and conditionally unstable. On the other hand, the 1200 GMT sounding at Midland, TX. (MAF) was absolutely stable to 800 mb. The surface dewpoint temperature increased through the morning hours over Louisiana and southern Arkansas as the southerly flow from the Gulf of Mexico increased in that area.

Although not shown here, it should be noted that the ACC in Fig. 1 lies just to the east of a major trough line at 500 mb. It is possible that a short wave is moving through this trough at this time but it also is possible that the minor changes that could be made in the NWS analysis of heights and temperatures simply reflect the influence of the ACC on the larger-scale environment.

The GOES-EAST IR imagery for 1230 GMT is given in Fig. 2 and the visible imagery of 1300 GMT is Fig. 3. The arc cloud appears in Fig. 2 only as a faint band of clouds at a temperature warmer than -32°C, according to the MB scale; however, it is easily seen in the visible imagery of Fig. 3. By this time the parent storm has essentially split into an eastern and a western portion. It is the eastern portion which appears to be connected with the arc cloud and to a large degree matches Gurka's type 1B gust front. However, rather than cirrus blowoff, the clouds behind the arc cloud are middle and lower level clouds having temperatures around -20°C to -30°C. The arc cloud marks the position of the squall line in Fig. 1 from Waco, TX. (ACT) to west of ABI. It is seen from this that the clouds behind the arc cloud

were still producing precipitation. As will be seen later (Fig. 6) this region eventually became essentially clear of clouds. The western portion of the ACC also slowly dissipated; by 1330 GMT the cloud top temperatures were everywhere in Texas warmer than -32°C and remained that way for the next 6.5 hrs.

By comparing Figs. 1-3, it can be seen that Stephenville, TX (SEP) lies in the outflow region behind the arc cloud and between the two main convective region appearing in Fig. 2. It was the only upper-air sounding station to be so located; Oklahoma City (OKC) lies to the north underneath the upper-level cloud shield. The 1200 GMT sounding at SEP is given in Fig. 4. It is seen that the atmospheric column over SEP was essentially saturated from the ground to somewhere around 500 mb and that the cloudy air was no colder than about -20°C, thus verifying the IR indications in Fig. 3. The wind reports on the right-band side of Fig. 4 show that from the ground to about 830 mb the wind was from a northeasterly direction. Also, the air in this layer can be seen from the sounding to be potentially colder than the air above it, hence it is hypothesized that this is air which has descended in saturated downdrafts and is spreading out behind the arc cloud. This would make the depth of the cold air layer at SEP about 1100m. This may provide an explanation for the superadiabatic layers appearing in the SEP sounding between 500 and 600 mb. The air in the surface layer has wet-bulb potential temperature (θ_w) of 13° - 14°C. The same values of θ_w are found in the layers from 545 to 562 mb and from 458 to 515 mb. Intrusions of colder, dryer air in these layers would produce superadiabatic layers just below them and also provide air for saturated downdrafts with θ_w values matching those in the cold-air dome.

The 1200 GMT sounding at OKC also shows a cold, saturated layer with the same values of θ_w as at SEP. However, at OKC this layer is confined to the lowest 30mb and it is capped by what appears to be a subsidence inversion. Saturated conditions are again found above 640mb, representing the middle and high clouds seen over OKC in Figs. 2 and 3.

A question to be answered then is, where is the intrusion air coming from? The 1200 GMT soundings at MAF and AMA both show air moving from the west with values of θ_w in the mid levels of the troposphere which are close to the required values.

As mentioned earlier, once the arc cloud was formed it expanded outward toward the south. This required a divergent wind field in the surface layer of the sort shown in Fig. 5 for 1700 GMT. The analysis was obtained objectively using the McIDAS and the lines are drawn at an increment of $5 \times 10^{-5} s^{-1}$. The divergence center coincides with the position of the mesohigh at this time and the axis of the convergent region in southeast Texas lies almost along the arc cloud position. A large part of the area encompassed by this convergent region was experiencing rain at this time.

It was possible to accurately pinpoint the time of the arc cloud passage at College Station, TX. (CLL) on the basis of recorded measurements at the Department of Meteorology at Texas A&M University. There, the wind shifted from 120° to 270° at 1610 GMT and the pressure jumped 0.5 mb. The maximum wind gust of 27 mi hr^{-1} (12 ms^{-1}) occured at 1620 GMT. This gust speed matched the arc cloud speed obtained by tracking the arc cloud in the satellite imagery. Rainfall actually started at CLL at 1540 GMT, prior to the arrival of the arc cloud due to a thunderstorm that developed to the west of the station. However, otherwise sequence of events agree with those reported by Charba (1974) in his study of gust fronts.

By 1930 GMT the arc cloud had expanded into a ring of about 800 km diameter (Fig. 6). Continuous thunderstorm activity had occurred on its eastern flank while clearing took place in the central portion of the area. A thin line of only low level convection marks the southernmost portion of the arc cloud and an expanse of stratacumulus remains on the western flank. This situation most clearly resembles a type 1C arc cloud. The positions of the arc cloud at 1400 and 1600 GMT are shown by lines of crosses. A small square in north central Texas gives the position of SEP. All that remains of the western portion of the ACC is the patch of stratacumulus and cirrus over western Oklahoma and the line of cumulus in an arc shape just to the west of SEP and intersecting the western flank of the arc cloud. A close examination of this portion of Fig. 6 reveals a cumulus cell just to the west of this intersection near the New Mexico border. This point also is in a convergent region (Fig. 5) as well as being at the position of the stationary front in Fig. 1. An hour later a cluster of at least 10 towering cumulus appeared at this point (see Fig. 8). In yet another half hour these cumuli melded into a single storm area which in turn became part of a line of storms extending across the eastern portion of New Mexico into Colorado.

The surface analysis for 2000 GMT (Fig. 7) shows the changes that took place over Texas in the 8 hr. period after the time of Fig. 1. The mesohigh became poorly defined and the main precipitation area (shaded) became elongated into a squall line. The isotherms in Fig. 7 still show considerable packing along the squall line and its extension into far west Texas, indicating that the dissipating arc cloud still had the thermal properties of a quasi-cold front but was incapable of initiating new convection in the stable air of south Texas.

The temperatures in Fig. 7 over central Texas indicate warming in that area of 15° - 20°F. Plots of surface temperature versus time were made for MWL, ABI, DFW, ACT, SJT and CLL and compared with plots for DRT and SHV. The latter two stations remained outside the arc cloud through 2000 GMT. It was found that as the arc cloud passed a given station, there was a drop in temperature to a value 6°- 8°C below that at the stations outside the arc. However, within a few hours, the exact period varying from one station to another, the temperature began to rise at a rate which matched that at DRT and SHV. All of the stations reached their maximum temperature within an hour of one another and as the temperature again fell in late afternoon,

the rates again nearly matched. By 0400 GMT on 18, May 1982 a temperature difference of 4°-6°C still existed between stations inside and outside of the arc. This indicates that all of the stations were experiencing the diurnal temperature variation and that the boundary layer within the arc cloud is very slow in modifying for systems as large as ACC's.

Darkow and Livingston (1975) have recommended the use of a quantity called total energy or static energy (Kreitzberg, 1964) in the study and prediction of severe storms. A good approximation to this quantity for a parcel following and invisid, adiabatic process is

$$E_T = C_p T + qz + wL,$$

where the first term on the right is specific enthalpy, the second term is potential energy per unit mass, and the last term is specific latent heat energy (the mixing ratio, w, has been used as an approximation to specific humidity). Kinetic energy has been ignored in this statement because it generally is two orders of magnitude smaller than the other energy components. It follows that E_T shoud be conservative property of a parcel like θ_w or θ_e if the assumptions are satisfied. This quantity was calculated from surface observations for sever l selected times between 0000 GMT, 17 May and 0000 GMT 18 May, 1982. As would be expected, the patterns of E_T were found to primarily reflect the temperature patterns with values, at 0900 GMT as an example, outside the ACC ranging from 325 to 345 Jg^{-1} and from 310 to 320 Jg^{-1} in the cold air inside the ACC perimeter. Parcels at the ground are constantly being replaced by other parcels with different values of E_T or in actuality may be modified by diabatic processes. In particular, the diurnal temperature variation appears in E_T. Also, it was found that the dew-point temperatures inside the arc cloud increased with time at a number of stations, presumably as a consequence of evaporation of rainfall from the earth's surface. Consequently, the difference in values of E_T between the two masses of air had largely vanished at many of the stations by 0000 GMT, 18 May, 1982. Therefore, from the point of view of the total energy, the recovery of energy at the ground which might then be available for future storm development is more rapid than if only internal energy is considered.

Case 2 - 17 May, 1982

Gurka (1976) defined his type 3 gust front cloud pattern as being "a narrow arc-shaped line of convective clouds with fairly uniform tops and no vigorous development along the arc. The arc is clearly separated from the originating cumulonimbus cell or cluster which is usually in its dying stage." This type of arc cloud appears to have developed in western Missouri on the same day as Case 1.

A reexamination of Fig. 1 reveals a mesoscale trough associate with warm temperatures extending from Oklahoma into eastern Kansas. Fig. 2 and 3 show a band of clouds extending roughly along this trough from the broad

cloud mass over Nebraska and western Iowa. The 1300 GMT surface analysis (not shown here) reveals the association of the cloud band with the warm trough even better.

By 1600 GMT the trough had shifted eastward somewhat into Missouri, the associated cloud band also shifted and was composed of high and middle clouds, and growing cummulus. It was beginning to look like a convective arc cloud. A temperature gradient of about 3°C per 100 km existed across Missouri but a packing of isotherms was not evident.

By 1700 GMT rain was falling from the better-developed cumuli in Iowa and northern Missouri and an hour later the cloud band was a thin line of towering cumulus and cumulonimbus stretching from north to south across central Missouri. Severe thunderstorm watches had been issued for eastern Iowa, northeastern Missouri and western Illinois. It may be noted that the presence of vigorous development along the arc in this case is not in agreement with the definition of type 3 cloud patterns.

The situation at 2000 GMT can be seen in Fig. 7 and 8. By this time a pocket of colder temperature (Fig. 7) appeared in central Missouri and the isotherms had become packed along the arc cloud, denoted in Fig. 7 by the squall line symbolism. A mesohigh had formed at the three-state corners of Missouri, Oklahoma, and Arkansas. Over the next several hours, a number of thunderstorms developed in the vicinity of this mesohigh and a convection was forged between the Missouri and Texas squall lines.

As described above, the development of the arc cloud in this case involved a somewhat different scenario than that in Case 1. Here, the arc cloud formed in a preexisting trough and without the presence of a well-developed mesohigh. Rainfall came later. Convergent flow is indicated along this trough by the winds in Fig. 1 and confirmed by the contours in Fig. 5.

The scenario parallels that described by Ulanski and Garstang (1978) for Florida thunderstorms, based on measurements over a dense network (660 km^2) of anemometers and rain guages. They found that convergence and cyclonic vorticity preceded radar echoes and rain by up to 90 min. In the case of the arc cloud developing into a squall line, the space and time scales are much greater than those for individual thunderstorms; however, the chain of events was the same.

Case 3 - 19 May 1982

As in Case 1, the ACC of 19 May, 1982 had its origin during the nighttime hours. Figure 9 is the IR image for 1100 GMT on 19 May and shows a type 2 ACC over Oklahoma. Earlier satellite observations show that this storm area moved northeastward from Texas into Oklahoma and is part of a flow of moisture from the tropics across Mexico and western Texas. Some evidence of this connection can still be seen in Fig. 1.

At this time Oklahoma lies on the east side of a deep longwave trough. There is no indication of a short wave at 850 mb; however, a pronounced short wave (meso β) can be analyzed at the 700 mb level at 1200 GMT over Oklahoma. It is impossible to tell if it is the cause or the effect of the ACC. It appears also with much reduced amplitde at 500 mb.

A portion of the surface map at 1200 GMT appears as Fig. 10. The heavy lines represent a reanalysis of the NWS analysis of pressure at an interval of 1 mb and the thin lines are temperature at 2 deg. interval. The shaded area represents the MDR values according to the 1135 GMT Radar Summary. An area of level 5 echos is seen just to the north of Wichita Falls, TX. (SPS). These analyses show that the storm area is a cold-core mesohigh at the ground A particularly pronounced axis of warmer temperatures appears on the east side of the radar echo pattern which played an important role in subsequent events. The region of warmer temperatures in the south and southeastern portion of Fig. 10 also has higher dewpoint temperatures and thus greater static energy.

This ACC underwent a rapid decay in the next few hours and exhibited a much different behavior than was seen in Case 1. For ease in the following discussion, certain features in Fig. 9 have been labeled. The main storm has been labeled A. B marks the left-hand segment of an arc cloud wich also can be seen in Fig. 9 to extend along the south side of A. Label C is a band of middle and high clouds which had no apparent connection with the ACC at this time. Fig. 11 shows these same features at 1200 GMT. The cloud band, C, has moved eastward as has the mass, A. However, B has remained nearly stationary and in this visible image from GOES-EAST, it can be seen that B contains many towering cumuli. The isolines in Fig. 11 represent surface values of equivalent potential temperature, θ_e, obtained objectively by use of McIDAS. A leading digit, 3, is missing from the θ_e values. The outflow region between A and B has the minimum values of θ_e while the axis of maximum values underneath the cirrus outflow of A reflects the warm axis in Fig. 10.

The field of horizontal divergence for 1200 GMT at the surface is given in Fig. 12 in units of $10^{-5}s^{-1}$. Again, the analysis was obtained objectively. It is seen that divergence dominates within the limits of the ACC. Convergence appears to the south and west of the ACC. In particular, note the divergence maximum just to the north of SPS where level 5 echos were being observed. It is expected that strong downdrafts were occuring in this area.

Fig. 13 shows the situation at 1600 GMT. Again, features A, B and C from Fig. 9 have been identified. The isolines are isotherms in deg. F. It is seen that the cloud mass had dissipated in the strongly-divergent region shown in Fig. 12. It appears that rain-out has occurred here, leaving a thin arc cloud on the south side of the ACC. Also, it appears that the outflow has spread westward to the cloud band, C, making it an extension of the arc cloud. Cloud band C is composed of stratacumulus with some cirrus according to the hourly observations. At this time, the greatest temperature differences exist between OKC and DFW to the south and between OKC and AMA to the west. This is because the temperature outside the arc cloud had gone up by a greater amount than they had at stations inside the arc

cloud. After 1600 GMT, these temperature difference decreased and the arc cloud in north Texas lost much of its definition by 1630 GMT.

This ACC differed from the one in Case 1 in that the arc cloud itself in this instance showed no independent motion. The entire mass, including the arc cloud once it was formed (will delineated by 1445 GMT), drifted eastward at about $10ms^{-1}$; however, this translation speed is difficult to ascertain from the satellite image because of the rapid dissipation of the west side of the main cloud mass.

Also, the arc cloud in this case was inactive in the sense of interacting with its environment to produce continuous convection. However, two interesting things did occur. By 1800 GMT, the axis of warm surface temperature had moved into eastern Oklahoma; the warmest temperature in the area was reported at Ft. Smith, Ark. (FSM). As the remains of the ACC moved across this area into Arkansas, there was a sudden rejuvination of the system starting with the appearance in the 1832 GMT satellite imagery of two new convective cells on the Oklahoma-Arkansas border. The other interesting thing was the explosive growth of deep convection in the Texas panhandle just to the west of cloud band C (see Fig. 13). Both of these developments can be seen in Fig. 14 which gives the satellite imagery at 2200 GMT. The superimposed analysis is the surface temperature field in deg. C. Over the next 4.5 hr., the systems in western Kansas and the Texas panhandle were responsible for eight reports of tornadoes and two reports of large hail. It is impossible to tell what if any role cloud band C may have played in this development.

Some factors probably contributing to the short life and relative unimportance of the arc cloud in this case (Fig. 13) may be seen in the sounding at 1200 GMT for OKC (Fig. 15). First, it is seen that the cold-air layer at the ground is very shallow, amounting to only about 200 m in depth. Secondly, the wind in this layer has no component to the south; therefore, the outflow is not undercutting and lifting the warmer, moister, surface air in northern Texas to maintain the convection. Thirdly, despite the fact that at 1200 GMT OKC is in the middle of the ACC (Fig. 11) it is seen that the sampled column is not saturated between roughly 600 and 750 mb-two intrusions of dryer air are evident. The source of this air must lie somewhere in the triangle formed by AMA, MAF, and SEP. The soundings at those stations show that the dewpoint spread in the source region is of the order of 15°C. Finally, an objective analysis of divergence shows convergence of the order of $5x10^{-5}s^{-1}$ over western Oklahoma between 500 and 850 mb. It thus appears that this storm was simultanously raining itself out and drawing dryer air into the system, thus reducing the energy supply.

Conclusions and Recommendations

This study has described the meteorological conditions associated with two arc cloud complexes (ACC) and one case of an arc cloud forming independently of a storm complex. It has not provided a definitive answer to the question of how arc clouds are formed, especially in the two ACC cases.

The answer to the question may depend upon the way in which individual thunderstorm cells develop and move relative to the storm mass as a whole. In Case 1, the MDR cells moved in a fashion suggestive of the radar echo behavior described by Fujita and Brown (1958), Browning and Ludlum (1960) and Browning (1982), prior to the formation of the arc cloud itself. Wilhelmson and Chen (1982) have simulated this behavior in a numerical model, showing that new cell development occurs after the rainfall from an earlier cell reaches the ground. The results of Case 3 make it appear that rainfall is an important factor in the formation of the arc cloud. Since the preferred region for a well-defined arc cloud seems to be on the south side of the storm complex, the formation may depend upon a correct set of circumstances involving cell positions and rainfall, and perhaps rainfall rates.

Other related unanswered questions are: (1) What is necessary for the arc cloud to be sustained and moving over long time periods? (2) Do all arc clouds form in the early morning hours, frequently before dawn?

In hopes of answering these questions, it is suggested that these studies be expanded upon by an examination of radar films in conjunction with rainfall records from the climatological network.

REFERENCES

1. Black, P.G., 1978: Mesoscale cloud patterns revealed by Apollo-Soyuz. Bull. Amer. Meteor. Soc., 59, 1409-1419.

2. Browning, K.A., 1962: Cellular structure of convective storms. Meteor. Mag., 91, 341-350.

3. _____, and F.H. Ludlam, 1960: Radar analysis of a hailstorm. Tech. Note No. 5, Dept. of Meteorology, Imperial College, London, 106 pp.

4. Byers, H.R., and R.R. Braham, 1949: The Thunderstorm. U.S. Dept. of Commerce, Weather Bureau, Washington, D.C., 282 pp.

5. Charba, J., 1974: Application of gravity current model to analysis of squall-line gust front. Mon. Wea. Rev., 102, 140-156.

6. Darkow, G.L., and R.L. Livingston, 1975: Hourly surface static energy as a delineator of thunderstorm outflow areas. Mon. Wea. Rev., 103, 817-822.

7. Fujita, T., 1963: Analytical Mesometerology: A review. Meteor. Monogr., 5, 77-122.

8. _____, and H.A. Brown, 1958: A study of mesosystems and their radar echoes. Bull. Amer. Meteor. Soc., 39, 538-554.

9. Goff, R.C., 1976: Vertical structure of thunderstorm outflows. Mon. Wea. Rev., 104, 1429-1440.

10. Gurka, J.J., 1976: Satellite and surface observations of strong wind zones accompanying thuderstorms. Mon. Wea. Rev., 104, 1484-1493.

11. Kreitzberg, C.W., 1964: The structure of occlusions as determined from serial ascents and vertically directed radar. Air Force Cambridge Research Lab., Research Rept. No. 64-26, 121 pp.

12. Maddox, R.A., 1980: Mesoscale convective complexes. Bull. Amer. Meteor. Soc., 61, 1374-1387.

13. Mitchell, K.E., and J.B. Hovermale, 1977: A numerical investigation of the severe thunderstorm gust front. Mon. Wea. Rev., 105, 657-675.

14. Orlanski, I., 1975: A rational subdivision of scales of atmospheric processes. Bull. Amer. Meteor. Soc., 56, 527-530.

15. Purdom, J.F.W., 1973: Picture of the Month: Mesohigh and satellite imagery. Mon. Wea. Rev., 101, 180-181.

16. _____, 1976: Some uses of high-resolution GOES imagery in the mesoscale forecasting of convection and its behavior. Mon. Wea. Rev., 104, 1474-1483.

17. _____, 1979: The development and evolution of deep convection. Preprints 11th Conf.Severe Local Storms, Kansas City, Mo., Amer. Meteor. Soc., 143-150.

18. Ulanski, S.L., and M. Garstang, 1978: The role of surface divergence and vorticity in the life cycle of convective rainfall. PartI: Observations and analysis. J. Atm. Sci., 35, 1047-1062.

19. _____, 1978: Part 2: Descriptive Model. J. Atm. Sci., 35, 1063-1069.

20. Wilhelmson, R.B., and C. Chen, 1982: A simiulator of the development of successive cells along a cold outflow boundary. J. Atm. Sci., 39, 1466-1483.

21. Zipser, E.J., 1969: The role of organized unsaturated convective downdrafts in the structure and rapid decay of an equatorid distrubance. J. Appl. Meteor., 8, 799-814.

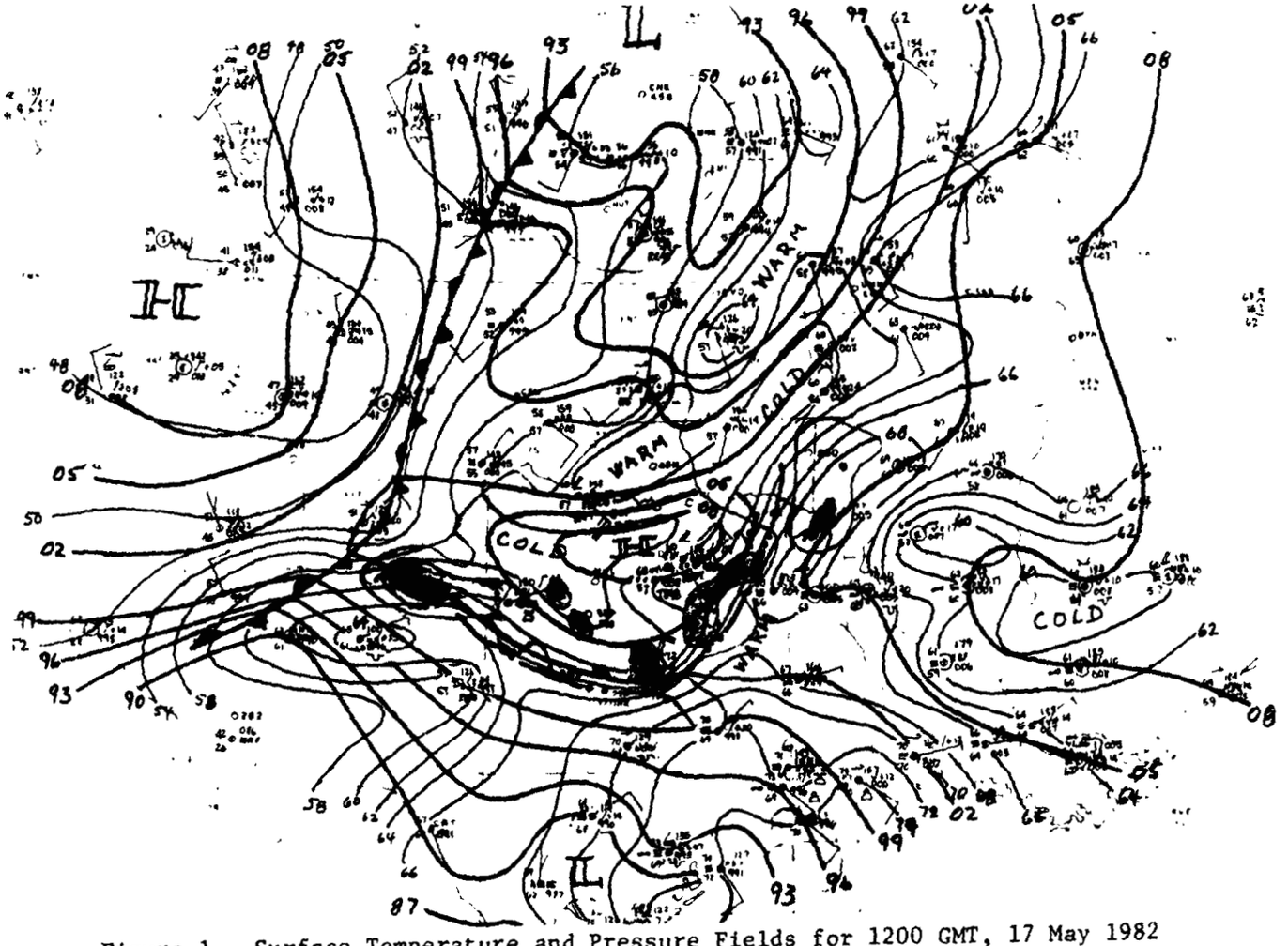

Figure 1. Surface Temperature and Pressure Fields for 1200 GMT, 17 May 1982

Figure 2. GOES-EAST Infrared Image at 1230 GMT

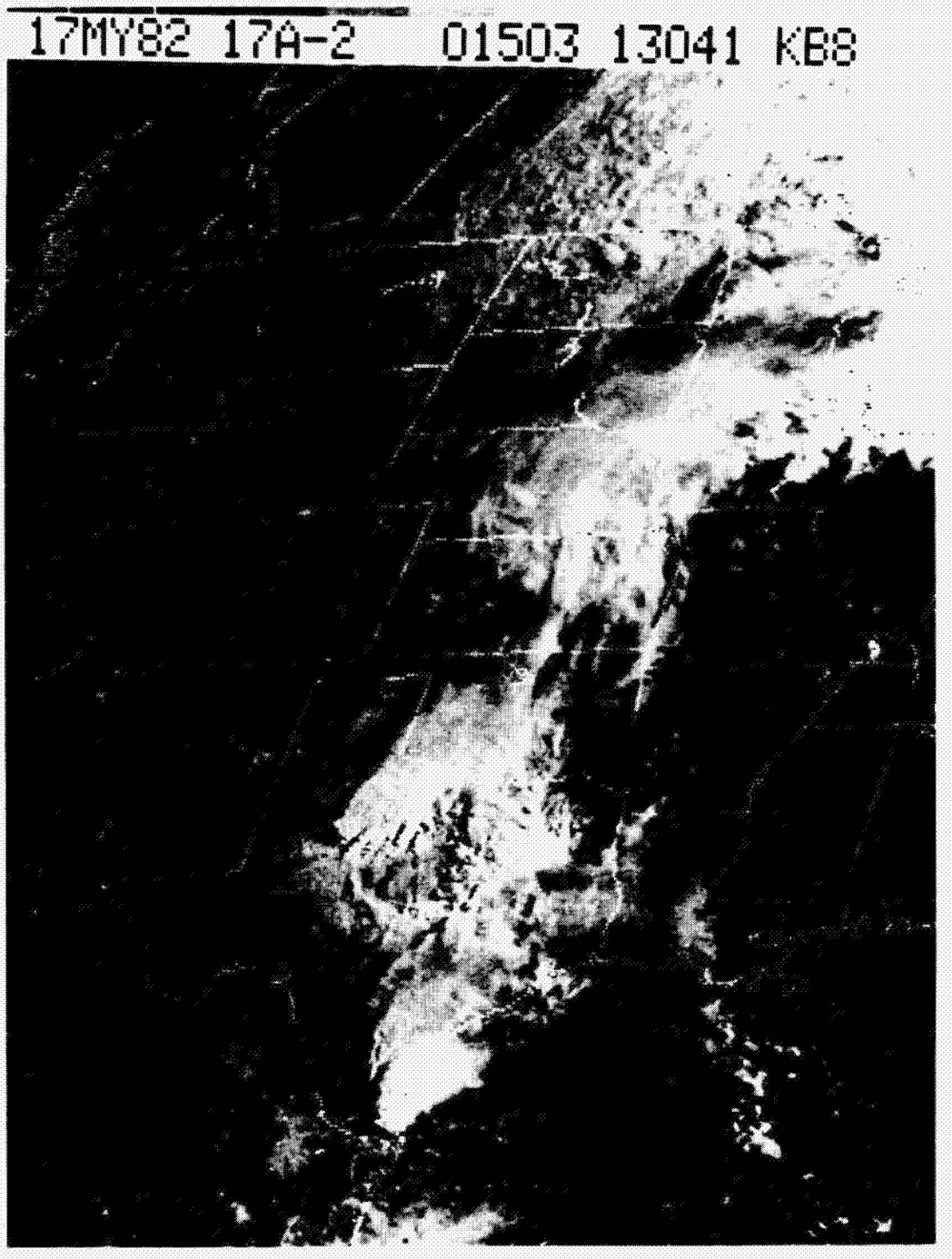

Figure 3. GOES-EAST Visible Image at 1300 GMT

Figure 4. RAOB Sounding at SEP
for 17 May 1982

Figure 5. Surface Divergence Field
at 1700 GMT

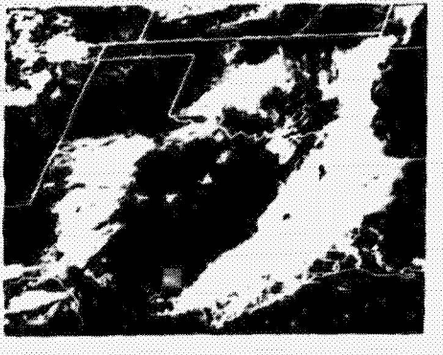

Figure 6. Arc Cloud Complex at 1900 GMT

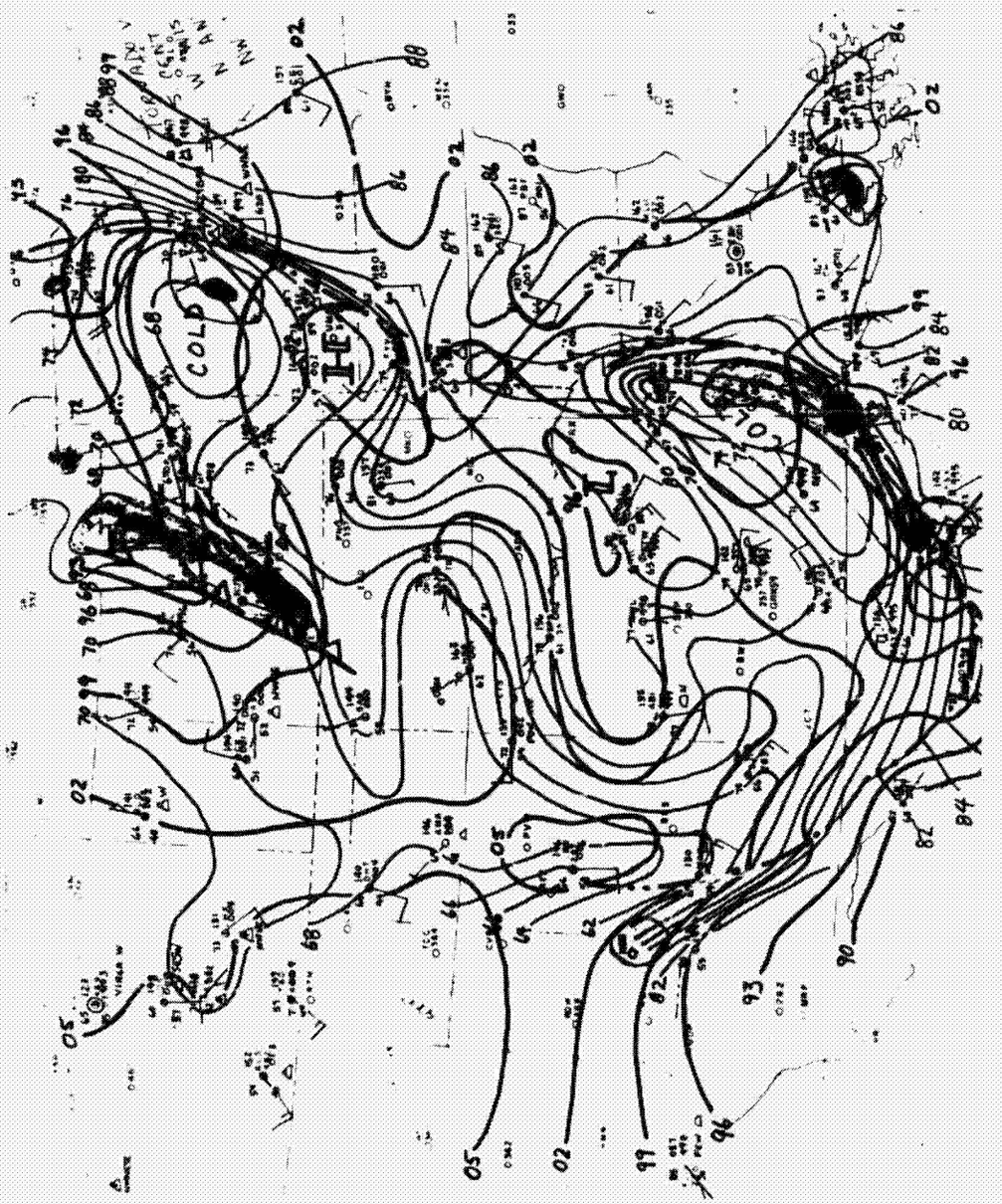

Figure 7. Surface Temperature and Pressure Fields for 2000 GMT

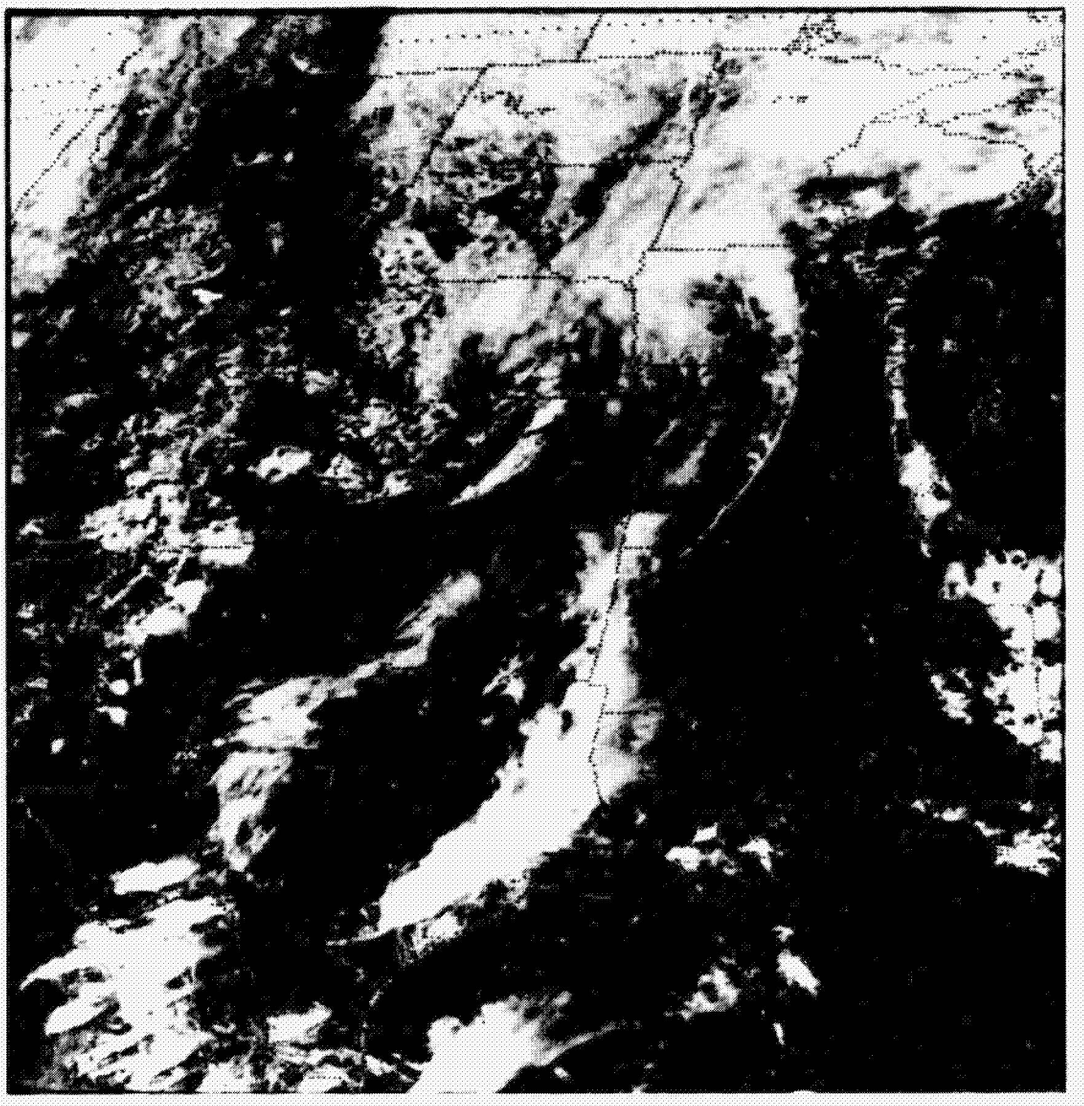

Figure 8. GOES-EAST Visible Image at 2001 GMT

Figure 9. GOES-EAST Infrared Image at 1100 GMT, 19 May 1982

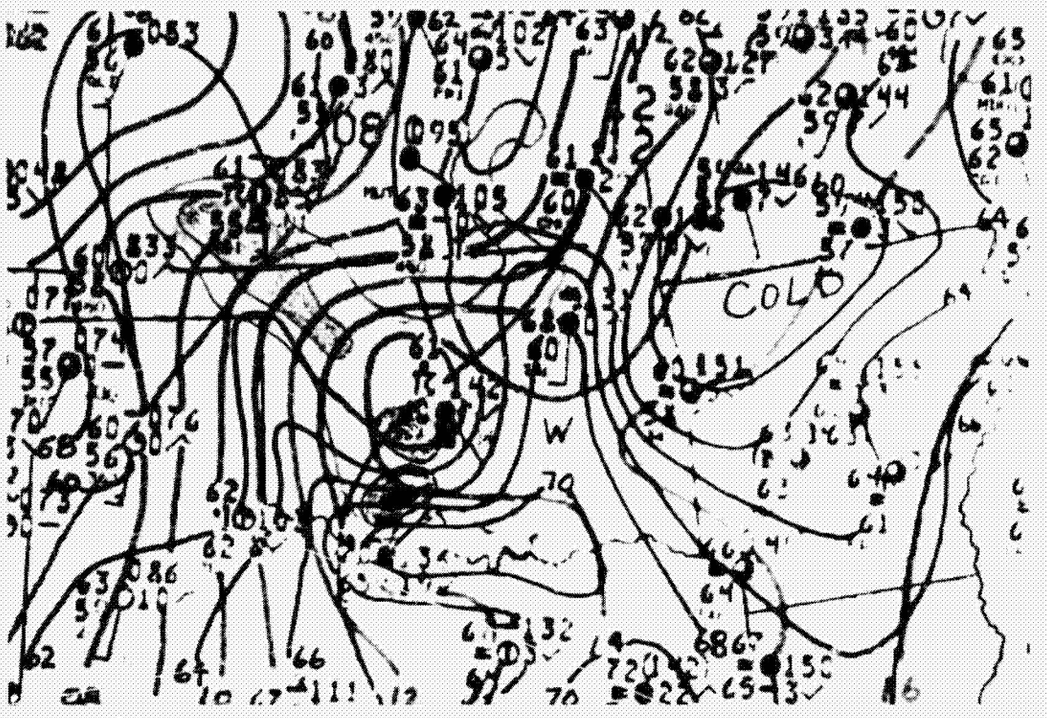

Figure 10. Surface Temperature and Pressure Fields for 1200 GMT, 19 May 1982

Figure 11. GOES-EAST Visible Image at 1200 GMT

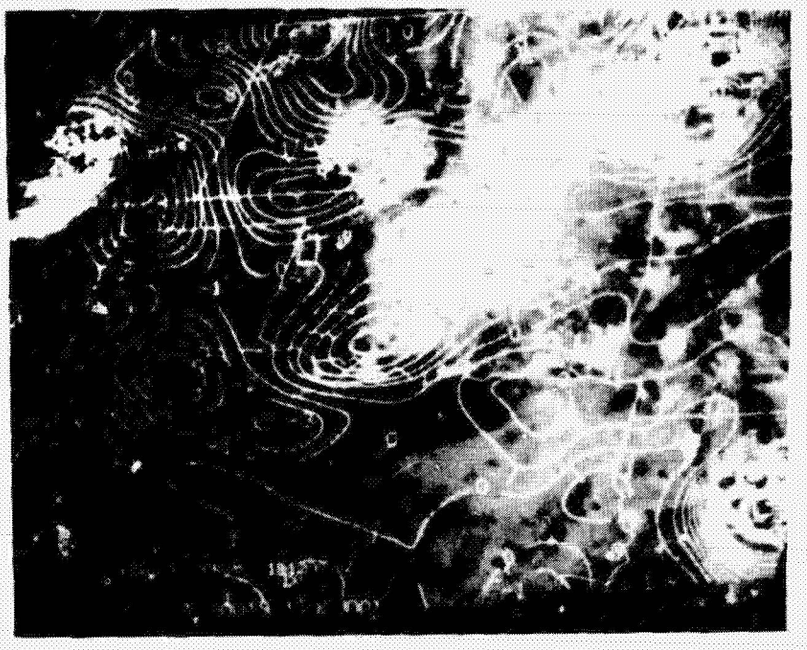

Figure 12. Surface Divergence at 1200 GMT, 19 May 1982

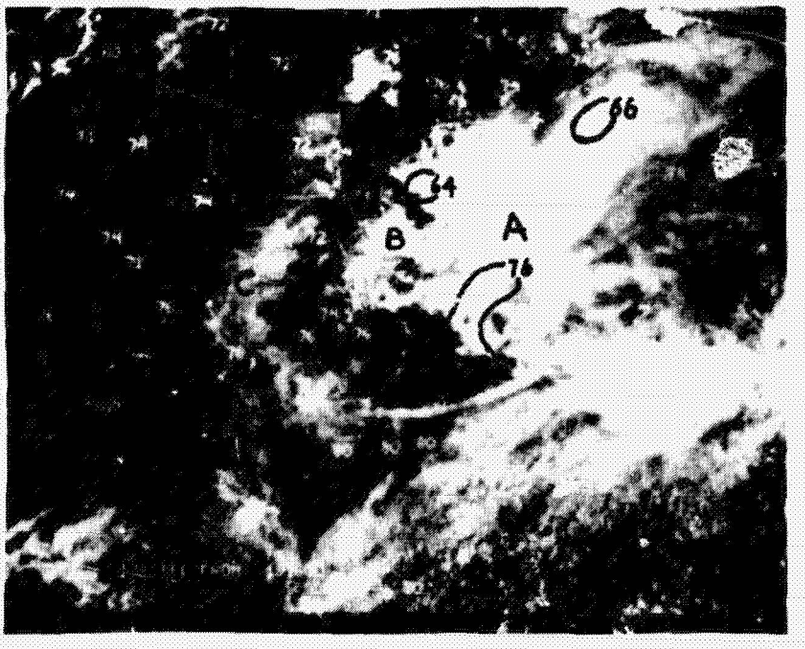

Figure 13. Visible Image and Temperature . 500 GMT

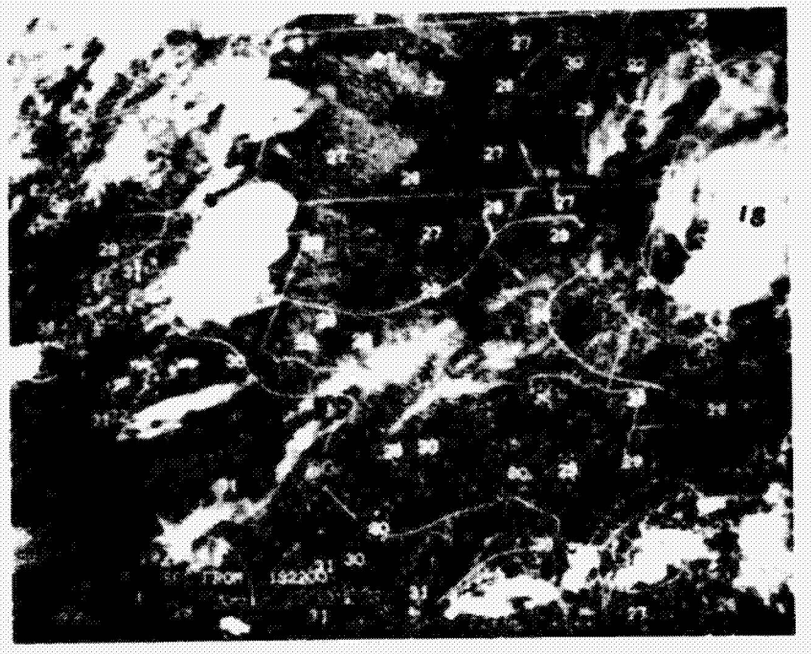

Figure 14. Visible Image and Temperature at 2200 GMT

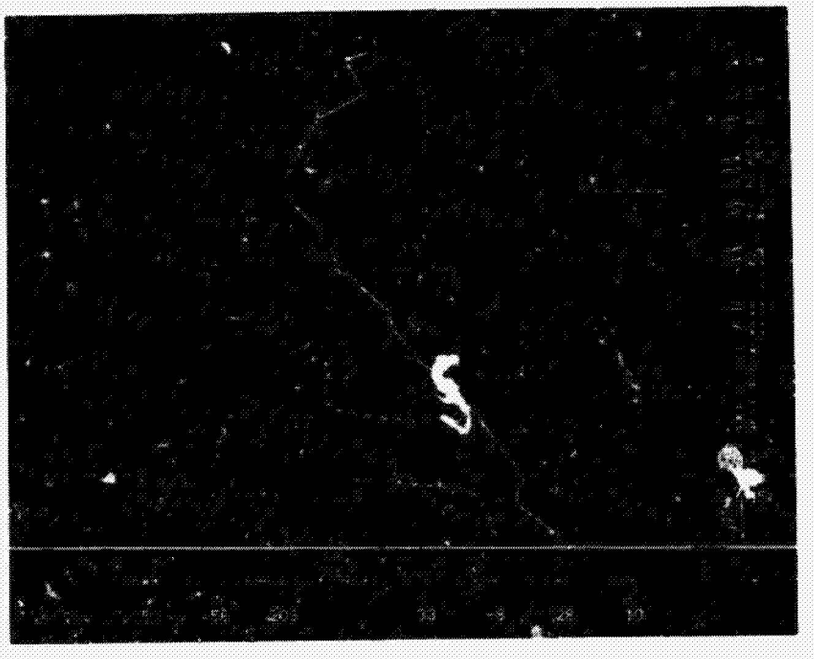

Figure 15. RAOB Sounding at OKC for 12 GMT, 19 May 1982

1983

NASA/ASEE SUMMER FACULTY RESEARCH FELLOWSHIP PROGRAM

MARSHALL SPACE FLIGHT CENTER
THE UNIVERSITY OF ALABAMA
IN HUNTSVILLE

PARTIAL ANALYSIS OF INSTA-FOAM

Prepared By:	Libby W. Chou, Ph. D.
Academic Rank:	Professor
University and Department:	Alabama A & M University Chemistry
NASA/MSFC Division: Branch:	 Materials & Processes Analytical Chemistry
MSFC Counterpart:	Robert Lynn
Date:	August 1, 1983
Contract No.:	NGT 01-008-021 The University of Alabama in Huntsville

PARTIAL ANALYSIS OF INSTA-FOAM

BY

Libby W. Chou
Professor of Chemistry
Alabama A & M University
Normal, Alabama

ABSTRACT

Insta-Foam is used as a thermal insulator for the non-critical area of the External Tank during the pre-launch phase to minimize icing. It has two components, A and B. There are three classes of compounds in A, and five in B. The purpose of this project is to identify the substances in each mixture, to determine the test variability and to recommend material acceptance criteria. Some work has been done on Component B. It was only possible to identify two species.

ACKNOWLEDGEMENTS

The author wishes to thank many individuals for their assistance, comments, and kindness, especially N. Hundley and D. Morris from the Polymer Branch; Dr. L. Ludwick, a fellow participant of this Program; J. Austin, C. Riddles and my NASA Counterpart, R. Lynn from the Analytical Chemistry Branch; and G. Smith from the Environmental & Energy Studies at UAH for a continuous supply of the water used in this study.

LIST OF FIGURES

Figure	Title	Page
1	Gradient Baselines/60 min.	i
2	NCFI Foam, 210 nm	ii
3	Insta-Foam (2321), 40 µl; 210 nm	iii
4	Insta-Foam (2321), 60 µl; 210 nm	iv
5	Insta-Foam (2321); 254 nm	v
6	Insta-Foam (20191); 210 nm	vi
7	Insta-Foam (20191); 254 nm	vii
8	Insta-Foam (22501); 210 nm	viii
9	Insta-Foam (22501); 254 nm	ix
10	Baselines and Polyol	x
11	Polyol; 210 nm	xi
12	Polyol, 40 µl; 254 nm	xii
13	Polyol, 60 µl; 254 nm	xiii
14	PCF; 210 nm	xiv
15	PCF; 254 nm	xv
16	Mixture of PCF and Polyol; 210 nm	xvi
17	Mixture of PCF and Polyol; 254 nm	xvii
18	Insta-Foam (22501), isocratic	xviii
19	Fraction A; 210 nm	xix
20	Fraction A; 254 nm	xx
21	Fraction A; NMR	xxi
22	Fraction A; Differential Thermal Analysis Curve	xxii

LIST OF FIGURES
(not presented in this report due to space, but can be obtained from Libby W. Chou or Robert Lynn.)

Figures	Title
2-i	Reference NCFI
2-ii	CPR 488 with impurities in water
2-iii	CPR 488; 210 nm
2-iv	Reference CPR 488
2-v	Reference Insta-Foam
6-i	Insta-Foam (20191), 40 µl; 210 nm
6-ii	Insta-Foam (20191), 60 µl.
7-i	Insta-Foam (20191), 40 µl; 254 nm
7-ii	Insta-Foam (20191), 60 µl.
8-i	Insta-Foam (22501), 60 µl; 210 nm
8-ii	Insta-Foam (22501), 90 µl
9-i	Insta-Foam (22501), 60 µl; 254 nm
10-i	Baselines
21-i	Solvent NMR
22	FractionA(no heating), 210 nm
23	Fraction A (no heating), 254 nm
24	Fraction 1, 210 nm
25	Fraction 1, 254 nm
26	Fraction 2, 210 nm
27	Fraction 2, 254 nm

INTRODUCTION

Insta-Foam is a urethane polymer. A urethane is an amide-ester of carbonic acid, R-NHC(=O)-O-R', product of an isocyanate and an alcohol:

$$R\text{-}N{=}C{=}O + H\text{-}O\text{-}R' \xrightarrow{\text{catalyst}} R\text{-}NHC(=O)\text{-}O\text{-}R'$$

Therefore, Insta-Foam is a two-component system. Component A has polyisocyanates, blowing agent, and stabilizers; Component B has the polyols, catalysts, blowing agents, stabilizers and fire retardant. The blowing agents are Freon 11 and Freon 12, the stabilizers are silicone surfactants, the catalysts are tertiary amines, and the fire retardant is tri-(β-chloro-isopropyl) phosphate (PCF). Methods for testing individual raw materials are tedius and not suitable for the present purposes (Ref. 1 - 7). High performance liquid chromatography (HPLC) was chosen for the instrumentation, because other urethane foams, such as CPR 488 and NCFI,have been analyzed for similar purposes. Even though identification of each compound has never been done on those foams, it was possible to show which would constitute a bad or good lot.

OBJECTIVES

1. Identify each substance in Component B.
2. Determine test variability in two or three determinations on each lot.
3. Recommend material acceptance criteria.

INSTUMENTATION AND RESULTS

The liquid chromatography instrument with a gradient programmer is by Waters Associates. It has a uv detector at 254 nm and a RI detector, and is connected to a Perkin Elmer LC75 variable wavelength detector chosen at 210 nm. Each uv detector was connected to a recorder. After Sigma 15 data station was repaired in the mid-July, it replaced the recorder on LC75.

Different gradient curves (5,6 and 9) have been tried, and the linear gradient (6) seems to be the most

effective in this case.

Gel Permeation column, μ-styragel 100Å, was used with solvent THF. Four fractions (Figure 18) were separated by tedius collections, because the preparative LC is not in working order. The first fraction (A) was a crystalline needle. The melting point and the heat capacity as determined by differential thermal analysis (Figure 22) are 51°C and 16.21 cal/g, respectively. Chromatograms from C18 column and the NMR spectrum are shown in Figures 19-21. The other three fractions are viscous liquids. Their chromatograms are not included in this report, but can be obtained from the author or her counterpart (Figures 22-27).

μ-Bondpak C18 was used with gradient elution from 20% acetonitrile/80% water to 90% acetonitrile/10% water in 90 minutes. Two problems were encountered. One was pressure build-up. At about 2000 psi, leaks were obvious at the injection port which should withstand a pressure of 5000 psi or more. Another problem was solvent purity, especially of water. A good lot of Burdick Jackson brand acetonitrile and very pure water (Ref. 8) produced baselines shown in Figure 1. When that batch of acetonitrile ran out, the Fisher HPLC brand was used, and the baselines are not as good (Fig. 10). Since relatively straight baselines were never obtained during this summer, even after filtering the water through C18 Sep-Pak and acetonitrile through Silica-Porasil Sep-Pak, the other chromatograms must be viewed with the residual baselines in mind. (Guard colums may alleviate this problem). After being very careful with the purities of the solvents, reproducible results with known urethane foams were obtained (Ref.9). NCFI is shown in Figure 2. Chromatograms of CPR 488 and references are not shown here (2-i through 2-v).

Three lots of Insta-Foam, Polyol raw material and fire retardant (PCF) were then analyzed. With the exception of PCF, part of the chromatograms seems to be dependent on the quantity injected (all approximately 5% solutions). Only those of the lot no. 2321 and polyol are presented as a function of quantity in this report (Fig. 3,4, 5,10c, 11, 12 and 13).

From chromatograms with 254 nm detector (Figures 5, 9, 12, 13, 17), the presence of PCF can be easily seen as a sharp peak at a retention time of 20 min. and poly-

ols at approximately 2, 4, 15, and 28 min. Which compounds produced the two other sharp peaks (35 and 42 min) are not known at this time.

With chromatograms using 210 nm detector (Fig. 3,4, 6, 8, 10c, 11, 14, 16), it is a little more difficult. The peak at approximately 20 min. for PCF sometimes becomes a shoulder or even being buried under a strongly absorbing peak. Polyols can be detected at 5.9, 11.00, 11.65 and 19.15 which may coalesce, particularly the latter three, as the amount of material injected increases. Sharp peaks at 35 and 42 min. in the 254 nm are also sharp at 210 nm. Two peaks at around 82 min. are present in all three lots of Insta-Foam and absent in polyol and PCF. They may be due to the amine catalysts or silicone surfactants. However, for lot no. 22501, there are two other peaks (79, 84 min.) which are absent in other lots.

CONCLUSION AND RECOMMENDATION

1. Polyols and PCF can be identified qualitatively by HPLC.
2. An intrinsic limitation of HPLC is the requirement for each compound in the mixture to absorb in the uv region. An extension of this is that some substances absorb more strongly than the others. Unless the absorbances of individual compounds are known, peak heights or areas can only be used comparatively but not quantitatively.
3. Ask the Insta-Foam Manufacturer for samples of amine catalysts, and silicone surfactants in order to identify the remaining peaks.
4. A much more time-consuming alternative is to fix the PrepLC, separating the unidentified peaks for further study.
5. Peaks at 79 and 84 min. in lot 22501 but absent in others need to be investigated of their importance for acceptance criteria: Do they contribute any difference as far as flatwise tension, bond tension, compressive strength and density are concerned?
6. The number of theoretical plates for HPLC columns need be be checked from time to time. Therefore, the standard chemicals for various columns should be purchased.

REFERENCE

1. ASTM D1638, D2849 (1980)
2. L. Mulder, Anl. Chim. Acta. 38 (1967)
3. J. J. Armstrong, et. al., J. Chem. Soc. 1958 4344
4. C. J. Hardy, J. Chromatog. 13 372 (1964)
5. R. Wittendorfer, Analytical Chem. 36 930 (1964)
6. P. Saliman, Analytical Chem., 36 112 (1964)
7. C. A. Bache and D. J. Lisk, Analy. Chem., 37 1477 (1965)
8. D. J. Runser, "Maintaining & Troubleshooting HPLC System" Wiley-Interscience (1981)
9. B. Ranganathan, Martin Marietta, privat comm.

Figure 1

Gradient Baselines: 20-90% Acetonitrile in Water/60 min
(A) 210 nm; 2.56x
(B) 254 nm; 0.2x

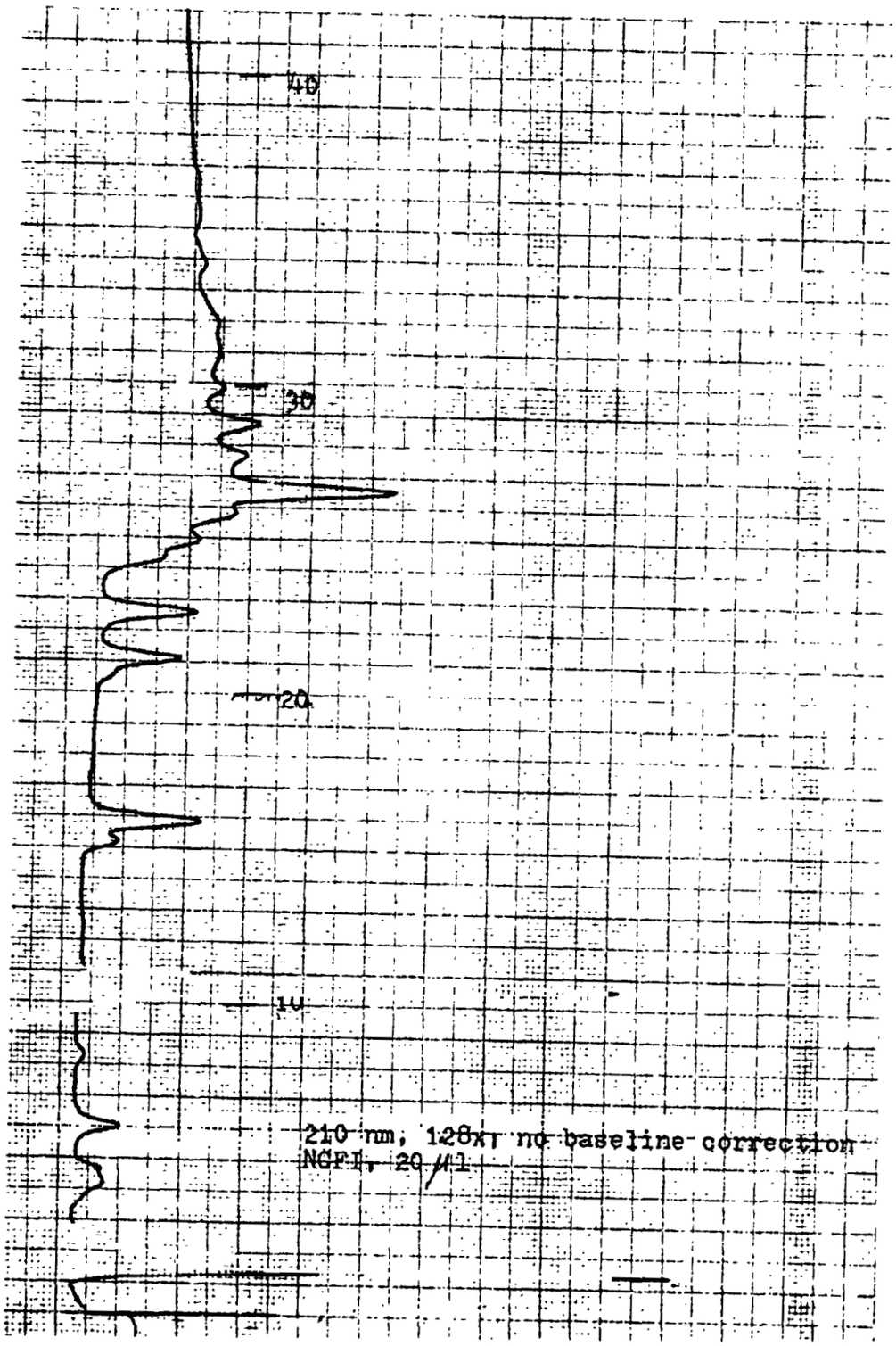

Figure 2

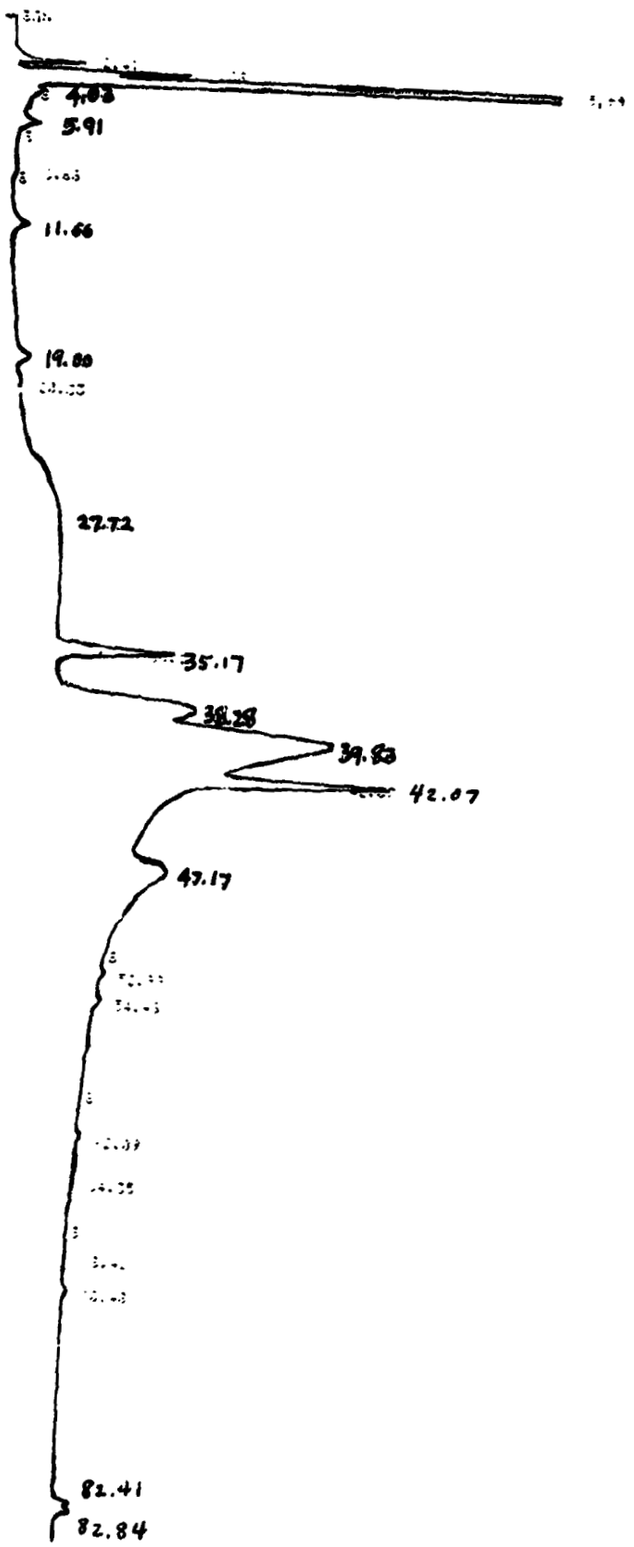

Figure 3

INSTA FOAM - lot no. 2321, 40 µl.
210 nm

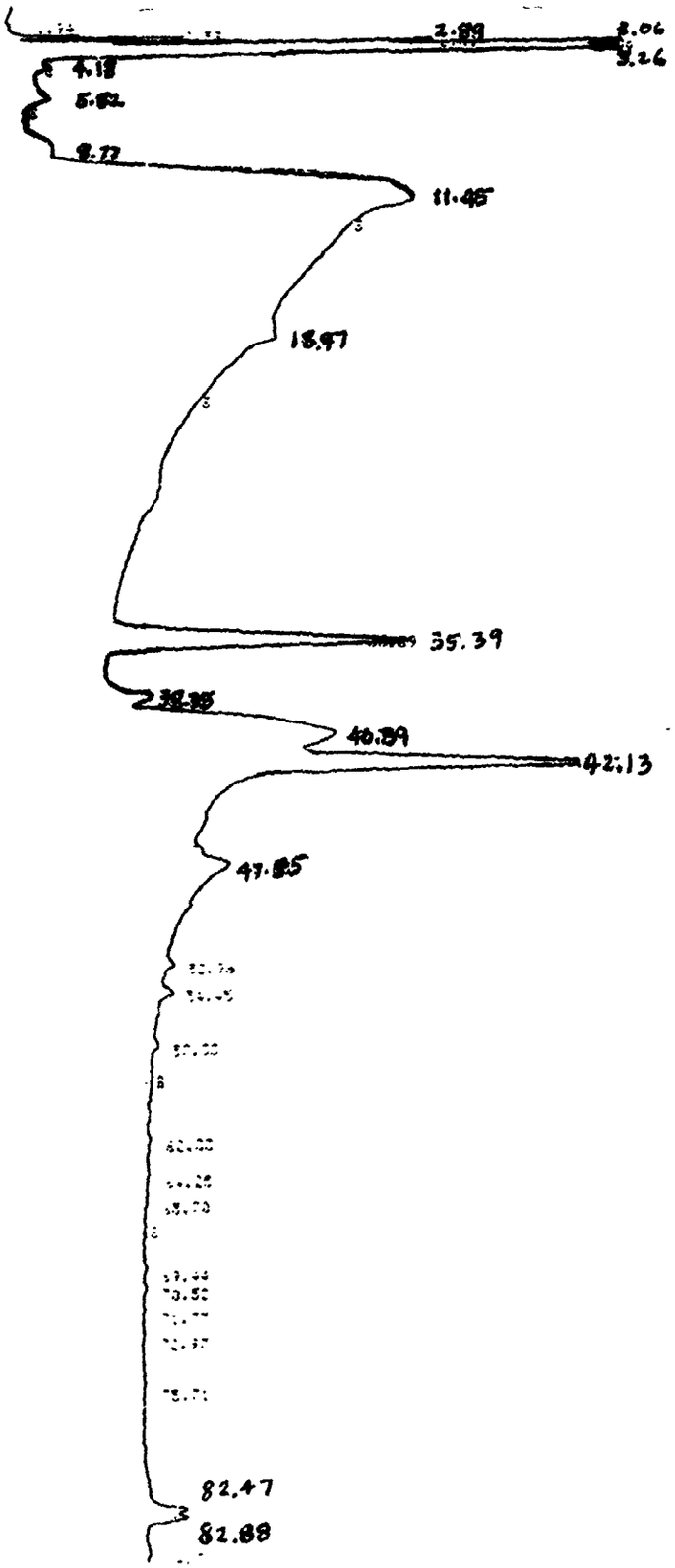

Figure 4
INSTA FOAM - lot no. 2321, 60 µl.
210 nm

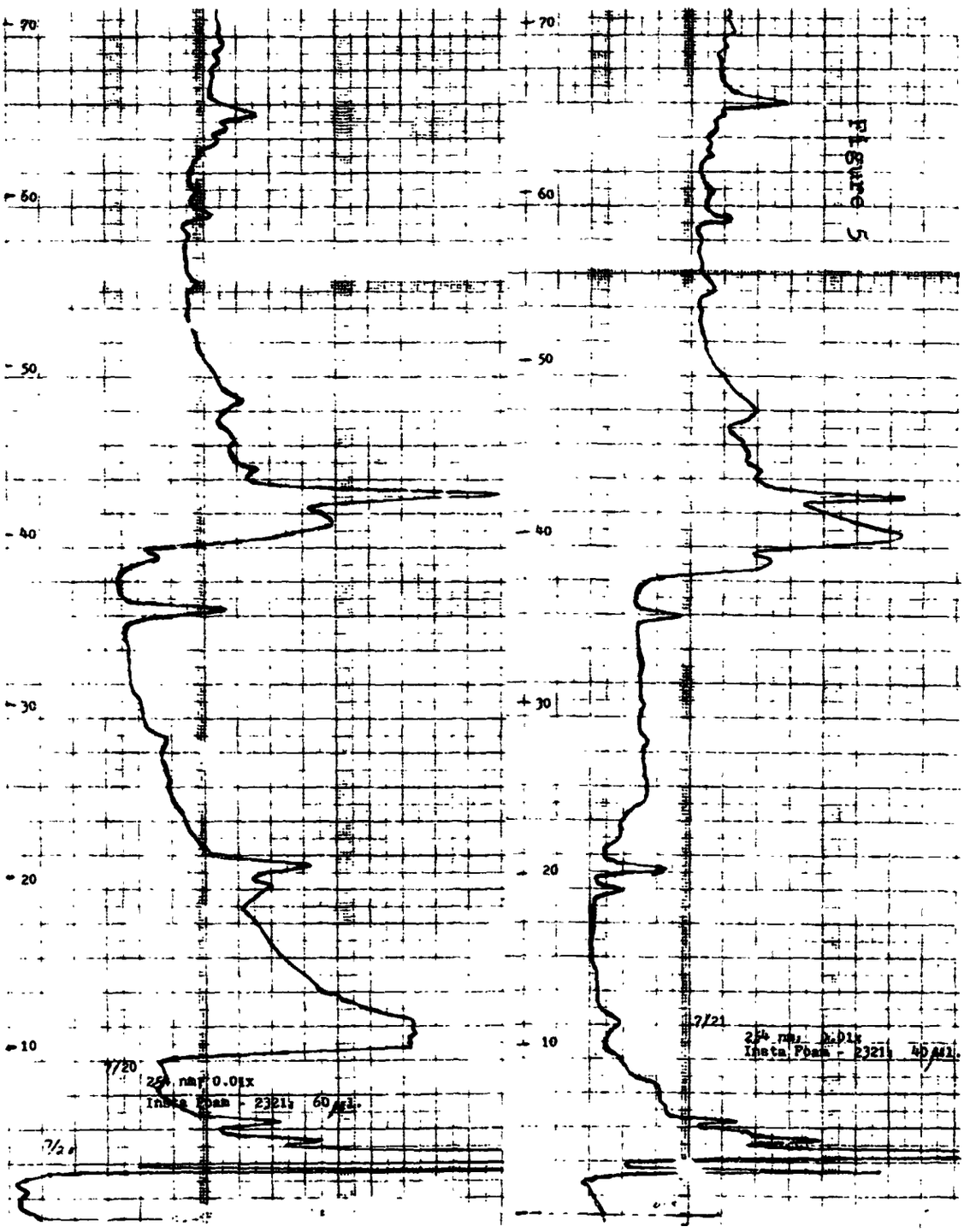

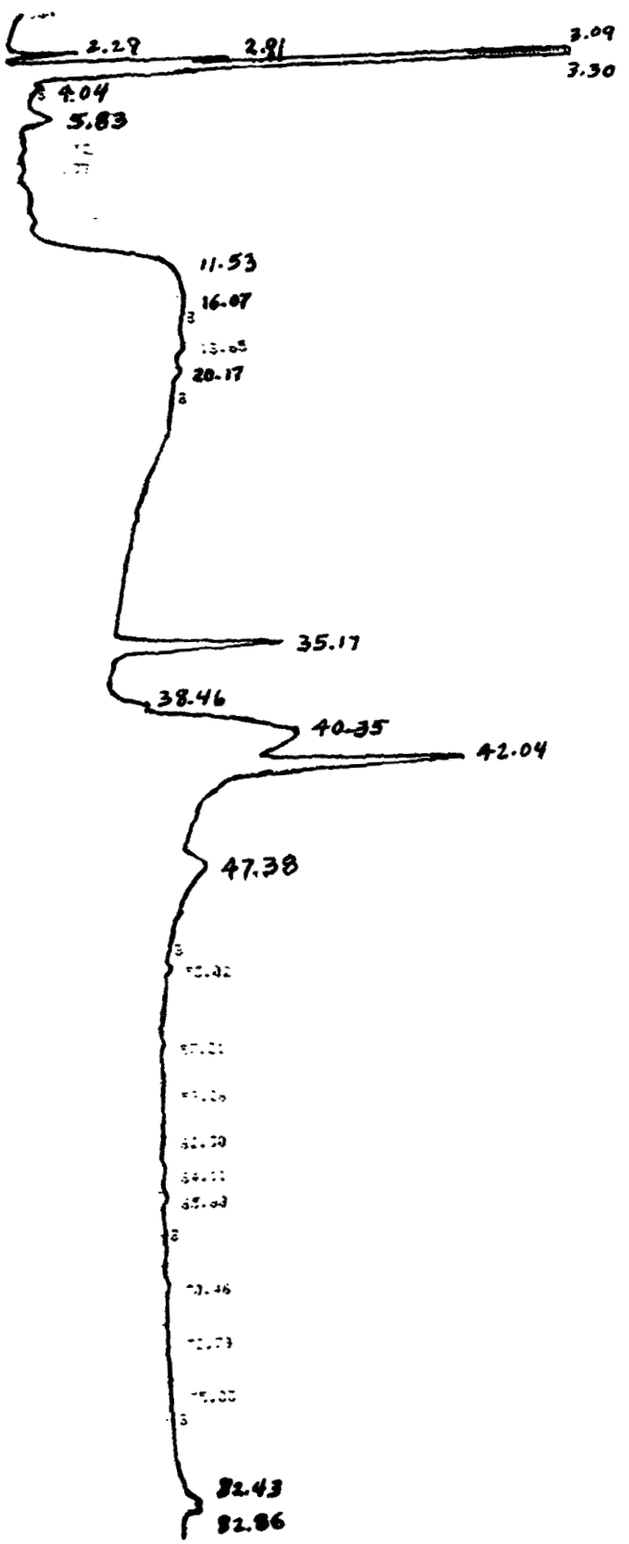

Figure 6

INSTA FOAM - lot no. 20191, 30 µl.; 210 nm
90 min. gradient

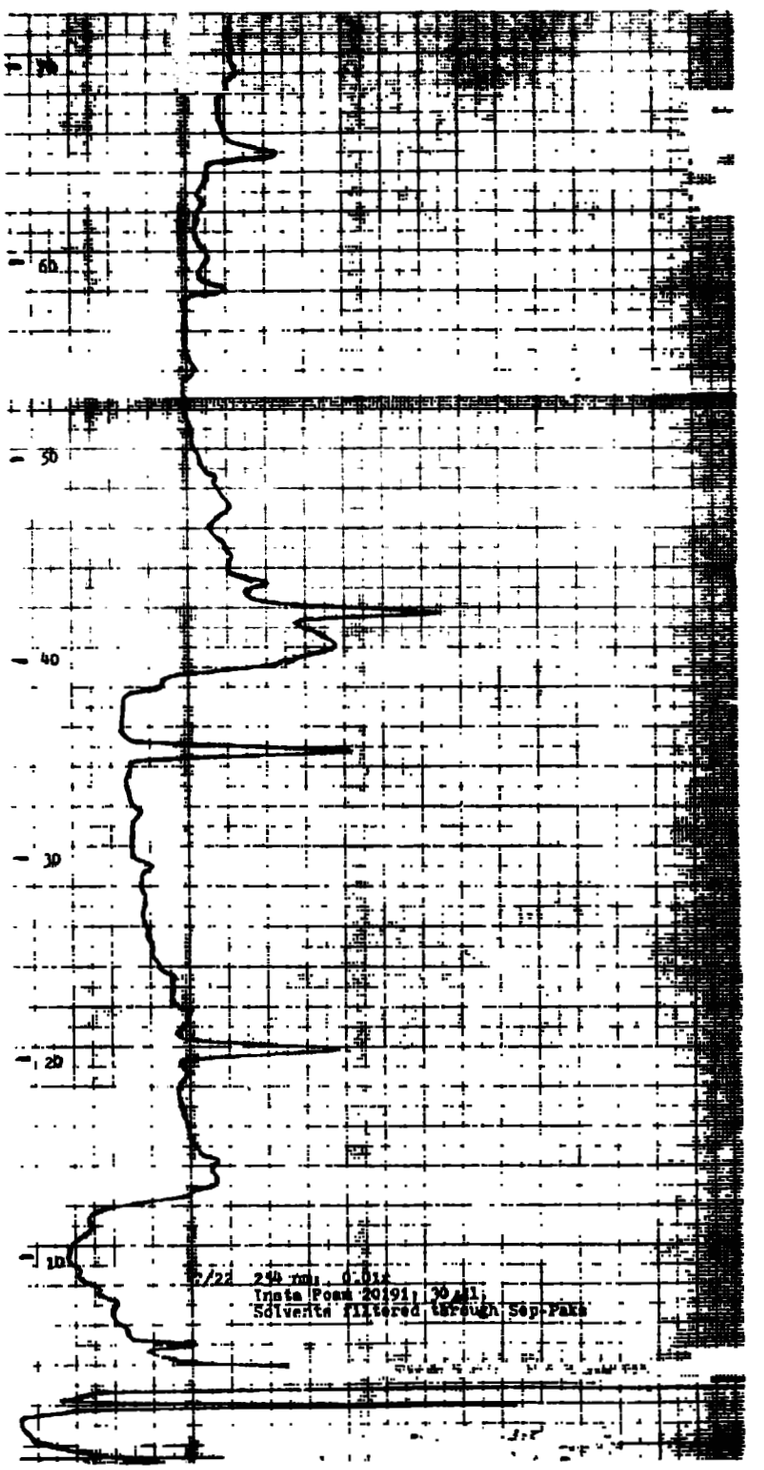

Figure 7

INSTA FORAM - lot no. 20191, 30 µl.; 254nm, 0.01x
90 min. gradient

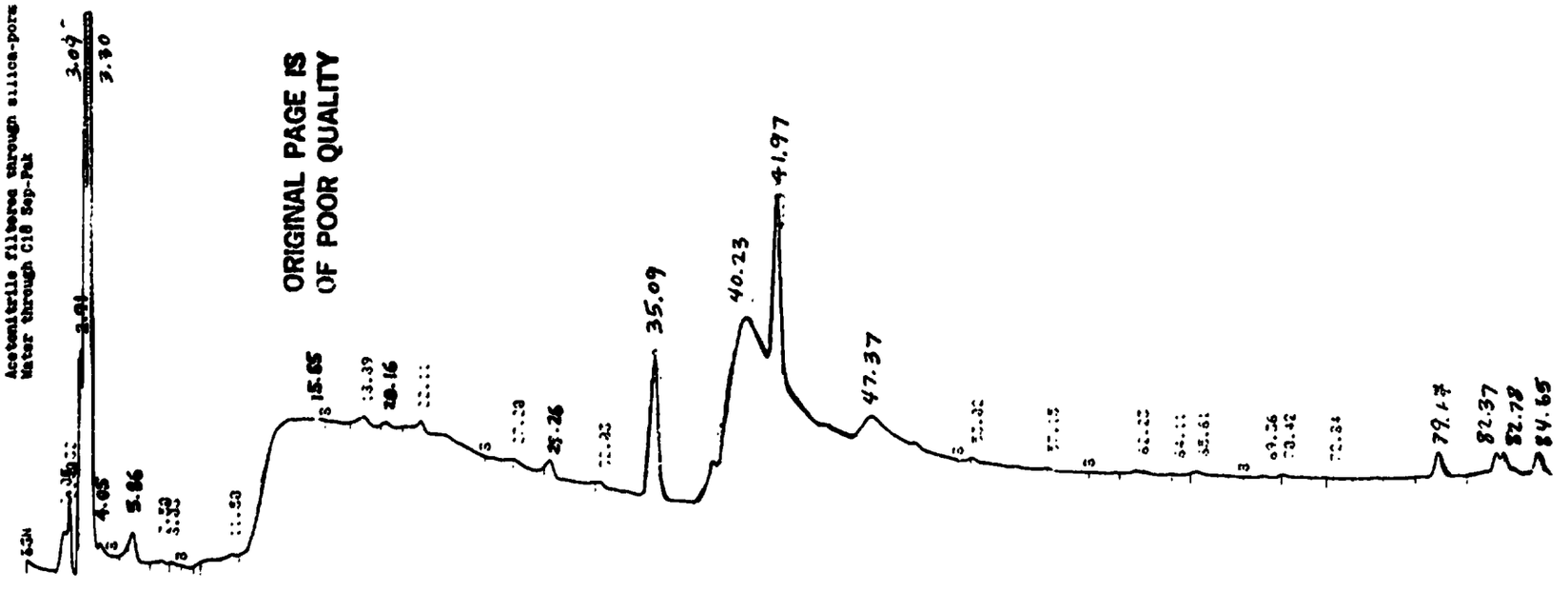

Figure 8

INSTA FOAM - lot no. 22501, 30 μl.; 210 nm
90 min. gradient

Figure 9

INSTA FOAM - lot no. 22501, 30 µl.; 254nm, 0.01x
90 min. gradient

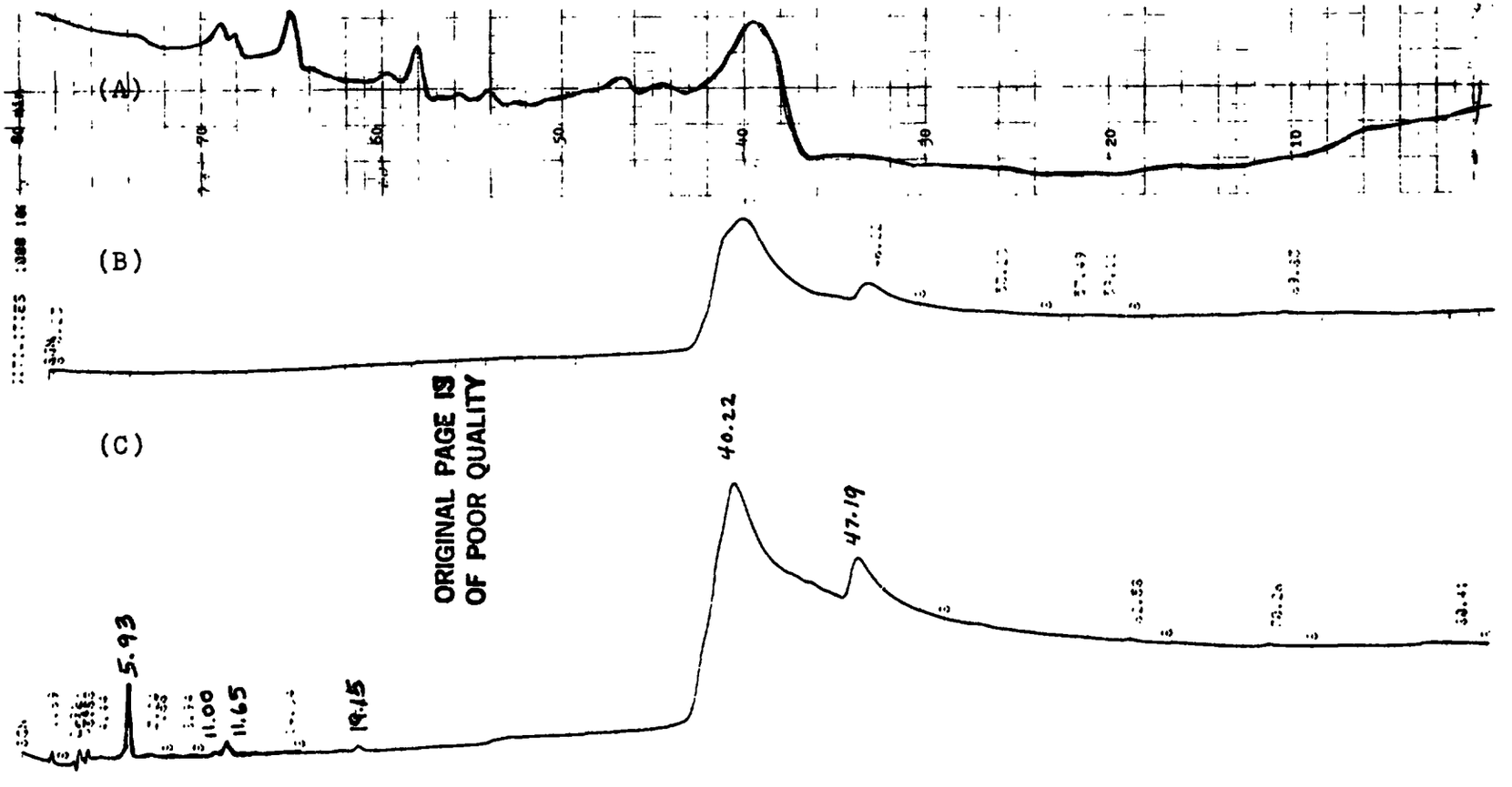

Figure 10

(A) Baseline, 254 nm; (B) Baseline, 210 nm; (C) POLYOL, 40 μl.

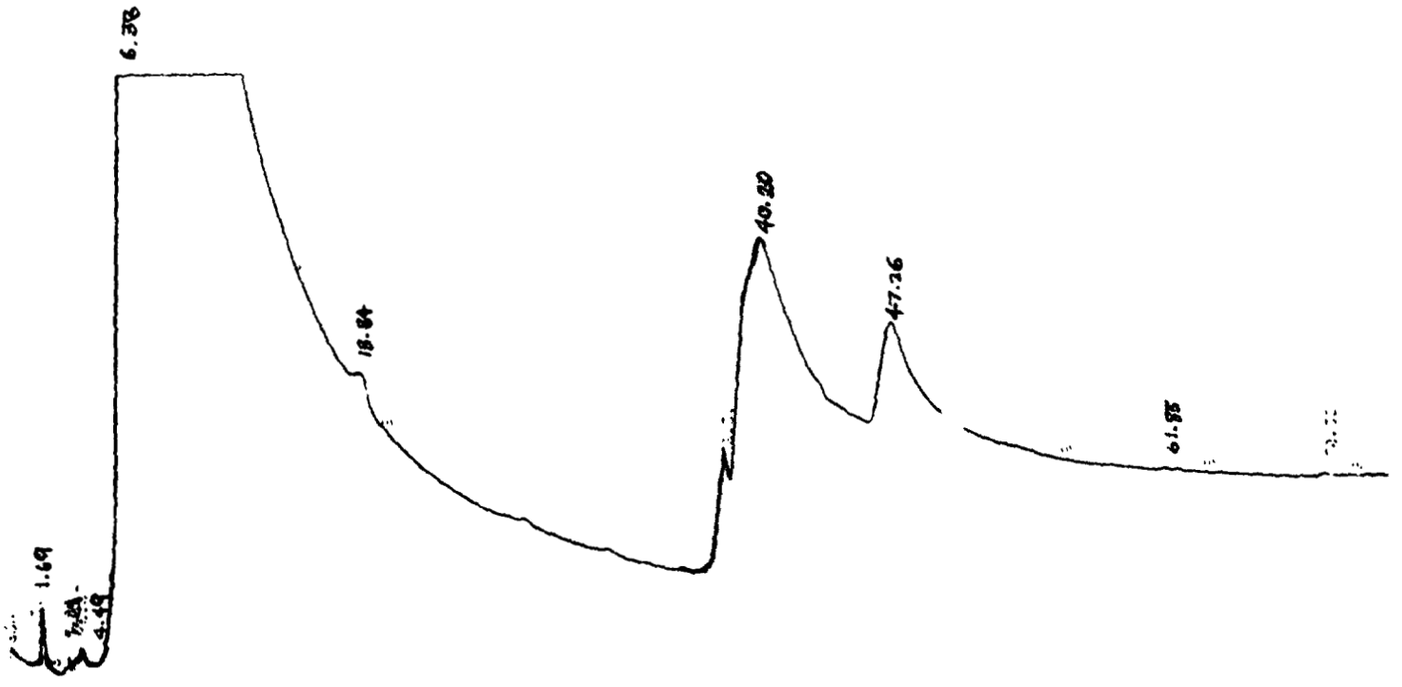

Figure 11

POLYOL, 60 μl.; 210 nm

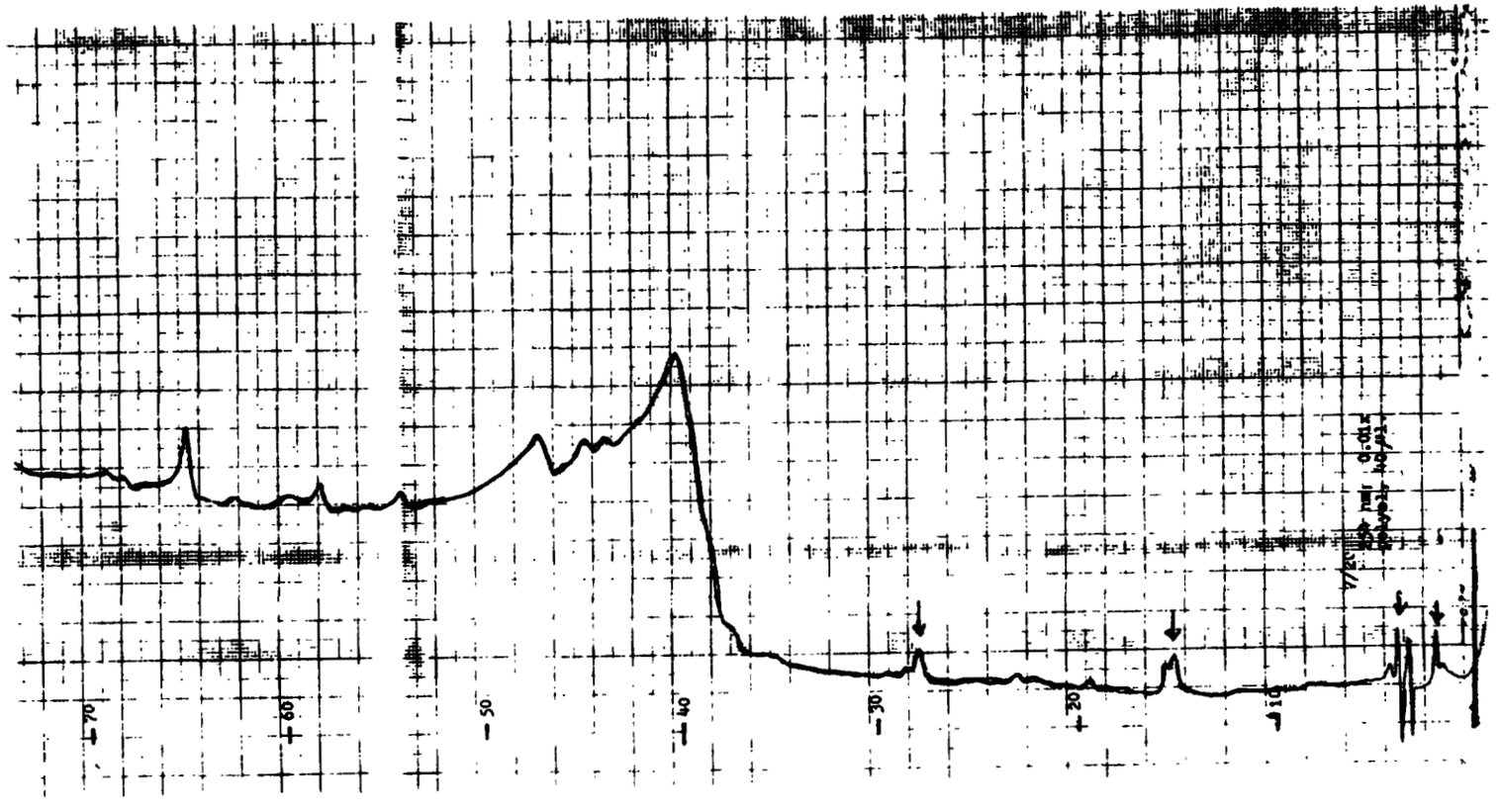

Figure 12

POLYOL, 40 µl.; 254 nm, 0.01x

90 min Gradient

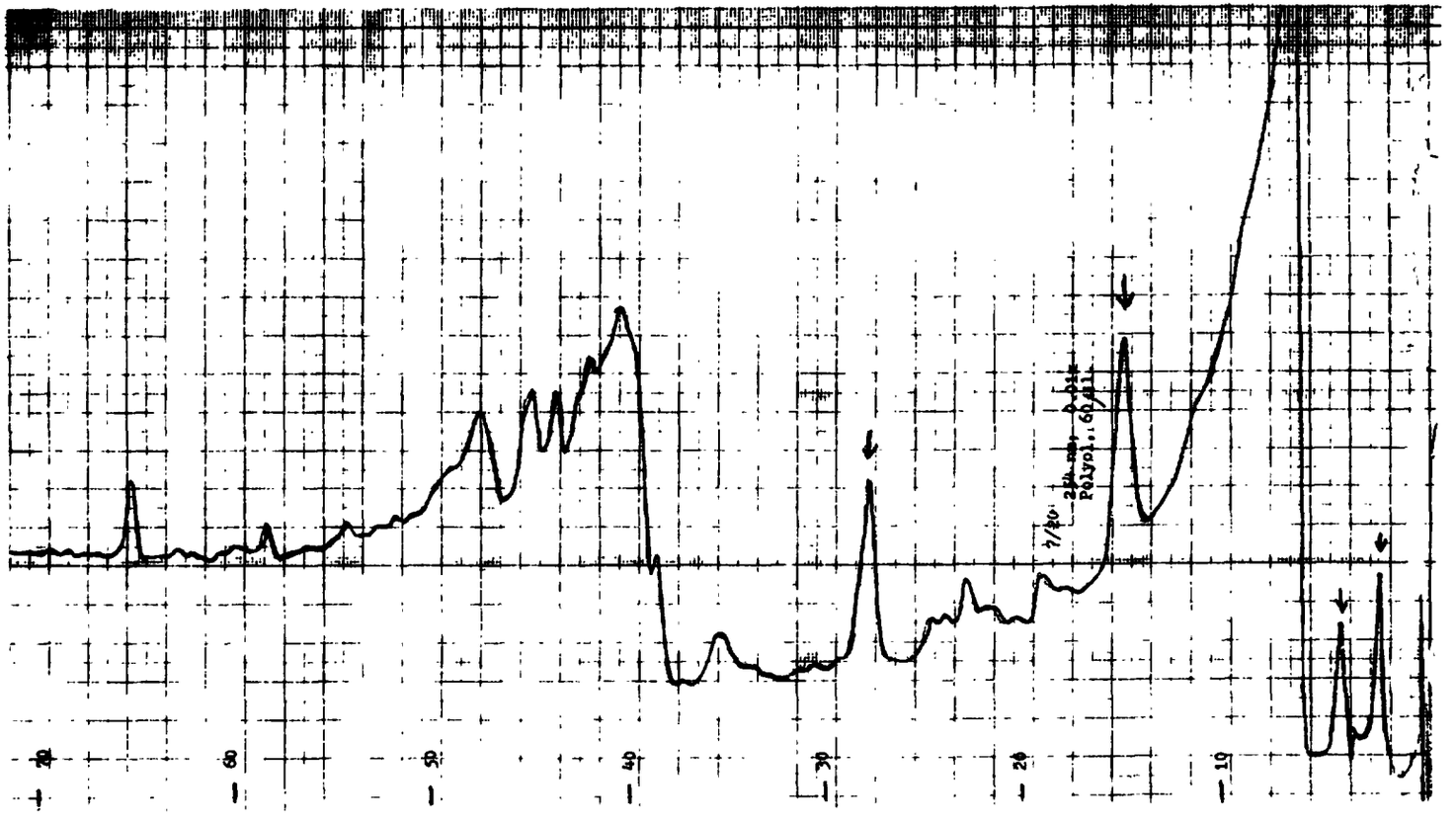

Figure 13
POLYOL, 60 µl., 254 nm, 0.01x
90 min Gradient

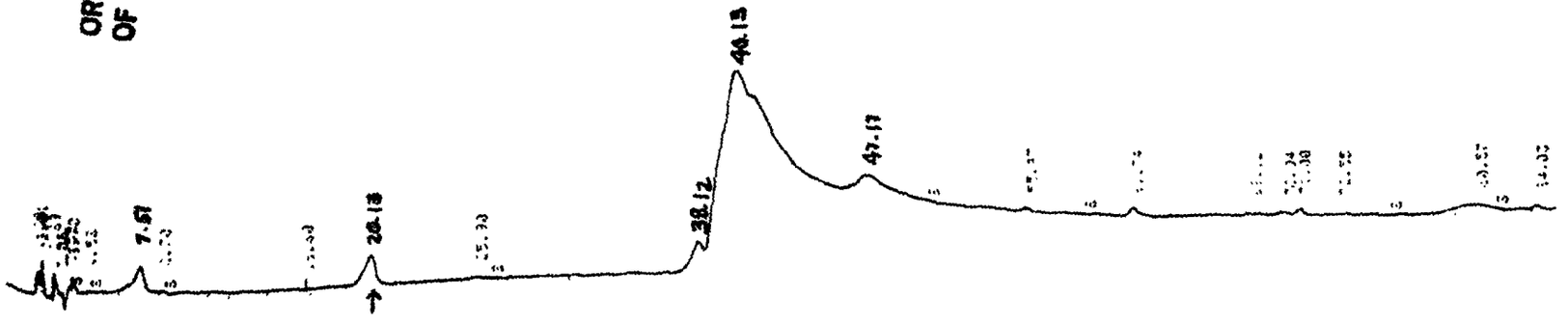

Figure 14

PCF, 50 µl.; 210 nm

Gradient: 20 to 90% ACN/90 min

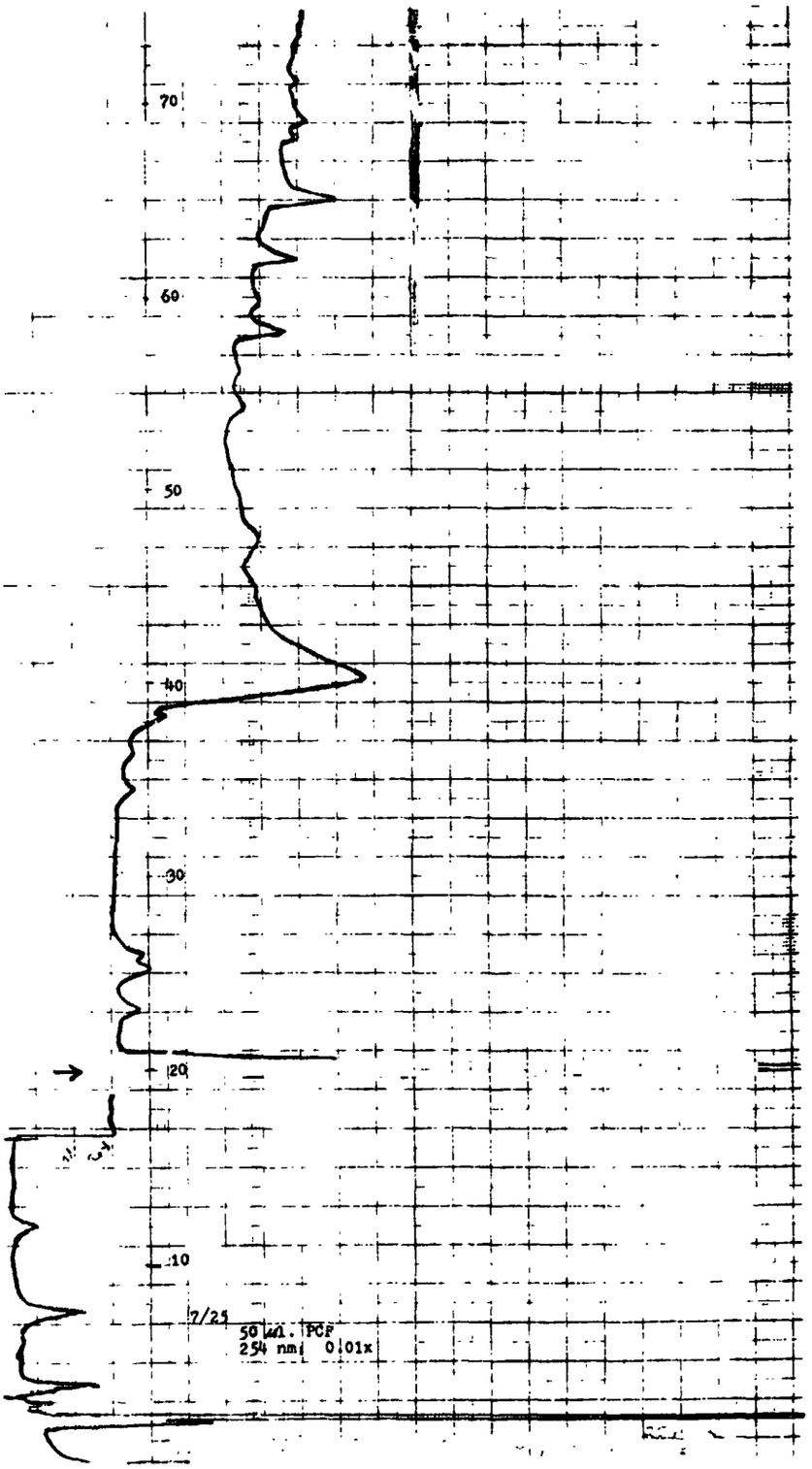

Figure 15
PCF, 50 μl.; 254 nm, 0.01x

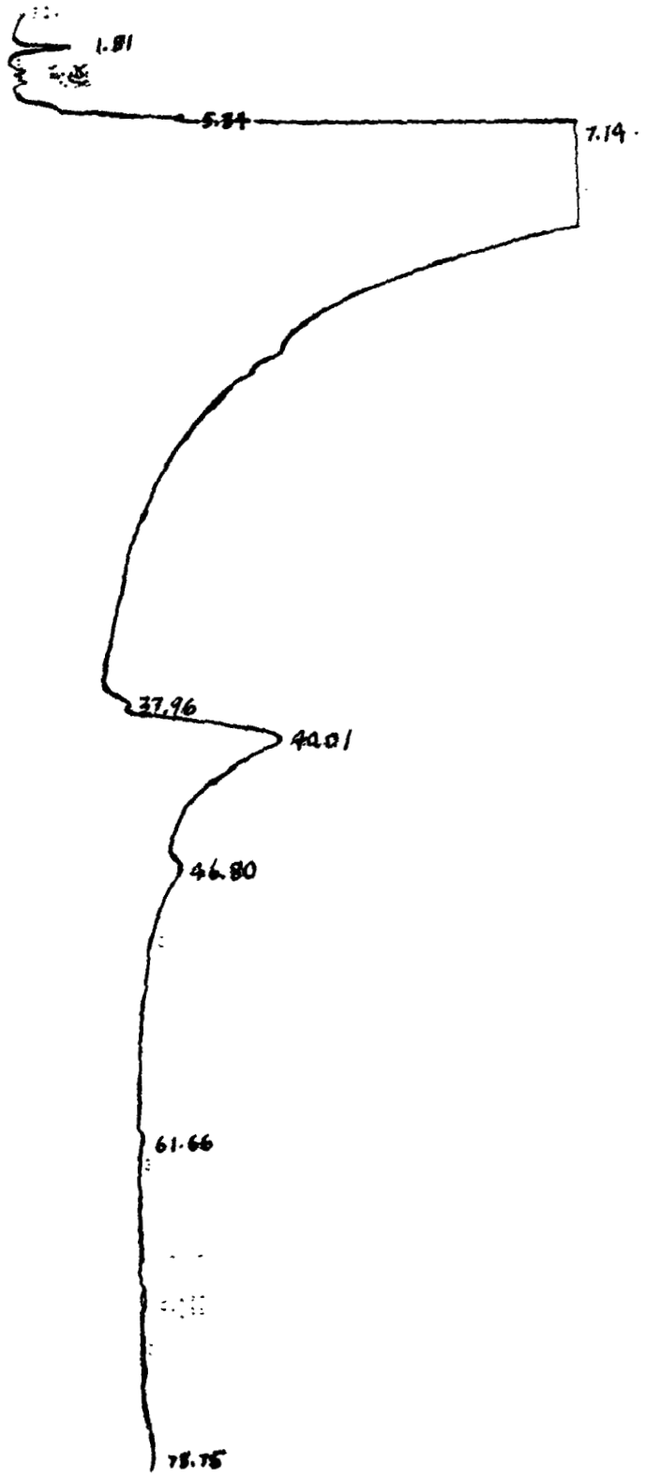

Figure 16
Mixture of PCF and Polyol (20/60), 50 µl.
210 nm

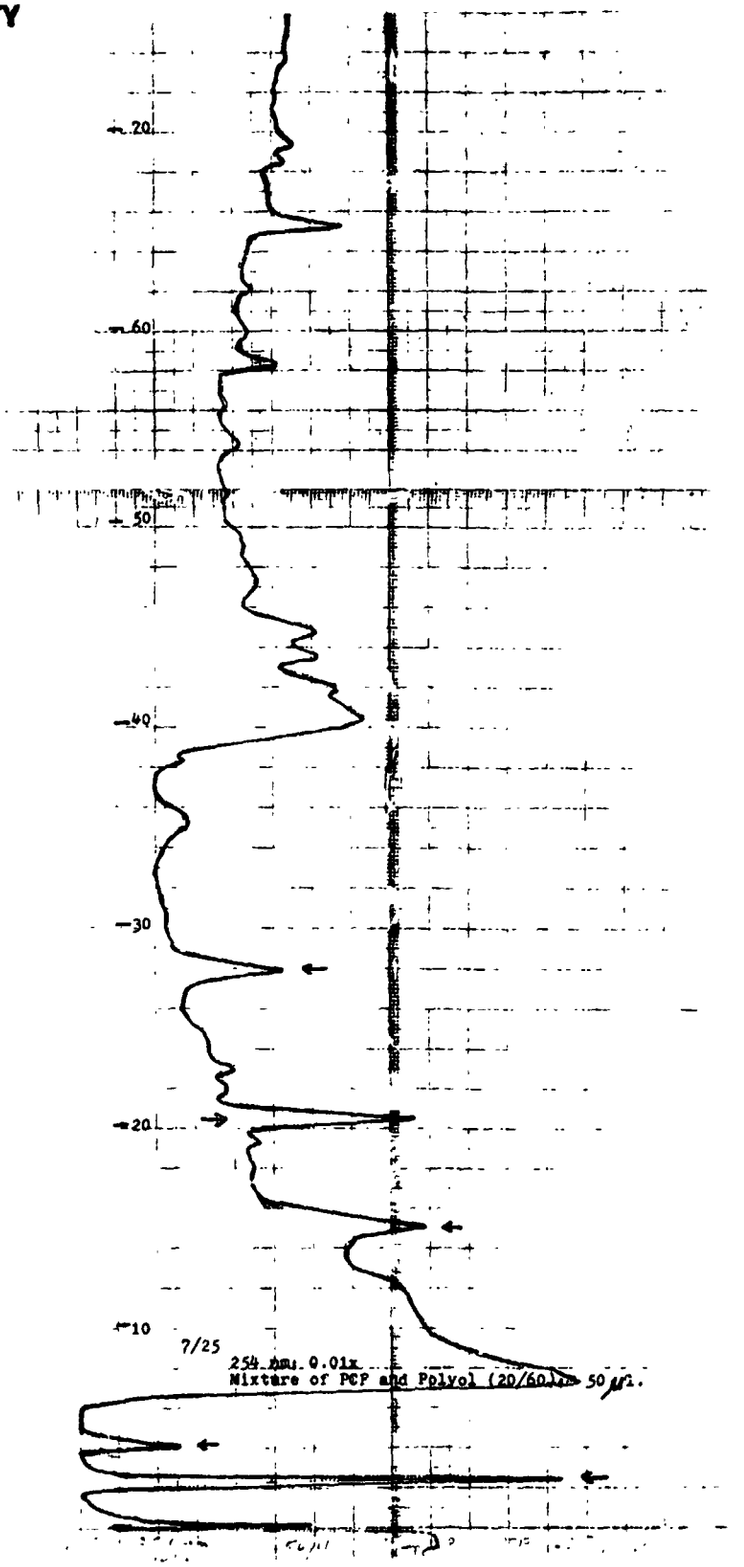

Figure 17

Mixture of PCF and Polyol (20/60), 50 µl.
254 nm, 0.01x

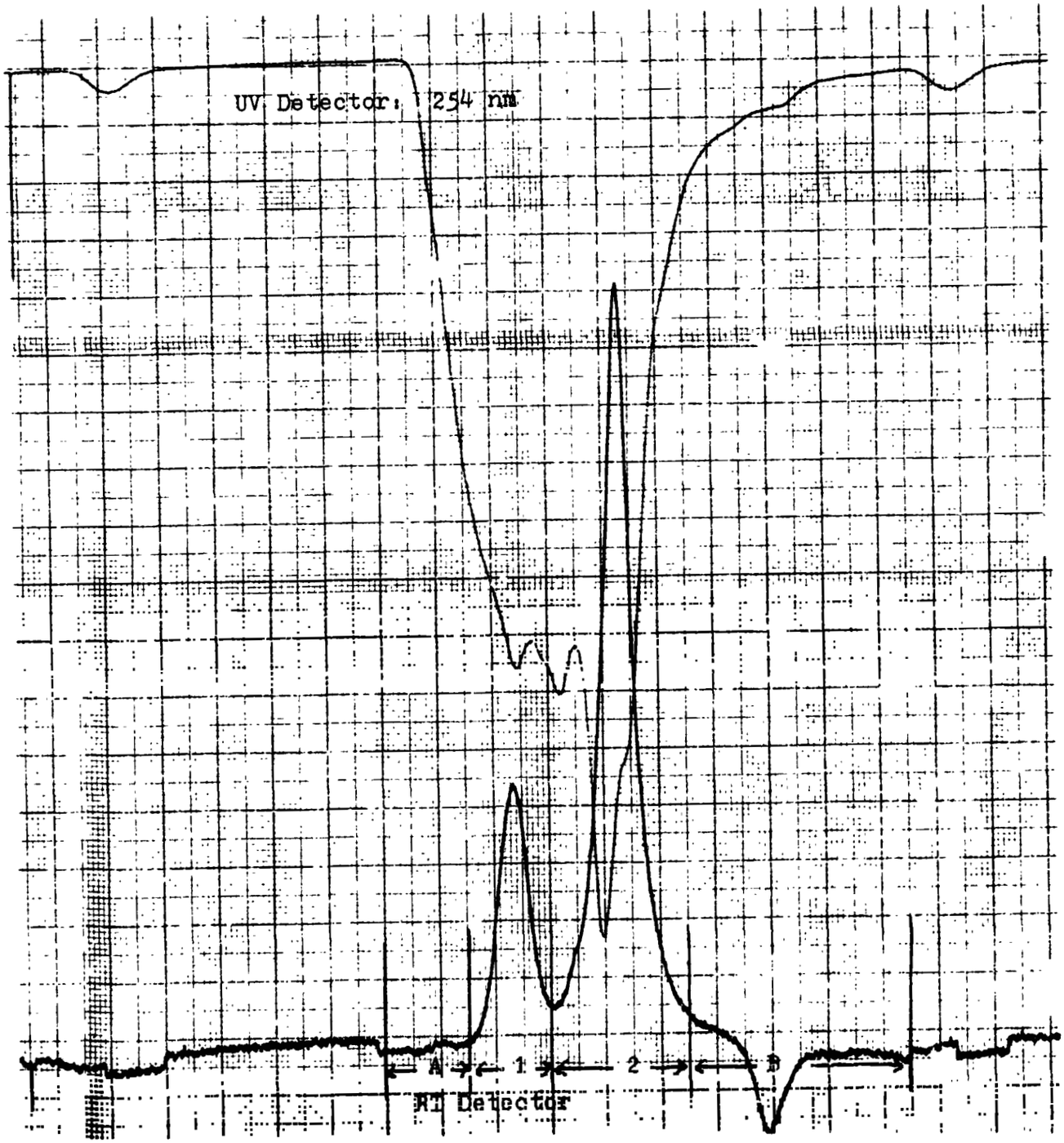

Figure 18
Insta Foam - lot n. 22501; Solvent: THF; Isocratic

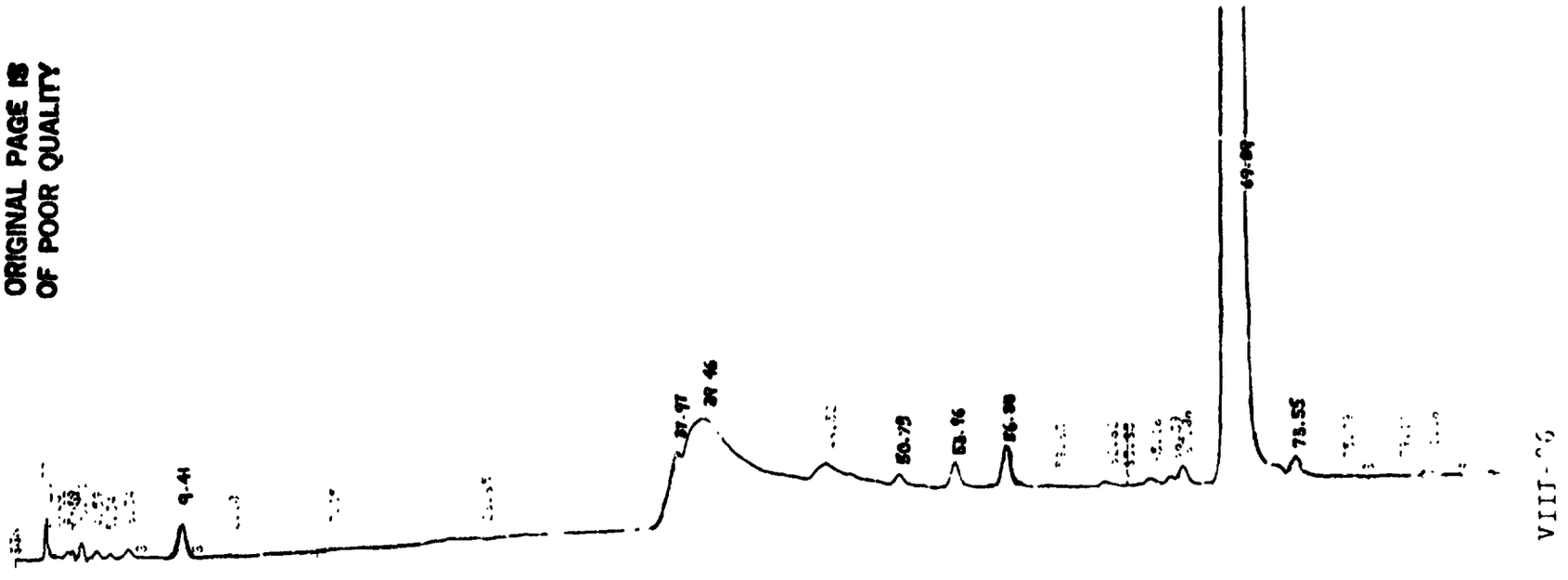

Figure 19
Fraction A (with heating), 50 μl.; 210 nm

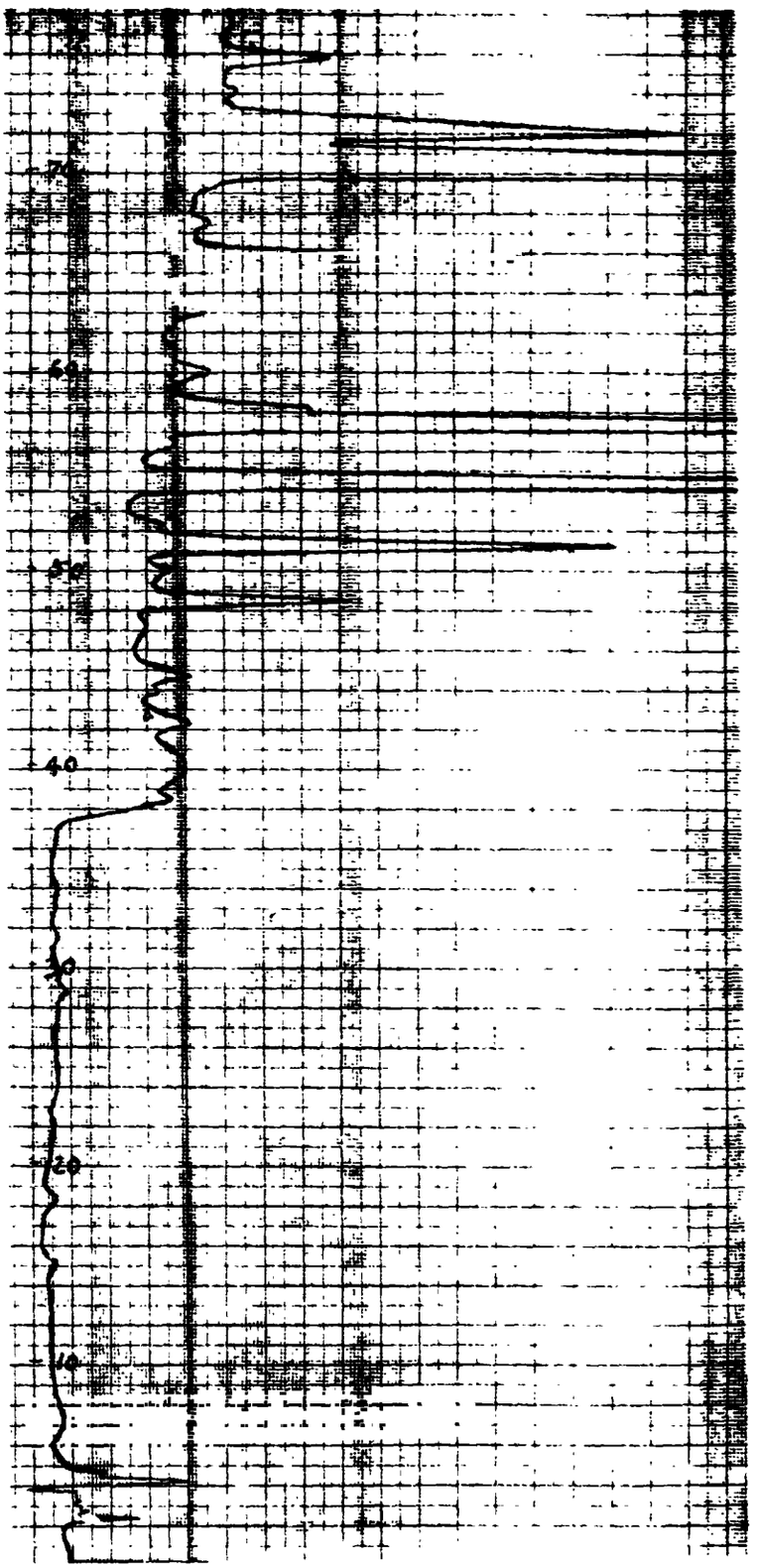

Figure 20

Fraction A (with heating), 40 µl.; 254 nm, 0.01x

ORIGINAL PAGE IS
OF POOR QUALITY

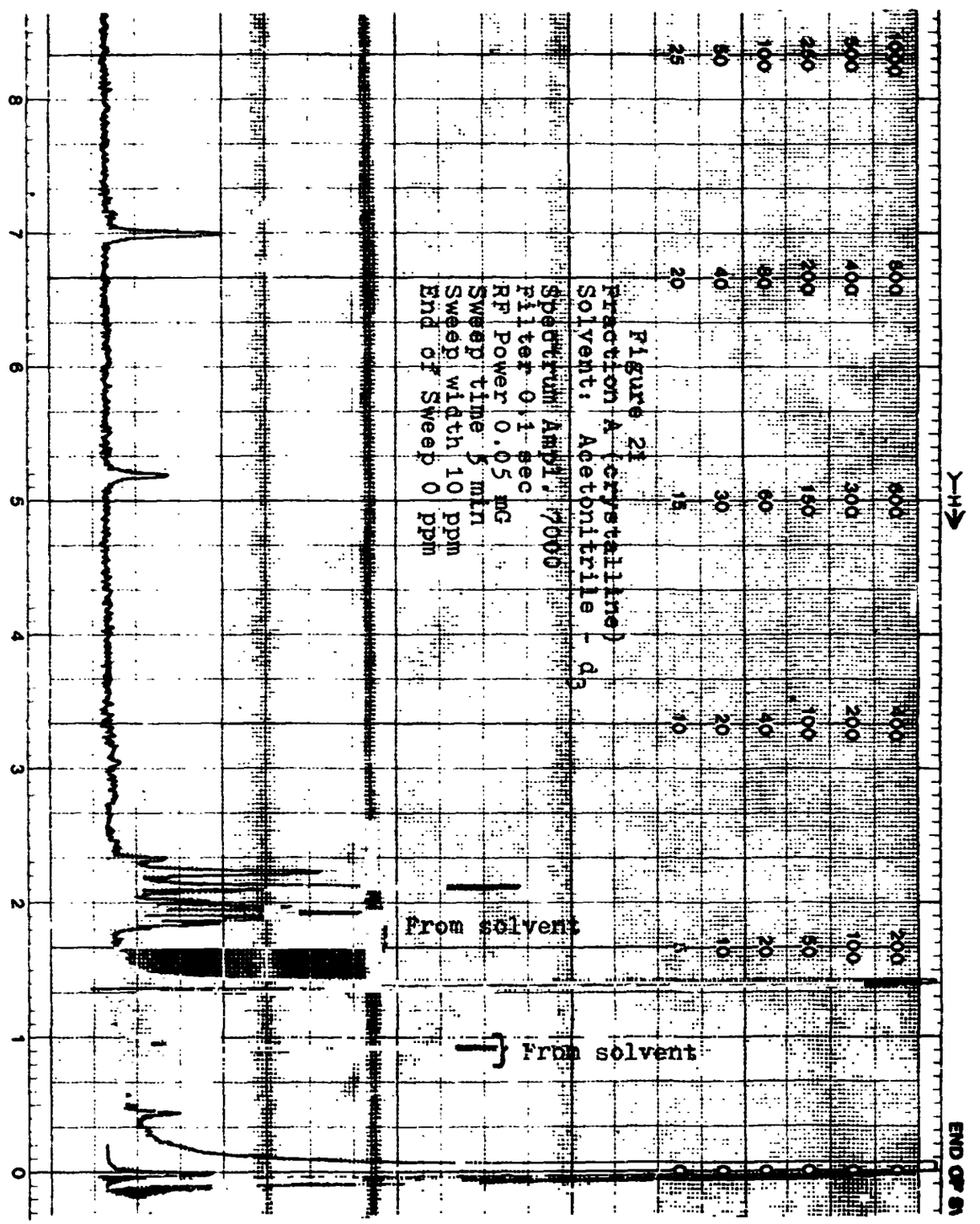

Figure 21
Fraction A (crystalline)
Solvent: Acetonitrile - d_3
Spectrum Ampl. 7000
Filter 0.1 sec
RF Power 0.05 mG
Sweep time 5 min
Sweep width 10 ppm
End of Sweep 0 ppm

Figure 22: Differential Thermal Analysis

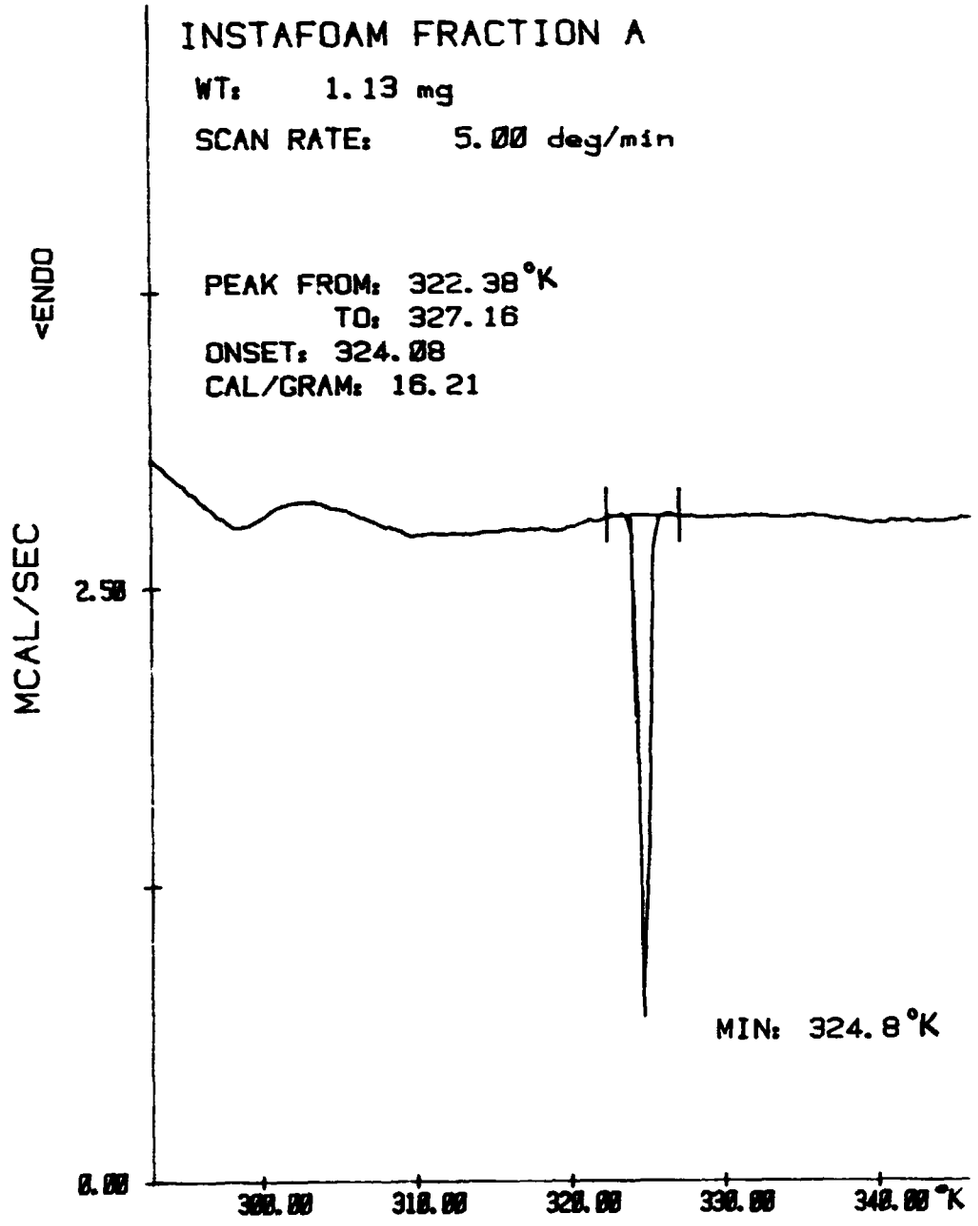

1983

NASA/ASEE SUMMER FACULTY RESEARCH FELLOWSHIP PROGRAM

MARSHALL SPACE FLIGHT CENTER
THE UNIVERSITY OF ALABAMA IN HUNTSVILLE

MECHANICAL PROPERTY CHARACTERIZATION OF P-100/934 GRAPHITE-EPOXY COMPOSITE MATERIAL

Prepared by:	Raymond G. Clinton, Jr., Ph.D.
Academic Rank:	Instructor
University and Department:	Georgia Institute of Technology School of Mathematics
NASA/MSFC:	
Division:	Nonmetallic Materials
Branch:	Ceramics and Coatings
MSFC Counterpart:	H. M. King
Date:	August 19, 1983
Contract No:	NGT 01-008-021 The University of Alabama in Huntsville

MECHANICAL PROPERTY CHARACTERIZATION OF P-100/934 GRAPHITE-EPOXY COMPOSITE MATERIAL

By

Raymond G. Clinton, Jr.
Instructor of Mathematics
Georgia Institute of Technology
Atlanta, Georgia 30332

ABSTRACT

The objective of this research project was to define procedures for the evaluation of properties of advanced fiber-reinforced composite materials and to demonstrate this technology on a specific material system. The procedures included quality control, fabrication techniques, specimen machining, test methodologies, and data collection and interpretation strategies. The material selected for study was Union Carbide's Thornel P-100 carbon fiber combined with Fiberite's 934 epoxy resin in unidirectional tape form.

The success of any project of such nature is primarily dependent on quality control, and thus major emphasis was placed on this area. Tests on the prepreg material, including gel time, resin solids content, tack, volatile content, and flow are detailed. The steps of the fabrication and machining processes are described. Both destructive and nondestructive techniques were employed to assess the properties of the cured laminates.

Tests to determine tensile strength and modulus, compressive strength and modulus, interlaminar and inplane shear strength, and flexural strength and modulus are discussed. The results of these experiments are compared with data generated by researchers at Union Carbide.

ACKNOWLEDGEMENTS

The author would like to express sincere appreciation to NASA and to ASEE for providing this opportunity. The research program was definitely a rewarding experience. The author is especially indebted to Ben Goldberg for his unfailing support and assistance throughout the effort and to Marshall King for sharing his experience and insight. Special thanks also to K. Woodiss and B. Bankston for their ultrasonics work, and to the personnel of the Ceramics and Coatings, and Polymers and Composite Branches of the Materials and Processes Laboratory, who helped to make this a most enjoyable summer.

1. Introduction

Research on advanced fiber-reinforced composite materials began only twenty years ago. During these years, the strength and stiffness properties of the fibers have been steadily improved. The development of stronger and more specialized matrix materials also has helped to overcome limitations and extend the applications of this technology. Such applications are increasing rapidly due to the advantages these materials offer over conventional isotropic materials. The primary advantages are high strength-to-weight and high stiffness-to-weight ratios, dimensional stability, and the capability to tailor the material to satisfy specific design requirements. To properly utilize these materials, a reliable data base of properties which may be used as guides in establishing design allowables is critical.

One area in which the benefits derived from the use of composites are being realized, and in which composites are counted upon to play an increasingly significant role is space structures. Two major requirements in space structures are a high stiffness-to-weight ratio and dimensional stability, e.g., the space telescope. The P-100 graphite fiber is ideally suited to space applications because of its ultra-high modulus and potential low cost. Before this fiber can be used to its full potential, accurate, reliable material properties must be established.

The objective of this research project was to define procedures necessary for the characterization of mechanical properties of advanced fiber-reinforced composite materials, and to demonstrate this technology on the P-100/934 material system. Procedures which were involved included quality assurance tests employing both destructive and nondestructive techniques, fabrication process, specimen production, test methodologies, and data collection and analysis. Particular effort was devoted to quality control.

2. Test Materials

The carbon fiber studied in the investigation was Union Carbide Corporation's Thornel P-100. This recently developed continuous filament which is produced from a pitch precursor has an ultra high modulus (100 Msi). It is important to note that the fibers did have UC-304 sizing but were not shear treated. Typical fiber properties supplied by the manufacturer are shown in Table 1. The graphite filaments were combined with 934 epoxy resin and supplied by Fiberite Corporation in 6 inch wide prepreg tape form, product designation hy-E 2034E. The Fiberite 934 epoxy is a 350°F resin system used for a variety of high performance aerospace applications including the payload bay doors of the space shuttle.

2.1 Prepreg Quality Tests

Visual inspection of the prepreg material revealed severe flaws. Along one edge of the tape, fibers had been badly skewed. This damage extended into the material to a depth which varied between one and two inches, and continued throughout the entire length of the roll. The problem was overcome by cutting off a portion of the edge as will be explained in Section 2.2.

Another serious flaw involved the epoxy resin system. The characteristics observed in the material were similar to those commonly found in prepregs in which the resin has advanced beyond B-stage. There was a marked loss of flexibility and a complete lack of tack. Quality control tests were conducted in an attempt to determine the nature and severity of the problem. Samples were also returned to Fiberite for parallel tests.

The quality tests included the following: resin solids content (method R-15), volatile content (method QCI-C-V-14), resin flow (method QCI-C-F-42), gel time (method G-2), and tack (method QCI-C-T-1). The procedures followed were those recommended by Fiberite, as designated in parentheses above. These property tests, with the exception of the tack test, are also covered by ASTM standards D3529, D3530, D3531, and D3532, respectively, which for practical purposes are identical. Briefly, the tack test consists of attaching one strip of material, (1" x 3" with fiber direction parallel to 1" dimension) to a clean corrosion resistant steel plate with light pressure and then similarly attaching a second strip to the first strip. The plate is positioned such that the specimen length is vertical. The specimen must remain in the position for 30 minutes.

The results of these tests are presented in Table 2. Fiberite did not conduct a tack test on the returned samples due to the obvious condition of the material[1]. The values obtained for the remaining properties were typical of those one would expect from a "normal" batch i.e., well within specifications. It appeared that the resin system had not advanced to a detectable or deleterious level beyond B-stage.

The presence of the previously described undesirable properties was not explained by the test results. But, it was necessary that the problems be eliminated before test panel fabrication for several reasons. Principal among these

were the greatly increased possibility of damage to the fibers during handling, a possible effect on the resin distribution in the cured laminate, and excessive difficulty in maintaining correct ply orientation and butt joint tolerances during the fabrication process.

Formation of a thin surface layer was assumed to be the source of both problems. This assumption was not inconsistent with the findings of the quality tests in that the size of the proposed layer was insufficient to influence the macro scale properties measured. At the time, it was believed that the layer consisted of highly polymerized resin*. A short-duration soak in an acetone-rich atmosphere was used in an attempt to restore tack and flexibility to the material. The treatment was successful in these areas; however, it also introduced two potential problems: (1) a retarding effect on polymerization due to plasticization and (2) an increase in volatile content which could lead to an increase in void formation in the laminate.

Volatile content, gel time and tack tests were conducted on several groups of samples which has been exposed to different duration soaks. All passed the tack test, but it was determined that the volatile content increased with exposure time. A five minute exposure appeared the most suitable, as the volatile content was found to be in the range 1.53% $\pm$ .14%, safely below the vendor recommended maximum of 2.0%. Also, the gel time was unaffected, measuring 12.4 $\pm$ 0.5 minutes.

Differential scanning calorimetry (DSC) tests were also run on the samples to investigate the effect of the five minute acetone-atmosphere soak on the polymerization process of the 934 resin. A representative plot in which the responses of the treated and virgin material are shown is presented in Figure 1. Two principal results of the tests may be observed in this graph. First, if the treatment had resulted in residual acetone being left in the matrix, a peak would be expected in the range around 60°C where the acetone would have been driven off. No such peaks were seen. Second, the polymerization peak of the treated sample, near 215°C, was not shifted with respect to that of the virgin sample. The curve size difference is due simply to the variation in sample size.

The above results and the similarity of the characteristics of both curves support the conclusion that the polymerization process was not affected by exposure to the acetone atmosphere. The treatment was therefore incorporated into the fabrication procedure.

2.2 Test Panel Description and Fabrication

The number and sizes of the panels were selected to optimize the use of the limited and costly material. A total of five panels were produced from which specimens were obtained for the five different mechanical property tests. Test panel dimensions and ply orientations are provided in Table 3. The mechanical properties were used as panel designations.

*Subsequent evidence has suggested that the layer may instead have been an oxide film.

Table 1. Typical Fiber Properties "Thornel" P-100 Fiber Grade VS-0054

Property	U.S. Customary Units	Value
Tensile Strength	$lb/in^2 \times 10^3$	325
Tensile Modulus	$lb/in^2 \times 10^6$	100
Density	lb/in^3	0.078
Filament Diameter	μ	11
Elongation at Break	%	0.5
Elastic Recovery	%	100
Carbon Assay	%	99 +
Surface Area	m^2/g	1
Thermal Conductivity	BTU-ft./hr.$(ft.^2)^oF$	300
Electrical Resistivity	Ohm-cm $\times 10^{-4}$	2.5
Longitudinal CTE at 70^oF (21^oC)	$PPM/^oF$	-0.9
Specific Heat at 70^oF (21^oC)	BTU/lb^oF	0.22

Table 2. Results of Prepreg Quality Tests

	MSFC	Fiberite
Resin Solids Content	37.4%	39%(1)
Volatile Content	.62%	.60%
Resin Flow	12.6%	22.1%
Gel Time	12.6 min(2)	9.8 min(3)
Tack	Failed	-

(1) Value supplied in vendor certification

(2) Test conducted at 325^oF

(3) Test conducted at 350^oF

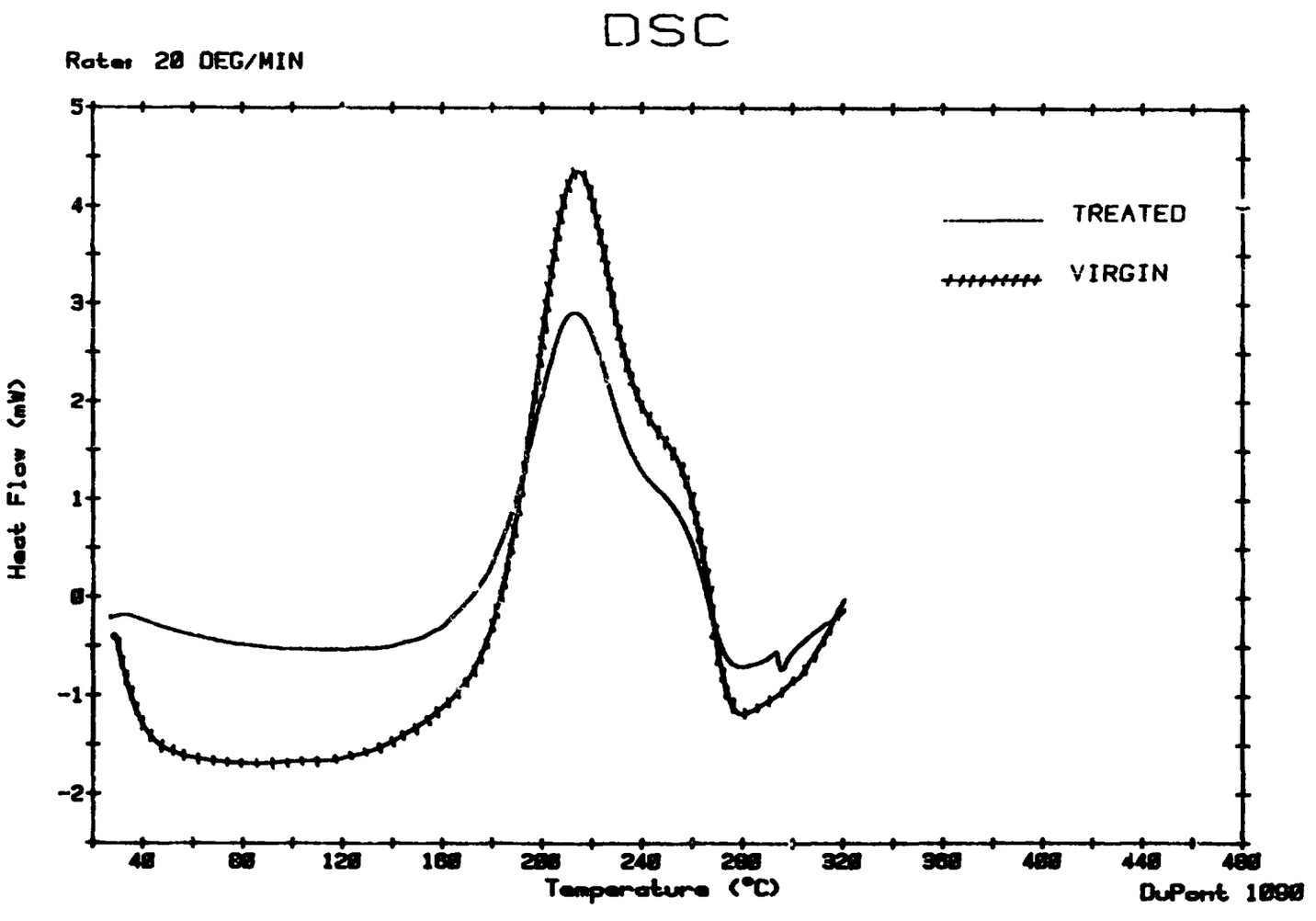

Figure 1. Differential scanning calorimetry results from virgin and acetone-atmosphere treated P-100/934 prepreg material.

Table 3. Test Panel Dimensions and Ply Orientation

Panel	Dimension	Fiber Orientation	Stacking Order
Tensile	11" x 14"	Parallel to 11" dimension	0_5
Compressive	7.5" x 11.5"	Parallel to 7.5" dimension	0_{12}
Inplane Shear	10" x 12"	$\mp 45^{o}$ with respect to 12" dim.	$\mp 45_{2s}$
Short Beam Shear	3" x 6"	Parallel to 3" dimension	0_{24}
Flexure	8" x 6"	Parallel to 8" dimension	0_{12}

Laminate construction for the tensile, compressive, and inplane shear panels was complicated by the fiber damage near the edge of the tape as previously described. These areas were cut from the sections used in the interior of the panel. But, since one inch of material was trimmed from the perimeter of the cured panel, a one inch wide flawed region was left on those sections which were positioned at the edges of the laminate. All edge splices in the above three panels were staggered a minimum of one inch in adjacent plies, and the pattern was not repeated within a 5 ply thickness. The short beam shear and flexure panels did not require butt joints.

The fabrication process was begun by thawing the prepreg and cutting the required number of sections from the roll. Each section was then placed in an acetone-rich atmosphere for five minutes, with the single ply of backing paper remaining on the material. The individual plies were inspected to determine the extent of fiber damage and assigned a specific position in the layup sequence on this basis.

The laminate and support materials were assembled and enclosed within a cork dam constructed around the perimeter of the laminate. The following stacking order was used:

1. One half inch aluminum cure plate
2. Teflon-coated, adhesive-backed separator film covering cure plate working surface
3. One ply of Teflon film (1 mil)
4. One ply of porous Teflon-coated glass cloth (TX1040)
5. Graphite/epoxy laminate
6. One ply of porous Teflon-coated glass cloth (TX 1040)
7. Bleeder paper
8. Lightweight glass cloth bleeder
9. One ply of Teflon film (1 mil)
10. One half inch aluminum cure plate coated with a release agent (Release All 75)
11. Two plies of 181 glass for overbleed
12. A vacuum bag covering the entire assembly and sealed to the cure plate.

The amount of resin to be removed from the layup was calculated, and the

appropriate number of plies of each bleeder material was selected to achieve the proper absorption.

Test panels were cured in a heated press. Fiberite cure cycle A-9, listed below, was followed.

1. Vacuum bag entire assembly
2. Apply full vacuum at room temperature for 30 minutes to debulk
3. Maintain vacuum throughout entire cycle
4. Raise temperature to 250°F (+5 - 10°F) at 2° - 5°F per minute under minimal pressure
5. Hold at 250°F (+5 - 10°F) for 15 ± 5 minutes
6. Apply 100 (+5 -0) psi pressure
7. Hold at 250°F (+5 - 10°F) and 100 (+5 -0) psi for 45 ± 5 minutes
8. Raise temperature to 350°F (+10 - 0°F) at 2° - 5°F per minute
9. Hold at 350°F (+10 - 0°F) for 2 hours ± 15 minutes
10. Cool under pressure and vacuum to below 175°F.

Thermocouples were inserted in the edges of the laminate to monitor the temperature. Using these readings, the heating elements of the press were cycled on and off to achieve the desired temperature rise rate.

2.3 Laminate Quality Tests

Several different methods were employed in an attempt to ensure that the panels were of acceptable quality. The major interests were the fiber volume fraction and the possible effects of the acetone treatment on the polymerization process of the resin and the void content of each panel. The methods utilized to investigate these areas were ultrasonic C-scan, differential scanning calorimetry, thermomechanical analysis, optical microscopy, and resin digestion.

All ultrasonic C-scans were run using a Sperry Reflectoscope Model S80. The tensile panel was the first to be scanned. Due to a combination of the manner in which the laminate was supported and the equipment settings, only the surface characteristics were recorded. The scan was dotted with what were apparently sizeable voids. The panel was immediately cut into specimens so that the edges could be microscopically examined for voids. None were observed at a magnification of 200X. The scan procedure was re-examined and the problem corrected. Unfortunately, the tensile specimens were not scanned individually.

The C-scan results for the compressive (COM), inplane shear (IPS), short beam shear (SBS), and flexure (FLEX) panels* are shown in Figures 2-5, respectively. The spots near the corners were produced by the posts which supported the laminates. With few exceptions, the scans indicate a high degree of uniformity in all panels and a lack of voids.

Prominent areas of high attenuation (noted by the disappearance of the trace) were the upper right corner of the IPS panel, Figure 3, and the left and right edges of the SBS panel, Figure 4. In fabrication of the SBS panel, none of the damaged edges were removed from the plies. So, the high attenuation was not

* The one inch trim area around the perimeter of the panels was not removed before scan.

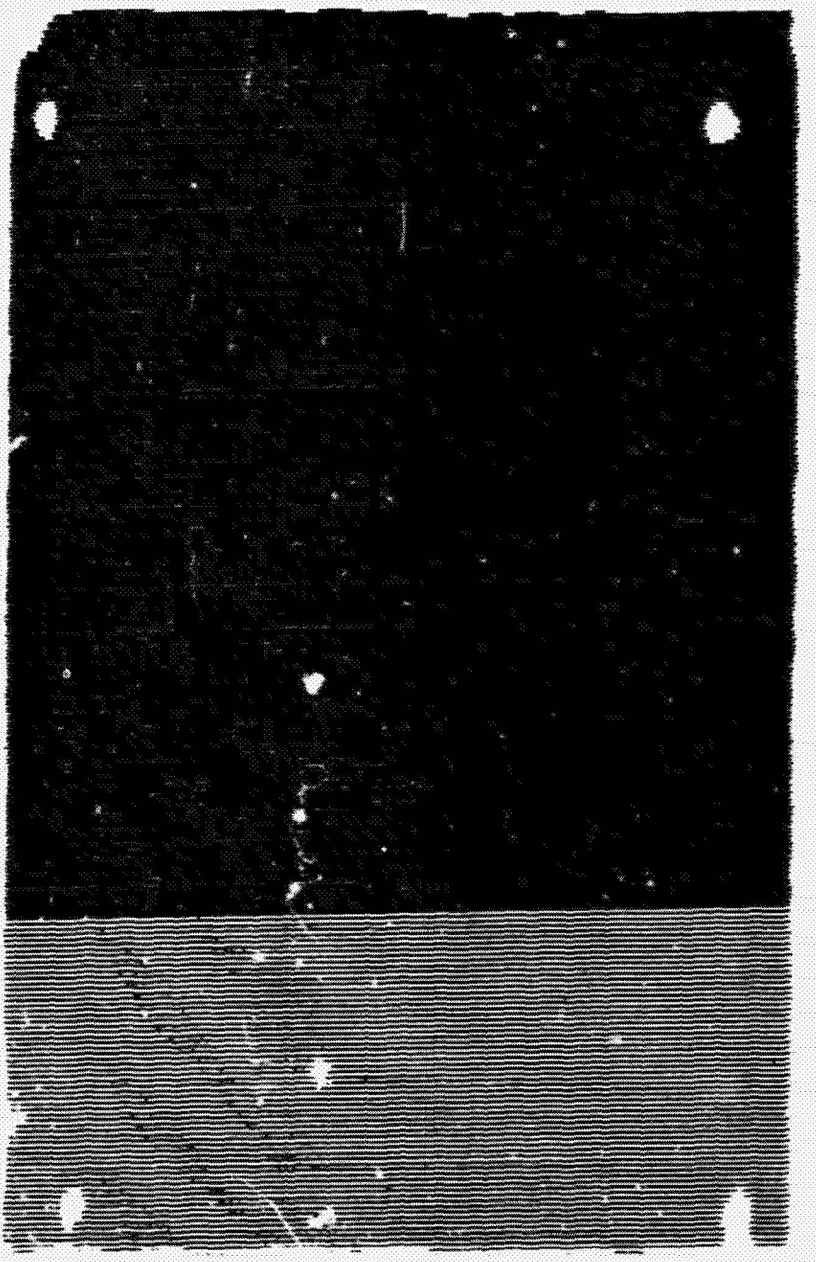

Figure 2. Ultrasonic C-scan of compression panel.

Figure 3. Ultrasonic C-scan of inplane shear panel.

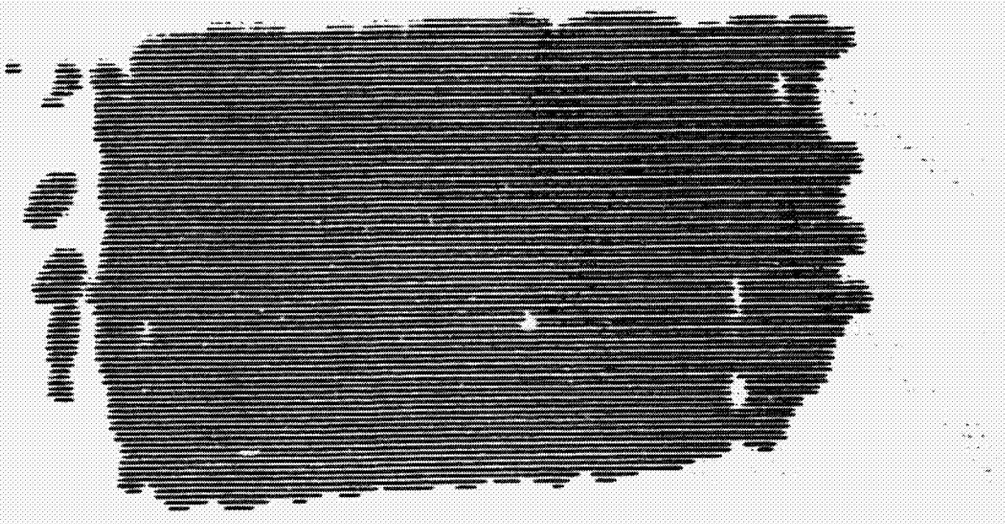

Figure 4. Ultrasonic C-scan of short beam shear panel.

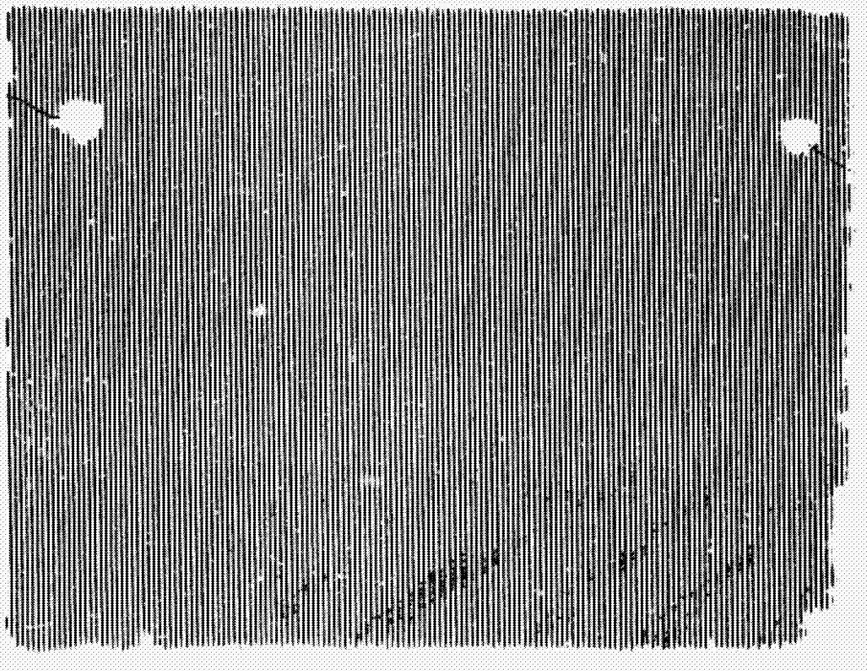

Figure 5. Ultrasonic C-scan of flexure panel.

surprising nor was it of any concern since the specimens were taken from the heart of the panel which was quite uniform.

The cause of the nonuniform response around the corner of the IPS panel was not completely determined. It was observed that the region closely corresponded to a surface pattern on the laminate. Also, fiber content samples taken from the area displayed a lower percentage of resin than was measured in other parts of the panel. It is important to note that microscopic examination of the two specimens containing portions of the region did not reveal voids at 200x magnification factor. The above evidence tends to support the hypothesis that the response was due to an uneven resin distribution, or overbleed in the area.

Results of the microscopic inspection strengthened the conclusions drawn from the C-scans relating to the quality of the panels. Several specimens were selected from each test group and examined under an optical microscope at a magnification factor of 200x. No voids were observed.

The weight percent of fiber in the cured laminates was determined in accordance with ASTM D3171. The results of tests conducted on five specimens cut from various parts of each panel are presented in Table 4. Due to the limited amount of available material, several of the samples were taken from the trim area as noted. The average fiber volume percent was calculated using the fiber density and resin density values supplied by the manufacturers and the experimentally determined weight percent. Data from high attenuation areas was omitted for obvious reasons.

Table 4. Fiber Content Results

Panel	Percent Weight				Percent Volume	
TEN	72.1	70.3	75.3[T]	72.9	73.3	61.0
COM	68.2[T]	67.1[T]	70.0	71.2	70.7[T]	57.9
IPS	69.0	68.3	76.1[A]	69.9	76.7[A]	57.5
SBS	69.1	70.0	72.4	69.3	71.7	59.1
FLEX	68.7	74.1[T]	67.2	70.1	75.2[A]	58.6

T Specimen taken from trim
A Specimen taken from an area of high attenuation.

The consistency of the measurements within and among the panels was an encouraging result, as was the fact that the fiber volumes were all close to the targeted value of 60%. Furthermore, in comparisons of the ultrasonic scans and the fiber content data, good qualitative correlations were evident. Thus, the results from these quality assurance tests strongly indicated that all of the panels

were of acceptable quality. However, for completeness, an investigation of one additional issue was conducted, and it is described below.

Although no adverse effects on the prepreg material due to the acetone treatment were discovered, it was necessary to study the behavior of the cured resin to ensure that the glass transition temperature (T_g) and the polymerization process had not been altered. DSC and TMA tests were conducted on both 934 resin samples and P100/934 composite samples using a DuPont 1090 Thermal Analyzer.

The principal result from the DSC series was that the polymerization process had not been influenced by the treatment. A representative plot supporting this conclusion is presented in Figure 6. In the figure, the responses of two samples of 934 epoxy which contained no fibers are shown for comparison. Both samples were initially heat treated to 300°C at 20° C per minute to remove any residual monomer. The response represented by the slashed line was from a specimen which was cut from the edge of the FLEX panel. The other specimen was taken from the edge of a T300/934 laminate which was subsequently used for end tabs. The material used in the latter panel was of good quality, and the fabrication process was the same as followed in the production of the test panels, with the notable exception of the acetone treatment. It is readily apparent that the characteristics of both curves are very similar, especially the polymerization peaks near 240°C. Apparent T_g regions around 200°C are observable in the response patterns of both specimens. The T_g of Fiberite 934 resin has been shown to be in this temperature range[2,3].

The effect of acetone in the matrix is evident by comparison of the two curves shown in Figure 7. The behavior of a P-100/934 composite specimen taken from the SBS panel is represented by the slashed line. The other was a similar sample which had been immersed in liquid acetone for ten seconds and then oven dried at 160°C for one hour before testing. The elevated temperature drying would certainly have evaporated any acetone remaining on the sample surface. Nevertheless, the shapes of the curves differ noticeably. This difference may be ascribed to the presence of acetone in the matrix as evidenced by the acetone peak in the solid curve around 60°C.

The salient points observed in the DSC tests are supported by the results of the TMA series. In Figure 8, the dimensional change of a T300/934 composite sample taken from the tab panel is plotted versus temperature. A similar measurement made on a P-100/934 composite sample from the COM panel is presented in Figure 9. Of significance are the correspondence of the inflection points of the two curves and the correlation with similar transition regions observed in the DSC traces.

In the initial analysis of the two samples described above, monomer was polymerized during the 10°C/minute temperature rise to 300°C. The second runs, shown in Figure 10, provide evidence of this further polymerization by the facts that the curves were smoother and the inflection points occured at slightly lower temperatures. Glass transition temperature regions around 200°C are evident which agree well with the apparent T_g range noted in the DSC tests.

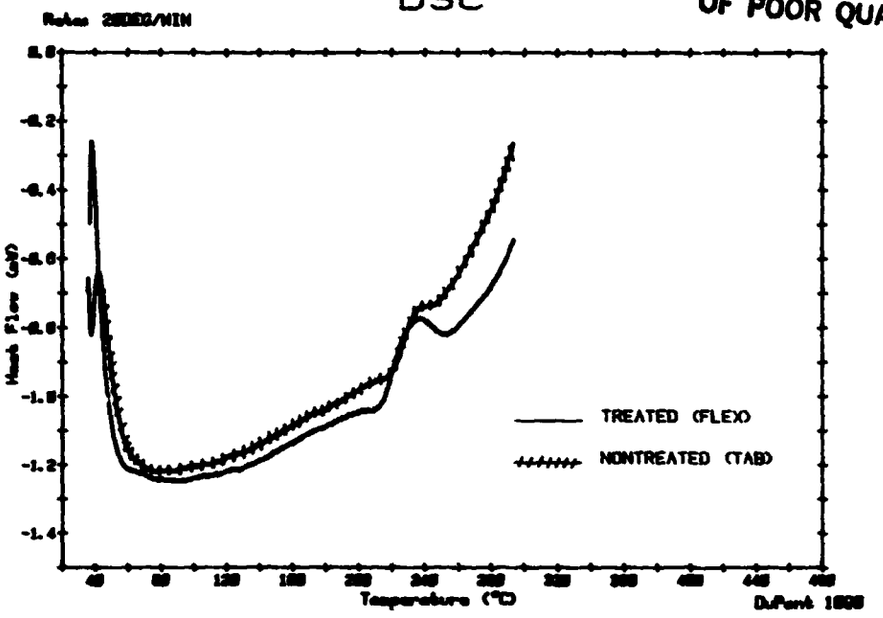

Figure 6. Differential scanning calorimetry results from cured resin samples of acetone-atmosphere treated 934 (P-100/934 FLEX) and nontreated 934 (T300/934 TAB).

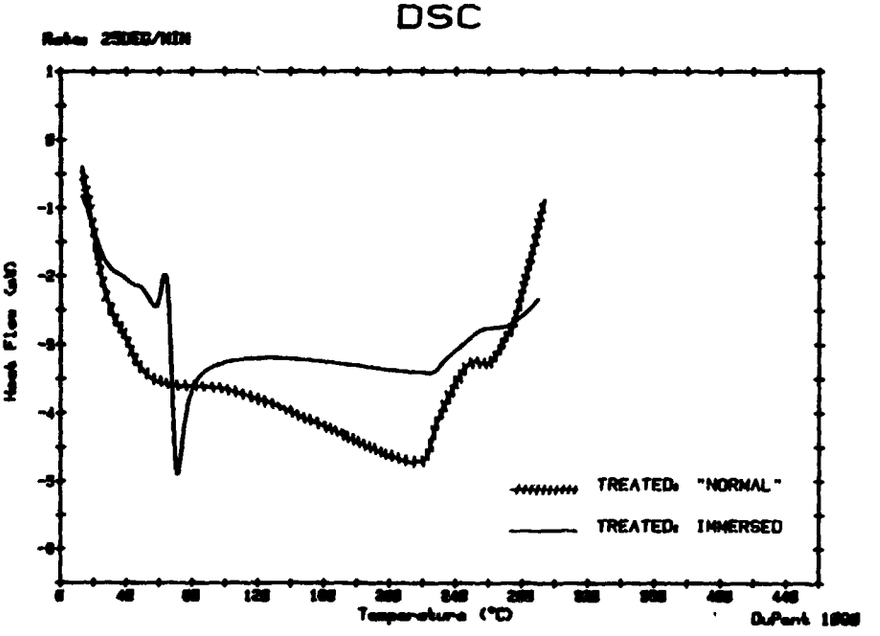

Figure 7. Differential scanning calorimetry results from (a) "normal" (b) liquid acetone immersed samples of atmosphere treated P100/934 composite.

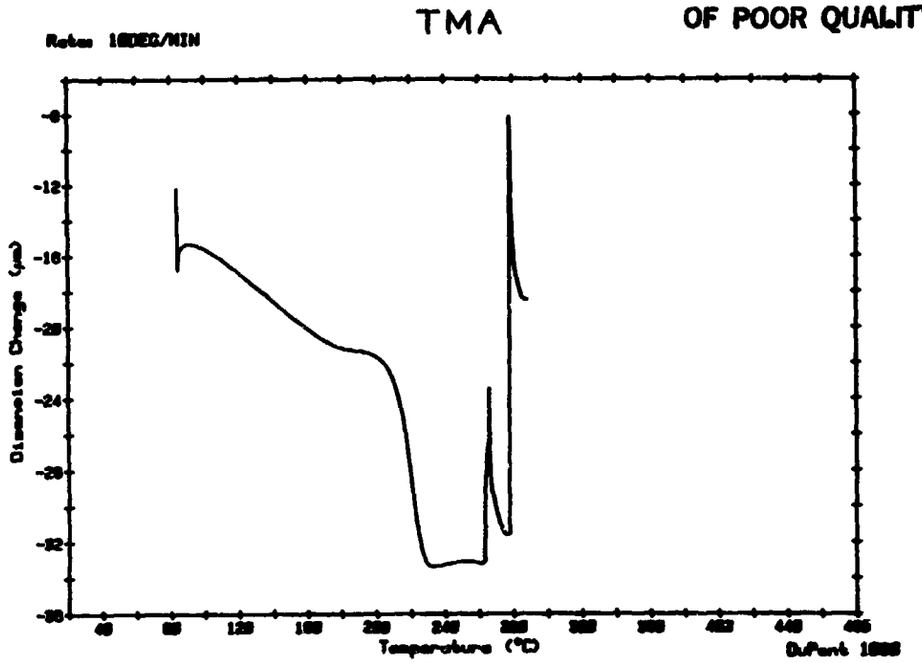

Figure 8. Thermomechanical analysis of P-100/934 composite (COM panel). First heat cycle.

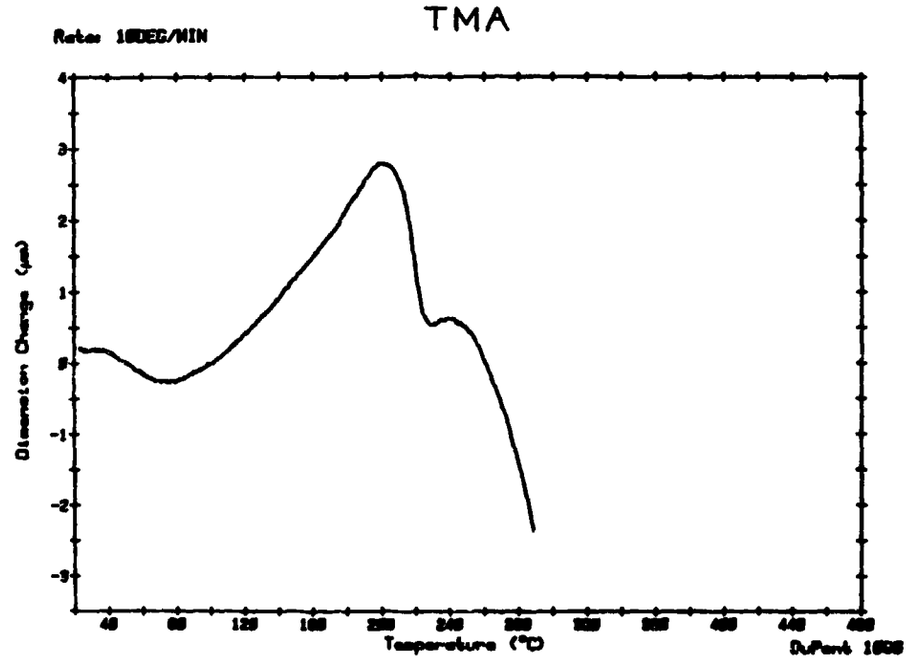

Figure 9. Thermomechanical analysis of T300/934 composite (TAB panel). First heat cycle.

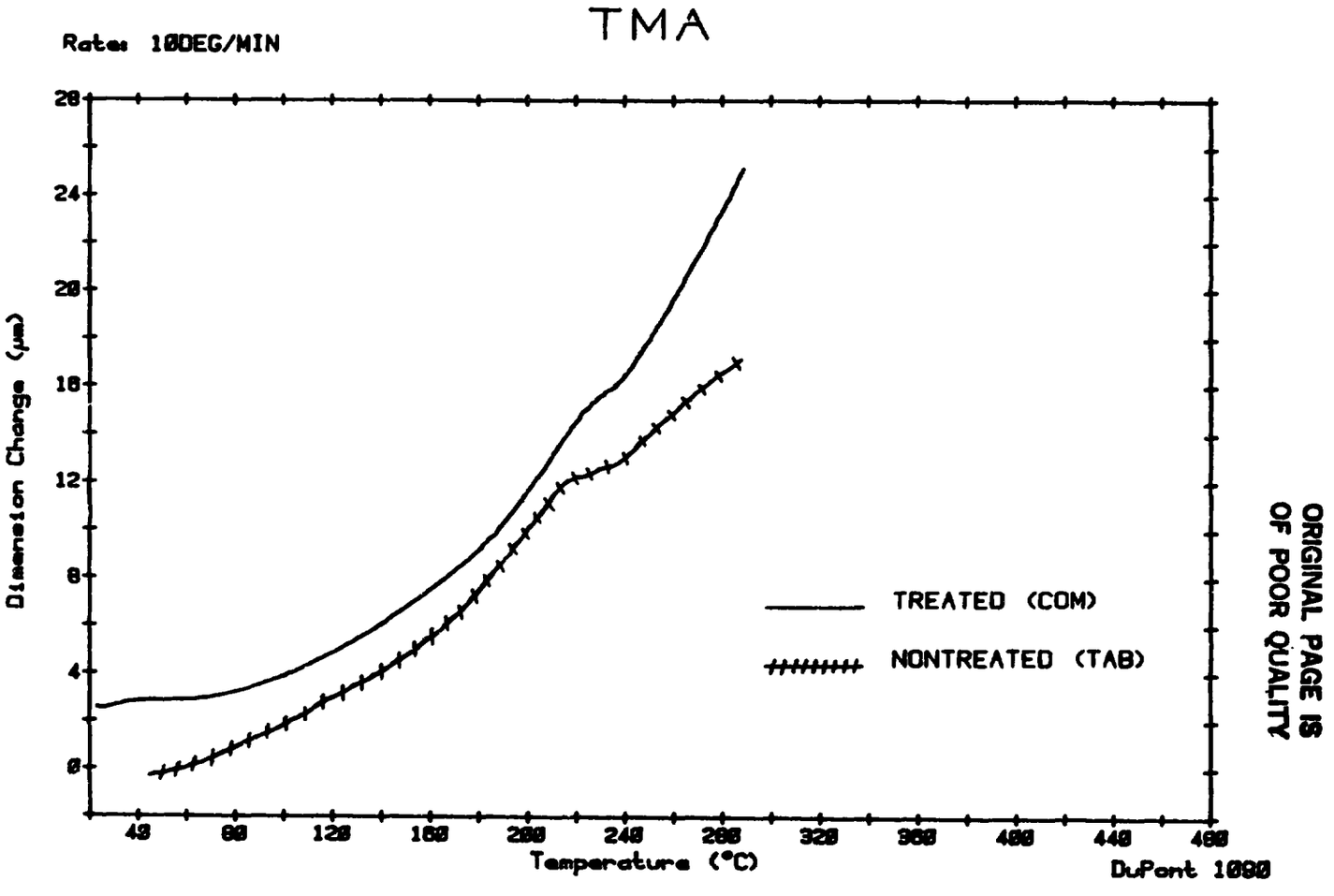

Figure 10. Thermomechanical analysis of P-100/934 composite (COM panel) and T300/934 composite (TAB panel). Second heat cycle.

It was concluded from the results of the DSC and TMA tests that the five minute exposure to the acetone atmosphere did not result in any residual acetone of a measurable amount in the matrix as evidenced by the absence of acetone peaks in all of the responses. Furthermore, the polymerization process was not altered nor was the glass transition temperature affected by the treatment.

2.4 Specimen Description

Test specimens were machined from the panels using a 220 grit diamond wheel mounted on a Strasbaugh slitting saw. Table feed was approximately three inches per minute, and coolant flow was used for all cuts. Initially, a one inch width of material was trimmed from the perimeter of each panel to remove the flawed material which had been used at the edges as noted previously. Visual and microscopic inspection of the specimens revealed no rough edges or machining induced flaws.

Specimen dimensions were established in accordance with ASTM standards. The dimensions used are provided in Table 5. Two different lengths of compression specimens were chosen to investigate whether a variation in the length of the tabbed area would affect the results. The gage section was held constant at 0.5 inch for all tests. For similar reasons, two different widths of short beam shear specimens were tested.

Specimens used for the determination of tensile, compressive, and inplane shear properties required end tabs. A fiberglas-reinforced laminate was used as tab material for the tension and inplane shear specimens. It was constructed from ten plies of a satin weave fabric (Clark-Schwebel style 7781 - Volan finish) and Fiberite 934 epoxy resin. Tabs cut from this panel were 1.5 inches in length, with an appropriate width matching that of the specimen type. All had a 45° bevel.

Table 5. Test Specimen Di · ensions

Specimen Type	Overall Length	Width	Average Thickness
0° Tension	9.0"	0.5"	0.031"
90° Tension	6.5"	1.0"	0.033"
0° Compression	5.0"	0.250"	0.063
	5.5"		
90° Compression	5.0"	0.250"	0.063
	5.5"		
Inplane Shear	10.0"	1.0"	0.046"
Short Beam Shear	0.75"	0.136"	0.135"
		0.232"	
Flexure	3.0"	1.0"	0.067

Unidirectional graphite-epoxy tabs were used for the compression specimens. Fiberite hy-E 1034C prepreg was used to construct the eight-ply laminate. The number of plies was chosen such that the overall thickness of the tabbed portion of the specimens would comply with ASTM tolerances. Two different lengths of tabs, 2.25 inches and 2.50 inches were cut from the panel. A 0.25 inch taper was milled into each piece.

All tabs were bonded to the specimens with AF-163-3M, a supported structural adhesive manufactured by 3M. This product is an improved version of the 250°F curing 3M adhesive, AF-126, suggested in ASTM D3039 and is widely used in the aerospace industry. Bonding was accomplished using a heated press according to the cure cycle recommended by the vendor. No vacuum was applied.

3. Test and Measurement Procedures

All tests were conducted according to currently approved ASTM standards. Not all of these standards enjoy universal acceptance; the compression and inplane shear tests are two prime examples. There are three standard test procedures recognized by ASTM for compression testing of composite materials. ASTM D3410-75, Test for Compressive Properties of Oriented Fiber Composites, was followed in this study. The standard requires use of the so-called "Celanese" test fixture, and the specimen design features an unsupported gage length of 0.5 inch. The other two methods are ASTM D695-69 and ASTM C393-62. Additional methods of compression testing are evaluated and compared by Clark and Lisagor[4] in a well written article which also contains a discussion of the problems involved in this type of testing.

Inplane shear properties are also determined in a variety of ways. The ASTM standard for Inplane Shear Stress-Strain Response of Unidirectional Reinforced Plastics, D3518-76, was used to obtain these properties in the present investigation. In this method, shear stress-strain data is calculated from the results of a uniaxial tension test of a $\pm 45^{\circ}$ laminate. The theoretical basis for the standard is discussed by Rosen[5]. In the aerospace industry, the rail shear test is generally preferred, but again the issue is unsettled, as both two-rail and three-rail fixtures are used. An excellent analysis of the two-rail shear test is given by Whitney, et al.[6], and a comparison of the $\pm 45^{\circ}$ tensile coupon test and the symmetric three-rail shear test is presente by Yeow and Brinson[7]. These are the more popular methods, but a substantial research effort has focused on this topic and a number of test procedures have been proposed.

The ASTM test methods for the determination of tensile, interlaminar shear, and flexural properties, which were used in this study, are generally accepted as standard. Although some imperfections exist, these can normally be overcome. An example is ASTM D790-81, the method for obtaining flexural properties. In an investigation of this standard, Zweben et. al.[8] reported that the specified procedures provided reliable strength data, but that the flexural modulus values could be misleading. Sufficiently high span-to-depth ratios or a correction for shear deformation are suggested to correct the problem.

The principal experimental difficulty which arises in tension tests is failures which occur outside the gage section. To promote failure in the test

section, the solution recommended in the standard, ASTM D3039-76, is a re-examination of those portions of specimen design relating to the tabs, material, adhesive, and configuration, and the gripping method.

Apparent interlaminar shear strength of composites is determined by the short-beam method, ASTM D2344-76. The procedure can normally be used with success on carbon fiber reinforced plastics. Problems occur when the short-beam specimens break in a complex mode involving both shear and tensile failures. Data from such tests cannot be used even as a conservative estimate of the shear strength[9]. Thus it is necessary to examine the specimen to determine the failure mode.

All tests were conducted in an Instron machine. The crosshead speed used for the short beam shear, compression, and transverse (90^{o}) tension tests was a constant 0.05 inches per minute. For the flexure, inplane shear, and longitudinal (0^{o}) tension tests, the speed was 0.10 inches per minute.

The selected span-to-thickness ratio for the short-beam shear test was 4 to 1. The actual ratio was reduced to approximately 3.7 to 1 because the support span was fixed at one half inch and the specimen thickness exceeded the design limit.

The three-point loading method was used in the flexure tests. A span-to-depth ratio of 32 to 1, which had been used by Union Carbide[10], was chosen in an effort to hold test conditions as constant as possible and thereby enable a better comparison of results. However, for the reasons cited above, the actual ratio was approximately 30 to 1.

All tension, compression, and inplane shear specimens were instrumented with strain gages. Both longitudinal and transverse gages were attached to the shear specimens and five of the 0^{o} tension samples. Back to back longitudinal gages were used on the compression specimens to ascertain whether buckling was occurring. The strains and the load cell output were recorded automatically by the John Fluke computerized data acquisition system. Strain and calculated stress values were stored on a floppy disk. At the conclusion of the test, a printout of the results and a stress-strain plot were produced.

4. Data Presentation and Discussion

Results of the mechanical property tests are presented in Table 6. Also included in the table are the values obtained by investigators at Union Carbide Corporation [10, 11]. These data were generated with an unspecified epoxy which was reportedly representative of commercial systems. Fiber volume content was 60%.

Comparison of the 0^{o} tensile strength results reveals excellent agreement, within 2%. Strengths within the ten sample group varied substantially, as evidenced by the coefficient of variation of 12%. However, such a value is not unreasonable in composite material tests, especially fiber dominated properties which characteristically exhibit greater variability than matrix controlled properties. The modulus values did not correlate as well, although the difference is

Table 6. Results of Mechanical Property Tests

Property	Union Carbide	Present Investigation Mean	Standard Deviation	Coefficient of Variation
0° Tensile Strength	165 ksi	162 ksi	19.45	12.04%
0° Tensile Modulus	62 Msi	68.4 Msi	3.99	5.84%
Maximum Strain	2500μin/in	2287μin/in	311.5	13.62%
90° Tensile Strength	NR	1.44 ksi	.249	17.33%
90° Tensile Modulus	NR	0.88 Msi	16.89	1.92%
0° Compressive Strength[1]	45 ksi	39.9 ksi	5.34	13.4%
0° Compressive Modulus	62 Msi	59.4 Msi	4.70	7.92%
90° Compressive Strength[2]	NR	19.9 ksi	-	-
90° Compressive Modulus	NR	1.04 Msi	-	-
Flexural Strength	70 ksi	84.66 ksi	3.577	4.23%
Flexural Modulus	46 Msi	39.3 Msi	2.99	7.61%
Inplane Shear Strength	NR	4.75 ksi	.249	5.24%
Inplane Shear Modulus	800 ksi	0.58 Msi	15.91	2.76%
Short Beam Shear	3 ksi	2.62 ksi[3]	.060	2.33%
		2.47 ksi[4]	.045	1.80%

(1) Compression specimen length was 5.0 inches
(2) Results of a single test, reported for completeness
(3) Square cross-section
(4) Rectangular cross-section

only 10%. The difference is apprently due to the variation in measured strains, which was also in the neighborhood of 10%. Using the simple rule of mixtures given in equation (1) a modulus value of 61.2 Msi is predicted for the P-100/934 material.

$$E_l = E_f V_f + E_m V_m \qquad (1)$$

where

E_l = longitudinal modulus

E_f = modulus of fiber, 100 Msi

V_f = volume fraction of fiber

E_m = modulus of matrix, 0.5 Msi[1]

V_m = volume fraction of matrix.

A representative stress-strain plot is presented in Figure 11.

The strength data from the transverse tension tests were low and quite inconsistent for a matrix dominated property. It is suspsected that the substandard performance may have been due to damage suffered by the specimens before testing. Several fo the extremely fragile six-ply samples were fractured while being mounted in the grips, and it is possible that the four specimens which survived were damaged in the process of mounting. This explanation is supported by the modulus results. The experimentally determined value averaged 0.88 Msi. The transverse modulus calculated from a mechanics of materials approach[12], expressed in equation (2), is 0.72 Msi.

$$E_2 = \frac{E_f E_m}{V_M E_F + F V_f E_m} \qquad (2)$$

Flaws, as a result of damage or improper fabrication may affect the strength and not alter the modulus, whereas substandard quality of the constituent materials normally will influence both properties.

The compressive properties were obtained from tests on 5 inch long specimens. Tests of the standard 5.5 inch specimens are included in the continuation of this project currently in progress at MSFC. Correlations of the 0^o strength and modulus values with those reported by Union Carbide are reasonable, the differences being 11% and 4%, respectively. The variability within the group was moderately high, but again the inconsistency is due in part to the strong influence of the fiber on the property. A representative stress-strain property is presented in Figure 12.

The 90^o compressive data was generated from a single test and is reported for the sake of completeness. As was the case with the transverse tension speci nens, difficulties in mounting the specimens in the fixture resulted in the loss of several samples.

Flexural properties were determined from three-point loading tests, as explained in the prior section. The flexural strength is defined in the ASTM standard to be equal to the maximum stress in the outer fibers. Maximum fiber

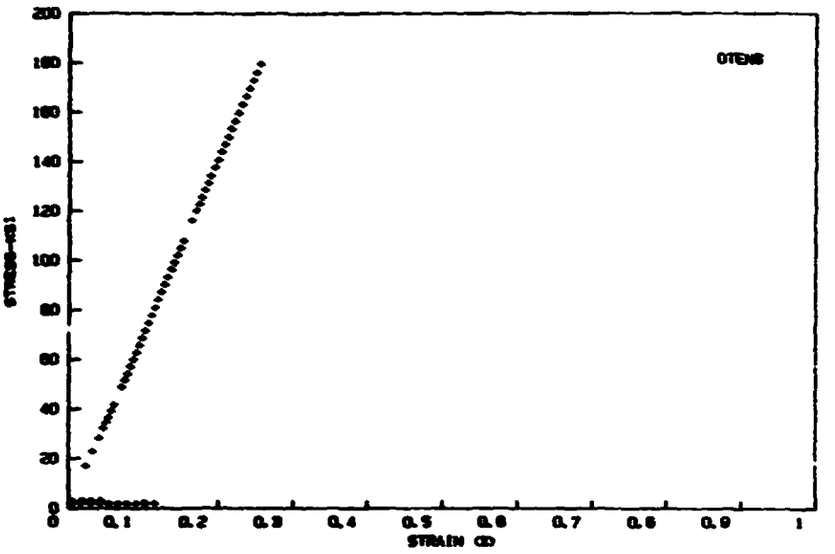

Figure 11. Stress-strain response of 0^{o} tension specimen #9.

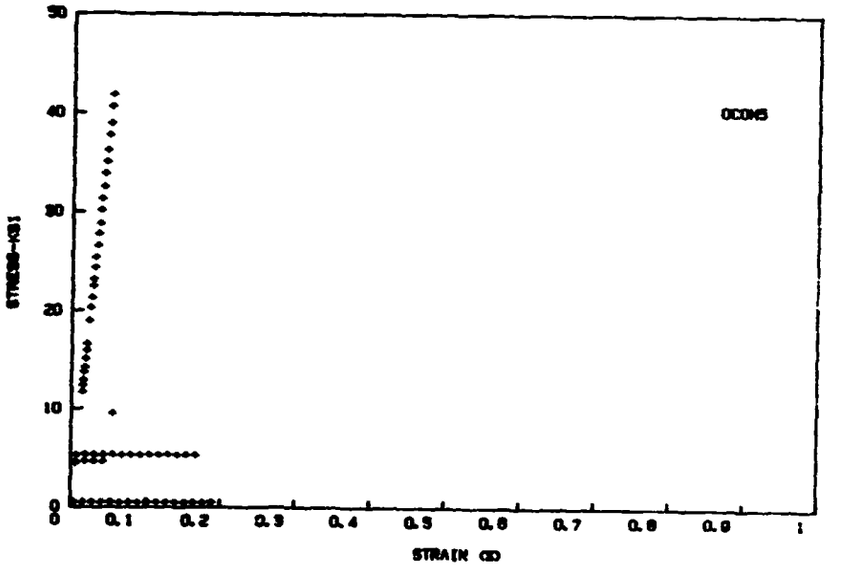

Figure 12. Stress-strain response of 0^{o} compression specimen #5.

stress was calculated in accordance with the standard, using the following equation:

$$S = \frac{3PL}{2bd^2} \qquad (3)$$

where:

S = Flexural strength,

P = maximum load,

L = support span,

b = beam width, and

d = beam depth.

The tangent modulus formula, given below, was used to calculate the flexural modulus,

$$E_B = \frac{L^3 m}{4bd^3}$$

where m is the slope of the tangent to the initial straight-line portion of the load-deflection curve.

The details of the flexural test procedure were not reported by Union Carbide. Since the manner in which the strength and modulus calculations were made is unknown at this time, a meaningful comparison of data is not possible. A difference in procedure may account for the significant differences in the results.

The shear modulus value of 5.75×10^5 psi is substantially lower than that reported by Union Carbide[11]. Both values were obtained experimentally using uniaxial tension tests of $\pm 45^\circ$ coupons. However, there are several factors which must be examined for a clearer interpretation of the results. Foremost among these is the resin systems used. Inplane shear properties are strongly dependent upon the matrix material. Since the resin systems differed, a straightforward comparison is not meaningful. A value of 6.6×10^5 psi[13] has been reported for a T300/934 composite having a fiber volume content of 63%. The test method, which may also influence the results, was not specified. The impact of differences in fiber type, fiber volume fractions, and resin type on the experimental results is difficult to precisely define. The situation is complicated by the variety of test methods employed, the complex interactions among the several factors involved, and the lack of a data base. The value of 5.75×10^5 psi appears reasonable, perhaps a bit conservative, but further testing is required to establish the shear modulus for this system.

Interlaminar shear strength is another property which is matrix dominated. Again, since the resin system used by Union Carbide was not specified, a direct comparison of data is not valid. A general trend is indicated by the proximity of the results. It must be emphasized that both strengths were obtained from specimens constructed with fibers that were not shear treated. Shear treatment increases the strength to 7 ksi[10].

Two groups of short beam shear specimens were tested. One group had a width-to-depth ratio of 1-to-1, while that of the second group was 1.7-to-1. The consistency within the data sets was excellent as evidenced by the coefficients of variation. In a comparison of results, a 5% decrease in the strength of the wider specimens was observed. This behavior agrees with the analysis of Sattar and Kellogg[14] for 0° unidirectional specimens which was later confirmed by Kedward[15]. As the width-to-depth ratio increases, the shear stress calculated using elementary beam theory becomes increasingly inaccurate. The actual stress may be greater than is predicted by theory. The correction factor estimated from a graph presented by Sattar and Kellogg is in the range of 3% to 4%, in which case, the correlation is quite good.

5. Conclusions

The procedures involved in the mechanical property characterization of P-100/934 graphite-epoxy composite material have been described. Quality assurance tests were conducted on the prepreg in an attempt to determine the nature and severity of a surface layer which had formed on the material. The results of these tests did not indicate any abnormality. A five minute exposure in an acetone-rich atmosphere was successfully used to restore tack and flexibility to the prepreg. Both destructive and nondestructive testing techniques were employed to determine whether this treatment had adversely affected the prepreg and the cured laminates. No deleterious effects were discovered during these tests. Mechanical property tests were conducted in accordance with currently approved ASTM standards. The results were compared with data generated by researchers at Union Carbide. The agreement between the two sets of data was good for the fiber-dominated properties. Although two different resin systems were used and direct comparisons of matrix dominated properties were not meaningful, supporting evidence indicated that these results were quite reasonable.

The objectives set forth at the initiation of this project were successfully accomplished.

References

1. Private communication, Carl Smith, Fiberite Corporation, Winona, Minnesota.

2. De Iasi, R., and Whiteside, J.B., "Effect of Moisture on Epoxy Resins and Composites," Advanced Composite Materials - Environmental Effects, ASTM STP 658, J.R. Vinson, Ed., American Society for Testing and Materials, 1978, pp. 2-20.

3. Dynes, P.J., and Kaelble, D.H., "Physiochemical Analysis of Graphite-Epoxy Composite Systems," Composite Materials: Testing and Design (Fifth Conference) ASTM STP 674, S.W. Tsai, Ed., American Society for Testing and Materials, 1979, pp. 566-577.

4. Clark, R.K., and Lisagor, W.B., "Compression Testing of Graphite/Epoxy Composite Materials," Test Methods and Design Allowables for Fibrous Composites," ASTM STP 734, C.C. Chamis, Ed., American Society for Testing and Materials, 1981, pp. 34-53.

5. Rosen, B.W., "A Simple Procedure for Experimental Determination of the Longitudinal Shear Modulus of Unidirectional Composites," Journal of Composite Materials, Vol. 6, October 1972, pp. 552-554.

6. Whitney, J.M., Stansbarger, D.L., and Howell, H.B., "Analysis of the Rail Shear Test - Applications and Limitations," Journal of Composite Materials, Vol. 5, June 1971, p. 24.

7. Yeow, Y.T., and Brinson, H.F., "A Comparison of Simple Shear Characterization Methods for Composite Laminates," Composites, Vol. 9, Jan. 1978, p. 49.

8. Zweben, C., Smith, W.S., and Wardle, M.W., "Test Methods for Fiber Tensile Strength, Composite Flexural Modulus, and Properties of Fabric Reinforced Laminates," Composite Materials: Testing and Design (Fifth Conference) ASTM STP 674, S.W. Tsai, Ed., American Society for Testing and Materials, 1979, p. 228.

9. Pipers, P.M.W., "The Interlaminar Shear Strength of Unidirectional Boron-Aluminum Composite," Journal of Composite Materials, Vol. 12, Jan. 1978, p. 53.

10. Private communication, M.K. Towne, Union Carbide Corporation, Cleveland, Ohio.

11. Private communication, R. Bacon, Union Carbide Corporation, Cleveland, Ohio.

12. Jones, R.M., Mechanics of Composite Materials, Scripta Book Co., Washington, D.C., 1975.

13. Greszczuk, L.B., "Application of Four-Point Ring Test for Determining Shear Modulus of Filamentary Composites," Test Methods and Design Allowables for Fibrous Composites, ASTM STP 734, C. C. Chamis, Ed., American Society for Testing and Materials, 1981, pp. 21-33.

14. Sattar, S.A., and Kellogg, D.H., "The Effect of Geometry on the Mode of Failure of Composites in the Short Beam Shear Test," Composite Materials: Testing and Design, ASTM STP 460, American Society for Testing and Materials, 1969, pp. 62-71.

15. Kedward, K.T., "On the Short Beam Test Method," Fibre Science and Technology, Vol. 5, 1972, pp. 85-95.

1983

NASA/ASEE SUMMER FACULTY RESEARCH FELLOWSHIP PROGRAM

MARSHALL SPACE FLIGHT CENTER
THE UNIVERSITY OF ALABAMA IN HUNTSVILLE

PRELIMINARY DESIGNS FOR MODIFICATIONS TO THE X-RAY SOURCE AND BEAM MONITOR OF THE MARSHALL SPACE FLIGHT CENTER'S X-RAY CALIBRATION FACILITY

Prepared By:	W. L. Croft, Ph.D.
Academic Rank:	Professor
University and Department:	Mississippi State University Department of Physics
NASA/MSFC:	
Laboratory:	Test
Division:	Systems and Components Test
Branch:	Environmental Test
MSFC Counterpart:	J. C. Reily, Jr.
Date:	August 12, 1983
Contract No.:	NGT 01-008-021 The University of Alabama in Huntsville

PRELIMINARY DESIGNS FOR MODIFICATIONS TO THE X-RAY SOURCE AND BEAM MONITOR OF THE MARSHALL SPACE FLIGHT CENTER'S X-RAY CALIBRATION FACILITY

BY

W. L. Croft
Professor of Physics
Mississippi State University
Mississippi State, Mississippi

ABSTRACT

The objective of this investigation is to develop preliminary designs for modifications to the X-ray source and beam monitor of the MSFC X-Ray Calibration Facility to meet requirements for the calibration of the Advanced X-Ray Astrophysics Facility. A Rhodium plated copper target and Rhodium foil filter are proposed as a source of X-rays of approximately 2.6 kev energy. Bragg scattering of the unpolarized X-ray beam from the present source through an angle of 90° by a single crystal placed on the axis of the guide tube is proposed as a source of approximately monoenergetic plane polarized X-rays. A sealed Xenon proportional counter with a Beryllium window is proposed as a beam monitor for use between 2.5 and 8 kev to obtain improved detection efficiency.

ACKNOWLEDGEMENTS

I would like to express my appreciation to the NASA/ASEE Summer Faculty Fellowship Program for providing this opportunity for research and learning. Thanks are extended to Dr. Gerald Karr, Dr. Jim Dozier, Mr. Leroy Osborn and Mr. Marion Kent for their assistance with a variety of problems and for the outstanding seminar series. I appreciate the hospitality extended me by Messrs. J. H. Newton, W. E. Dickson and R. N. Stone, and their staffs. I also appreciate valuable discussions with Dr. Martin Weisskopf, AXAF Project Scientist, of the Space Sciences Laboratory. Special thanks go to my NASA Counterpart, Mr. Cary Reily, for his friendly and helpful direction of this work and to Mrs. Pat Blackmon who typed this report.

NOMENCLATURE

Symbols	Definition
α	Constant that determines X-ray absorption in gas chamber when only pressure varies.
ϵ	Proportional counter efficiency.
λ	X-ray wavelength.
μ	Linear absorption coefficient.
θ	Angle of incidence and reflection in Bragg Scattering.
ρ	Mass density.
C_3	Proportional counter counting rate.
d	Distance between two adjacent crystal planes.
E	X-ray energy.
I	X-ray intensity.
K	Proportionality constant between gas density and pressure at constant temperature.
m	Mass of gas sample.
M	Molecular mass of a gas.
N	Number of moles in gas law; order of reflection in Bragg equation.
P	Absolute pressure of a gas.
R	Universal gas constant.
T	Absolute temperature.
V	Volume of gas.
X	Thickness of absorbing material.
Z	Atomic number of a chemical element.

INTRODUCTION

The Marshall Space Flight Center's X-Ray Calibration Facility was constructed in 1976 for use in the calibration of the High Energy Astronomical Observatory-2 (HEAO-2 or the Einstein Observatory).[1] The facility (Fig. 1) consists of: (1) a source chamber which contains a modified industrial X-ray generator, (2) an instrument chamber which contains an optical bench, LN_2 panels and heating panels, (3) a 1000 ft by 3 ft diameter guide tube which connects the two chambers, (4) a flow-type proportional counter X-ray beam monitor, (5) a vacuum pumping system which can maintain pressures of the order of 10^{-6} torr, and (6) the associated instrumentation for the measurement of pressures, temperatures and X-ray spectra. In addition to its use in the calibration of HEAO-2 and rocket payloads, and in testing the X-ray scattering properties of other systems, the instrument chamber has proved to be valuable for the vacuum bakeout of flight hardware.

HEAO-2 was launched in November 1978 and during its approximately 3 years of operation it returned data which revolutionized X-ray astronomy.[2] The Advanced X-Ray Astrophysics Facility (AXAF) is being developed to produce another quantum-jump in man's understanding of the X-ray universe.[3] AXAF will have an angular resolution of approximately 0.5 arc-seconds (a factor of 8 better than HEAO-2) and a sensitivity of 100 or more times better than HEAO-2. AXAF will be launched and serviced on orbit from the Space Shuttle and is expected to have a useful life of 10-15 years.

The MSFC X-Ray Calibration Facility is scheduled to be used for the testing of the AXAF Test Mirror Assembly in 1984. A proposal to modify the facility by, among other things, lengthening the guide tube by the addition of 700 ft of 5 ft diameter tube and enlarging the instrument chamber to accommodate AXAF is currently under review. If this extension of the capability of the facility is approved, it will be used to calibrate AXAF in the late 1980's.

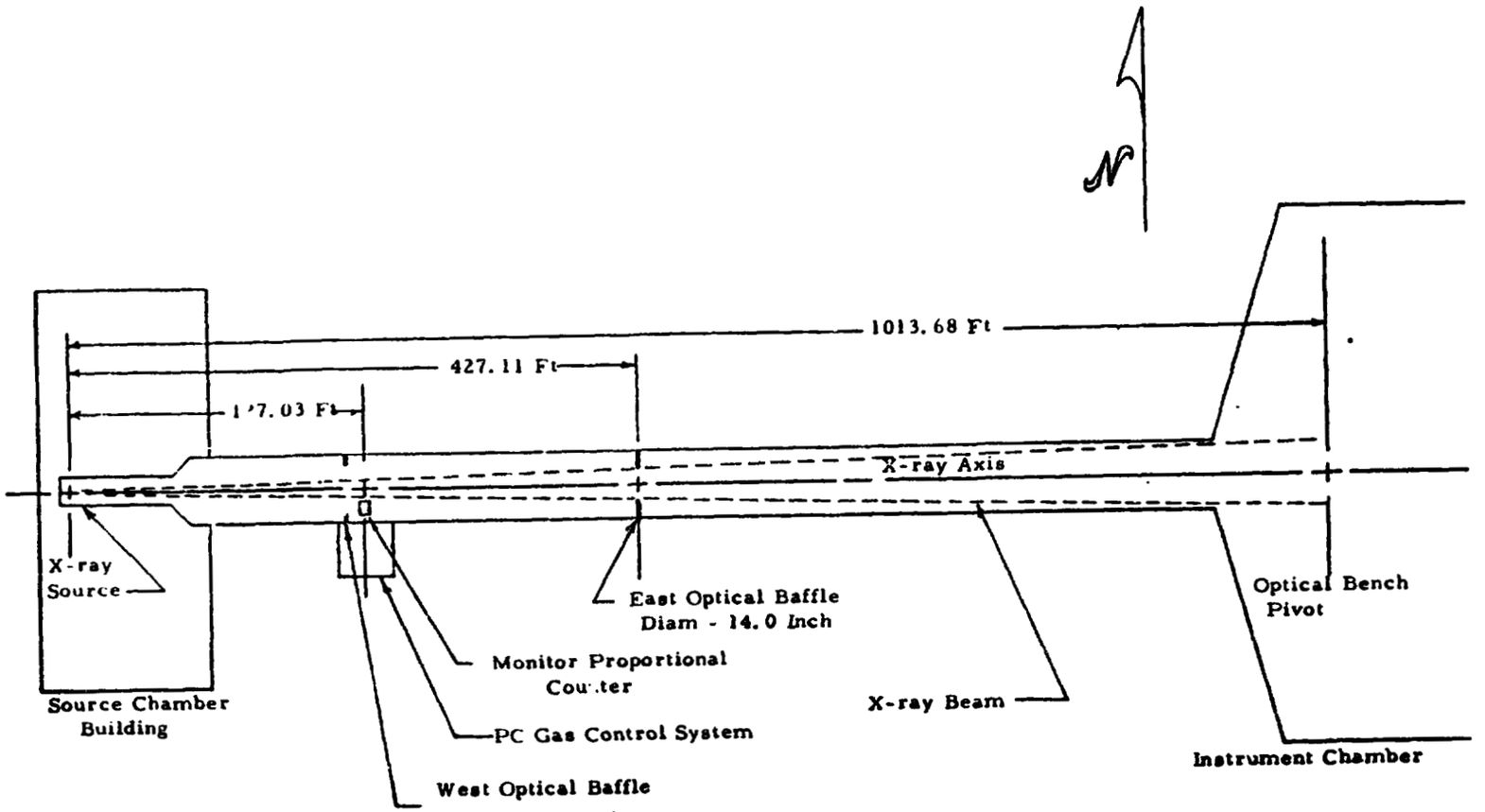

FIGURE 1. X-RAY CALIBRATION SYSTEM LAYOUT

OBJECTIVES

The primary objectives of this project are to produce the preliminary designs for modifications to the X-ray source and beam-monitor needed to extend their capabilities to meet the requirements for testing and calibrating AXAF and to provide reprints and references to relevant scientific articles. The following topics are discussed.

(1) Thin Film Techniques.

(2) A Boron Filter for Use at Low X-Ray Energies.

(3) Isolation of an X-Ray Line at Approximately 0.1 kev.

(4) An X-Ray Target and Filter System to produce an X-Ray Beam at an Energy of Approximately 2.6 kev.

(5) A System for Measuring the Absorption of X-Rays in the Monitor Proportional Counter.

(6) A Xenon Filled Proportional Counter for Improved Efficiency in the Energy Range of 2.5 to 10 kev.

(7) A Source of Approximately Monoenergetic Plane-Polarized X-Rays.

(8) Comments on Some Operating Procedures.

THIN FILM TECHNIQUES

The X-ray energy range for AXAF is 0.1 to 8 kev. Work at these low X-ray energies requires thin windows for proportional counters and thin substrates for X-ray filters. Techniques for routinely producing strong, thin (less than 100$\mu g/cm^2$) plastic films of Formvar have been described.[4,5] One popular technique is to let a small volume of Formvar dissolved in ethylene dichloride spread into a thin film on a water surface. The film is usually removed from the water by pushing an open rectangular frame down perpendicular to the center of the film. This produces a double layer of the film on the frame and the process is often repeated several times to build up a laminated film of several layers of this film which can have a thickness of the order of 3$\mu g/cm^2$. This procedure leads to strong films which are usually free of pin hole leaks. These films can be packaged for later use and have a long shelf life.

THIN FILM TECHNIQUES (Continued)

In order to prevent poor resolution and reduced counting rates at low X-ray energies, thin plastic films used for counter windows should have approximately 500Å of aluminum vacuum-evaporated onto them.[6] This prevents the window from charging positively and producing a region of charge combination and a poor field distribution.

The capability to produce one's own thin films can result in a superior product, the flexibility to produce films for specific applications, and all this with considerable savings in time and expense.

BORON FILTER

The Boron/Polypropylene filter used in the HEAO-2 calibration was made by air-brushing a suspension of very fine particles of boron onto a 1.5 micron polypropylene film. There is some uncertainty about the uniformity of the boron layer and since no binder was used the boron is not firmly attached to the plastic.[7]

A technique for producing a boron filter with good uniformity and adherence to a thin substrate has been reported.[4] This method uses a suspension of boron in ethyl alcohol with a small amount of binder. A thin Formvar film is coated with boron by lowering it into a tank containing the boron suspension and then slowly withdrawing it by means of a mechanical drive. The amount of boron which adheres to the film depends on the boron concentration and the speed with which the film is withdrawn from the suspension.

Techniques for producing thin boron films by vacuum evaporation have also been reported.[8,9] However, this method is more difficult than the one described above.

ISOLATION OF AN X-RAY LINE AT APPROXIMATELY 0.1 KEV

In the HEAO-2 calibration, the lowest energy characteristic X-ray line used was the boron K-line at 0.185 kev, while the beryllium target was used with a boron filter to produce a continuum of low energy X-rays.

ISOLATION OF AN X-RAY LINE AT APPROXIMATELY 0.1 KEV (Continued)

The beryllium K X-ray line at an energy of 0.1085 kev could probably be made available for the AXAF calibration, if needed, by installing a thin Formvar window (made as described above) on the proportional counter and by using a beryllium filter (commercially available) with the Be target on the X-ray source. Energy resolution could probably be improved, if necessary, by use of a more sensitive preamplifier.

AN X-RAY LINE AT APPROXIMATELY 2.6 KEV

Some celestial X-ray sources of astrophysical interest have energy spectra which peak near 2.6 kev. The X-ray sources used in the calibration of HEAO-2 did not provide an X-ray of this energy. However, an energy of this value will be needed in the calibration of AXAF and Rhodium has been suggested as a possible target material.[10]

Table 1 shows that the six L X-ray lines in $_{45}Rh$ are in the energy range of interest.[11] If a target of Rhodium can be fabricated for use in the X-ray source, the energy requirement will be met.

TABLE 1
RHODIUM L X-RAY LINES

X-RAY LINE	ENERGY (kev)
L_2M_1	2.5191
L_2M_4	2.83441
L_3M_1	2.3765
L_3M_4	2.69205
L_3M_5	2.69674
$L_3N_{4,5}$	3.0013

Rhodium plating was first introduced about 50 years ago and produces a finish which is a good reflector, is resistant to tarnishing and is wear resistant.[12] It is used for coatings on jewelry, mirrors, search light reflectors, electrical contacts, etc. Although it would be difficult to develop a satisfactory procedure for Rhodium plating starting with commonly available chemicals, proprietary solutions for this purpose are available.[13] Rhodium is plated from these solutions using directions supplied with the solutions. Since Rhodium is routinely used to plate copper circuit elements, an interchangeable target for the X-ray source anode could be made of copper and this copper target could be plated with Rhodium using a solution and directions obtained commercially if the expertise is not already available locally.

AN X-RAY LINE AT APPROXIMATELY 2.6 KEV (Continued)

A Rhodium foil filter a few microns in thickness used with the Rhodium plated copper target should produce low background characteristic L X-rays with energies near 2.6 kev. Rhodium foil is available commercially or can be produced by vacuum evaporation of the metal onto glass where it is said to be poorly adherent and easily removed.[14] Rhodium, like the other platinum metals, is expensive.

A SYSTEM FOR MEASURING THE ABSORPTION OF X-RAYS IN PROPORTIONAL COUNTER GASES

It may sometimes be desirable to measure the absorption of X-rays in the gas being used in a proportional counter. Measurements of this kind have been made for many years.[15]

The proposed experimental arrangement is shown in Fig. 2. Chamber 2 is a proportional counter while Chamber 1 holds the gas which is to be investigated. A narrow beam of approximately monoenergetic X-rays is incident on Window 1 and those X-rays which are not absorbed in Window 1 or in Chamber 1 are incident on the window of the proportional counter, Window 2. The thicknesses of Window 1, Chamber 1, Window 2, and Chamber 2 are X_0, X_1, X_2 and X_3 respectively.

Figure 2

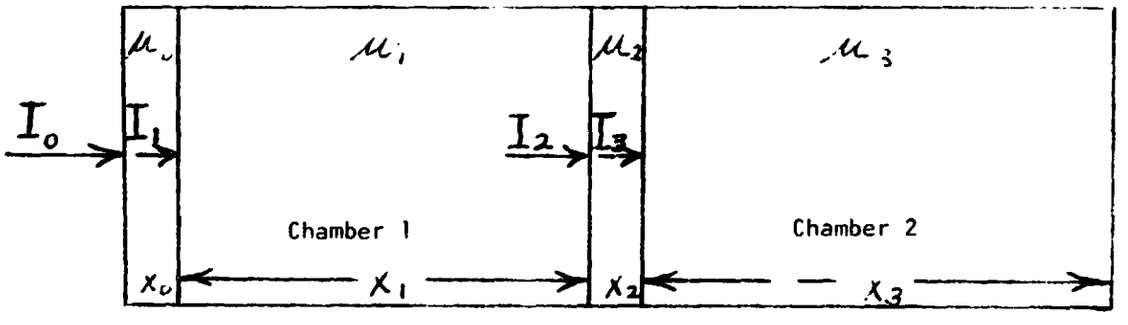

GAS ABSORPTION APPARATUS

A SYSTEM FOR MEASURING THE ABSORPTION OF X-RAYS IN PROPORTIONAL COUNTER GASES (Continued)

The intensities of X-ray beams incident on Window 1, Chamber 1, Window 2 and Chamber 2 are I_0, I_1, I_2 and I_3 respectively. In terms of the linear absorption coefficients, the following equations can be written to express the various intensities in terms of the initial beam intensity and the thicknesses and linear absorption coefficients of the regions.

$$I_1 = I_o e^{-\mu_o x_o} \qquad (1)$$

$$I_2 = I_1 e^{-\mu_1 x_1} = I_o e^{-\mu_o x_o} e^{-\mu_1 x_1} \qquad (2)$$

The counting rate in the proportional counter, C_3, can be expressed in terms of the intensity of X-rays incident on the counter window, I_2, and the efficiency of the counter, ϵ, as

$$C_3 = \epsilon I_2 \qquad (3)$$

In the following measurements, the geometry of the chambers and the energy and intensity, I_0, of the X-rays incident on Window 1 will be held constant. Chamber 1 will be filled with the counter gas to be investigated at the temperature and pressure of interest. The counting rate, C_{3p}, at this pressure will be determined. Chamber 1 will then be evacuated and the counting rate C_{30} will be determined. The ratio of C_{3p} to C_{30} gives:

$$\frac{C_{3P}}{C_{30}} = \frac{\epsilon I_o e^{-\mu_o x_o} e^{-\mu_1 x_1}}{\epsilon I_o e^{-\mu_o x_o} (1)} = e^{-\mu_1 x_1}. \qquad (4)$$

Thus the linear absorption coefficient μ_1 of the gas can be determined by measuring the depth of Chamber 1, X_1, and the counting rates with Chamber 1 evacuated and filled with gas under the desired conditions, C_{30} and C_{3p} respectively. Note that this method will work only if the absorption in Chamber 1 is not near 100%.

A SYSTEM FOR MEASURING THE ABSORPTION OF X-RAYS IN PROPORTIONAL COUNTER GASES (Continued)

The results can be expressed in terms of the mass absorption coefficient by making use of the following relationship:

$$I = I_0 e^{-\mu x} = I_0 e^{-(\mu/\rho)(\rho x)} \qquad (5)$$

where ρ is the density of the absorbing material and μ/ρ is the mass absorption coefficient.

It may be convenient to express the absorption of X-rays by gases in chambers of fixed geometry in terms of the absolute pressure of the gas. This can be achieved as follows. The ideal gas law can be expressed as PV=NRT where P is absolute gas pressure, V is volume, N is the number of moles of the gas, R is the universal gas constant and T is the absolute temperature. For a gas of molecular mass M, a mass m of the gas can be expressed in moles as N=m/M. Thus the ideal gas law can be written as

$PV = (m/M)RT$ (6) and rearranged to give

$P \frac{M}{RT} = \frac{m}{V} = \rho$ (7). When temperature is held constant, density is directly proportional to pressure and can be expressed as

$$\rho = KP \qquad (8)$$

with the constant K defined by $K = \frac{M}{RT}$. Thus for a given gas at a given temperature the density is directly proportional to the pressure.

This leads to the following result which may be useful:

$$I = I_0 e^{-\mu x} = I_0 e^{-(\mu/\rho)(\rho x)} = I_0 e^{-(\mu/\rho)\left(\frac{Mx}{RT}\right)P} \qquad (9)$$

For a given gas, constant X-ray energy, constant geometry, and constant temperature:

$(\mu/\rho)\left(\frac{Mx}{RT}\right)$ is a constant which will be called α.

Thus $I = I_0 e^{-\alpha P}$ (10) and the transmitted intensity is seen to be a decreasing exponential function of gas pressure.

XENON PROPORTIONAL COUNTER

Proportional counters are often used in the study of low energy X-rays because of several favorable characteristics. These counters are relatively simple and reliable and for low energies they are efficient and have relatively good energy resolution. The construction and operation of these counters is thoroughly discussed in the literature.[16,17,18] X-ray proportional counters usually have a cylindrical or rectangular metal enclosure with a thin window in one end or a side. A small uniform diameter metal wire is centered along the length of the enclosure. This metal wire is well insulated from the enclosure and the counter is operated with this anode wire at a high positive electrical potential with respect to the enclosure which serves as the cathode. Proportional counters are usually operated with one of the noble gases as the primary counter gas. These gases give higher initial ionization and larger gas gains since energy is not used in exciting rotational and vibrational states as would be the case with diatomic and polyatomic gases. To prevent counting instabilities which have several origins, a few torr of an organic quench gas such as CH_4 is usually added to the noble gas.

The proportional counter used in the HEAO-2 calibration was a Diano Model SPG-9A gas-flow counter with a 1.8 micron polypropylene window covered with several hundred angstroms of aluminum and supported by a metal mesh. For X-rays below about 1.5 kev pure methane at 5.0 PSIA was used as the counter gas while at energies above 1.5 kev, P-10 gas (90% Argon and 10% Methane) was used at a pressure of approximately 1 atm.

There are several problems with an Argon filled counter in the energy range of 2.5 to 10 kev. The Ar K-edge is at about 3.2 kev. This results in a rather large discontinuity in the mass absorption coefficient for Ar at this energy which produces a correspondingly large discontinuity in the counter efficiency and also leads to a K-escape peak as some Ar K-Xrays escape from the counter. Also the efficiency of the counter decreases with energy and is down to about 17% at 8 kev.[1]

At energies below 100 kev X-rays are much more likely to interact with matter by means of the photoelectric effect than by the Compton effect and in this energy range the photoelectric absorption coefficient varies approximately as Z^4 where Z is the atomic number of the absorbing material involved. Thus in this energy range, $_{54}Xe$ is a much more efficient absorber of X-rays than is $_{18}Ar$. Also since the K-edge in Xe is at 34.6 kev there is no large discontinuity in its mass absorption coefficient below 10 kev and similarly, no troublesome K-escape peak.

A Xenon proportional counter 2.5 cm deep with 700 torr of Xe and 60 torr of CH_4 at 20°C will have efficiencies as shown in Fig. 3. As an example, such a counter with a 2 mil (9.2 mg/cm^2) Be window has an efficiency of 97% at 8 kev.

FIGURE 3: EFFICIENCY OF A XENON PROPORTIONAL COUNTER

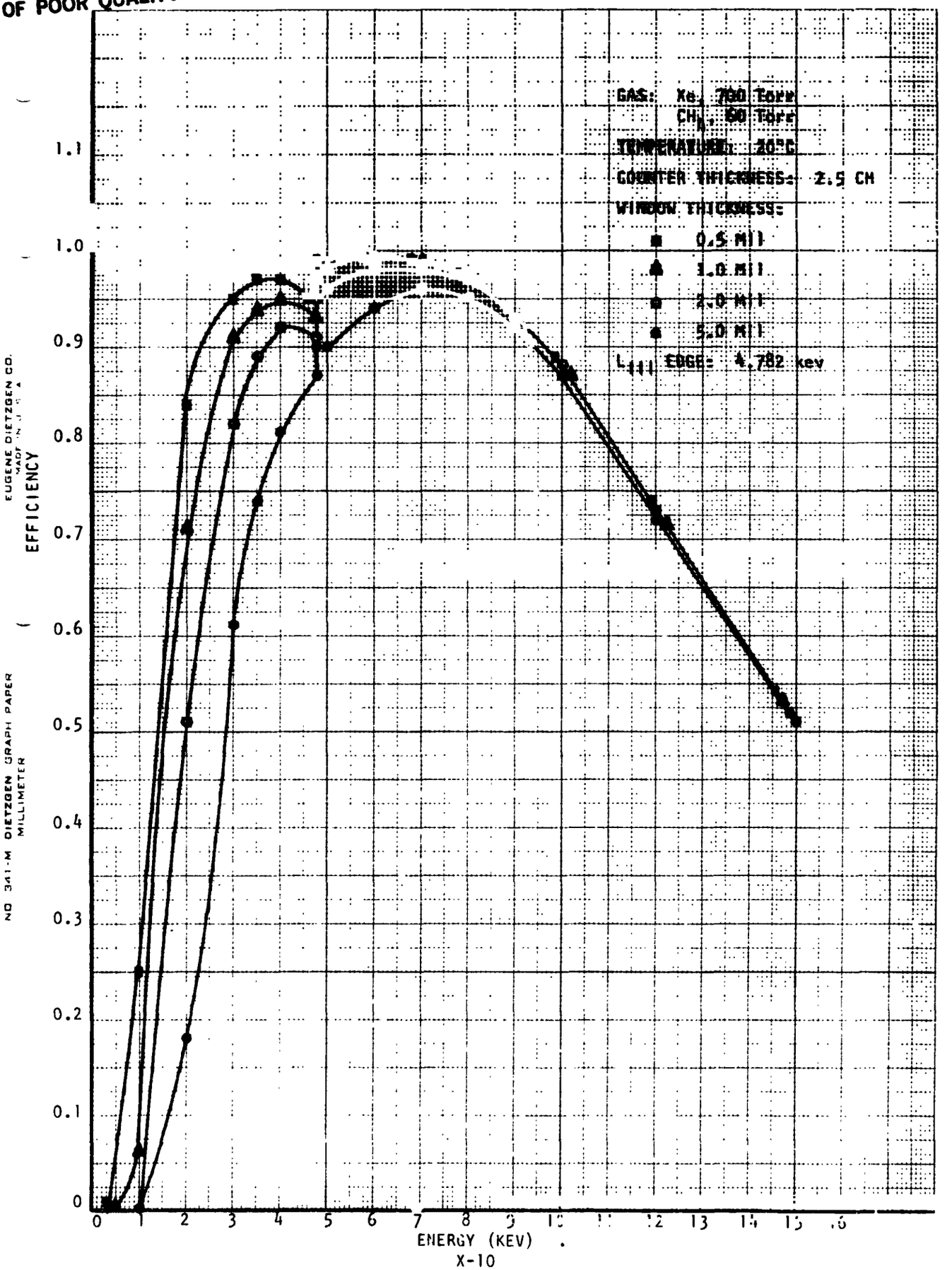

The efficiency of a proportional counter is given by the expression

$$\epsilon(E) = [\exp(-\mu_w x_w)][1 - \exp(-\mu_g x_g)] \qquad (11)$$

where the symbols have their usual meanings and the subscripts w and g refer to the counter window and counter gas respectively. The first term is the fraction of the incident X-rays which pass through the counter window while the second term is the fraction of the X-rays which get into the counter which are absorbed in the counter gas. Note that the absorption of X-rays due to the CH_4 quench gas is negligible above 2 kev. This can easily be shown by treating the absorption due to the carbon and the hydrogen independently.

It should be clear from the above discussion that a Xenon counter offers advantages near the high end of the AXAF energy range, 8 kev. A Xenon counter would need to be a sealed counter rather than a flow counter since Xenon is rather expensive.

Small quantities of gaseous impurities can seriously degrade the performance of a proportional counter. Therefore, the parts of a newly constructed counter should be carefully cleaned prior to assembly. Following assembly but prior to filling with Xenon, the counter should be evacuated and pumped for several hours at a temperature well above 20°C to ensure outgassing.

To avoid problems with "end effects" in side-window counters, the size of the window should be small enough that the metal side of the counter shields at least 1 cm at each end of the anode wire from X-rays. The anode wire itself should be of uniform diameter to avoid a non-uniform electric field which also degrades performance. If one end of the anode wire is free, it should terminate with a small sphere of metal.

THE PRODUCTION OF PLANE POLARIZED X-RAYS

The technique for producing a beam of plane polarized X-rays by scattering an unpolarized beam through 90° off of a low Z scatterer has been known for sometime.[19,20] The polarized state of this scattered beam can be confirmed by scattering it through 90° off of a second low Z scatterer, See Fig. 4.

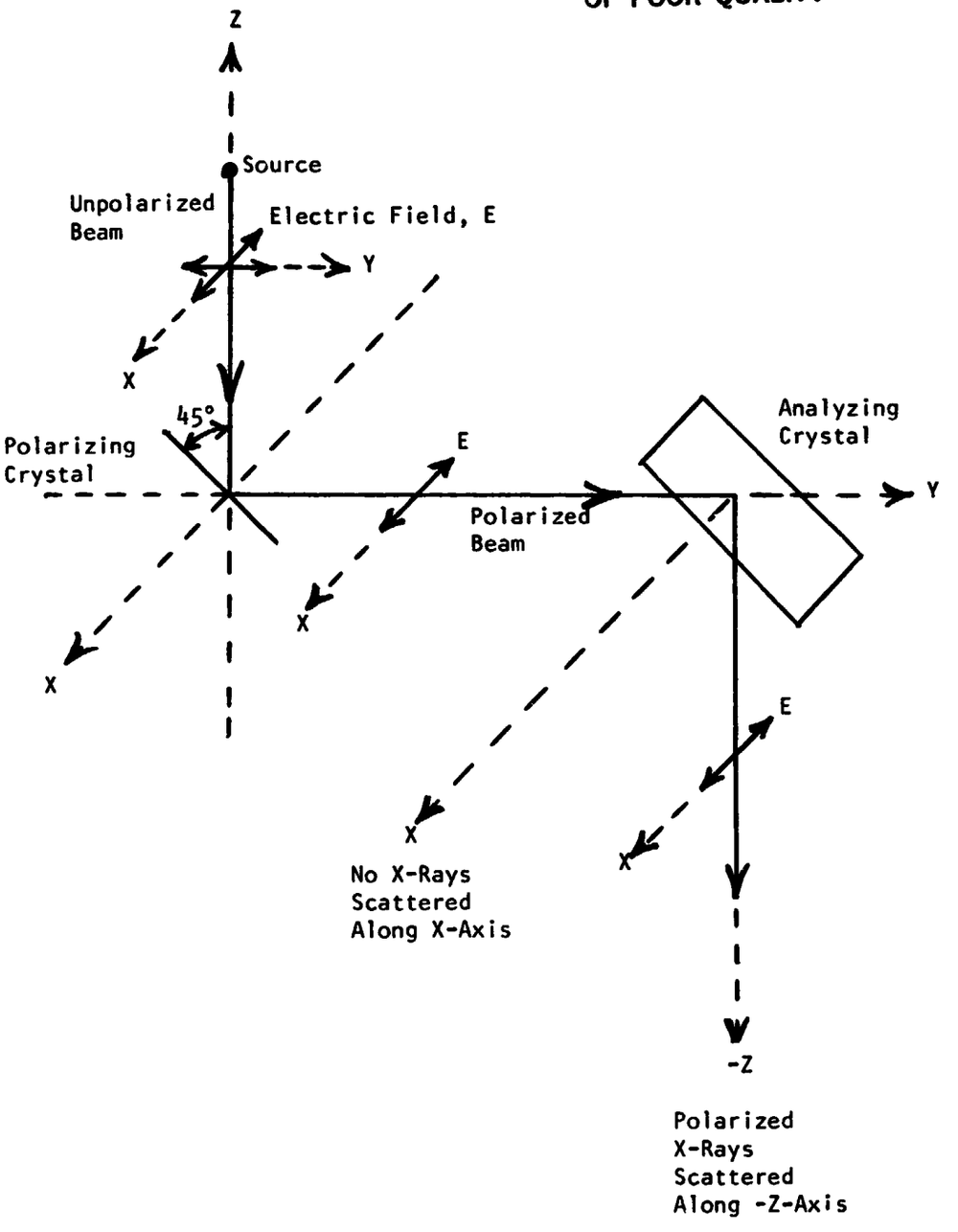

FIGURE 4: PRODUCTION OF POLARIZED X-RAYS

Since X-rays and other electromagnetic waves are transverse (the oscillating electric and magnetic fields are perpendicular to the direction of propagation), the waves scattered at 90° have their electric field vectors perpendicular to the plane formed by the incident and scattered waves.

The selection of X-ray energies by the process of Bragg scattering, "reflection", from a crystal is well known.[21] The Bragg equation is

$$n\lambda = 2d\sin\theta \qquad (12)$$

where n is the order of the reflection, usually one, d is the spacing between adjacent parallel reflecting planes in the crystal, and θ is the angle of incidence and reflection measured with respect to the reflecting crystal plane, not its normal.

If an unpolarized beam of X-rays is reflected off of a judiciously chosen crystal at an incident angle of 45°, then a monoenergetic beam of plane polarized X-rays will result. From the Bragg equation the wave length of the reflected X-rays is given by

$$\lambda = \frac{2d\sin\theta}{n} \qquad (13).$$

Notice that as n increases, λ decreases. This means that as n increases the energy of the X-rays scattered at a particular angle increases. An experimenter can ensure that no reflections of order higher than one occur by operating at anode voltages too low to excite X-rays with energies which correspond to larger values of n.

As an example, if a graphite crystal is used 2d=6.708 Å. Then for N=1 and scattering at θ=45°, λ =4.743 Å which can be shown to be equivalent to an X-ray energy of 2.62 kev by use of the formula

$$E = \frac{12.43\ \text{keV}\,\text{Å}}{\lambda} \qquad (14).$$

In practice, the crystals are often bent slightly so that a narrow range of energies centered on the desired energy is reflected.

A graphite crystal will be used with the Rhodium plated X-ray target and Rhodium filter to produce a plane polarized beam of approximately 2.6 kev photons for the calibration of the AXAF polarimeter.

OPERATING PROCEDURES

The procedures used in calibrating the equipment and in taking and analyzing the data for the HEAO-2 calibration appear to have been well thought out and carefully applied.[1,7] The author sees no reason to suggest that changes be made for the AXAF calibration. It may be worth noting, however, that the peak shift with counting rate in the X-ray spectra which was observed and correctly handled in the HEAO-2 calibration is most likely a characteristic of the proportional counter itself, and not an indication of a problem with the counting electronics.[22]

RECOMMENDATIONS

(1) An in-house thin-film capability should be developed for the purpose of producing counter windows and absorber substrates.

(2) A new boron filter should be constructed by use of techniques discussed above and its performance should be compared with the present boron filter.

(3) A Rhodium-plated copper target for the X-ray generator should be built and tested with a Rhodium filter to characterize it as a source of X-rays with an energy of approximately 2.6 kev.

(4) A sealed Xenon proportional counter with a beryllium window should be constructed and its performance in the energy range from 2.5 to 10 kev should be compared with that of the present proportional counter.

(5) The X-ray source should be modified to produce plane polarized X-rays by scattering unpolarized X-rays at 90° off of a graphite crystal. The polarization characteristics of the scattered beam should be investigated by means of a second graphite crystal and movable proportional counter in the instrument chamber.

REFERENCES

1. Reily, J. C.: Test Report X-Ray System Operation HFAO-B Telescope Calibration, NASA ET44-HEAO-411 Addendum, April 1978.

2. Giacconi, Riccardo: Scientific American 242, 80, 1980.

3. Advanced X-Ray Astrophysics Facility (AXAF) Science Working Group Report, NASA TM-78285, May 1980.

4. Williamson, F. and Maxon, C. W.: Rev. Sci. Instrum. 46, 50, 1975.

5. Grader, R. J., et al.: Rev. Sci. Instrum. 42, 465, 1971.

6. Charles, M. W. and Cooke, B. A.: Nucl. Instr. and Meth. 61, 31, 1968.

7. Reily, J. C.: Private Communication, MSFC, 1983.

8. Hill, H. A.: Rev. Sci. Instrum. 27, 1086, 1956.

9. Erdman, K. L., et al.: Rev. Sci. Instrum. 35, 122, 1964.

10. Weisskopf, M. C.: Private Communication, MSFC, 1983.

11. Burr, Alex, Handbook of Spectroscopy Volume I, 10, J. W. Robinson, CRC Press, Cleveland, 1975.

12. Lowenheim, F. A., Electroplating, 294, McGraw-Hill, New York, 1978.

13. See Advertisements in the Journal Metal Finishing.

14. Holland, L., Vacuum Deposition of Thin Films, 99, Chapman and Hall Ltd., London, 1963.

15. Compton, A. H. and Allison, S. K., X-Rays in Theory and Experiment, 518, D. Van Nostrand, New York, 1935.

16. Curran, S. C., Handbuch der Physik 45, 174, S. Flugge; Springer-Verlag, Berlin, 1958.

17. Curran, S. C. and Wilson, H. W., Alpha-Beta-and Gamma-Ray Spectroscopy Volume I, 303, K. Siegbahn; North Holland, Amsterdam, 1965.

18. Rossi, B. B. and Staub, H. H., Ionization Chambers and Counters, McGraw-Hill, New York, 1949.

REFERENCES

19. Compton, A. H. and Hagenow, C. F.: J. Optical Soc. Am. and Rev. Sci. Instruments 8, 487, 1924.

20. George, W. H.: Proc. Roy. Soc. Lond., Ser. A 156, 96, 1936.

21. Wehr, M. R. and Richards, J. A., Physics of the Atom Second Edition, 184, Addison-Wesley, Reading, Mass., 1959.

22. Spielberg, N. and Tsarnas, D. I.: Rev. Sci. Instrum. 46, 1086, 1975.

1983

NASA/ASEE SUMMER FACULTY RESEARCH FELLOWSHIP PROGRAM

MARSHALL SPACE FLIGHT CENTER
THE UNIVERSITY OF ALABAMA IN HUNTSVILLE

SYNTHESIS OF N-SUBSTITUTED SILANEAMINES: MONOMERIC PRECURSORS OF SILICON CARBIDE-NITRIDE FIBERS

Prepared by:	David J. Crouse, Ph.D.
Academic Rank:	Assistant Professor
University and Department:	Tennessee Technological University Department of Chemistry
NASA/MSFC:	
Laboratory:	Materials and Processes
Division:	Non-Metallic Materials
Branch:	Polymers and Composites
MSFC Counterpart:	Benjamin G. Penn, Ph.D.
Date:	August 19, 1983
Contract No.:	NGT 01-008-021 The University of Alabama in Huntsville

SYNTHESIS OF N-SUBSTITUTED SILANEAMINES: MONOMERIC PRECURSORS OF SILICON CARBIDE-NITRIDE FIBERS

BY

David J. Crouse
Assistant Professor of Chemistry
Tennessee Technological University
Cookeville, Tennessee

ABSTRACT

The objective of this project is to prepare a series of N-alkyl substituted silanetriamines. These compounds are to be the monomers leading to polycarbosilazane resins which are used to prepare silicon carbide-silicon nitride fibers for use in composite materials.

Silanetriamines are prepared by the condensation of methyl or phenyl trichlorosilane with a primary amine. The amines used in this

$$R\text{-}SiCl_3 \quad + \quad R'\text{-}NH_2 \longrightarrow R\text{-}Si\text{-}(NH\text{-}R')_3$$

study are methyl, n-propyl, n-butyl and allyl. The silaneamines were prepared by adding the chlorosilane to a solution of the amine in either petroleum ether or toluene. The compounds were purified by distillation and characterized by infrared and nuclear magnetic resonance spectroscopy.

INTRODUCTION

The technological demand for materials of improved strength and stiffness has led to considerable research in the area of fiber-reinforced resin-matrix composites. Fibers made from glass, boron or carbon exhibit high mechanical strengths, high moduli of elasticity and low density. When combined with epoxy, polyester or polyimide resins, composite materials are produced that are exceptionally strong and stiff for their weight(1). Carbon (graphite) fibers are the predominant high-strength, high-modulus reinforcing agent currently used in high-performance composites. They are widely used in aerospace and other scientific applications. They also contribute to energy conservation in the form of lightweight transportation vehicles.

Despite the advantages of carbon fibers, there are areas where improvement can be made by the development of alternate fibers for composite materials. Carbon fibers show high electrical conductivity which has led to concern about safety (2). During combustion, carbon fibers released into the atmosphere may enter electronic equipment causing short circuits (3). Carbon fibers are also subject to oxidative degradation. Severe oxidation occurs above 400^{0}C in air (4). Another problem is poor adhesion between carbon fibers and thermoplastic or metal matrices (5). This can result in debonding of the fibers from the matrix at low stress. Many of the most desirable applications of composite materials are in high temperature areas, such as gas turbine blades, plasma devices and rocket motors. Current carbon fibers show insufficient temperature stability for applications of this type.

These limitations necesitate the search for new materials with potential as carbon fiber replacements. Silicon carbide - silicon nitride ($Si_xN_yC_z$) materials have been suggested as one promising candidate (6). Such materials are oxidation resistant at high temperatures and possess other properties similar to carbon fibers. Work in the Materials and Processes Laboratory of the Marshall Space Flight Center has produced fibers of this type (7). These fibers showed a tensile modulus of approximately 29 X 10^6 psi. At this stage of development, this compares favorably with that of graphite fibers with an average value of 55 X 10^6 psi. The electrical resistivity value of $Si_xN_yC_z$ fibers is measured at 7 X 10^8 ohm-cm. This lies in the semiconductor range but approaches the value of a true insulator ($\geq 10^{12}$).

The fibers tested above were prepared by a method derived from that of Verbeek. The first step was the synthesis of the monomer, tris (methylamino)methylsilane, by the reaction of methyltrichlorosilane with methyl amine (Eq. 1). The monomer was then converted into a polycarbosilazane

$$CH_3SiCl_3 + 6\ CH_3NH_2 \longrightarrow CH_3Si(NHCH_3)_3 + 3\ (CH_3NH_3^+)Cl^-$$

EQUATION 1

resin by passing over glass rings at 520°C. Although the structure of this polymer is not completely characterized it is believed to be analogous to other polysilazanes (8) (Eq. 2). Fibers were then hand drawn

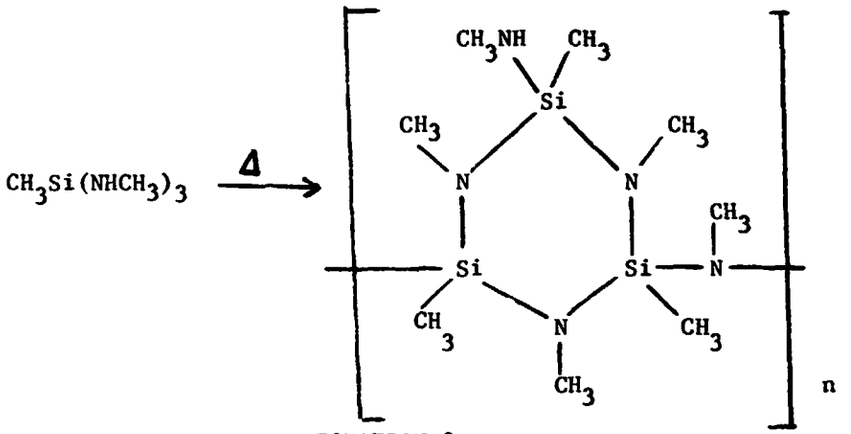

EQUATION 2

from the resin melt. The fibers were next humidity conditioned to a noncombustible material. Finally, the hydrolyzed fibers were pyrolyzed to the inorganic $Si_xN_yC_z$ by heating to approximately 1500°C.

The objective of this project is to prepare a series of substituted silaneamines for use in the production of $Si_xN_yC_z$ fibers. With the initial promise demonstrated by fibers formed from the tris(methylamino)methylsilane monomer, the next logical step is structural modification of the polymer. Each silane amine monomer will hopefullyprovide a different polymer precursor with modified properties.

During pyrolysis, mass is lost due to elimination of volatile byproducts. Excessive mass loss is undesirable because it can result in fiber defects and high shrinkage (9). Incorporation of higher molecular weight carbon groupings may decrease this problem. In particular, it has been shown that in the production of carbon fibers, loss of volatile byproducts is lowest when the precursor material contains aromatic groups.

EXPERIMENTAL

Reagent grade aniline and allyl amine were distilled over zinc metal. Phenyltrichlorosilane (PCR Research Chemicals) was vacuum distilled and stored under nitrogen in a dark bottle. All other chemicals were used without further purification. Boiling points of the products are uncorrected.

Infrared spectra were recorded neat between sodium chloride plates on a Perkin-Elmer 137 spectrophotometer with absorptions reported in wave-numbers (cm^{-1}). Nuclear magnetic resonance spectra were obtained in carbon tetrachloride solution on a Varian EM-306L spectrometer. Chemical shifts are reported in parts per million delta (δ) using either chloroform methylene chloride or tetramethylsilane as standards.

General Procedure for the Preparation of Tris(alkylamino)silanes

Approximately 300 mL of the appropriate solvent[a] was placed in a clean, dry one liter 3-neck flask. That was equipped with an addition funnel and mechanical stirrer. A gas inlet was placed atop the funnel. The apparatus was placed in an ice-water bath while flushing the system with dry nitrogen gas. The desired amine (1.5-2.0 moles[b]) was added to the solvent and stirring started. The alkyltrichlorosilane (0.2 moles) was placed in the addition funnel taking care to avoid extensive exposure to moist air. The silane was then added dropwise to the amine solution with vigorous stirring under an inert, dry atmosphere.

After silane addition was complete, the stirrer and funnel were removed and replaced with a condenser. The resultant mixture of solution and amine hydrochloride precipitate was then refluxed for one hour under dry nitrogen. The mixture was allowed to cool to room temperature and then vacuum filtered through a medium or coarse fritted glass funnel[c]. The precipitate was washed with 100 mL of the solvent. Exposure to humidity was kept to a minimum at all times.

The filtrate was then evaporated in vacuo to remove excess unreacted amine and the majority of the solvent. The residue from this was then vacuum distilled storing the desired fraction under dry nitrogen.

Silaneamines Prepared by the Preceding Method

The following compounds obtained were all clear, colorless liquids.

Tris(n-propylamino)methylsilane $(CH_3CH_2CH_2NH)_3SiCH_3$
b.p. 225°C/760 torr, 98°C/4 torr
Percent yield = 79.8
IR (Fig. 1); 3400w, 2910s, 2850s, 1450m, 1390s, 1250s, 1225m, 1120s, 1075m, 1025w, 1010s, 900m, 840m, 770m, 745m.
NMR (Fig. 2); -0.27 (s, 3H), 0.30 (broad s, 3H), 0.63 (t, 9H), 1.17 (m, 6H), 2.50 (t, 6H).

Tris(n-butylamino)methylsilane $(CH_3CH_2CH_2CH_2NH)_3SiCH_3$
b.p. 185°C/6 torr
Percent yield = 82.0
IR (Fig. 3); 3410w, 2950s, 1475m, 1400s, 1290w, 1260s, 1220w, 1130s, 1050m, 980w, 895m, 845m, 800m, 780m, 735w.
NMR (Fig. 4); -0.20 (s, 3H), 0.35 (broad s, 3H), 0.77 (t, 9H), 1.20 (m, 12H), 2.58 (t, 6H).

Tris(allylamino)methylsilane $(CH_2{=}{=}CHCH_2NH)_3SiCH_3$
b.p. 66°C/0.5 torr
Percent yield = 81.0
IR (Fig. 5); 3400w, 3050w, 2950w, 2850w, 1640w, 1440w, 1390s, 1255m, 1220m, 1150m, 1100s, 1025, 995m, 915s, 850m, 785w.
NMR (Fig. 6); -0.07 (s, 3H), 0.62 (broad s, 3H), 3.33 (m, 6H), 4.73-6.17 (m, 9H).

Preparation of Tris(anilino)methylsilane $(C_6H_5NH)_3SiCH_3$

Toluene[d] (300 mL) was placed in a clean, dry one liter 3-neck flask fitted with a mechanical stirrer and addition funnel. Aniline (135 g, 1.45 moles) was added to the flask. A gas inlet is placed on the addition funnel and the apparatus was cooled in an ice-water bath while flushing with dry nitrogen. Methyltrichlorosilane (29.9 g, 0.20 moles) was placed in the addition funnel and added dropwise while stirring under nitrogen.

After the silane addition was complete, the mixture was warmed to 40-60°C for one hour. After cooling to room temperature, the mixture was filtered through a medium fritted glass funnel, washing the precipitate with 100 mL of toluene. The filtrate was then evaporated in vacuo.

The residue was transferred to a small distilling flask and a short-path distillation apparatus (no condenser or fraction cutter) was assembled. The residue was then vacuum distilled collecting 49.2 g (77.1%) of a highly viscous yellow oil (b.p. 220°/1 torr, lit. (10) 212°/ 1 torr).

IR (Fig. 7); 3400m, 3050w, 1600s, 1490s, 1380s, 1280s, 1230w, 1180w, 1160w, 1080m, 1030m, 1000m, 915s, 780m, 755s, 735m, 695s.
NMR (Fig. 8); 0.82 (s, 3H), 4.27 (broad s, 3H), 6.87-7.52 (m, 15H).

Preparation of Tris(methylamino)phenylsilane $(CH_3NH)_3SiC_6H_5$

Toluene (600 mL) was placed in a two liter 3-neck flask equipped with a mechanical stirrer, gas inlet and Dewar condenser. The flask was placed in a cooling bath at approximately -40°C (liquid nitrogen/acetonitrile). A similiar cooling mixture was placed in the condenser. Methylamine gas was passed into the system through the condenser. This was continued until the total volume was about 800 mL. The apparatus was then flushed with dry nitrogen.

Phenyltrichlorosilane (84.5g, 0.40 mole) was placed in an addition funnel and inserted in one neck of the flask placing the nitrogen inlet on the funnel. The silane was added dropwise under nitrogen with vigorous stirring, maintaining the bath temperature at about -40°C.

After the addition was complete, the system was allowed to warm to room temperature. The mixture was then refluxed under nitrogen for one hour. The mixture was then cooled and filtered to remove the amine salt. The precipitate was washed with 200 mL of toluene. The filtrate was evaporated in vacuo. The residue was vacuum distilled collecting 53.7g (68.8%) of a clear colorless liquid (b.p. 113°/2 torr, 250°/760 torr).

IR (Fig. 9); 3430m, 3050w, 2900s, 2800m, 1600w, 1480w, 1430m, 1370s, 1110s, 1015m, 730s, 700m.
NMR (Fig. 10); 0.60 (broad s, 3H), 2.60 (s, 9H), 7.13-7.73 (m, 5H).

[a]Petroleum ether or toluene can be used in most cases. Toluene has the advantage that the amine salt is somewhat less soluble in it.

[b]The stoichiometric ratio of amine to silane is 6:1. In order to guarantee excess amine, at least 2.4 moles of amine per mole of halogen is used. If a volatile amine is used, a larger excess is recommended.

[c]In some instances it may be desirable to evaporate the unreacted amine before filtration. This allows for more complete precipitation.

[d]Tris(anilino)methylsilane is not sufficiently soluble in petroleum ether to allow use of that solvent here.

RESULTS AND DISCUSSION

The synthesis of silanetriamines was carried out beginning basicly with the procedure outlined by Penn, et al. The initial preparation attempted was that using methyltrichlorosilane and n-propyl amine (Eq. 3, R = $-CH_2CH_2CH_3$). The reaction was carried out at 0°C as the amine was

$$CH_3SiCl_3 + 6\ RNH_2 \longrightarrow CH_3Si(NHR)_3 + 3\ (RNH_3^+)Cl^-$$

EQUATION 3

liquid at room temperature unlike the methyl amine used by Penn. The reaction proceeded much as expected except that the boiling point of this product was too high for high yield distillation at atmospheric pressure. The product obtained here was a clear, colorless liquid which would react with moisture from the air. This corresponded to observations of the original monomer.

The initial preparation gave a fairly low yield but by the third trial a very satisfactory yield of 80 percent was obtained. Two other compounds were synthesized without major problems. Silanetriamines made from n-butyl (R = $-CH_2CH_2CH_2CH_3$) and allyl (R = $-CH_2CH{=}CH_2$) were prepared in good yields of 82 and 81 percent respectively.

The major problem which had arisen up to this point was the difficulty in successfully separating all the amine hydrochloride ($RNH_3^+Cl^-$) salt from the reaction mixture. If the salt were present during the distillation, it would sublime over contaminating the product. Experience with the methyl amine monomer indicated that the presence of salt would produce unsatisfactory precursor resin. In addition, Rochow indicates that cyclization of silane amines is catalyzed by ammonium salts.

The next monomer prepared was that from the reaction of the chlorosilane with aniline (R = $-C_6H_5$). Initial attempts resulted in no silaneamine isolated from the filtrate. Since significant quantities of amine salt were produced, it was believed that the reaction had proceeded as planned. The literature indicated that this compound had been previously prepared by Anderson (11) using benzene as the solvent. This and experiments in the laboratory led to a new attempt using toluene instead of petroleum ether. This attempt resulted in the successful isolation of the desired product. Apparently, the tris(anilino)methylsilane was insoluble in petroleum ether and was left behind with the salt during filtration. Some difficulty still remained because the product was an exceedingly viscous glassy material at room temperature. This necesitated the use of a short-path distillation in the final purification. After sitting for some time, the oil showed some signs of crystallization but the process was imperceptibly slow. Until this monomer can be obtained in crystalline

form, it will prove to be difficult to work with.

A second series of monomers was initiated using phenyltrichlorosilane (Eq. 4). Once the purity of the phenylsilane was assured, reac-

$$C_6H_5SiCl_3 + 6\ RNH_2 \longrightarrow C_6H_5Si(NHR)_3 + 3(RNH_3^+)Cl^-$$

EQUATION 4

tion with methyl amine (R = $-CH_3$) was carried out smoothly. A percent yield of 69 was obtained. Due to the inherent simplicity of this substance, it was selected for the initial polymerization experiments. This is work is in initial stages and will be reported on in future publications. The preparation of a second monomer to be made from n-propyl amine was attempted. Although the reaction appeared to proceed normally, a nonvolatile solid was obtained upon distillation. It resembles a polymeric material but confirmation of this is yet to be made.

All of the compounds prepared were characterized by infrared (IR) and nuclear magnetic resonance (NMR) spectroscopy. Samples of each have been submitted for elemental analysis.

CONCLUSIONS AND RECOMMENDATIONS

The preparation of N-alkyl substituted silaneamines can be carried out easily with good yields. This has provided several new compounds for polymerization and fiber formation. The data obtained from these fibers will provide clues to the direction of future work. In particular, two distinctly differently different monomers containing aromatic rings were synthesized. Future tests will indicate whether predictions about the effects of substitution are valid. At the very least, even if these new compounds do not produce vastly superior fibers, some of the monomers may be more amenable to mass production.

This area of polymer and composite work has only just opened and many tasks remain. The mechanism of polymerization is only partially understood at this time. An examination of the effect of structure on the conditions and rate of polymerization is ultimately necessary. With the variety of monomers available now and in the near future, this study is feasible. In addition, current structural modifications have not drasticall; altered the intermolecular attractive forces. Incorporation of funtionality into the side chain also offers a future project. In conclusion, this area is ripe for extended study, especially if the original fibers continue to live up to their initial promise.

REFERENCES

1. Lubin, G., "Handbook of Composites" Van Nostrand Reinhold Company, 1982.

2. Cagliostro, D.E., Textile Research Journal 632, Oct. 1980.

3. Springer, G.S., Mashtizadeh, S.A. and Keller, R.B., J. Composite Materials 13, 225 (1979).

4. Jenkins, G.M. and Kawamura, K., "Polymeric Carbon-Carbon Fiber, Glass and Char" Cambridge University Press, 1976.

5. Langley, M., "Carbon Fibers in Engineering", McGraw-Hill, 1973.

6. Verbeek, W., Ger. Offen. 2, 218, 960 (1973).

7. Penn, B.G., Ledbetter, F.E., Clemons, J.M. and Daniels, J.G., J. App. Polym. Sci. 27, 3751 (1982).

8. Kruger, C.R. and Rochow, E.G., J. Polym. Sci. A 2, 3179 (1964).

9. Fitzer, E., Angew. Chem. Int. Ed. Engl. 19, 375 (1980).

10. Fessenden, R. and Fessenden, J.S., Chem. Reviews 61, 361 (1961).

11. Anderson, H.H., J. Amer. Chem. Soc. 73, 5802 (1951).

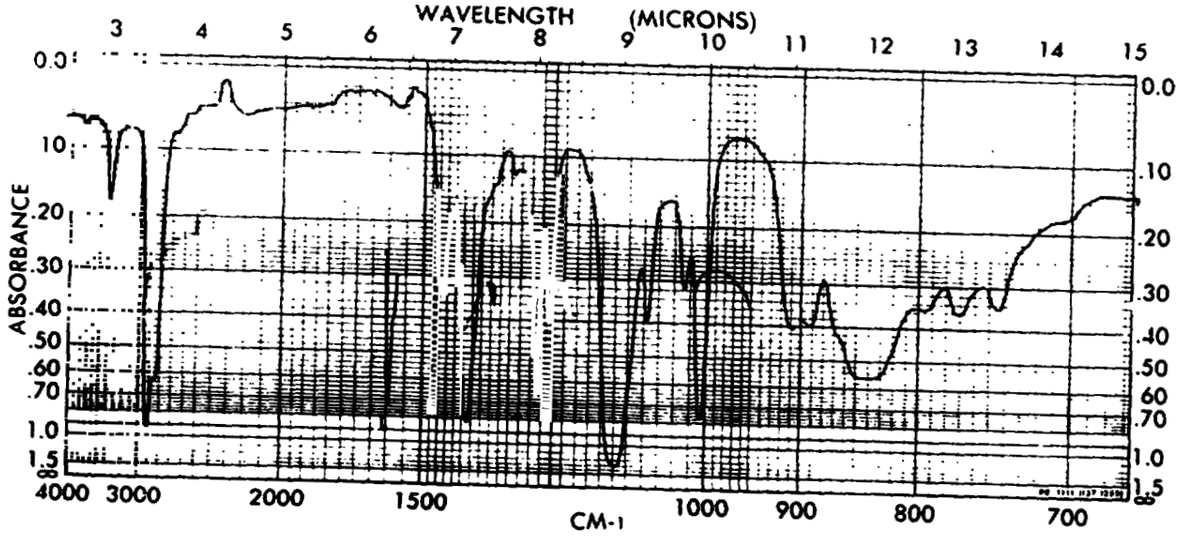

FIGURE 1 IR SPECTRUM OF TRIS(N-PROPYLAMINO)METHYLSILANE

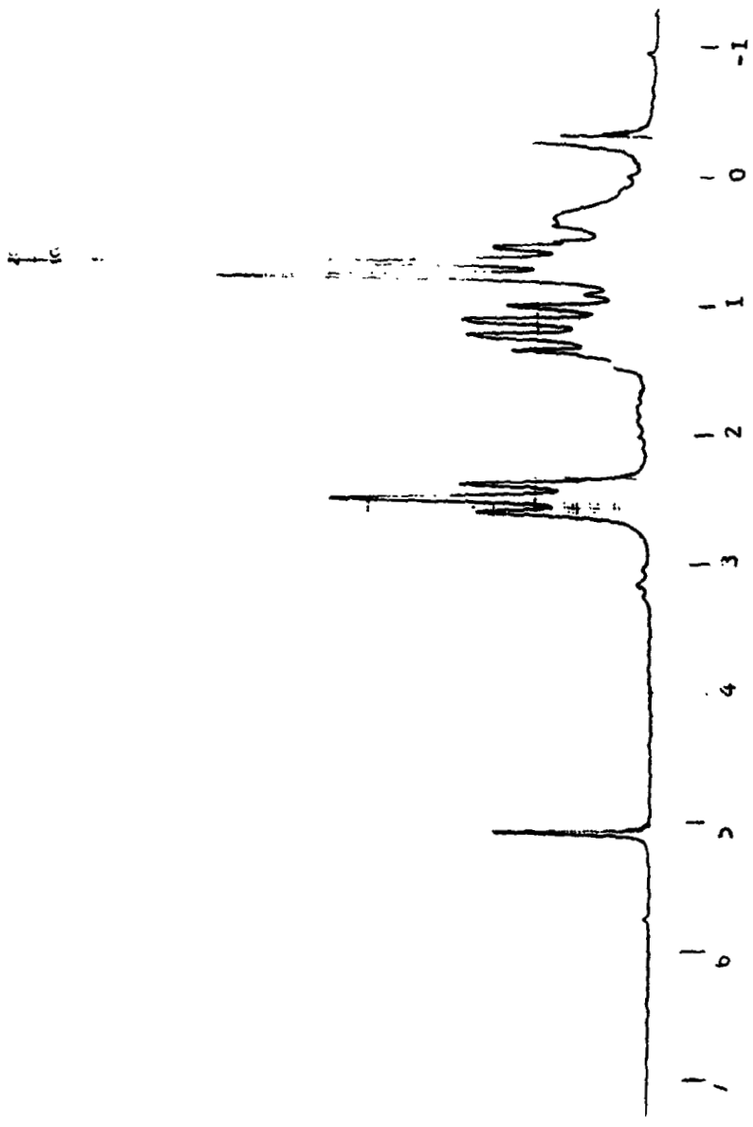

FIGURE 2 NMR SPECTRUM OF TRIS(N-PROPYLAMINO)METHYLSILANE

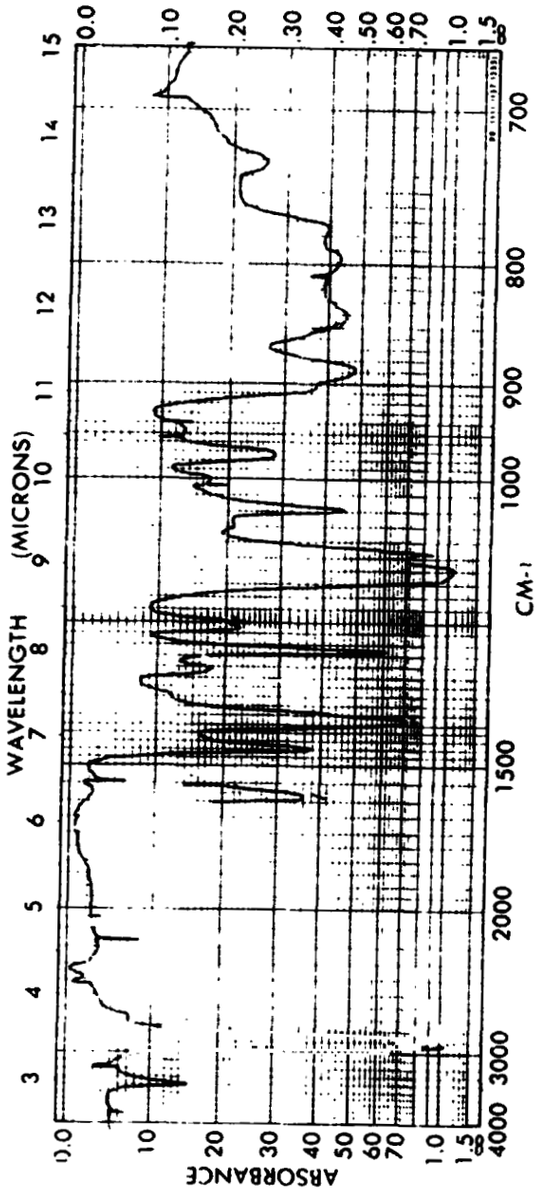

FIGURE 3 IR SPECTRUM OF TRIS(N-BUTYLAMINO)METHYLSILANE

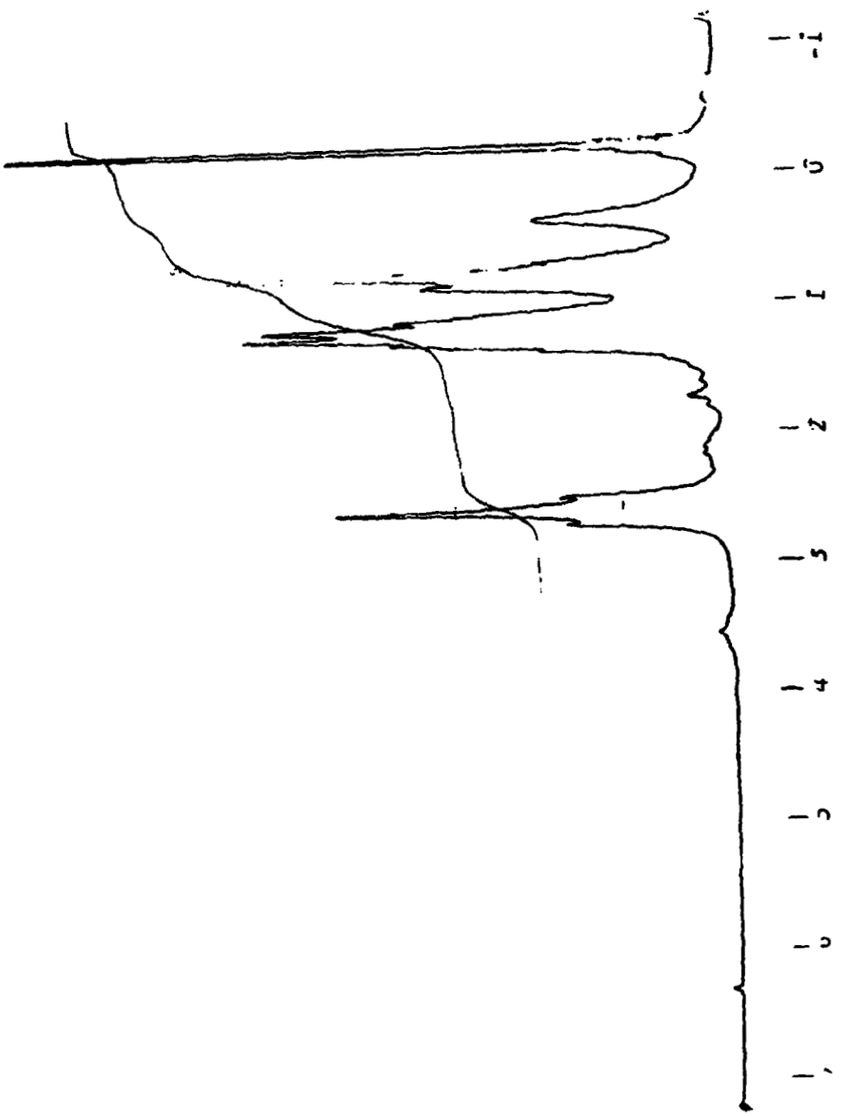

FIGURE 4 NMR SPECTRUM OF TRIS(N-BUTYLAMINO)METHYLSILANE

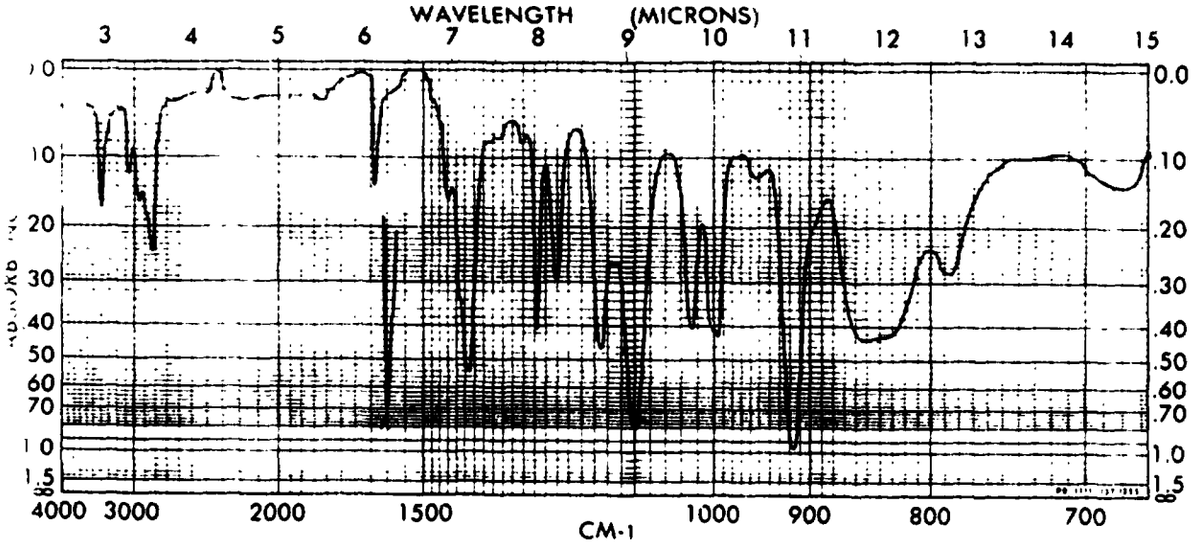

FIGURE 5 IR SPECTRUM OF TRIS(ALLYLAMINO)METHYLSILANE

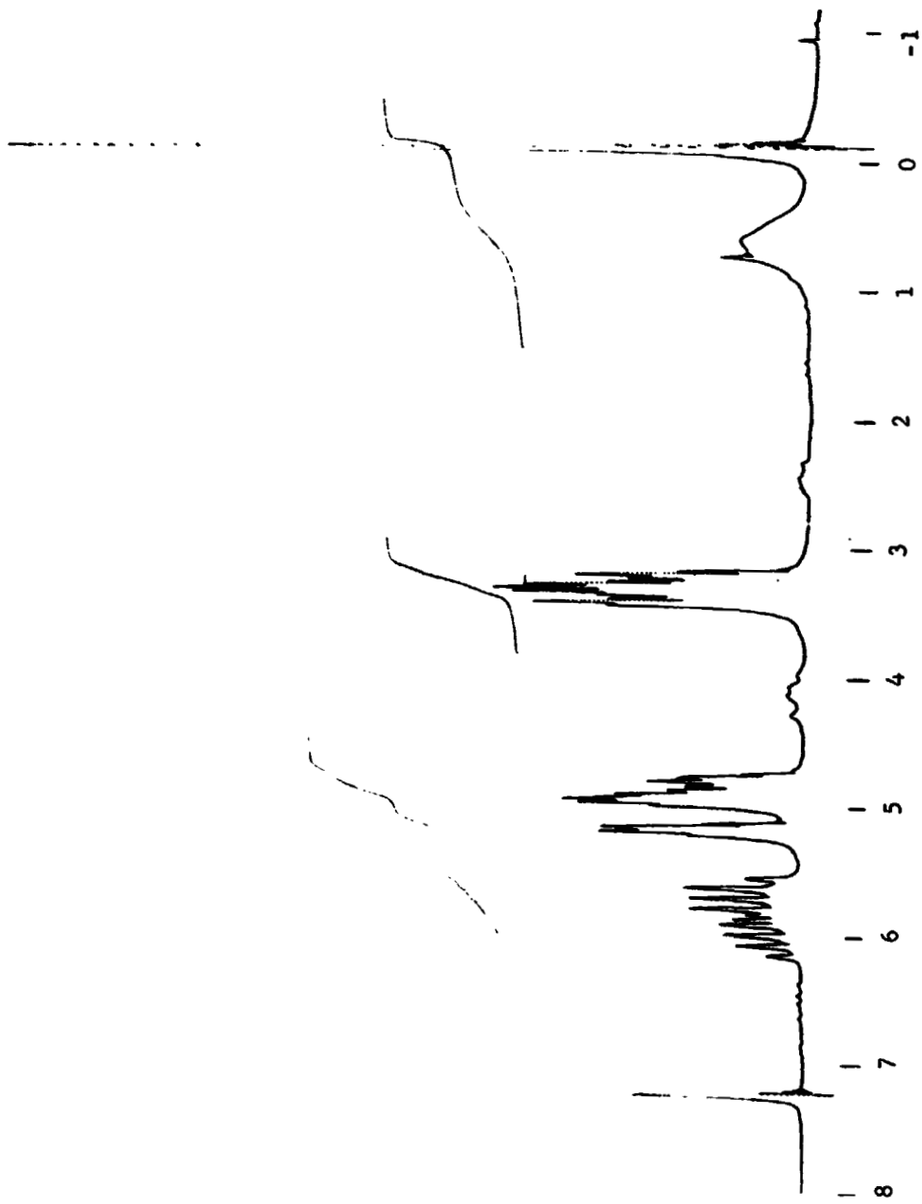

FIGURE 6 NMR SPECTRUM OF TRIS(ALLYLAMINO)METHYLSILANE

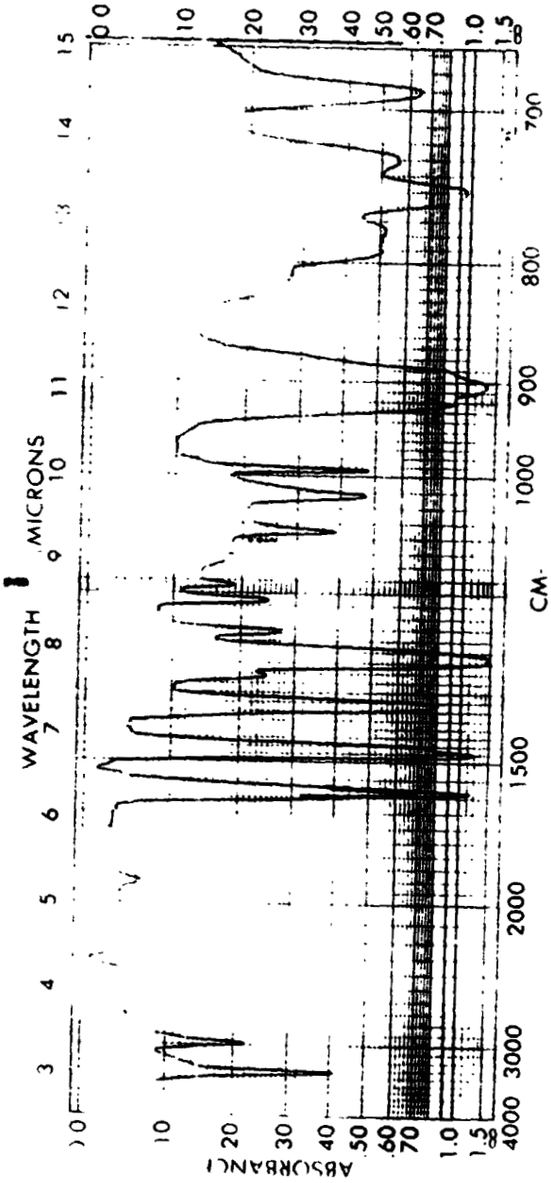

FIGURE 7 IR SPECTRUM OF TRIS(ANILINO)METHYLSILANE

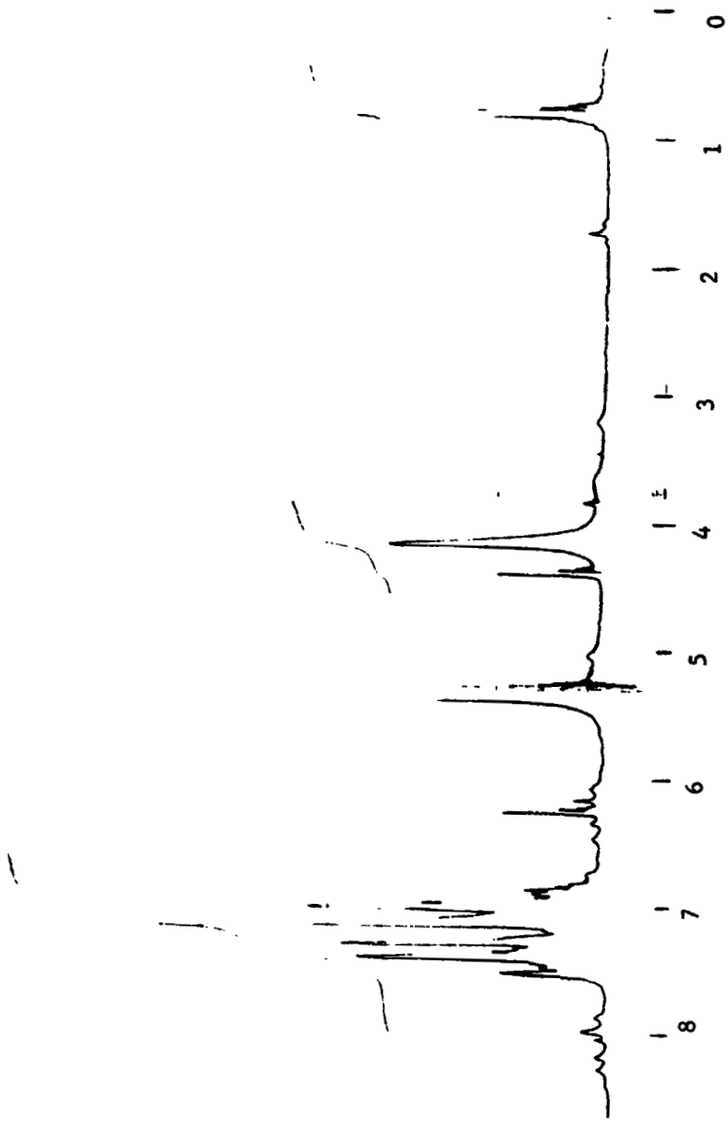

FIGURE 8 NMR SPECTRUM OF TRIS(ANILINO)METHYLSILANE

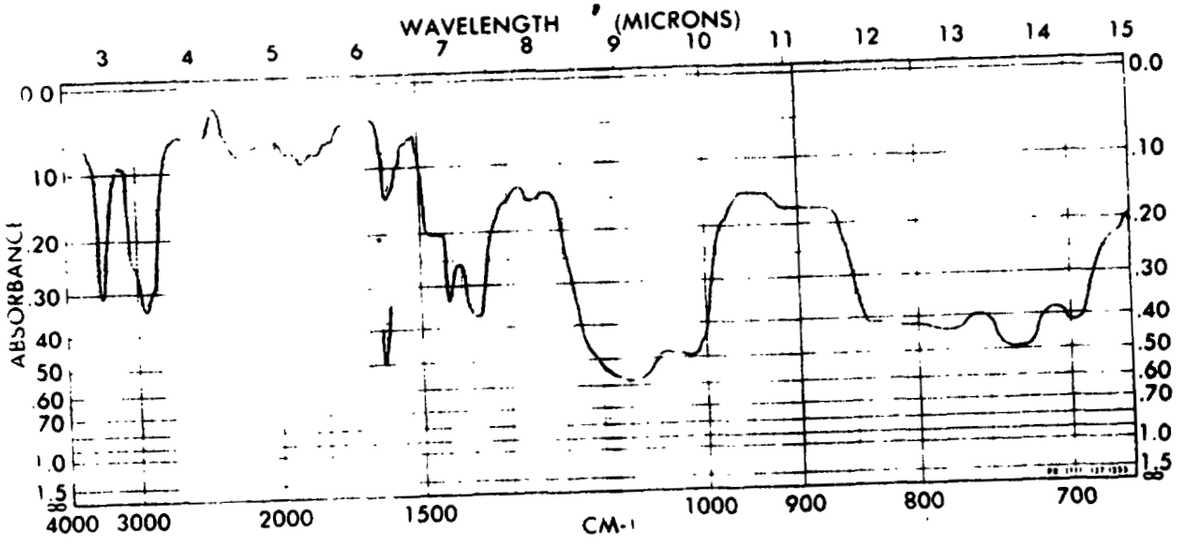

FIGURE 9 IR SPECTRUM OF TRIS(METHYLAMINO)PHENYLSILANE

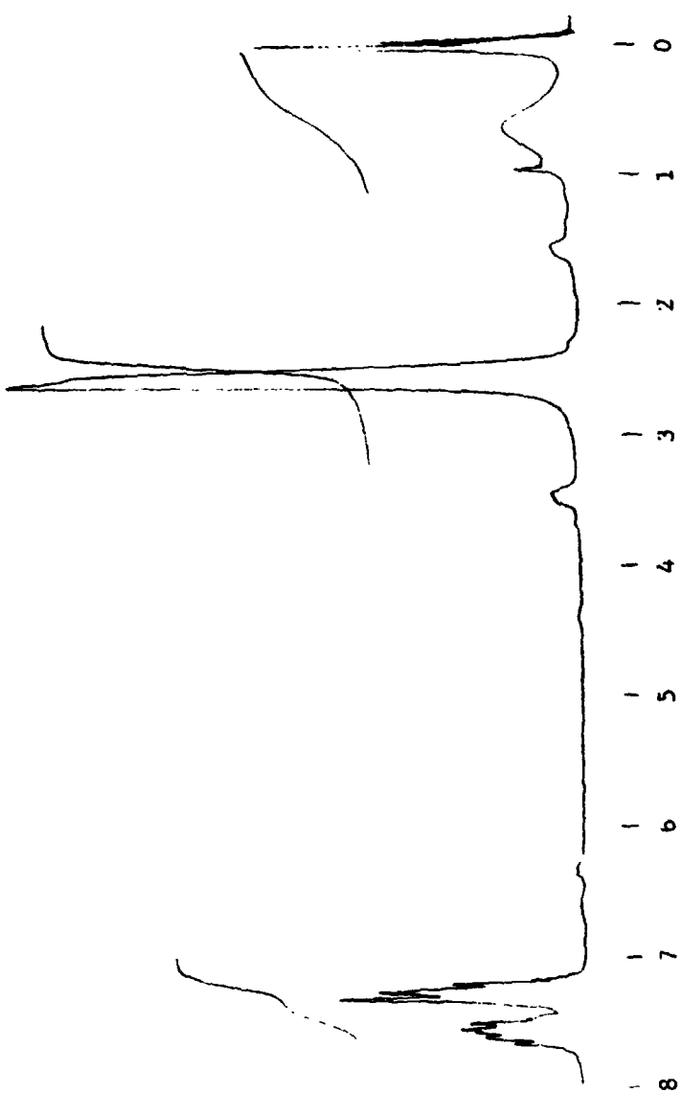

FIGURE 10 NMR SPECTRUM OF TRIS(METHYLAMINO)PHENYLSILANE

1983

NASA/ASEE SUMMER FACULTY RESEARCH FELLOWSHIP PROGRAM

MARSHALL SPACE FLIGHT CENTER

THE UNIVERSITY OF ALABAMA IN HUNTSVILLE

LINEAR AND NONLINEAR ASPECTS OF ROTORDYNAMICS

Prepared by:	William B. Day, Ph.D.
Academic Rank:	Associate Professor
University and Department:	Auburn University
	Department of Mathematics
NASA/MSFC:	
Division:	Control Systems
Branch:	Servomechanisms & Systems Stability
MSFC Counterpart:	Luke A. Schutzenhofer, Ph.D.
Date:	August 12, 1983
Contract Number:	NGT-01-008-021
	The University of Alabama in Huntsville

LINEAR AND NONLINEAR ASPECTS OF ROTORDYNAMICS

BY

William B. Day, Ph.D.

Associate Professor of Mathematics

Auburn University, Alabama

ABSTRACT

Excessive vibrations of the liquid oxygen pump in the Space Shuttle's Main Engine have been recorded during hot firing ground testing. We have examined the differential equations which describe the rotordynamics of the pump in order to determine mathematical explanations of this possibly destructive phenomenon.

To this end we have considered modeling the rotor as a random eigenvalue problem and derived statistical properties of the solutions. Secondly, we have derived analytical expressions for the solution in the case of symmetric damping and stiffness. This enables one to determine accuracy estimates when testing numerical techniques to solve both asymmetric and nonlinear problems. Finally, the rotor model has had nonlinear elements incorporated to improve its simulation of the pump and to expand the corresponding mathematical theory.

LIST OF FIGURES

FIGURE		PAGE
1	y vs. z - Motion with Deadband	XII-16
2	t vs. R - Motion with Deadband	XII-16
3	PSD of y (0 to 600 Hertz)	XII-17
4	PSD of R (200 to 800 Hertz)	XII-17
5	PSD of R (800 to 2000 Hertz)	XII-17
6	PSD of R (2000 to 5000 Hertz)	XII-17
7	PSD of Y (500 to 700 Hertz)	XII-18
8	PSD of y (600 to 1000 Hertz)	XII-18
9	PSD of y (1000 to 2000 Hertz)	XII-18

1. Introduction: In this report we examine three aspects of the rotordynamics of the Space Shuttle Main Engine High-Pressure Liquid Oxygen Fuel Turbopump. The mathematical model for rotordynamics problems originated with Jeffcott [3] and describes axisymmetric motion of a rotor which contains stiffness and damping. The rotor is driven by mass imbalance and mathematically the motions in the y- and z-directions are the solutions of

$$(1.1)\quad m\ddot{y} = -k_{11}y+k_{12}z-c\dot{y}+A\cos\omega t$$

$$(1.2)\quad m\ddot{z} = -k_{21}y-k_{22}z-c\dot{z}-A\sin\omega t.$$

Hereafter, we shall assume that the mass m is a non zero constant and that both equations have been divided by m. The four k's are generally unrelated; however, we shall often use the symmetric case where $k_{11} = k_{22}$ and $k_{12} = k_{21}$. The symmetric case occurs frequently in reality, and the modifications to be made in other situations are usually straight-forward. We also limit our discussion to equations with no cross-damping and equal damping for the two directions of motion.

In section 2 we solve equations (1.1) - (1.2) when the coefficients are random variables. Following the methods of Soong et al., [4], [5], and [6], we derive expressions for the random eigenvalues and eigensolutions. In section 3 two transformations are presented for our equations. Under these transformations, the solutions of equations (1.1) and (1.2) are most easily obtained. Section 4 examines the effect of including the nonlinear phenomenon deadband in our equation. Using asymptotic expansions we are able to derive analytic expressions for the solutions. These solutions reveal the apparent shift of the natural frequencies. Extensive bibliographies of work on this nonlinear problem are given by Childs [1] and Yamamoto [7].

2. Random Eigenvalues: We initially examine the case for which system (1.1) - (1.2) contains only one random variable coefficient. We replace this constant c_{ee} by $C+\Gamma$ where $C=\langle c_{ee}\rangle$, the expected value of c_{ee} and Γ is a random variable with zero expectation.

Following the identical procedure used in the deterministic problem, we are lead to solve the characteristic equation

$$(2.1)\quad \lambda^4+a_3\lambda^3+a_2\lambda^2+a_1\lambda+a_0=0$$

for the exponents of the solution; i.e., assuming $y=y_0 \exp(\lambda t)$ and $z=z_0 \exp(\lambda t)$, we must find the roots of equation (2.1).

The coefficients of equation (2.1) are random variables since they depend on the constants of equations (1.1) - (1.2), which now involve a random variable. Therefore, we assume λ also depends on this random variable Γ and write

$$(2.2) \quad \lambda = \sum_{n=0}^{\infty} b_n \lambda^n.$$

This expansion for λ can be substituted into equation (2.1) and the unknown coefficients can be determined recursively. The lowest order (in λ) equation obtained will always be

$$(2.3) \quad b_0^4 + a_3 b_0^3 + a_2 b_0^2 + a_1 b_0 + a_0 = 0$$

where the a's are those used in the deterministic problem; i.e., $Cee = C = \langle Cee \rangle$. We distinguish among the four roots by

$$(2.4) \quad \lambda_i = \sum_{n=0}^{\infty} b_{ni} \Gamma^n \text{ for } i = 1,2,3,4.$$

Since we are ultimately interested in the statistics (moments) of the solutions which have the form

$$y = d_1 e^{\lambda_1 t} + d_2 e^{\lambda_2 t} + d_3 e^{\lambda_3 t} + d_4 e^{\lambda_4 t}$$

$$z = c_1 e^{\lambda_1 t} + de_2 e^{\lambda_2 t} + e_3 e^{\lambda_3 t} + e_4 e^{\lambda_4 t},$$

we are lead to examining

$$\exp(\lambda t)$$

$$= \exp\left(b_{0i} t + \sum_{n=1}^{\infty} b_{ni} \Gamma^n t\right)$$

$$= \exp(b_{0i} t)\left[1 + (\Sigma b_{ni} \Gamma^n t) + \tfrac{1}{2}(\Sigma b_{ni} \Gamma^n t)^2 + \ldots\right]$$

Thus, to find $\langle y(t_1) y(t_2) \rangle$ we are reduced to considering terms of this form:

$$\langle \exp(\lambda_i t_1)\exp(\lambda_j t_2)\rangle$$

$$= \exp(b_{oi}t_1+b_{oj}t_2)\cdot$$
$$\cdot\langle(1+(b_{1i}\Gamma+b_{2i}\Gamma^2+\ldots)t_1+\tfrac{1}{2}(b_{1i}\Gamma+b_{2i}\Gamma^2+\ldots)^2t_1^2+\ldots)$$
$$\cdot(1+(b_{1j}\Gamma+b_{2j}\Gamma^2+\ldots)t_2+\tfrac{1}{2}(b_{1j}\Gamma+b_{2j}\Gamma^2+\ldots)^2t_2^2+\ldots)\rangle$$

$$= \exp(b_{oi}t_1+b_{oj}t_2)\cdot$$
$$\cdot\langle(1+(b_{1i}t_1)\Gamma+(b_{2i}t_1+\tfrac{1}{2}b_{1i}^2t_1^2)\Gamma^2+\ldots)\cdot$$
$$\cdot(1+(b_{1j}t_2)\Gamma+(b_{2j}t_2+\tfrac{1}{2}b_{2j}^2t_2^2)\Gamma^2+\ldots)\rangle$$

$$= \exp(b_{oi}t_1+b_{oj}t_2)\cdot$$
$$\cdot[1+b_{1i}t_1+b_{1j}t_2)\langle\Gamma\rangle$$
$$+(b_{1i}b_{1j}t_1t_2+b_{2i}t_1+\tfrac{1}{2}b_{1i}^2t_1^2$$
$$+b_{2j}t_2+\tfrac{1}{2}b_{2j}^2t_2^2)\langle\Gamma^2\rangle+\ldots]$$

Similar results hold for higher moments; i.e., for

$$\langle y^n(t_1)y^m(t_2)\rangle, \langle z^n(t_1)z^m(t_2)\rangle \text{ and } \langle y^n(t_1)z^m(t_2)\rangle.$$

Example 1:

$$\ddot{y} = -5y-z-(5+\zeta)\dot{y}$$

$$\ddot{z} = -y-5z-5\dot{z}$$

The characteristic equation is

$$\lambda^4+(10+\zeta)^3+(35+5\zeta)\lambda^2+(50+5\zeta)\lambda+24=0$$

with $\lambda_i = \sum_{nc^0}^{\infty} b_{ni}\zeta^n, \quad i=1,2,3,4.$

we have $(b_{oi}+b_{1i}\zeta+b_{2i}\zeta^2+\ldots)^4+(10+\zeta)(b_{oi}+b_{1i}\zeta+b_{2i}\zeta^2+\ldots)$
$$+(35+5\zeta)(b_{oi}+b_{1i}\zeta+b_{2i}\zeta^2+\ldots)^2$$
$$+(50+5\zeta)(b_{oi}+b_{1i}\zeta+b_{2i}\zeta^2+\ldots)+24=0$$

or $b_{oi}^4+4b_{oi}^3b_{1i}\zeta+(6b_{oi}^2b_{1i}^2+4b_{oi}^3b_{2i})\zeta^2+\ldots$

$+10(b_{oi}^3+3b_{oi}^2b_{1i}\zeta+(3b_{oi}b_{1i}^2+3b_{oi}^2b_{2i})\zeta^2+\ldots)$

$+\zeta(b_{oi}^3+3b_{oi}^2b_{1i}\zeta+\ldots)$

$+35(b_{oi}^2+2b_{oi}b_{1i}\zeta+(b_{1i}^2+2b_{oi}b_{2i})\zeta^2+\ldots)$

$+5\zeta(b_{oi}^2+2b_{oi}b_{1i}\zeta+\ldots)$

$+50(b_{oi}+b_{1i}\zeta+b_{2i}\zeta^2+\ldots)+5\zeta(b_{oi}+b_{1i}\zeta+\ldots)+24=0$

Thus ζ^o: $b_{oi}^4+10b_{oi}^3+35b_{oi}^2+50b_{oi}+24=0$

$(b_{oi}+1)(b_{oi}+2)(b_{oi}+3)(b_{oi}+4)=0$

$b_{oi}=-i, i=1,2,3,4$

ζ: $4b_{oi}^3b_{1i}+30b_{oi}^2b_{1i}+b_{oi}^3+70b_{oi}b_{1i}$

$+5b_{oi}^2+50b_{1i}+5b_{oi}=0$

$b_{1i}=-(b_{oi}^3+5b_{oi}^2+5b_{oi})/(4b_{oi}^3+30b_{oi}^2+70b_{oi}+50)$

$b_{11}=-(-1)(1-5+5)/(-4+30-70+50)=1/6$

$b_{12}=-(-2)(4-10+5)/(-32+120-140+50)=-2/-2=1$

$b_{13}=-(-3)(9-15+5)/(-108+270-210+50)=-3/2=-3/2$

$b_{14}=-(-4)(16-20+5)/(-256+480-280+50)=4/-6=-2/3$

ζ^2: $6b_{oi}^2b_{1i}^2+4b_{oi}^3b_{2i}+30b_{oi}b_{1i}^2+30b_{oi}^2b_{2i}$

$+3b_{oi}^2b_{1i}+35b_{1i}^2+70b_{oi}b_{2i}+10b_{oi}b_{1i}$

$+50b_{2i}+5b_{1i}=0$

$$b_{2i}=\frac{-(6b_{0i}^2b_{1i}^2+30b_{0i}b_{1i}^2+3b_{0i}^2b_{1i}+35b_{1i}^2+10b_{0i}b_{1i}+5b_{1i})}{4b_{0i}^3+30b_{0i}^2+70b_{0i}+50}$$

$$= \frac{-b_1\ [(6b_{0i}^2+30b_{0i}+35)b_{1i}+3b_{0i}^2+10b_{0i}+5]}{4b_{0i}^3+30b_{0i}^2+70b_{0i}+50}$$

$$b_{21}=-(1/6)[(6-30+35)(1/6)+3-10+5]/6$$

$$=-(11/6-12/6)/36=1/216$$

$$b_{22}=-[(24-60+35)+12-20+5]/-2=-2$$

$$b_{23}=\frac{3}{2}[(54-90+35)(-3/2)+27-30+5]/2=21/8$$

$$b_{24}=\frac{2}{3}[(96-120+35)(-2/3)+48-40+5]/-6$$

$$=\frac{2}{3}[-22/3+39/3]/-6=17/27$$

Finally, $\lambda_1 =-1+\zeta/6+\zeta^2/216+\ldots$

$\lambda_2 =-2+\zeta-2\zeta^2+\ldots$

$\lambda_3 =-3-3\zeta/2+21\zeta^2/8+\ldots$

$\lambda_4 =-4-2\zeta/3+17\zeta^2/27+\ldots$

It is a straight-forward, although cumbersome extension to allow two or more of the coefficients in equations (1.1)-(1.2) to be random variables. We need only assume a series of the form

$$\lambda_i=\sum_{n_1=0}^{\infty}\ \sum_{n_2=0}^{\infty}\cdots\ \sum_{n_k=0}^{\infty} b_{n_1n_2\ldots n_ki}\zeta_1^{n_1}\zeta_2^{n_2}\ldots\zeta_k^{n_k},\ i=1,2,3,4.$$

The following example of two random coefficients is typical.

Example 2: $\ddot{y} = -5y-z-(5+\zeta)\dot{y}$

$\ddot{z} = -y-5z-(5+\theta)\dot{z}$

The characteristic equation is

$$\lambda^4+\lambda^3(10+\zeta+\theta)+\lambda^2(10+25+5\zeta+5\theta+\theta\zeta)$$
$$+\lambda(25+5\zeta+25+5\theta)+24=0$$

Then $\lambda_i = \sum_{n=0}^{\infty} \sum_{m=0}^{\infty} b_{nmi}\, \zeta^n \theta^m, i=1,2,3,4.$

or substituting into the equation

$$(b_{00i}^4+4b_{00i}^3b_{01i}\theta+4b_{00i}^3b_{10i}\zeta+6b_{00i}^2b_{01i}^2\theta^2$$
$$+6b_{00i}^2b_{10i}^2\zeta^2+4b_{00i}^3b_{20i}\zeta^2+4b_{00i}^3b_{11i}\zeta\theta+4b_{00i}^3b_{02i}\theta^2+\ldots)$$

$$+(10+\zeta+\theta)(b_{00i}^3+3b_{00i}^2b_{10i}\zeta+3b_{00i}^2b_{01i}\theta+3b_{00i}^2b_{11i}\theta\zeta$$
$$+\theta^2[3b_{00i}b_{01i}^2+3b_{00i}^2b_{02i}]+\zeta^2[3b_{00i}b_{10i}^2+3b_{00i}^2b_{20i}]+\ldots)$$

$$+(35+5\zeta+5\theta+\zeta\theta)(b_{00i}^2+2b_{00i}b_{01i}\theta+2b_{00_i}b_{10_i}\zeta$$
$$+(2b_{00i}b_{20i}+b_{10i}^2)\zeta^2+(2b_{00i}b_{02i}+b_{01i}^2)\theta^2$$

$$+\theta\zeta(2b_{01i}b_{10i}+2b_{00i}b_{11i})+\ldots)$$

$$+(50+5\zeta+5\theta)(b_{00i}+b_{10i}\zeta+b_{01i}\theta+b_{20i}\zeta^2+$$

$$b_{11i}\zeta\theta+b_{02i}\theta^2+\ldots)+24=0$$

Ultimately, we have

$$\lambda_1=-1+\zeta/6+\theta/6+\zeta^2/216-23\zeta\theta/108+\theta^2/216+\ldots$$

$$\lambda_2=-2+\zeta+\theta-2\zeta^2+32\zeta\theta-20^2+\ldots$$

$\lambda_3=-3-3\zeta/2-3\theta/2+21\zeta^2/8-303\zeta\theta/4+21\theta^2/8+...$

$\lambda_4=-4-2\zeta/3-2\theta/3+17\zeta^2/27+62\zeta\theta/27+17\theta^2/27+...$

3. Transformations: In the case of symmetric stiffness, equations (1.1) and (1.2) become

(3.1) $\ddot{y}=-ay+bz-c\dot{y}+A\cos\omega t$

(3.2) $\ddot{z}=-by-az-c\dot{z}-A\sin\omega t.$

We can solve these equations more easily by performing two transformations.

First of all, since the damping, c, is the same for the two equations, define

$$u(t)=\exp(ct/2)y(t)$$

$$v(t)=\exp(ct/2)z(t).$$

Then equations (3.1) and 3.2) become

(3.3) $\ddot{u}=(-a+c^2/4)u+bv+A\exp(ct/2)\cos\omega t$

(3.4) $\ddot{v}=(-bu+(-a+c^2/4)v-A\exp(ct/2)\sin\omega t$

and damping has been removed.

Next, with the transformations

$$x(t)=u(t)+iv(t)$$

$$w(t)=u(t)-iv(t),$$

we have

$$\ddot{x}=(-a+c^2/4-ib)x+A\exp(c/2-i\omega)t$$

$$\ddot{w}=(-a+c^2/4+ib)w+A\exp(c/2+i\omega)t$$

Thus

(3.5) $\ddot{x}+\omega_x^2 x=A\exp(\mu t)$

(3.6) $\ddot{w}+\bar{\omega}_x^2 w=A\exp(\bar{\mu}t)$

where the bar is complex conjugation and $\omega_x^2=a-c^2/4+ib$, and $\mu=c/2-i\omega$.

The solution of equation (3.5) is

$$x(t)=A\sin\omega_x t+B\cos\omega_x t+C\exp(\mu t)$$

where $C=A/(\omega_x{}^2+\mu^2)$ and A and B are determined by the initial conditions. Since $w(t)=\overline{x(t)}$, the solution of equation (3.6) is

$$w(t)=\bar{A}\sin\bar{\omega}_x t+\bar{B}\cos\bar{\omega}_x t+\bar{C}\exp(\bar{\mu}t).$$

Now if we reverse the two transformations, we find

$$y(t)=\exp(-ct/2)\,\mathrm{Re}\;x(t)$$

$$=\exp(-ct/2)\,\mathrm{Re}[A\sin\omega_x t+B\cos\omega_x t+C\exp(\mu t)]$$

and

$$z(t)=\exp(-ct/2)\,\mathrm{Im}\;x(t)$$

$$=\exp(-ct/2)\,\mathrm{Im}[A\sin\omega_x t+B\cos\omega_x t+C\exp(\mu t)].$$

The natural frequency ω_x can be found from

$$\omega_x{}^2=(a-c^2/4)+ib$$

$$=[(a-c^2/4)^2+b^2]^{\frac{1}{2}}\exp(i\,\mathrm{Arctan}(b/(a-c^2/4)));$$

hence,

$$\omega_x=[(a-c^2/4)^2+b^2]^{\frac{1}{4}}\exp(.5i\,\mathrm{Arctan}(b/(a-c^2/4))).$$

Finally, we note that a reduction to equations of the form (3.5) and 3.6) can be accomplished even in the case of non-symmetric stiffness; however, the initial transformation fails when the damping coefficients for the two equations are different.

4. Nonlinear Deadband: Because the impellers of the space shuttle main engine (SSME) liquid oxygen (LOX) turbopump cause a pressure differential and thereby a large axial thrust, it is necessary to reduce this force by creating a radial clearance between the bearings of the rotor and the support structure. This radial gap, the bearing deadband, is generally filled with a fluid which acts as a damper of small magnitude.

Accounting for deadband leads to nonlinearities in the Jeffcott equation; see Yamamoto (7) for a derivation. We have

(4.1) $\ddot{y} = bz - c\dot{y} - k(1-\Delta/R)(y-\mu z) + A\cos\omega t$

(4.2) $\ddot{z} = -by - c\dot{z} - k(1-\Delta/R)(\mu y+z) - A\sin\omega t$

where Δ is the size of the deadband, $R^2=y^2+z^2$, and ω is the frequency of rotation, which is assumed to be constant. We use b, c, k, μ, and A as constants only. Although this problem can be generalized somewhat (e.g., non-symmetric coefficients), we restrict our attention to this form since the solutions exhibit typical nonlinear behavior.

Yamamoto (7), Childs (1), and Gupta et al. (2) have examined some of the consequences of including deadband in the rotor's description, but analytic solutions have not been presented heretofore. We use asymptotic expansions to obtain zero- and first-order expressions for the solutions of problems (4.1)-(4.2).

These equations are easily solved numerically using a fourth-order Runge-Kutta algorithm. Figure 1 shows the motion for the case

$b=115700.\ S.^{-2}$	$A=285.\ in./S.^2$
$c=240.\ S.^{-1}$	$\omega=1000\pi$ rad./S.
$k=1305000.\ S.^{-2}$	$y(0)=.0001$ in.
$\Delta=.0000285$ in.	$z(0)=0=\dot{y}(0)$
$\mu=.1$	$\dot{z}(0)=-1000\pi y(0)$ in./S.

The motion has become periodic for the time interal ($.5\le t\le 1.S.$) shown. The graph of t vs. R given in Figure 2 displays R in the form

$$R=.71+.39\sin 720\pi t=a_1+a_2\sin\alpha t.$$

It is this second figure that leads us to consider solving our nonlinear equations by asymptotic expansions.

Now $$\frac{\Delta}{R} = \frac{\Delta}{a_1+a_2\sin\alpha t} = \frac{\Delta}{a_1}\left(\frac{1}{1+\frac{a_2}{a_1}\sin\alpha t}\right)$$

$$= \frac{\Delta}{a_1}\sum_{n=0}^{\infty}\left(-\frac{a_2}{a_1}\right)^n \sin^n\alpha t$$

or

$$(4.3)\quad \frac{\Delta}{R} = (\Delta/a_1)(1-(a_2/a_1)\sin\alpha t+(a_2/a_1)^2\sin^2\alpha t+\ldots).$$

We shall use a_2/a_1 as our expansion parameter ε. Thus,

$$\frac{\Delta}{R} =(\Delta/a_1)(1-\varepsilon\sin\alpha t+\varepsilon^2\sin^2\alpha t+\ldots).$$

Next we expand our solutions y and z asymptotically in ε

$$(4.4)\quad y =y_0+\varepsilon y_1+\ldots$$

$$(4.5)\quad z =z_0+\varepsilon z_1+\ldots \quad .$$

Substitution into equations (4.1) and (4.2) yields

$$(\ddot{y}_0+\varepsilon\ddot{y}_1+\ldots)=b(z_0+\varepsilon z_1+\ldots)-c(\dot{y}_0+\varepsilon\dot{y}_1+\ldots)$$
$$-k(1-\Delta/a_1+\varepsilon(\Delta/a_1)\sin\alpha t-\ldots)*$$
$$*(y_0+\varepsilon y +\ldots-\mu z_0-\varepsilon\mu z_1-\ldots)+A\cos\omega t$$

$$(\ddot{z}_0 +\varepsilon\ddot{z}_1+\ldots)=-b(y_0+\varepsilon y_1 t\ldots)-c(\dot{z}_0+\varepsilon\dot{z}_1+\ldots)$$
$$-k(1-\Delta/a_1+\varepsilon(\Delta/a_1)\sin\alpha t-\ldots)*$$
$$* (\mu y_0+\varepsilon\mu y_1+\ldots+z_0+\varepsilon z_1+\ldots)-A\sin\omega t.$$

Consequently, our zero-order problem is

$$(4.6)\quad \ddot{y}_0 =bz_0-c\dot{y}_0-k(1-\Delta/a_1)(y_0-\mu z_0)+A\cos\omega t$$

$$(4.7)\quad \ddot{z}_0 =-by_0-c\dot{z}_0-k(1-\Delta/a_1)(\mu y_0+z_0)-A\sin\omega t$$

and our first-order problem is

$$(4.8)\quad \ddot{y}_1 =bz_1-c\dot{y}_1-k(1-\Delta/a_1)(y_1-\mu z_1)-k(\Delta/a_1)\sin\alpha t(y_0-\mu z_0)$$

$$(4.9)\quad \ddot{z}_1 =-by_1-c\dot{z}_1-k(1-\Delta/a_1)(\mu y_1+z_1)-k(\Delta/a_1)\sin\alpha t(\mu y_0+z_0).$$

In operator notation, we have

$$L[Y_0] = F_0(t)$$

$$L[Y_1] = F_1(t, Y_0)$$

and in general

$$L[Y_n] = F_n\ (t, Y_0, Y_1, \ldots, Y_{n-1}).$$

We content ourselves with solving the zero-and first-order problems. The prescribed initial conditions are used with the zero-order problem. The initial conditions for all higher-order problems are all zero.

The solutions of the zero-order problem can be found easily by transforming the dependent variables by

$$y(t) = \exp(-ct/2)\ u(t)$$

$$z(t) = \exp(-ct/2)\ v(t)$$

to remove the damping and by

$$x(t) = u(t) + iv(t)$$

$$w(t) = u(t) - iv(t).$$

The resulting equations are

$$\ddot{x}+\lambda^2 x = A\exp(\nu t) \qquad (4.10)$$

$$\ddot{w}+\bar{\lambda}^2 w = A\exp(\bar{\nu} t) \qquad (4.11)$$

where the bar indicates complex conjuntion, $\lambda^2 =$

$(k(1-\Delta/a_1)-c^2/4) + i(b+\mu k(1-\Delta/a_1))$, and $\nu = c/2 - i\omega$. Since

equation (4.11) is the complex conjugate of equation (4.10), we examine (4.10) only and find

$$x = A_1 \sin\lambda t + A_2 \cos\lambda t + A_3 \exp(\nu t)$$

and ultimately

$$y_0(t) = \exp(ct/2)\,\mathrm{Re}\ x(t)$$

$$z_0(t) = \exp(ct/2)\,\mathrm{Im}\ x(t).$$

For the numbers used for Figures 1 and 2, we have

$$y_o = C_1(t)\sin 280\pi t + C_2(t)\cos 280\pi t + C_5\cos 1000\pi t + C_6\sin 1000\pi t$$

$$z_o = C_3(t)\sin 280\pi t + C_4(t)\cos 280\pi t - C_5\sin 1000\pi t + C_6\cos 1000\pi t$$

where $C_1(t) = b_1(\exp(\beta_1 t)+\exp(\beta_2 t))/2 + b_2(\exp(\beta_1 t)-\exp(\beta_2 t))/2$

$C_2(t) = -b_3(\exp(\beta_1 t)-\exp(\beta_2 t))/2 + b_4(\exp(\beta_1 t)+\exp(\beta_2 t))/2$

$C_3(t) = b_3(\exp(\beta_1 t)+\exp(\beta_2 t))/2 - b_4(\exp(\beta_1 t)-\exp(\beta_2 +))/2$

$C_4(t) = b_2(\exp(\beta_1 t)-\exp(\beta_2 t))/2 + b_1(\exp(\beta_1 t)+\exp(\beta_2 t))/2$

$C_5 = -.31249595\ E\text{-}4$

$C_6 = .19260378\ E\text{-}5$

$b_1 = -.46227656\ E\text{-}4$

$b_2 = -.19260378\ E\text{-}5$

$b_3 = -.46091025\ E\text{-}3$

$b_4 = .13124959\ E\text{-}3$

$\beta_1 = -120. + 109.71576$

$\beta_2 = -120. - 109.71576$

$\lambda = 280\pi + i(109.71576)$

We refer to the real part of λ as the natural frequency of the linearized problem (or of the zero-order problem). Notice that in general it is not the same natural frequency that one obtains from the linear problem with no deadband ($\Delta=0$), but rather is smaller since the effective stiffness is $k(1-\Delta/a_1)$ instead of k.

To solve the first-order problem, equations (4.8) and (4.9), we substitute for y_o and z_o and expand the new forcing functions using the usual trigonometric identities. We examine the details of equation (4.8) here:

$$\ddot{y}_1+c\dot{y}_1+k(1-\Delta/a_1)y_1-(b+k\mu(1-\Delta/a_1))z_1=f_1(t)$$

where

$$f_1(t) = -k(\Delta/a_1)y_o\sin\alpha t+k\mu(\Delta/a_1)z_o\sin\alpha t.$$

Then

$$f_1(t)=U_1\exp(\beta_1 t)\cos440\Pi t+U_2\exp(\beta_1 t)\sin440\Pi t$$
$$+U_3\exp(\beta_2 t)\cos440\Pi t+U_4\exp(\beta_2 t)\sin440\Pi t$$
$$+U_5\exp(\beta_1 t)\cos1000\Pi t+U_6\exp(\beta_1 t)\sin1000\Pi t$$
$$+U_7\exp(\beta_2 t)\cos1000\Pi t+U_8\exp(\beta_2 t)\sin1000\Pi t$$
$$+U_9\cos280\Pi t+U_{10}\sin280\Pi t$$
$$+U_{11}\cos1720\Pi t+U_{12}\sin1720\Pi t$$

with

$$L=k\Delta(1-\mu)/a_1$$

$$U_1=-L(b_1+b_2)/4=-U_5$$

$$U_2=L(b_3-b_4)/4=U_6$$

$$U_3=L(-b_1+b_2)/4=-U_7$$

$$U_4=-L(b_3+b_4)/4=U_8$$

$$U_9=-k(\Delta/a_1)(C_6+\mu C_5)/2=-U_{11}$$

$$U_{10}=k(\Delta/a_1)(C_5-\mu C_6)/2=-U_{12}$$

A similar analysis of equation (4.9) leads to same forcing function where the coefficients listed above have the following replacements:

For the y solution	For the z solution
$1-\mu$	$1+\mu$
b_1	b_3
b_2	$-b_4$
$-b_3$	b_2
b_4	b_1
$C_5-\mu C_6$	$-C_6-\mu C_5$
$C_6+\mu C_5$	$C_5-\mu C_6$

The solutions of this first-order problem are straightforward but tedious. We note here that y_1 and z_1 will be of this form:

$$V_1\exp(\beta_1 t)\cos 440\Pi t+V_2\exp(\beta_1 t)\sin 440\Pi t$$

$$+V_3\exp(\beta_2 t)\cos 440\Pi t+V_4\exp(\beta_2 t)\sin 440\Pi t$$

$$+V_5\exp(\beta_1 t)\cos 1000\Pi t+V_6\exp(\beta_1 t)\sin 1000\Pi t$$

$$+V_7\exp(\beta_2 t)\cos 1000\Pi t+V_8\exp(\beta_2 t)\sin 1000\Pi t$$

$$+V_9\cos 280\Pi t+V_{10}\sin 280\Pi t$$

$$+V_{11}\cos 1720\Pi t+V_{12}\sin 1720\Pi t$$

$$+V_{13}\exp(\beta_1 t)\cos 280\Pi t+V_{14}\exp(\beta_1 t)\sin 280\Pi t$$

$$+V_{15}\exp(\beta_2 t)\cos 280\Pi t+V_{16}\exp(\beta_2 t)\sin 280\Pi t$$

where the last four terms result from the homogeneous problem and are determined by the initial conditions (all are zero). The first twelve terms are due to the forcing functions of the first-order problem and can be calculated using undetermined coefficients.

Our purpose here is to demonstrate that the anticipated frequencies (viz. 440Π, 1000Π, 280Π, and 1720Π) are those revealed through examination of the power spectrum density (PSD) applied to the Runge-Kutta solutions.

The PSD of y is shown in Figure 3 and verifies our analysis for frequencies 140, 720, and 500 Hertz. The response at 860 Hertz is much smaller than these other three and is shown in Figure 8.

Figures 4, 5, and 6 show the PSD of R, and all peaks occur at multiples of our fundamental frequency of R, 360 Hertz. This result in precisely what our asymptotic analysis uses since the second-order problem would present combinations of sin 2α and the y_0 and z_0 solutions; i.e., for order ε^2 we anticipate frequency responses at 580 and 1220 Hertz, in addition to the four other frequencies. Figures 7, 8, and 9 attest to this. Finally, these last three figures also show (very small magnitude) responses for 940, 1300, and 1580 Hertz. These are third-order responses.

There are several unresolved questions connected with these expansions. The first query is how to determine analytically the constants a_1, a_2, and α related to R. Secondly, how can one find analytic expressions for the transition points from stable to unstable regions for the solutions as functions of the parameter k? Next, how is this stability affected by changes in magnitude of the deadband Δ or of the eccentricity, a part of the driving coefficient A? Finally, we should examine how bifurcation theory may be applied to our problem in order to account for the two "new" eigenvalues at 140 and 220 Hertz replacing the "old" eigenvalue at 185 Hertz which is found in the linear problem with zero deadband.

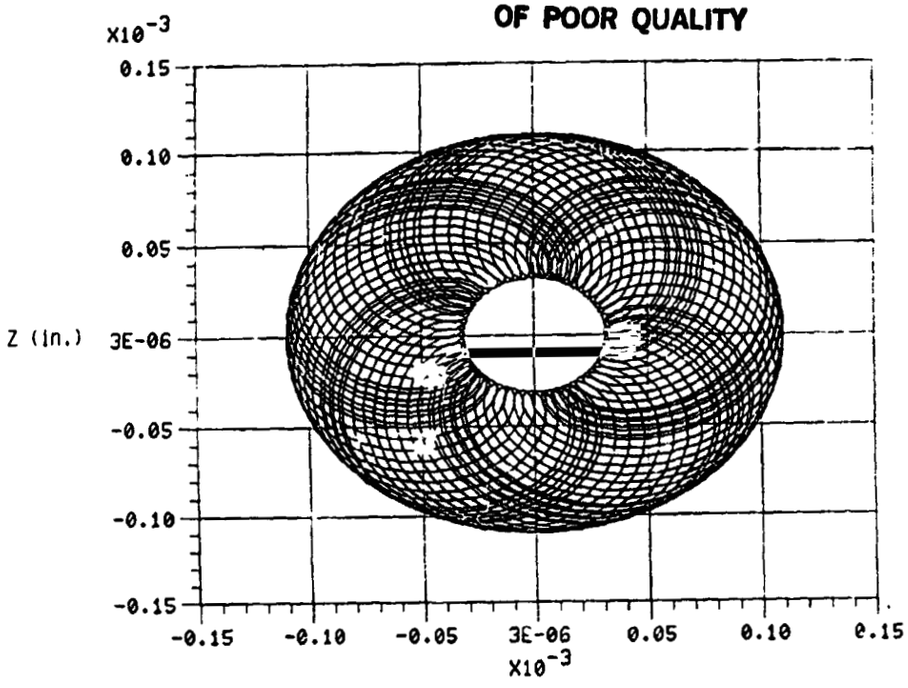

FIGURE 1

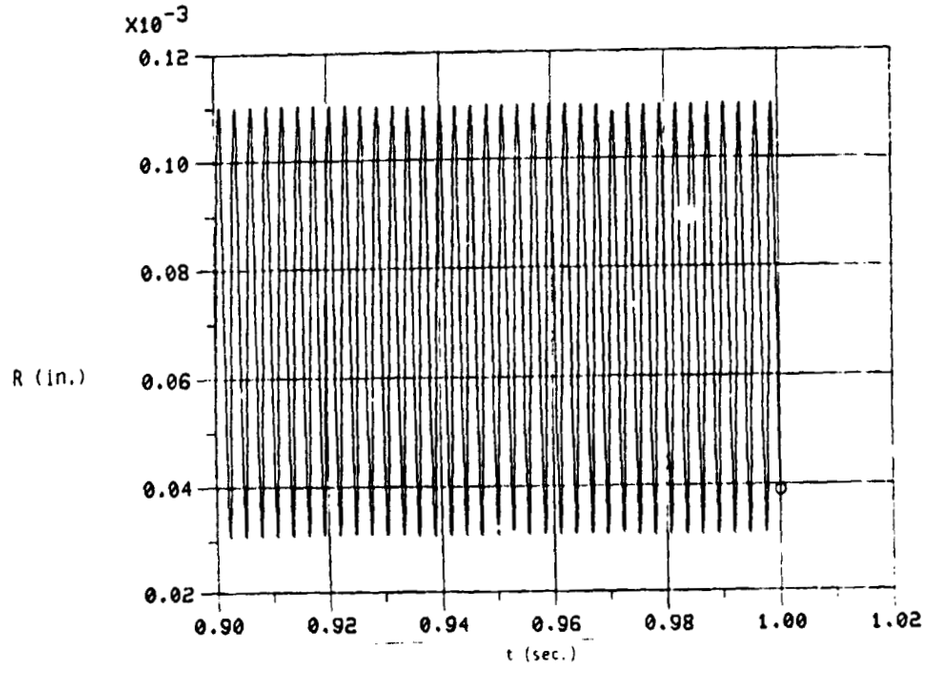

FIGURE 2

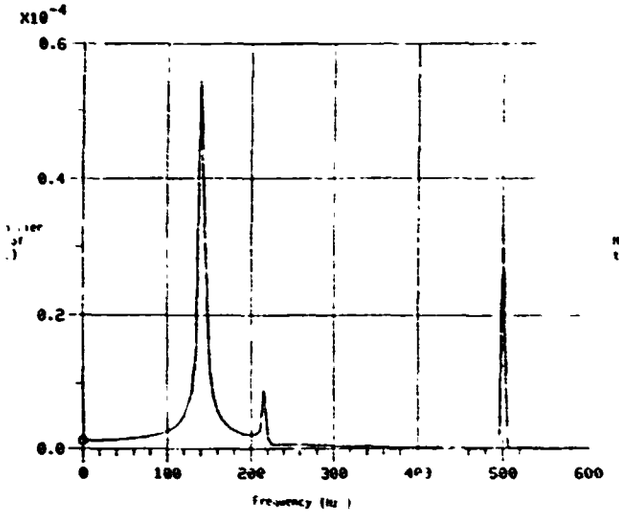

FIGURE 3

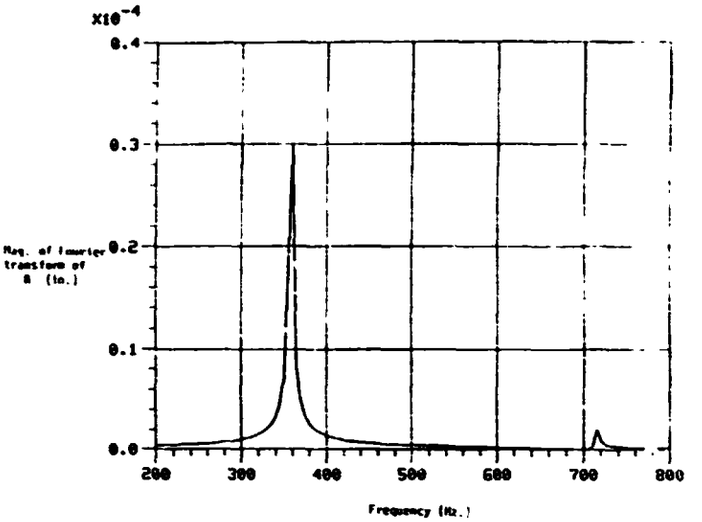

FIGURE 4

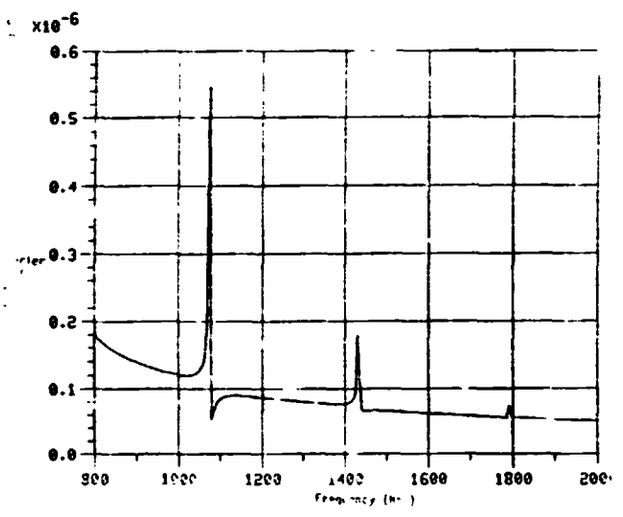

FIGURE 5

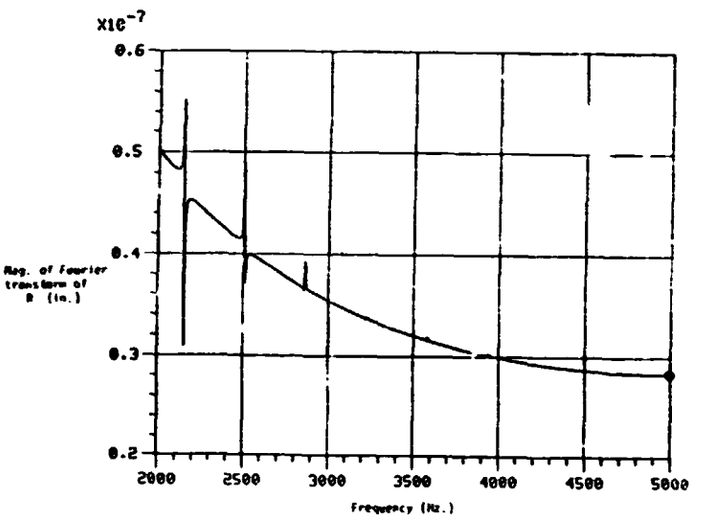

FIGURE 6

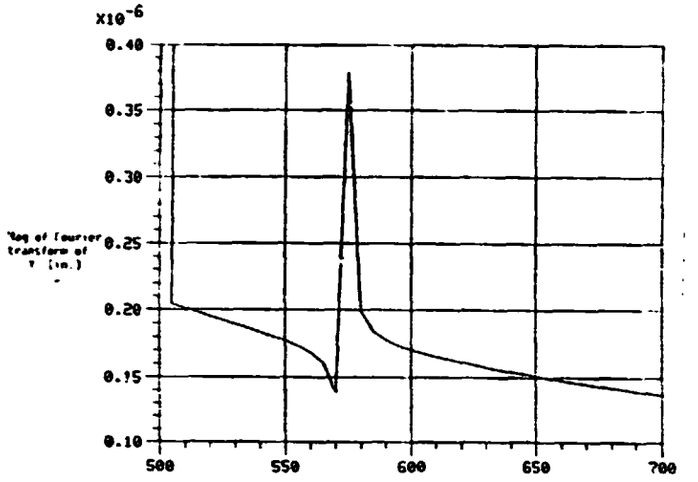

FIGURE 7

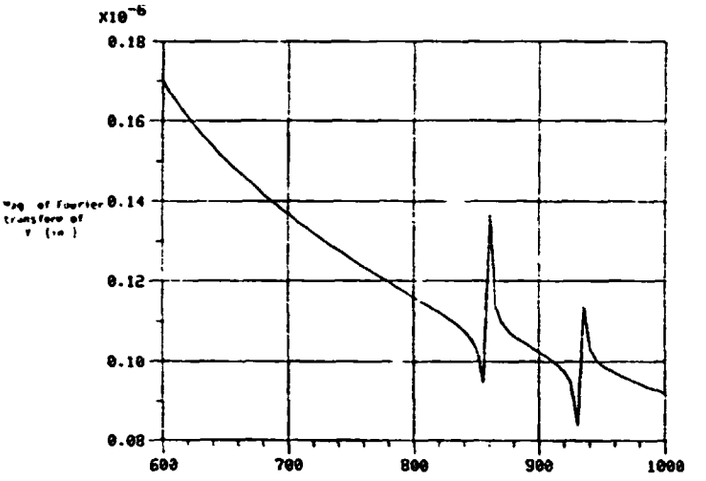

FIGURE 8

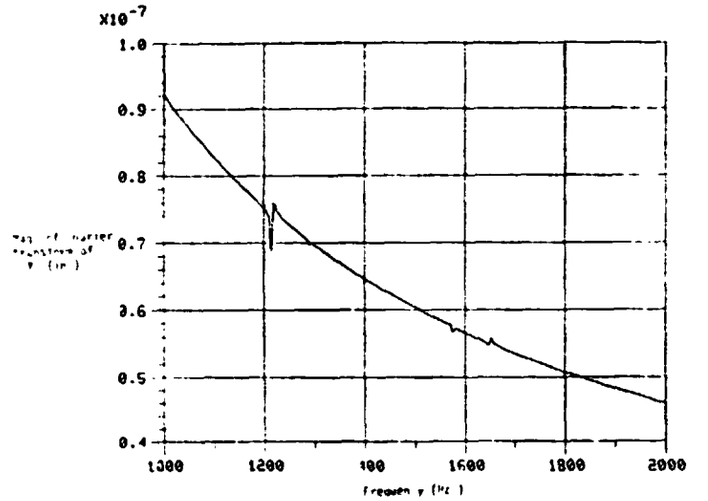

FIGURE 9

5. References:

1. Childs, D. W., "The Space Shuttle Main Engine High-Pressure Fuel Turbopump Rotordynamic Instability Problem", Trans. ASME, Journal of Engineering for Power, Jan. 1978, pp. 48-57.

2. Gupta, P.K., Winn, L. W , and Wilcock, D. F., "Vibrational Characteristics of Ball Bearings", Journal of Lubrication Technology, ASME Trans., Vol. 99F, No. 2, 1977, pp. 284-289.

3. Jeffcott, H. H., "The Lateral Vibration of Loadee Shafts in the Neighborhood of a Whirling Speed-The Effect of Want of Balance", Philosophical Magazine, Series 6, Vol. 37, 1919, p. 304.

4. Soong, T. T., and Bogdanoff, J. L., "On the natural frequencies of a disordered linear chain of N degrees of freedom", Int. J. Mech. Sci. 5, 1963, pp. 237-265.

5. Soong, T. T., and Bogdanoff, J. L., "On the impulsive admittance and frequency response of a disordered linear chain of N degrees of freedom", Int. J. Mech. Sci. 6, 1964, pp. 225-237.

6. Soong, T. T., and Chuang, S. N., "Solutions of a class of random differential equations", SIAM J. Appl. Math. 24, 1973, pp. 449-459.

7. Yamamoto, T., "On the critical speeds of a shaft", Memories of the Faculty of Engineering, Nagoya (Japan) University, Vol. 6, No. 2, 1954.

1983

NASA/ASEE SUMMER FACULTY FELLOWSHIP PROGRAM

MARSHALL SPACE FLIGHT CENTER
THE UNIVERSITY OF ALABAMA IN HUNTSVILLE

INTERFACING A TWO-STAGE IMAGE INTENSIFIER TUBE TO AN ECHELLE SPECTROGRAPH

Prepared by: Terry R. Flesch, Ph.D.
Associate Professor
Physics Dept.
North Georgia College

NASA/MSFC: Infrared Astronomy Branch
Space Science Lab

NASA Counterpart: Walter F. Fountain

Date: August 12, 1983

Contract No. NGT 01-008-021
The University of Alabama
in Huntsville

INTERFACING A TWO-STAGE IMAGE INTENSIFIER TUBE TO AN ECHELLE SPECTROGRAPH

By

Dr. Terry R. Flesch
Associate Professor of Physics
North Georgia College
Dahlonega, Georgia

ABSTRACT

An Echelle spectrograph has been in use at the Marshall Space Flight Center for a number of years. Research has been carried out in the study of the internal motions of ionized gas clouds in the interstellar medium. In order to extend the ability of the spectrograph to allow investigations of the faint outer regions of the gas clouds and to make possible the initiation of new research programs dealing with the study of sunspots and the zodiacal light, a two-stage image intensifier tube was incorporated into the instrument. The objective of this work was to interface the image tube with the spectrograph.

ACKNOWLEDGEMENTS

It is a pleasure to acknowledge the assistance which I received from the scientists and technicians in my work on this project. All were willing to give of their time and talents to help me struggle to complete my task and I owe them a debt of gratitude.

In particular, I want to thank Mr. Walt Fountain. Our many discussions and his many suggestions made my work much more interesting and fruitful. Also a special thanks goes to Mr. Ed Hazle who provided his talents and time in offering me countless suggestions.

Finally, I would like to thank the National Aeronautics and Space Administration and the University of Alabama in Huntsville for making such a worthwhile program available to faculty members across the country.

INTRODUCTION

An Echelle spectrograph has been used in active research at the Marshall Space Flight Center since 1973. Research programs have concentrated on the study of the internal motions of interstellar ionized gas clouds. A better understanding of the dynamics of these regions has resulted from the investigations of the doppler shifts in the hydrogen alpha emission of the Balmer spectral series.

The basic optical system of the Echelle spectrograph is shown in Figure 1. The instrument is designed to utilize high spectral order numbers to increase angular dispersion in the spectrum. This is accomplished by blazing the Echelle diffraction grating at an angle of approximately 63 degrees. However, when high spectral orders are used, overlapping of adjacent orders becomes a serious problem. To compensate for this, a cross-disperser is oriented with its dispersion direction perpendicular to that of the Echelle grating's. This displaces the successive orders in a direction perpendicular to the wavelength dispersion, thus alleviating the problem.

In addition, the use of multiple slits allows the two dimensional spacial resolution necessary for the study of the extended sources mentioned above. Table I includes the characteristics of the spectrograph. The system has proven reliable in obtaining data on a number of HII regions, but new and extended observing programs have made an adaptation necessary.

To extend the investigations of the emission nebulae, a two-stage image intensifier tube is needed. Two important considerations make this mandatory. To observe the faint outer regions of the nebulae with a single-stage tube for a length of time sufficient to adequately expose the photographic emulsion would require an unrealistically long exposure time. In addition, the Echelle's construction results in a rotation of the field of view as an object is tracked across the sky, thus destroying the two dimensional resolution of the spectra. A two-stage image tube should provide sufficient gain to allow the exposure times to be short enough to retain the spacial resolution.

A new program designed to study the zodiacal light is being planned. Since this would entail observing an extremely faint extended source, a single-stage tube was thought to be inadequate. Thus the instrument needed to be upgraded to include a two-stage image intensifier tube.

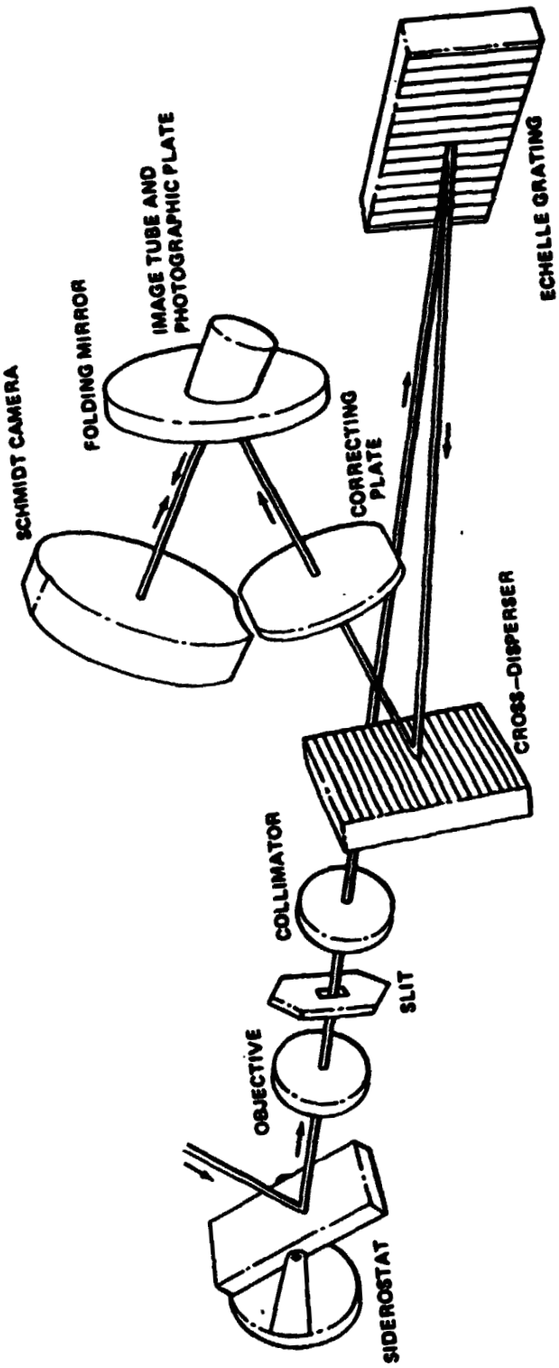

Figure 1 - Echelle spectrograph optics

Table I

Optical characteristics of the Echelle spectrograph in use at the Marshall Space Flight Center

Siderostat	- 10 inch x 15 inch flat front surface mirror
Objective	- 5 inch aperture f/4.8 achromat
Collimator	- 5 inch aperture f/4.8 achromat
Slits	- width: 0.16 mm length: 14.3 mm separation: 1.27 mm
Echelle grating	- 15 cm x 30 cm blaze angle: 63° 26' grooves/mm: 79
Cross disperser grating	- 20 cm x 25 cm grooves/mm: 300
Schmidt camera	- 12 inch aperture f/2
Image tube	- 40 mm diameter cathode surface S 20 photocathode surface single-stage
Useful spectral order range	- 26th order for near infrared to 45th order for near ultraviolet
Reciprocal dispersion	- 8.7 angstroms/mm in 26th order 5.0 angstroms/mm in 45th order
Resolution	- approximately 6 km/sec for radial velocity measurements
Photographic plates	- Kodak IIa-D emulsion baked at 58°C for 16 hours

OBJECTIVES

The goal of this project was the interfacing of a two-stage image intensifier tube to the Echelle spectrograph described previously. Modifications of the single-stage interface were necessary to insure the cooling of both photocathode surfaces of the two-stage tube and to compensate for the slightly longer length of the new tube.

THE IMAGE TUBE HOUSING

The construction of the housing for the image tube presented two fundamental problems. The fact that the tube contains two photocathode surfaces means that there are two major sources of dark noise. Also, the tube's longer length meant that the optical image produced by the camera could not be focused on the front photocathode surface. This resulted from the fact that the tube housing was restricted by the optics of the camera itself from being positioned far enough into the instrument. To compensate for this, a negative lens was mounted on the front of the image tube housing to bring the focus of the instrument out to the photocathode surface. The housing design finally adopted is shown schematically in Figure 2.

Cooling the photocathode surfaces is accomplished by passing cold nitrogen gas through cavities incorporated in the potting material which secures the image tube in its housing. The gas is produced by passing an electric current through a heating strip placed into a liquid nitrogen dewer. Approximately 120 watts are required to supply a sufficient gas flow for cooling the image tube. As shown in Figure 2, the gas is injected into a toroidal cavity enveloping the central portion of the image tube. On the opposite side of the cavity, an exit hole carries the nitrogen to the front cathode surface where the gas is vented into the camera interior. A thermocouple is mounted near the front cathode to enable monitoring the temperature of the nitrogen as it leaves the image tube housing. Four vent holes in the mask allow homogeneous gas flow across the entire photocathode surface. The vented nitrogen also serves to keep the interior of the camera moisture-free, thus preventing condensation from forming on the tube's front surface. This method of cooling has produced temperatures in excess of 50°C below ambient temperature in laboratory tests.

LABORATORY TESTING

Photoelectric and photographic tests were conducted in a darkroom laboratory setting to determine the dark noise levels of the image tube and the effectiveness of the cooling technique in reducing the noise.

The photoelectric tests were carried out by placing a photomultiplier tube's photocathode close to the back plate of the image tube. The PMT's output was monitored by pulse counting electronics and strip chart recordings were made after d.c. amplification of the signal.

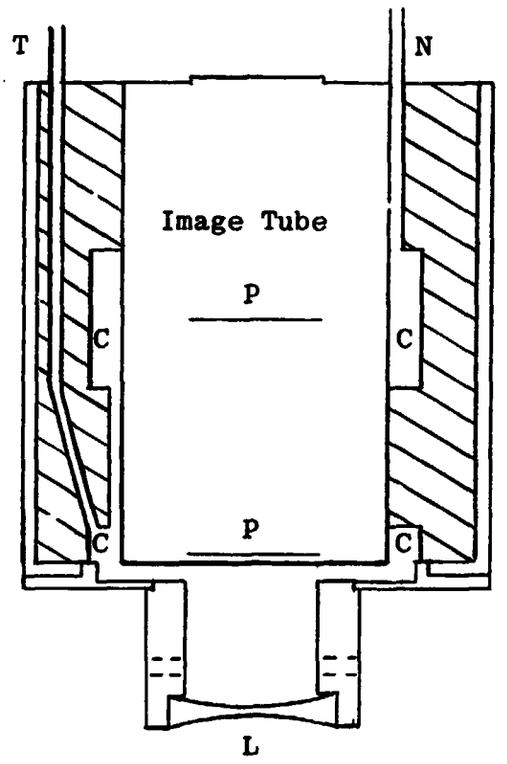

Figure 2 - Schematic of the image tube housing assembly

Notation:

P - Photocathode surface

T - Thermocouple tube

N - Nitrogen gas tube

C - cooling cavities for flow of Nitrogen gas

L - Negative lens

TEST I

The first test measured the dark noise level of the image tube as a function of the applied voltage. The test was conducted using pulse counting data. No strip chart recording was employed. The photomultiplier voltage was held at 900 volts and the test was conducted at the ambient room temperature of 20°C. Three twenty-second integrations were made at each voltage setting. The average of the three readings was used as an indication of the dark noise level. Two minutes were allowed after each voltage change before readings were taken to insure the image tube's coming to a steady level of activity. The results of the test are shown in Table 2. As expected, the dark noise did increase with increasing applied voltage. Readings were terminated at 2 6 volts in compliance with the manufacturer's suggested maximum voltage of 2.65 volts. The decrease in the number of counts above 2.4 volts is believed to be due to saturation in the pulse counting electronics and does not indicate a real decrease in dark noise.

TEST II

The ability of the cooling technique to reduce dark noise was tested by using d.c. amplification of the output from the PMT and recording the resultant signal on a strip chart recorder. The image tube was operated at 2.5 volts for all cooling tests. Temperatures ranged from the ambient room temperature of 20°C to a minimum of -35°C. An analysis of the chart recordings shows several consistent characteristics of the image tube.

I. The image tube's activity increases from zero to approximately one half of its final level of activity in the first 30 seconds after voltage is applied. Thereafter, approximately 5 minutes is required for the final steady state activity level to be reached.

II. When voltage is removed from the tube, approximately 3 minutes is required for the activity level to reach its quiet level. The reduction of activity follows a quasi-exponential decay with a time constant of 40 - 45 seconds.

III. The cooling technique dramatically reduces the dark noise level. After 30 minutes, noise levels are typically reduced by a factor of 3 to 5 with a corresponding decrease in the random noise in the signal.

The interpretation of the chart recordings was complicated by the fact that the signal showed variations of 10 to 20 % on a time scale of several minutes. This can probably be attributed to a drift in the amplifier electronics, though the cause is not certain. See Figures 3 and 4 for representative examples of these characteristics.

Photographic tests were also conducted to measure the dark noise levels by placing Kodak IIa-D plates in contact with the back plate of the image tube. Exposure times ranged from 5 seconds to 40 minutes. During these tests, it was noted that electrical arcing was occuring between the metal casing of the image tube and the surrounding material. This arcing did not noticably affect the exposures and was eliminated by grounding the metal casing. The cause of the arcing is not known.

A curious result was obtained upon analysis of the photographic plates. As expected, the level of dark noise decreased markedly as the tube cooled from ambient temperature to 0°C. Visual inspection of the plates indicated a reduction by at least a factor of two in the noise level. However, as the tube cooled further, no noticable decrease in the dark noise beyond that already observed was apparent, though the temperature was reduced to -35°C. The reason for this is not clear. However, it may be due to the increase in sensitivity of the emulsion as its temperature was decreased by being in contact with the cooling image tube. This seems possible especially in the context of the photoelectric data which shows a continued reduction in dark noise down to at least -17°C as can be seen from the chart recordings. Whether or not the decrease in dark noise below -17°C will be of any real benefit in an observing program is uncertain, since the emulsion will be cooled by the surface of the image tube in that case as it was in the laboratory tests.

CONCLUSIONS AND RECOMMENDATIONS

The mechanics of interfacing the two-stage image intensifier tube to the Echelle spectrograph has been accomplished and the cooling technique used to reduce the dark noise level of the tube has proven to be effective in laboratory tests. Obviously, the final determination of the capabilities of the instrument must be determined from observations of celestial objects. However, time did not permit this next step to be pursued. Observations of HII regions should be conducted to determine the real increase in the gain of the two-stage tube over the single-stage tube.

C-4

Figure 3

Increase in dark noise after application of voltage to image tube

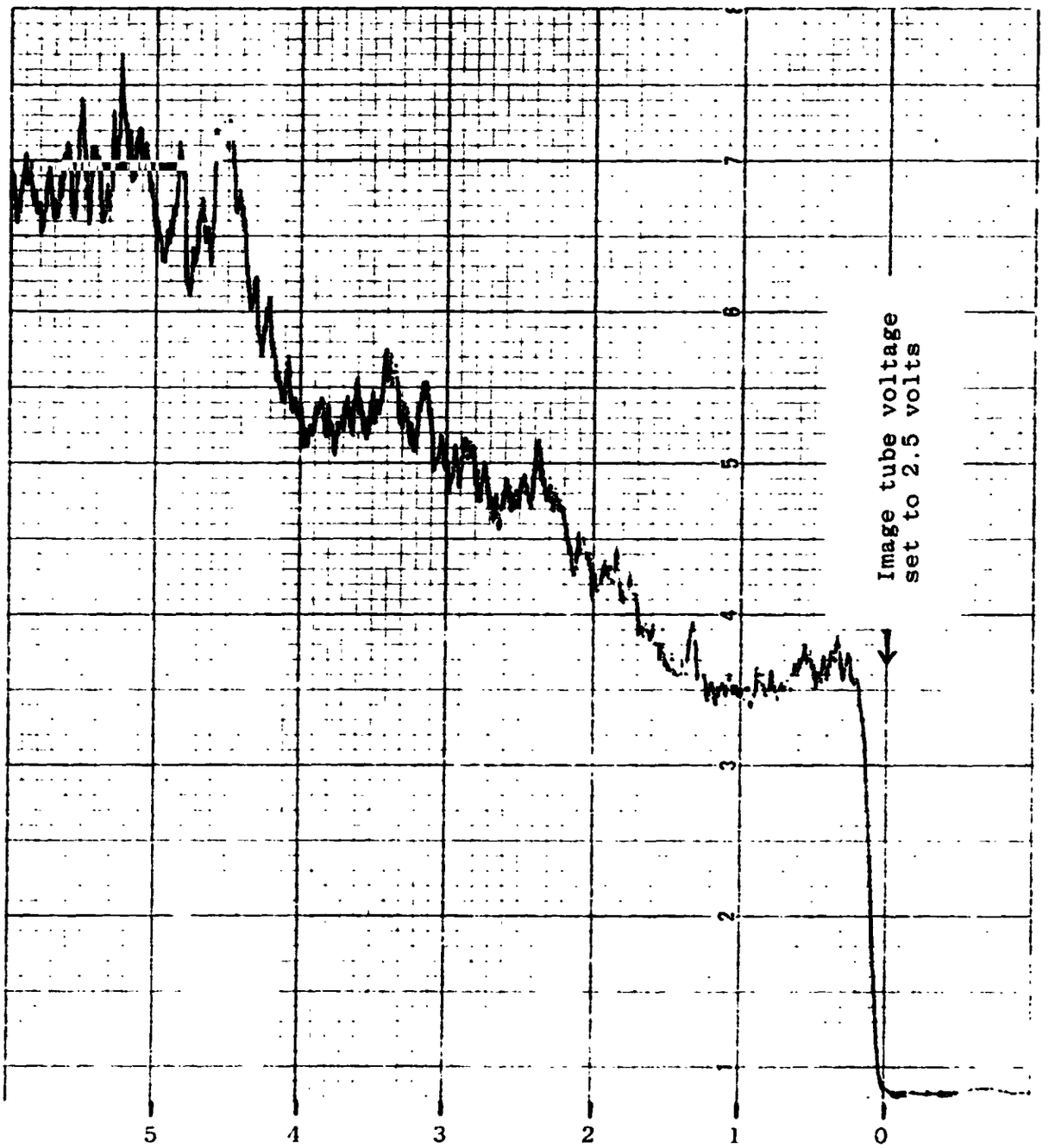

Figure 4

Decay of dark noise after removal of voltage from image tube

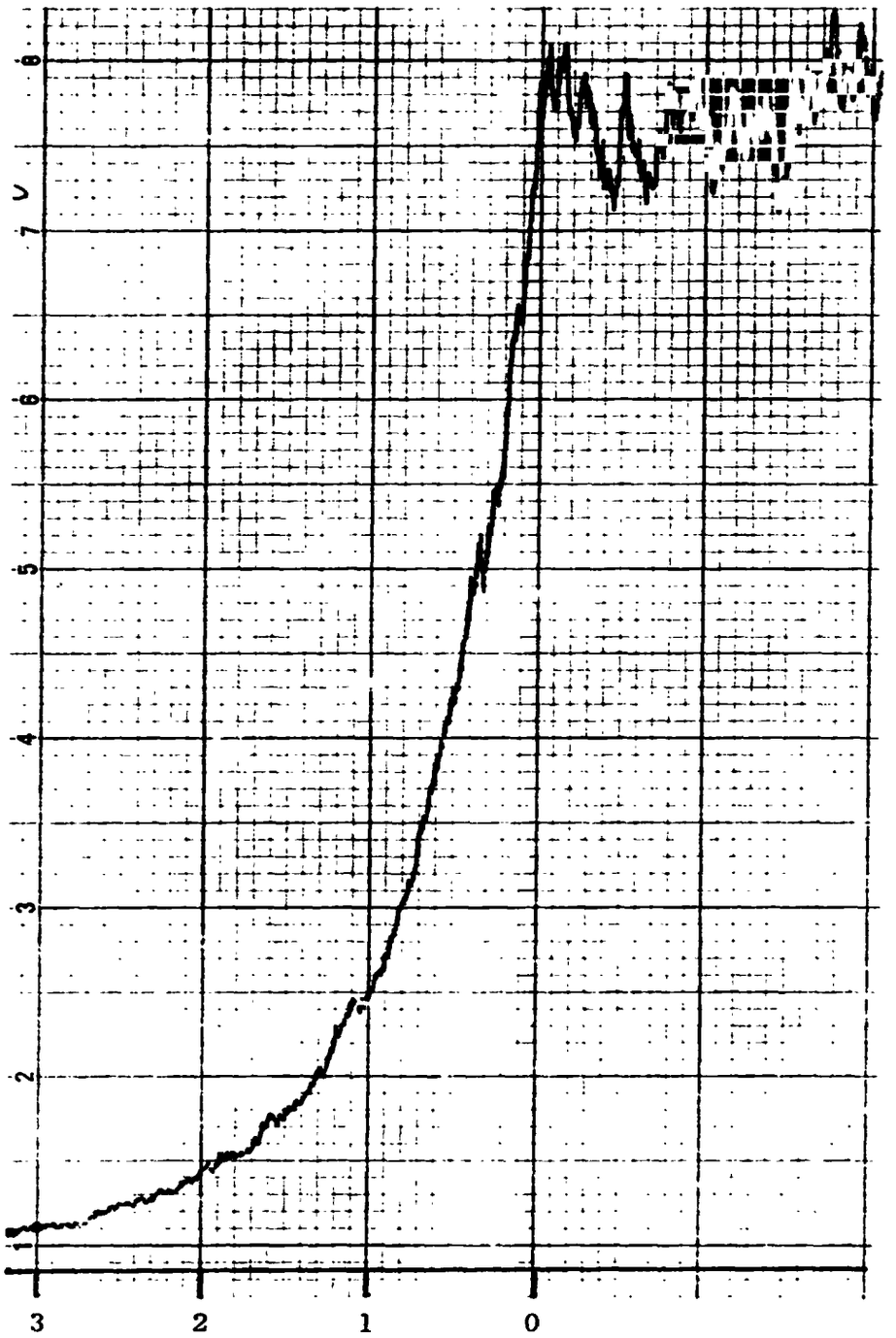

Only after these observations will it be possible to ascertain the feasibility of the zodiacal light program mentioned earlier in this report.

In addition, a recalibration of the instrument's image scale is necessary. The single-stage image tube utilized a field flattener lens whereas the two-stage tube does not. Also, the incorporation of the negative lens in the optics of the system will change the image scale at the back plate of the two-stage tube. Table III lists the modifications in the spectrographic system as a result of this project. All other characteristics are the same as those outlined in Table I.

Table II

Tabulation of dark noise counts as a function of voltage applied to the image tube.

Voltage	Counts	Voltage	Counts	Voltage	Counts
0.0	9110	0.9	9086	1.8	102185
.1	8894	1.0	10107	.9	176778
.2	8852	.1	10713	2.0	267378
.3	9522	.2	11759	.1	388956
.4	8773	.3	13746	.2	537472
.5	8474	.4	16504	.3	686783
.6	8456	.5	22308	.4	761876
.7	9111	.6	31121	.5	741593
0.8	8639	1.7	49998	2.6	638811

Table III

Modifications made to the Echelle spectrographic system as a result of the incorporation of the two-stage image intensifier tube.

Image tube	- 18 mm diameter cathode surface S 20 photocathode surface two-stage
Negative lens	- focal length: -86 mm position: approximately 1.6 cm in front of image tube
Reciprocal dispersion and Resolution	- to be determined from future tests

REFERENCES

1. Fountain, W. F. et al., "An Internal Velocity Study of the Rosette Nebula", Astrophysical Journal, 229, 971-980 1979 May 1.

2. Fountain, W. F., private communication.

3. Mufson, S. L. et al., "An Investigation of the Neutral and Ionized Gas in M16", Astrophysical Journal, 248, 992-1009, 1981 September 15.

4. Schroeder, Daniel J., "Design Considerations for Astronomical Echelle Spectrographs", Pub.A.S.P., 490, 1970.

1983

NASA/ASEE SUMMER FACULTY RESEARCH FELLOWSHIP PROGRAM

MARSHALL SPACE FLIGHT CENTER
THE UNIVERSITY OF ALABAMA IN HUNTSVILLE

ATOMIC OXYGEN EFFECTS ON MATERIALS

Prepared by:	Albert T. Fromhold, Ph.D.
Academic Rank:	Professor
University and Department:	Auburn University Department of Physics
NASA/MSFC:	
Laboratory:	Materials and Processes
Division:	Engineering Physics
Branch:	Physical Sciences
MSFC Counterpart:	Ann F. Whitaker
Date:	August 12, 1983
Contract No.:	NGT 01-008-021 The University of Alabama in Huntsville

ATOMIC OXYGEN EFFECTS ON MATERIALS

By

Albert T. Fromhold
Professor of Physics
Auburn University
Auburn University, AL 36849

ABSTRACT

One objective of this investigation has been to offer recommendations on the selection of metal samples to be exposed to ambient atomic oxygen on the STS-8 flight presently scheduled for August 30, 1983. (These samples constitute a small subgroup of a very large group of test specimens prepared by A. Whitaker and other members of the Physical Sciences Branch for this mission.) The metals selected and prepared for STS-8 are silver, lead, copper, nickel, tungsten, molybdenum, magnesium, platinum, and alloys of FeCrAl and NiCr. Literature data are reviewed concerning the oxidation properties of these materials with a view towards understanding which oxides might be formed, the state of the oxide (surface film or volatile form), and the reaction rate. In addition, various techniques for characterizing the parent metals and the surface oxides are reviewed.

ACKNOWLEDGEMENTS

The author appreciates the kind hospitality extended during his tenure at Marshall Space Flight Center. He was impressed with the extensive efforts made by the organizers of the NASA-ASEE Summer Faculty Fellowship Program to see that it provided a meaningful and broadening experience for the participant as well as being fruitful from the standpoint of the laboratory.

LIST OF TABLES

Table No.	Title	Page
I.	Base Metals and Alloy Components Considered for Test Specimens in STS-8	XIV-2
II.	Characterization of Technique by Excitation and Detection Particle	XIV-3

INTRODUCTION

The ultraviolet radiation from the sun decomposes the atmospheric molecular oxygen quite extensively above 100 km in altitude, and the resulting atomic oxygen environment is far more chemically reactive for materials on space vehicles than is the corresponding molecular oxygen atmosphere near the earth's surface. Consequently, metals which are quite inert on earth (e.g., silver) may oxidize rapidly in the upper atmosphere. This has serious implications for components used in long-term missions, such as, for example, the one contemplated for the Space Telescope.

OBJECTIVES

My task has been to offer recommendations on choice of samples and make some estimates based on literature data concerning the oxidation rates and the reaction products to be expected for ten metal samples to be exposed to ambient atomic oxygen on the STS-8 flight presently scheduled for August 30, 1983. The interest in the metals stems partly from mission-oriented applications, and partly from their potential usage in an atomic oxygen flux and total fluence monitor to be developed for on-orbit use.

The body of the report is in three parts, first a presentation of oxide characteristics[1, 2] and oxidation data for the selected metals in molecular oxygen[3] and in atomic oxygen taken from the references cited, second a review of certain surface analysis techniques[4], and third a discussion of atomic oxygen monitors.

Information relating to the metal specimens is listed in Table I. Information regarding analysis techniques is given in Table II.

TABLE I

BASE METALS AND ALLOY COMPONENTS CONSIDERED FOR TEST SPECIMENS IN STS-8

Elemental Metal (or Material)		At. Wt.	Sp. Gr.	Melting Temp.	Crystal Structure	Color
Aluminum	Al	26.98	2.702	659.7	Cubic	Silver-White
Chromium	Cr	52.01	7.20	1890	Cubic	Steel-Gray
Copper	Cu	63.54	8.92	1083	Cubic	Reddish
Iron	Fe	55.85	7.86	1535	Cubic	Silver
Lead	Pb	207.21	11.34	327.4	Cubic	Silver Blue-White
Magnesium	Mg	24.32	1.74	651	Hexagonal	Silver-White
Molybdenum	Mo	95.95	10.2	2620	Cubic	Silver-White
Nickel	Ni	58.71	8.90	1455	Cubic	Silvery
Platinum	Pt	195.09	21.45	1773.5	Cubic	Silvery
Silver	Ag	107.88	10.5	960.8	Cubic	White Metallic
Tungsten	W	183.86	19.3	3370	Cubic	Gray-Black
Carbon	C	12.01	1.8-2.1	3650 (subl.)	Amor.	Black
Boron	B	10.82	2.3-3.3	2300	Amor. or Monoclinic	Brown or Yellow

TABLE II

CHARACTERIZATION OF TECHNIQUE BY EXCITATION AND DETECTION PARTICLE

	Technique	Excitation Particle	Detection Particle
XRF	X-ray fluorescence	Photon	Photon
ESCA	Electron spectroscopy for chemical analysis	Photon	Electron
PES	Photoelectron spectroscopy	Photon	Electron
AES	Auger electron spectroscopy	Photon	Electron
EMP	Electron microprobe	Electron	Photon
SEM	Secondary electron microscopy	Electron	Electron
AES	Auger electron spectroscopy	Electron	Electron
EM	Electron microscopy	Electron	Electron
IEX	Ion-excited x-ray fluorescence and impact radiation	Ion	Photon
SCANIIR	Surface composition by analysis of neutral and ion impact radiation	Ion	Photon
SEM	Secondary electron microscopy	Ion	Electron
IMMA	Ion microprobe mass analyzer	Ion	Ion
SIMS	Secondary ion mass spectroscopy	Ion	Ion
ISS	Ion scattering spectroscopy	Ion	Ion
RUTH	Rutherford scattering	Ion	Ion

OXIDATION DATA

Molybdenum

Many oxides of molybdenum exist, from the dioxide MoO_2 to the pentoxide to the sesquioxide to the trioxide. The latter, MoO_3, has a molecular weight of 143.94 and is colored or whitish-yellow with a rhombohedral structure. Its density is 4.692 and its melting point is 795°C. The dioxide has a molecular weight of 127.94 and a density (viz., specific gravity) of 6.47; it is lead gray in color, and is tetragonal or monoclinic in crystal structure.

While molybdenum remains shiny under a two-hour exposure to air at 200°C, it tarnishes to a steel-blue color at 300°C, and up to 600°C it forms a coherent oxide. Above 600°C, the outer layer of MoO_3 becomes granular and then begins to melt and volatize with an attendant high rate of oxidation. Next to the metal, the oxide MoO_2 has been observed, with the outer layer being MoO_3. Oxides having stoichiometric composition between these two have also been reported. Parabolic oxidation is the predominant rate law during the protective stage, with transition to a linear law taking place after 20 hours at 525°C in dry air. The transition occurs almost immediately at 650°C. At lower oxygen pressures, such as 76 mm. Hg, the transition to linear oxidation has been encountered at 450°C. Oddly enough, the oxygen pressure does not seem to affect the rate in the linear region once a threshold pressure is reached. The threshold may be of the order of one atmosphere at 550 to 650°C. Below 600°C, MoO_3 is not noticeably volatile. The activation energy for volatilization is 53 Kcal/mole up to a temperature of 650°C, and it is 89.6 Kcal/mole above this temperature. The vapor pressure of MoO_3 is relatively high in the higher temperature region, and is even higher in the presence of water vapor.

In another study, the formation of MoO_3 was found to be parabolic up to 700°C, with the maximum rate occurring at 600°C. Cracking of the oxide probably occurred at 750°C because the time dependence was linear with breaks in the curves. A limiting thickness was observed at 770°C, at which point the rate of formation was balanced by the rate of volatilization.

Marker experiments were carried out to ascertain the nature of the diffusing species causing oxide growth. The indications were that the growth occurs almost entirely by the inward diffustion of oxygen towards the metal interface. This likewise is believed to be the mechanism for the oxidation of tungsten.

The thickness of the underlying MoO_2 layer was insignificant when compared with the MoO_3 layer. MoO_3 melts at 795°C. The oxidation tends to become catastrophic above about 725°C due to heating caused by oxide formation, but such catastrophic oxidation could be prevented by first producing an oxide film at a lower temperature.

The reaction of molybdenum with atomic oxygen has been studied rather extensively in the high temperature regime in the laboratory. The reaction probability is quite high, is temperature-dependent, but is relatively insensitive to oxygen pressure. The reaction product is apparently MoO_3 which volatilizes rapidly as it is formed [see "Kinetics of High-Temperature Oxidation of Molybdenum by Dissociated Oxygen" by D. E. Rosner and H. D. Allendorf, J. Chem. Phys. 40, 3441-3442 (1964)]. The most informative presentation of the data for the reaction of molybdenum with atomic oxygen is given by Figs. 4 and 5 in the article entitled "Kinetics of the Attack of High-Temperature Molybdenum and Tungsten by Atomic Oxygen" by D. E. Rosner and H. D. Allendorf [J. Electrochem. Soc. 114, 305-314 (1967)]. Figure 4 in that article shows a comparison between the oxidation probabilities for atomic and molecular oxygen as a function of reciprocal temperature. Both probabilities are of the order of 0.5 at 2800 K, and decrease with decreasing temperature. It is interesting to speculate that the reaction probability for molecular oxygen at the high-temperature end of the range may be due to thermal dissociation of the oxygen molecules to form atomic oxygen. It is difficult to estimate the heating effect of a hot filament on the ambient gas because of the collisions between gas molecules and the attendant kinetic energy exchanges. (That is, the filament temperature may be 2800 K, but the effective temperature of the ambient gas will be lower.) At 1000 K, the reaction probability for atomic oxygen is approximately 0.03, whereas the reaction probability for molecular oxygen is less than 0.0001. The great divergence in the reaction probabilities of atomic and molecular oxygen has its onset as the temperature is decreased below 1700 K, and the divergence steadily increases with decreasing temperature. Figure 5 in the above-listed article illustrates the independence of the reaction probability for atomic oxygen pressures extending from 0.001 to 0.1 torr. From that figure it can be noted that the reaction probability increases from 0.04 at 1150 K to 0.07 at 1400 K, and then to 0.15 at 1760 K.

The laboratory technique for studying the interaction of molybdenum and other metals with atomic oxygen is an interesting one. A microwave discharge is utilized to generate the atomic oxygen from molecular oxygen in a fast-flow Pyrex vacuum system containing the sample to be studied. The microwave technique is a non-thermal process. The atomic oxygen concentrations are obtained by means of an NO_2 light-titration technique, which can be understood from the following reactions:

$$O + NO_2 \longrightarrow NO + O_2 \qquad \text{(fast reaction)}$$

$$O + NO \longrightarrow NO_2 + h\nu\,(\text{yellow-green}) \qquad \text{(slow luminescent reaction)}$$

Increasing amounts of NO_2 are added to the system until the yellow-green glow becomes extinguished. This indicates that all of the atomic oxygen has been used up in the fast reaction indicated above. At that point the flow rate of NO_2 equals the original atomic oxygen flow rate. The observation can be made visually, or else a photomultiplier can be used. It is interesting to speculate that these reactions producing a yellow-green glow may also provide an explanation for observations on previous Shuttle missions of a luminous glow seen on the windward side of the orbiter during night-time passes.

Tungsten

Oxides of tungsten (wolfram) exist in several stoichiometries, starting with the dioxide WO_2 which is a brown cubic material having molecular weight of 215.85, a density of 12.11, and a melting point of 1500 to 1600°C. Next is the pentoxide W_2O_5 (or W_4O_{11}) called mineral blue which has a molecular weight of 447.70 (or 911.39). This is a blue-violet triclinic material which sublimes at 800 to 900°C. The most common oxide is the trioxide WO_3 called Nat. wolframite. It is a yellow orthorhombic crystal, or a yellow-orange powder, having a molecular weight of 231.85, a density of 7.16, and a melting point of 1473°C.

Tungsten remains shiny during exposure to air for 2 hours at 300°C. At higher temperatures, temper colors appear and a blue-black adherent oxide forms up to 600°C. At yet higher temperatures, yellow or yellow-green WO_3 forms on the surface. After oxidizing at temperatures of 700 to 1000°C, a thin adherent dark blue oxide of uncertain composition has been found underneath the surface layer of WO_3. This could be the pentoxide, but it could also be one of the other suboxides which are known to exist. A porosity of 30% has been reported for the WO_3 layer. At temperatures of the order of 1000°C, WO_3 is sufficiently volatile so that a net loss in weight can be observed. This point depends somewhat on oxygen pressure, varying from about 1050°C for oxygen pressures below 5 mm. Hg and increasing to approximately 1200°C at pressures exceeding 76 mm. Hg.

The oxidation rate law is parabolic in the lower temperature range, with a transition to a linear law taking place at higher temperatures. The transition point seems to be in question, since some experimenters have observed parabolic growth at temperatures as high as 1100°C whereas others have noted linear growth at temperatures as low as 500°C. The linear growth law seems to be favored at pressures above atmospheric pressure, though little dependence of the rate constant on oxygen pressure was observed in some experiments.

Volatilization of the WO_3 was not detected at 700°C in 1 atmosphere of moist oxygen. However, it was found that volatilization of WO_3 was greatly accelerated at 1000°C by the presence of water vapor exceeding 30% by volume.

The relatively low melting point of WO_3 relative to W metal means that the protective character of the oxide film will be lost long before the tensile properties of the metal will be affected by the temperature. In common with molybdenum, the volatility of the trioxide causes tungsten to be a relatively poor high temperature material (or alloy component) for use in an oxygen environment.

A fairly extensive study of the interaction of tungsten with atomic oxygen has been carried out [cf. "Kinetics of the Attack of High-Temperature Molybdenum and Tungsten by Atomic Oxygen", D. E. Rosner and H. D. Allendorf, J. Electrochem. Soc. 114, 305-314 (1967)]. As in the case of molybdenum, the reaction probability for atomic oxygen with tungsten was found to be independent of the oxygen pressure over the range investigated, which was between 0.001 and 0.1 torr. Figure 8 of the cited paper illustrates this pressure-independence, and in addition shows the reaction probability to be 0.08 at 1560 K and approximately 0.12 at 1830 K. Figure 7 of that paper illustrates the temperature-dependence of the oxidation probability for both atomic oxygen and molecular oxygen. For molecular oxygen, the probability exceeds 0.1 at 2600 K, decreases to approximately 0.04 at 2000 K, and drops to values of the order of 0.002 at 1500 K. A semi-logarithmic plot of the oxidation probability versus (1/T) is linear over the range 2600 to 1800 K, but drops more rapidly than this over the 1800 to 1500 K range. At all temperatures, the reaction probability for atomic oxygen was significantly higher than described above for molecular oxygen. For example, at 2000 K the reaction probability for atomic oxygen would be approximately 0.2 compared to 0.03 for molecular oxygen, and the difference is much greater at lower temperatures. At 1500 K, the reaction probability for atomic oxygen is about 0.08 compared to the value of 0.002 for molecular oxygen, a difference of a factor of 40, whereas the difference at 2000 K was of the order of a factor of 7. The observations for molybdenum (described above) were similar to these over the comparable temperature range, the numbers being the same to within a factor of 2. The primary difference is that the reaction probability for molecular oxygen with molybdenum at the higher temperature (2000 K) is greater by a factor of 2 than the corresponding reaction probability of molecular oxygen with tungsten. The experimental temperature range studied was far greater for molybdenum than for tungsten, however, so that greater ratios of the reaction probability for atomic relative to molecular oxygen were recorded for molybdenum. For example, at 1100 K the probability for reaction of atomic oxygen with molybdenum is approximately 0.04, whereas the probability for reaction of molecular oxygen with molybdenum is down to 0.0002, the difference being a factor of 200.

Tungsten and molybdenum represent two of the most promising metals for use in the design of an atomic oxygen monitor. Both have a suitable data base for the atomic oxygen reaction probability, and both have relatively high values for the reaction probability. Furthermore, both metals have good mechanical properties, and are readily available in wire and filament form.

Carbon

Carbon differs from the most of the elements and alloys described in this report insofar as it is non-metallic. However, its interaction with atomic oxygen has been studied, and it shows promise as a material for use as an atomic oxygen monitor. Graphite comes in two forms, namely, pyrolytic and isotropic. The isotropic form has a higher reaction probability with both atomic and molecular oxygen. Data for the temperature-dependence of the two forms in both atomic and molecular oxygen are given in Figure 5 of a paper entitled "Kinetic Studies of the Attack of Refractory Materials by Oxygen Atoms and Chlorine Atoms" by D. E. Rosner and H. D. Allendorf [High Temperature Technology, Proceedings of the 3rd International Symposium, Asilomar, CA, 1967 (Butterworths, London, 1969)]. One quite interesting feature illustrated by these data is the very high reaction probability in atomic oxygen between 1000 and 2000 K, the probability being between 0.1 and 1.0 for both graphite forms. The lower values of the reaction probability, namely those around 0.1, are characteristic of the pyrolytic graphite at the lower temperatures. In molecular oxygen, however, the reaction probability for pyrolytic graphite is down to 0.0001 at about 1300 K, with the highest values measured for this form being only of the order of 0.01 at 1800 K. In molecular oxygen, the isotropic form shows a pronounced peak at a temperature somewhere in the range of 1500 to 1600 K, but even at the peak the value is only of the order of 0.1. [Also see Figure 2 in "High Temperature Oxidation of Carbon by Atomic Oxygen" by D. E. Rosner and H. D. Allendorf, Carbon 3, 153-156 (1965).]

A study has been made to ascertain the difference in the reaction products formed by graphite interacting with atomic and molecular oxygen. [See "Primary Products in the Attack of Graphite by Atomic Oxygen and Diatomic Oxygen above 1100 K" by H. D. Allendorf and D. E. Rosner, Carbon 7, 515-518 (1969)]. Appreciable amounts of CO and CO_2 were found in both cases, with the CO/CO_2 ratio varying between 1.0 and 10 over the temperature range 1200 to 2000 K. Thus CO is the most abundant product. It was found that a noticeably greater fraction is CO_2 in the case of reaction with atomic oxygen. From the peak carbon atom removal probability it was concluded that, at most, some 60% of the incident atomic oxygen leads to reaction with carbon, with the remainder being reflected or recombining to form O_2 gas.

It appears that, insofar as carbon is concerned, the best choice for an atomic oxygen monitor would be the isotropic form held at a temperature of about 1600 K. The reaction probability would be about 0.6 and would be relatively insensitive to temperature changes of as much as 100 K on either side of this mean temperature. (By relatively insensitive, we mean variations not greater than 20% or so.)

There is another reason for choosing isotropic graphite over the pyrolytic form, namely, in the case of pyrolytic graphite, there is a tendency for the

oxidation probability to increase somewhat with atomic oxygen pressure, whereas the reaction probability for isotropic graphite is apparently independent of the atomic oxygen pressure [see "Comparative Studies of the Attack of Pyrolytic and Isotropic Graphite by Atomic and Molecular Graphite by Atomic and Molecular Oxygen at High Temperatures" by D. E. Rosner and H. D. Allendorf, AIAA Journal 6, 650-654 (1968), and also Figure 4 in the article already cited by these authors: Carbon 3, 153-156 (1965]. Figure 3 in the latter article illustrates reaction probabilities which are independent of the atomic oxygen pressure and which have values of approximately 0.6 at 1180 K and 0.7 at 1450 K.

Lead

Lead forms a number of oxides, the dioxide Pb_2O, the monoxide PbO, red oxide Pb_3O_4, the sesquioxide Pb_2O_3, and the suboxide Pb_2O. The monoxide exists in two forms, litharge and massicot. The molecular weight is 223.19. Litharge is a yellow tetragonal material with density of 9.53 and a melting point of 888°C. Massicot has a density of 8.0 and is a yellow orthorhombic material. The dioxide PbO_2 has molecular weight of 239.19, a density of 9.375, and it decomposes at 290°C. Pb_3O_4 has molecular weight of 685.57, is in the form of red crystalline scales or an amorphous powder, has a density of 9.1, and decomposes at 500°C. The sesquioxide Pb_2O_3 has a molecular weight of 462.38, is an orange-yellow powder (or else amorphous), and decomposes at 370°C. The suboxide Pb_2O is a black amorphous material having molecular weight 430.38, a density of 8.342, and decomposes.

Red tetragonal PbO transforms to yellow orthorhombic PbO at 486°C. Pb_3O_4 dissociates in air at 540°C to form PbO. PbO_2 decomposes in air in equilibrium with Pb_3O_4 at approximately 400°C.

In the temperature range 250 to 320°C, lead oxidizes in accordance with the parabolic growth law, forming a reddish-brown oxide which is smooth and tightly adherent to the parent metal surface. At temperatures up to 550°C, oxidation remains essentially parabolic, though there may be a succession of rate constants. A second parabolic region seems to consist of Pb_3O_4 together with red or yellow PbO, depending upon whether the temperature is below or above the 486°C transition temperature. Above 550°C, structural changes occur and there is a transition from a parabolic to a linear rate of oxidation.

It is known from experiments on the plasma oxidation of lead [see, for example, A. T. Fromhold, Jr. and John M. Baker, "Oxide Growth in an rf-Plasma", J. Appl. Phys. 51, 6377-6392 (1980)] that the oxide forms much more rapidly than it forms in molecular oxygen at the same temperature. It is interesting to speculate whether or not this vastly-increased rate is due to the atomic oxygen produced in the discharge, or whether it may be due to sputter-imbedding of oxygen ions with the attendant increase in the concentration gradient of the

diffusing oxygen species, or else due to electric-field-enhanced transport caused by the potential differences set up across the oxide film during the gaseous discharge. Perhaps a definitive answer to the question of whether it is due to atomic oxygen will be given by the results obtained on the lead sample prepared for the STS-8 mission.

Magnesium

The normal oxide of magnesium is MgO, although the Chemical Rubber Handbook also lists a peroxide of magnesium having the composition MgO_2. MgO has molecular weight 40.31, a density of 3.58, and a melting point of 2800°C. It is a colored cubic material with a refractive index of 1.736. The peroxide is a white powdered substance.

Magnesium chemically reacts with dry molecular oxygen to form cubic MgO with a lattice constant of 4.20 Å. The fast initial oxidation leads to an oxide film thickness of 70 Å or so in thickness. The oxide remains protective at temperatures below 450°C in dry oxygen. In moist oxygen, the oxide remains protective below 380°C. The protective stage is governed by a parabolic growth law. In the non-protective temperature range of 475 to 575°C, a linear rate law is found which has an activation energy of 50.5 Kcal/mole and a pre-exponential factor of 1.7×10^6 g/sq. cm.-sec. The ignition temperature of magnesium, which varies with the oxygen pressure, is 623°C at one atmosphere.

No data have been located which characterize the interaction of magnesium with atomic oxygen other than recombination coefficients cited below.

Copper

Copper forms two major oxides, Cu_2O and CuO. In addition, a suboxide Cu_4O is listed. Cu_2O, called Nat. cuprite, has a molecular weight of 143.08, a density of 6.0, and a melting point of 1235°C. It is a red octahedral cubic crystal with a lattice constant of 2.705 Å. CuO, called Nat. tenorite, has a molecular weight of 79.54, a density of 6.3 to 6.49, and a melting point of 1326°C. It is a black monoclinic crystal with a lattice constant of 2.63 Å. The suboxide is listed as olive green in color, but is has not been completely characterized or even substantiated.

In general, oxidation at temperatures of the order of 150°C leads to a limiting thickness growth law, while oxidation at temperatures between 200 and 1000°C is essentially parabolic. For oxidation in air, the quoted activation energies are 20.14 Kcal/mole between 300 and 550°C, and 37.70 between 550 and 900°C. The corresponding pre-exponential factors are 1.5×10^{-5} and 0.266 in units of gm^2/cm^4-sec.

A cubic rate law has also been observed, usually at intermediate temperatures above 120°C and extending as high as 750°C. The effect of moisture seems to be small, seemingly in the direction of slightly reducing the oxidation rate.

An attempt to measure the effect of atomic oxygen on the oxidation rate of copper was made more than three decades ago, but the results seemed to be somewhat inconclusive [see "The Oxidation of Several Metals in Activated Oxygen at High Temperatures" by A. Dravnieks, J. Am. Chem. Soc. 72, 3761-3767 (1950)]. Dravnieks noted many interesting features, as for example, that cuprous oxide was pure reddish until traces of cupric oxide appeared, at which time the surface of the oxide scale became grey. He also noted that even though both the cupric and cuprous oxides were thermodynamically possible under the experimental conditions, the color of the oxide scale and the x-ray patterns indicated clearly that at the beginning of the oxidation only cuprous oxide was formed, with the cupric oxide appearing in the more advanced stages of oxidation. The conclusions relating to the effect of atomic oxygen were complicated by the same factors which give rise to the peculiar pressure dependence of the oxidation rate of copper in molecular oxygen. It was concluded that atomic oxygen could accelerate or it could retard the oxidation, and furthermore it could change the composition of the oxide film.

The experiment by Dravnieks described above utilized a platinum resistance thermometer as a device to measure the concentration of oxygen atoms. The experimental details are described in the paper, but in brief the principle is based on a resistance measurement of the platinum filament, the resistance being a function of heating due to the current passed through the filament and heating due to atom recombination in forming oxygen molecules. An auxiliary method employing a platinum and platinum-rhodium junction was likewise used. In these methods, certain assumptions were made which may not be quantitatively valid, such as the assumption that the accommodation coefficient is unity for oxygen atoms, and the assumption that atoms will recombine principally on a platinized surface so the non-platinized junction can serve as a reference. Platinum resistance thermometers have also been used to study the temperature variation of the recombination probability [see "Variation with Temperature of the Recombination of Oxygen Atoms on a Platinum Surface", by G. C. Fryburg and H. M. Petrus, J. Chem. Phys. 32, 622-623 (1960)].

It should also be pointed out that atomic oxygen also recombines on copper and copper oxide surfaces. The room temperature recombination coefficient on copper is given as 0.17 and that on copper oxide (stoichiometry unstated) is stated to be 0.02 [see "The Recombination of Oxygen Atoms at Surfaces" by J. C. Greaves and J. W. Linnett, Trans. Faraday Soc. 54, 1323-1330 (1958)]. Other measured values for copper oxide at 300 K are higher, namely 0.11 for Cu_2O and 0.045 for CuO [see "Recombination of Oxygen Atoms on Oxide Surfaces" by P. G. Dickens and M. B. Sutcliffe, Trans. Faraday Soc. 60,

1272-1285 (1964)]. Recombination coefficients are also given in the first paper for magnesium (0.0026), silver (0.24), nickel (0.028), magnesium oxide (0.0035), nickel oxiae (0.0077), and lead oxide (0.0058), and in the second paper for MgO (0.011)and NiO (0.0015).

Boron

While boron was not selected as a sample for the STS-8 mission, nevertheless its interaction with atomic oxygen has been studied (see the symposium paper by Rosner and Allendorf cited in the subsection on Carbon). The most interesting feature of the data illustrated in Figure 6 in the paper is that the reaction probability exceeds 0.9 at a temperature of about 1900 K. This high probability is for the reaction of boron with atomic oxygen, the reaction probability in molecular oxygen being a factor of 3 or so lower. The very high reaction probability would seem to make this material a very good candidate for use in an atomic oxygen monitor. On the negative side, however, is the strong temperature-dependence observed for the reaction probability. At 1600 K, the probability has dropped to approximately 0.1. Thus, some way to maintain filament temperature control would be required if one were to have an accurate monitor. This might present a problem, since thermocouples utilized as sensors would be influenced by the heat of atomic oxygen recombination. (The measurement of the rate of heat generation due to recombination of atomic species such as hydrogen or oxygen is a well-known method for determining the atomic concentrations in mixtures of atoms and molecules of the same species [see, for example, J. W. Fox, A. C. H. Smith, and E. J. Smith, Proc. Phys. Soc. (London) 73, 533 (1959). The use by Dravnieks of a platinum resistance thermometer and platinum and platinum-rhodium junctions for this purpose is mentioned in the subsection on Copper.]

Platinum

Although platinum in bulk is not easily converted to an oxide in molecular oxygen, a very strongly adherent adsorbed layer of oxygen does form on the surface during exposure to air. This layer is very difficult to remove. The major reaction between Pt and oxygen at high temperatures consists in the formation of gaseous oxide. This is indicated by the fact that above 1100°C, the metal evaporates in oxygen with a rate which increases with increasing temperature, whereas the metal does not evaporate in this manner in argon or nitrogen atmospheres. The oxide formed in gaseous oxygen appears to be PtO_2.

A number of oxides of platinum are listed in the Chemical Rubber Handbook. Among them is the monoxide PtO, the dioxide PtO_2, and the trioxide PtO_3. PtO is a violet-black substance with a melting point of 550°C, a density of 14.9, and a molecular weight of 211.09. The dioxide is black, has a melting point of 450°C, a density of 10.2, and a molecular weight of 227.03.

The trioxide is reddish-brown and has a molecular weight of 243.09.

The oxidation of platinum by atomic oxygen has been studied extensively by G. C. Fryburg [see "Enhanced Oxidation of Platinum in Activated Oxygen", J. Chem. Phys. 24, 175-180 (1956); also "II. Identity of Active Species and Oxide Formed", ibid. 42, 4051-4052 (1965) and "III. Kinetics and Mechanism", J. Phys. Chem. 69, 3660-3662 (1965)]. A microwave power supply was used to activate the oxygen, and the concentration of oxygen atoms thereby produced was determined by the NO_2 titration and NO-O afterglow technique. The temperature was maintained by current through the platinum specimen from a highly-stabilized d.c. power supply, with a fast-response digital voltmeter used to monitor the resistance of the specimen. The thinning of the specimen was small during oxidation, being typically less than one part in 500 at 1000°C for the longest oxidation runs. Some of the most important results are illustrated in Figure 1 in paper III listed above, where curves for the oxidation rate versus partial pressure of atomic oxygen are given for temperatures of 900, 1050, 1100, and 1150°C. The atomic oxygen pressure range extends from zero to 0.04 torr. The curves are linear with respect to the atomic oxygen partial pressure. The reaction was observed to occur with essentially zero activation energy, as deduced from the temperature-independence of the slopes of the curves. The oxide formed by the reaction was PtO_2, although it was noted to be brown in color. The oxide was volatile and was produced at a rate which was independent of time. That is, a linear rate law was obtained for the oxidation of platinum. The intercepts of the curves served to give the rates of formation of PtO_2 in molecular oxygen at the several temperatures.

The dissociation temperature of both PtO and PtO_2 is 750°C under standard pressure conditions, and would be even lower at reduced pressures. Thus the PtO_2 produced in the experiments outlined above must have volatilized from the surface of the filament in a time shorter than the lifetime of the compound, and then was deposited on the cooler wall of the enclosing glass tube. A sensitive chemical analysis technique was used to determine the stoichiometry of the oxide produced, and it was found that PtO_2 was the favored oxide. The compound PtO_2 was also confirmed by means of electron diffraction studies of the condensed oxide film. The rate of oxidation was too slow to be followed by loss of weight of the platinum or by the increase in the resistance of the platinum due to changes in its physical dimensions produced by oxidation. Thus a more sensitive method, based on collection of the deposited oxide, dissolving it, and analyzing it colorimetrically for the amount of platinum, was employed. The formation of PtO_2, as opposed to PtO, agrees with the rule-of-thumb that metals are usually oxidized to their highest valence state in activated oxygen.

Whereas the reaction probabilities for atomic oxygen forming volatile molybdenum oxide and volatile tungsten oxide were of the order of 0.1, depending upon the temperature, the reaction probability was found to be much lower

for platinum. At 1000°C, each incident oxygen atom was found to have a reaction probability of only 1.3×10^{-5}. (This was deduced from the experimental result that the number of platinum atoms leaving the filament per oxygen atom striking the surface was 6.7×10^{-6}.) The corresponding probability for reaction of oxygen molecules with platinum was 3.3×10^{-8}. Thus, the oxygen atoms were approximately 400 times more effective than oxygen molecules in causing oxidation of the platinum. These values were the ones cited in first publication. In paper III, the given values were somewhat different, partly due, however, to interpretation. Assuming that one incident oxygen atom is capable of producing a PtO_2 molecule, the reaction probability for atomic oxygen was given as 5×10^{-6}, which moreover was found to be independent of the temperature. On the other hand, the collision efficiency of the O_2 molecules was given as 1.8×10^{-8} at 900°C and 8.7×10^{-6} at 1500°C. Thus it was concluded that the oxygen atoms are roughly 300 times more reactive than the O_2 molecules at 900°C, but the two were equally reactive at 1500°C. It was also inferred from the results that the oxidation of platinum by O_2 molecules and the oxidation by O atoms occur independently of one another.

Given the relatively low reaction probabilities for platinum oxide formation above, it is of interest to compare these numbers with the corresponding recombination coefficients giving the probability that the incident oxygen atoms will chemically combine on the filament surface (heterogeneous catalysis) to form molecular oxygen. In paper III, it is stated that the recombination coefficient for oxygen atoms on hot platinum is probably 0.1 or higher. That process is first order with respect to the atomic oxygen concentration, as is the oxidation process, and likewise occurs with zero activation energy (at least for temperatures above 800°C). The recombinations coefficient was deduced to be temperature-independent above 800°C. This temperature is above the dissociation temperature of platinum oxide, and the fact that a platinum sample will remain bright and shiny in an oxygen stream above this temperature indicates that no oxide film adheres to the surface to poison the catalytic properties of the surface. However, the interesting observation was made that heating and cooling a platinum device in molecular oxygen gives a surface which is sluggish and unresponsive, whereas heating and cooling in the presence of atomic oxygen results in an active responsive surface. Another study of the recombination of atomic oxygen on platinum indicated little if any recombination [see "Atomic Oxygen - Metal Surface Studies as Applied to Mass Spectrometer Measurements of Upper Planetary Atmospheres" by G. W. Sjolander, J. Geophysical Research 81, 3767-3770 (1976)]. However, that study was apparently under room temperature conditions with carbon and hydrogen present, since copious amounts of H_2O, CO, and CO_2 were observed coming off the platinum surface. Some information was also given in that paper for the recombination of atomic oxygen on silver, the probability apparently being of the order of 0.02.

The use of platinum devices to measure the concentration of atoms present in activated gases is relatively well known. The method hinges on the ability of platinum to effect catalytic recombination of the atoms into molecules, and involves a measurement of the heat liberated. This is usually done by a measurement of the increase in the temperature of a filament or ribbon specimen due to the heat released in the recombination reaction. In large atomic oxygen concentrations, platinum can be heated to a bright red by this heat. It would seem that occurrence of the two independent processes of oxidation and oxygen atom recombination might complicate considerably the use of either reaction as the basis for design of an atomic oxygen monitor utilizing the resistance of a platinum filament as the measurable quantity. That is, at very high temperatures the oxidation reaction can indeed change the physical dimensions of the filament, due to loss of metal in the formation of volatile oxide, but the heat released during recombination may contribute appreciably to the heating of the filament. Ascertaining the temperature of the filament from a resistance measurement alone would thus seem impossible, and conversely, deducing the change in the physical cross-sectional area of the filament from a resistance reading alone, without having an independent measurement of the temperature of the filament, would seem equally impossible. Namely, the resistance depends on both the cross-sectional area and the resistivity, the latter varying markedly with temperature for most materials.

Silver

Two oxides of silver exist, the oxide Ag_2O and the peroxide AgO. Ag_2O has a molecular weight of 231.74 and a density of 7.143. It is a brown-black cubic substance which decomposes at 300°C. AgO (sometimes listed as Ag_2O_2) has molecular weight 247.74 (the peroxide Ag_2O_2 symbolism) and it decomposes at temperatures above 100°C. It is a gray-black cubic material having a density of 7.44.

Silver is fairly noble in molecular oxygen, having a low tendency to react. The tarnish layer commonly observed on household silver is not an oxide, but instead, is a sulfide.

The adsorption and occlusion (viz., reaction with solid phase) of oxygen atoms with silver has been studied at 300 K [see "The Rate and Mechanism of Interaction of Oxygen Atoms and Hydrogen Atoms with Silver and Gold" by B. J. Wood, J. Phys. Chem. 75, 2186-2195 (1971)]. Figure 4 in that paper shows the mass of adsorbate as a function of the sorption time, and it is demonstrated that silver takes up atomic oxygen at an almost constant rate well beyond monolayer coverage. In fact, results of McBee and Yolken were cited which showed that oxide film growth on a silver surface exposed to a flux of oxygen atoms was nearly linear in time to thicknesses exceeding 1000 Å. The results contrast dramatically with results for gold, which indicate that gold adsorbs up

to a maximum of one monolayer of oxygen atoms at 300 K with a rate that diminishes with coverage. Gold exhibits no occlusion of atomic oxygen nor gives any evidence of oxide formation. Neither silver norgold was observed to adsorb oxygen when exposed to O_2 only. Atomic oxygen recombines to form molecular oxygen in the presence of silver, one value for the probability being given as 0.24 (see the subsection on Copper) and another value being 0.02 (see the subsection on Platinum). Both values were based on room temperature measurements.

The reaction of silver interconnects with atomic oxygen during the STS-5 mission is described in an unpublished report by P. N. Peters, J. C. Gregory, and A. F. Whitaker. It was concluded that a layer of Ag_2O formed which was of the order of one micron in thickness. The high reflectivity of silver was thereby destroyed. These experimental results prompted the further studies on silver samples scheduled for the STS-8 mission.

Chromium

The only oxide formed on heating in molecular oxygen at various temperatures has been reported to be Cr_2O_3. Only 5000 Å of oxide form when chromium is heated in molecular oxygen at a pressure of 76 mm. Hg and a temperature of 1000°C for one hour. At 700°C and the same pressure, a 5000 Å oxide film forms in about six hours. The oxide film is quite protective for chromium in molecular oxygen under these conditions. On the other hand, at higher temperatures the Cr_2O_3 scale oxidizes to form CrO_3 which is volatile, and the overall weight of the sample decreases with time of exposure. Studies of this phenomena in molecular oxygen have been carried out [see "Oxidative Vaporization Kinetics of Cr_2O_3 in Oxygen from 1000 to 1300°C" by C. A. Stearns, F. J. Kohl, and G. C. Fryburg, J. Electrochem. Soc. 121, 945-951 (1974)]. In the presence of atomic oxygen, the vaporization was markedly enhanced [see "Enhanced Oxidative Vaporization of Cr_2O_3 and Chromium by Oxygen Atoms" by G. C. Fryburg, F. J. Kohl, and C. A. Stearns, J. Electrochem. Soc. 121, 952-959 (1974)]. The investigations were conducted over the temperature range of 200 to 1250°C. The enhancement was found to be 10^9 at 550°C in oxygen containing 2.5% atomic oxygen. The enhancement is so large that, whereas the oxidative vaporization of Cr_2O_3 could only be detected above 900°C in molecular oxygen, it could be readily measured down to 200°C in the partially atomic oxygen environment. In addition to these remarkable observations, it was found during the course of the investigation that below 800°C, a direct oxidative vaporization of chromium metal occurred in atomic oxygen. The temperature-dependence of both rates is quite peculiar, as can be noted from Figure 5 in the last paper cited above. At 550°C, the maximum values for the probability of reaction of an oxygen atom is 0.03 for Cr_2O_3 oxidation to CrO_3, and 0.014 for Cr oxidation to CrO_3. In the 950 to 1250°C region, the probability for Cr_2O_3 oxidation is 0.002. Below 800°C, the chromium ribbon

samples remained bright and shiny after a series of oxidations in atomic oxygen.

Atomic oxygen also recombines to form molecular oxygen in the presence of chromium. At room temperature the rate is very low, but the recombination coefficient increases rapidly with increasing temperature.

The implications of the above-described enhancement of the evaporation of the protective layer of Cr_2O_3 by atomic oxygen should not be overlooked, not only for pure chromium itself but also regarding high chromium steels. The low temperature enhancement is truly enormous, being of the order of 10^{20} at 200°C. At 550°C, the enhancement is still a factor of a billion, though at 1000°C it drops to a factor of 100. With larger concentrations of atomic oxygen, the enhancements would be even larger. Both the high rate of removal of the protective Cr_2O_3 layer and the high rate of removal of the parent chromium by atomic oxygen pose a potential problem for use of chromium steels and similar alloys for space vehicles.

FeCrAl

Aluminum additions greatly increase the oxidation resistance of iron due to the formation of alumina (Al_2O_3) or an alumina-containing surface layer. Under some conditions the spinel $FeO \cdot Al_2O_3$ is formed, which itself slows the diffusion much more than layers of pure iron oxide.

Steels containing chromium are among the best of the oxidation resistant commercial alloys. More than 12% Cr below 1000°C and more than 17% Cr above 1000°C will increase the oxidation resistance approximately a hundredfold relative to pure iron. Initial oxidation of such alloys is relatively rapid until 1000 Å or so of the oxide layer is formed, and thereafter the rate falls dramatically. The protective layer in some cases is Cr_2O_3, but in other cases it consists of $FeCr_2O_4$ or $(Cr, Fe)_2O_3$. Although the protective film $FeO \cdot Cr_2O_3$ has a tendency to crack above 800°C, it can be self-healing. The protective character is better if the film is formed initially at low temperatures and low oxygen pressures. The oxidation rate of iron-chromium alloys increases with the oxygen concentration in the gas.

It is important to note that small weight percentages of aluminum are much more effective in increasing the corrosion resistance of iron than are corresponding weight percentages of chromium. For example, 4% Al dramatically increases the corrosion resistance of iron, even as much as would be produced by 14% Cr, as observed at 890°C after 4 hours exposure. During the oxidation of iron-chromium-aluminum alloys, the aluminum is usually oxidized preferentially. The upper portion of the bulk alloy is thus impoverished in aluminum to a considerable depth.

Nickel

Nickel forms only one stable oxide, the monoxide NiO called Nat. bunsenite. It has a molecular weight of 74.71, a density of 6.67, and a melting point of 1990°C. It is green-black in color and is cubic in structure with a lattice constant of 2.1818 Å.

There exist in addition some unstable oxides of nickel, but NiO is the only oxide observed at temperatures in the range 300 to 700°C. The parabolic growth law is usually found to be applicable for the oxidation of nickel in molecular oxygen, although some deviations from parabolic growth have been observed for reaction times exceeding 50 hours. In the temperature range 400 to 850°C, the rate constant has an activation energy of 41.2 Kcal/mole and a pre-exponential factor (in gm^2/cm^4-sec) of 8×10^{-4}. In the temperature range 900 to 1050°C, the corresponding numbers are 68.3 and 120.

No data were found for the oxidation of nickel by atomic oxygen. Data for the recombination coefficients for atomic oxygen on Ni and NiO are listed in the subsection on Copper.

NiCr

It is interesting to note that chromium additions to nickel below 10% by weight actually decrease the corrosion resistance of nickel. This only prevails so long as NiO remains the predominant oxide. Alloys containing more than 15% of chromium have, on the other hand, good corrosion resistance in molecular oxygen. At these concentrations, Cr_2O_3 or $NiO \cdot Cr_2O_3$ layers are formed. In 80/20 Ni-Cr alloys in the 400 to 700°C range and at oxygen pressures of 1 mm. Hg, the main oxide formed is Cr_2O_3. At higher temperatures, the spinel $NiCr_2O_4$ becomes important. Although it is not clear what exactly determines the good oxidation resistance of nickel-chromium alloys, it can be said that a large proportion of Cr_2O_3 is generally beneficial. As outlined in the subsection on Chromium, atomic oxygen can volatilize Cr_2O_3, thus possibly leading to a failure in its protective character. For this reason, a sample of NiCr was chosen for exposure in the STS-8 mission.

ANALYSIS TECHNIQUES

X-Ray Production and Fine Structure

The continuous x-ray spectrum (bremsstrahlung) is due to the braking of a particle (usually an electron) impinging on a target. All or part of the incident particle's energy can be lost in the deceleration of the particle, so the spectrum of x-rays extends from a minimum wavelength (with all kinetic energy converted) to longer wavelengths (where only part of the kinetic energy of the particle has been converted). Actually, the impinging particle interacts one or more times with the screened nuclei of the target, so the x-ray spectrum is created in quantum increments. The short wavelength limit (SWL) is a function of the incident electron energy and is independent of the atomic number Z of the target. The x-ray intensity is proportional to the Z of the target but is inversely proportional to the square of the mass of the incident particle. The peak in the x-ray spectrum occurs at approximately 1.5 SWL.

If, instead of interacting with the screened nucleus of the target, the incident particle knocks out one of the inner shell electrons of the target atoms, thus creating a vacancy, such a vacancy may be filled by one of the electrons in the outer shells of the atom. If, as a consequence, an x-ray is thereby created, it will be one of the characteristic lines of the spectrum for the target material.

Chemical reaction produces wavelength shifts to both longer and shorter wavelengths in the x-ray spectra of various elements. The energy level changes are due to modifications in the electrical screening as the valence electrons form a bond. Low atomic number elements undergo the greatest shifts. Shifts of the order of 1 to 4 eV are common. In addition to the shifts, there is also a change in shape of the emission spectrum. Large intensity changes are also noted for certain lines. The transition probabilities are modified by chemical combination because of several factors: changes in electron character, electron depopulation of a given level and the attendant formation of excitation states, and nonradiative transition modifications.

EXAFS

X-ray absorption fine structure analysis can be used to deduce the position of neighboring atoms to the one emitting the x-ray. The emitted photoelectron is diffracted, thus giving rise to fine structure in the spectrum.

X-Ray Appearance Potential Spectroscopy

The surface is bombarded by electrons, and as the electron energy is varied through an ionization threshold the atom begins to emit its characteristic x-rays. This serves to identify the element. This technique is simple, but is rather insensitive in the case of many elements.

Electron Microprobe

Electron excitation (typically at 10 to 30 kV) of a sample causes it to emit its characteristic x-rays by creating an inner-shell vacancy. The beam is focused to a small diameter so that a mass as small as 10^{-11} gram and a volume as small as one cubic micron can be analyzed. The chemical analysis is accomplished by dispersion of the x-ray spectrum so obtained and quantitatively measuring the wavelength and intensity of each characteristic line. The wavelengths identify the emitting elements, and the line intensities give a measure of the concentrations of the elements. The advantage over other analytical methods is the ability to analyze quantitatively samples of such small size.

X-Ray Fluorescence Analysis

An x-ray source is used to excite a sample to emit its own characteristic x-rays. The word "fluorescence" indicates the excitation of photons by other photons. This is one of the most useful analytical methods for chemical analysis since it is rapid and economical. Whether or not this x-ray spectrochemical analysis technique is a surface technique is debatable since the x-rays emitted originate in a surface layer of 50 microns or so in thickness. When radiation from an x-ray tube is used for excitation, the continuum portion of the spectrum provides most of the excitation. Gamma rays can be used as well as x-rays for excitation of the sample.

ESCA

"Electron Spectroscopy for Chemical Analysis" (ESCA), a technique originated by Siegbahn at Uppsala, involves the ejection of core electrons of the target material by incident soft x-rays of well-known energy. The analysis of the kinetic energies of the ejected electrons, together with the known energy of the incident x-rays, allows a calculation to be made of the core-electron binding energies. The binding energy reflects the oxidation state. The binding energy is markedly affected by the chemical environment, and is also a function of the atomic charge. Measurement of the chemical shifts in this way provides a sensitive and quantitative method of chemical analysis which moreover is applicable to nearly every element in the periodic table, with the exception of hydrogen and helium.

As an example of the use of ESCA, the quantitative analysis of mixed MoO_2/MoO_3 oxides can be better than 2% in mixtures containing more than 15% MoO_2. Other successful analyses have been carried out on the mixed oxides PbO/PbO_2, Cr_2O_3/CrO_3, and AsO_3/As_2O_5. It has been demonstrated that PtO_2 can be distinguished from Pt. Oxide films on Ni and Ni-Cu alloys have been studied, and the metals and oxidation states of the oxides identified. Spectra obtained on NiO could be distinguished from spectra of Ni, and Ni foils were found to exhibit characteristics of Ni/NiO mixtures.

The technique is a surface technique since the ejected electrons generally emerge from the upper 100 Å of the sample. One restriction is to samples which are stable to x-ray bombardment. Although most materials are stable under such bombardment, nevertheless, some do decompose. The sensitivity of the technique is very high, typical amounts of material being of the order of a microgram. Two orders of magnitude less material has on occasion been successfully analyzed. The technique is so sensitive that 0.01 monolayers can produce a detectable signal for many materials. One problem which does arise in the analysis of dielectrics, however, is surface-charging, which leads to a shift in the absolute positions of the peaks in the spectrum, although there is not much relative shift between neighboring peaks.

The soft x-ray source for the technique is typically a conventional x-ray tube, with heated cathode and cooled anode. The power required is about 5 kw, thus requiring that large amounts of heat be dissipated. This is accomplished by water cooling. The electron energy analyzer can be one of several types, viz.

(a) retarding electrostatic field applied to grids,
(b) inhomogeneous magnetic field,
(c) concentric spheres with electrostatic potential difference.

The magnetic type is rather touchy because shielding of the earth's field is so critical. The detectors are usually electron multipliers, though photographic plates likewise can be used.

Auger Electron Emission

Auger emission is complementary to x-ray fluorescence in the sense that both processes result from an outer shell electron dropping to fill an inner-shell vacancy in an excited ion decay event. If the energy is emitted as a photon, the process is called x-ray fluorescence, whereas if the energy is emitted as a second electron ejection, the process is called Auger emission. In both cases, the energy of emission is independent of the exciting radiation. For example, Auger electron emission lines are characteristic of the sample which is excited, and are not characteristic of the exciting particle type or exciting particle energy. Different exciting quanta generate characteristic fluorescence or Auger peaks with varying

degrees of efficiency, but all can be used for chemical analysis.

In the lighter target atoms ($Z < 11$), the probability for Auger emission is approximately 1, but with increasing Z, the probability increases for x-ray fluorescence. At $Z = 33$, the probabilities are approximately the same, namely, 50% - 50%. In Auger spectroscopy, a series of accelerator plates and baffles provides the energy selection for the electron beam. After Auger ejection, the atom is doubly ionized, thus resulting in a modification of its energy-level diagram.

Ion milling can be employed with Auger spectroscopy to determine depth profiles of chemical compositions. The surface is bombarded with 200 to 5000 eV ions to sputter away the surface. Noble gases, such as Ar^+, are used to avoid reaction with the surface. Actually, two different sputtering ions are desirable, because the incident ions are imbedded in the surface and thus create additional Auger spectra. There are additional complications involved in ion milling, among them the following: Surface roughening, homogenization of the surface, different sputtering rates for different elements in a compound, and surface charging. The latter can be eliminated by using an auxiliary electron beam.

Ion Neutralization Spectroscopy

The surface of the sample is bombarded with low-energy ions. Auger electrons are ejected from the surface, which are energy analyzed to infer the density of states of the surface.

Photoelectron Spectroscopy

Ultraviolet photons are used for the excitation of valence-shell electrons having binding energies in the range of 0 to 40 eV. Some of the commonly-used excitation lines to produce the photons are:

He^+	(40.812 eV)
He	(21.218 eV)
Kr	(10.032 eV)
Hg	(4.8878 eV)

The emitted electrons are energy analyzed to give intensity versus energy. This spectrum can be unfolded to yield many electronic properties of the target sample, as for example, the electronic density of states.

Mössbauer Effect Studies

A wealth of detailed information can be obtained for the limited number of elements readily available for Mössbauer work. This is a gamma ray technique

based on the principle of zero phonon transitions. In principle, information can be obtained on the valence state and the type of bonding of an atom to the surface, and on the dynamics of motion of an atom oscillating about its equilibrium position on the surface. Additional information concerning the electric field symmetry at the atom site and the existence and strength of any magnetic field at the atom can be obtained. Also, the surface mobility and diffusion rate of the atom can be deduced. Although there are only a limited number of elements which are amenable to Mössbauer studies, it is worthwhile to note that among them are the important elements Fe and Sn.

EPR

Electron paramagnetic resonance has been used to establish that O_2^- lattice vacancies exist at the surface of ZnO at temperatures above 150 K in evacuated systems. At higher oxygen pressures, chemisorbed O_2^- has been observed. Similar results have been reported for CaO, SrO, ZrO_2, TiO_2, and ZnS.

NMR

Protons can be positively identified by nuclear magnetic resonance techniques. Surface hydroxyl groups have been deduced from the resonance line shape and its temperature dependence. Physically-adsorbed water on silica has been detected through the temperature-dependence of T_1 and T_2, the nuclear spin-lattice and spin-spin relaxation times. It is interesting that the water detected on silica was found to demonstrate a two-phase behavior.

ATOMIC OXYGEN MONITORS

It is of interest to obtain a continuous measurement of the atomic oxygen concentration in the upper atmosphere of the earth by space vehicles during orbit and reentry. The most straightforward method would seem to be the use of a mass spectrometer. There is a problem, however, in that the atomic oxygen tends to interact with the mass spectrometer ion source, thus leading to a reading for the atomic oxygen concentration which is too low. Therefore it is worthwhile to consider other possible methods.

A. Whitaker and R. DeHaye have proposed a method and device for on-orbit monitoring of the atomic oxygen flux and total fluence. Basically the device consists of a thin film strip of material with an applied voltage. The current through the material is to be monitored continuously. The resistance of the film is inversely proportional to its thickness. As the atomic oxygen impinges on the film its surface is oxidized to form a volatile oxide or an oxide layer which is less conductive than the parent material. The change in current flow with time should be proportional to the incident flux, and the total current change should be proportional to the total incident fluence. The proportionality factors depend upon the reaction probability. The metals molybdenum and tungsten have high reaction probabilities, as well as carbon. The temperature-dependence of the reaction probabilities and the heating effects of the catalytic recombination of atomic oxygen are also germane to this problem. This explains to a large extent the attention which has been devoted to these quantities in this report.

One method used to determine the actual temperature of a filament-type specimen is to employ the known temperature-dependence of the resistivity of the material, and measure very carefully the physical cross-sectional area and length of the specimen. The measured resistance can then be used to deduce the temperature. This method is good at the start of the atomic oxygen reaction, but since the cross-sectional area of the specimen steadily decreases as the reaction proceeds, it cannot be used subsequently in the reaction unless it is possible to measure the temperature (or else the cross-sectional area) independently by some other means. That is, there are two unknowns affecting the resistance, the physical cross-sectional area of the specimen (which is constantly changing) and the resistivity (which changes as the filament temperature changes), so the measurement of only one quantity (namely, the resistance of the filament) is insufficient to determine the two unknown parameters. The temperature of the filament specimen is sometimes monitored independently with an optical pyrometer, so that any resistance changes leading to an increase in temperature for fixed

current due to decreasing filament diameter can be continuously compensated for by a decrease in the filament heating current as the metal filament reacts. However, the continuous use of an optical pyrometer would seem to be impractical on board the Space Shuttle. It would also be possible to photograph the filament periodically with sufficient resolution to ascertain the changes in diameter which occur during flight, but such data would not be available on a continuous basis for adjusting the filament current accordingly to maintain a fixed temperature. It is because of this problem of maintaining a fixed filament temperature that a choice of material for the atomic oxygen monitor needs to take into consideration the sensitivity of reaction rate to temperature, the ideal being that of finding a substance which has a reaction rate which is essentially independent of temperature. This, of course, must be coupled with the requirement that the substance have a high reaction probability, since otherwise the monitor will not have the requisite sensitivity. This problem will require further study.

It is informative to list the steps utilized by Rosner and Allendorf in their study of the high-temperature oxidation of Mo and W by atomic oxygen. These steps are as follows:

1. NO_2 light titration technique used to measure the atomic oxygen concentration.
2. The filament temperature was measured absolutely with an optical pyrometer, and the current through the filament was adjusted continuously as required to keep the temperature constant.
3. The voltage drop was measured across the central part of the filament to obtain the resistance, and with the known temperature and the known functional dependence of the resistivity of the filament material on temperature, the cross-sectional diameter of the filament could be obtained as a function time.
4. The rate of decrease of the cross-sectional diameter of the filament gives the reaction rate of the filament material, since the reaction product was volatile.
5. The incident atomic oxygen flux was obtained from the partial pressure of atomic oxygen measured in step 1 and the use of the Hertz-Knudsen equation, assuming the atomic oxygen attacking the filament to be at the same temperature as the filament obtained in step 2.
6. The reaction probability was then obtained by taking the ratio of the incident atomic oxygen flux to the reaction rate of the filament atoms.

As an alternative to the filament technique of measuring the atomic oxygen flux, or the NO_2 light titration technique, a technique whereby the surface conductivity of a ZnO single crystal is monitored could be used. Atomic

oxygen adsorbed on zinc oxide single crystals causes a decrease in surface conductivity. It would be necessary to provide a means of heating the ZnO to 500 to 800 K in a cyclic process to restore the crystal, but this would not be a major difficulty. A typical response curve for such a device can be seen in Figure 5 of the paper entitled "New Method for the Detection of Atomic Oxygen Beams" by H. Nahr, H. Hoinkes, and W. Wilsch [J. Chem. Phys. 54, 3022-3025 (1971)]. The linearity of the response is demonstrated, but an absolute calibration would be required in order to have a quantitative device. This calibration would probably be different from one ZnO crystal to another, and would require an atomic oxygen beam with a known (i.e., independently-measurable) flux. An interesting property of the ZnO detector is that it will detect atomic hydrogen as well as atomic oxygen, the surface conductivity changes being in opposite directions for the two cases. That is, adsorbed hydrogen increases the conductivity, whereas adsorbed oxygen decreases the conductivity. This can be understood by noting that ZnO is an n-type defect semiconductor, so that the conductivity will decrease if atomic oxygen depletes the conduction electron concentration by becoming a chemisorbed O^- ion.

CONCLUSIONS AND RECOMMENDATIONS

1. Several metals were recommended for experimental investigation on the STS-8 mission.

2. The thickness of the surface oxide films should be measured by ellipsometry.

3. The oxides should be characterized at minimum by x-ray diffraction, ESCA, and Auger electron spectroscopy.

4. The possible effects of the spurious heating of the filament-type specimens due to recombination of atomic oxygen should be carefully considered in the selection of a material for use in a resistance-type atomic oxygen monitor.

5. Careful thought should be given to the problem of deducing simultaneously the filament size and the temperature of the filament in the proposed resistance-type atomic oxygen monitor.

REFERENCES

1. Hodgman, C. D., Weast, R. C., and Selby, S. M., Handbook of Chemistry and Physics, Chemical Rubber Publishing Co., Cleveland, Ohio, 1974.

2. Samsonov, G. V., The Oxide Handbook, Plenum, New York, 1973.

3. Kubaschewski, O. and Hopkins, B. E., Oxidation of Metals and Alloys, Butterworths, London, 1962.

4. Kane, Philip F. and Larrabee, Graydon B., Characterization of Solid Surfaces, Plenum Press, New York, 1976.

[N84 16037

NASA/ASEE SUMMER FACULTY RESEARCH FELLOWSHIP PROGRAM

MARSHALL SPACE FLIGHT CENTER
THE UNIVERSITY OF ALABAMA IN HUNTSVILLE

AN EVALUATION OF TECHROLL SEAL FLEXIBLE JOINT MATERIAL

Prepared by:	William B. Hall, Ph.D.
Academic Rank:	Professor
University and Department:	Mississippi State University Department of Chemical Engineering
NASA/MSFC: Division: Branch:	 Non-Metallic Ceramics & Coatings
MSFC Counterpart:	Ron L. Nichols
Date:	August 12, 1983
Contract No:	NGT 01-008-021 The University of Alabama in Huntsville

ABSTRACT

An Evaluation of Techroll Seal Flexible Joint Material

William B. Hall
Professor, Chemical Engineering
Mississippi State University
ASEE-NASA Fellow

Ron L. Nichols
Ceramics Unit, EH34
Marshall Space Flight Center
ASEE-NASA Counterpart

On April 7, 1983 a Tracking and Data Relay Satellite (TDRS) launched from Space Shuttle 6 failed to reach geosynchronous orbit. The conclusion reached from an intensive investigation was that the satellite tumbled out of control due to failure of an oil seal in the rocket system known as Inertial Upper Stage (IUS). The oil seal is a flexible joint permitting swivel or gimbal of the rocket nozzle to control direction of flight.

This study evaluated the materials utilized in the flexible joint for possible failure modes. Studies undertaken included effect of temperature on the strength of the system, effect of fatigue on the strength of the system, thermogravimetric analysis, thermomechanical analysis, differential scanning calorimeter analysis, dynamic mechanical analysis, and peel test.

These studies indicate that if the joint failed due to a materials deficiency, the most likely mode was excessive temperature in the joint. In addition, the joint material is susceptible to fatigue damage which could have been a contributing factor.

Introduction

The Air Force Space Division Inertial Upper State (IUS) is a three-axis stabilized, two-stage vehicle used to take payloads from low earth orbits to other regions of space such as a geosynchronous orbit. The primary propulsion system is composed of two solid rocket motors built by Chemical Systems Division (CSD) of United Technologies Corporation. The first stage (SRM-1) contains 2.,400 lb of propellant and is used as a perigee kick motor to provide the energy required to go from low earth orbit to geosynchronous orbit. The second stage (SRC-2) contains 6000 lbs of propellant and is used as an apogee kick motor to provide the energy to circularize the geosynchronous orbit. On a typical shuttle mission the IUS could place up to 5100 lbs into geosynchronous orbit. SRM-1 and SRM-2 were designed with as much commonality as practical to improve reliability and minimize cost. Common items include case material and strength level, insulation and liner material, nozzle material, thrust vector control, thrust vector control actuators, ignition system, flexible joint concept, and identical manufacturing procedures and techniques.

The flexible joint concept (Techroll seal) was developed to permit the use of a low-weig' electromechanical actuation system as required by the stringent use parameters in the shuttle program. The movable Techroll seal is a constant volume, fluid-filled bearing using a seal configured with two rolling convolutes which permit omniaxial deflection of the nozzle assembly. The Techroll seal consists of two layers of Kevlar-29 fabric layered between two sheets of neoprene rubber with steel cable beads for seal retention. One layer of the Kelvar-29 fabric is sufficient for load carrying. The second layer is redundant for extra

safety.

Typical operating temperature for the motors ranges from 45°F to 82°F. These temperatures are maintained at this level by insulation and heaters. However, prior to use the motors are exposed to other temperatures in various transportation sequences.

A Tracking and Data Relay Satellite (TDRS) launched from Space Shuttle 6 failed to reach geosynchronous orbit. The ensuing investigation concluded that the satellite went out of control due to the failure of the Techroll seal. This study was conducted to identify possible failure modes for the flexible joint. Specific materials properties were determined regardless of probability of the Techroll seal system being exposed to exactly the same physical parameters.

Material Evaluation

Several tests were conducted to determine possible failure modes of the composite Techroll seal material. These tests included:

a. Strength versus temperature

   Tests were conducted utilizing a Model 1113 Instron Universal Testing machine with a 5000 lb capacity. Specimens were brought up to temperature, held for five minutes, and pulled to failure in tension, at a pull rate of 10 in/min.

b. Strength versus number of fatigue cycles

   Flexural fatigue cycles were obtained at room temperature on a MIT Folding Indurance Testor per ASTM D-2176-63T under an applied load of 1 kg. Strength was then determined at room temperature by pulling the flexed specimens to failure in tension utilizing a Model 1113 Instron Universal Testing Machine with a 5000 lb capacity.

c. TGA

   Thermogravimetric analysis in Air and N_2 was conducted utilizing the DuPont 1090 system with the Model 951 TGA attachment. Additional TGA tests were conducted in vacuum utilizing a Mettler Model TA-2.

d. TMA

Thermomechanical analysis was conducted utilizing the DuPont 1090 system in conjuction with the Model 943 TMA attachment.

e. DSC

Differential scanning calorimeter tests were conducted utilizing the DuPont 1090 system with the Model 910 DSC attachment.

f. DMA

Dynamic mechanical analysis was performed utilizing the DuPont 1090 system in conjunction with the Model 982 DMA attachment.

g. Peel Test

Bond strength of the various layers of the Techroll seal composite was determined utilizing the Model 1113 Instron Universal Testing Machine.

h. SEM Evaluation

Scanning electron microscope analysis was conducted utilizing a Cambridge Stereoscan Model 250 MK2.

Results

Strength of the Techroll seal composite at various temperatures is shown in Figure 1. This data indicates the strength deteriorates rapidly at temperatures in excess of 200°F with only 54% of the original room temperature strength remaining at 500°F.

The slight increase in strength from 75°F to 200°F is attributed to increase in ductility of the Kevlar fibers, whereby a greater load sharing capacity overides the decrease in individual fiber strength. The decrease in strength of the composite material as it is subjected to flexure cycles is shown in Figure 2. The strength decreases rapidly with number of flexure cycles up to 1000 cycles, where the rate of decline in strength decreases.

The differences in rate of strength deterioration between flat sheet material and Techroll seal material is attributed to the difference in

the lay-up configuration and bond strength between layers. The flat sheet material had 47% of non-flexed strength left after 1000 cycles while the Techroll seal had 57% after 1000 cycles.

Thermogravimetric analysis (TGA) results as shown in Figures 3,4,5 and Table 1 show that the material is stable over the anticipated operating temperature range. However, if the temperature should exceed 75°C, the neoprene begins to decompose, with rapid decomposition occurring above 285°C. The Kevlar fibers begin to deteriorate at 350°F, with the rate dependent upon environment. The vacuum environment causes the greatest loss of weight up to the 350°F range, while air causes the greatest loss of weight above that temperature. This latter weight loss is attributed to an oxidation process.

TMA results shown in Figure 6 indicate uniform properties in the range of -33°C up to 100°C. No change in these properties would be anticipated until decomposition temperatures are reached The abrupt change in the slope of the curve shown at -33.3°C is connected to the Tg of the system.

DSC results shown in Figure 7 indicate no reactions in the range of 0-100°C, with two minor indothermic reactions occurring between -45°C and 0°C, with the first reaction occurring at the Tg of neoprene.

DMA results shown in Figure 8 indicate stable conditions in the anticipated use temperature range of 7°C up to 28°C. No further change would be anticipated until decomposition temperatures are reached. The large decrease in E and increase in damping capacity at approximately -30°C is connected to the Tg of the system.

Peel test results shown in Table 2 indicate that bonding between layers in the composite is very weak, a known problem with Kevlar fibers. A good bond strength would be in the range of 15 lb/in.

SEM analysis indicates the primary mode of damage to the fiber during flexure is splitting of fiber into many other fibers of much smaller diameter, and breakage of these smaller fibers. This type of damage is shown in Figure 9.

Discussion of Results

The evaluation of the flexible joint materials revealed the following:

a. The strength of the composite degrades rapidly at temperatures above 200°F.

b. The Kevlar fibers are very susceptible to flexural cyclic damage.

c. Bonding rubber to Kevlar, and Kevlar to Kevlar produces a very weak bond which percludes much load-sharing ability of the system.

d. Neoprene begins to decompose at 75°C with rapid decomposition above 285°C in vacuum. This would permit the fluid to escape from the seal, causes loss of swivel ability and thereby loss of control.

The most likely mode of failure of the Techroll seal would be excessive temperature with flexure damage being a contributing factor.

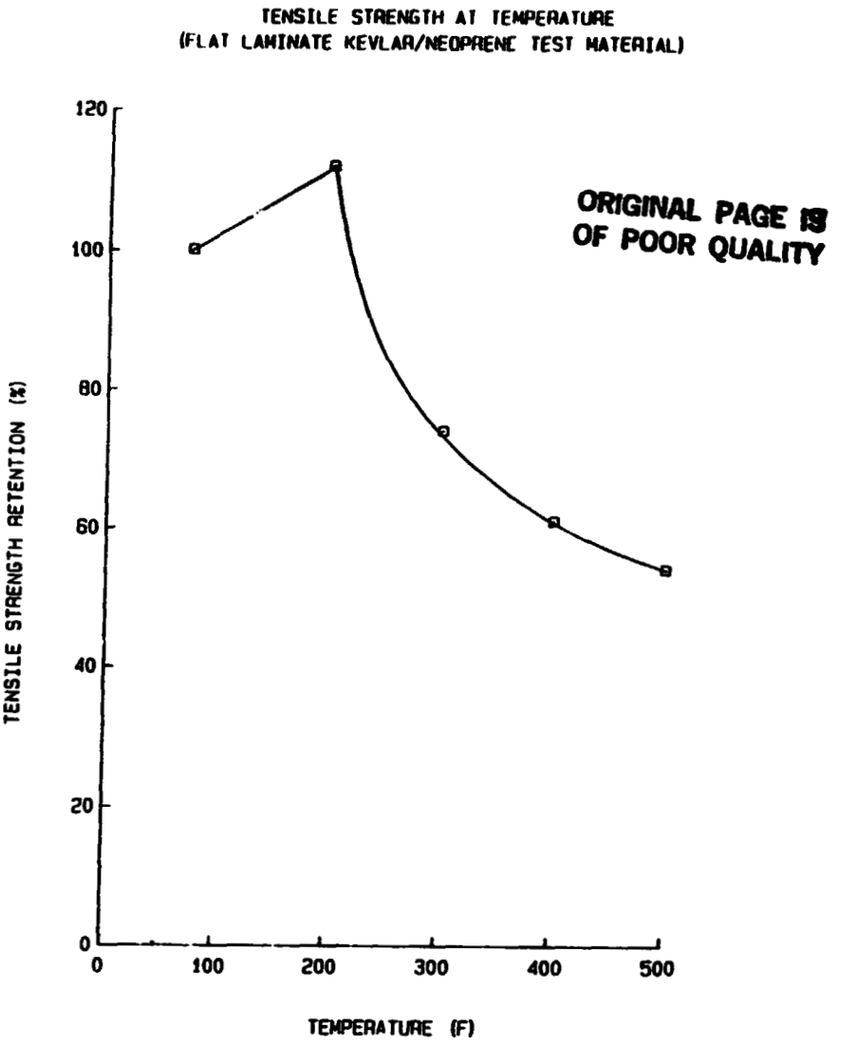

Figure 1. Per cent room temperature tensile strength retained versus test temperature.

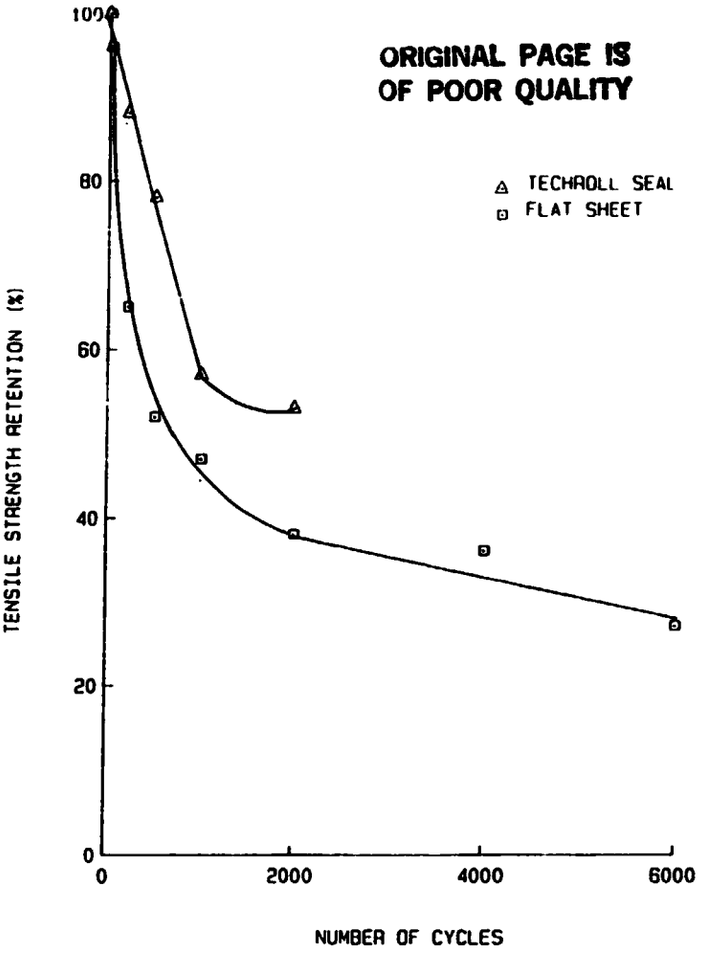

Figure 2. Per cent unflexed tensile strength retained versus number of flexed cycles.

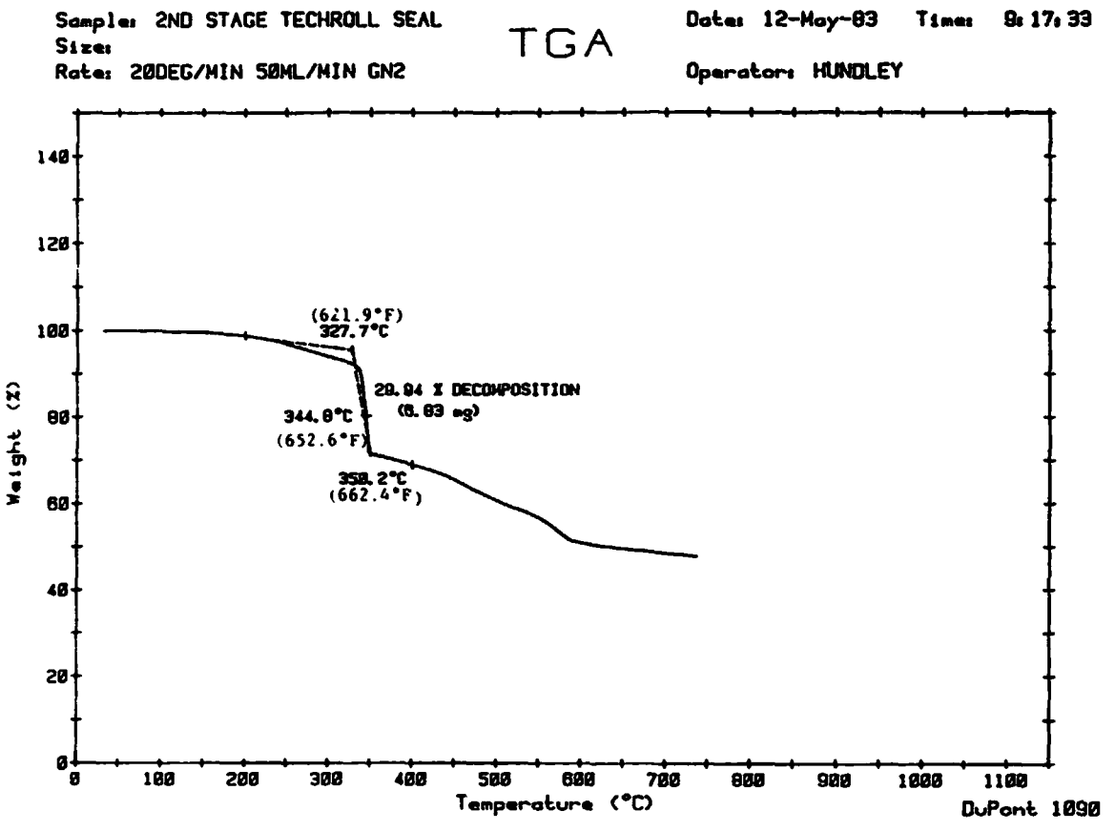

Figure 3. Thermogravimetric analysis of Techroll seal material in N_2 atmosphere

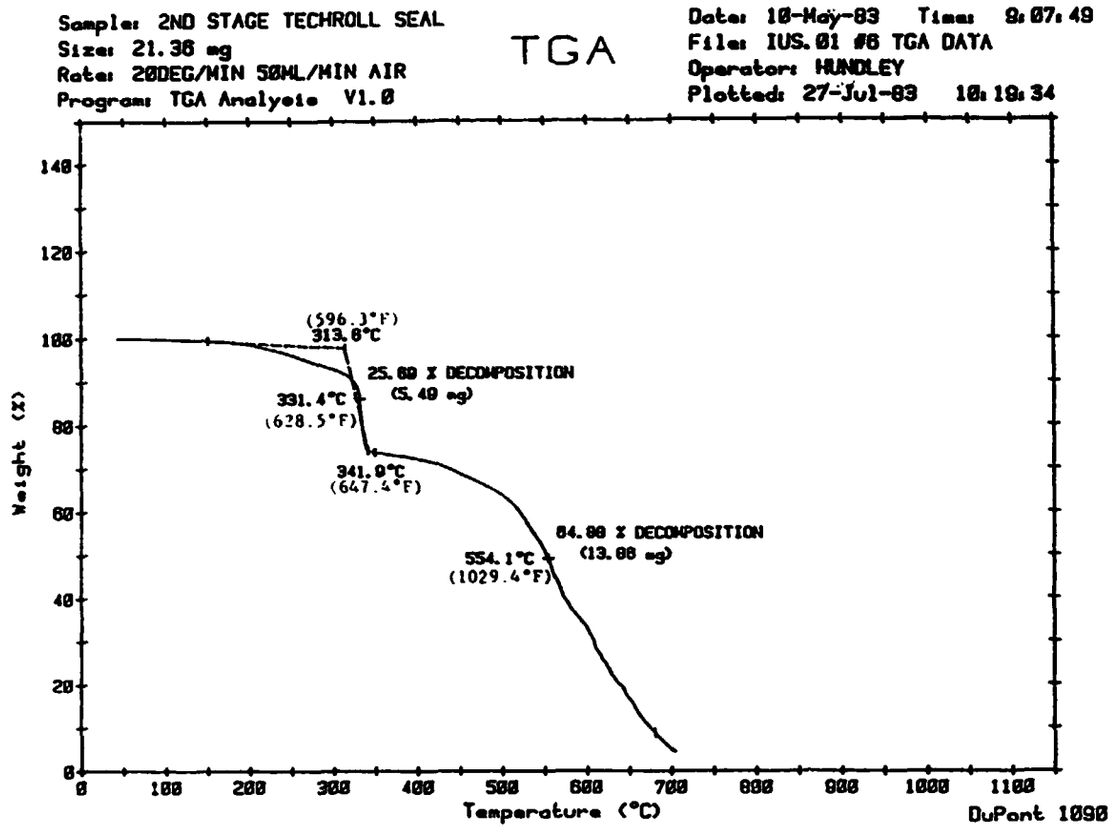

Figure 4. Thermogravimetric analysis of Techroll seal material in air atmosphere.

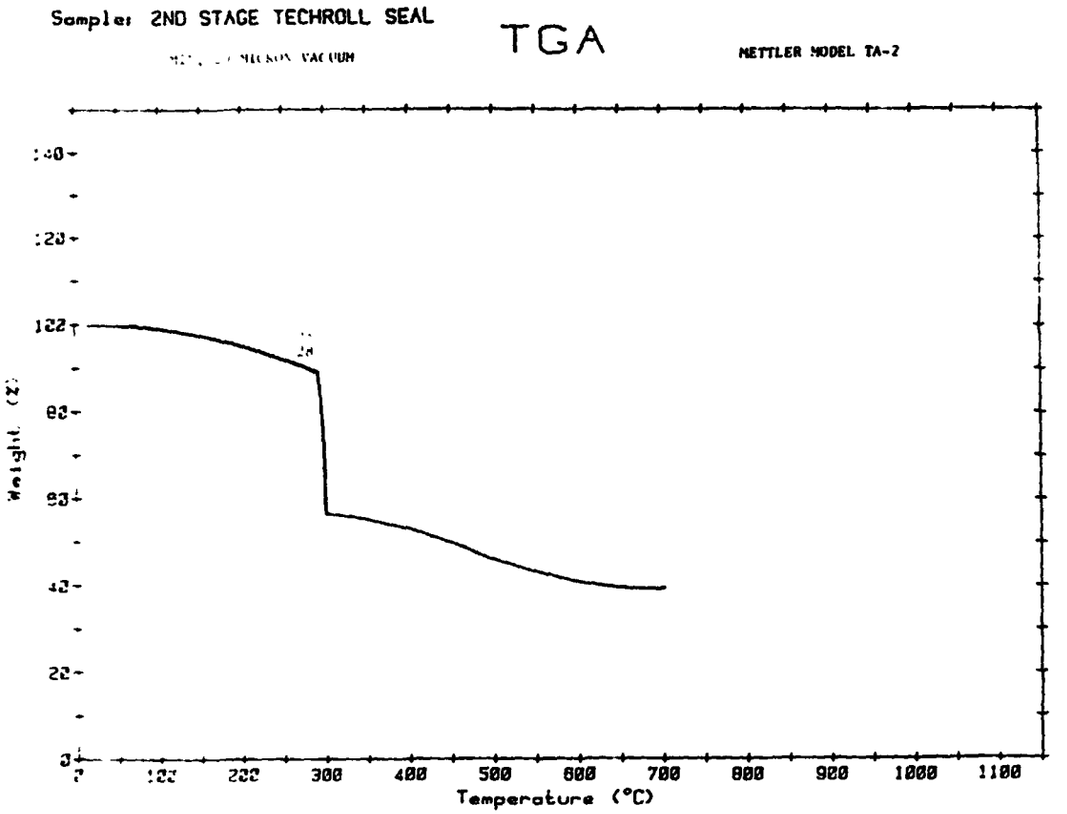

Figure 5. Thermogravimetric analysis of Techroll seal material in vacuum.

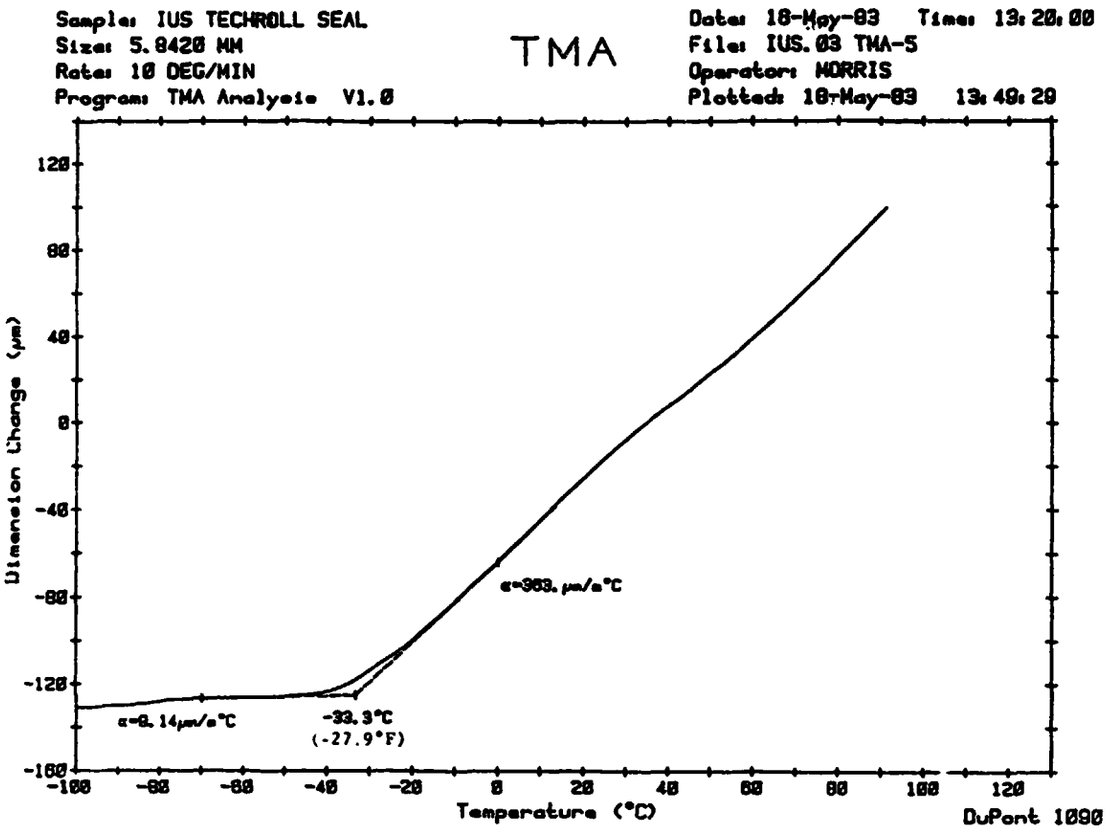

Figure 6. Thermomechanical analysis of Techroll seal material.

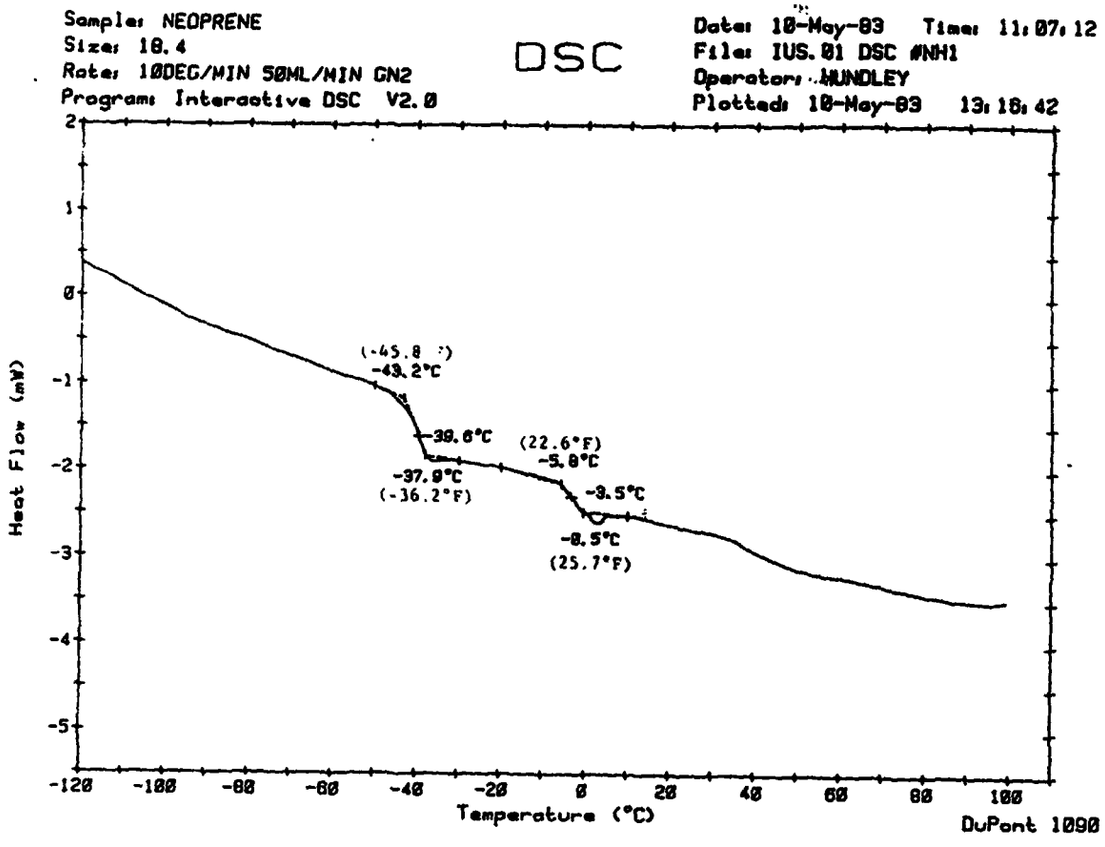

Figure 7. Differential scanning calorimeter analysis of Neoprene.

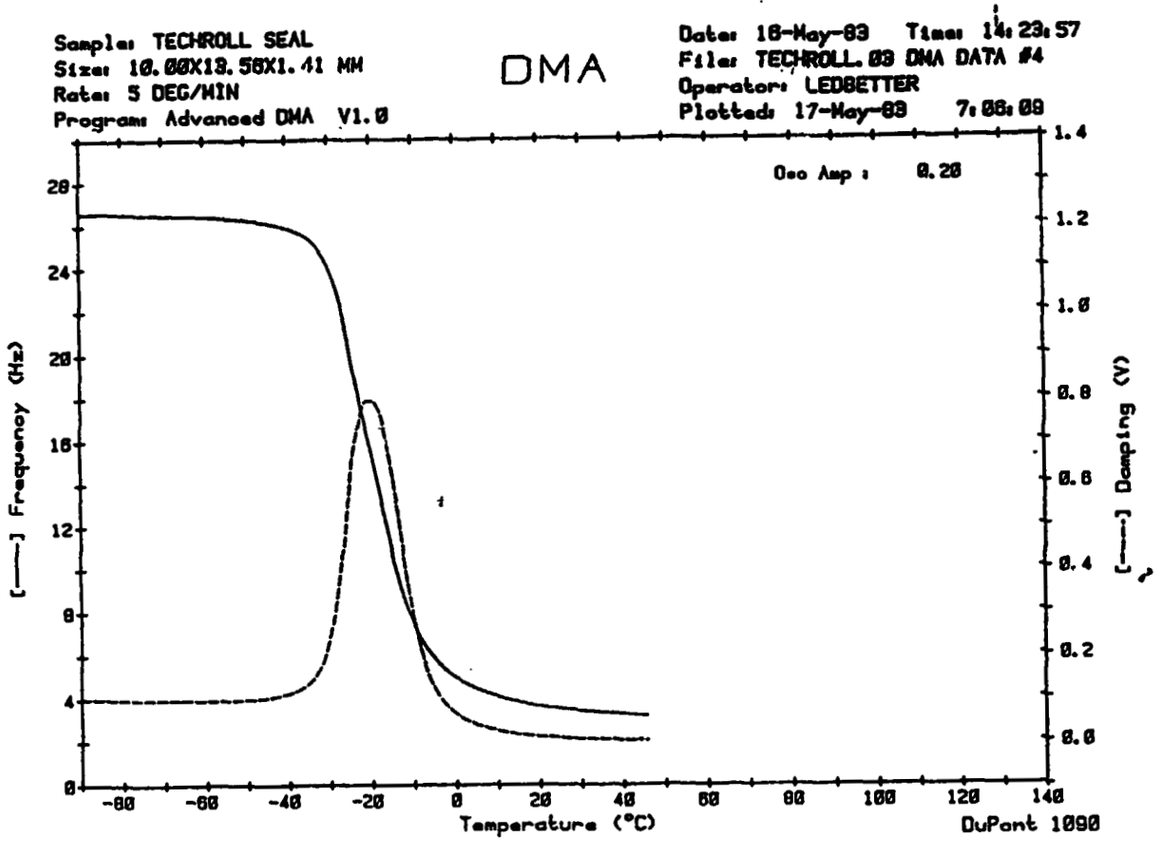

Figure 8. Dynamic mechanical analysis of Techroll seal material

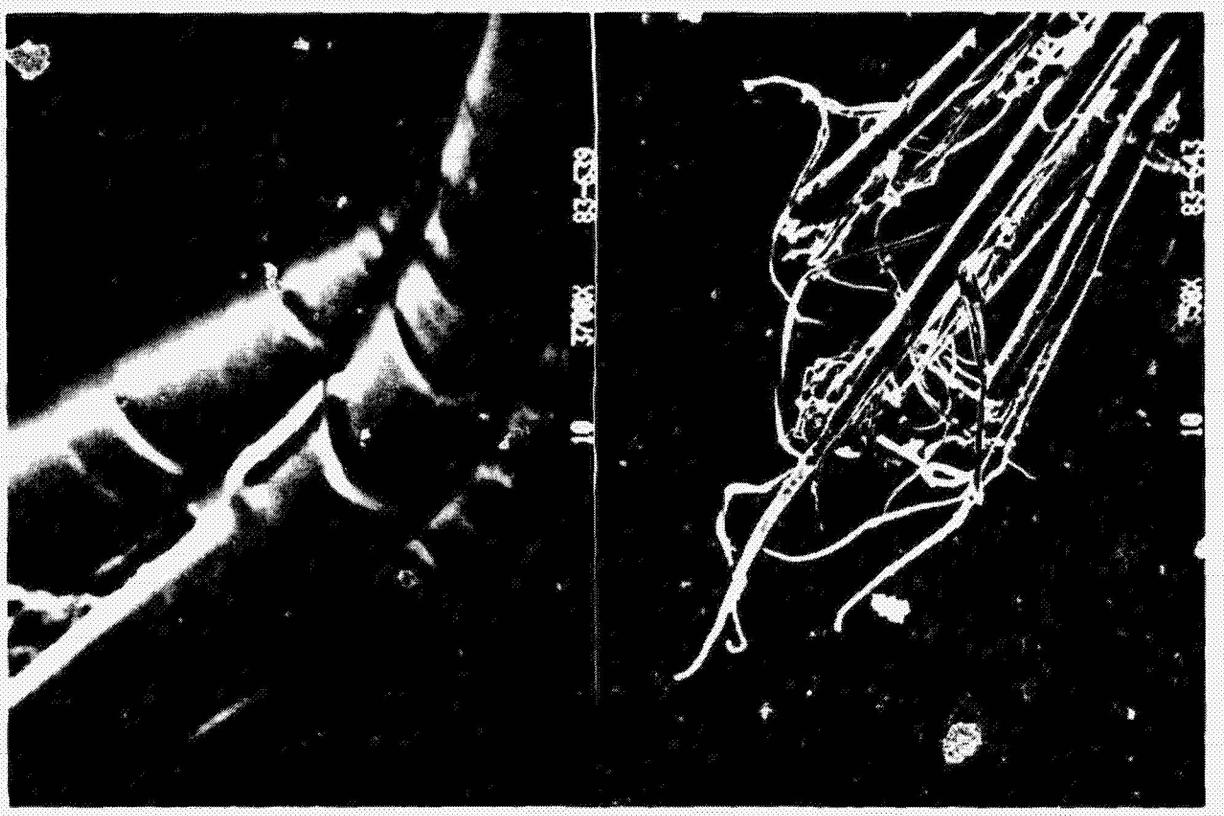

Figure 9. SEM analysis of Kevlar fiber degradation due to flexure.

Atmosphere	Temperature of first weight loss (°C)	Neoprene Decomposition Temperature (°C)	Total weight loss (%)
Vacuum	75	285	57
Air	150	314	95
N_2	200	328	52

Table 1. Comparison of Thermalgravimetric analysis of Techroll seal material in different environments.

180 DEGREE PEEL TEST

FLAT SHEET	PEEL STRENGTH, LBS./INCH
0.010" RUBBER TO KEVLAR	2.0
0.010" KEVLAR TO KEVLAR	4.5
0.035" RUBBER TO KEVLAR	4.0
TECH ROLL SEAL	
0.013" RUBBER TO KEVLAR	3.0
0.013" KEVLAR TO KEVLAR	0 - 4.0
0.040" RUBBER TO KEVLAR	4.0

INHERENTLY LOW BOND STRENGTH BETWEEN KEVLAR AND NEOPRENE OBSERVED

LARGE AREAS OF DELAMINATION PRESENT IN TRS

Table 2. Peel strength of Techroll seal composite.

1983

NASA/ASEE SUMMER FACULTY RESEARCH FELLOWSHIP PROGRAM

MARSHALL SPACE FLIGHT CENTER
THE UNIVERSITY OF ALABAMA
IN HUNTSVILLE

A STUDY OF ACCRETION IN COMPACT SOURCES: DISK PRECESSION AND JET HELICITY

Prepared By:	Philip E. Hardee, Ph.D.
Academic Rank:	Assistant Professor
University and Department:	University of Alabama Dept. of Physics & Astronomy
NASA/MSFC Division: Branch:	 Astrophysics High Energy Physics
MSFC Counterpart:	Dr. Martin Weisskopf
Date:	8/24/83
Contract No:	NGT 01-008-021 The University of Alabama in Huntsville

ABSTRACT

The effect of adiabatic expansion on the propagation and growth of helical twisting on a supersonic jet is investigated. Cooling of the jet material increases the jet's Mach number and increases the jet's density relative to that of the external medium. This has the effect of decreasing the maximum rate of growth and increasing the maximally unstable wavelength relative to the jet's radius. Propagation effects cause the wavelength of helical waves to change at a rate different from that of the maximally unstable wavelength with the result that the characteristic wavelength of helical twisting is not equal to this wavelength. The most rapidly growing helical wave will have a wavelength as much as a factor of 2 different from the instantaneous maximally unstable wavelength. Decrease in the growth rate along the jet is shown to imply an upper limit to the number of e-foldings and, therefore, an upper limit to the wave amplitude even in the absence of non-linear effects. This upper limit is dependent on the jet's Mach number at the point on the jet where the helical wave is initially produced.

I. Introduction

Extragalactic radio jets are unstable to helical twisting that is driven by centrifugal forces associated with lateral displacement of the jet fluid. The rate of amplitude growth of helical twisting along cylindrical jets and the characteristic wavelength of helical twisting can be important diagnostic tools in an investigation of the properties of extragalactic radio jets and the associated radio sources. The potentially distruptive properties of growing helicity to jet flow has led to a thorough investigation of the growth rate of this instability in the limit of small wave amplitude, on cylindrical jets of constant radius (Hardee 1979; Ferrari, Trussoni, and Zaninetti 1981; Ray 1981). This research has shown that the growth rate is peaked at some maximally unstable wave number which is primarily a function of the jet Mach number and density ratio between the jet and the external medium as well as the jet radius, and secondarily a function of the magnetic field. The effect of jet expansion and velocity shear on helical instability has also been investigated. For a constantly expanding fluid jet that remains isothermal in an isothermal external medium, it has been shown that results obtained for the cylindrical jet of constant radius scale with the jet radius, i.e., the growth rate is inversely proportional to the jet radius and the maximally unstable wavelength is proportional to the jet radius (Hardee 1982). Studies of magnetized shear layers in two-dimensional slab geometry have led Ferrari, Massaglia, and Trussoni (1982) to conclude that helical twisting is not strongly influenced by the presence of a shear

layer; and this conclusion is strengthened by the fact that in three-dimensional cylindrical geometry, the helical wavelength in the direction of wave propagation around the jet is on the order of the jet circumference which is much greater than the thickness of a shear layer (Hardee 1983).

It might appear that helical twisting in the regime of small wave amplitude is adequately described by a characteristic wavelength equal to the maximally unstable wavelength with amplitude growth given by the instantaneous maximum growth rate combined with the phase velocity of the helical wave. If this were the case, subsequent research would involve extension of the nonlinear calculations performed by Benford (1981). However, most of the research performed has not considered the effect of changing conditions in the jet and in the external medium. Changing conditions imply Mach number and density gradients which can affect the wavelength and growth of helical twisting. In a previous paper (Hardee 1983), the effect of changing jet conditions on the growth rate, phase velocity, and maximally unstable wave number for a representative sample of unstable wave modes was studied. The results showed that changing conditions affect the wave phase velocity, and thus the wavelength of propagating waves, differently from the effect on the maximally unstable wavelength. As a result, the characteristic wavelength of helical twisting will not be equal to the instantaneous maximally unstable wavelength, and wave growth will be considerably modified from previously considered situations.

In this paper we will study the effects of changing jet conditions on wave propagation and growth of the helical wave mode on a jet expanding adiabatically in an isothermal medium. In § II, we rederive the dispersion relation describing wave propagation and growth for small wave amplitude along a jet of cylindrical cross section for the general case of wave frequency and wave number varying in arbitrary manner. Spherical coordinates are used to describe constant jet expansion and gradients in the jet and external medium are included. In § III, we present the results of the numerical analysis which are computations of the wave phase velocity and growth rates as a function of position along the expanding jet. We use these results to find the most rapidly growing helical wavelengths on the jet. Finally, in § IV, we discuss the implications for models of twisted jets.

II. Dispersion Relation

We investigate the stability of a constantly expanding jet in which densitites and temperatures in the jet and the external medium are varying in different fashion. The variation is constrained by the requirement that the jet be constantly expanding and in static pressure balance with the external medium. We begin with the linearized equations of continuity and momentum in spherical coordinates (r, θ, ϕ) for fluids in which $\rho_o >> P_o/c^2$ where ρ_o is the density and P_o is the pressure, and in which the sound speed, a, is much less than the speed of light, c:

$$\frac{\partial \rho'}{\partial t} + v_{or}\frac{\partial \rho'}{\partial r} + \rho_o\left[\frac{1}{r^2}\frac{\partial}{\partial r}(r^2 v'_r) + \frac{1}{r\sin\theta}\frac{\partial}{\partial \theta}(\sin\theta\, v'_\theta) + \frac{1}{r\sin\theta}\frac{\partial v'_\phi}{\partial \phi}\right] + v'_r\frac{\partial \rho_o}{\partial r} = 0 \qquad (1)$$

and

$$\rho_o\left(\frac{\partial v_\phi}{\partial t}' + v_{or}\frac{\partial v_\phi}{\partial r}'\right) = -\frac{1}{r\sin\theta}\frac{\partial P}{\partial \phi}' \qquad (2a)$$

$$\rho_o\left(\frac{\partial v_\theta}{\partial t}' + v_{or}\frac{\partial v_\theta}{\partial r}'\right) = -\frac{1}{r}\frac{\partial P}{\partial \theta}' \qquad (2b)$$

$$\rho_o\left(\frac{\partial v_r}{\partial t}' + v_{or}\frac{\partial v_r}{\partial r}'\right) = -\frac{\partial P}{\partial r}' \qquad (2c)$$

In these linearized equations $\rho = \rho_o + \rho'$, $P = P_o + P'$, and $v = v_o + v'$, and $\rho_o = \rho_{in}(r)$ and $P_o = P_{in}(r)$ are solutions of the time-independent equations inside the jet of velocity $v_o = v_{or}$ given $\rho_o = \rho_{ex}(r)$ and $P_o = P_{ex}(r)$, $v_o = 0$ in the external medium. Equations 1 and 2 all contain the differential $(\partial/\partial t) + v_{or}\,(\partial/\partial r)$ and this allows us to transform away the velocity in the jet fluid v_{or} and then introduce it as a condition at the boundary.

We assume that a perturbation to the time-independent quantities can be expressed in terms of fourier components. In particular, we assume that

$$\rho' = \rho_1\, g(\theta)\, e^{i\kappa(r,\theta,t)} \tag{3}$$

where ρ_1 is the amplitude of the density perturbation and the function $g(\theta)$ specifies the angular dependence inside and external to the jet whose surface is at $\theta = \theta_o$. From equation (3) for ρ' and equations (2a), (2b), and (2c) with $v_{or} = 0$, it can be shown that velocity perturbation v' must be of the following form:

$$v_\phi' = v_{\phi 1}(r)\, \frac{g(\theta)}{\sin\theta}\, e^{i\kappa(r,\ \phi,\ t)} \tag{4a}$$

$$v_\theta' = v_{\theta 1}\,(r,\ \theta)\, e^{i\kappa(r,\ \phi,\ t)} \tag{4b}$$

$$v_r' = v_{r1}(r)\, g\,(\theta)\, e^{i\kappa(r,\ \phi,\ t)} \tag{4c}$$

and

$$v_{\phi 1}(r) = -\frac{1}{r}\,\frac{\rho_1}{\rho_o}\,\frac{(\partial\kappa/\partial\phi)}{(\partial\kappa/\partial t)}\,\left(\frac{\partial P'}{\partial \rho'}\right) \tag{5a}$$

$$v_{\theta 1}(r, \theta) = \frac{i}{r} \frac{\rho_1}{\rho_o} (\partial\kappa/\partial t)^{-1} \left(\frac{\partial P'}{\partial \rho'}\right) \frac{\partial g(\theta)}{\partial \theta} \qquad (5b)$$

$$v_{r1}(r) = - \frac{\rho_1}{\rho_o} \frac{(\partial\kappa/\partial r)}{(\partial\kappa/\partial t)} \left(\frac{\partial P'}{\partial \rho'}\right) \qquad (5c)$$

When conditions internal and external to a cylindrical jet are constant, $\kappa = kr + n\phi - \omega t$ and we identify the derivatives of $\kappa(r, \phi, t)$ in equations (5a), (5b), and (5c) as $(\partial\kappa/\partial t) = -\omega$, $(\partial\kappa/\partial\phi) = n$, and $(\partial\kappa/\partial r) = k$ where ω, n and k are constants. A perturbation is described by fourier components of form $A = A_1 \exp\left(i(kr + r\phi - \omega t)\right)$. The fourier components are waves which propagate around the cylindrical jet with angle of propagation determined by k, the wavenumber parallel to the jet axis and n the wavenumber around the jet circumference. Since waves must be periodic around the jet circumference, n is an integer. This remains true when conditions internal and external to the jet change and when the jet radius changes. In the most general case, ω and k need not remain constant but can be functions of r and we write $(\partial\kappa/\partial t) = -\omega(r)$, $(\partial\kappa/\partial r) = k(r)$ but $(\partial\kappa/\partial\phi) = n$. For an isothermal constantly expanding jet and isothermal external medium, it has been shown that $\omega(r) = \omega_o(r_o/r)$ and $k(r) = k_o(r_o/r)$. Since $R \equiv r \sin\theta$ is the instantaneous jet radius, the frequency and wavenumber of a fourier component change universely proportional to the jet radius (Hardee 1982).

Equations (2a, b, c) along with equations (4a, b, c) and (5a, b, c) can be used in equation (1) to write a differential

equation for $g(\theta)$ (equation A8, Hardee 1982). In the limit of small angular displacement from the polar axis where $\psi^2 \equiv \sin^2\theta << 1$ this differential equation can be written in the form (equation A10, Hardee 1982)

$$\psi^2 \frac{\partial^2 g(\psi)}{\partial \psi^2} + \psi \frac{\partial g(\psi)}{\partial \psi} + \{(\beta^2(r) - n^2)\psi^2 - n^2\} g(\psi) = 0 \quad (6)$$

where

$$\beta^2(r) = \frac{\omega^2(r)r^2}{a^2(r)} - k^2(r)r^2 + i\{2k(r)r + \frac{\omega(r)r^2}{a^2(r)} \frac{\partial}{\partial r} [a^2(r) \frac{k(r)}{\omega(r)}]\} \quad (7)$$

and we have assumed adiabatic perturbations to the jet for which $(\partial P'/\partial \rho') = a^2(r)$. Equation (6) becomes Bessel's equation when $\beta(r) = \beta$ independent of r. When both jet and external medium are isothermal, the sound speed is independent of r. In this case, it is clear that $\beta(r) = \beta$ independent of r if $\omega(r)r \equiv \omega$ and $k(r)r \equiv k$ are independent of r and it has been shown that this is a self-consistent solution of the resulting dispersion relation (Hardee 1982). A choice of $\omega(r)$ and $k(r)$ that will make $\beta(r)$ independent of r in the general case is not readily apparent. However, we can restrict our attention to a fixed value of r at which point equation (6) becomes Bessel's equation

$$\beta_{rn}^2 \psi^2 \frac{\partial^2 g(\psi)}{\partial(\beta_{rn}\psi)^2} + \beta_{rn}\psi \frac{\partial g(\psi)}{\partial(\beta_{rn}\psi)} + [\beta_{rn}^2\psi^2 - n^2] g(\psi) = 0 \quad (8)$$

where $\beta_{rn}^2 \equiv \beta^2(r) - n^2$.

The solution of equation (8) gives $g(\psi) = c_1 J_n(\beta_{rn}\psi) + c_2 N_n(\beta_{rn}\psi)$ where J_n and N_n are the Bessel and Neuman functions, respectively. The subsequent derivation of the dispersion relation is given in Appendix A of Hardee (1982) and can be summarized as follows: The result for $g(\psi)$ is used to find the dependence of $v_{\theta 1}(r, \theta)$ on the angle θ. This result and equation (3) for ρ' can be combined with equation (4b) to write an equation for the velocity perturbation in the θ direction. If the displacement of the jet boundary is written in terms of velocity perturbation inside and outside the jet and the two expressions are equated, an eigenvalue equation for adiabatic perturbations to the surface of discontinuity is the result:

$$\frac{\beta^{in}_{rn}}{\omega_{in}^2(r)\rho_{in}(r)} \frac{J_n'(\beta^{in}_{rn}\Psi)}{J_n(\beta^{in}_{rn}\Psi)} = \frac{\beta^{ex}_{rn}}{\omega_{ex}^2(r)\rho_{ex}(r)} \frac{H_n^{(1)'}(\beta^{ex}_{rn}\Psi)}{H_n^{(1)}(\beta^{ex}_{rn}\Psi)} \quad (9)$$

where $\Psi \equiv \sin\theta$.

If we specify $\omega_{ex}(r) = \omega$ and $k_{ex}(r) = k$ then $\omega_{in}(r) = \gamma(\omega - ku)$ and $k_{in}(r) = \gamma[k - (\omega/c^2)]$ with result that

$$\beta^{ex}_{rn} = \{\frac{\omega^2 r^2}{a_{ex}^2} - k^2 r^2 - n^2 + ikr\,[2 + \frac{2r}{a_{ex}} \frac{\partial a_{ex}}{\partial r} - \frac{r}{v^*_{ph}} \frac{\partial v^*_{ph}}{\partial r}]\}^{1/2} \quad (10a)$$

and

$$\beta^{in}_{rn} = \{\gamma^2 \frac{(\omega - ku)^2 r^2}{a_{in}} - \gamma^2[k - (u/c^2)\omega]^2 r^2 - n^2 + i\gamma[k - (u/c^2)\omega] r \cdot \quad (10b)$$
$$[2 + \frac{2r}{a_{in}} \frac{\partial a_{in}}{\partial r} - r\{(v^*_{ph} - u)^{-1} + (u^2/c^2)\,[u - (u^2/c^2)\, v^*_{ph}]^{-1}\} \frac{\partial v^*_{ph}}{\partial r}]\}^{1/2}$$

where $v^*_{ph} \equiv (\omega/k)$. The isothermal case is the case for which $\partial a/\partial r = 0$ and $\partial v^*_{ph}/\partial r = 0$. For the more general case we expect the sound speeds and complex phase velocity to be slowly varying functions of r. When $\beta^{ex}_{rn} \equiv kr\zeta_{rn}$ and $\beta^{in}_{rn} \equiv kr\xi_{rn}$ equation (9) takes on the form (A23 Hardee 1982)

$$\frac{J_n'(k\Psi\xi_{rn})}{J_n(k\Psi\xi_{rn})}\frac{H_n^{(1)}(k\Psi\zeta_{rn})}{H^{(1)'}(k\Psi\zeta_{rn})}\frac{\xi_{rn}}{\zeta_{rn}} = \gamma^2\eta\frac{(\Phi-M_{in})^2}{\Phi^2} \qquad (11)$$

which is identical to that for jets of cylindrical cross section but with η, M_{in} and Φ now functions of r and ξ_{rn} and ζ_{rn} contain derivatives of a and v^*_{ph}. Given a particular model for the jet and the external medium which specifies P, ρ_{in} and ρ_{ex} as functions of r we can use equations (10) along with an estimate of v_{ph}^* to provide a first order estimate for propagation and growth of the eigenmodes of equation (11).

III. The Adiabatic Jet

Suppose we consider the case of adiabatically expanding jet in an isothermal external medium. This is the case if there is little energy dissipation and it follows that the jet velocity remains constant. In this example we will also consider the jet to be constantly expanding with radius $R = r\Psi$. We assume that the jet is in static pressure balance with the external medium and that the pressures can be written as $P_{ex} = P^{o}_{ex}\rho_{ex}^{\gamma_{ex}}$ and $P_{in} = P^{o}_{in}\rho_{in}^{\gamma_{in}}$. The restriction of static pressure balance requires that $M_{in} = u/a_{in} \propto \rho_{in}^{(\gamma_{in} - 1)/2}$ and that $\eta = \rho_{in}/\rho_{ex} \propto \rho_{in}^{-(\gamma_{in}/\gamma_{ex}-1)}$. For the adiabatic jet and isothermal external medium $\gamma_{in} = \Gamma_{in}$ and $\gamma_{ex} = 1$. Jet density decreases with $\rho_{in} \propto (r\Psi)^{-2}$ and the internal pressure decreases with $P_{in} \propto (r\Psi)^{-2\Gamma_{in}}$. For convenience we will choose the adiabatic index $\Gamma_{in} = 3/2$. Static pressure balance requires that conditions in the jet and external medium vary as indicated in Table 1 with $x = 3$. Of particular interest to us is the fact that this set of assumptions means that the jet Mach number $M_{in} = M^{o}_{in}(r\Psi)^{1/2}$ and that the density ratio $\eta = \eta^{o}(r\Psi)$ and both are increasing along the jet. Since the external medium is isothermal $M_{ex} = u/a_{ex}$ remains constant.

Some changes in the growth rate and maximally unstable wavenumber resulting from inclusion of the gradients in sound speed and wave phase velocity in the wave dispersion equation (11) might be expected. Analytically we can compute the sizes of the different terms in

equations (10). The jet sound speed $a_{in} = a^{o}_{in}(r\Psi)^{-1/2}$ and the gradients of the complex phase velocity, v^{*}_{ph}, can be computed in some limiting cases. The complex phase velocity can be written as $v^{*}_{ph} = \alpha(\eta)u + i\,\beta(\eta)u$ provided the ratio $k/k^{p} \sim 1$ or k is much less than or much greater than k^{p}, where $k^{p}$is the fastest growing wavenumber. If we specialize to the helical wave mode $\alpha(\eta)$ and $\beta(\eta)$ are given by

$$\alpha_1(\eta) \sim \begin{cases} \eta/(1+\eta) & k_1 << k_1^{p} \\ \log\left[(1.6 + 10\eta^{0.5})/(1.6 + \eta^{0.5})\right] & k_1 \sim k_1^{p} \\ 1 - M_{in}^{-1} & k_1 >> k_1^{p} \end{cases} \tag{12}$$

$$\beta_1(\eta) \sim \begin{cases} \eta/(1+\eta) & k_1 << k_1^{p} \\ \log\left[1.0 + 1.7\eta^{0.3}/(1.0 + 2.3\eta^{0.7})\right] & k_1 \sim k_1^{p} \\ 0 & k_1 >> k_1^{p} \end{cases}$$

For the helical wave mode the maximally growing wave-number k_1^{p} corresponds to a wave with wavelength

where

$$\lambda^{p}_{1} \sim [f(\eta)M_{in} - 2.5]\,R \tag{13}$$

$$f(\eta) \sim 4.2/(1.0 + \eta^{0.5})$$

(Hardee 1983). We find that the contribution from these additional terms is on the same order as terms involving jet expansion. Terms involving jet expansion were found to affect growth rate and maximally unstable wavenumber on the 10% level.

In order to fully consider all possibilities, let us assume that a jet might initially be much less dense than the surrounding medium and be only weakly supersonic. Parameters for seven positions along such a jet are given in Table 2. Distance along the jet is normalized to the point at which the jet density is equal to the external density. For our particular choice of parameters, static pressure balance requires that the jet Mach number in the external medium be $M_{ex} = 14$. While we have chosen this set of parameters to illustrate the effects of changing η and M_{in} a real jet might be propagating with velocity $u \sim 9 \times 10^8$ cm s^{-1} through an external medium with temperature $T_{ex} \sim 1.5 \times 10^7$K and sound speed $a_{ex} \sim 6.5 \times 10^7$ cm s^{-1}. Figure 1 shows the growth rate ω_I (R/u) as a function of the wavenumber $k = 2\pi R/\lambda$ of the helical wave mode. For these calculations, we have set $\Psi = 0.04$. The results displayed in Figure 1 can be compared with results obtained for an isothermal jet and external medium (Hardee 1982). We find that the wave phase velocity, the growth rate, and the maximally unstable wavenumber are only minimally affected by the inclusion of the gradient terms. Thus, expressions for wave phase velocities and the maximally unstable wavenumber will be relatively independent of the rate of jet expansion or the rate of change of sound speeds and densities.

We are particularly interested in following the growth rate and wavelength evolution of helical waves as they are convected outwards on a jet. For an isothermal jet, it was shown that the wavelengt was proportional to the jet radius. This particular solution occurred because the density ratio and Mach number

remained, constant with result that the wave phase velocity, v_{ph}, and the ratio λ_1/λ_1^p remained constant. This is no longer the case for an adiabatic jet. On the adiabatic jet, v_{ph} is a function of the density and wavelength relative to λ_1^p (see eq. 12) and λ_1^p is a function of density ratio and Mach number. Following the development of a wave with initial wavelength λ_1 is accomplished by first ascertaining the evolution of the wavelength as the wave propagates outward and then computing the growth rate corresponding to the appropriate wavelength and position on the jet. For propagating waves the real part of the wave frequency should remain an invarient along the jet. For an expanding jet, the quantity $\omega_R(R/u)$ is an invarient and the frequency ω_R is inversely proportional to the instantaneous jet radius (Hardee 1982). This means that the wavelength of waves propagating on the jet surface will scale with the wave phase velocity as well as the jet radius and $\lambda = [\alpha(\eta)/\alpha(\eta_o)]\ (R/R_o)\ \lambda^o$ where η_o, R_o, and λ^o are the density ratio, jet radius, and wavelength at any arbitrary position along the jet. In the long and short wavelength limits $\alpha_1(\eta)$ is given by equation (12) and helical waves in these wavelength limits will evolve with wavelength given by

$$\lambda_1(r) \sim \begin{cases} (\eta/\eta_o)[(1+\eta_o)/(1+\eta)]\ (R/R_o)\lambda_1(r_o) & \lambda^o{}_1 >> \lambda^p{}_1 \\ (M^o{}_{in}/M_{in})[(1+M_{in})/(1+M^o{}_{in})](R/R_o)\lambda_1(r_o) & \lambda^o{}_1 << \lambda^p{}_1 \end{cases} \quad (14)$$

In general, helical waves with initial wavelength within an order of magnitude of λ^P_1 must be followed numerically. Figure 2 shows the phase velocity of helical waves as a function of wavenumber for the seven positions along the jet. The dashed line shows how k^P_1 changes along the jet. Note that vertical lines correspond to changes in wavelength proportional to the jet radius. The dashed and dotted lines show the evolution of the wavenumber for four separate cases of initial wavenumber: (a) $k^o_1 < k^P_1$, (b) $k^o_1 \lesssim k^P_1$, (c) $k^o_1 \gtrsim k^P_1$, and (d) $k^o_1 > k^P_1$. For cases (a) and (d) in which the initial wavenumber is about one order of magnitude away from $k_1{}^P$ the change in helical wavelength is given reasonably well by equation (13). We also find that the change in helical wavelength for case (c) in which the initial wavelength is $k_1{}^P$ is given reasonably well by using the value of $\alpha_1(\eta)$ when $k_1 \sim k^P_1$ (eq. 12). However, a similar analytic approach when $k_1 \lesssim k^P_1$ like case (b) fails to be sufficiently accurate. We conclude that waves with wavelength a few times longer than $k_1{}^P$ initially must be followed numerically.

The rate of growth of any helical wave is found by computing the number of e-foldings that the wave undergoes as it propagates out along a jet. The wave amplitude grows as $A = A_o e^{N_e}$ and N_e, the number of e-foldings, is given by

$$N_e = \int^r_{r_o} l_e^{-1}(r)\, dr \qquad (15)$$

where $l(r) = v_{ph}(r)/\omega_I(r)$ is the instantaneous e-folding length. With $v_{ph}(r) = \alpha_1(\eta)u$ and $\omega_I(r) = \beta_1(r)k_1(r)u$

where $k_1(r) = [\alpha_1(r_o)/\alpha_1(r)]\ (r_o/r)\ k_1(r_o)$ we can write equation (14) in the form

$$N_e = \alpha_1(r_o)\ k_1{}^o\Psi^{-1} \int^r_{r_o} \beta_1(r)\ \alpha_1{}^{-2}(r)\ r^{-1}dr, \qquad (16)$$

where

$$k^o{}_1\Psi^{-1} = k_1(r_o)r_o.$$

For helical waves with initial wavelength $\lambda_1 >> \lambda^p{}_1$ we can use the long wavelength forms for α_1 and β_1(eq. 12) with result that

$$N_e \simeq \frac{\eta_o}{1+\eta_o}\ k^o{}_1\Psi^{-1} \int^{\eta}_{\eta_o} (1+\eta)\eta^{-5/2}\ d\eta \qquad (17)$$

when $k^p{}_1 << k_1{}^p$.

While equation (17) can be integrated exactly the assumption that $\eta_o << \eta$ reveals an interesting upper limit to N_e which is

$$N_e < 2/3\eta_o{}^{-1/2}\ [(1 + 3\eta_o)/(1 + \eta_o)]\ k^o{}_1\Psi^{-1} \qquad (18)$$

valid when $k^o{}_1 << k^p{}_1$. For initial wavelengths within an order of magnitude of the maximally unstable wavelength, the number of e-foldings can be obtained numerically. In table 3 we show the number of e-foldings between the seven positions on the jet for four initial wavenumbers (cases (a), (b), (c), and (d) in figure 2). The total number of e-foldings for a particular evolving

helical wave is found by summing the appropriate column. For example, the helical wave with initial wavelength $\lambda_1 \gtrsim \lambda_1^P$ (case b) would e-fold 18 times between positions 1 and 2, 14 times between positions 2 and 3, etc. We learn three things from this computation. First it is clear that the fastest growing helical wavelengths will be longer than λ_1^P. Second, the large number of e-foldings that occur when the Mach number is low , between positions 1 and 3, imply that "light" jets must have initial Mach numbers greater than about five to be reasonably stable to helical waves. Third, there is an upper limit to the number of e-foldings for any initial helical wavelength and the maximum number of e-foldings is a function of the initial conditions.

Now let us consider the case of a "heavy" jet with initial density equal to the density in the surrounding medium. For purposes of comparison with the previous case of a "light" jet, we assume that the jet is weakly supersonic initially. Parameters for this jet at six positions along the jet are given in Table 4. Our choice of initial density ratio and Mach number and assumption of static pressure balance imply that the Mach number in the external medium be $M_{ex} = 2.4$. If $T_{ex} \sim 1.5 \times 10^7$ K and $a_{ex} \sim 6.5 \times 10^7$ cm s^{-1} the jet velocity would be $u \sim 1.6 \times 10^8$ cm s^{-1}. Figure 3 shows the growth rate ω_I (R/u) as a function of the wavenumber $k = 2\pi R/\lambda$ of the helical wave mode for the six positions along the jet. Note that the maximally unstable wavenumber is increased compared to the "light" jet and that the growth rate is more sharply peaked with reduced plateau at higher wavenumbers. These changes are the result of the

increased density of the "heavy" jet. The wavelength of helical waves with initial wavelength more than an order of magnitude different from λ^P_1 evolve according to equation (14) and an upper limit to the number of e-foldings of helical waves with initial wavelength more than an order of magnitude different from λ^P_1 is given by equation (18). For waves with initial wavelength within an order of magnitude of the maximally unstable wavelength we obtain the number of e-foldings numerically. Figure 4 shows the wave phase velocity as a function of wavenumber for the six positions along the "heavy" jet and shows the evolution of the wavenumber for four separate cases of initial wavenumbers: (a) $k^o_1 < k^P_1$, (b) $k^o_1 \lesssim k^P_1$, (c) $k^o_1 \gtrsim k^P_1$, and (d) $k^o_1 > k^P_1$. For cases (a) and (d) in which the initial wavenumber is about one order of magnitude away from k^P_1 the wavelength evolution is given reasonably well by using $\alpha_1(\eta)$ when $k_1 \sim k_1{}^P$ (eq. 12). The wave phase velocity changes much less along the "heavy" jet compared to the "light" jet, but the resulting change in wavelength is still important.

For helical waves with wavelength more than an order of magnitude greater than λ^P_1 the upper limit to the number of e-foldings is given by equation (18) as before. The number of e-foldings for helical waves with shorter wavelength is given for the cases (a), (b), (c), and (d) in Table 5. If the initial Mach number is low, the fastest growing waves are those with wavenumber $k_1 \gtrsim k_1{}^P$. This result is different from what we found on the "light" jet on which the fastest growing helical waves are those with $k_1 \lesssim k_1{}^P$. If the initial Mach number is greater

than about 5, wavegrowth is about equally rapid for a broad wavenumber region around k_1^P (see cases (b) and (c) for N_e between positions 3 to 6). We also find that the intial Mach number needs to be greater than about 5 for the jet to be reasonably stable to helical waves. This suggests that there is little difference in stability properties of jets over a broad range of density ratio. We can see this by directly comparing the fastest growing helical wave on the "light" jet with the fastest growing helical wave on the "heavy" jet. To eliminate the effect of different Mach numbers, begin at position 3 for case (b) on the "light" jet (Table 3) and position 2 for case (c) on the "heavy" jet (Table 5). Comparison shows approximately the same number of e-foldings between successive positions independent of the density ratio. The principal difference between "light" and "heavy" jets is the difference in the range of wavelengths which grow the most rapidly.

IV. Discussion

It is useful to compare our present results with earlier results obtained for an isothermal expanding jet. For the isothermal jet $\gamma_{in} = 1$ and the temperature in the jet is constant. The assumption of constant expansion and static pressure balance with an isothermal external medium means that $\rho_{ex} \propto (r\Psi)^{-2}$, $x = 2$ in Table 1, and $\eta = \eta_o$ remains a constant. Since the density ratio and Mach numbers are constants, the variation in growth rate and maximally unstable wavelength is a function of jet radius only, while the wave phase velocity remains constant if the ratio k_1/k_1^P remains constant. The self-consistent solution is the one for which the ratio k_1/k_1^P and the wave phase velocity are constant. Therefore, all waves scale with jet radius only, and the fastest growing helical wave has wavelength λ^P_1. For this case equation (15) for N_e becomes

$$N_e = [\beta_1^P/\alpha_1^P]\, k_1^P(r)\Psi^{-1}\, \ln(r/r_o) \qquad (19)$$

where α_1^P and β_1^P are constants given by equation (17) and $k_1^P(r_o)$ is the maximally growing wavelength at the initial position r_o. For $\eta = 1$ and $\lambda^P_1 \sim 2.1 M_r R$ equation (19) becomes

$$N_e \sim 0.83(M_{in}\Psi)^{-1}\, \ln(r/r_o). \qquad (20)$$

and we have ignored the slow variation of N_e as a function of η. Thus, on the isothermal jet helical twisting should have a characteristic wavelength of λ^P_1 given by equation (13) and the

wave amplitude will grow as

$$A \sim A_o (r/r_o)^{0.83/M_{in}\Psi} \qquad (21)$$

where $A = A_o e^{N_e}$, N_e is given by equation (20) and A_o and r_o are the initial amplitude and position, respectively. Note that $M_{in}\Psi < 1$ for static pressure confinement.

Now let us consider the response of an adiabatically expanding jet to helical twisting. As an example, we assume a jet with density ratio $\eta = 0.1$ and initial Mach number $M_{in} = 4.7$. This corresponds to position 3 along the "light" jet (see Table 2). We also pick $\Psi = 0.06$ which gives the jet an opening angle of about 7°. Table 6 shows how the adiabatic jet evolves and shows the number of e-foldings the fastest growing helical wave undergoes between successive positions along the jet. The number of e-foldings shown here is less than the number of e-foldings in Table 3 for the fastest growing wave (case (b) $k_1 \lesssim k_1^p$) because we have assumed a more rapidly expanding jet with $\Psi = 0.06$ instead of $\Psi = 0.04$. For illustrative purposes, we have chosen $r = 5$ Kpc when $\eta = 1$. The wavelength of the helical wave at the point of maximum growth at each position, calculated from equation (13), is given in the final column of the Table. Recall that the helical wave which will actually grow the most rapidly will have a wavelength longer than λ^p_1. Thus the characteristic helical wavelength on the adiabatically expanding jet will be greater than the instantaneous value of λ^p_1 and our earlier results indicate that the characteristic wavelength could

be a factor of 2 or so greater than the instantaneous value of λ^{P}_{1}. The maximum number of e-foldings that the fastest growing helical wave experiences in this example is $N_e^{max} \sim 8$. Thus along the adiabatic jet, the maximum possible amplification in amplitude of helical twisting is a factor of about 3000. For identical initial conditions, i.e., $M_{in} = 4.7$ and $\Psi = 0.06$, the amplitude of helical twisting on an isothermal jet increases according to equation (21) as $(r/r_o)^3$. An amplification factor of 3,000 is reached at a distance 10 times the initial distance or by 5 Kpc in our example. Note that if growth were exponential, the amplification factor would be $e^{10} \sim 22,000$ at 5 Kpc. In reality this implies that a "linear" description of wave growth more closely approximates reality on the adiabatically expanding jet on which wave amplitudes grow more slowly.

These calculations show that changing jet conditions such as occur along an adiabatically expanding jet have a large impact on the growth of perturbations to the jet surface. While we have only considered growth of the helical wave mode in detail, the related fluting wave modes will behave similarly. The difference in wave growth between an adiabatically expanding jet and an isothermallly expanding jet are solely the result of variations in the phase velocity of propagating waves, and the rapid increase in the maximally unstable wavelength with consequent rapid decrease in the maximum growth rate which occurs along an adiabatically expanding jet. Our comparison between these two cases reveals two important fundamental consequences. Firstly, the characteristic wavelength associated with helical twisting

will only be within a factor of 2 or so of the instantaneous maximally unstable wavelength. The calculations also reveal that a broad range of wavelengths can grow at about the same rate. Thus, the characteristic wavelength that appears on a jet may depend on conditions near the jet origin and details of the initial wave excitation. Secondly, the rate of wave growth is considerably reduced by cooling jet expansion and wave growth of a particular wave can effectively cease as the wave propagates out along a jet. We have also found that the maximum number of e-foldings for a particular wave is sensitively dependent on the initial conditions where the wave is produced.

Suppose we consider the implication of these results for an expanding extragalactic jet. Necessarily we must restrict ourselves to qualitative analysis because a quantitative comparison with real jets can only be made when calculations are performed for a specific model of the jet and the external medium. Note that a more realistic model will be one in which the jet cools more slowly than adiabatically and the temperature in the external medium increases, i.e., cooling accretion flow. Nevertheless, the present calculations will be similar to this more realistic case. A more slowly cooling jet combined with slowly warming external medium will result in approximately the same increse in the jet density relative to the density in the external medium so the effect will be about the same. The primary difference will be the slower increase in jet Mach number because of the slower jet cooling. This implies somewhat faster wave growth and shorter characteristic wavelength but

qualitatively the results will be similar on such a jet. We expect the initial point of wave excitation to be near the origin of the jet. Because the true wavelength of helical waves is on the order of several times the jet radius, random perturbations to the jet surface can produce only very small amplitude helical waves. From the point of view of a fourier analysis of the perturbation most of the power is in shorter wavelengths which will be associated with higher order fluting wave modes. Even if initial amplitudes are very small, our calculations imply that the jet Mach number must be sufficiently suspersonic at the point of wave excitation, because wave growth is extremely rapid if the Mach number is less than about four (see Tables 3 and 5). While faster jet expansion than used for the calculation in Tables 3 and 5 decreases the number of e-foldings, nearly free jet expansions would be required of an initially low Mach number jet to keep wave amplitudes from becoming large. Either case would seem to rule out jet formation by a deLaval nozzle in which the flow must go through a transonic region before becoming suspersonic. We take our results to imply that jets must be formed with initially high Mach numbers, say $M > 4$. If jets were produced with lesser Mach numbers they should show large amplitude helical twisting near the origin with amplitude regulated by non-linear effects.

There is at least one additional interesting consequence of wave growth on a cooling expanding jet that is a result of the rapidly decreasing growth rate as waves propagate out along the jet that would be particularly obvious if jet expansion were to

be reduced. It is clear that waves can grow rapidly and be convected far enough from the maximally unstable wavelength that growth effectively ceases. From this point, the waves amplitude remains approximately constant. If, at the same time, jet expansion ceases or slows, these waves propagate along the jet with approximately constant amplitude. If jet expansion continues or begins again, these waves would disappear when the jet radius became large relative to the wave amplitude. While some wavelengths disappeared, longer wavelengths may appear because amplification is now more rapid at a longer wavelength. This behavior is suggested by examing Table 5 in which we see helical waves with wavelength $\lambda \sim \lambda^P$ growing most rapidly but those with $\lambda > \lambda^P$ growing equally rapidly further out along the jet. Because waves with longer wavelengtn can reach greater amplitude before non-linear effects become important, i.e., motions of the fluid at the sound speed transverse to the flow velocity in the wave frame mean larger transverse oscillation for longer wavelength, these initially more slowly growing waves can come to dominate. In general, we might expect these transitions to result in changes in the characteristic wavelength by factors of 2 or 3 but not by an order of magnitude.

Finally we note that the existence of precession of the central power source may provide the initial trigger for wave like helical twisting. In fact, if the jet is not ballistic, i.e., 'light" jet, the helical twisting induced by precession propagates as a wave phencmenon. The manner of wave propagation and growth if its wave amplitude is small is exactly as

described by the dispersion relation (eq. 11) in Section II. If this is the case, then the precession frequency can be related to observed helical twisting only after the wave propagation effects are taken into account. This implies faster precession frequencies than would be assumed if the jet were ballistic because long wavelength, low frequency helical twisting evolves from shorter wavelength, higher frequency helical twisting at the origin. Also in this case, amplitude growth is not strictly linear but is governed at small amplitude by the growth rate found from the linearized dispersion relation .

References

Benford, G. 1981, Ap.J., 247, 792.

Ferrari, A., Trussoni, E., and Zaninetti, L., 1981, M.N.R.A.S., 196, 1051.

Ferrari, A., Massaglia , S., and Trussoni, E., 1982, M.N.R.A.S., 198, 1065.

Hardee, P. E., 1979 Ap.J., 234, 47.

Hardee, P. E., 1982, Ap.J., 257, 509.

Hardee, P. E., 1983, Ap.J., 252, 775.

Hardee, P. E., 1983, Ap.J., (in press).

Ray, T. P., 1981, M.N.R.A.S., 196, 195.

TABLE 1

Variation in density temperature and sound speed for an adiabatic jet and arbitrary external medium in static pressure balance.

$$P_{in} = P^{o}_{in}(r\Psi)^{-2\Gamma_{in}} \qquad P_{ex} = P_{in}$$

$$\rho_{in} = \rho^{o}_{in}(r\Psi)^{-2} \qquad \rho_{ex} = \rho^{o}_{ex}(r\Psi)^{-x}$$

$$T_{in} = T^{o}_{in}(r\Psi)^{-2(\Gamma_{in}-1)} \qquad T_{ex} = T^{o}_{ex}(r\Psi)^{-2(\Gamma_{in}-x/2)}$$

$$a_{in} = a^{o}_{in}(r\Psi)^{-(\Gamma_{in}-1)} \qquad a_{ex} = a^{o}_{ex}(r\Psi)^{-(\Gamma_{in}-x/2)}$$

For static pressure balance $x = 2\gamma_{in}/\gamma_{ex}$ and we have set $\gamma_{in} = \Gamma_{in}$.

TABLE 2

Parameters at seven positions along a "light" jet

Position #	$(r/r_1) = \eta$	M_{in}	$k_1{}^P = 2\pi R/\lambda^P{}_1$ (± 10%)
1	0.015	1.8	1.50
2	0.03	2.6	0.95
3	0.10	4.7	0.50
4	0.30	8.1	0.33
5	1.0	14.8	0.23
6	3.0	25.6	0.18
7	10.0	46.7	0.14

TABLE 3

Numbers of e-foldings, N_e, between the seven positions along the "light" jet with opening angle corresponding to $\Psi = 0.04$.

Position #	M_{in}	(a) $k_1 < k^P{}_1$	(b) $k_1 \lesssim k^P{}_1$,	(c) $k_1 \gtrsim k^P{}_1$	(d) $k_1 > k^P{}_1$
1	1,8	--	--	--	--
2	2.6	18	18	11.5	2.9
3	4.7	12	14	8.4	2.0
4	8.1	3.1	5.5	3.3	0.7
5	14.8	1.0	3.0	1.7	0.3
6	25.6	0.3	1.4	0.8	0.2
7	46.7	0.2	0.8	0.4	0.1

TABLE 4

Parameters at six positions along a "heavy" jet

Position #	$(r/r_1) = \eta$	M_{in}	$k^P{}_1 = 2\pi R/\lambda^P{}_1$ (±10%)
1	1	2.6	2.5
2	3	4.5	1.6
3	10	8.2	1.1
4	30	14.2	0.90
5	100	26.0	0.75
6	300	45.0	0.70

TABLE 5

Number of e-foldings, N_e, between the six positions along the "heavy" jet.

Position #	M_{in}	(a) $k_1 < k^P_1$	(b) $k_1 \lesssim k^P_1$	(c) $k_1 \gtrsim k^P_1$	(d) $k_1 > k^P_1$
1	2.6	--	-- --	--	--
2	4.5	1.6	6.4	12.9	0.1
3	8.2	0.8	5.6	6.3	0.9
4	14.2	0.4	2.7	2.6	0.6
5	26.0	0.2	1.6	1.5	0.4
6	45.0	0.1	0.8	0.7	0.2

TABLE 6

Conditions and number of e-foldings of the fastest growing helical wave along an adiabatically expnding jet with opening angle of about 7° ($\Psi = 0.06$).

M_{in}	n	r(kpc)	$R = r\Psi$(pc)	$N_e(k_1 < k^P_1)$	λ^P_1
4.7	0.1	0.5	30	--	12.5R
8.1	0.3	1.5	90	3.7	19.5R
14.8	1.0	5	300	2.0	28.6R
25.6	3.0	15	900	0.9	39.4R

Figure Captions

Figure 1: Growth rate, $\omega_I(R/u)$, of the helical wave mode as a function of the wavenumber, $k = 2\pi R/\lambda$, for seven positions along the adiabatically expanding "light" jet.

Figure 2: Phase velocity, v_{ph}/u, of the helical wave mode as a function of the wavenumber, $k = 2\pi R/\lambda$ for seven positions along the "light" jet. The dashed line gives the position of the maximally unstable wavenumber and the dashed and dotted lines show the evolution of the wavenumber of a propagating helical wave for cases (a) $k < k^P$, (b) $k \lesssim k^P$, (c) $k \gtrsim k^P$, and (d) $k > k^P_1$.

Figure 3: Growth rate, $\omega_I(R/u)$, of the helical wave mode as a function of the wavenumber, $k = 2\pi R/\lambda$, for six positions along the adiabatically expanding "heavy" jet.

Figure 4: Phase velocity, v_{ph}/u, of the helical wave mode as a function of the wavenumber, $k = 2\pi R/\lambda$, for six positions along the "heavy" jet. The dashed line gives the position of the maximally unstable wavenumber and the dashed and dotted lines show the evolution of the wavenumber of a propagating helical wave for cases (a) $k < k^P$, (b) $k \lesssim k^P$, (c) $k \gtrsim k^P$, and (d) $k > k^P$.

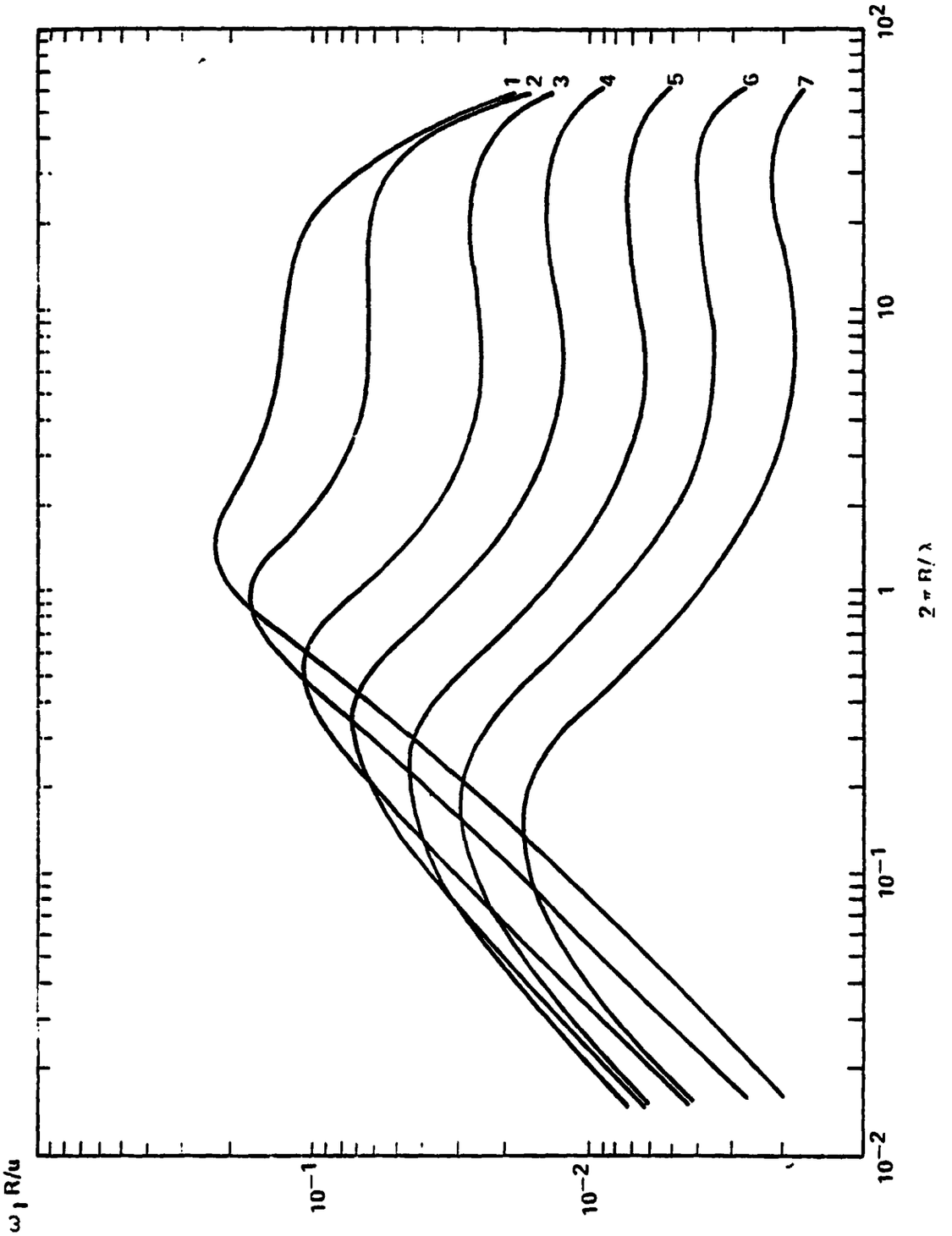

Figure 1.

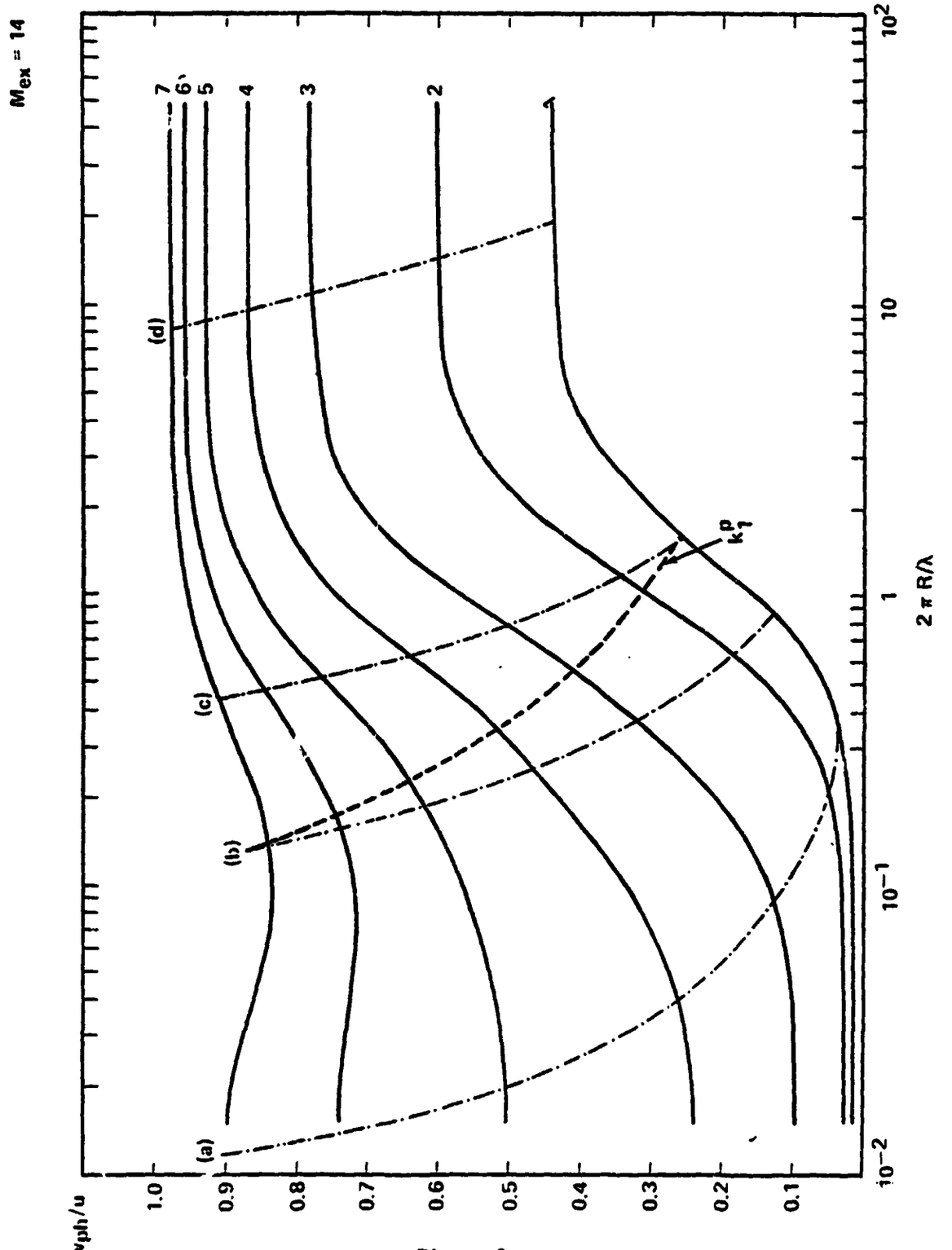

Figure 2.

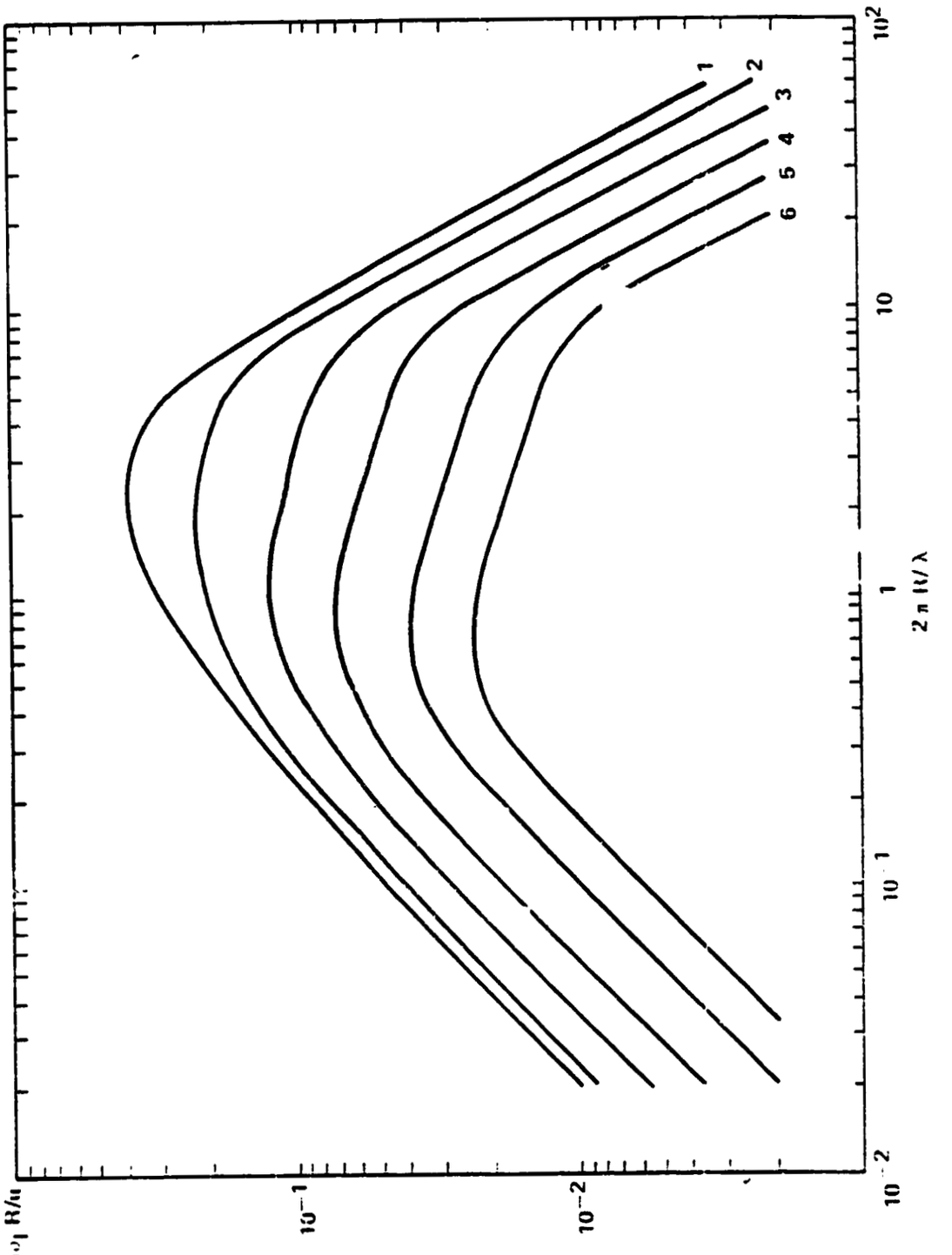

Figure 3.

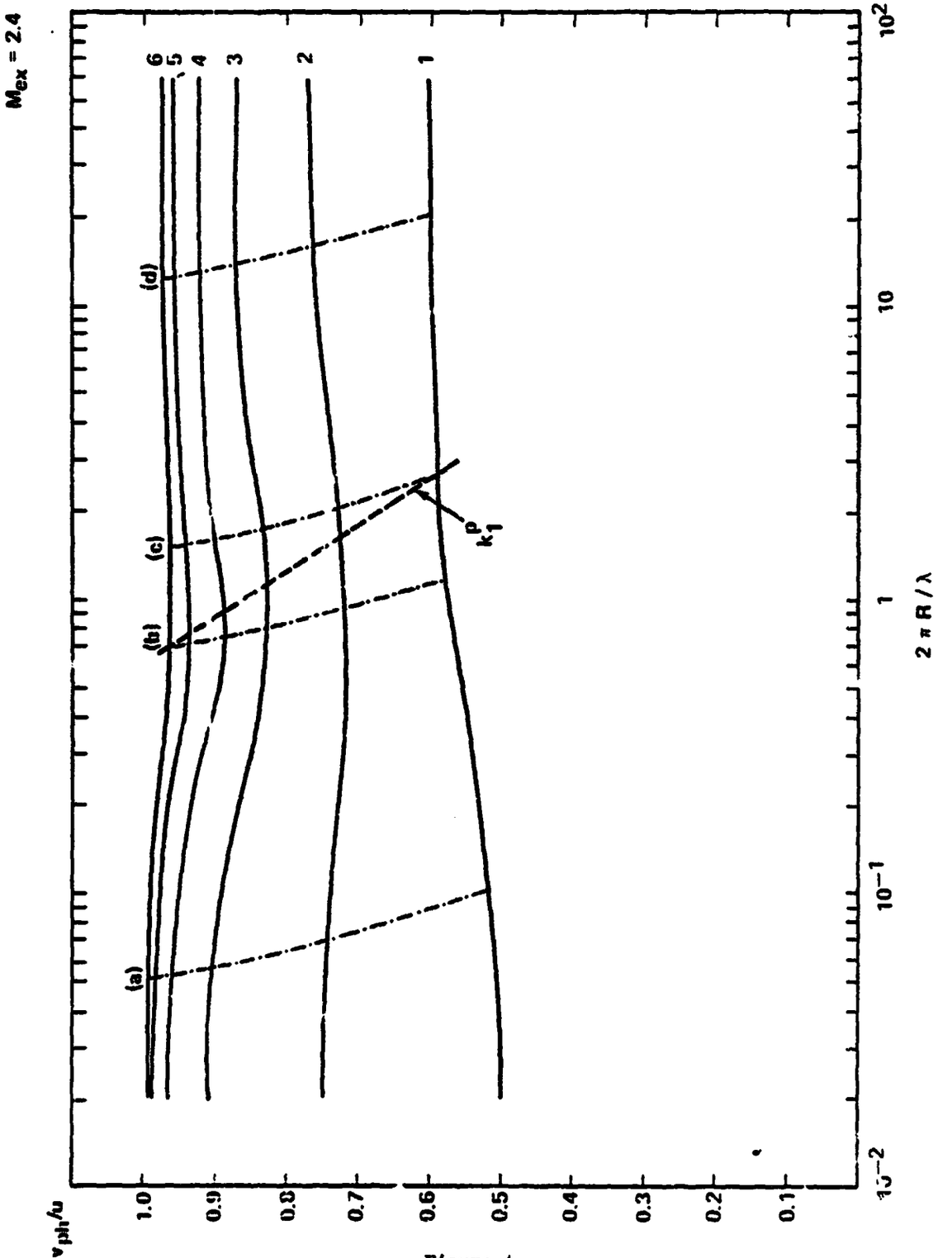

Figure 4.

N84 16039

1983

NASA/ASEE SUMMER FACULTY RESEARCH FELLOWSHIP PROGRAM

MARSHALL SPACE FLIGHT CENTER

THE UNIVERSITY OF ALABAMA

CHARACTERISTICS OF RF LIGHTNING EMISSIONS AT 2 GHz AND 250 MHz

PREPARED BY:	FEREYDOUN JALALI, PH. D.
ACADEMIC RANK:	ASSOCIATE PROFESSOR
UNIVERSITY AND DEPARTMENT:	ELECTRONIC ENGINEERING TECHNOLOGY
NASA/MSFC:	
LABORATORY	INFORMATION & ELECTRONIC SYSTEMS
DIVISION	COMPUTER AND COMMUNICATION
BRANCH	COMMUNICATIONS SYSTEMS
MSFC COUNTERPART:	DONALD STONE
DATE:	AUGUST 1983
CONTRACT NO:	UNIVERSITY OF ALABAMA IN HUNTSVILLE NGT 01-008-021

C-5

ACKNOWLEDGEMENT

The project started with some of the key equipment malfunctioning apparently as a result of having sustained a close strike!

The troubleshooting and repair of the system provided the opportunity for me to experience the fine spirit of cooperation that exists among the branch personnel. My sincere thanks to Messrs. Bill Reed, Leon Bell, Al Kosis, Ed Gleason, Grover Tucker, and Dave Harris for all their assistance in putting the system back on its feet.

Also it gives me great pleasure to thank Mr. Lee Malone for his continued support and useful suggestions and Mr. Don Stone, my counterpart, for all of his help and encouragement and for driving to the "Anderson Road Trailer" at odd hours (often on weekends) in our pursuit of lightning data.

CHARACTERISTICS OF RF LIGHTNING EMISSIONS AT 2 GHZ AND 250 MHZ

F. JALALI
ASSOCIATE PROFESSOR, EET DEPARTMENT
FORT VALLEY STATE COLLEGE

ABSTRACT

Radio frequency emissions in the S-band and VHF range from lightning discharges are recorded by a facility developed at MSFC as part of a feasibility study of a satellite-based lightning mapping system. The recording facility receives rf emissions in both vertical and horizontal polarization and stores the data on magnetic tape. Output from any one antenna may also be selected for high speed digitization and disk storage. Improvement in both hardware and software have enhanced significantly the accuracy of data characterization and the speed of data collection.

Emission records at VHF have higher signal strength than the S-band as expected. The records of cloud-to-ground discharges obtained so far give a 7-33 V/M peak equivalent signal strength (1 KHz at 10 kilometer) in the S-band range. The CG discharge structure is recognizable in most of the data collected. Considerable rf activity is present throughout the VHF records. The S-band data shows signals associated with limited portions of discharge history. The records obtained are from lightning activities within a 10 mile range.

Introduction and Ojectives

Considerable interest, both scientific and commercial, in lightning information has lead NASA to study the feasibility of a satellite-based lightning mapping system. (1) This has involved consideration of systems based on detecting the optical and/or radio frequency emissions from lightning.

A system based on RF detection requires operation in or above the VHF range in order to avoid the ionospheric effects on propagation present at the lower frequencies and to limit antenna size. Since the characteristics of lightning emissions at the desired frequency range have not been fully defined, a RF lightning program was initiated at MSFC for collecting emission data at 2.0 GHz and 250 MHz. A recording facility was implemented and its basic element set up in 1981; it was enhanced and completed in 1982 and some data collected. The program was continued with the objective of acquiring a large number of emission records in 1983. This has not been completely realized because of the unusually dry summer. Only two local thunderstorms (on July 14 and 17) produced significant activity from which data was collected.

This report outlines the measurement system and data collection procedure and presents the results of the analysis of the emission data that has been obtained.

RECORDING SYSTEM AND DATA COLLECTION PROCEDURE

The instrumentation facility is composed of receiving, recording, and processing equipment for this project.[2] RF emissions at two frequencies, 251 MHz and 2.0 GHz, are received using two linearly polarized antennas for each frequency. An Ampex FR-2000 multi-channel recorder is employed to record the outputs of the four RF receivers as well as those of two electric-field antennas. In addition, the time code and a trigger pulse marking the initiation of digitization are also recorded on two other tracks of the magnetic tape. The digitizer unit actually consists of a display card, a digitizer card, a total of 128 kilobyte of solid-state memory, and an HPIB interface. It is triggered when the input analog signal goes above a preset threshhold. Immediately following the trigger, the memory registers are filled with the digitized samples. After the last memory register is filled, the unit stops digitization and switches to display mode. In this mode, the memory content may be displayed on an oscilloscope. The digitizer may be operated at a maximum rate of 20 Mbs. During data collection, it is normally connected to the receiver output of the vertically polarized S-band antenna and is operated at 10 or 20 Mbs. The record thus produced is saved on hard disk by the operator. The use of a video camera installed on the receiver antenna cluster mounting board has enabled observation of the optical emissions. The camera output along with that of a field microphone is recorded on video tape. The blockdiagram of the recording system is shown in Figure 1.

Four antennas identical to the receiving antennas are used for the calibration of the RF receiving system. The source antennas are installed 44 feet away from, and at the same height as, the receiving antenna cluster. Calibration is performed by radiating a known level of CW power and recording the digitized output of a receiver obtained directly or through the magnetic tape medium. Thus, a complete RF system calibration requires eight test runs. Each run is conducted by stepping the source generator power through a total range to change the receiver output from noise level to saturation. The RF calibration test is performed in conjunction with a program that computes the magnitudes of the E-field and the power density at a receiver antenna corresponding to the digitized level of its receiver output.

A major improvement in data collection speed was realized as a result of modification of the computer program that is used during data collection activities. The program's original purpose was to transfer the content of any selected portion of the solid state memory to the hard disk for permanent storage. All of the associated data relative to a record had to be manually recorded by the operator. This required

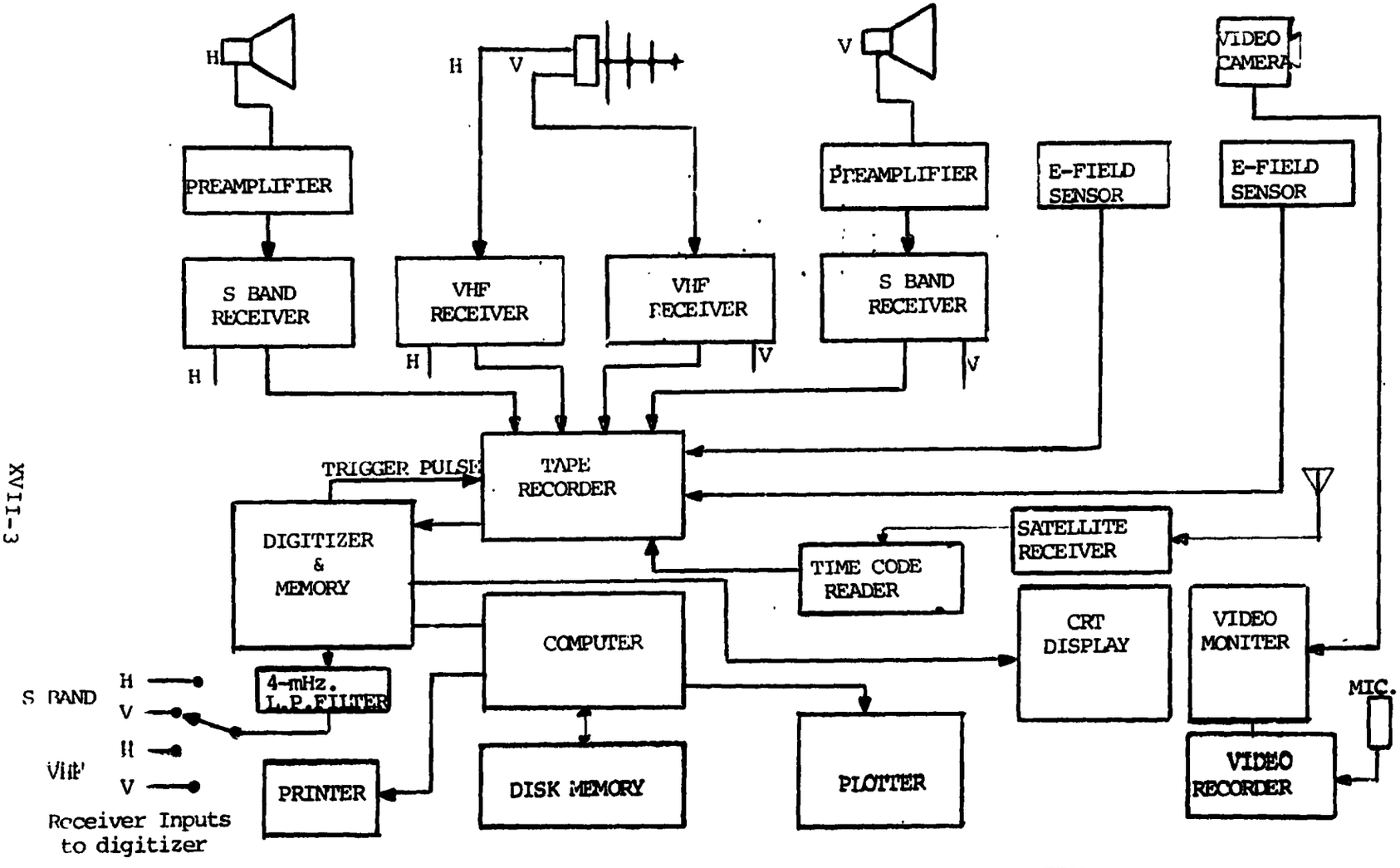

Fig. 1. LIGHTNING EMISSION RECORDING FACILITY

noting and recording the time of the digitizer's triggering and the time of the audio return, providing the necessary input to the computer to transfer to hard disk a desired segment of the solid-state memory, and resetting the digitizer to prepare for the next record. The modified program performs the logging of all of the supplementary data by presenting several menues from which selections based on observed parameters of the event are made and entered with a few key strokes. In addition, the program automatically registers the time of the trigger event and resets the digitizer upon completion of a data cycle.

Data

The data examined in this report were obtained on July 9, 16, 19, 22, 1982, and on July 14, 17, 1983, during afternoon or early evening local thunderstorms. Only the emission records with reliable information on their range and the type of discharge were included in the quantitative analysis. All results are for ground discharges which occurred within a 10-mile range of the facility and were extracted from records stored on magnetic tape at 60 ips. The tape medium proved very useful as its records could easily be digitized and displayed for examination, plotting and other data manipulations. It also allowed comparison of simultaneous events of different channels by use of the recorded trigger pulse of the digitizer as a reference marker.

Peak Signal Strength Computations

Table 1 gives the peak signal strength computed for 13 ground strikes recorded in summer 1983. Also included on the lower section of the table are the results obtained in 1982. It is noteworthy that the range of equivalent peak intensity of the entire data is within one order of magnitude.

To determine the degree of approximations inherent in the result shown, the sources of errors should be considered. Two obvious sources of errors are the system tolerances and the errors in measurement of range. System tolerances, such as calibration errors due to misalignment of antennas, etc., are expected to be low. Repeated calibration runs on different days showed a repeatability error of less than 2% (power level measurement are performed using calibrated power meters and precision attenuators). The distance of a ground flash to the facility is computed by: $C_s * t$ in which Cs is the sound velocity and t the difference between the time of the flash and the audio signal. Flash time can be determined accurately by playback of the video record in single-frame mode. The audio signal in playback, however, gradually builds up and, because of the poor low frequency response of the microphone, does not contain the thunder peaks usually audible directly from a ground strike. The error in the 10Km-1 KHz-equivalent signal strength due to time measurement errors may be computed by noting the linear relation between the two:

$$Eeq = (Er)(BW/10)^{-1/2}(D),$$
$$= (Er)(BW/10)^{-1/2} Cs(t \pm \Delta t)$$

TABLE 1

PEAK SIGNAL STRENGTH OF CG RADIATION @ 2GHz

Er (μV/m)	Distance (Km)	Eeq (1KHz @ 10 km) (μV/m)	ΔEeq/Δt (%)	Log(Eeq)
850	5.97	8.02	5.8	0.90
850	8.78	11.80	3.9	1.07
330	10.88	5.70	3.2	0.75
1000	8.40	13.30	4.1	1.12
720	5.27	6.00	6.5	0.78
720	8.78	10.00	3.9	1.00
750	3.86	4.58	8.9	0.66
580	8.40	7.7	4.1	0.89
400	8.75	5.5	3.9	0.74
900	8.40	11.95	4.1	1.08
1200	8.40	15.94	4.1	1.20
900	8.40	11.95	4.1	1.08
900	7.35	10.49	4.7	1.02
		(1982 - RESULTS)		
600	8.30	7.9	4.0	0.9
740	6.60	7.7	5.2	0.89
3100	6.60	32.5	5.2	1.51
1600	7.30	18.5	4.7	1.27
1050	8.00	13.2	4.3	1.12
1600	5.60	14.3	6.2	1.16

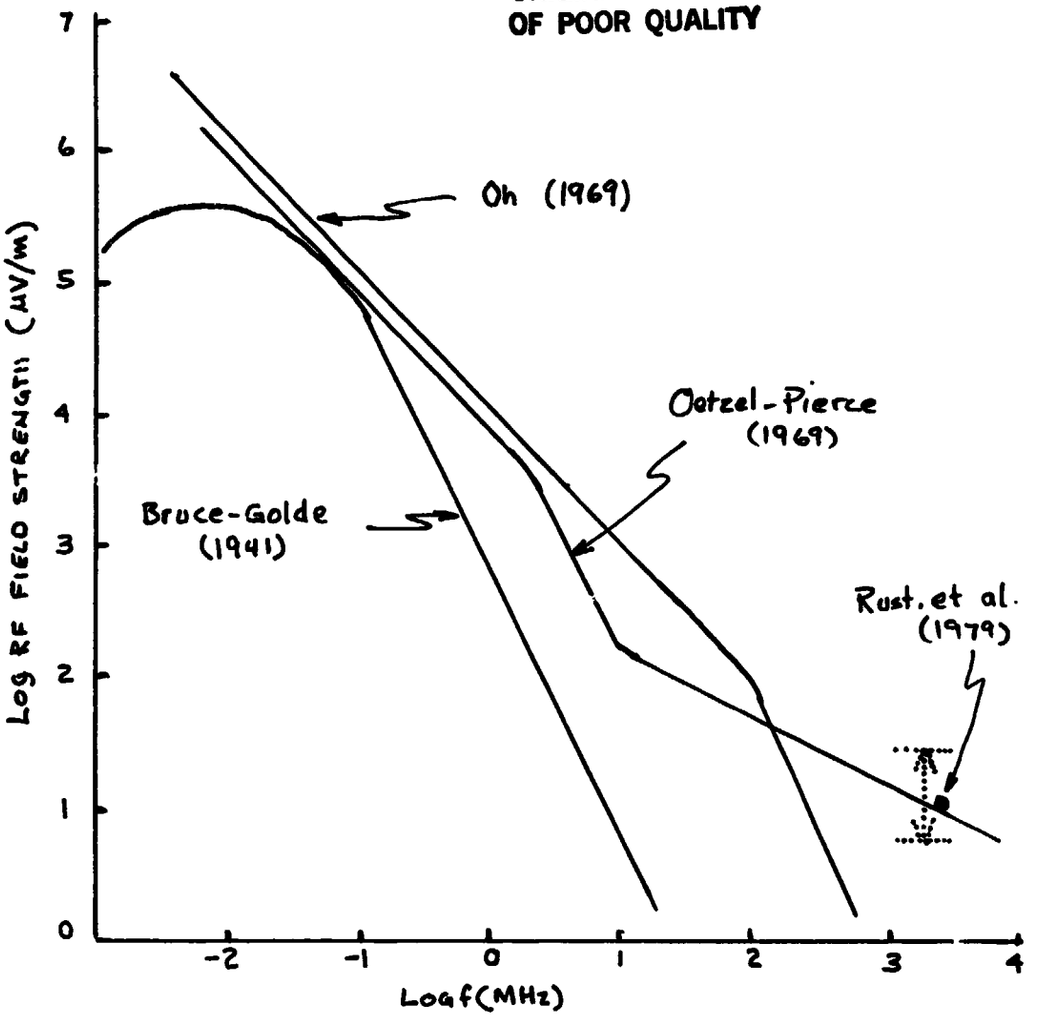

FIGURE 2 - COMPOSITE LIGHTNING AMPLITUDE SPECTRUM
FROM DATA PRESENTED BY OETZEL AND PIERCE

In which Er is the received signal strength, BW the receiver bandwidth, D the range of flash in kilometer, and t the time of travel of thunder. Since Eeq is linearly related to t, the percent error in Eeq is equal to the error in t. The 4th Column in Table 1 shows the error Eeq per one second error in t. 2-second average error in the time measurements yields a $\pm$10% error in the average Eeq values. The Eeq and its range for the data obtained are shown in Figure 2 superimposed on the composite experimental lightning amplitude spectrum reported by Oetzel and Pierce (3).

Signature Analysis

Figure 3 is a composite graph of E-field and radiation signals (S-band, vertically polarized antenna) received from a ground strike at 2056:34 UT, on July 16, 1982. The distance of the flash from the recording facility was between 6 and 8 kilometers. The digital levels of the vertical scale apply only to the radiation signal; the time axis is synchronized for both signals. The leader region and the first and second return strokes are labelled on the by L, R1, and R2 respectively. This and other 2 GHz CG records show signal peaks associated with the first and subsequent return strokes. Also, a few bursts of lower intensity radiation are always associated with the stepped leader process. These are consistent with the observations reported by Rust, et al., (1979) at 2200 MHz.

An interesting feature observed in all of the CG signals is the behavior of the level of the rf signal during the stepped leader. The expanded graph of the stepped leader and the 1st return stroke for the emission recorded at 1417:24 CST, on July 17, 1983, along with the video record of the flash are given in Figure 4. The rf radiation appears to follow an exponentially increasing mean which levels off just prior to the 1st return stroke. We have not determined if this is a system effect (for example, the coupling of the d.c. field onto the rf) or a discharge characteristic. The peak-to-peak value of the rf noise is significantly higher in the leader region than in the intervals between the return strokes. This characteristic may be noted more clearly in the graph of Figure 5 which is for the 2GHz signal received at 1421:17 CST, July 17, 1983.

The radiation at the VHF generally has a greater number of pulses associated with the entire C-G discharge history. This is evident in the example of Figure 6 which shows the graphs of 2 GHz (a) and 250 MHz signals of a CG discharge at 1421.33 CST, on July 17, 1983. The S-band graph shows the first return stroke and about 16 msec of activity associated with the stepped leader. Both of these features are also recognized in the VHF record. The region of high activity in the VHF signal extend back for about 100 Milliseconds.

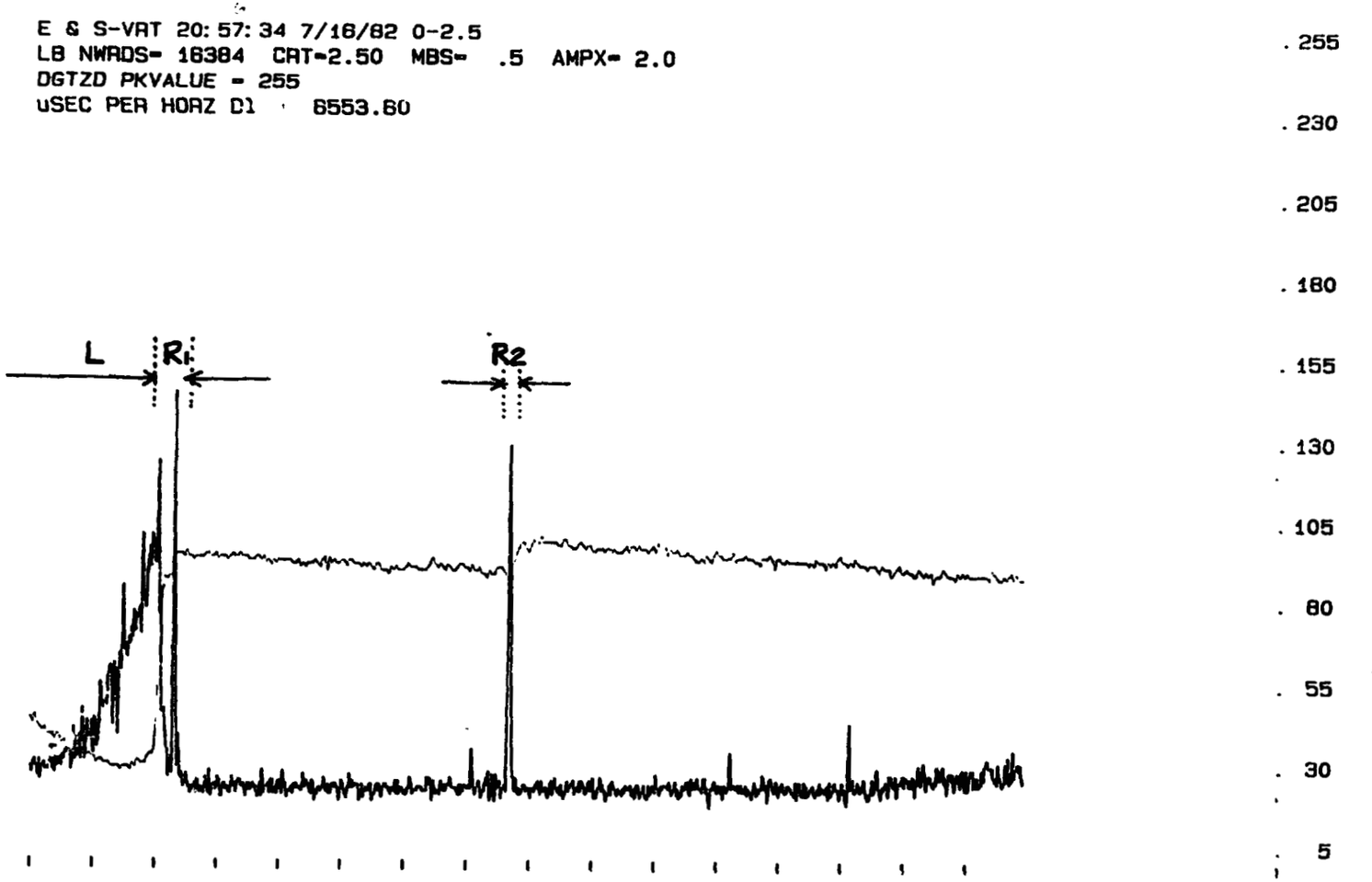

FIGURE 3 - E-FIELD AND 2 GHz RADIATION SIGNALS

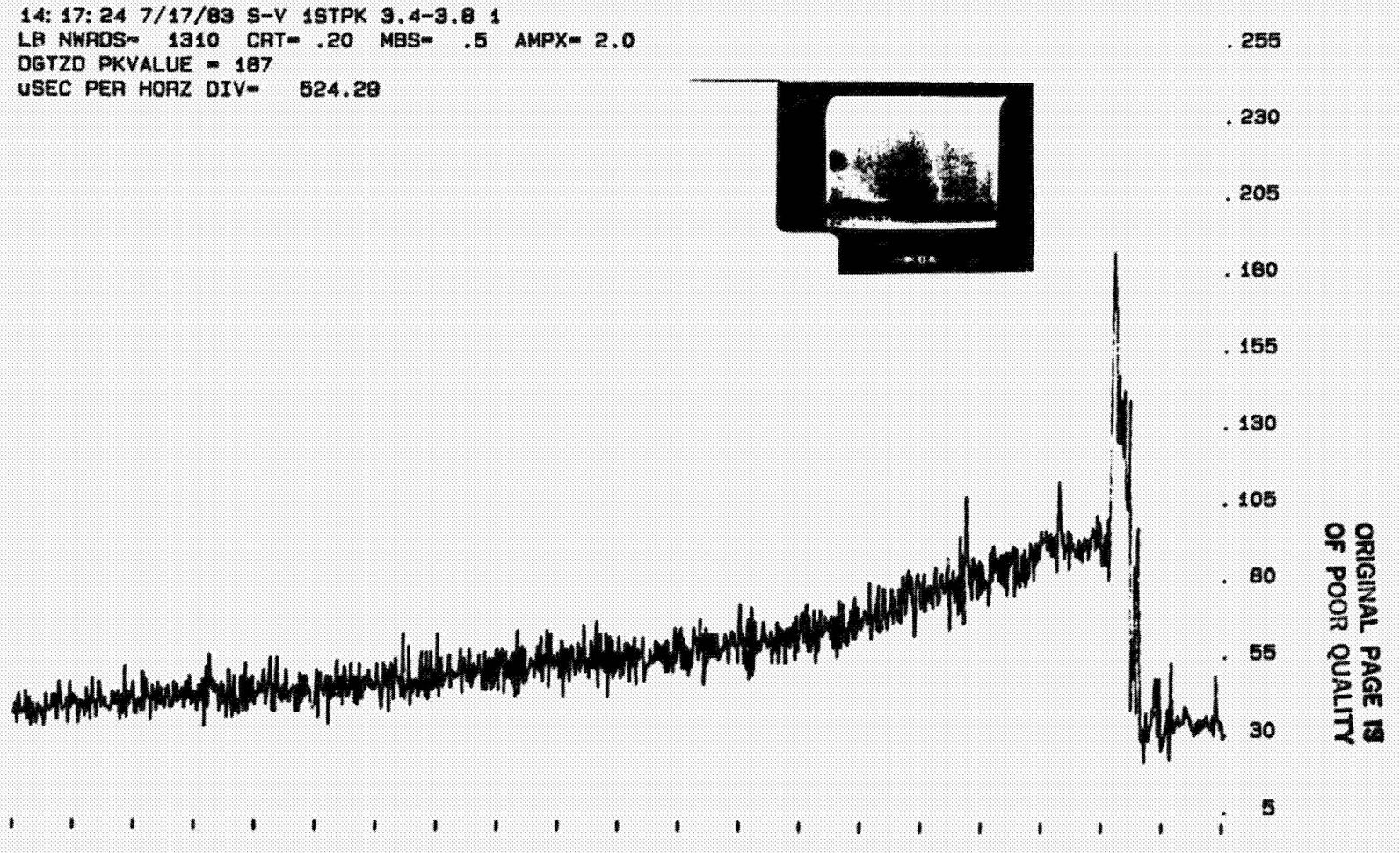

FIGURE 4 - 2 GHz SIGNAL ASSOCIATED WITH THE STEPPED LEADER

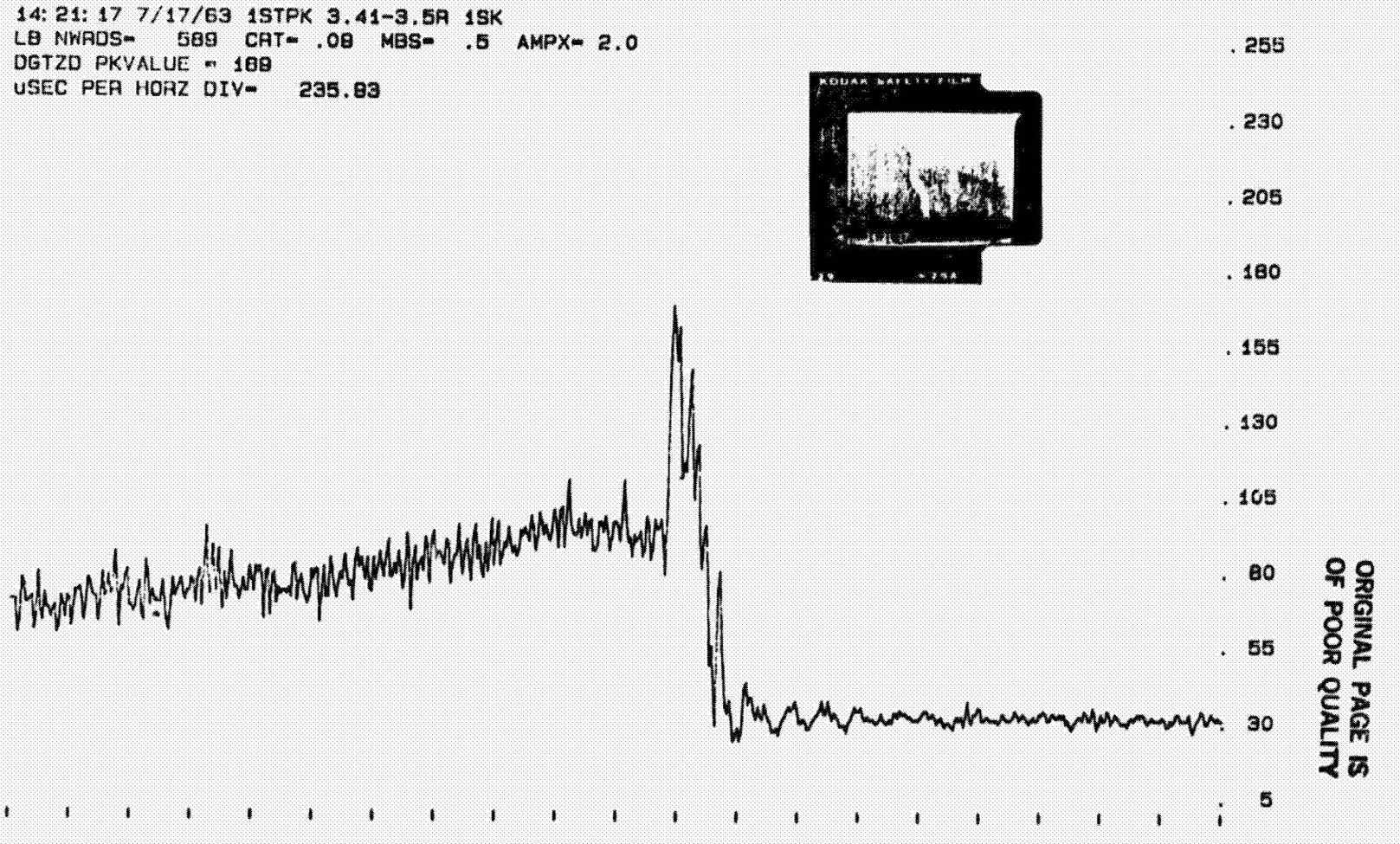

FIGURE 5 COMPARISON OF NOISE LEVEL PRIOR AND AFTER 1ST RETURN SHAKE (2 GHz)

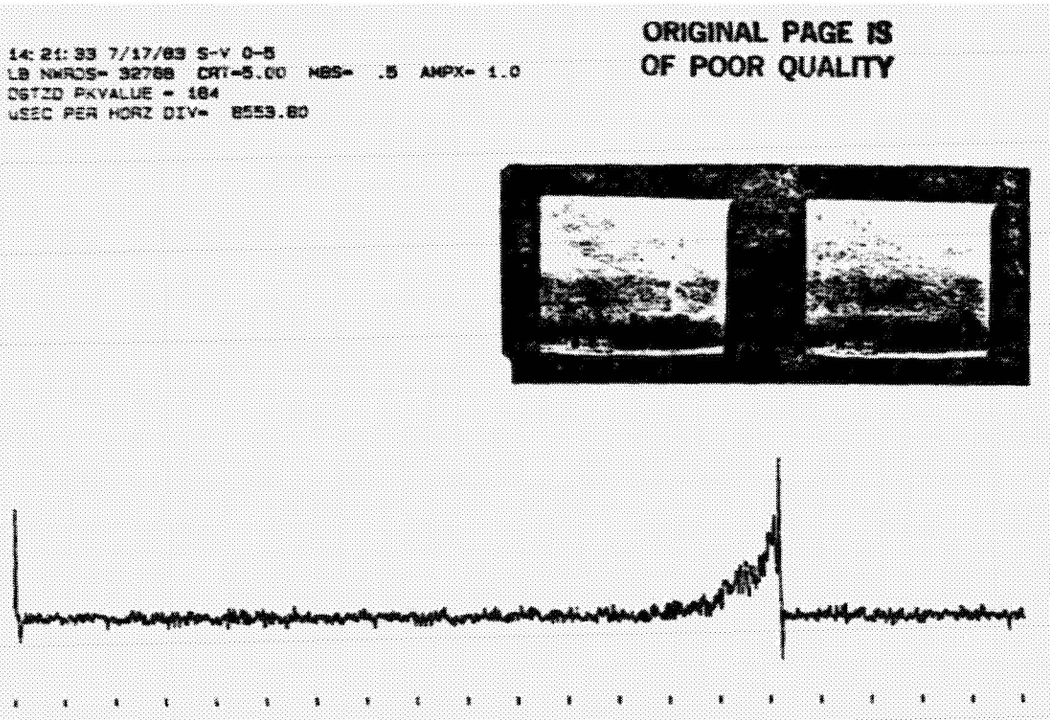

FIGURE 6 2 GHz (TOP) AND 250MHz SIGNALS ASSOCIATED WITH 1ST RETURN STROKE AND THE LEADER

Comparison of the records of the two polarizations at each frequency did not show any significant difference in signatures. The peak intensities of the horizontally-polarized signals, however, were generally lower than those of their orthogonal counterparts. Figure 7 shows the signals received in each polarization for 2 GHz and 250 MHz from a CG flash at 1416:55 CST, on July 17, 1983.

ORIGINAL PAGE IS
OF POOR QUALITY

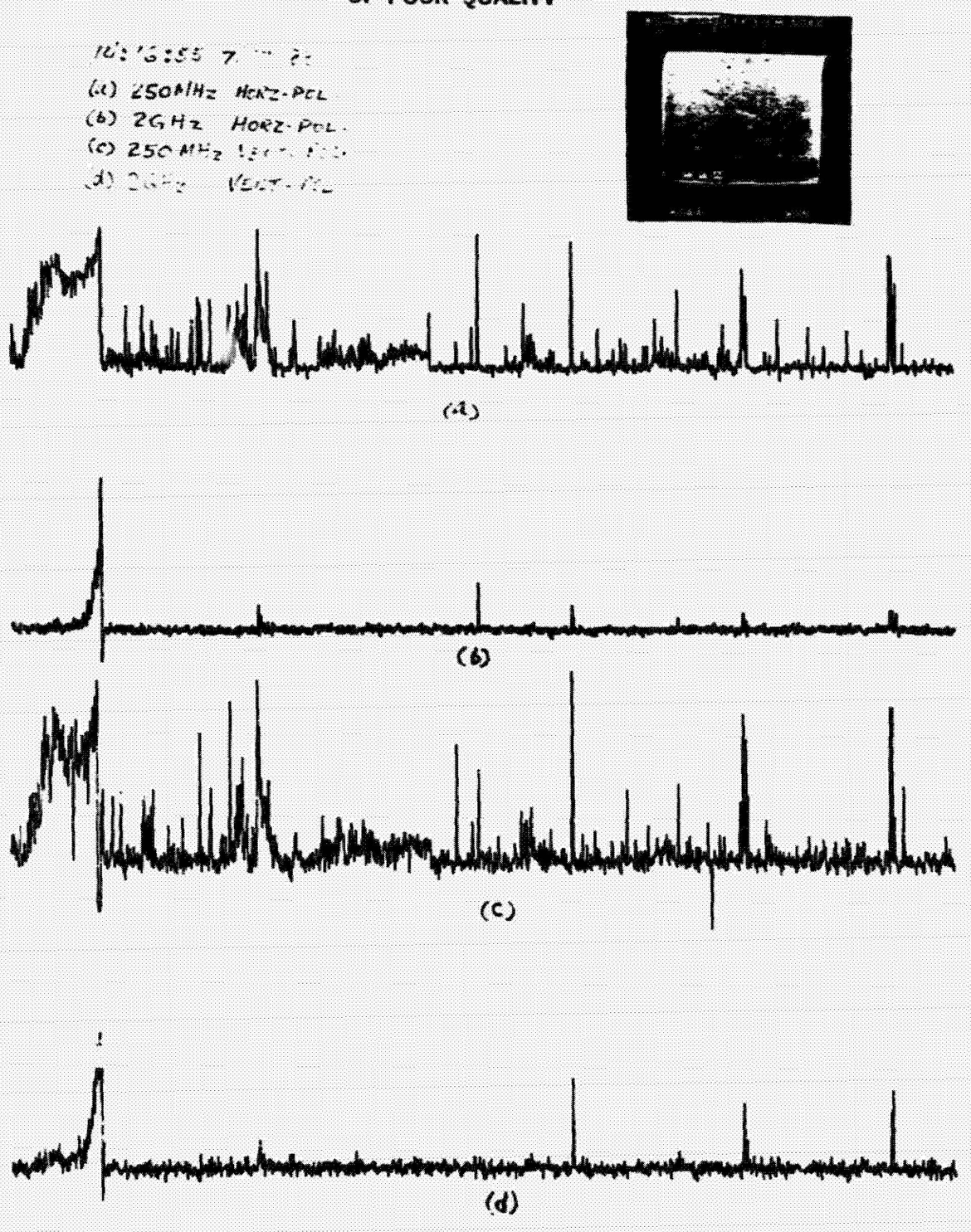

FIGURE 7 COMPARISON OF VERTICAL AND HORIZONAL POLARIZATION SIGNALS AT 2GHz AND 250 MHz

SUMMARY AND CONCLUSIONS

The MSFC lightning recording facility is an excellent system for the study of the high frequency emissions from close lightning discharges. Hardware and software modifications have improved the facility making rapid data collection and one-man operation possible.

Although the unusually dry summer prevented obtaining the anticipated quantity of data, two local thunderstoms in July resulted in recording of RF signals from 18 CG flashes. Analysis of the data obtained (including those of 1982) indicate the following:

(a) The peak intensities at 2 GHz are in the 6 to 32 μV/M (1 KHz @ 10Km) range. For the collected data the average intensity is 11.4 μV/M with 10 records (58%) having intensilies at or above this value.

(b) The CG discharge 2 GHz signals show radiation peaks associated with the first and secondary return strokes. The stepped leader appears as an active region and is easily recognizable in each CG record. The discharge hisotry is otherwise quiet except for isolated pulses of much weaker amplitude. The signature at 250 MHz parallels that of the S-band with a 2 to 5 times longer region of rf activity previous to the first return stroke and more frequent pulses during the entire discharge process.

(c) No significant differences were observed between the signatures registered through the horizontally and vertically polarized antennas at either frequencies. The signal strengths were, however, weaker in the horizontally polarized records.

RECOMMENDATIONS

In order to develop an adequate data base of lightning characteristics at the low microwave frequencies, the recording facility should be maintained for additional data collection, This is specially important in view of the improved capability of the facility for rapid collection and accurate characterization of lightning data.

The S-band signature observed in the present data, may suggest the possibility of identification of the under 15Km CG discharges by the rf radiation in the S-band. One objective of the project would be to determine the existance of any system effect in the stepped leader's signature. Furthermore, collection of a few verified cloud-to-cloud records would provide additional evidence on the uniqueness of the CG signature observed.

If the facility is continued for additional data collection, the following suggestions for further instrumentation improvement should be considered:

(a) The mounting boards of both receiving and calibration antenna clusters should be replaced. The present boards are slightly deformed due to weathering.

(b) A wide-angle lens should be used on the video camera to enable verification of the presence of flashes near or just outside the main beam of the S-band horns.

(c) The field microphone be replaced by a directional unit with good low frequency response. This will enhance the time measurements of the audio signal from the flash and hence yield more accurate intensity figures.

REFERENCES

1. Bent, R. B., Operational Application Committee, Proceedings of the 1979 Workshop on the Need for Lightning Observations from Space, NASA CP-2095, Washington, D.C., 1979.

2. Jalali, F., Detection and Analysis of Radio Frequency Lightning Emissions, NASA/ASEE Summer Research Program Report, NGT 01-008-021, UAH, 1981.

3. Oetzel, G.N. and E.T. Pierce, Radio Emissions from Close Lightning, Planetary Electrodynamics, Vol.I, Gordon and Breach Publishers, New York, 1969.

4. Rust, W.D., P.R. Krehbiel, and A. Shlanta, Measurement of Radiation from Lightning at 2200 MHz, Geophys. Res. Lett., 6, 85, 1979.

1983

NASA/ASEE SUMMER FACULTY RESEARCH FELLOWSHIP PROGRAM

MARSHALL SPACE FLIGHT CENTER
THE UNIVERSITY OF ALABAMA IN HUNTSVILLE

A FEASIBILITY STUDY OF ELECTROMAGNETIC DE-SPIN SYSTEM FOR EARTH ORBITING SATELLITES

Prepared By:	Prasad K. Kadaba, Ph. D.
Academic Rank:	Professor
University and Department:	University of Kentucky Department of Electrical Engineering
NASA/MSFC:	Advanced Systems Office
MSFC Counterpart:	G. von Tiesenhausen
Date:	August 12, 1983
Contract No.:	NGT 01-008-021 The University of Alabama in Huntsville

A FEASIBILITY STUDY OF ELECTROMAGNETIC DE-SPIN SYSTEM FOR EARTH ORBITING SATELLITES

BY

Prasad K. Kadaba
Professor of Electrical Engineering
University of Kentucky
Lexington, Kentucky 40506

ABSTRACT

This investigation is a feasibility study of electromagnetic satellite de-spin systems based on induced eddy-currents in the satellite by an external d.c. magnetic field. Two concepts have been investigated: (1) one based on a large diameter coil positioned around the satellite such that the axis of the satellite rotation is in the plane of the coil; and (2) a magnet, either permanent or electromagnet, positioned close to the satellite by the orbiter RMS. A comparison is made of the two concepts by varying the appropriate parameters with a view to reduce the de-spin time to a reasonable value. Design parameters for the magnets and the coil are indicated.

ACKNOWLEDGEMENTS

The author wishes to acknowledge with thanks the valuable assistance of Mes. George von Tiesenhausen, R. W. Parks during his stay at the Marshall Space Flight Center. He wishes to thank Mr. Lott W. Brantley, Jr. for extensive discussions during the course of the project. Thanks are also due to Mr. Howard Lanier for the computer calculations and Ms. Sharlene Stratton for typing the final report.

INTRODUCTION

The servicing of disabled satellites requires that the units be de-spun before any repair can be done. One way to accomplish this is by physical attachment of equipment or astronauts with equipment that would take the rotational energy out of the satellite. This procedure may be quite hazardous. As an alternative, a system without physical contact with the satellite that would reduce the spin to a very low value within a reasonable time is desirable. One such possibility is to induce eddy-currents in the satellite by electromagnetic means. This eddy-current power input would act in such a way as to reduce the rotat' energy of the satellite.

In this study two schemes for inducing eddy-currents have been investigated: (1) one based on a large diameter current loop positioned around the satellite such that the axis of the satellite rotation is in the plane of the loop; and (2) a magnet, either permanent or electro-magnet, positioned close to the satellite by the orbiter RMS. Both the systems have been parametrically analyzed with a view tc reduce the de-spin time to a reasonable value. Design parameters for the magnets and the current loop are given.

OBJECTIVES

The objectives of this study are to investigate and assess the practical applicability of an electromagnetic satellite de-spin system based on the induction of counteracting eddy-currents in the satellite. This system without physical contact with the satellite and using moderate amount of power is expected to reduce satellite spin to a very low value within a reasonable time.

DETAILS OF THE STUDY

i) Theoretical considerations:

Current-loop Analysis: The spinning satellite configuration assumed as a cylinder of thickness, t, is shown in Figure 1 positioned symmetrically with respect to the current loop such that the axis of rotation of the cylinder is in the plane of the current loop. In order to evaluate the eddy-current power input to thesatellite, as a first step, the expression for the magnetic flux density at a general point in the skin of the satellite is derived. The procedure is as follows: The magnetic flux density $\overline{B}$ is related to the magnetic vector potential $\overline{A}$ by $\overline{B} = \nabla X \overline{A}$. The vector potential at a general point P shown in the sketch is given by:

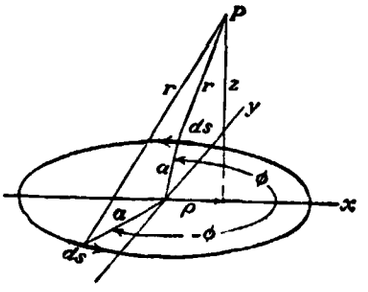

$$A_\phi = \frac{\mu_o I}{4\pi} \oint \frac{dL_\phi}{r}$$

$$= \frac{\mu_o I}{2\pi} \int_0^\pi \frac{a \cos\phi d\phi}{(a^2 + \rho^2 + z^2 - 2a\rho\cos\phi)^{1/2}} \qquad (1)$$

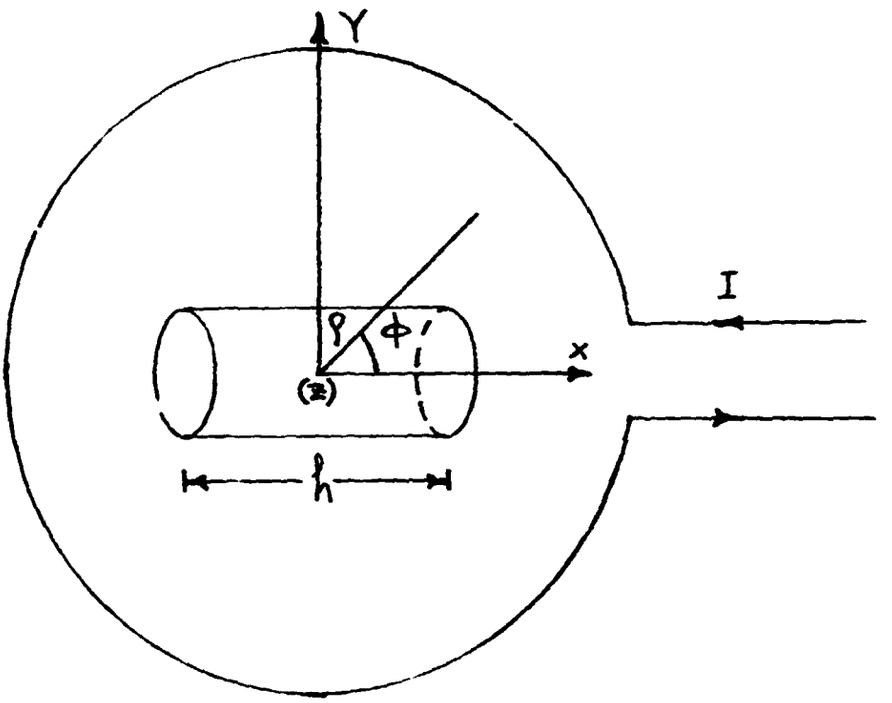

Fig. 1: Configuration of the satellite positioned symmetrically with respect to the current loop; Rotation axis of the cylinder is in the plane of the current loop.

The vector potential $\bar{A}$ has only the ϕ-component A_ϕ because when equidistant elements of the loop (dL) at $+\phi$ and $-\phi$ are paired, the resultant is normal to (ρz). $d\bar{L}$ in equation (1) is the component of $\overline{dL}$ in this direction. Let $\phi = (\pi+2\theta)$; then $d\phi = 2d\theta$ and $\cos\phi = (2\sin^2\theta - 1)$ and equation (1) becomes:

$$A = \frac{\mu_o a I}{\pi} \int_0^{\pi/2} \frac{(2\sin^2\theta - 1)d\theta}{[(a+\rho)^2 + z^2 - 4a\rho\sin^2\theta]^{1/2}} \qquad (2)$$

Rearranging and letting:

$$k^2 = 4a\rho\,[(a+\rho)^2 + z^2]^{-1} \text{ and } m = [1-(1-k^2)^{1/2}][1+(1-k^2)^{1/2}]^{-1} \qquad (3)$$

A_ϕ becomes (1):

$$A_\phi = \frac{\mu_o I}{\pi k}\left(\frac{a}{\rho}\right)^{1/2}\left[\left(1-\frac{k^2}{2}\right)K - E\right]$$

$$= \frac{\mu_o I}{32}\left(\frac{a}{\rho}\right)^{1/2} k^3\left(1 + \frac{3}{4}k^2 + \frac{15}{128}k^4 + \ldots\ldots\right)$$

$$= \frac{\mu_o I}{\pi}\left(\frac{a}{m\rho}\right)^{1/2}[K(m) - E(m)]$$

$$= \frac{\mu_o I}{2\pi}\left(\frac{a}{\rho}\right)^{1/2} m^{3/2}\left(1 + \frac{3}{8}m^2 + \frac{15}{128}m^4 + \ldots\ldots\right) \qquad (4)$$

where K and E are complete elliptic integrals of the first and second kind respectively.

To determine the magnetic flux density $\bar{B}$, using cylindrical coordinates:

$$\bar{B} = \bar{a}_\rho B_\rho + \bar{a}_\phi B_\phi + \bar{a}_z B_z$$

and

$$B_\rho = -\frac{1}{\rho}\frac{\partial}{\partial z}\left(\rho A_\phi\right) + \frac{1}{\rho}\frac{\partial}{\partial \phi}\left(A_z\right)$$

$$= -\frac{\partial A_\phi}{\partial z} \qquad \text{since only } A_\phi \text{ exists}$$

$$B_\phi = \frac{\partial}{\partial z}\left(A_\rho\right) - \frac{\partial}{\partial \rho}\left(A_z\right) = 0$$

$$B_z = -\frac{1}{\rho}\frac{\partial}{\partial \phi}\left(A_\rho\right) + \frac{1}{\rho}\frac{\partial}{\partial \rho}\left(\rho A_\phi\right)$$

$$= \frac{1}{\rho}\frac{\partial}{\partial \rho}\left(\rho A_\phi\right)$$

$$\frac{\partial K}{\partial k} = \left[\frac{E}{k(1-k^2)} - \frac{K}{k}\right] \; ; \quad \frac{\partial E}{\partial k} = \left[\frac{E}{k} - \frac{K}{k}\right]$$

From equation (3),

$$\frac{\partial k}{\partial z} = -\frac{zk^3}{4a\rho} \; ; \quad \frac{\partial k}{\partial \rho} = \left[\frac{k}{2\rho} - \frac{k^3}{4\rho} - \frac{k^3}{4a}\right]$$

Carrying out the differentiation, collecting terms, and substituting for k finally yields:

$$B_\rho = \frac{\mu_o I}{2\pi} \frac{z}{\rho[(a+\rho)^2 + z^2]^{1/2}} \left[-K + \frac{(a^2 + \rho^2 + z^2)}{[(a-\rho)^2 + z^2]} E\right] \tag{5}$$

$$B_z = \frac{\mu_o I}{2\pi} \frac{1}{[(a+\rho)^2 + z^2]^{1/2}} \left[K + \frac{(a^2 - \rho^2 - z^2)}{[(a-\rho)^2 + z^2]} E\right] \tag{6}$$

If the current loop has N turns, B_ρ and B_z in (5) and (6) is each multiplied by N. Numerical values of B_ρ and B_z can be computed for any value of ρ and z by finding k from equation (3) and then solving for the elliptic Integrals K and E.

Expression for the Motional EMF Generated:

Vector direction of the area swept by filamentary conductor, h, is parallel to the (yz) plane. This unit vector, $\bar{l}$, can be resolved in terms of cartesian coordinate unit vectors defined with respect to the coordinate axes shown in Figure 1.

$$\bar{l} = (\cos\theta)\,\bar{A}_y + (\sin\theta)\,\bar{A}_z$$

$$\bar{B} = \bar{A}_\rho\, B_\rho + \bar{A}_z\, B_z$$

$$\bar{B}.\bar{l} = (B_\rho \sin\phi \cos\theta + B_z \sin\theta)$$

$\sin\phi = \frac{A_s}{\rho}$ where A_s = radial distance to a point in the skin of the satellite (cylinder) from the rotational axis of the cylinder. Therefore,

$$\bar{B}.\bar{l} = \left(\frac{B_\rho A_s}{\rho}\cos\theta + B_z \sin\theta\right)$$

The flux linkage $d\psi$ when, h, rotates by an angle $d\theta$ is then given by:

$$d\psi = \left[\left\langle\!\left\langle \frac{B_\rho}{\rho}\right\rangle\!\right\rangle A_s \cos\theta + \left\langle\!\left\langle B_z\right\rangle\!\right\rangle \sin\theta\right] h\, A_s\, d\theta \qquad (7)$$

The motional EMF, ε generated is given by:

$$\varepsilon = \int_{\theta=0}^{\theta=\theta_1}\left[\left\langle\!\left\langle \frac{B_\rho}{\rho}\right\rangle\!\right\rangle A_s \cos\theta + \left\langle\!\left\langle B_z\right\rangle\!\right\rangle \sin\theta\right] h\, A_s\, d\theta \qquad (8)$$

The upper limit $\theta=\theta_1$ in equation (8) is fixed by the rpm of the satellite. For example, for 10 rpm $\theta_1 = \frac{\pi}{3}$ and so forth. The double averages $\left\langle\!\left\langle \frac{B_\rho}{\rho}\right\rangle\!\right\rangle$ and $\left\langle\!\left\langle B_z\right\rangle\!\right\rangle$ are obtained as follows. For a given θ, ρ varies from $A_s \cos\theta$ to $\sqrt{(A_s\cos\theta)^2 + h^2/4}$. $\left\langle \frac{B_\rho}{\rho}\right\rangle$ and $\langle B_z\rangle$ are the averages for the run of values of ρ from $A_s\cos\theta$ to $\sqrt{(A_s\cos\theta)^2 + h^2/4}$ with θ fixed. The second averages $\left\langle\!\left\langle \frac{B_\rho}{\rho}\right\rangle\!\right\rangle$ and $\left\langle\!\left\langle B_z\right\rangle\!\right\rangle$ are obtained by varying θ from $\theta=0$ to $\theta=\theta_1$ where θ_1 is fixed by the rpm value. Similar to the derivation in reference (2) the eddy current power input, P_s, to the satellite is given by

$$P_s = \int_{r = A_{si}}^{(A_{si} + t/2)} \frac{\varepsilon^2\, \pi\, r\, dr}{2\, \rho_{Al}\, h} \qquad (9)$$

In equation (9), A_s in the expression for ε obtained from (8) is changed to the variable r in the integrand. A_{si} is the inner radius of

the cylinder and t, is the thickness of the cylinder wall. ρ_{Al} is the resistivity of aluminum, the material assumed for the satellite skin. After substituting for ε in equation (9) from (8) we have:

$$P_s = \int_{r=A_{si}}^{r=(A_{si}+t/2)} \pi \frac{\left[\sin\theta_1 \left\langle\!\left\langle \frac{B_\rho}{\rho} \right\rangle\!\right\rangle hr^2 + \left\langle\!\left\langle B_z \right\rangle\!\right\rangle (1-\cos\theta_1)\frac{hr}{2}\right]^2}{2\rho_{Al}\, h} \, rdr \quad (10)$$

Magnet System Analysis:

The configuration for this case is shown in Figure 2 with the origin of coordinates at the center of the magnet and the coordinate axes as shown. The magnetic flux density $\bar{B}$ is related to the magnetic field intensity $\bar{H}$ and the magnetization $\bar{M}$ in a medium by

$$\bar{B} = \mu_o \mu \bar{H} = \mu_o (\bar{H} + \bar{M}) \quad Wb/m^2$$

In the sketch shown assuming uniform polarization parallel to the axis, $\nabla.\bar{M} = 0$ where $\bar{M}$ is the magnetization in the magnet. There is then, only an equivalent surface charge at the ends, and the derivation of the field expression is similar to that given in reference (3).

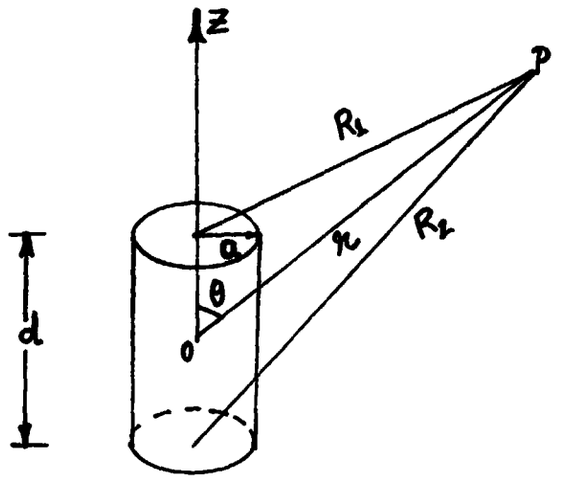

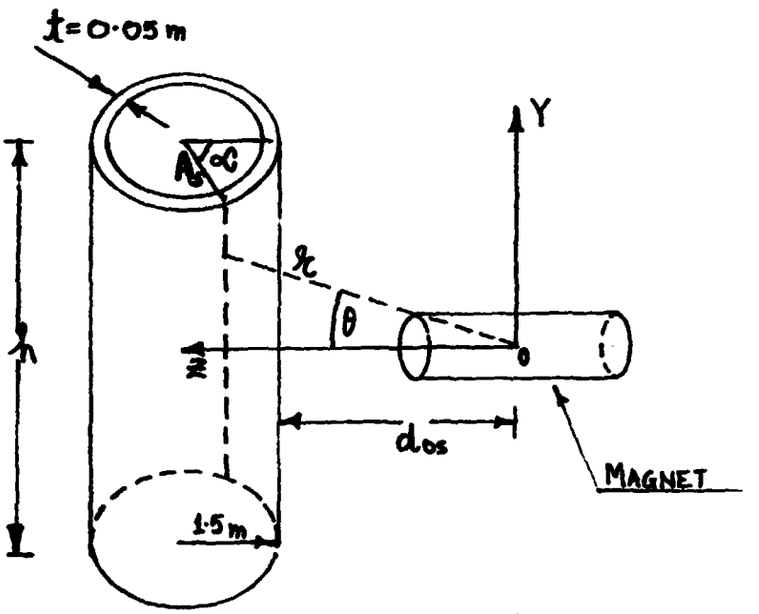

Fig. 2: Configuration for the Magnet System; origin of coordinates is at the center of the magnet with the axes as shown.

This surface charge q_M is $q_M = \pm \pi M a^2$ where a is the radius of the magnet. The problem is then analogous to the electric dipole* and the scalar magnetic potential $\Phi_M(P)$ is:

$$\Phi_M(P) = \frac{q_M}{4\pi}\left(\frac{1}{R_1} - \frac{1}{R_2}\right) \tag{11}$$

The magnetic field intensity $\bar{H}$ is then given by:

$$\bar{H} = -\nabla'\Phi_M(P)$$

$$= -\frac{\pi a^2 M}{4\pi}\,\nabla'\left(\frac{1}{R_1} - \frac{1}{R_2}\right) \tag{12}$$

Where ∇' refers to differentiation with respect to field point coordinates (P).

$$\nabla'\left(\frac{1}{R_1}\right) = -\frac{\bar{A}_{R_1}}{R_1^2}\ ;\ \nabla'\left(\frac{1}{R_2}\right) = -\frac{\bar{A}_{R_2}}{R_2^2} \tag{13}$$

Substituting in equation (12) we have:

$$\bar{H} = \frac{Ma^2}{4}\left(\frac{\bar{A}_{R_1}}{R_1^2} - \frac{\bar{A}_{R_2}}{R_2^2}\right) \tag{14}$$

$$\bar{B} = \mu_o \bar{H} = \frac{\mu_o Ma^2}{4}\left(\frac{\bar{A}_{R_1}}{R_1^2} - \frac{\bar{A}_{R_2}}{R_2^2}\right) \tag{15}$$

$$\bar{A}_{R_1} = \frac{\bar{R}_1}{R_1} \quad \text{where } \bar{R}_1 = \bar{A}_x X + \bar{A}_y Y + \bar{A}_z\left(Z - \frac{d}{2}\right)$$

and

$$\bar{A}_{R_2} = \frac{\bar{R}_2}{R_1} \quad \text{where } \bar{R}_2 = \bar{A}_x X + \bar{A}_y Y + \bar{A}_z\left(Z + \frac{d}{2}\right)$$

Substituting for $\bar{A}_{R_1}$, $\bar{A}_{R_2}$, R_1 and R_2 in equation (15), we have:

---

*This analogy is very close especially for a magnet whose $\frac{d}{a}$ ratio is large.

$$\bar{B} = \frac{\mu_o MA^2}{4}\left[\frac{\bar{A}_x X + \bar{A}_y Y + A_z(Z - \frac{d}{2})}{\{X^2 + Y^2 + (Z - \frac{d}{2})^2\}^{3/2}} - \frac{\bar{A}_x X + \bar{A}_y Y + \bar{A}_z(Z + \frac{d}{2})}{\{X^2 + Y^2 + (Z + \frac{d}{2})^2\}^{3/2}}\right] \tag{16}$$

Flux linkage in time (dt) by the rotating cylinder is

$$\bar{B}.\overline{dS} = B_y dS_y + B_z dS_z \tag{17}$$

$$dS_z = -(dxdy);\quad dS_y = \frac{Xdxdy}{\sqrt{(A_s^2 - X^2)}}$$

The motional EMF, ε is:

$$\varepsilon = \int_{\alpha=0}^{\alpha=\alpha_1} \bar{B}.\overline{dS} \tag{18}$$

Where α_1 is the angle of rotation of the cylinder in unit time corresponding to a given rpm

When $\alpha=0$, $x=0$; $\alpha=\alpha_1$, $x=A_s\sin\alpha_1$ and $z=[K-\sqrt{(A_s^2-x^2)}]$; so combining equations (16), (17), and (18) and using the above relations, we have finally the expression for the motional EMF, (ε):

$$\varepsilon = \frac{\mu MA^2}{2}\int_{y=0}^{y=\frac{h}{2}}\int_{x=0}^{x=A_s\sin\alpha_1} \frac{xy}{\sqrt{(A_s^2-x^2)}}\left[\frac{1}{\left\{x^2 + y^2 + \left(K - \frac{d}{2} - \sqrt{A_s^2-x^2}\right)^2\right\}^{3/2}} - \frac{1}{\left\{x^2 + y^2 + \left(K + \frac{d}{2} - \sqrt{(A_s^2-x^2)}\right)^2\right\}^{3/2}}\right] dxdy$$

$$+\frac{\mu MA^2}{2}\int_{y=0}^{y=\frac{h}{2}}\int_{x=0}^{x=A_s\sin\alpha_1}\left[\frac{\left(K+\frac{d}{2}-\sqrt{A_s^2-x^2}\right)}{\left\{x^2+y^2+\left(K+\frac{d}{2}-\sqrt{A_s^2-x^2}\right)^2\right\}^{3/2}}\right.$$

$$\left.-\frac{\left(K-\frac{d}{2}-\sqrt{A_s^2-x^2}\right)}{\left\{x^2+y^2+\left(K-\frac{d}{2}-\sqrt{A_s^2-x^2}\right)^2\right\}^{3/2}}\right]\,dxdy \qquad (19)$$

In the above equation, α_1, is related to the rpm of the satellite as follows: for 10 rpm, $\alpha_1 = \frac{\pi}{3}$; for 8 rpm, $\alpha_1 = \frac{4\pi}{15}$ etc. The eddy current power input, P_s, to the satellite is, as before, given by:

$$P_s = \int_{r=A_{si}}^{(A_{si}+t/2)} \frac{\varepsilon^2\,\pi\,r\,dr}{2\,\rho_{Al}\,h} \qquad (20)$$

Again, in equation (20), A_s in the expression for ε obtained from (19) is changed to the variable r, in the integrand.

Expression for the Motional EMF (Approximate Solution):

If one makes the approximation that the radial distance r, is large compared to d, the length of the magnet, the expression for the motional EMF ε, would be much simpler compared to equation (19). In the following, this approximate procedure is followed:

In equation (11), using the approximation $r>>d$ $R_1R_2\simeq r^2$ and (R_2-R_1) $\simeq d\cos\theta$, equation (11) becomes:

$$\Phi_M(P) \simeq \frac{MA^2}{4}\,\frac{d\cos\theta}{r} \qquad (21)$$

The magnetic field intensity $\bar{H}$ is given by:

$$\bar{H} = -\nabla\Phi_M(P) = -\left[\bar{A}_r \frac{\partial\Phi_M}{\partial r} + \bar{A}_\theta \frac{\partial\Phi_M}{\partial\theta} + \bar{A}_\phi \frac{\partial\Phi_M}{r \sin\theta\, \partial\phi}\right]$$

$$= \frac{MA^2d}{4\, r^2}\left[2\cos\theta\, \bar{A}_r + \sin\theta\, \bar{A}_\theta\right] \tag{22}$$

$$\bar{B} = \mu_o \bar{H} = \frac{M\mu_o A^2 d}{4r^2}\left[2\cos\theta\, \bar{A}_r + \sin\theta\, \bar{A}_\theta\right] \tag{23}$$

$\bar{B} = \bar{A}_r B_r + \bar{A}_\theta B_\theta$, and the components B_r and B_θ are given by:

$$\left.\begin{aligned} B_r &= \frac{\mu_o MA^2 d\cos\theta}{2r^2} \\ B_\theta &= \frac{\mu_o MA^2 d\sin\theta}{4r^2} \end{aligned}\right\} \tag{24}$$

Motional EMF generated:

Vector direction of the area swept by filamentary conductor h, in Figure 2 is parallel to the x-z plane. This unit vector, $\bar{l}$, can be resolved into:

$$\bar{l} = -\cos\alpha\, \bar{A}_z + \sin\alpha\, \bar{A}_y$$

and

$$\bar{B}.\bar{l} = B_r\,[\sin\alpha\sin\theta\sin\phi - \cos\alpha\cos\theta] + B_\theta\,[\cos\alpha\sin\theta + \sin\alpha\cos\theta\sin\phi] \tag{25}$$

The flux linkage $d\Psi$, when h, rotates by an angle $d\alpha$, is:

$$d\Psi = [\langle\langle B_r{}^1\rangle\rangle + \langle\langle B_\theta{}^1\rangle\rangle]\, h\, A_s\, d\alpha \tag{26}$$

where,

$$\left.\begin{aligned} B_r{}^1 &= B_r\,[\sin\alpha\sin\theta\sin\phi - \cos\alpha\cos\theta] \\ \text{and} \\ B_\theta{}^1 &= B_\theta\,[\cos\alpha\sin\theta + \sin\alpha\cos\theta\sin\phi] \end{aligned}\right\} \tag{27}$$

The double averages $\langle\langle B_r^1 \rangle\rangle$ and $\langle\langle B_\theta^1 \rangle\rangle$ in equation (26) are found as follows:

For a given α, B_r^1 and B_θ^1 are evaluated for the run of values, y=0 to $\frac{h}{2}$; for example, y=0, 0.15, --1.5 if h = 3 meters. Then $\langle B_r^1 \rangle$ and $\langle B_\theta^1 \rangle$ is determined. Then α is varied at suitable intervals and $\langle B_r^1 \rangle$, $\langle B_\theta^1 \rangle$ are obtained for these different values of α and the second averages $\langle\langle B_r^1 \rangle\rangle$ and $\langle\langle B_\theta^1 \rangle\rangle$ are computed. The motional EMF generated for a given rpm is given by:

$$\varepsilon = \int_{\alpha = 0}^{\alpha = \alpha_1} [\langle\langle B_r \rangle\rangle + \langle\langle B_\theta \rangle\rangle] \, h \, A_s \, d\alpha \tag{28}$$

and the eddy current power input P_s is:

$$P_s = \int_{r = A_{si}}^{(A_{si} + t/2)} \frac{\varepsilon^2 \, \pi \, r dr}{2 \, \rho_{Al} \, h} \tag{29}$$

where the A_s in ε^2 obtained from equation (28) is replaced by the variable r in the integrand of equation (29). As before A_{si}, is the inner radius of the cylinder. The time required to dissipate the rotational energy of the satellite, is the ratio of the rotational kinetic energy of the satellite divided by the eddy current power input. Calling this time the de-spin time, T:

$$T \text{ in minutes} = \frac{\text{Kinetic Energy of the Satellite in Joules}}{60 \text{ (Eddy current power input-in watts)}}$$

The kinetic energy of the rotating cylinder is, $E = \frac{1}{2} I\omega^2$, where ω is the angular velocity and I is the moment of inertia of the rotating cylinder. $I = \frac{m}{2} (r_1^2 + r_2^2)$ for a hollow cylinder rotating on its axis. Here m, is the mass of the cylinder and r_1 and r_2 are the inner and outer radii of the cylinder.

The dynamics of the spinning satellite can be treated by solving the the following first order equation:

$$\frac{d\omega}{dt} = - \frac{K_e B^2}{I} \omega \qquad (30)$$

where K_e is the configuration constant given by

$$K_e = \pi\sigma r^3 L t \left[1 - \frac{2t}{L} \tanh \frac{L}{2t}\right] \qquad (31)$$

In this equation, σ is the conductivity of the cylinder, r is the outer radius, L is the height of the cylinder and t, is the thickness of the cylinder wall. B is the average magnetic flux density. Letting $K = \frac{K_e B^2}{I}$, equation (30) becomes:

$$\frac{d\omega}{dt} = - K\omega \qquad (31)'$$

the solution of which is, $\omega=\omega_o e^{-Kt}$. The plot of this equation for a typical case is shown in figure 3.

ii) Design considerations

Current Loop: The results which will be outlined in the next section indicate 9000 A-T as a suitable upper limit to yield a reasonable de-spin time. At room temperature using a reasonable value of about 3 mm diameter wire which can carry 45 amps, the number of turns of the loop required is 200. This leads to a total length of wire in the coil to about 4400 meters using a 10 meter diameter coil. Using aluminum as the material for the wire, the resistance of the wire is around 14 ohms. This leads to too much power requirement to energize the coil. Low temperature coil would remedy the situation. For example, at liquid nitrogen temperature the resistivity of aluminum is estimated to be 10^{-9} ohm-meter using data at 100^o K and 50^o K (4). With a current of 45 amps, this leads to a total resistance of 0.53 ohm. The voltage drop across thecoil is then 23.8 V and the I^2R power input is 1.073 KW. Based on AWG8 wire capable of carrying 45 amps at room temperature the diameter of the aluminum wire at liquid nitrogen temperature keeping the total resistance the same is 0.61 mm. So, choosing 1 mm diameter wire, for the 200 turn-coil, the total cross-sectional diameter for the coil conductor without the cooling jacket is 1.4 cm. With cooling jacket and insulation, the overall diameter of the insulated coil conductor is about 7.5 cms or 3 inches, an acceptable dimension. The overall weight of the current loop is also a reasonable value, less than 200 lbs.

A computer search was made to investigate the possibility of using superconducting conductors at liquid nitrogen temperature. Nothing turned up in the search. In conversation with the superconducting division at Westinghouse (5) it was learned that the state-of-the art

ORIGINAL PAGE IS
OF POOR QUALITY

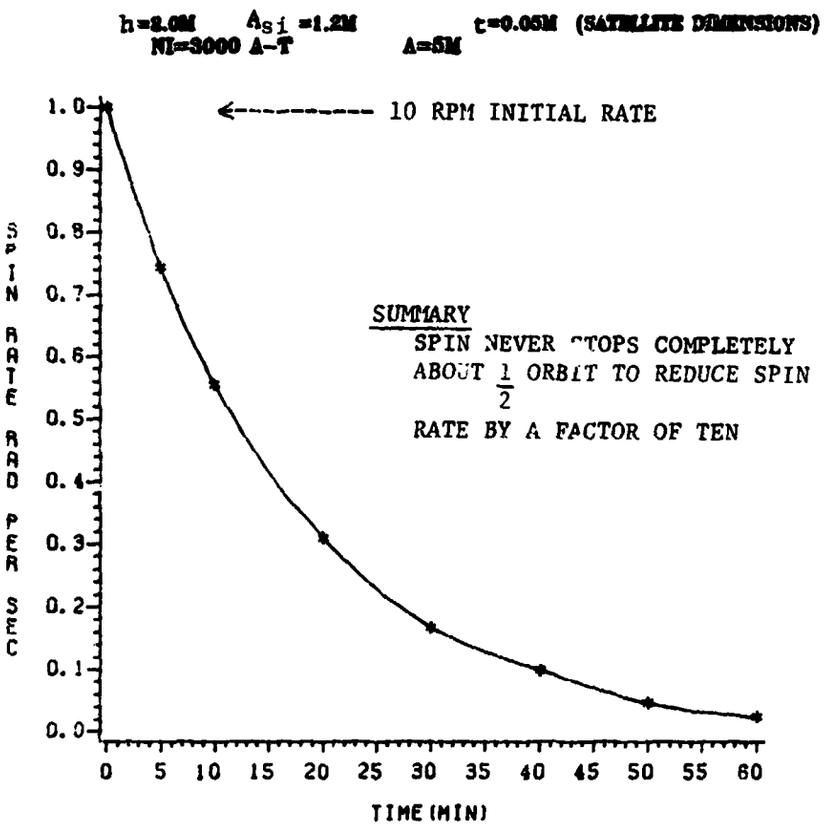

FIG. 3 SPIN RATE VS DE SPIN TIME

superconducting commercial material available at temperatures higher than liquid helium is Niobium-Germanium tape operated at slush hydrogen temperature -- around 17 or 18° K. Niobium-Germanium film 10μ thick is deposited on copper substrate by CVD and plated with hastelloy to provide strength. The overall thickness of the tape is 15 mils and $\frac{1}{4}$" wide. The use of liquid hydrogen would be practical in the present application involving the shuttle as liquid hydrogen is readily available.

Magnet Design Considerations:

Permanent Magnet: The use of a permanent magnet, if one of suitable size and weight can be designed, to achieve de-spinning would be desirable as this would mean no external power source. In view of this, design criteria for permanent magnet are summarized. Commercial sources for permanent magnets which can provide the rather high magnetization necessary for this application are not readily available.

The important parameters in the design of a permanent magnet are: i) the residual induction, B_r, ii) the coercive force, H_c, iii) the maximum energy product (BH) max and iv) the permeance coefficient, $B/\mu_o H$. The material used should have a high B_r and H_c. The permeance coefficient defines the actual operating point on the demagnetization curve for the material from which the magnet is made. $(BH)_{max}$ is the highest value that can be obtained when multiplying values of B and H along the demagnetization curve. $(BH)_{max}$ defines the greatest capability of the material and the operating point should approach $(BH)_{max}$. B_r is the maximum flux density that can occur in the magnet with no air gap. A magnet with an air gap has a 'self demagnetizing' effect that acts to reduce the flux density in the magnet and this flux density can never equal B_r. The bar magnet is the case of the greatest air gap.

For the specific case of round bar magnets the following design equations are relevant (6):

$$\frac{B}{H} = \frac{K_1}{\left(\frac{D}{2}\right)^2} \sqrt{\frac{D}{2}\left(\frac{D}{2} + L\right)}$$

for axially oriented types, with $K_1 = 0.7L$ for Alnico types and $K_1 = L$ for all ferrites.

$\frac{B}{H} = \frac{4}{L}\sqrt{\frac{D}{2}\left(\frac{D}{2} + L\right)}$ for diametrically oriented types. In both these

equations L is the length and D is the diameter of the bar magnet. For a given L and D use of these equations will give the permeance coefficient which defines the operating point on the demagnetization curve.

Cobalt-rare earth alloy permanent magnets are, perhaps, the best material to use in the present application. In view of this, the information on this type of magnet material is summarized below:

Cobalt-rare earth alloy permanent magnets (7):

The cobalt-rare earth alloys have the general formula R Co_5, where R, is one of the rare-earth elements samarium, praseodymium, etc. They are made by pre-alloying the constituents under an inert atmosphere, reducing the alloy to a fine powder, pressing to the required shape in a strong magnetic field, and finally sintering in an inert atmosphere. They owe their permanent magnet properties to the extremely high magnetocrystalline anisotropy of their hexagonal crystal structure.

Sm Co_5: B_r = 0.85 Wb/m^2; $(BH)_{max}$ = 135 KJ/m^3; H_c = 640 KA/m; specific gravity = 8.1; working temperature limit = 200° C; Composition: Co 66%; Sm 43%. Magnetizing considerations: the magnet can be magnetized by a solenoid powered by d.c., supplied by batteries, a rectifier or a motor generator. The winding should be designed to match the available supply, and since magnetization can usually be accomplished in a second or less, it may not be necessary to design for continuous running. For anisotropic materials the magnetizing force should be at least three and for isotropic materials, five times the coercivity. For materials such as ferrites and cobalt-rare earths, where the intrinsic coercivity, H_{ic} is much greater than H_c, it is H_{ic} that should be considered. For producing very large magnetizing forces, large current pulses lasting for only a fraction of a second are used. This can be obtained from the discharge of a capacitor. Superconducting coils have sometimes been used for magnetizing rare-earth-cobalt magnets.

Specifically for the present application a permanent magnet with a magnetization M, of about 7.96 x 10^5 A/M would be desirable in order to achieve a reasonable value of de-spinning time. This value of magnetization is a good compromise between reasonable size and strong enough interacting magnetic flux density at the skin of the satellite. The magnetic flux density in the magnet corresponding to M = 7.96 x 10^5 A/M is 10,000 gauss whereas 15,000 gauss is about the limit for a bar magnet. From the information provided by Ithaco, Inc., New York (8) the largest magnet available corresponds to a magnetization M = 4 x 10^5 A/M and weighs 50 Kgms. Based on this data, the magnetization of M = 7.96 x 10^5 can be provided by a bar magnet with a diameter of 10 cms and 2.5

meters long. Its weight would be around 187 Kgms. According to information available the weight of the magnet increases linearly with dipole moment.

As regards the electromagnet (a solenoid with a magnetic core), the ampere-turns (A-T) necessary to yield a magnetization of 7.96×10^5 A/M would be:

$$\frac{7.96 \times 10^5}{\mu} \simeq NI$$

where μ is the appropriate permeability. Using a value of μ=5, (9) for flux density of 10,000 gauss, the ampere-turns NI would be 1.59×10^5. For a current of I=45 amps, the same value used in the current loop design, the number of turns N would be 3500 turns/meter.

iii) RESULTS AND ANALYSIS

Both in the case of the current loop and the magnet system the various parameters have been parametrically analyzed and the results are shown in the following figures. Figures 4 and 5 are respectively plots of eddy current power input and de-spin time vs. rpm of the satellite for the following ampere-turns (A-T): 6000, 9000 and 12,000. The satellite (cylinder) dimensions chosen are the height of the cylinder h=3m, the inner radius A_{si} = 1.45 m, the thickness of the cylinder wall, t=0.05 m and the radius of the current loop, A=5 m. Figures 6 and 7 are similar plots for a smaller size spinning satellite. Here h=2.5 m, A_{si}=1.2 m, t=0.05 m and A=3.5 m. The ampere-turns chosen are 6000 and 9000.

The de-spin time increases, as one would expect, when the rpm of the satellite decreases. Also as the ampere-turns increases the de-spin time decreases. By doubling the number of ampere-turns, the de-spin time is reduced by about $\frac{1}{4}$. For the smaller satellite very good values of de-spin times are obtained when the radius of the current loop is reduced to 3.5 m for the case of 6000 A-T. For example, for 10, 8 and 6 rpms the de-spin times range from 20.3 to 39.4 minutes a time span within the orbital daylight. For the larger satellite, as indicated in figure 5, desirable de-spin times are obtained by going to 9000 or even 12,000 A-T. The data shown in figure 5 is for the case where the radius of the coil is 5 m. The ampere-turns needed could, of course, be reduced by using a smaller diameter coil. As mentioned earlier in the report in section (ii) under design considerations, good values of power input around 1.1 KW are obtained by using cryogenic cooled coils. The value stated is for the case of 9000 A-T aluminum coil at liquid nitrogen temperature. The power requirement is quite modest compared to the available power of 6 KW. The overall weight of the current loop is also a reasonable value, less than 200 lbs.

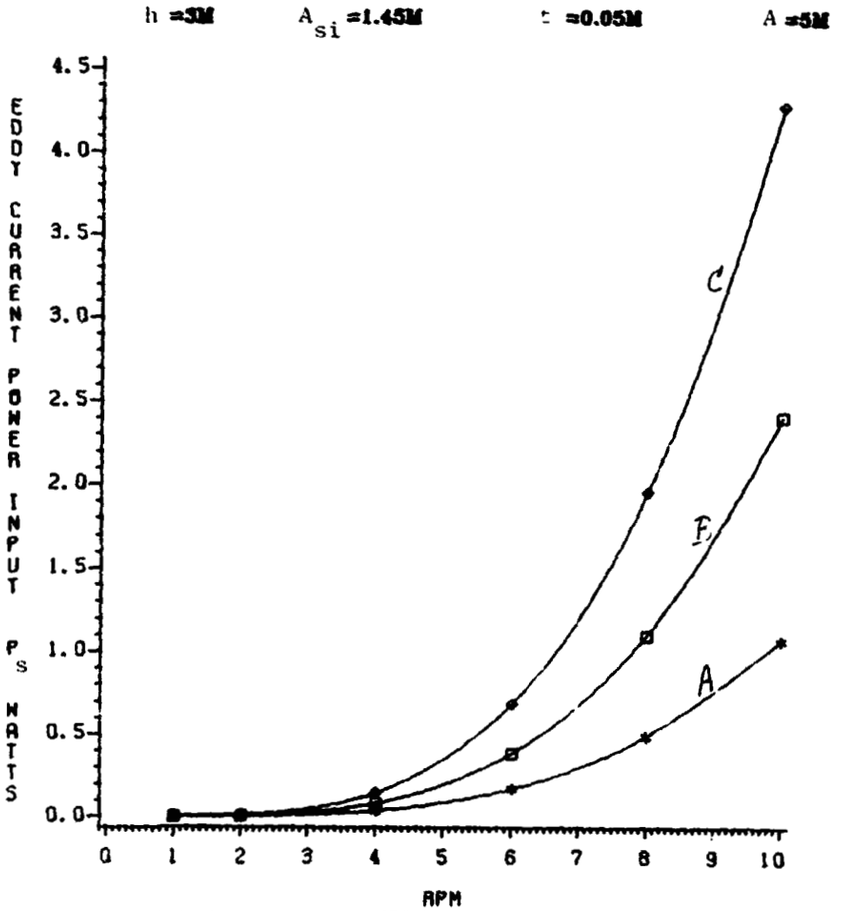

FIG. 4 EDDY CURRENT POWER INPUT P_S VS RPM
(A) NI=6000 A-T, (B) NI=9000 A-T, (C) NI=12000 A-T

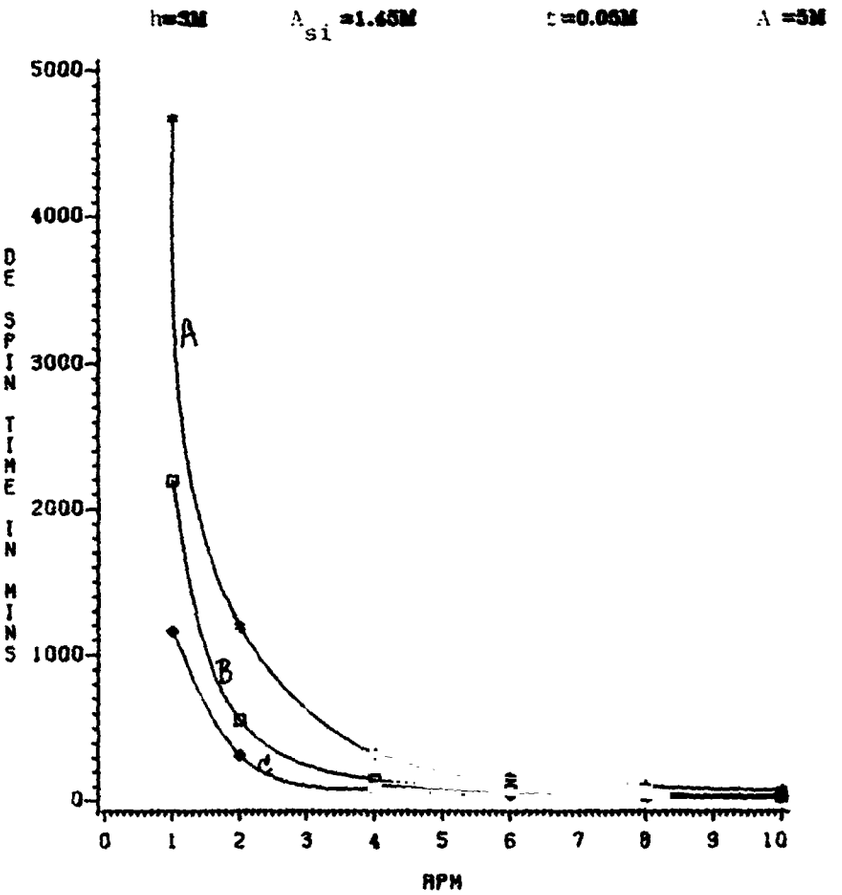

FIG. 5 DE-SPIN TIME VS RPM
(A) NI=6000 A-T. (B) NI=9000 A-T. (C) NI=12000 A-T

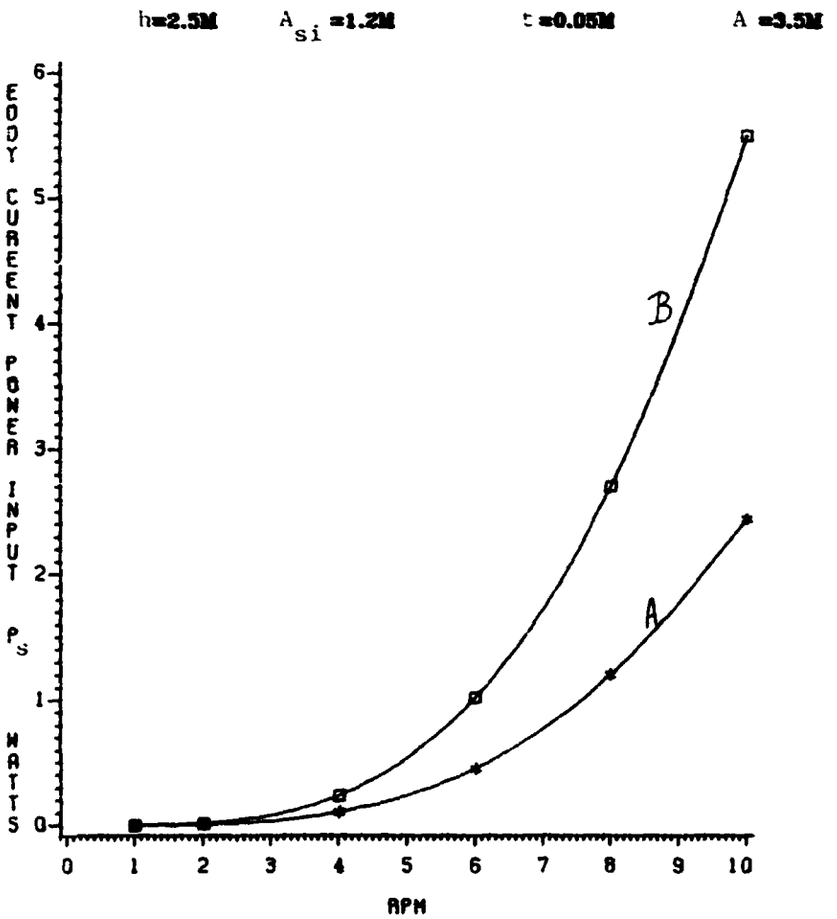

FIG. 6 EDDY CURRENT POWER INPUT P_s VS RPM
(A) NI=6000 A-T, (B) NI=9000 A-T

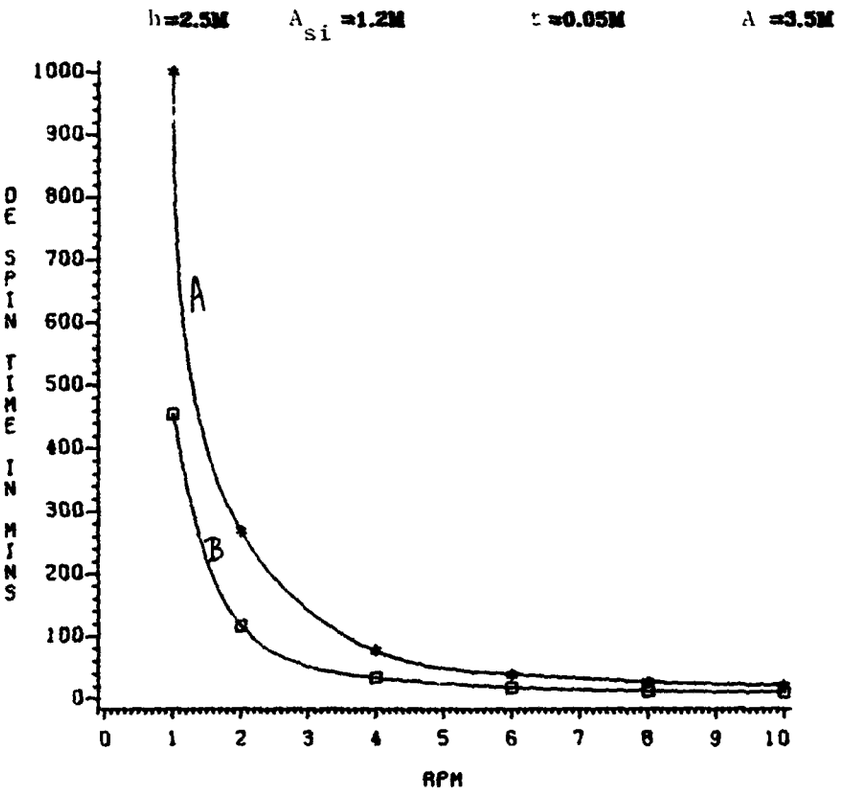

FIG. 7 DE-SPIN TIME VS RPM
(A) NI=6000 A-T. (B) NI=9000 A-T

Figures 8 and 9 are, respectively, the eddy-current power input and de-spin time vs. rpm for different positions of the magnet relative to the spinning satellite (d_{0s} ranging from 1.85 m to 2.85 m). The magnetization M of the magnet is 7.9×10^5 A/M and the magnet dimensions are: radius A=0.05 m and length d=2.5 m. The dimensions of the spinning satellite are: h=2.5 m, A_{si}=1.2 m, and t=0.05 m. As one would expect, the de-spin time for a given rpm increases as the distance d_{0s} is increased. There is about a two-fold increase in de-spin time as the distance of the magnet from the satellite is increased by 1 meter. What is puzzling, however, is that the de-spin time decreases as the rpm of the spinning satellite decreases. This is opposite to that for the current loop case. One possible explanation is that the eddy-current power input P_s does not vary a great deal compared to the rotational energy as the rpm of the spinning satellite changes. A thorough explanation would involve three dimensional plots of the interacting flux density. Figure 10 shows the plot of de-spin time vs. rpm for three values of magnetization M=7.9×10^5, 1.2×10^6 and 2×10^6 A/M. For a given rpm, as M is increased the de-spin time decreases from 139 minutes to 21.7 minutes as M is increased from 7.9×10^5 A/M to 2×10^6 A/M. The data shown in figure 10 is for a satellite whose dimensions are: h=3 m; A_{si}=1.45 m; t=0.05 m. The magnet dimensions are: the radius A=0.05 m and length d=2.5 m. The data shown in tables I and II are interesting in that there is a significant change in de-spin time as the radius of the magnet is changed keeping the length constant. For example, as shown in tables I and II for the case of 10 rpm the de-spin time is 268 minutes with M=4×10^5 A/M and A=0.05 m whereas the time is 9.53 minutes with M=7.9×10^5 A/M and A=0.087 m.

By comparing the data of the current loop with the magnet system, it would seem that the current loop design is to be preferred from the point of view of shorter de-spin time and smaller weight of the cryogenic cooled coil. As indicated in section (ii) under design considerations for a permanent magnet with a diameter of 10 cms and 2.5 meters long the weight of the magnet is 187 Kgms. to provide a magnetization of 7.96×10^5. However permanent magnet has the desirable feature that no external power source is required to energize it. Before a final evaluation can be done the magnet system needs to be researched further.

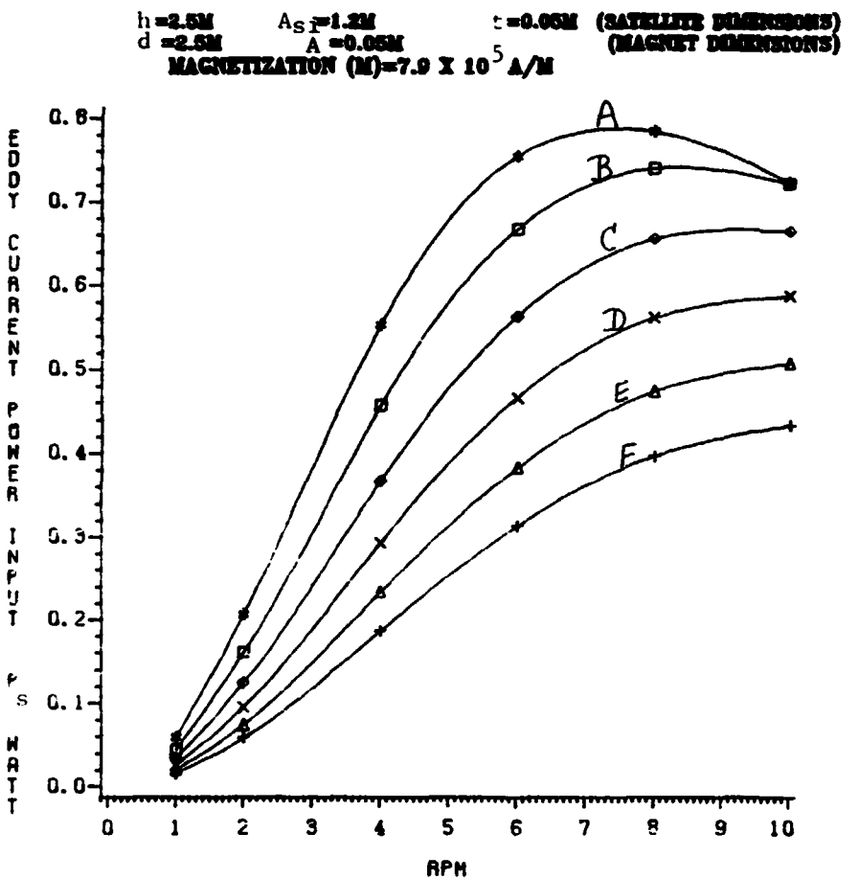

FIG. 8 EDDY CURRENT POWER INPUT P_S VS RPM
(METERS)=(A):1.85,(B):2.05,(C):2.25, (D):2.45,(E):2.65,(F):2.85

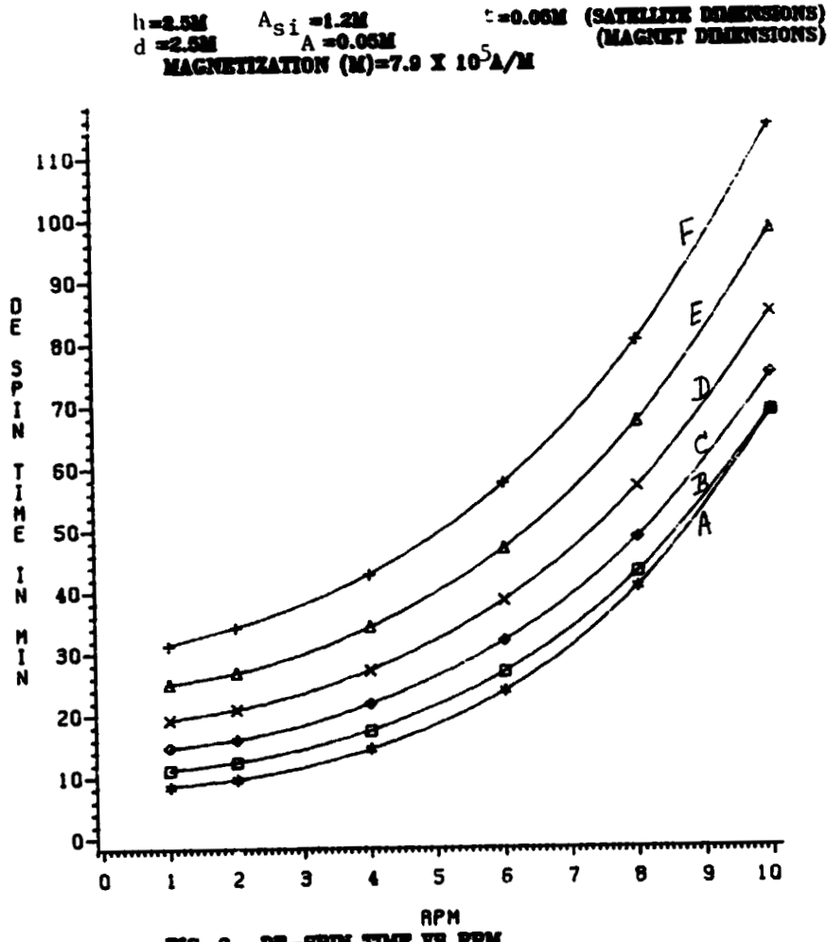

FIG. 9 DE-SPIN TIME VS RPM
(METERS)= (A):1.85, (B): 2.05,(C):2.25,(D):2.45,(E):2.65,(F):2.85

ORIGINAL PAGE IS
OF POOR QUALITY

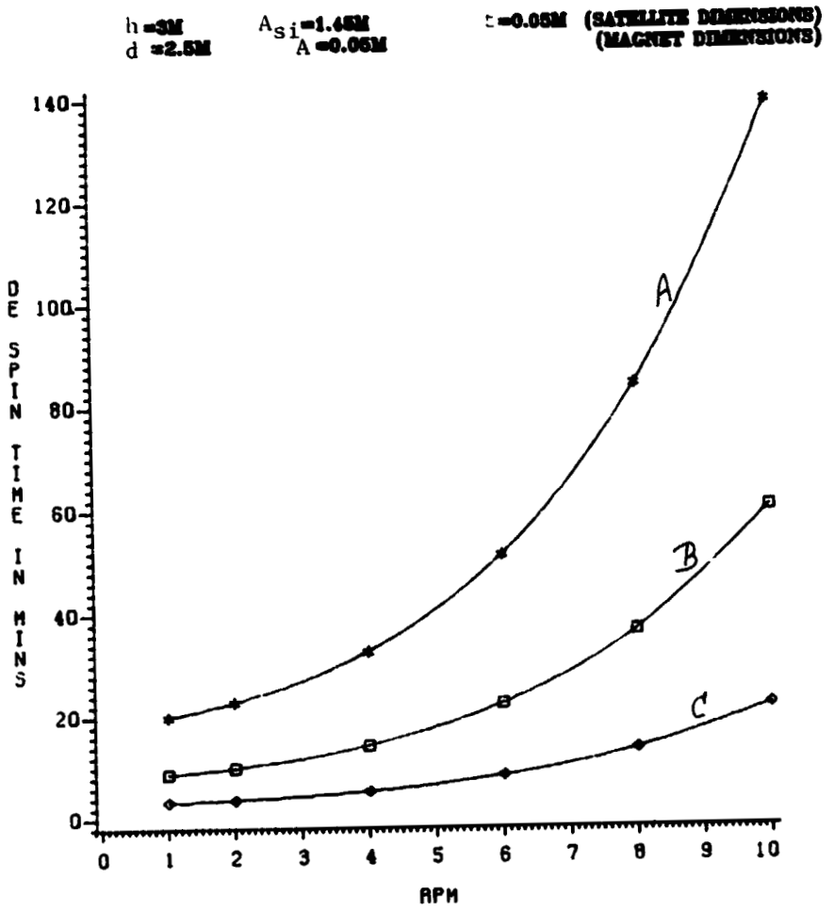

FIG. 10 DE-SPIN TIME VS RPM
(A)=7.9 X 10^5 A/M,(B)=1.2 X 10^6 A/M,(C)= 2.0 X 10^6 A/M

Table I: Eddy-current power input and de-spin times for different rpm; Magnet parameters: $M=4 \times 10^5$ A/M, A=0.05 m, d=2.5 m. Satellite dimensions: h=2.5 m, A_{si}=1.2 m; t=0.05 m, d_{0s}=1.85 m.

RPM	10	8	6	4	2	1
P_s (Watts)	0.185	0.201	0.193	0.142	0.053	0.015
De-spin time (minutes)	268	158	93	56	37.4	33.3

Table II: De-spin times for different rpm. Magnet parameters: $M=7.9 \times 10^5$ A/M, A=0.087 m, d=2.5 m. Satellite dimensions same as in Table I. d_{0s}=1.85 m.

RPM	10	8	6	4	2	1
De-spin time (minutes)	9.53	6.01	3.80	2.50	1.80	1.60

CONCLUSIONS AND RECOMMENDATIONS

The theoretical study undertaken indicates that the non-contacting electromagnetic satellite de-spin system based on the induction of counter acting eddy-currents in the satellite is practical and requires only moderate amounts of power. It would be possible to reduce satellite spin to a very low value within a reasonable time of the order of orbital daylight or less.

A comparision of the two systems, one based on a large diameter coil positioned symmetrically around the satellite and the other using a magnet positioned close to the satellite indicates that the current loop design is to be preferred from the point of view of shorter de-spin time and lighter weight of the cryogenic cooled coil compared to the weight of the magnet. The permanent magnet, however, has some merit in that it does not involve any external power source In particular, the current loop design using a coil radius of 3.5m and 6000 A-T gives very good values of de-spin times within the orbital daylight for the smaller of the two satellites investigated. The power input to the coil using cryogenically cooled coils is around 1 kw. The satellite (cylinder) size is 2.5m long and 2.5m in diameter with a wall thickness of 0.05m. Even for the heavier satellite - 3m long and 3m in diameter - reasonable de-spin times can be obtained using a 9000 A-T coil. The magnet design using reasonable size magnets seems to be practical for lighter satellites with the magnet positioned close to the satellite - about 2 feet away. The interesting result that the de-spin time decreases as the rpm of the spinning satellite decreases in case of the magnet design seems to suggest that the two designs are complimentary. The current loop design is a good method when the spin rate is high and the magnet design is, perhaps, better when the spin rate is low.

The recommendations are as follows:

i) The theoretical analysis of the magnet system needs to be pursued further. In particular the reason why the de-spin time decreases as the rpm of the spinning satellite decreases needs to be investigated in greater detail. A three-dimensional computer plot of interacting flux density profile would be helpful in the analysis. The design of a cost-effective and reasonable size permanent magnet with a rather high magnetization needs to be pursued further. The possibility of commercial sources other than Ithaco needs to be looked into.

ii) A scaled-down laboratory model of the proposed de-spin system could be constructed with a view to test the results of the theoretical analysis outlined in this report.

iii) A computer simulation of a complete de-spin mission profile using a

series of representative satellite characteristics that have a bearing on the de-spin process is suggested.

Finally, it is appropriate to mention that the designs envisaged in this study will provide a safe and effective satellite de-spin system which could replace the present concept of direct astronaut EVA intervention for de-spinning.

REFERENCES

1. Smythe, William R., Static and Dynamic Electricity, McGraw-Hill Book Co., New York, N.Y., 1968, p. 290.

2. Del Toro, Vincent, Principles of Electrical Engineering, Prentice-Hall, Inc., Englewood Cliffs, New Jersey, 1965, pp. 600-604.

3. Nussbaum, Allen, E. M. Theory for Engineers and Scientists, Prentice-Hall, Inc., Englewood Cliffs, New Jersey, 1965, pp. 287-288.

4. Hanby, K. R., 'Handbook on Materials for Superconducting Machinery' Technical Report, Battelle Columbus Labs., Ohio, Nov., 1975. Mueller, A., 'Superconducting tape with A15-phase Nb-Ge' Zeitschrift fuer Metalkunde, 71, 1980, pp. 507-510.

5. Braginski, A. I., et al., "Niobium-Germanium Superconducting Tapes for High-Field Magnet Applications" Contract NAS3-20233, Westinghouse Research and Development Center, November, 1977.

6. Moskowitz, Lester R., Permanent Magnet Design and Applications Handbook, Cahners Books International, Inc., Boston, Mass., 1976, p. 45.

7. Wright, W., and McCaig, M., Permanent Magnets, Oxford Univ. Press, 1977, pp. 10-11.

8. IPS 0009: 'Magnet Acquisition/Despin System', Ithaco, Inc., Ithaco, N.Y , July, 1979.

9. Liwschitz-Garik, Michael, D. C. Machines, Van Nostrand Co., Princeton, New Jersey, 1961, p. 9.

1983

NASA/ASEE SUMMER FACULTY RESEARCH FELLOWSHIP PROGRAM

MARSHALL SPACE FLIGHT CENTER
THE UNIVERSITY OF ALABAMA
IN HUNTSVILLE

STUDIES OF NEUTRON AND PROTON NUCLEAR ACTIVATION IN LOW-EARTH ORBIT II

Prepared by:	C. E. Laird, Ph.D.
Academic Rank:	Professor
University:	Eastern Kentucky University
Department:	Physics and Astronomy
NASA/MSFC:	
(Laboratory)	Space Science
(Division)	Astrophysics
(Branch)	High Energy Physics
MSFC Counterpart:	Gerald J. Fishman
Date:	August 12, 1983
Contract No.:	NGT 01-008-021 The University of Alabama in Huntsville

STUDIES OF NEUTRON AND PROTON ACTIVATION IN LOW-EARTH ORBIT II

BY

C. E. Laird, Ph. D.
Professor of Physics
Eastern Kentucky University

ABSTRACT

The study of neutron and proton nuclear activation in low-earth orbit reported in NASA CR-162051 has been continued with increasing emphasis given to primary and secondary neutron activation. The previously reported activation due to protons has been modified to include 1. flux attenuation caused by all inelastic reactions; 2. the modification of the proton flux distribution caused by sample covering material; and 3. the activation of the sample as a function of the distance into the sample from the surface of incidence. A method has been developed for including the effects on the activation of the finite width and length of the samples. The reactant product spectra produced by proton-induced reactions has been studied. Cross sections needed for neutron induced reactions leading to long-lived (half-life>1 day) radioisotopes have been indentified and, in some cases, compiled. Reactions for which cross sections are unavailable have been indentified for further study. From data found in the literature an estimate has been made as to the flux of primary neutrons in the planned LDEF orbit.

LIST OF TABLES

Table No.	Title	Page
I.	Total Inelastic Cross Sections	XIX-18
II.	Activation of Cobalt Sample	XIX-18
III.	Effects of Aluminum Covering on Proton Flux	XIX-19
IV.	Activation as a Function of Sample Depth without Inelastic Scattering	XIX-20
V.	Activation including Inelastic Scattering for Co-59(p,n) Reaction	XIX-21
VI.	Expected Neutron Flux for LDEF Orbit	XIX-22

INTRODUCTION

The radiation environment experienced by scientific equipment placed in low-Earth orbit is a subject of continuing study by NASA. An understanding of the primary and secondary radiation and their effects on spacecraft materials and experiments is needed to assure the proper operation of orbiting scientific and engineering instrumentation; especially, for radiation detection equipment planned for satellites such as the Gamma Ray Observatory. While the effects of prompt radiation produced by incident charged particles may be suppressed by using anti-coincidence shielding, the effects of induced radioactivity are much more difficult to counter. The feasibility of orbital experiments requires a better understanding both of the primary radiation environment and of the induced radioactivity in orbiting spacecraft.

The High Energy Physics Branch of the Space Science Laboratory at Marshall Space Flight Center has developed an experiment to gain further knowledge of spacecraft radiation environments. This experiment consists of measuring the radioactivity induced in small metal samples scheduled to be flown in the Long Duration Exposure Facility and on Spacelabs I and II. An analysis of the activation of these samples will yield information related to the primary and secondary fluxes of particles encountered by the samples.

In order to anticipate the activation of these samples, preliminary calculations were begun during the Summer of 1982 under the NASA/ASEE Summer Faculty Fellowship Program. The results of that study have been published<1>. As a continuation of that work this report contains the activation caused by primary protons as a function of depth into the sample, the reduction in activation caused by inelastic nuclear processes attenuating the proton flux, the effects of covering the samples with a 3/8 inch aluminum covering, and a method for calculating the activation of the samples in the situation where the activating particles may leave the sides. Also, the expected primary neutron flux is estimated from atmospheric and orbital neutron flux measurements. Finally, suggestions are made for further study.

A. EFFECTS OF INELASTIC SCATTERING

While both protons and neutrons passing through matter interact through nuclear processes, protons also experience electromagnetic forces. The electromagnetic forces, acting between charged projectiles and atomic electrons, result in a loss of kinetic energy and may cause the total stopping of the particle. The rate of energy loss (stopping power) and the range of charged particles in matter have been extensively studied<2>. Recently, Zaidens<3> has established useful semi-empirical equations for these processes and Andersen et al.<4> have tabulated "best-fit" values using a modification of the Bethe formula. The Zaidens' equations and the effects of the stopping power and range have been discussed in a previous report<1>.

The nuclear interactions between nucleons and nuclei include elastic and inelastic scattering. Elastic scattering results in the deflection of the nucleon with the recoiling nucleus carrying off the kinetic energy lost by the nucleon. Inelastic scattering results in the capture of the nucleon, with other particles (p',n,D,T,etc.) being emitted. As protons pass through matter, they continually lose energy through electromagnetic scattering where the Coulomb force between the proton and the atomic electrons results in a continual reduction in the mean energy of the protons and a spreading of the energy distribution of the protons through straggling. Most nuclear reaction excitation functions peak within a few MeV of the reaction threshold; especially when barrier penetration effects have been overcome and when there are sufficient numbers of high-spin protons to populate high spin ground states. As the protons lose energy, those with energies greater than the peak of the excitation function have an increasing probability of reacting with the nucleus as they lose energy. As the energy drops below the peak energy, effects of barrier penetration rapidly reduces the interaction probability. Thus, electromagnetic interactions may increase the probability of an interaction for some protons but decrease that probability for other protons.

Nuclear interaction may also modify the energy of the nucleon through elastic scattering or may capture that nucleon with other particles being emitted. Elastic nuclear scattering of protons and neutrons from moderate-to-heavy nuclei, as in the LDEF samples,

results in scattering with rather small energy loss (2% for A > 50) and with an angular distribution having a dominant peak in the forward direction. Since the calculations of this report assume a random distribution of incident particles and since there is only a small energy loss per nuclear elastic collision, the resultant distribution of nucleons will not be seriously affected by elastic scattering. Thus, elastic scattering was not included in the present calculations.

Inelastic scattering processes result in a reduction of the flux of primary nucleons as they pass through the material; not simply a modest change in energy or directions. Excitation functions for total inelastic scattering have been measured for a wide variety of targets<5,6,7>. The procedure for inelastic scattering experiments<5> involves measuring the reduction in the incident beam intensity after it passes through a given target and the angular distribution both of the elastically scattered nucleons and of the charged secondaries produced in a reaction. Corrections for elastic and inelastic scattering into the forward direction are made to the measured transmitted intensity to obtain the reaction cross section. The quoted accuracy for such measurements are from 3 to 4% <5,6> including both statistical and non-statistical errors.

Renberg et al.<5> have measured the inelastic-scattering cross sections for a large number of targets for incident protons energies from 184 to 560 Mev. Also, they have graphically presented other inelastic-scattering data taken from the literature for proton energies from 10 MeV to 2 GeV. More recently, Abegg et al.<6> have determined inelastic scattering cross sections for proton energies up to 30 MeV measured with targets of tantalum, gold and terbium. Barashenkov et al.<7> have tabulated total, elastic, and inelastic cross sections for nucleons, antinucleons, pi- and K-mesons for energies greated than 50 MeV. Unfortunately, above 200 MeV these results exhibit large inconsistancies. But, the more recent measurements, noted above, remove some of the inconsistancies.

Abegg et al. <6> compared their results both to black nucleus and optical model calculations. They found that the optical model, which specifically calculates the proton penetrability and which uses global optical model parameters, gave the better fit. However, in their black-nucleus model they only used a geometri-

cal cross section modified to have an effective radus of R+λ where λ is the reduced wavelength of the incident particle.

Renberg et al.<5> used a more complicated model which included an approximate Coulomb repulsion factor and an approximation for the transparency of the nucleus. Their data was analyzed using

$$Sin = \pi(R+\lambda)^2(1-V/E)(1-T) \qquad (1)$$

where $R=RoA^{1/3}$ is the nuclear radius, Sin is the inelastic scattering cross section, and V is the Coulomb barrier of the nucleus defined by

$$V = zZe^2/(R+\lambda), \qquad (2)$$

E is the kinetic energy of the incident particle, K is an "effective intra-nuclear" wave number, and T is the transparency of the nucleus to the proton given by

$$T = (1 - (1 + 2KR)\exp(-2KR))/2K^2R^2. \qquad (3)$$

This function fits their data but does not do very well for the data below 100 Mev. There, this model tends to poorly account both for the rapid rise of the cross section to a peak near 25 MeV and the rapid fall off to a valley near 100-200 MeV. More complicated model calculations do give the required cross-sectional behavior but at a substantially greater computational effort. A recent treatment by Townsend et at. <8> using eikonal scattering theory fits the data very well for energies from 25 MeV up to 22.5 GeV.

Since there seemed to be no simple analytical function with which to calculate inelastic cross sections, it was decided to make use of the experimental cross sections and of interpolation for the activation calculations. However, the A dependence seen in the model fit to the inelastic scattering data was used to scale the measured data for a given nucleus such as Fe to nuclei such as Co which were not studied by these authors. Thus, for this report the unmeasured inelastic cross-sections for V, Ni, and Co were scaled

from Fe, for Ta from Pb, and for In from Sn(In). Table I contains the scaled inelastic cross sections used in this report. The expected accuracy of these tabulated values should be on the order of 10%.

Also, Table I contains, for each element, the appropriate parameter, C which is used in Zaiden's equation<1,3> to calculate charged particle range and stopping power. The units of C are such that the stopping power is in MeV per grams/sq. cm. and range in grams/sq. cm. if the energy is in MeV.

The computer program IRTRAP.1> used in these calculations was modified to correct for the flux attenuation due to inelastic processes using the well-known exponential law

$$F(x) = F(0)\exp(-N\ \mathrm{Sin}(E)\ x) \qquad (4)$$

where F is the proton flux, Sin(E) is the inelastic cross section at an energy E, N is the number of atoms/cubic centimeter, and x is the distance (in grams per sq. cm.) into the sample. Since E is continually decreasing due to stopping effects, the inelastic cross section must be evaluated at an average energy within the distance x. For proton energies between the tabulated values a semi-log interpolation was used.

Table II contains, in column B, the activation produced in the Cobalt sample when inelastic attenuation is included. A comparison of col. B with col. A, which contains the activation without absorption, shows only a small reduction in the activation. Typical reductions of a few percent indicate that the attenuation of the proton flux by all inelastic processes will not significantly affect the activation of the LDEF samples.

B. COVERING MATERIAL

The LDEF samples are mounted at various locations around the facility and, thus, are affected by varying amounts of material on the different sides. For most samples the side facing outward will have only a small layer of insulating material. However, on one set of samples the covering material consists of 3/8 inches of

aluminum and silicon. On all samples, enough material is usually present on the sides that incident particles would not impinge at right angles to the sides. On the back of each sample, at least 5 g/sq.cm. of material will drastically reduce the activation from the omni-directional trapped-proton flux found in the planned orbit. Thus, activation by trapped-protons incident on the spacecraft side of the samples is not considered to be significant. However, if there should be a significant proton flux onto the sample from inside the facility, it will show up as a significant activation on the inside surface(see Section C). For further calculational purposes it was assumed that protons strike neither the backs nor at right angles to the sides of the samples. Also, since silicon has nearly the same Z as Al, calculations are presented only for the effects of 3/8 inch of aluminum covering material.

The inelastic-scattering cross sections used in these calculations are taken from Ref. 5. Cross sections are evaluated from this data using a semi-log interpolation. Stopping powers and ranges are calculated using Zaidens' semi-empirical equations <3>. In the calculation of the activation the samples were considered to be square segments which are part of an infinitely wide and long sample as previously outlined <1>. The activation /unit area (# of nuclei/day of flight/unit area of sample) was calculated for a unit area on the surface and scaled to the required surface area. It was assumed that the proton is incident at an angle θ and thus, it has passed through a thickness of covering material given by $t/\cos(\theta)$ where t is the thickness normal to the surface. For a given incident energy the energy degradation and the flux attenuation is calculated. This lower-energy, attenuated flux is then used for calculating the activation of the sample. Table III contains the effects of the covering material on the incident flux at a variety of incident angles as well as the flux for no covering material for comparison. While the flux is not dramatically reduced for protons of a specific energy unless the proton is stopped, the energy of the emerging proton is greatly reduced.

Column C of Table II contains the total activation per day produced in the Cobalt sample covered by aluminum. This covering reduces the activation by more than 50% in each reaction. The stopping of protons in the covering material greatly reduces the flux reaching the samples as well as reducing the energy of those that do. Both effects strongly reduce the total activation.

Table V contains the activation as a function of depth into a covered Cobalt sample. This will be discussed in Section C.

C. ACTIVATION AS A FUNCTION OF DISTANCE INTO SAMPLE

As previously mentioned, a proton passing through the sample continuously loses energy until it stops or leaves the sample. For protons having energy above the peak of the reaction cross section the probability of a reaction increases as the energy decreases. If the proton energy is at, or below, the peak the reaction probability decreases as the energy decreases. Since the proton energies decrease in approximately a linear fashion with the distance into the sample, variation in activation with distance into the sample might be observed.

In Table IV the activation of a vanadium sample is presented as a function of distance (grams/sq. cm.) into the sample (along the z axis). The activation reaction listed here is (p,n) and has been calculated with the flux of protons expected in orbit but, in case 1, assuming only normally incident protons and, in case 2, assuming an omnidirectional flux ($<\theta>$). In both cases it is obvious that the activation is greatest near the surface of the sample. However, the $<\theta>$ average result has an overall greater activation and a distribution of activation that is greatest near the front surface.

Further confirmation of these conclusions can be seen in Table V where the activation as a function of distance into the sample is given for the Co(p,3n) reaction. These results include flux attenuation by inelastic processes whereas those in Table IV did not. In both V(p,n) and Co(p,3n) reactions a similar pattern of decreasing activation with distance is seen. Results for other reactions not tabulated support the proposition that this will hold in most, if not all, reactions.

Once the LDEF samples have been returned from orbit, careful counting of both the front and back surfaces of the samples will give an indication of the proton flux onto those surfaces. The attenuation of the intensity of gamma rays passing from one surface through the sample and counted after leaving the second

surface will yield data related to the position of greatest activation. For example, if the greatest activation is at surface A, then the count rate with surface A nearest the detector will obviously be greater than with surface B there. Assuming that the energy dependence of the proton flux is approximately correct, then deviations of the front to back counting ratio from that predicted by the model may indicate a significant proton flux from inside the spacecraft. This would be seen in the spectra of low-energy gamma rays which are highly attenuated by the sample. The attenuation for gamma rays passing through one-half, or 1/16 inch, of the Cobalt sample is 6.7% at 1377 MeV and 26% at 158 keV. By comparing the ratio of the intensity of widely separated gamma-ray peaks measured from the LDEF samples with that expected from thin sources-both gamma rays produced in a specific reaction-an effective activation depth can be obtained. Therefore, if the gamma-ray spectra taken with the back of the sample facing the detector yield a greater than expected intensity, then a significant proton flux will be incident from inside the spacecraft.

D. TECHNIQUE FOR MEASURING ACTIVATION AS A FUNCTION OF POSITION WITHIN THE SAMPLE

The finite width and length of the samples reduce the overall activation because some particles leave the edges of the material and others enter through the sides and do not encounter as much material as those passing through the total thickness. A technique which could be used to accurately calculate an approximation to the expected activation would break the sample into a large number of cubical (or parallelopiped) cells each surrounding a lattice point. The surface cells have particles incident on the top, whereas the cells on the sides have particles incident upon them. For a sample of length and width W and thickness t and cell size d, we would have N X N X NZ cells where N = W/d and NZ = t/d. The activation in a given cell at lattice point i, j, k produced by particles incident on cell i', j', o; N, j', k'or i', N, k' would be given by

$$A(i,j,k) = \sum_{i',j'} A(i,j,k;i',j',0)$$

$$+ \sum_{i',k'} A(i,j,k;i',N,k') + \sum_{j',k'} A(i,j,k;N,j',k'). \quad (5)$$

Protons entering the sides (k = 0) may or may not have reduced or modified fluxes depending on the material, if any, adjacent to the sample.

A straight forward approach to this problem would require (assuming incidence on only one surface and the four sides) calculating the activity produced on each cell (1000 cells if N = NZ = 10) by protons (or neutrons) incident on N surface cells and 4N x NZ side cells. This can be reduced by a factor of eight using the symmetry of the sample. If one breaks the sample into a figure consisting of an equilateral triangle of side W and thickness t, recursion relationships will allow for calculating the total activation in all cells by protons incident only on one-eighth. The coordinates of the centers of the surface cells are (i - 1/2, j - 1/2, k = 0) for i,j = 1 to N. Since only one half of the area of the cells for i = j (i.e., i - 1/2 = j - 1/2) are in the triangle, they must be weighted by a factor of a half. We, therefore, have 1/2 N(N-1) full surface squares and N one-half squares. The sides of this figure is made up of N X NZ rectangular segments.

A particle incident on the surface at point (x,y, 0) will subtend an angle θ with respect to a normal to the surface and an angle ϕ with respect to an x axis arbitrarily taken to be parallel to one of the two sides of the square and through the center. The range of θ will be 0° to 90° and of ϕ from 0° to 360°. Assuming the particle follows a straight line through the sample, its position after traveling a distance L will be given by

$$\begin{aligned} X &= x + L \sin\theta \cos\phi \\ Y &= y + L \sin\theta \sin\phi \\ Z &= z - L \cos\theta \end{aligned} \quad (6)$$

where z = 0 for surface incidence. The particle leaves the sample when L takes a value such that X,Y > a, or Z > T. If T is greater than or equal to the range of the particle, then it stops in the sample.

For the particles incident on the sides θ must be less than 90° and $-90^\circ < \phi < 90^\circ$. If adjacent material

is flush with the exposed surface of the sample, then we assume no 90° incident particles are present. Likewise, we assume particles cannot be incident at angles greater than 90°. Although particles may be elastically scattered off of adjacent surfaces into the sample if there is no side material, particles are also elastically scattered off of the sample in such a way that the two effects are expected to cancel. After traveling a distance L into the sample, the position is given by Eqs. 6 where Z is a negative number. The condition for the particle to cease interacting is the same as in surface incidence.

The activation at a given cell can be determined by calculating the activation along a small segment of the assumed linear path and assigning that activation to the closest lattice point. Once the particle has stopped, leaves the sample or falls below the lowest reaction threshold, then no further activation is possible.

Once the activation in each cell has been calculated, symmetry can be used to total the activation in all cell for total-surface incidence. If Po(i,j,k) is the activation at a lattice point i,j,k due to particles incident on the triangle or its sides, then the total activation for a point inside the triangular slab will be given by

$$P(i,j,k) = Po(i,j,k) + Po(-i,j,k) + Po(-i,-j,k) + Po(i,N-j,k) + Po(-i,N-j,k) + Po(-i,j-N,k) + Po(i,-j,k). \quad (9)$$

Once this has been determined, the activation at a point corresponding to a reflection about the diagonal is given by

$$P(i,j,k) = P(j,i,k) \quad (8)$$

where $i,j > 0$. This gives the activation for the square $i,j > 0$ and then the symmetry about the x- and y-axes gives the activation over the entire slab.

This procedure should yield an accurate estimation of the activation at any point in the lattice. The ultimate accuracy would be dependent upon the total

number of cells used in the calculation. However, there is a linear relationship between the number of cells and the computer time required to perform the calculation. An analysis of the optimal number of cells required to obtain sufficient accuracy for these calculation is needed, but has not yet been undertaken. The computer code IRTRAP has not been modified to include this method of computing the activation.

E. SECONDARY PARTICLES AND REACTIONS

Since the energies of the expected proton flux go well above 100 MeV, the types of particles emitted in proton reactions on the samples are numerous. However, the exponentially decreasing nature of the proton flux means that the probability of the emission of particles having high production thresholds is small. Since neutrons have larger low-energy penetrabilities than charged particles, they are the dominant type of particle emitted in these reactions. The emitted charged particles will have average energies much less than the incident protons and will be stopped by electromagnetic processes before producing significant secondary activation. The uncharged neutrons will not be stopped and could seriously compete with primary activations, especially primary neutron activation.

Secondary neutrons emitted in proton-induced reactions are usually classified as coming from compound nuclear or direct nuclear reactions. Compound nuclear reactions yield particle distributions which peak at low energy (typically below 1 MeV) and fall off rapidly with energy. Secondary neutrons fluxes fall off rapidly to 1/10 of the maximum at an energy of 5 MeV<9>. The angular distribution of these neutrons is isotropic. The energy dependence is given as a Maxwellian energy distribution having the form

$$N(E) = C(E/T^2)\exp(-E/T) \qquad (9)$$

where E is the neutron energy, C is a normalization constant and T is the effective nuclear temperature. Since the neutrons come from (p,xn) and other reactions, the effective nuclear temperature must be determined for each reaction and, then, a series of

distribution functions must be used in activation calculations.

Direct nuclear reactions result in anisotropic, higher energy neutrons. Direct reaction neutrons are emitted predominately in the forward direction with the probability of emission decreasing sharply with angle. Furthermore, direct reactions to isobaric analog states and to specific low-energy states in the daughter nucleus lead to peaks in the neutron spectra. These peaks are very difficult to model, but are not sufficiently strong to cause large discrepancies in activation calculations. Direct reactions can be treated using the exciton or pre-equilibrium model <10>. As a matter of fact, since the direct reactions are small compared to compound reactions, the activation through low threshold reactions, such as (n,γ) or (n,p), can be accurately calculated without considering direct reactions. However, the activation produced by high-threshold proton reactions will demand the energy and angular distributions of direct-reaction secondary neutrons.

Previous work <1> on activation of these samples centered on compiling cross sections leading to long-lived isotopes. Activation calculations for secondary neutrons (and secondaries in general) requires a more thorough compilation of reaction cross sections as well as the energy and angular distributions of the emitted particles. Sufficient data for these calculations have yet to be compiled.

F. ORBITAL NEUTRON FLUXES

The activation of the LDEF metal samples will be produced by primary protons, primary neutrons, cosmic rays, and secondaries produced within the sample and by other material in the facility. A careful interpretation of the measured activation by neutrons will be greatly facilitated by a preliminary calculation of their expected activation effect. In order to perform this calculation an estimate of the neutron flux to be ecountered by LDEF is needed.

Many studies have been done on neutron fluxes as a function of altitude and latitude<11-19>. These have been performed using various types of neutron counters attached to high altitude balloons or placed in

orbiting satellites. This data indicates that the total neutron flux decreases in energy above 1 MeV, that it increases with latitude above and below the equator, and that it decreases with altitude above about 20 km.

Bhatt<11> has extrapolated the results of neutron fluxes measured in balloon flights at 7.8° N latitude to the top of the atmosphere, usually defined to be 50 km. These fluxes show (for E>10MeV) a rapid decrease with energy. Although there are indications of a slightly greater upward neutron flux than downward, his data are total fluxes and may be approximated as omnidirectional.

Klumpar et al.<17> measured the neutron flux at 42° N latitude at an altitude of 3.5 g/sq. cm. (37 km) for neutron energies from 3 MeV to 20 MeV. For the range 3<E<10 MeV they found an energy power dependence with an exponent of -1.8.+/-.2. Matching this functional dependence to Bhatt's 50 km neutron flux at 10 MeV, we find a flux of $3.5\ E^{-1.8}$ N/sec cm MeV for neutron energies 3<E<10 MeV.

Lockwood et al.<16> reported the neutron flux as measured by instruments aboard OGO 6. Two aspects of that measurement are useful to this study. First, the latitude dependence of the neutron count rate was presented. For latitudes less than 40° the dependence is approximately quadratic in latitude. A least-squares fit to their data for θ <32° yielded the result

$$y = 1 + .00152\,\theta^2 \qquad (9)$$

for a 400-500 km orbit where θ is the latitude in degrees. The quality of the fit is as good as one's ability to read the data in Fig. 1 of their article. Furthermore, they observed the count rate as a function of altitude and stated that the flux is reduced at 400-500 km to 43% of the value at 50 km.

The equatorial neutron flux at 500 km can be crudely approximated by taking 43% of the flux at 50 km using Bhatt's extrapolation and the Klumpar et al. energy dependence normalized to Bhatt's value. Integrating the latitudinal dependence of the flux over a 24 hour period of the 28.5°,500 km planned orbit for LDEF yields the fluxes found in Table VI.

The activation caused by the flux can be calculated given the properties of the materials and the cross sections for the various reaction of interest. Although some of the cross sections are found in ENDF/B-V (Evaluated Nuclear Data File) library from Brookhaven National Laboratory, other necessary cross sections are not presently available. Once a more complete compilation is available, the neutron activation calculations can be done with a modified form of IRTRAP.

G. SUMMARY AND CONCLUSIONS

The computer program IRTRAP has been modified to include the effects of trapped-proton attenuation and energy degradation in sample and covering material and to calculate the activation profile within the LDEF metal samples. The calculations indicate that an uncovered sample will have a decreasing level of activation with distance from the surface facing outward from the facility. The 3/8 inch aluminum covering material will reduce the activation by more than half and will "wash-out" the activation energy distribution. However, the covered-sample activation will yield useful information concerning the flux of high-energy protons passing through the covering.

The effects of secondary charged particles on the samples seems to be negligible. This is due to the expected evaporation spectra of these particles and their short mean-free-paths in materials. However, secondary neutrons have much greater paths and will be the dominate particle emitted by reactions in the samples. These neutrons will offer serious competition to some trapped-proton interactions and all secondary neutron reactions.

Finally, an attempt to profile the expected primary neutron flux has been made. The reliability of these estimated fluxes is, as of yet, not known and need additional study.

H. RECOMMENDATIONS

1. An experimental program needs to be initiated at a proton accelerator to obtain empirical data on

sample activation. This data can be used to ascertain the reliability of the IRTRAP calculations and to provide a means of testing the counting and analysis techniques to be used in the LDEF experiment. It also will provide experience to the investigators needed to assure that all appropriate factors have been considered.

2. The effects of finite width and length of the samples on the activation should be given further study. Modifying IRTRAP in the manner suggested in this report should be undertaken.

3. The search for cross sections needed to calculate the expected activation or to unfold the activating fluxes should be continued. Contacts at Indiana University Cyclotron Facility and at Oak Ridge National Laboratory need to be continued or initiated in order to obtain this data by locating tabulated data or by experimentation.

4. A careful study should be made of the local background at the proposed sample counting site, of any temporal changes in that background, of both mechanical and electronic means of reducing that background, and the efficiency of the detector for extended, low level sources. Also, the self-attenuation of the gamma rays by the samples should be studied. Furthermore, the gamma-ray spectra taken with a high-resolution Ge(Li) detector should be analyzed with data analysis software available at Eastern Kentucky University.

REFERENCES

1. C. E. Laird, "Studies of Neutron and Proton Nuclear Activation in Low-Earth Orbit", NASA CR-162051, August, 1982.

2. M. S. Livingston and H. A. Bethe, Rev. Mod. Phys. 9, 245(1937).

3. C. S. Zaidens, NIM120, 125 (1974).

4. H. H. Andersen and J. F. Ziegler, The Stopping and Range of Ions in Matter, 1977, Pergamon Press.

5. P. U. Renberg, D. F. Measday, M. Pepin, P. Schwaller, B. Favier and C. Richard-Serre, Nuc. Phy. A183, 81 (1972).

6. R. Abegg, J. Birchall, N. E. Davison, M. S. De Jong, D. L. Ginther, D. K Hasell, T. N. Nasr, W. T. H. Van Oers, R.F. Carlson, and A. J. Cox, Nuc. Phys. A324, 109 (1979).

7. V. S. Barashenkov, K. K. Gudima, and V. D. Toneev, Progr. Phys. 17, 683(1969).

8. L. W. Townsend, John W. Wilson, and H. B. Bidasaria, "Nucleon and Deuteron Scattering Cross Sections from 25 MeV/Nucleon to 22.5 GeV/Nucleon", NASA TM84636, 1983.

9. T. Nakamura, M. Fujii, and K. Shin, Nuc. Sci. Eng. 83, 444(1983).

10. M. Blann, Ann. Rev. Nuc. Sci. 25, 423(1975).

11. V. L. Bhatt, J. Geo. Res. 88, 4941(1983).

12. V. L. Bhatt, J. Geo. Res. 81, 4601(1976).

13. A. M. Preszler, S. Moon, amd R. Stephen White, J. Geo. Res. 81, 4715(1976).

14. J. A. Lockwood, C. Chen, L. A. Friling, and R. N. St. Onge, J. Geo. Res. 81, 6211(1976).

15. A. M. Preszler, G. M, Simnett, and R. Stephen White, J. Geo. Res. 79, 17(1974).

16. J. A. Lockwood, S. O. Ifedili, and R. W. Jenkins, J. Geo. Res. 78, 7978(1973).

17. D. M. Klumpar, J. A. Lockwood, R. N. St. Onge, and L. A. Friling, J. Geo. Res. 78, 7959(1973).

18. R. Stephen White, Rev. Geo. Space Phys. 11, 595(1973).

19. W. Zobel, T. A. Love, J. T. DeLorenzo, C. O. McNew, R. H. Baldy, and H. W. Parker, ORNL-TM-3877.

TABLE I

Total Inelastic Cross Sections
(millibarns)

	Material					
E(MeV)	Al	V	Co	Ni	In	Ta
10	610	738	813	813	550	
17	690	836	922	922	1270	
20						1611
25						1617
30	700	846	932	932	1510	1649
35	660	837	922	922	1510	1703
40	650	827	911	911		1740
45						1729
50						1748
60	500	752	828	828	1425	1776
100	425	705	777	777	1270	1662
225	400	643	708	708	1180	1600
340	402	638	703	703	1157	1626
460	422	662	730	730	1188	1559
550	427	663	731	731	1188	1595
C	184	148	148	148	110	90

TABLE II

Activation of Cobalt Sample
(100000 nuclei per day)

Isotope Produced	A	B	C
Ni-57	.1849	.1769	.0721
Ni-56	.00788	.00756	.00338
Co-58	10.25	9.823	3.971
Co-57	6.489	6.215	2.586
Co-56	1.944	1.865	.8509
Cr-51	.8178	.7883	.3712
Mn-54	1.598	1.534	.6784

A-uncovered sample without inelastic scattering corrections
B-uncovered sample with inelastic corrections
C-covered sample with inelastic corrections

TABLE III

Effects of Aluminum Covering on Proton Flux
(10000 protons /day sq. cm. MeV)

A. No Covering

E(MeV)

4.5	6.0	10.0	15.0	30.0	50.0	100.0	200.00

Flux

11.34	10.82	8.654	5.987	4.384	3.679	2.581	1.079

B. 3/8 inch Aluminium Covering

Angle (degrees)	Threshold Energy	Incident Energy (MeV) 50	100	200	
					exit
0	45.9	15.2	83.9	190.9	energy
	3.82	3.556	2.516	1.0484	flux
22	47.9	10.1	82.6	190.2	
	3.70	3.546	2.5111	1.0465	
44	55.4		77.1	187.2	
	3.55	-	2.4905	1.0389	
66	76.7		54.9	176.9	
	2.77	-	2.4155	1.0127	
77	107.6			156.7	
	2.06	-	-	.9665	
88	312.1	-	-	-	

TABLE IV

Activation as a Function of Sample Depth
Without Inelastic Scattering
for the V-51(p,n) Reaction
(100000 nuclei per day)

Depth (g/sq. cm.)	Normal Incidence	Theta Averaged
.1	1.29	3.70
.2	1.40	2.68
.3	.91	2.21
.4	.95	1.67
.5	1.04	1.79
.6	.78	1.46
.7	.77	1.29
.8	.79	1.09
.9	.57	1.14
1.0	.69	.92
1.1	.68	1.14
1.2	.66	.79
1.3	.45	.86
1.4	.63	.89
1.5	.61	.65
1.6	.59	.84
1.7	.45	.42
1.8	.43	.71
1.9	.58	.54
2.0	.56	.44

TABLE V

Activation Including Inelastic Scattering
for Co-59(p,3n) Reaction
(1000 nuclei/day)

Depth (g/sq. cm.)	Normal Incidence no covering	Theta Averaged material	Theta Averaged with covering
.1	.43	1.64	.224
.2	.42	1.38	.253
.3	.41	1.29	.307
.4	.40	.99	.227
.5	.40	.99	.281
.6	.39	.89	.300
.7	.38	.82	.278
.8	.37	.69	.246
.9	.37	.70	.273
1.0	.37	.60	.242
1.1	.36	.67	.307
1.2	.35	.51	.225
1.3	.35	.56	.285
1.4	.34	.50	.274
1.5	.34	.39	.246
1.6	.34	.48	.300
1.7	.33	.38	.240
1.8	.33	.45	.287
1.9	.32	.36	.231
2.0	.31	.35	.224
2.1	.31	.43	.275
2.2	.31	.37	.235
2.3	.31	.35	.225
2.4	.30	.35	.229
2.5	.29	.34	.219
2.6	.29	.41	.263
2.7	.29	.35	.224
2.8	.29	.28	.179

TABLE VI

Expected Neutron Flux for LDEF Orbit
(1000 neutrons/day sq. cm. MeV)

E(MeV)	Flux	E(MeV)	Flux
3	26.7	5	10.6
7	5.8	9	3.7
10	3.0	20	1.8
30	1.4	40	1.1
50	.99	60	.72
70	.55	80	.40
90	.26	100	.17

1983

NASA/ASEE SUMMER FACULTY RESEARCH FELLOWSHIP PROGRAM

MARSHALL SPACE FLIGHT CENTER
THE UNIVERSITY OF ALABAMA IN HUNTSVILLE

ULTRAHIGH MOLECULAR WEIGHT AROMATIC SILOXANE POLYMERS

Prepared By:	Larry M. Ludwick, Ph.D.
Academic Rank:	Professor
University and Department:	Tuskegee Institute Department of Chemistry
NASA/MSFC:	
Division:	Non-Metallic Materials
Branch:	Polymers and Composites
MSFC Counterpart:	William J. Patterson, Ph.D.
Contract No:	NGT 01-008-021 The University of Alabama in Huntsville

ULTRAHIGH MOLECULAR WEIGHT AROMATIC SILOXANE POLYMERS

by

Larry M. Ludwick, Ph.D.
Professor of Chemistry
Tuskegee Institute
Tuskegee Institute, Alabama

ABSTRACT

Silphenylene-siloxane polymers can be prepared by the

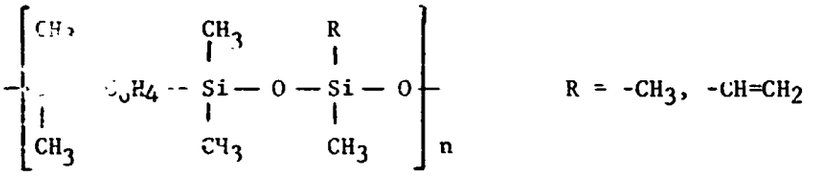

condensation reaction of a diol [1,4-bis(hydroxydimethylsilyl)benzene] and a silan [bis(dimethylamino)dimethylsilane]. Using a stepwise condensation technique, a polymer ($R=-CH_3$) with a molecular weight in excess of 1.0×10^6 has been produced. The polymer exhibits increased thermal stability, compared to a methyl siloxane polymer without the aromatic phenyl ring in the backbone.

The use of bis(dimethylamino)methylvinylsilane should allow for ready crosslinking at the vinyl sites ($R=-CH=CH_2$) introduced into the backbone. However, under the conditions of the reaction system a high molecular weight polymer was not obtained or the polymer underwent a crosslinking process during the synthesis.

INTRODUCTION

Polysiloxanes have been noted for their ability to exhibit desirable mechanical properties over a wide range of temperature. These characteristics are the result of both high thermal stability and low-temperature flexibility. Numerous attempts have been made to improve these properties by structural modifications. Most success has been obtained by incorporating different functional groups within the polymer backbone. (1) This alteration can serve to improve both the thermal stability and the backbone flexibility. Thermal stability improvements result because the stable functional groups in the backbone apparently prevent the silicon-oxygen backbone from reverting to thermally stable cyclic trimers and tetramers. Carboranes and arylene units have shown notable success in this respect. (2,3,4)

The condensation of a bis(hydroxysilyl)benzene with bis(amino)-silanes produces a silphenylene siloxane copolymer (SPS) in which the backbone has an exactly alternating sturcture. Using a

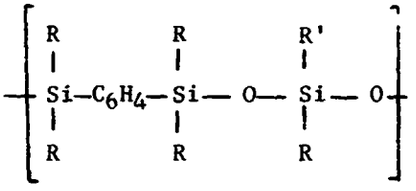

$R = -CH_3$
$R' = -CH_3, -CH=CH_2$

multistep synthetic approach involving 1,4-bis(hydroxydimethylsilyl)-benzene and bis(dimethylamino)dimethylsilane, the methyl SPS polymer ($R' = -CH_3$) has been prepared in 50-gram quantities with a weight average molecular weight in excess of 1×10^6 as determined by gel permeation chromatography. (5) Verification of high molecular weights has been obtained by light scattering experiments. (6) In addition the polymer exhibits improved thermal stability over the polymethylsiloxanes. Improved thermal stability and mechanical properties have also been observed for the vinyl/methyl SPS polymer ($R' = -CH=CH_2$). (7)

The purpose of this project was to prepare sufficient quantities of the high molecular weight vinyl/methyl SPS polymer so that cure/formulation studies could proceed. These studies would provide vulcanized elastomer samples for extensive evaluation of the mechanical properties. In order to facilitate the cure/formulation studies, it was desired to incorporate the vinyl substituent to provide built-in sites for crosslinking. These polymers have been synthesized using a low temperature reaction involving a highly reactive bis(ureido)silane. (8) Since this monomer is extremely reactive, the use of bis(dimethylamino)methylvinyl silane in a multistep approach provides an attractive route to this terpolymer.

EXPERIMENTAL

Materials

Toluene was dried for use in synthesis by distillation from calcium hydride. It was stored over molecular sieves until use. Methanol and tetrahydrofuran (THF) (Burdick and Jackson) were used without additional treatment. 1,4-Bis(hydroxydimethylsilyl)benzene (Silar Laboratories, Inc. and Petrarch Systems, Inc.) was purified by recrystallization from carbon tetrachloride. Two recrystallizations produced a material with a purity greater than 98%, as shown by gel permeation chromatography (GPC) analysis. Bis(dimethylamino)dimethylsilane and bis(dimethylamino)methylvinylsilane (Silar Laboratories, Inc.) were both used as obtained. Analysis by gas chromatography showed no significant additional components. Quantities of these silanes, sufficient for several syntheses, were kept in a closed nitrogen-filled glove bag. Transfers were made using gas tight syringes. Stock quantities of the silanes were stored in a freezer in plastic bags containing Drierite.

Polymer Preparation

Polymer syntheses were performed in 3-necked flasks fitted with a reflux condenser, an addition funnel and a thermometer. The system, including the reactant disilanol, was dried in a 50°C vacuum over for several hours, preferably overnight, before use. It was assembled with a continuous purge of dry nitrogen gas which was maintained during the reaction. Dry toluene was added to the system and stirred with a magnetic stirrer. The mixture was kept at reflux (105-112°C) with a heating mantle.

The silane was added in various modes, including direct addition to the reaction flask. Normally the silanes were mixed with dry toluene in the addition funnel and added over a period of several hours either in a dropwise fashion or in several portions at 1-2 hour intervals. Additional toluene was added as needed to maintain adequate mixing in the reaction flask. After approximately 24 hours the heating was discontinued and the reaction mixture poured into rapidly stirred methanol. The oily or semi-solid product which separated was washed with additional methanol and dried in a 50°C vacuum oven.

The polymer synthesis was normally conducted in two steps. In the first step, approximately 95% of the calculated molar amount of the silane was used. Following reaction the product was isolated. In the second step, the amount of silane used was two to three times the amount deficient in the first step. The product was isolated as before. The progress of molecular weight advancement was monitored by observing the retention times with a gel permeation chromatograph.

Polymer Characterization

Intrinsic viscosities were determined at 30.0°C (±0.1°C) using a Cannon-Ubbelohde dilution viscometer. Four dilutions (75, 60, 43 and 25%) were made from stock solutions.

Nuclear magnetic resonance (NMR) spectra were obtained using a Varian EM-360L instrument. Polymers were dissolved either in $CDCl_3$ of d_8-toluene. The silanes were used neat. Tetramethysilane or methylene chloride served as references.

Gas chromatographic analysis of the silane monomers was performed on a Hewlett-Packard 5710A gas chromatograph.

Gel permeation chromatorgaphy used a Waters Associates liquid chromatograph. 20-50 μl samples of approximately 3% solutions in THF were used with a solvent flow of 1.0 ml/min. The output of the ultraviolet dector was displayed on either a Hewlett-Packard 3380A integrator or a Perkin-Elmer Sigma 15 Chromatographic Data Station. The refractive index unit was also employed as the detector when toluene was used as solvent for the less soluble polymers. A single 30-cm column of 100 Å ultrastyragel (waters Associates) was used for the analysis of the disilanol starting material. For the characterization of the prepolymers and polymer products, a set of three 30-cm ultrastyragel columns (1×10^4, 1×10^5 and 1×10^5 Å pore sizes) was used. Later a set of two ultrastyragel columns (1×10^4 and 1×10^5 Å) was also used with essentially the same result. The retention time was used as a rough indication of molecular weight advancement. During certain parts of the experimental work the times varied considerably. A series of polystyrene standards (Waters Associates) was injected as a single mixture at regular intervals to assess retention times. Typical values are shown in Table 1.

Table 1

Standard Polystyrene Retention Times (Min)

Peak M[a]	Two-Columns		Three-Columns
	THF	Toluene	THF
2.3×10^6	-[b]	17.0	28.3
1.75×10^6	19.8	18.0	30.3
6.55×10^5	21.3	19.3	32.7
3.70×10^5	22.8	20.6	34.8
1.96×10^5	25.0	22.4	37.6
1.11×10^5	26.2	23.4	39.2
3.45×10^4	29.0	25.9	42.7
2.05×10^4	30.2	26.8	44.1

[a] Supplied by Waters Associates
[b] Not resolved

RESULTS AND DISCUSSION

Several attempts were made to synthesize a high molecular weight SPS polymer containing 5-10% of the vinyl pendant (R' = $-CH=CH_2$). Some typical results are shown in Table 2. Since the Sigma 15 Chromatographic Data Station was not available for much of the time period, molecular weight characterization for most preparations was not attempted. In all cases the relative retention time was used to assess the advancement in molecular weight. This was done by comparing retention times with the set of polystyrene standards. While this method does not take into consideration the viscosity of the materials, it did provide a qualitative measure of the success of each synthesis.

None of the experiments produced a polymer with a molecular weight (short retention time) comparable to that of the previously prepared SPS dimethyl polymer. In fact most preparations achieved basically the same GPC retention time. This occurred in several experiments: (1) when a high polymer was achieved (unintentionally) during the first step with little subsequent advancement in molecular weight, (2) when the first step produced a low molecular weight product which was advanced further in the second step, and (3) when the vinyl silane was added only during the second step to a dimethyl SPS prepolymer.

The reasons for these results have not been fully determined. However, a number of possibilities exist. Primary among these must be the purity of the starting monomers. In the case of the disilanol used, the materials purchased from two suppliers both contained a number of minor components. Although most of these impurities were removed by recrystallization from carbon tetrachloride, even two recrystallizations could not a small impurity which exhibited a slightly longer retention time. Typical chromatograms are shown in Figure 1. This peak may be due to a monofunctional impurity which, if present, would significantly decrease the length of the polymer backbone possible. The disilanol used in the preparation of the high molecular weight dimethyl SPS polymers did not exhibit this peak, and in fact was never recrystallized prior to use. (5)

A second factor is the concentration of the disilanol/toluene mixture. While this aspect has not been fully investigated, it appears to be important to keep the reacting disilanol concentration as high as possible. This is somewhat difficult to control as the disilanol does not readily dissolve in the toluene until the solvent nears reflux temperature. In this regard it also may mean that the silane should be added directly to the disilanol mixture, or at least in a minimum amount of toluene. Additional toluene may then be added as required during the experiment.

The results of experiment #7, and to some extent experiment #5, were unlike those of previous trials. In experiment #7 the concentration of disilanol was kept very high. During the second step the reaction

Table 2

Methyl/vinyl SPS Polymer Syntheses

#	Prepolymer			Polymer		
	Mol % Silane Used[a] M/M	M/V	Retention Time (min)	Silane Used[b] M/M	M/V	Retention[c] Time (min)
1	95	6	40	x	-	40
2	87	6	45[d]	x		37
3	89	5	45[e]			
4	90	5	36	x	-	36
5	92	6	--f	x	x	--f
6	91	6	--	x	x	36
7	86	10	--f	x	-	--f
8	96	0	44	x	-	37
				-	x	37

[a]Mole percent based on disilanol used.
[b]Excess (2-4 times) silane based on disilanol used.
[c]LML-6 (dimethyl SPS polymer prepared 1982) 33 min.
[d]Silane mixture added dropwise over several hours.
[e]Silane added directly to reaction mixture.
[f]Could not be determined due to solubility decrease and changes in retention times.

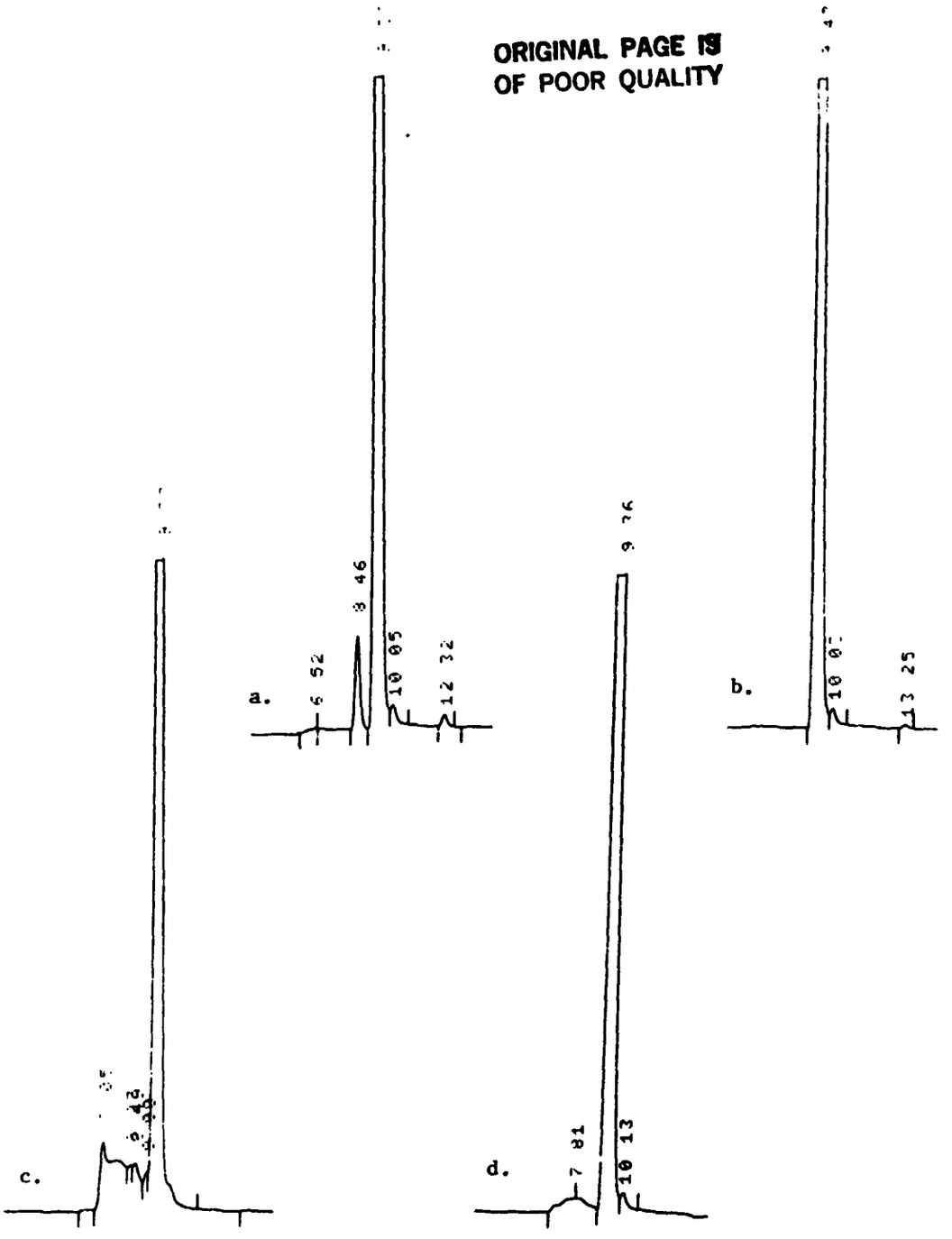

Figure 1. GPC Analysis of 1,4-Bis(hydroxydimethylsilyl)benzene
a. Silar Laboratories
b. Silar Laboratories, Recrystallized Twice from CCl_4
c. Petrarch Systems
d. Petrarch Systems, Recrystallized Twice from CCl_4

mixture became nearly solid very quickly and required large amounts of toluene. In addition a mechanical stirrer was necessary to maintain stirring. The product appeared to be a solid gelatinous mass. It did not appear to be soluble in toluene but rather seemed to absorb it. The product did not dissolve in THF, acetone, hexane, chloroform, methylene chloride or acetonitrile. In most cases the solvent was absorbed, leaving a gelatinous material. Even extremely dilute solutions were difficult, if not impossible, to filter through anything other than paper or a course glass frit. This apparently contributed to the increasing retention times observed during GPC analysis. When the solvent was removed the whitish solid was extremely elastic and only slightly sticky. The solid readsorbed solvent, reforming the gelatinous mass. These observations suggest that these preparations had crosslinked during the reaction. This was also indicated by the NMR of the product (See Figure 2). With polymer #7 the vinyl signal at $\sim\delta$ 5.9 was less intense than that in polymer #5, even though polymer #7 was prepared with nearly twice the amount of vinyl silane monomer. This observation is highly qualitative because the extremely low solubilities of both polymers in $CDCl_3$ required the use of very high instrument settings.

The reaction temperature and/or reaction time also appears to be important. The rubbery product was most tenacious and thick on the bottom surface of the flask, next to the heating mantle. This seems to suggest that the reaction temperature and/or time may need to be reduced when using the vinyl silane, particularly during the second step of the reaction sequence. An alternative would be to use the more reactive bis(ureido)silanes to react at much lower temperatures.

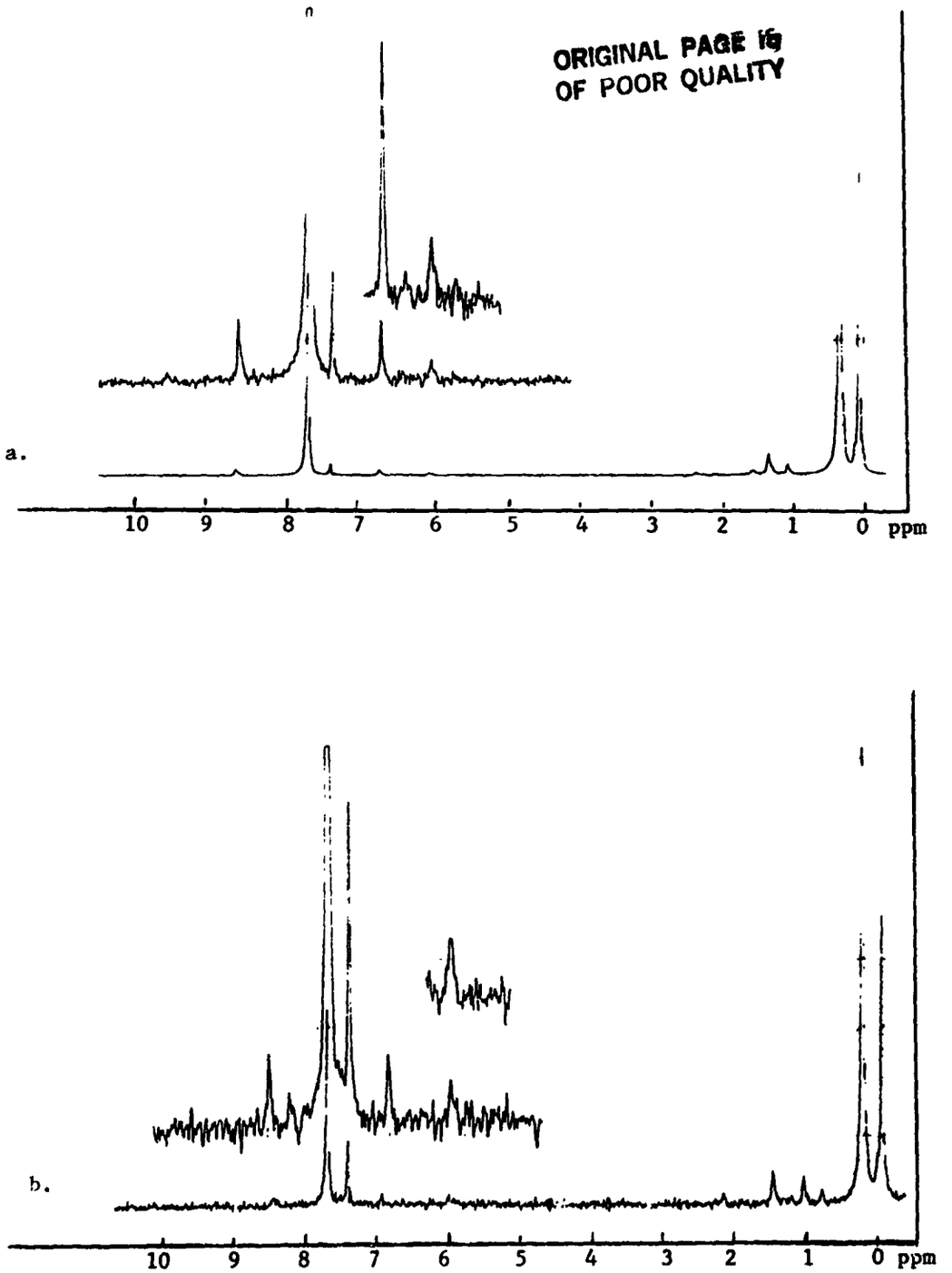

Figure 2. ^{1}H NMR Spectra of Methyl/vinyl SPS Polymers in $CDCl_3$.
a. Polymer 5 - 6% Vinyl Substitution
b. Polymer 7 - 10% Vinyl Substitution

CONCLUSIONS AND RECOMMENDATIONS

The synthesis of high molecular weight SPS polymers containing vinyl pendants to aid in crosslinking studies has not yet been successful. However the results indicate some probable causes for the problems. The purity of the disilanol monomer needs to be increased. This may be accomplished by using other recrystallizing solvent or solvent combinations, sublimation or perhaps preparative liquid chromatography techniques. Increased purity, along with more careful attention to the concentration of the reaction mixture, should produce higher molecular weight products.

The apparent crosslinking problem which occurred during several of the syntheses may be avoided in several ways. Using lower temperatures and shorter reaction times may reduce this problem. However, previous work also suggested that the condensation reaction does not occur below about 90°C so that a more reactive aminosilane may be required.

REFERENCES

1. Cassidy, Patrick E., Thermally Stable Polymers, Marcel Dekker, Inc., New York, 1980.

2. Pittman, C.U. Jr., W.J. Patterson and S.P. McManus, J. Polym. Sci. Polym. Chem. Ed., 14, 1715 (1976).

3. Dvornic, P.R., and R.W. Lenz, J. Polym. Sci. Polym. Chem. Ed., 20, 593 (1982).

4. Stewart, D.D., E.N. Peters, C.D. Beard, G.B. Duncks, E. Hedaya, G.T. Kwiatkowski, R.D. Moffitt and J.J. Bohan, Macromolecules, 12, 373 (1979).

5. Ludwick, L.M., NASA/ASEE Summer Faculty Report, NASA CR-162051, Section XXV, August, 198?.

6. Patterson, W.J. N. Hundley and L.M. Ludwick, NASA Technical Report, Marshall Space Flight Center, TMX Number Unassigned, August, 1983.

7. Dvornic, P.R., and R.W. Lenz, Polymer, 24, 716 (1983).

8. Dvornic, P.R., and R.W. Lenz, J. Polym. Sci. Polym. Chem. Ed., 20, 951 (1982).

1983

NASA/ASEE SUMMER FACULTY RESEARCH FELLOWSHIP PROGRAM

MARSHALL SPACE FLIGHT CENTER
THE UNIVERSITY OF ALABAMA IN HUNTSVILLE

A REPORT ON SUPERFLUID HELIUM FLOW THROUGH POROUS PLUGS FOR SPACE SCIENCE APPLICATIONS

Prepared by:	Franklin Curtis Mason, Ph.D.
Academic Rank:	Associate Professor
University and Department:	Middle Tennessee State University Department of Chemistry and Physics
NASA/MSFC Division: Branch:	 Astrophysics Infrared Astronomy
MSFC Counterparts:	Eugene Urban and Dan Ladner
Date:	August 12, 1983
Contract No.:	NGT 01-008-021 The University of Alabama in Huntsville

A REPORT ON SUPERFLUID HELIUM FLOW THROUGH POROUS PLUGS FOR SPACE SCIENCE APPLICATIONS

By

Franklin Curtis Mason
Associate Professor of Physics
Department of Chemistry and Physics
Middle Tennessee State University
Murfreesboro, Tennessee

ABSTRACT

The need for cryogenically cooled experimental space science apparatus, such as the infrared telescope being readied for the Spacelab 2 mission, has brought about the perfecting of techniques for utilizing superfluid helium as the primary cryogen for producing the desired cooling. At the heart of the matter is the ability of superfluid helium to flow through diminishingly small pores, and based on this fact, the flow of the superfluid through a porous metal plug serves as the method of achieving a controlled flow process which produces the desired cooling effect.

As a background for the study of the nature of superfluid helium flow through porous plugs for other space science uses, preliminary tests on various plugs of a given material, diameter, height, and filtration grade have been performed. Two characteristics of the plugs, pore size and number of channels, have been determined by the bubble test and warm flow test of helium gas through the plugs, respectively.

Tests on the flow of He II through the plugs have also been performed. An obvious feature of the results of these tests is that for isothermal measurements of pressure versus mass flow rate below approximately 2.10 K, the flow is separated into two different regimes, indicative of the occurrence of a critical phenomenon.

In order to provide a more complete understanding of the nature of the superfluid flow of helium through porous plugs, tests of a similar nature to those cited above are still being conducted, and future methods for advanced testing of the plugs are being developed.

ACKNOWLEDGEMENTS

The author wishes to acknowledge the NASA/ASEE Summer Faculty Fellowship Program, along with the NASA Directors Jim Dozier and Leroy Osborn, and Gerald Karr, the UAH Director.

To NASA Counterparts Dr. Eugene Urban and Dr. Dan Ladner of the Infrared Astronomy Branch of the Marshall Space Flight Center Space Science Laboratory, an expression of thanks is offered.

A debt of gratitude is owed to Dr. John Hendricks and Mr. Mark Tcherneshoff, both of The University of Alabama in Huntsville, for the availability of the data analyzed in this paper.

A further word of thanks is expressed to Dr.'s Hendricks, Karr, Urban, and Ladner for the useful and informative discussions concerning space cryogenics in general and porous plugs in particular.

To Mr. J. O. Jolley and Mr. Dale Armstrong, whose help in matters of a technical nature was of great assistance, an expression of gratitude is offered.

And finally, the typing of the paper was by Mrs. Sue Davis of the Infrared Astronomy Branch, and the author is grateful to her for that service.

INTRODUCTION

The use of porous plugs as phase separators to control superfluid helium (He II) flow in space cryogenic systems is a well established concept (1-4), with a working application to the IRAS system presently in space. Also, the infrared telescope (IRT) and the gravity probe (GP-B) experiment, both of which are to be carried into space on future Spacelab flights, will be utilizing this method of cryogenic flow control. Even with these various applications, research is still being done on the superfluid flow of helium through porous plugs. The Infrared Astronomy Branch of the Marshall Space Flight Center Space Science Laboratory is currently engaged in porous plug research. In the capacity of a NASA/ASEE Summer Faculty Fellow, the author of this paper has been a part of this effort for the summer of 1983.

OBJECTIVES

The objective of the research being reported on here is to gain a better understanding of the superfluid flow of helium through porous plugs for other cryogenic applications to space science. On the way to realizing this objective, plug performance data useful in the design of future space cryogenic systems are also being acquired.

The objectives of this paper are to discuss porous plugs and some recent tests on the flow of fluids through the plugs, including the superfluid flow, and to discuss future tests presently being considered by the Infrared Astronomy Group of the MSFC Space Science Lab.

DISCUSSION

Porous Plugs

In the physics of porous plugs, the main factors to be considered here are porosity, pore size, and permeability. In a porous sample, such as a porous plug, there are two types of porosity to consider, closed and open porosity (5). Closed porosity forms as the pores pinch closed during the fabrication process. Open porosity refers to the interconnection to the material surface and is the basis for the

property of permeability. Quantitatively, porosity is defined as the volume of the voids divided by the total volume. The term total porosity relates to the combination of open and closed porosity, and it is of interest in regard to the thermal conductivity of the plugs. Effective porosity is a measure of open porosity, and it relates directly to the mass flow rate. Qualitatively, permeability relates to the ease with which fluids pass through a porous plug. It is measured by the application of Darcy's law, or, when assuming a model of laminar flow through parallel channels, by applying the Poiseuille flow formula (7,8). The three factors defined above in turn are related to other factors such as pore shape and pore density.

Porous plugs are available in several materials, and they are usually manufactured from powders (5). In the process of fabrication, sized powders, the particles of which are typically irregularly shaped, are pressed and then sintered. In this seemingly straight forward process, the necessary control to produce precise pore characteristics is often difficult. For space science applications this virtually necessitates the testing of individual plugs in order to determine the performance characteristics of each.

Two sets of porous plugs are currently being tested by the infrared astronomy group this summer. They are a set of stainless steel and a set of bronze plugs. The supplier of these plugs if the Pacific Sintered Metals Company (9). The diameter of all the plugs is one-half inch. Plug thicknesses range from one-sixteenth inch to one-half inch. The filtration rating of the stainless steel plugs is 2-5 microns, while the filtration rating of the bronze plugs is about 10 microns. Other plug characteristics are given in Table 1.

Flow

The definitive work on the flow of fluids through porous media was by Darcy, whose work was reported in 1856 (10). Studies by Darcy on the flow rate of water through filter beds led to the formulation of Darcy's law. This law states that the flow rate (Q) through a porous medium is proportional to the cross-sectional area (A) of the medium, directly proportional to the pressure drop (ΔP) across the medium, and inversely proportional to the length (ℓ) of the flow path. In equation form, this law is written as

$$Q = KA(\Delta P)/\ell \qquad (1)$$

where K is a constant of proportionality, and is known as

the hydraulic conductivity (11). The permeability of the medium is related to the hydraulic conductivity.

Darcy also noted the similarity between flow through porous media and laminar pipe flow. In this connection, a porous medium may be thought of as consisting of a bundle of circular parallel flow channels, all of which have the same diameter and length. This model will be applied to the porous plugs being discussed here.

The Parallel Channel Model

In the parallel channel model, known also as the Kozeny hydraulic model (12), the flow rate of an ordinary fluid such as warm helium gas or liquid helium above the superfluid transition temperature, assuming laminar flow in both cases, is given by the Poiseuille flow formula. This formula is, assuming the fluid to be incompressible,

$$\dot{m} = \frac{\pi N d^4 \rho \Delta P}{128 \ell \mu} \tag{2}$$

where $\dot{m}$ is the mass flow rate, N is the number of channels, ℓ is the plug length, ρ is the fluid density, μ is the fluid viscosity, and ΔP is the pressure difference across the plug.

If warm gas laminar flow data for $\dot{m}$ versus ΔP are gathered and plotted on a graph, the slope of the graph would yield information on the number of channels. That is,

$$\text{SLOPE} = \frac{\pi N d^4 \rho}{128 \ell \mu} \tag{3}$$

or

$$N = \frac{128 \ell \mu (\text{SLOPE})}{\pi \rho d^4} \tag{4}$$

For laminar superfluid helium flow through porous plugs, the above expression for the mass flow rate is altered to (13)

$$\dot{m} = \frac{\pi N d^4 \rho (ST/L) \Delta P}{128 \ell \mu} \tag{5}$$

We note here that ρ in this expression is the superfluid

density, and μ is the normal fluid viscosity. S is the entropy, T is the absolute temperature, and L is the latent heat of vaporization. For calculational purposes, values of these quantities are well known (14).

To get the diameter of the flow channels, a test known as the bubble test is performed. This test is based on gas-pressure displacement of a wetting fluid (such as isopropyl alcohol) from the pore structure, and what is being measured is the minimum constriction in the largest pore (5). On the basis of capillarity, the pore diameters are given by

$$d = 4\ \gamma/P \tag{6}$$

where d is the diameter, γ is the surface tension, and P is the pressure. It should be noted here that this test is said to be of limited validity in analyzing pore structure (5).

In the Kozeny model, the effective porosity is found by computing the total volume of the channels and then dividing by the plug volume. The resulting expression is

$$\varepsilon_{eff} = \frac{Nd^2}{D^2} \tag{7}$$

where D is the plug diameter. The remaining symbols have been previously defined.

EXPERIMENTAL CONSIDERATIONS

The details of the three different tests associated with the porous plugs are shown in Figures 1, 2, and 3.

Figure 1 depicts the details of the warm flow gas test. In this test helium gas from a regulated helium supply bottle at room temperature is conducted through a 1/4 inch o.d. copper line in which a Hastings LF-20 flow transducer and a DM-525 pressure transducer have been placed. Signals from these transducers are fed to the appropriate electronic meters and registered on an x-y recorder, with the mass flow rate on the "y" axis, and the pressure difference across the plug on the "x" axis. The gas exits the line through the porous plug as shown. Information from this test gives the permeability of the plug in addition to the number of channels involved in the flow.

The details of the bubble test are shown in Figure 2. Again, helium gas at room temperature from a supply bottle is conducted through a tube. In this case there is only a DM-525 transducer for registering pressure, which is read on a Hewlett-Packard digital voltmeter. The flow is regulated until the smallest bubble can be seen emerging from the plug into the isopropyl alcohol on top of the plug. The observation of the bubble formation is made by the use of a binocular microscope. This test is repeated five times for each plug and an average pressure is calculated. The bubble test gives the size of the pores in the plug to the approximation stated above.

In the superfluid test, the details of which are shown in Figure 3, the porous plug is sealed in by indium O-rings at the bottom of a thin-walled 1/2 inch i.d. stainless steel tube that extends into the cryostat. Below the tube, the plug is in contact with the liquid helium in the bath. Immediately above the plug, a static pressure line inside the stainless steel tube measures the pressure on the down stream side of the plug. The stainless steel tube conducts the fluid which emerges from the plug to a vacuum pump. The flow is measured in a similar way to that associated with the two previous tests discussed above. Pressures are also measured in a similar fashion to the warm flow test and the bubble test. It should be noted that on the pressure tube radiation baffles have been placed, and that both this tube and the gas conduction tube are enclosed in a larger evacuated tube that serves to isolate them from the bath. In this way the tests are isothermal.

One outstanding feature of the superfluid tests is that data taking has been automated by the use of a Hewlett-Packard 9835 computer in conjunction with a Hewlett-Packard 3497A Data Acquisition Control Unit.

RESULTS

The various characteristics of the two sets of porous plugs are given in Table 1. For the bronze plugs, designated as the 83-20 Series in the table, one notes that the pore diameters range in value from 49 microns to 73 microns. The number of channels varies from approximately 3,200 to 28,000. The effective porosity ranges from 0.037 to 0.63. For the stainless steel series, labelled as the 83-40 series, the pore diameters vary from about 6.6 microns to about 15 microns. The number of channels ranges from 40,000 to 121,000. The effective porosity varies from 0.015 to 0.077. These results hardly make it necessary to retract the statement about the need for testing individual plugs.

Superfluid tests were run for four porous plugs early in the summer. The plugs tested were 83-20, 83-21, and 83-22 of the bronze series, and 83-40 of the stainless steel series. During these tests a series of flow rate versus pressure difference measurements were made at a fixed temperature for temperatures from 2.15 K to 1.80 K in steps of 0.05 K temperature increments. For comparison purposes the data for plugs 83-20 and 83-40 have been plotted on log-log graphs. These graphs, designated as Figures 4 and 5, reveal the gross features of the flow of superfluid helium through the porous plugs. The data from these particular plugs were selected to be displayed because of the plug lengths being the same, which is one-sixteenth of an inch. Of notable significance in both cases is the fact that the data separate into two distinct regions for temperatures below 2.10 K. Between the lambda-point temperature of 2.17 K and 2.10 K the flow is characterized by a curve which is more in keeping with the flow of gaseous helium. As the temperature decreases and a bigger fraction of the superfluid helium becomes converted to the superfluid component of He II, one sees the onset of the data breaking into two regimes.

Another feature of the superfluid flow data is an apparent effect of pore size on flow rate. In Figure 4 for the bronze plug flow rates as high as 5,000 SCCM (standard c.c.'s per minute) occur at relative low pressure differences. Furthermore, for this case one notes that for a given ΔP, the flow rate increases with decreasing temperature. For the stainless steel plug of Figure 5 the flow rates differ by a factor of ten or so from those of the bronze plug at pressures somewhat larger, comparatively speaking. In the data plots for the stainless steel plug we see that for a given ΔP, the

flow rate decreases with decreasing temperature. This is just the opposite of the behavior of the bronze plug, and at a given ΔP in the lower branch of Figure 5 the flow rate is somewhat insensitive to a temperature change.

To test the parallel channel model against superfluid flow data, constants of proportionality at a temperature of 1.8 K were calculated from Equations (2) and (5) for plugs 83-20 and 83-22, and the straight lines indicated by these constants were plotted on a graph along with the experimental data. The calculations were based on the numbers given in Table 1 for pore diameters and numbers of channels. Other required data for these calculations were found in a previously cited source (14) and from tables available in the laboratory (15). The resulting plots are displayed in Figure 6. Since the two plugs are of different lengths, the plots suggest a dependence of flow rate on plug length. Also of note in the plots is the fact that the experimental points lie below the calculated ones. In this respect, for plug # 83-20 the ratio of the experimental to the calculated slope for the upper regime is 0.70, and 0.35 for the lower one. For plug # 83-22 these respective ratios are 0.62 and 0.31. The calculated curves are plotted in such a way that the two branches for each plug intersect at the critical flow rate as determined from the experimental plots. The experimental critical flow rates themselves are different, with plug # 83-20 having a higher critical mass flow rate than that of plug # 83-22. However the percent difference is only about 21.5%. In summary, this analysis shows not too good agreement between the model and the actual data, but the two only differ by factors ranging from 1.4 to 3.2 for the collective data.

CONCLUSIONS AND RECOMMENDATIONS

In this report, the data analysis represents a precursory attempt to develop the author's understanding of the nature of the superfluid helium flow through porous plugs. Still left undiscussed here is the all-important occurrence of the transition from one flow regime to another in superfluid helium. Along these lines, there have been discussions held (16) this summer concerning counterflow experiments on the porous plugs. In these experiments one would envision measuring heat flow rates versus temperature differences and mass flow rates versus pressure difference on each plug in the hope of finding a correlation between the respective critical points in the flow. Low temperature thermometry and calorimetry would be involved in the counterflow experiments, and this would add several more complexities to the experimental set-up. However, the information to be gained from such

studies is seen as crucial to a more complete understanding of superfluid helium flow through porous plugs.

In addition to the critical mass flow rate occurrence, another important question to be resolved is that of the phase (or phases) of the fluid within the plug during the flow. In this respect, previous experimentation in the MSFC Space Science Laboratory has led to the statement that heat and mass transport below the critical flow rate is by counter-flow of superfluid helium, with the pores of the plug being filled with superfluid; above the transition, it is believed that the superfluid-vapor interface retreats into the plug; and at the higher temperatures just below the lambda point, the plug is almost completely filled with vapor (13).

One of the observations given in this report does rate further investigation. From Figures 4 and 5 concerning the behavior of the superfluid flow rate as a function of pore size, a recommendation for future research on this question is in order. The approach would be to measure the flow rate as a function of temperature and pore size for a given material in order to determine if there exists a pore size between about 5 microns and 60 microns such that the mass flow rate would be rather insensitive to temperature.

TABLE 1. PLUG CHARACTERISTICS TABLE

I. 83-20 Series, Bronze, 5-15 Micron Filtration Grade, 0.500 Inch Diameter

Plug Number	Length (inches)	Pore Diameter (microns)	Number of Channels	Effective Porosity
83-20	0.0625	63.0	6,230	0.037
83-21	0.125	60.2	28,100	0.631
83-22	0.250	60.5	5,780	0.131
83-22	0.375	49.0	12,500	0.186
83-23	0.500	73.2	3,195	0.106

II. 83-40 Series, Stainless Steel, 2-5 Micron Filtration Grade, 0.500 Inch Diameter

Plug Number	Length (inches)	Pore Diameter (microns)	Number of Channels	Effective Porosity
83-40	0.0625	6.56	54,800	0.0146
83-41	0.125	10.1	121,000	0.0766
83-42	0.250	15.2	40,200	0.0574

REFERENCES

1. Selzer, P. M., et al., "A Superfluid Plug for Space," Advances in Cryogenic Engineering, 16, (1971) 277-280.

2. Karr, G. R. and Urban, E. W., "Superfluid Plug as a Control Device for Helium Coolant," Cryogenics, (May 1980), 266-270.

3. Petrac, D., et al., "Performance of a Ceramic Porous Plug Superfluid Liquid-Vapor Phase Separator," Bulletin of the American Physical Society, 20, (1975) 698.

4. Denner, H. D., et al., "Flow of Helium Through Porous Plugs," Cryogenics, (March 1978), 166-170.

5. German, R. M., "Porous Materials," Chapter 10 in Advances in Powder Technology, (1982), 225-248.

6. Putterman, S. J., Superfluid Hydrodynamics, North Holland Publishing Co., Amsterdam, 1974.

7. Daily, J. W. and Harleman, D. R., Fluid Dynamics, Addison-Wesley, Reading, Mass., 1966.

8. De Wiest, J. M., Flow Through Porous Media, Academic Press, New York and London, 1969.

9. Pacific Sintered Metals Company, 16110 So. Figueora St., Gardena, Calif. 90248, Tel. 213/321-4595.

10. Darcy, H., Les Fontaines Publiques de la Ville de Dijon, Dalmont, Paris, 1856.

11. See Reference 8.

12. Michell, S. J., Fluid and Particle Mechanics, Pergamon Press, Oxford, 1970.

13. Hendricks, J. B. and Karr, G. R., "Characterization of Superfluid Porous Plug Performance," A Paper Presented at the Ninth International Cryogenic Engineering Conference (ICEC), May 11-14, 1982, Kobe, Japan.

14. Wilks, J., The Properties of Liquid and Solid Helium, Clarendon Press, Oxford, 1967.

References, Continued.

15. "The Thermodynamic Properties of Helium II from 0 K to the Lambda Transition," NBS Technical Note 1029, December 1980.

16. Ladner, D., Irfrared Astronomy Branch, Astrophysics Division, Space Science Laboratory, Marshall Space Flight Center, Huntsville, AL, Private Communication.

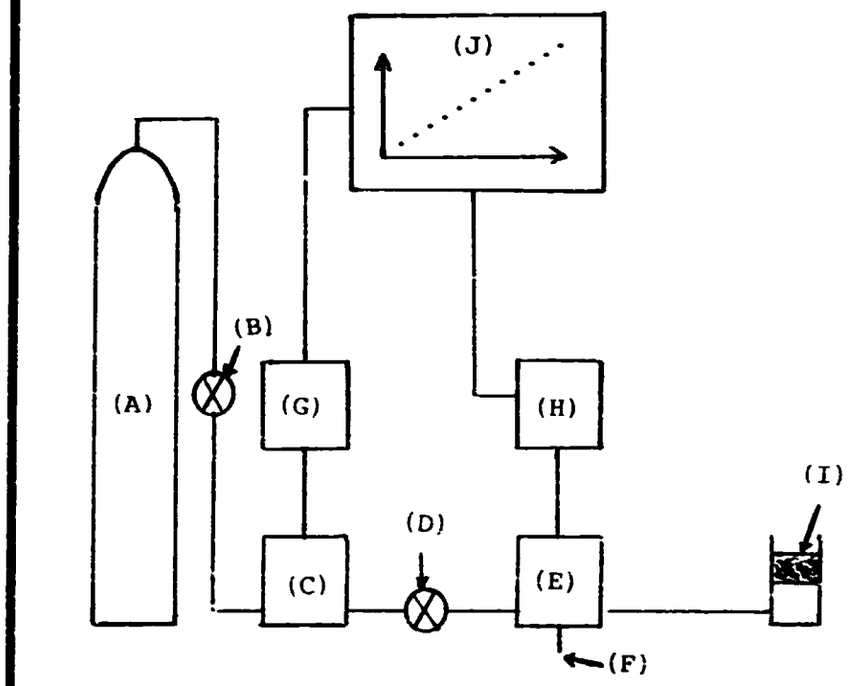

LEGEND

(A)----Regulated Helium Supply Bottle
(B)----Flow Control Valve
(C)----Flow Rate Transducer
(D)----Flow Control Valve
(E)----DM-525 Pressure Transducer
(F)----Port to Atmosphere
(G)----Hastings Flow Meter
(H)----Datametrics Pressure Meter
(I)----Porous Plug
(J)----x-y Plotter

FIGURE 1

DIAGRAM OF WARM FLOW TEST

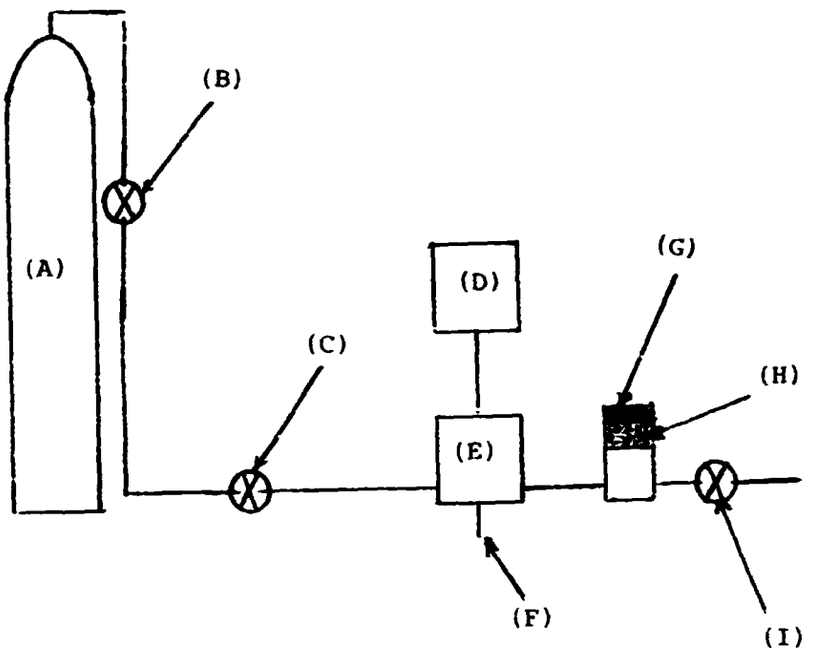

LEGEND

(A)----Regulated Helium Supply Bottle
(B)----Flow Control Valve
(C)----Flow Control Valve
(D)----Datametrics Pressure Meter
(E)----DM-525 Pressure Transducer
(F)----Port to Atmosphere
(G)----Isopropyl Alcohol Layer
(H)----Porous Plug
(I)----Flow Control Valve

FIGURE 2

BUBBLE TEST DETAILS

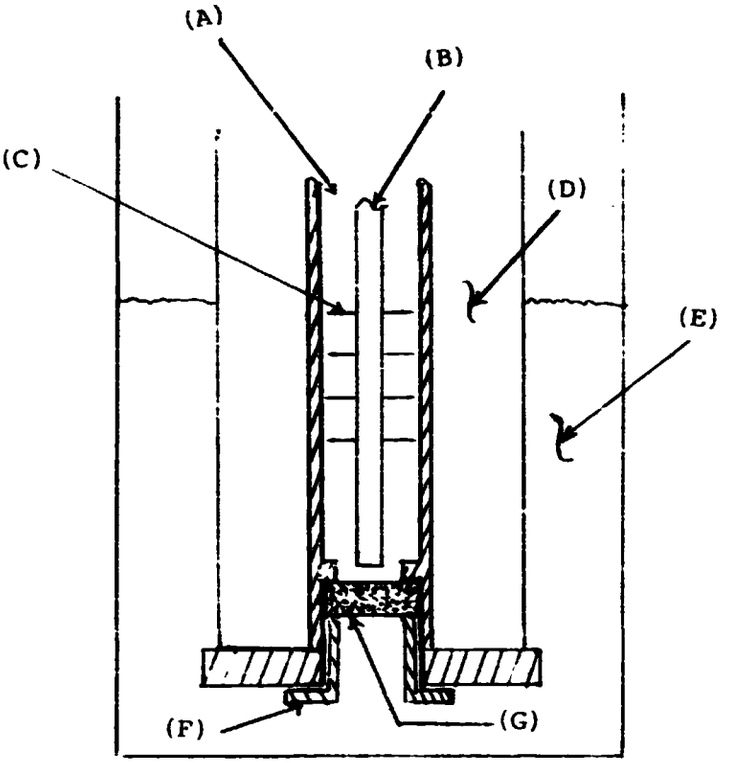

LEGEND

(A)----Vapor Exhaust Line
(B)----Pressure Measuring Line
(C)----Radiation Baffles
(D)----Insulating Vacuum Space
(E)----Liquid Helium Bath
(F)----Porous Plug Clamp
(G)----Porous Plug

FIGURE 3

SUPERFLUID TEST DETAILS

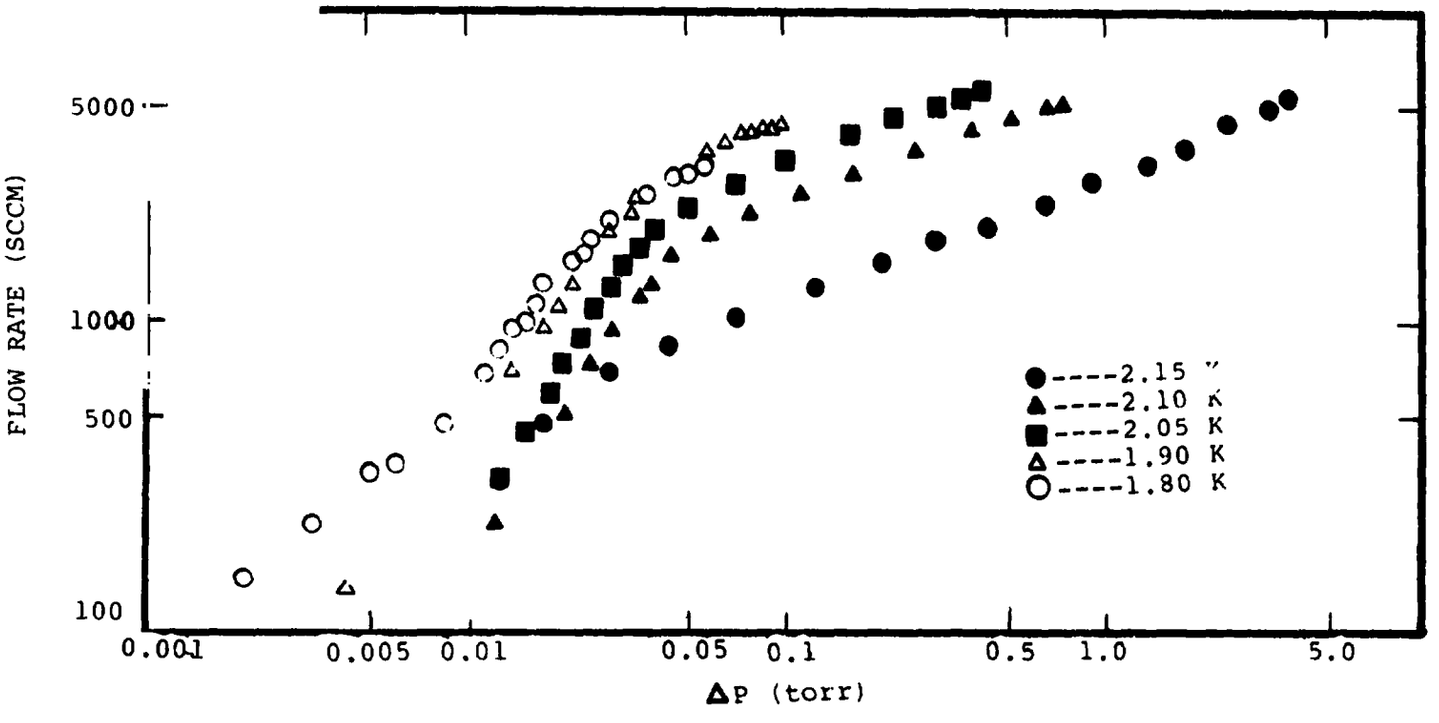

FIGURE 4

TEMPERATURE FLOW RATE PROFILE

BRONZE PLUG # 83-20

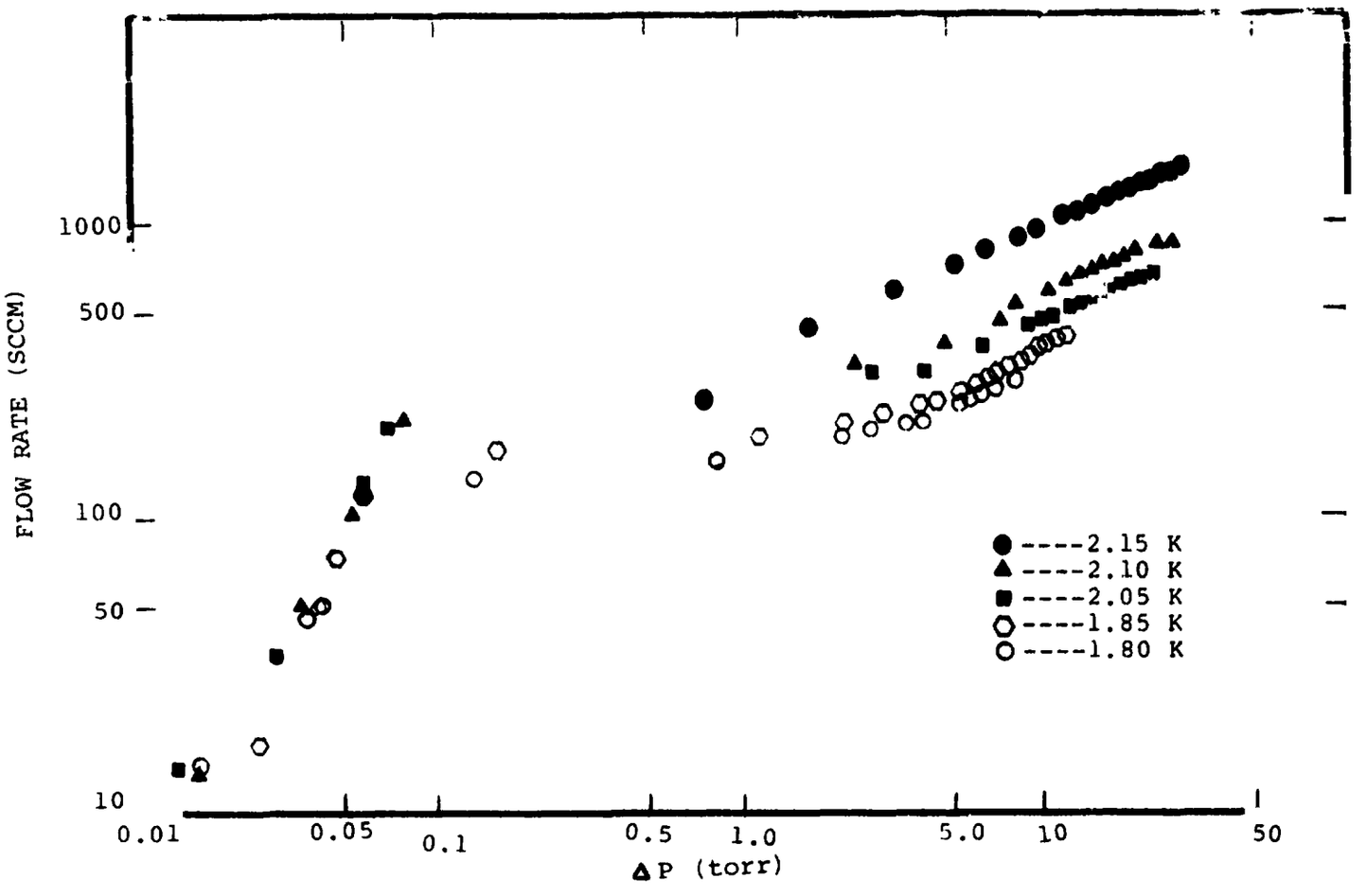

FIGURE 5

TEMPERATURE FLOW RATE PROFILE FOR S. S. PLUG # 83-40

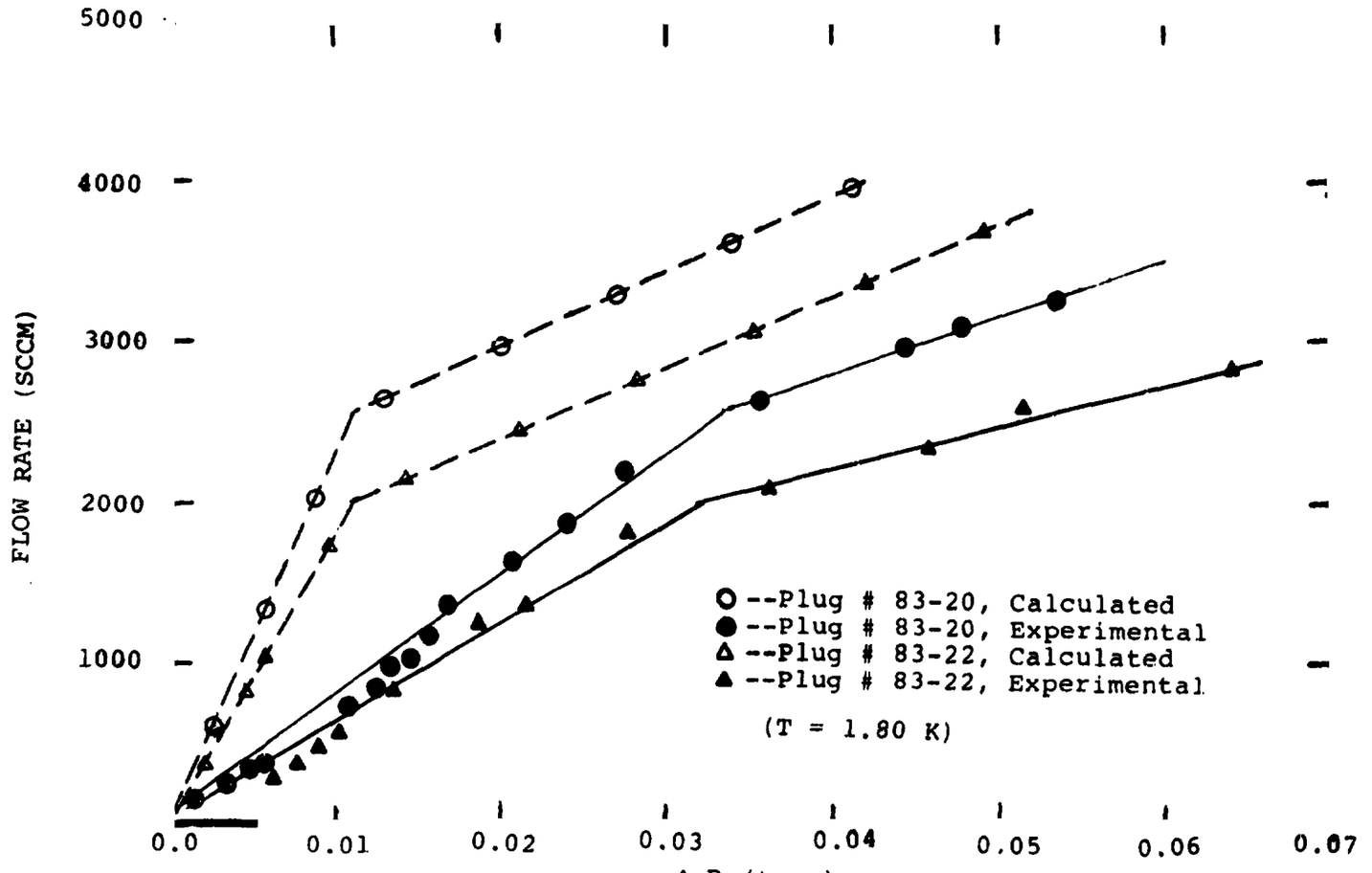

FIGURE 6

FLOW RATE COMPARISONS FOR PLUGS 83-20 AND 83-22

1983
NASA/ASEE SUMMER FACULTY RESEARCH FELLOWSHIP PROGRAM

MARSHALL SPACE FLIGHT CENTER
THE UNIVERSITY OF ALABAMA AT HUNTSVILLE

POPULATION CONTROL OF SELF-REPLICATING SYSTEMS; OPTION C

Prepared By:	Richard L. McCord, Ph.D.
Academic Rank:	Professor
University and Department:	Middle Tennessee State University
NASA/MSFC:	
Laboratory:	Space Science
Division:	Astrophysics
Branch:	High-Energy Physics
MSFC Counterpart:	Wesley A. Darbro
Date:	August, 1983
Contract No.:	NASA-NGT-01-008-021 The University of Alabama at Huntsville

POPULATION CONTROL OF SELF-REPLICATING SYSTEMS; OPTION C

BY

Richard L. McCord, Ph.D.
Professor of Mathematics
Middle Tennessee State University
Murfreesboro, Tennessee

ABSTRACT

From the conception and development of the theory of self-replicating automata by John von Neumann, others have expanded on his theories. In 1980, Georg von Tiesenhausen and Wesley A. Darbro developed a report which is a 'first' in presenting the theories in a conceptualized engineering setting. In that report several options involving self-replicating systems are presented. One of the options allows each primary to generate n replicas, one in each sequential time frame after its own generation. Each replica is limited to a maximum of m ancestors.

This study involves determining the state vector of the replicas in an efficient manner. The problem is cast in matrix notation, where $F = [f_{ij}]$ is a non-diagonalizable matrix. Any element f_{ij} represents the number of elements of type j = (c,d) in time frame k+1 generated from type i = (a,b) in time frame k. It is then shown that the state vector is:

$$\bar{f}(k) = \bar{f}(\emptyset) \cdot F^{K} = \bar{f}(\emptyset) \cdot M \cdot J^{K} \cdot M^{-1}$$

where J is a matrix in Jordan form having the same eigenvalues as F. M is a matrix composed of the eigenvectors and the generalized eigenvectors of F.

ACKNOWLEDGEMENTS

Indebtedness is due and appreciation is extended to the following:

Wesley A. Darbro, MSFC counterpart; for his patience, understanding, encouragement, and friendship to me and for his mathematical insight, awareness, and contribution in this area of research.

Billy G. Bass, Assistant to the Director, Space Science Laboratory; for his concern, comments, and introduction and indoctrination to the Space Science Laboratory.

Marion I. Kent, Former Director of University Affairs; for his influence, interest, support, and cooperation.

Gerald R. Karr, University Program Director; for his direction, excellent organization, and administration.

James B. Dozier, Research and Technology; for his programs, unique commentaries, and individual assistance.

Leroy Osborn, Acting University Affairs Director; for his enthusiastic support, assistance, and leadership.

B. F. Barfield, 1982 University Program Director; for his continued interest and support.

L. Michael Freeman, University Program Co-Director; for his support and interest.

LIST OF FIGURES

Figure no.	Title	Page
1.	Family tree of replicas (option B)	XXII-13
2.	Family tree of replicas (option C)	XXII-14
3.	Formation of Matrix F = $[f_{ij}]$	XXII-15
4.	Cumulative diagram of replicas option C; n = 2, m = 3	XXII-16

INTRODUCTION

In 1980, Georg von Tiesenhausen and Wesley A. Darbro [6] developed "a first approach to conceptualize self-replicating systems from past and present abstract theories." This development was based on theories composed by John von Neumann in the late 1940's and expanded by others. NASA officials and others have discussed the possible application of self-replicating systems to future space mission.

In the mathematics of self-replication presented in the study cited above and in the publication by Darbro and von Tiesenhausen [1], several options are described.

Option A is designed to allow simultaneous replication of a primary; that is, each primary may generate n replicas in each time frame after its own generation until cut-off.

Option B allows each primary to generate n replicas sequentially, one in each time frame after its own generation.

Option C is special case of option B in which the maximum number m of ancestors is specified.

A primary is an individual capable of replication and may or may not be a replica itself. The words generates, replicates, and reproduces are synonyms. Production refers to the process of deriving an end product (other than replicas) as a result of work done. The word cut-off indicates the end of the replication and the beginning of production.

OBJECTIVES

The aim of this study has been:

1. to review the literature relative to the Fibonacci sequence and the mathematics of self-replication.

2. to investigate diagonalization and Jordanization relative to certain special matrices.

3. to determine the state vector of the replicas in an efficient manner, in particular for option C, the system having a maximum number n of replicas per primary and a maximum number m of ancestors for a replica.

OPTION C

The major concern of this study is option C as presented by Darbro and von Tiesenhausen [1]. For this option a primary generates a fixed number n of replicas which in turn become primaries. Replication continues until either the number of ancestors for a primary reaches the value m or until cut-off. Each primary generates its n replicas in sequential time frames, beginning in the first time frame after its own generation. At cut-off, replication ceases and production begins.

The example depicted for option B when n = 2 by McCord [4] is sh. in Figure 1. Consider Figure 2 in which n = 2 and m = 3 for option The diagram is identical to the option B diagram up to time frame 4 at which time the restriction m = 3 begins affecting the number of replicas.

For R = (n+1) (m+1) types of replicas (which are or may become primaries) denote the types by the elements of AXB = $\{(\emptyset,\emptyset), (1,\emptyset),.., (n,\emptyset), (\emptyset,1), (1,1), \ldots, (n,1), \ldots, (\emptyset,m), (1,m), \ldots, (n,m)\}$, where A = $\{\emptyset,1, \ldots,n\}$, and B = $\{\emptyset,1, \ldots, m\}$. Each ordered pair (x,y) identifies the number x of replicas generated by the primary and the number y of ancestors of that primary. Consider a square matrix F = $[f_{ij}]$ of order R, where f_{ij} is the number of replicas of type j = (c,d) in time frame k+1 generated by a primary of type i = (a,b) in time frame k, where $\emptyset \leq a \leq n$, $\emptyset \leq c \leq n, \emptyset \leq b \leq m, \emptyset \leq d \leq m, \bigwedge k = \{\emptyset,1,2, \ldots, nm\}$. Matrix F can be constructed by the following relation:

$$\left.\begin{array}{l}(a,b) \longrightarrow (a+1,b)\\ (a,b) \longrightarrow (\emptyset,b+1)\end{array}\right\} \quad \text{if } a \neq n, b \neq m \qquad (1)$$

$$(a,b) \longrightarrow (a,b) \quad \text{if } a = n \bigvee b = m \qquad (2)$$

In particular, in the example of Figure 2;

$$\left.\begin{array}{l}(\emptyset,\emptyset) \longrightarrow (1,\emptyset)\\ (\emptyset,\emptyset) \longrightarrow (\emptyset,1)\end{array}\right\} \quad \left.\begin{array}{l}(1,\emptyset) \longrightarrow (2,\emptyset)\\ (1,\emptyset) \longrightarrow (\emptyset,1)\end{array}\right\} \quad (2,\emptyset) \longrightarrow (2,\emptyset)$$

$$\left.\begin{array}{l}(\emptyset,1) \longrightarrow (1,1)\\ (\emptyset,1) \longrightarrow (\emptyset,2)\end{array}\right\} \quad \left.\begin{array}{l}(1,1) \longrightarrow (2,1)\\ (1,1) \longrightarrow (\emptyset,2)\end{array}\right\} \quad (2,1) \longrightarrow (2,1) \qquad (3)$$

$$\left.\begin{array}{l}(\emptyset,2) \longrightarrow (1,2)\\ (\emptyset,2) \longrightarrow (\emptyset,3)\end{array}\right\} \quad \left.\begin{array}{l}(1,2) \longrightarrow (2,2)\\ (1,2) \longrightarrow (\emptyset,3)\end{array}\right\} \quad (2,2) \longrightarrow (2,2)$$

$$(\emptyset,3) \longrightarrow (\emptyset,3), \quad (1,3) \longrightarrow (1,3), \quad (2,3) \longrightarrow (2,3)$$

From Figure 3, a matrix F can be formed:

$$F = \begin{bmatrix} 0 & 1 & 0 & 1 & 0 & 0 & 0 & 0 & 0 & 0 & 0 & 0 \\ 0 & 0 & 1 & 1 & 0 & 0 & 0 & 0 & 0 & 0 & 0 & 0 \\ 0 & 0 & 1 & 0 & 0 & 0 & 0 & 0 & 0 & 0 & 0 & 0 \\ 0 & 0 & 0 & 0 & 1 & 0 & 1 & 0 & 0 & 0 & 0 & 0 \\ 0 & 0 & 0 & 0 & 0 & 1 & 1 & 0 & 0 & 0 & 0 & 0 \\ 0 & 0 & 0 & 0 & 0 & 1 & 0 & 0 & 0 & 0 & 0 & 0 \\ 0 & 0 & 0 & 0 & 0 & 0 & 0 & 1 & 0 & 1 & 0 & 0 \\ 0 & 0 & 0 & 0 & 0 & 0 & 0 & 0 & 1 & 1 & 0 & 0 \\ 0 & 0 & 0 & 0 & 0 & 0 & 0 & 0 & 1 & 0 & 0 & 0 \\ 0 & 0 & 0 & 0 & 0 & 0 & 0 & 0 & 0 & 1 & 0 & 0 \\ 0 & 0 & 0 & 0 & 0 & 0 & 0 & 0 & 0 & 0 & 1 & 0 \\ 0 & 0 & 0 & 0 & 0 & 0 & 0 & 0 & 0 & 0 & 0 & 1 \end{bmatrix} \quad (4)$$

As presented by Darbro and von Tiesenhausen [1] in the frameword of Klarner [3], the state vector may be formed for any time frame k. Specifically,

$$\bar{f}(0) = [1\ 0\ 0\ 0\ 0\ 0\ 0\ 0\ 0\ 0\ 0\ 0] \quad (5)$$

$$\bar{f}(1) = \bar{f}(0) \cdot F = [0\ 1\ 0\ 1\ 0\ 0\ 0\ 0\ 0\ 0\ 0\ 0] \quad (6)$$

$$\bar{f}(2) = \bar{f}(1) \cdot F = \bar{f}(0) \cdot F^2 = [0\ 0\ 1\ 1\ 1\ 0\ 1\ 0\ 0\ 0\ 0\ 0] \quad (7)$$

$$\vdots$$

$$\bar{f}(6) = \bar{f}(5) \cdot F = \bar{f}(0) \cdot F^6 = [0\ 0\ 1\ 0\ 0\ 2\ 0\ 0\ 4\ 0\ 0\ 0] \quad (8)$$

and generally,

$$\bar{f}(k) = \bar{f}(k-1) \cdot F = \bar{f}(0) \cdot F^K \quad . \quad (9)$$

At time frame 6, the steady state vector indicates the data displayed in Table 1:

a replica type	b ancestor type	f_{ab} number
0	0	0
1	0	0
2	0	1
0	1	0
1	1	0
2	1	2
0	2	0
1	2	0
2	2	4
0	3	8
1	3	0
2	3	0

Table 1. Frequence of replica-ancestor types.

Continuing with the same example in which n = 2 and m = 3, the cumulative diagram (Figure 4) is perhaps more revealing. If a,b index the number of replicas and ancestors, respectively, for any particular primary, the state vector for any time frame k can be expressed using the following format for a,b where $a \leq n$, $b \leq m$, $\bigwedge k = 6$:

$$\begin{matrix} b & \emptyset\ \emptyset\ \emptyset\ 1\ 1\ 1\ 2\ 2\ 2\ 3\ 3\ 3 \\ a: & \emptyset\ 1\ 2\ \emptyset\ 1\ 2\ \emptyset\ 1\ 2\ \emptyset\ 1\ 2 \end{matrix} \tag{10}$$

$$\bar{f}(6) = [\emptyset\ \emptyset\ 1\ \emptyset\ \emptyset\ 2\ \emptyset\ \emptyset\ 4\ 8\ \emptyset\ \emptyset], \tag{11}$$

that is

$$f_{00} = \emptyset,\ f_{10} = \emptyset,\ f_{20} = 1,\ f_{01} = \emptyset,\ f_{11} = \emptyset,\ f_{21} = 2,\ \ldots,\ f_{23} = \emptyset\ . \tag{12}$$

Since the vector $\bar{f}(k)$ which represents the state of the replicas at time k can be expressed by (9), then

$$\bar{f}(6) = [1\ \emptyset\ \emptyset\ \emptyset\ \emptyset\ \emptyset\ \emptyset\ \emptyset\ \emptyset\ \emptyset\ \emptyset\ \emptyset] \cdot \begin{bmatrix} \emptyset & 1 & \emptyset & 1 & \emptyset & \emptyset & \emptyset & \emptyset & \emptyset & \emptyset & \emptyset & \emptyset \\ \emptyset & \emptyset & 1 & 1 & \emptyset & \emptyset & \emptyset & \emptyset & \emptyset & \emptyset & \emptyset & \emptyset \\ \emptyset & \emptyset & 1 & \emptyset & \emptyset & \emptyset & \emptyset & \emptyset & \emptyset & \emptyset & \emptyset & \emptyset \\ \emptyset & \emptyset & \emptyset & \emptyset & 1 & \emptyset & 1 & \emptyset & \emptyset & \emptyset & \emptyset & \emptyset \\ \emptyset & \emptyset & \emptyset & \emptyset & \emptyset & 1 & 1 & \emptyset & \emptyset & \emptyset & \emptyset & \emptyset \\ \emptyset & \emptyset & \emptyset & \emptyset & \emptyset & 1 & \emptyset & \emptyset & \emptyset & \emptyset & \emptyset & \emptyset \\ \emptyset & \emptyset & \emptyset & \emptyset & \emptyset & \emptyset & 1 & \emptyset & 1 & \emptyset & \emptyset & \emptyset \\ \emptyset & \emptyset & \emptyset & \emptyset & \emptyset & \emptyset & \emptyset & 1 & 1 & \emptyset & \emptyset & \emptyset \\ \emptyset & \emptyset & \emptyset & \emptyset & \emptyset & \emptyset & \emptyset & 1 & \emptyset & \emptyset & \emptyset & \emptyset \\ \emptyset & \emptyset & \emptyset & \emptyset & \emptyset & \emptyset & \emptyset & \emptyset & 1 & \emptyset & \emptyset & \emptyset \\ \emptyset & \emptyset & \emptyset & \emptyset & \emptyset & \emptyset & \emptyset & \emptyset & \emptyset & 1 & \emptyset & \emptyset \\ \emptyset & \emptyset & \emptyset & \emptyset & \emptyset & \emptyset & \emptyset & \emptyset & \emptyset & \emptyset & 1 & \emptyset \\ \emptyset & \emptyset & \emptyset & \emptyset & \emptyset & \emptyset & \emptyset & \emptyset & \emptyset & \emptyset & \emptyset & 1 \end{bmatrix}^{6}, \tag{13}$$

and

$$\bar{f}(6) = [1\ \emptyset\ \emptyset\ \emptyset\ \emptyset\ \emptyset\ \emptyset\ \emptyset\ \emptyset\ \emptyset\ \emptyset\ \emptyset] \cdot \begin{bmatrix} \emptyset & \emptyset & 1 & \emptyset & \emptyset & 2 & \emptyset & \emptyset & 4 & 8 & \emptyset & \emptyset \\ \emptyset & \emptyset & 1 & \emptyset & \emptyset & 1 & \emptyset & \emptyset & 2 & 4 & \emptyset & \emptyset \\ \emptyset & \emptyset & 1 & \emptyset & \emptyset & \emptyset & \emptyset & \emptyset & \emptyset & \emptyset & \emptyset & \emptyset \\ \emptyset & \emptyset & \emptyset & \emptyset & \emptyset & 1 & \emptyset & \emptyset & 2 & 4 & \emptyset & \emptyset \\ \emptyset & \emptyset & \emptyset & \emptyset & \emptyset & 1 & \emptyset & \emptyset & 1 & 2 & \emptyset & \emptyset \\ \emptyset & \emptyset & \emptyset & \emptyset & \emptyset & 1 & \emptyset & \emptyset & \emptyset & \emptyset & \emptyset & \emptyset \\ \emptyset & \emptyset & \emptyset & \emptyset & \emptyset & \emptyset & \emptyset & \emptyset & 1 & 2 & \emptyset & \emptyset \\ \emptyset & \emptyset & \emptyset & \emptyset & \emptyset & \emptyset & \emptyset & \emptyset & 1 & 1 & \emptyset & \emptyset \\ \emptyset & \emptyset & \emptyset & \emptyset & \emptyset & \emptyset & \emptyset & \emptyset & 1 & \emptyset & \emptyset & \emptyset \\ \emptyset & \emptyset & \emptyset & \emptyset & \emptyset & \emptyset & \emptyset & \emptyset & \emptyset & 1 & \emptyset & \emptyset \\ \emptyset & \emptyset & \emptyset & \emptyset & \emptyset & \emptyset & \emptyset & \emptyset & \emptyset & \emptyset & 1 & \emptyset \\ \emptyset & \emptyset & \emptyset & \emptyset & \emptyset & \emptyset & \emptyset & \emptyset & \emptyset & \emptyset & \emptyset & 1 \end{bmatrix} \tag{14}$$

From Strang 5, any square matrix having s linearly independent eigenvectors is similar to a Jordan form matrix with s blocks, each block of the form

$$J_i = \begin{bmatrix} \lambda_i & 1 & & \\ & \lambda_i & 1 & \\ & & \ddots & \ddots \\ & & & 1 \\ & & & \lambda_i \end{bmatrix} \qquad (15)$$

where each blank is zero. Since there exists square matrices M, J, M^{-1} such that $F = MJM^{-1}$, where J is a Jordan form matrix, then it follows that

$$F^K = MJ^KM^{-1} \qquad (16)$$

and

$$\bar{f}(k) = \bar{f}(\emptyset) \cdot F^K = \bar{f}(\emptyset) \cdot MJ^KM^{-1} . \qquad (17)$$

Thus the problem of finding the state vector can be made to rest on raising a Jordan form matrix to an exponent. It may be pointed out that the eigenvalues of J are precisely those eigenvalues of F. Moreover, the columns of M are the eigenvectors and the generalized eigenvectors of F.

In the example of n = 2 and m = 3,

$$\bar{f}(6) = \begin{bmatrix} 1 & \emptyset & \emptyset & \emptyset & \emptyset & \emptyset & \emptyset & \emptyset & \emptyset & \emptyset & \emptyset \end{bmatrix} \cdot F^6, \text{ where} \qquad (18)$$

$$F = MJM^{-1}, \text{ so that} \qquad (19)$$

$$\bar{f}(6) = \begin{bmatrix} 1 & \emptyset & \emptyset & \emptyset & \emptyset & \emptyset & \emptyset & \emptyset & \emptyset & \emptyset & \emptyset \end{bmatrix} \cdot MJ^6M^{-1}. \text{ Specifically,} \qquad (20)$$

$$M = \begin{bmatrix} 1 & \emptyset & \emptyset & \emptyset & \emptyset & \emptyset & 1 & 2 & 4 & 8 & \emptyset & \emptyset \\ \emptyset & 1 & -1 & 1 & -1 & 1 & 1 & 1 & 2 & 4 & \emptyset & \emptyset \\ \emptyset & \emptyset & \emptyset & \emptyset & \emptyset & \emptyset & 1 & \emptyset & \emptyset & \emptyset & \emptyset & \emptyset \\ \emptyset & \emptyset & 1 & -1 & 1 & -1 & \emptyset & 1 & 2 & 4 & \emptyset & \emptyset \\ \emptyset & \emptyset & \emptyset & 1 & -2 & 3 & \emptyset & 1 & 1 & 2 & \emptyset & \emptyset \\ \emptyset & \emptyset & \emptyset & \emptyset & \emptyset & \emptyset & \emptyset & 1 & \emptyset & \emptyset & \emptyset & \emptyset \\ \emptyset & \emptyset & \emptyset & \emptyset & 1 & -6 & \emptyset & \emptyset & 1 & 2 & \emptyset & \emptyset \\ \emptyset & \emptyset & \emptyset & \emptyset & \emptyset & 1 & \emptyset & \emptyset & 1 & 1 & \emptyset & \emptyset \\ \emptyset & \emptyset & \emptyset & \emptyset & \emptyset & \emptyset & \emptyset & \emptyset & 1 & \emptyset & \emptyset & \emptyset \\ \emptyset & \emptyset & \emptyset & \emptyset & \emptyset & \emptyset & \emptyset & \emptyset & \emptyset & 1 & \emptyset & \emptyset \\ \emptyset & \emptyset & \emptyset & \emptyset & \emptyset & \emptyset & \emptyset & \emptyset & \emptyset & \emptyset & 1 & \emptyset \\ \emptyset & \emptyset & \emptyset & \emptyset & \emptyset & \emptyset & \emptyset & \emptyset & \emptyset & \emptyset & \emptyset & 1 \end{bmatrix} \qquad M^{-1} = \begin{bmatrix} 1 & \emptyset & -1 & \emptyset & \emptyset & -2 & \emptyset & \emptyset & -4 & -8 & \emptyset & \emptyset \\ \emptyset & 1 & -1 & 1 & \emptyset & -2 & \emptyset & \emptyset & -4 & -8 & \emptyset & \emptyset \\ \emptyset & \emptyset & \emptyset & 1 & 1 & -2 & 1 & \emptyset & -4 & -8 & \emptyset & \emptyset \\ \emptyset & \emptyset & \emptyset & \emptyset & 1 & -1 & 2 & 1 & -4 & -7 & \emptyset & \emptyset \\ \emptyset & \emptyset & \emptyset & \emptyset & \emptyset & \emptyset & 1 & 2 & -3 & -4 & \emptyset & \emptyset \\ \emptyset & \emptyset & \emptyset & \emptyset & \emptyset & \emptyset & \emptyset & \emptyset & \emptyset & \emptyset & \emptyset & \emptyset \\ \emptyset & \emptyset & 1 & \emptyset & \emptyset & \emptyset & \emptyset & \emptyset & \emptyset & \emptyset & \emptyset & \emptyset \\ \emptyset & \emptyset & \emptyset & \emptyset & \emptyset & 1 & \emptyset & \emptyset & \emptyset & \emptyset & \emptyset & \emptyset \\ \emptyset & \emptyset & \emptyset & \emptyset & \emptyset & \emptyset & \emptyset & \emptyset & 1 & \emptyset & \emptyset & \emptyset \\ \emptyset & \emptyset & \emptyset & \emptyset & \emptyset & \emptyset & \emptyset & \emptyset & \emptyset & 1 & \emptyset & \emptyset \\ \emptyset & \emptyset & \emptyset & \emptyset & \emptyset & \emptyset & \emptyset & \emptyset & \emptyset & \emptyset & 1 & \emptyset \\ \emptyset & \emptyset & \emptyset & \emptyset & \emptyset & \emptyset & \emptyset & \emptyset & \emptyset & \emptyset & \emptyset & 1 \end{bmatrix} \qquad (21)$$

and

$$J=\begin{bmatrix} 0 & 1 & 0 & 0 & 0 & 0 & 0 & 0 & 0 & 0 & 0 & 0 \\ 0 & 0 & 1 & 0 & 0 & 0 & 0 & 0 & 0 & 0 & 0 & 0 \\ 0 & 0 & 0 & 1 & 0 & 0 & 0 & 0 & 0 & 0 & 0 & 0 \\ 0 & 0 & 0 & 0 & 1 & 0 & 0 & 0 & 0 & 0 & 0 & 0 \\ 0 & 0 & 0 & 0 & 0 & 1 & 0 & 0 & 0 & 0 & 0 & 0 \\ 0 & 0 & 0 & 0 & 0 & 0 & 0 & 0 & 0 & 0 & 0 & 0 \\ 0 & 0 & 0 & 0 & 0 & 0 & 1 & 0 & 0 & 0 & 0 & 0 \\ 0 & 0 & 0 & 0 & 0 & 0 & 0 & 1 & 0 & 0 & 0 & 0 \\ 0 & 0 & 0 & 0 & 0 & 0 & 0 & 0 & 1 & 0 & 0 & 0 \\ 0 & 0 & 0 & 0 & 0 & 0 & 0 & 0 & 0 & 1 & 0 & 0 \\ 0 & 0 & 0 & 0 & 0 & 0 & 0 & 0 & 0 & 0 & 1 & 0 \\ 0 & 0 & 0 & 0 & 0 & 0 & 0 & 0 & 0 & 0 & 0 & 1 \end{bmatrix} \qquad J^6 = \begin{bmatrix} 0 & 0 & 0 & 0 & 0 & 0 & 0 & 0 & 0 & 0 & 0 & 0 \\ 0 & 0 & 0 & 0 & 0 & 0 & 0 & 0 & 0 & 0 & 0 & 0 \\ 0 & 0 & 0 & 0 & 0 & 0 & 0 & 0 & 0 & 0 & 0 & 0 \\ 0 & 0 & 0 & 0 & 0 & 0 & 0 & 0 & 0 & 0 & 0 & 0 \\ 0 & 0 & 0 & 0 & 0 & 0 & 0 & 0 & 0 & 0 & 0 & 0 \\ 0 & 0 & 0 & 0 & 0 & 0 & 0 & 0 & 0 & 0 & 0 & 0 \\ 0 & 0 & 0 & 0 & 0 & 0 & 1 & 0 & 0 & 0 & 0 & 0 \\ 0 & 0 & 0 & 0 & 0 & 0 & 0 & 1 & 0 & 0 & 0 & 0 \\ 0 & 0 & 0 & 0 & 0 & 0 & 0 & 0 & 1 & 0 & 0 & 0 \\ 0 & 0 & 0 & 0 & 0 & 0 & 0 & 0 & 0 & 1 & 0 & 0 \\ 0 & 0 & 0 & 0 & 0 & 0 & 0 & 0 & 0 & 0 & 1 & 0 \\ 0 & 0 & 0 & 0 & 0 & 0 & 0 & 0 & 0 & 0 & 0 & 1 \end{bmatrix} . \tag{22}$$

CONCLUSIONS AND RECOMMENDATIONS

In option C, the state vector $\bar{f}(k)$ can be generated in several ways.

1. Use of a diagram.
2. Recursively, by using $\bar{f}(k) = \bar{f}(k-1) \cdot F$.
3. Raising F to an exponent, $\bar{f}(k) = f(\emptyset) \cdot F^{k}$.
4. Jordanizing F, $\bar{f}(k) = \bar{f}(\emptyset) \cdot MJ^{k}M^{-1}$.

Some areas which may prove to be of interest are:

1. Defining and investigating the problems of placement of the replicas as they are generated.
2. Considering the demise of replicas; that is, replicas are no longer reproductive [2], [1].

REFERENCES

1. Darbro, Wesley A., and Georg von Tiesenhausen, "Sequences Generated by Self-Replicating Systems", The Fibonacci Quarterly, 21(1983), 97-106.

2. Hoggatt, V. E., Jr., and D. A. Lind, "The Dying Rabbit Problem", The Fibonacci Quarterly, 7(1969), 482-487.

3. Klarner, David A., "A Model for Population Growth", The Fibonacci Quarterly, 14(1976), 227-281.

4. McCord, Richard L., "Population Control of Self-Replicating Systems", 1982 NASA/ASEE Summer Faculty Fellowship Program, NASA Contractor Report, NASA CR-162051, August, 1982, XXVII-12.

5. Strang, Gilbert, Linear Algebra and Its Applications, Academic Press, New York, 1976, 181-189.

6. Von Tiesenhausen, Georg, and Wesley A. Darbro, Self-Replicating Systems - A Systems Engineering Approach, NASA Technical Memorandum, NASA TM 78304 Marshall Space Flight Center, Alabama, July 1980.

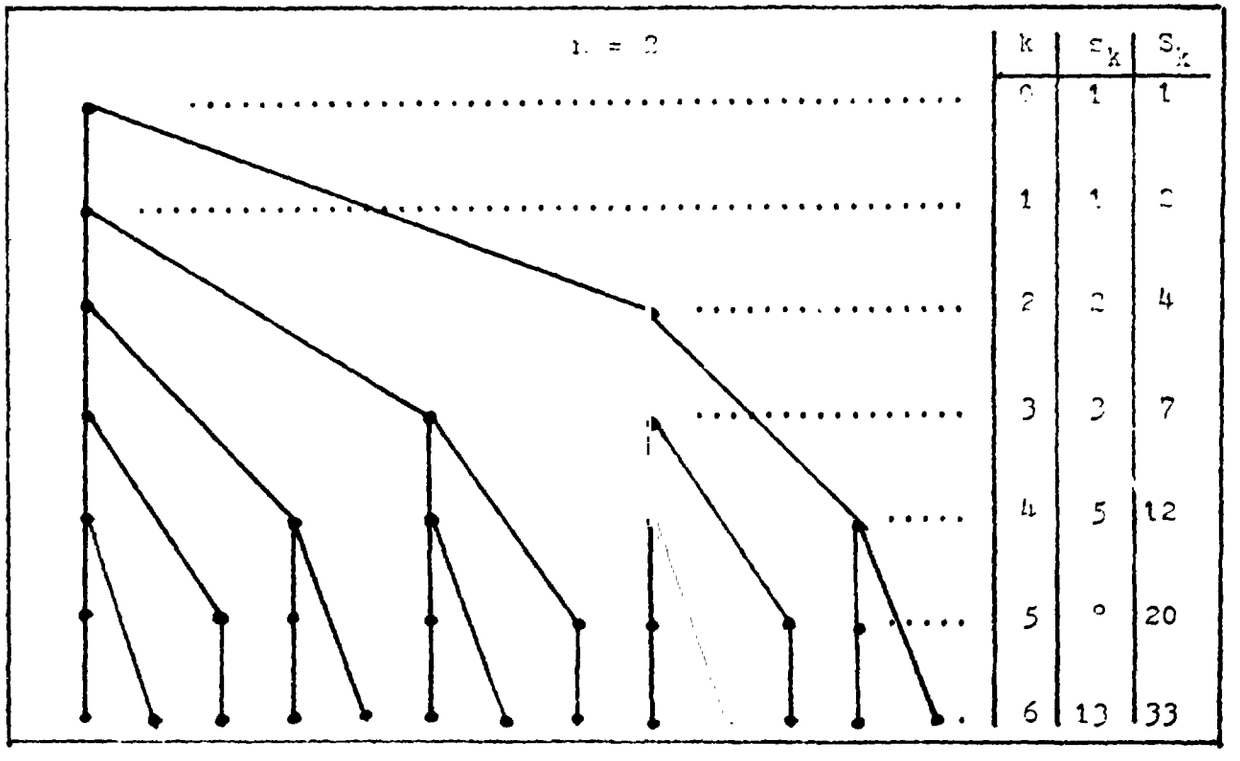

FIGURE 1. Family Tree of Replicas
Option B

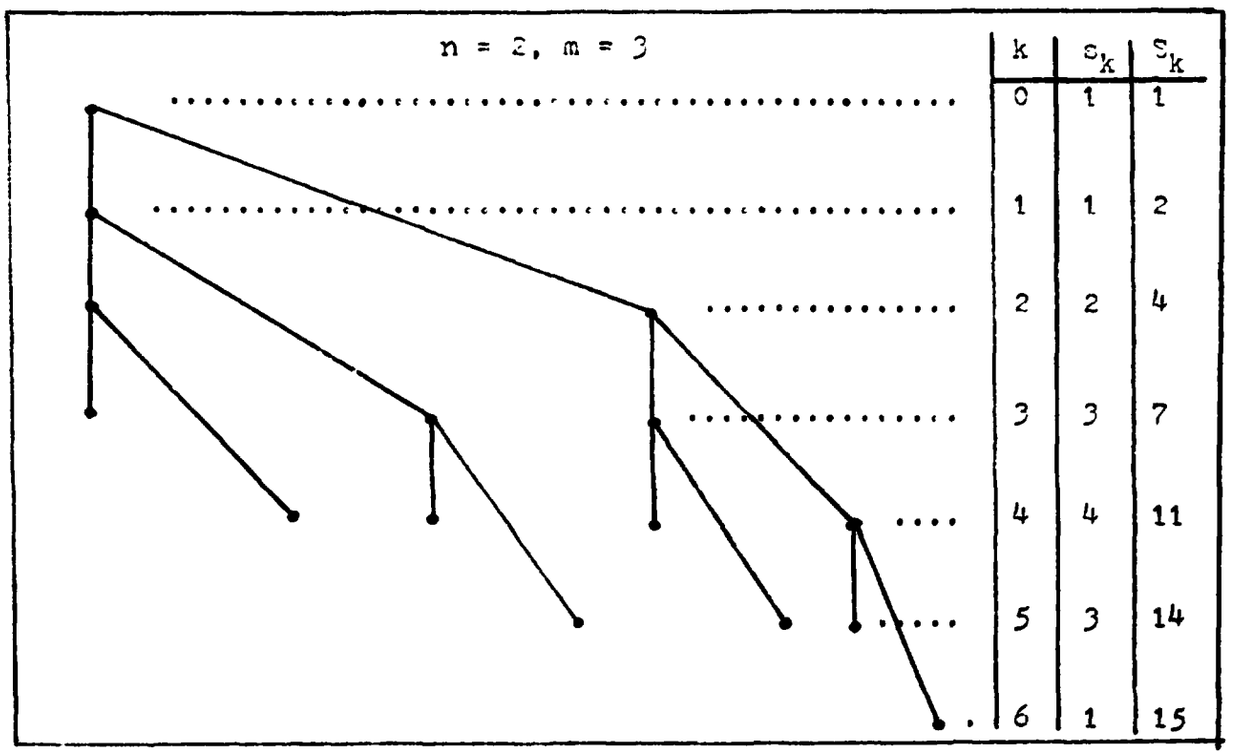

FIGURE 2. Family Tree of Replicas.
Option C.

i \ j	0^0	1^0	2^0	0^1	1^1	2^1	0^2	1^2	2^2	0^3	1^3	2^3
0^0	0	1	0	1	0	0	0	0	0	0	0	0
1^0	0	0	1	1	0	0	0	0	0	0	0	0
2^0	0	0	1	0	0	0	0	0	0	0	0	0
0^1	0	0	0	0	1	0	1	0	0	0	0	0
1^1	0	0	0	0	0	1	1	0	0	0	0	0
2^1	0	0	0	0	0	1	0	0	0	0	0	0
0^2	0	0	0	0	0	0	0	1	0	1	0	0
1^2	0	0	0	0	0	0	0	0	1	1	0	0
2^2	0	0	0	0	0	0	0	0	1	0	0	0
0^3	0	0	0	0	0	0	0	0	0	1	0	0
1^3	0	0	0	0	0	0	0	0	0	0	1	0
2^3	0	0	0	0	0	0	0	0	0	0	0	1

FIGURE 3. Formation of Matrix $F = [f_{ij}]$.
Option C; n = 2, m = 3.

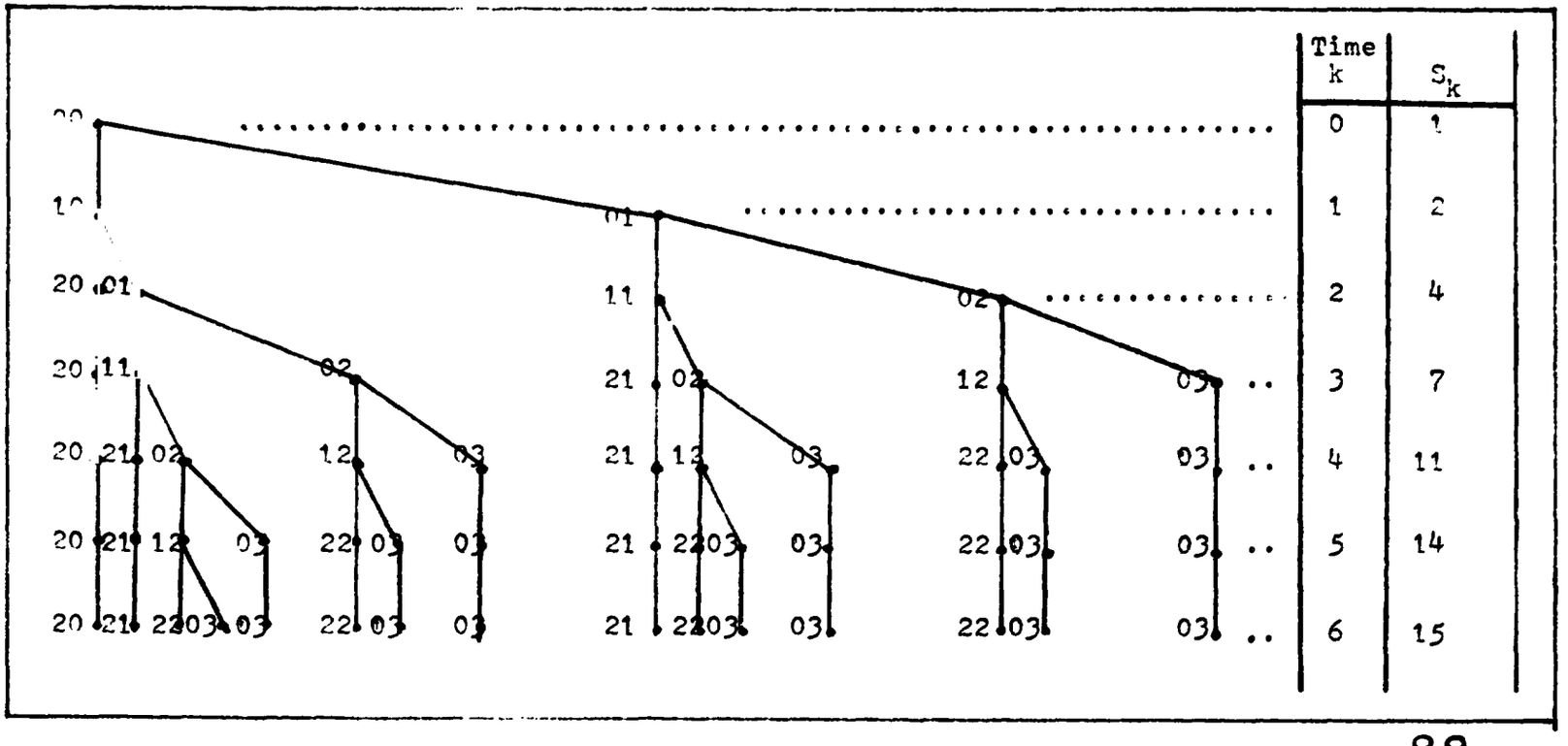

FIGURE 4. Cumulative Diagram of Replicas.

Option C; n = 2, m = 3.

1983

NASA/ASEE SUMMER FACULTY RESEARCH FELLOWSHIP PROGRAM

MARSHALL SPACE FLIGHT CENTER

THE UNIVERSITY OF ALABAMA IN HUNTSVILLE

A FMCW RADAR RANGING DEVICE FOR THE TELEOPERATOR MANEUVERING SYSTEM

Prepared By:	Malcolm W. McDonald, Ph.D.
Academic Rank:	Associate Professor
University and Department	Berry College Department of Physics
NASA/MSFC: (Laboratory) (Division) (Branch)	 Information & Electronic Systems Computers and Communication Communications Systems
MSFC Counterpart:	E. H. Gleason
Date:	August 12, 1983
Contract No.:	NGT-01-008-021 The University of Alabama in Huntsville

A FMCW RADAR RANGING DEVICE FOR THE TELEOPERATOR MANEUVERING SYSTEM

By

Malcolm W. McDonald, Ph.D.
Associate Professor of Physics
Berry College
Mount Berry, Georgia

ABSTRACT

A frequency-modulated continuous wave radar system is under development in the Communications Systems Branch of the Information and Electronic Systems Laboratory at Marshall Space Flight Center. The radar unit is being designed for use on the teleoperator maneuvering system. Its function is to provide millimeter-level accuracy in range and range rate measurements out to a range of thirty meters. This will facilitate "soft" docking with accuracy.

This report is an updating of previous developments reported on this system. An innovation in the system is the utilization of a standard reference signal generated by shunting a portion of the radar energy into a shorted coaxial delay line. The regular radar target return signal is constantly compared with the reference signal to provide internal error compensation. Within a five meter range, a limit imposed by present laboratory dimensions, the radar system exhibits reliable accuracy with range error less than 0.2%.

ACKNOWLEDGMENTS

I am extremely grateful to Marshall Space Flight Center, NASA, ASEE, and The University of Alabama in Huntsville, collectively, for providing this summer research program. Much credit goes to the able leadership and effective administration of the program by Dr. Gerald Karr, Dr. James Dozier, and Mr. Leroy Osborn.

My interaction with my NASA counterpart, Mr. Ed Gleason, was of an exceptional nature. He was exceedingly generous in allowing me full run of his laboratory and in permitting me total liberty in studying and attempting alternative approaches in the operation of the radar system. I thank him for sharing his expertise, insights, and friendship.

The sense of accomplishment and pleasure derived from this research project was heightened by stimulating dialogue and challenging ideas shared with Mr. Bill Reed. I offer my sincerest thanks for the warm camaraderie and evidence of personal acceptance extended me by all the persons in the Communications Systems Branch. In addition, it has been a pleasure working in a nearby area and engaging in conversation with two other faculty fellows, Dr. Al Pujol and Dr. Fereydoun Jalali, throughout the summer.

LIST OF FIGURES

Figure Number	Title	Page Number
1	FM Sweep Parameters	XXIII-8
2	Radar-Target Geometry	XXIII-8
3	Block Diagram of System	XXIII-10
4	Waveforms and Timing Relationships	XXIII-12

INTRODUCTION

As space exploration continues and the permanent space platform or station becomes a reality the need for a small "workhorse" vehicle will be met by the Teleoperator Maneuvering System. TMS, as it has been identified until recently, has been lately designated as the Orbital Maneuvering Vehicle, or OMV. Reference will continue to be made to TMS in this report.

The TMS vehicle will require an accurate close-range radar system to enable "soft" docking with the space station or other vehicles. The radar system described in this report is being developed to help meet that need. This system has evolved from an earlier system developed in this laboratory for the measurement of the thickness of coal seams in coal mining operations (ref. 1).

The microwave energy is generated in a voltage-controlled YIG (yttrium-iron-garnet) K_a-band oscillator. The oscillator frequency is modulated by a symmetric triangular voltage ramp which drives the output frequency through an adjustable sweep range Δf of one or two gigahertz that is centered on a frequency of 35 gigahertz (see fig. 1). This energy is transmitted from a 15 cm diameter dish antenna which also receives a component of returning energy reflected from a cubical corner reflector located at a range distance R. The time delay t for the returning energy is dependent upon the range R. The returning energy is homodyned in a microwave mixer with the frequency currently available from the oscillator to produce an audio frequency F (a few kilohertz) which is proportional to the range. Careful processing of the audio signal leads to a computed value of range. Computer processing of the range and time data will produce a reading of range rate (relative speed of approach or recession between the radar system and a moving target).

OBJECTIVES

The objectives guiding the scope of this research effort are:

1. to investigate the nature and source of the first-order and second order range determination errors indigenous to the FMCW radar system under development in the Communications Systems Branch laboratory at Marshall Space Flight Center,

2, to seek optimized signal processing techniques which will reduce the range errors to acceptable levels, and

3. to set a goal of minimizing the range determination errors to a value of $\pm$0.1% within the five-meter limited range available in the laboratory.

RESEARCH REPORT

I. General Description

The basic principles of frequency-modulated continuous wave (FMCW) radar operations are described in various references (see, for example, Skolnik, ref. 1). Figure 1 illustrates the frequency modulation used in the radar system under investigation.

A voltage-controlled microwave oscillator is swept linearly in time up and down through the extreme frequencies, f_1 (minimum) and f_2 (maximum), with a half-period T of approximately four milliseconds. The sweep frequency was actually about 122.5 Hz. The oscillator is a YIG (yttrium-iron-garnet) type, and its center frequency was set to a nominal value of 35 gigahertz. Thus the radar operates in the K_a band with a nominal wavelength emitted of 8.6 millimeters and is swept through a frequency range one or two gigahertz (adjustable).

The basic radar-target geometry is illustrated in Fig. 2. The microwave energy is fed to a transmit/receive dish antenna. After a range-dependent time delay t a portion of the energy returns to the antenna after reflecting from the target. The target is a copper-coated cubical corner reflector mounted on a calibrated five-meter optical bench. The returning energy is homodyned in a microwave mixer with the updated frequency available directly from the oscillator. The output of the mixer is a low frequency (audio, a few kilohertz) beat signal of a frequency F which is linearly related to the range of the target.

Investigations reported earlier (ref. 2) utilized direct measurement of the audio frequency F made during a selected time window in the latter part of the upsweep or downsweep half cycle for the purpose of computing range. That earlier method suffered from the fact that measurements of F were being made during either the up or downsweep, but not both, with whatever biases that fact might introduce into the range computation. It also had a problem with a Doppler error which was introduced when the target was in motion. A final shortcoming of the earlier method employed in the radar system originated in a type of "step" error which occurred unavoidably at certain range values when the zero-crossing detection circuitry was forced to step forward or backward one cycle of the F waveform to commence the measurement of frequency within the selected time window. The present system employs a signal processing scheme which obviates all of those difficulties in the earlier system. The new signal processing scheme will be discussed in the next section.

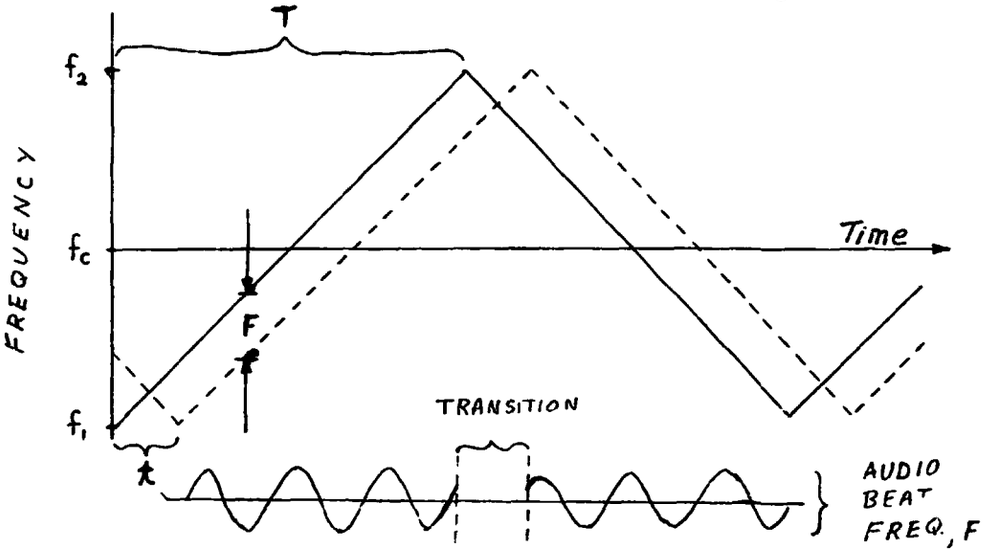

Figure 1. FM Sweep Parameters. The center frequency, f_c = 35 GHz. The sweep excursion, $\Delta f = f_2 - f_1$ = 1.25 or 2.5 GHz (adjustable). Parameters F, T, and t are described in the text.

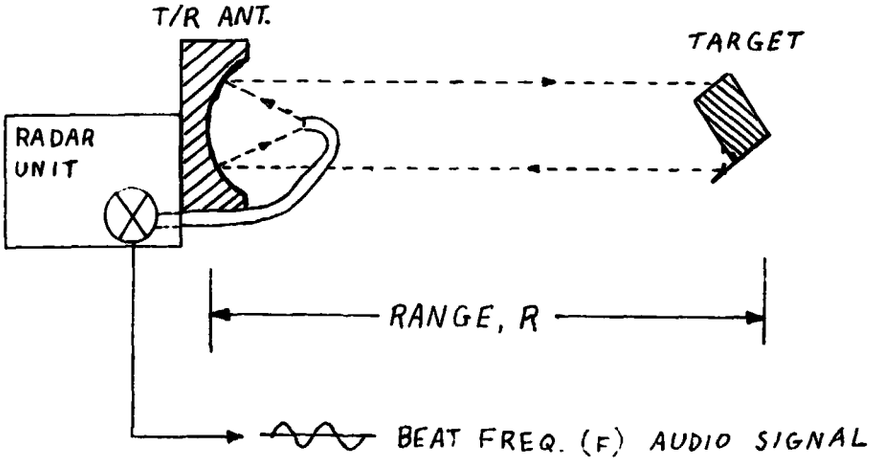

Figure 2. Radar-Target Geometry. The transmit/receive antenna is a dish of diameter 15.24 cm (6.00 inch) and 5.1 cm focal length. The target is a copper-coated cubical corner reflector which slides along a five-meter calibrated optical bench.

II. Circuit Description

A block diagram illustrates the microwave and electronic signal processing circuitry in Figure 3. The new system incorporates the following changes into the former system: 1) the introduction of a shorted coaxial delay line-generated audio signal (frequency denoted by G) which serves as an electronic drift compensation reference, 2) sampling of range data and calibration data during both the upsweep and the downsweep cycle (this enables a canceling of the Doppler error associated with a moving target), 3) the upconversion and FM discrimination of the range audio and calibration audio signals, and 4) the digitization of the analog voltage output from the FM discriminator.

The more important waveforms with their relative timing indicated are illustrated in Figure 4. The SYNC square wave serves as the fundamental clock timing reference throughout the system. It establishes the voltage ramp period which drives the YIG oscillator up on one half cycle and down in frequency during the other half cycle. The microwave energy from the oscillator is divided into two components by a hybrid microwave splitter. The first component is directed through a microwave circulator to the transmit/receive antenna. On the route to the antenna an in-line 10 dB directional coupler diverts a small portion of the energy out to the calibration delay line circuit.

The major portion of the first component is transmitted from the antenna with an energy return from the target. The target return energy is circulated around to rejoin the second component in a second hybrid splitter (combiner). The time-delayed range component is mixed with the undelayed to produce a range-dependent audio beat signal, referred to as the F signal. This signal passes through a bandpass filter and an automatic gain control circuit to the analog switch.

Picking up again at the 10 dB in-line directional coupler, the ten dB reduced signal is circulated into a shorted coaxial transmission line 3.5 meters in length. The reflected energy mixes with the reverse-path leakage energy that gets through this second circulator to produce a reference audio signal, referred to as the G signal. The G signal frequency is passed through a highpass filter/amplifier to the analog switch. The delay line length establishes the G signal frequency at a value corresponding to an equivalent range of about 4.6 meters.

The SYNC/2 pulse is derived from the SYNC pulse in a divide-by-two circuit. SYNC/2 drives the analog switch to pass alternately the range audio F and the calibration audio G signals. A full sweep cycle

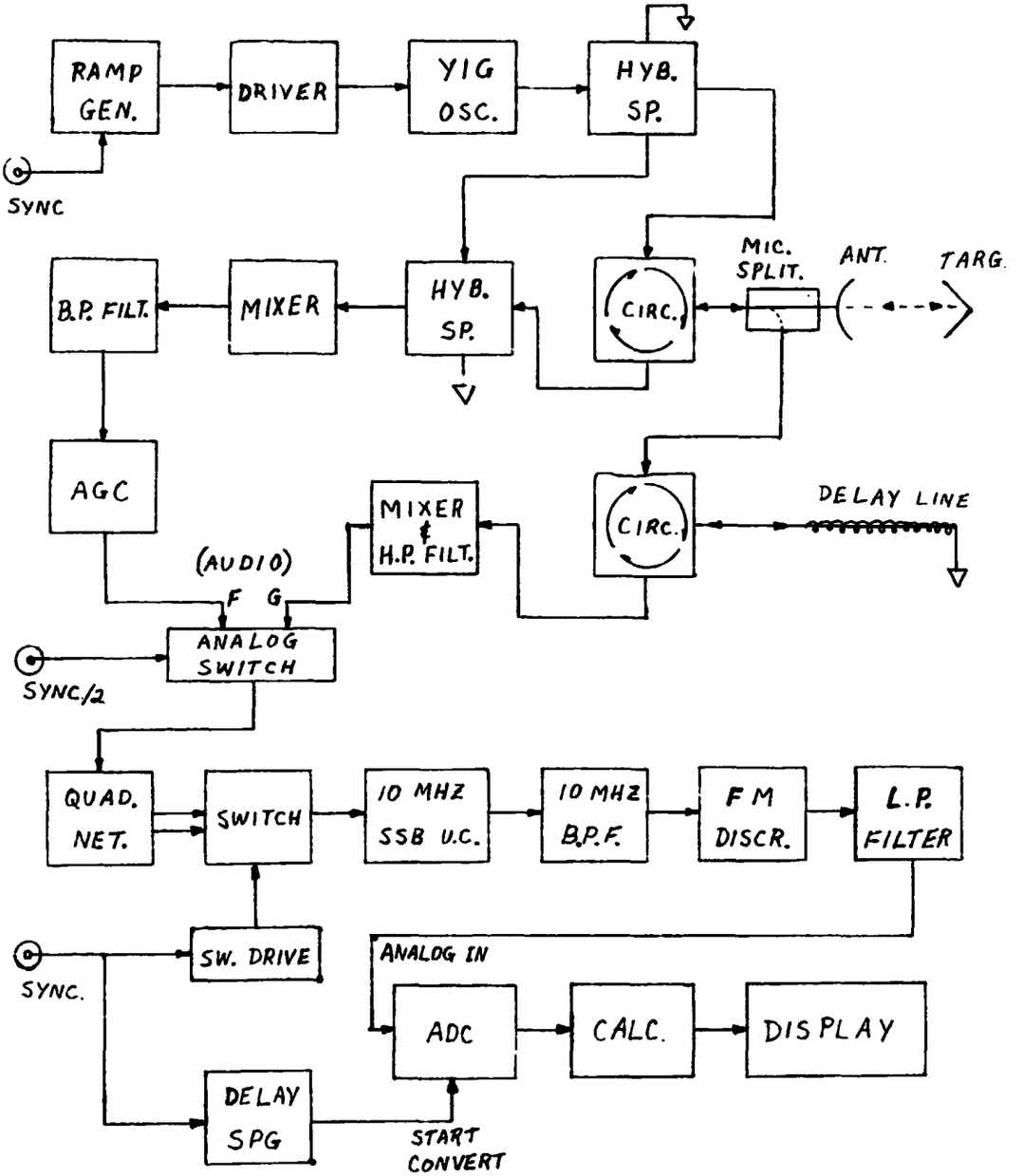

Figure 3. Block Diagram of System. Abbreviations are explained in text.

of the range audio F (upsweep plus downsweep) and then a full sweep cycle of the calibration audio is passed.

From the analog switch the audio frequency is fed to a quadrature network which produces two outputs bearing a ninety-degree phase relationship. These two outputs are switched at the SYNC rate into a ten-megahertz single sideband upconverter. The upconverter produces the upper sideband (local oscillator frequency plus audio frequency) during one half of the sweep cycle and the lower sideband (local oscillator frequency minus audio frequency) during the other half. The upconverted signals are directed through a 10 MHz bandpass filter into the FM discriminator.

The output from the FM discriminator is voltage offset to become the bipolar ANALOG IN signal. It is filtered to remove any transients or high frequency components and sampled by an analog-to-digital converter. A delay-sample pulse pulse generator circuit derives the START CONVERT pulse for the ADC. The digitized data is transferred into a calculator (Hewlett-Packard HP 9825A) through an interrupt-mode buffer. The range calculation is performed and an updated range reading is registered on a digital display. The displayed range represents an n-fold sliding average of the last n readings computed.

The SYNC and SYNC/2 pulses are also read into the calculator as peripheral status input levels STI$\emptyset$ and STI1, respectively. They enable the calculator to identify the input data and to establish an order for data transfer from the ADC.

III. Theory of Operation

As is illustrated in Figure 1, the YIG oscillator is driven in a linear fashion between frequency extremes f_1 and f_2 in a time T. The return signal from the target (dashed line) differs from the microwave energy it re-encounters (solid line) by a frequency difference F. This becomes the audio signal developed in the mixer in response to the target at range R. The time delay t for the return signal is defined by

$$t = 2R/c \qquad \text{(Equation 1)}$$

where R is the range and c is the propagation speed of the microwaves. The beat frequency F is related to the time delay t by

$$F/t = \Delta f/T \ . \qquad \text{(Equation 2)}$$

Combining the two equations allows range to be expressed in terms of the audio frequency F,

$$R = cFT/2\,\Delta f \ . \qquad \text{(Equation 3)}$$

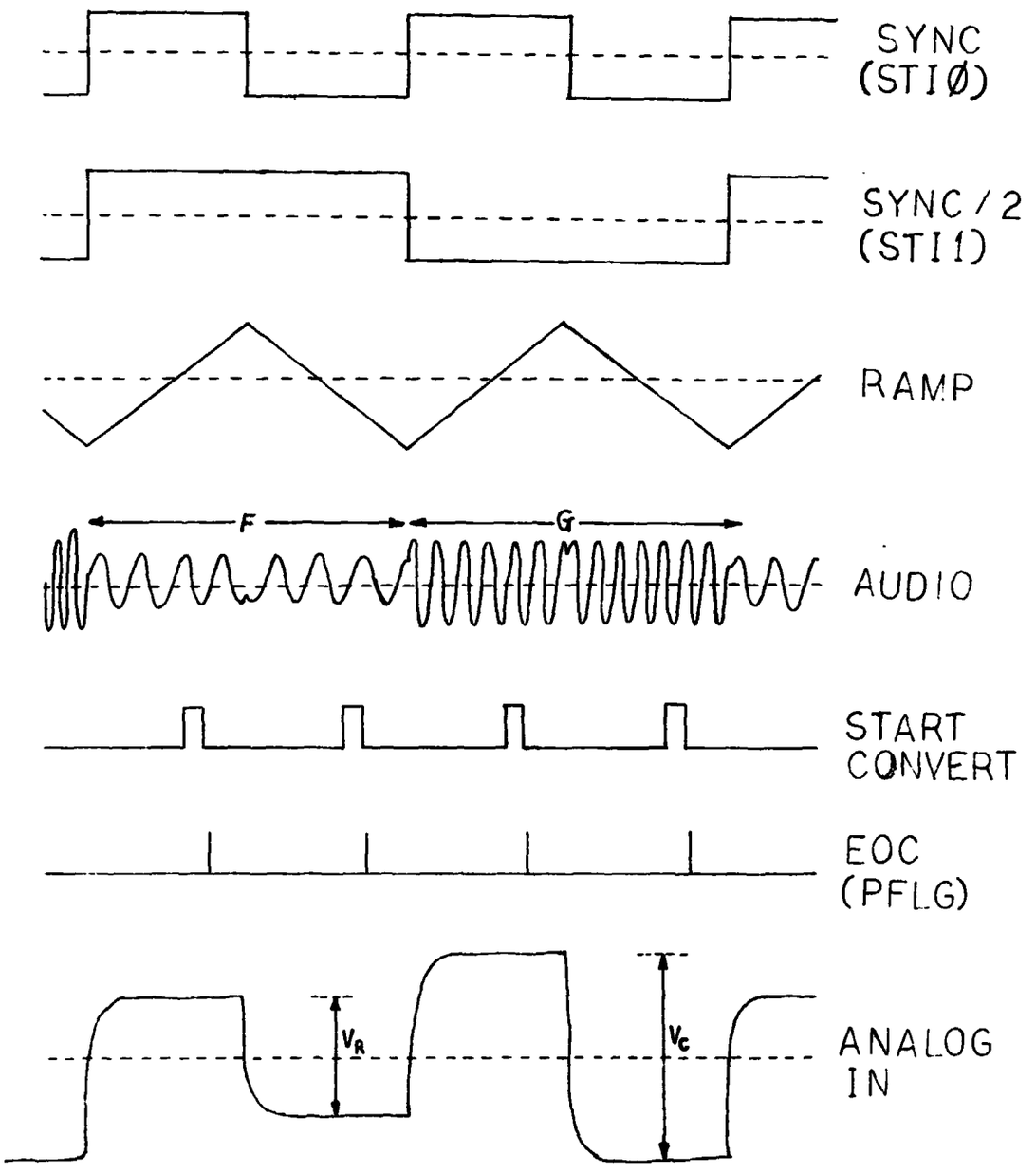

Figure 4. Waveforms and Timing Relationships.

In other words, since c, T, and Δf either have, or can be set at, fixed values, R is directly proportional to F.

In the FM discriminator the output voltage is linearly proportional to the (upconverted) input frequency. Thus, if we label the upper- and lower-sideband voltages V_2 and V_1, respectively, we can write

$$V_1 = mF_1 + b \text{ , and}$$

$$V_2 = mF_2 + b$$

where F_1 and F_2 represent the lower- and upper-sideband frequencies defined by

$$F_1 = f_{LO} - F \text{ , and}$$

$$F_2 = f_{LO} + F$$

and m and b are slope and intercept parameters characteristic of the V vs. F behavior of the FM discriminator. f_{LO} represents the local oscillator frequency in the upconverter.

Defining the range voltage $V_R = V_2 - V_1$ (see Figure 4) and substituting into Equation 3 yields

$$V_R = 2mF \text{ , and}$$

$$R = (cT/4m\Delta f)\cdot V_R \quad . \qquad \text{(Equation 4)}$$

In principle, then, R is directly proportional to V_R. In fact, however, electronic drift in the system can cause the value of V_R to vary in time for a fixed value of R. To compensate for such drift-related errors an approach adapted from that of Johnson and coworkers (see Ref. 3) was instituted. The calibration audio frequency G generated by the delay line undergoes precisely the same signal processing as does the range audio F. It generates a calibration voltage V_C (see Figure 4) analogous to the range voltage V_R. In fact the ratio of the two voltages, V_R/V_C, is directly proportional to R,

$$R = M(V_R/V_C) + B \quad . \qquad \text{(Equation 5)}$$

As V_R tends to drift, V_C drifts in a corresponding manner, thereby maintaining a fixed ratio at a fixed range. A measurement of the

slope M and intercept B characteristic of the relationship of the ratio V_R/V_C and the range R for the radar system need be made only one time. Thus, the voltage data sampled by the ADC enables the computation of the voltage ratio and the Equation 5 allows a method of establishing the corresponding range.

IV. Results and Conclusions

The radar system, as described in this paper, exhibits reliable range measurements with errors less than $\pm$ 0.2% out to a laboratory-restricted range limit of five meters. It was found that some degree of intermodulation of the calibration signal G due to insufficient isolation of the range signal from the calibration signal seems to account for the major portion of the range determination error in the system presently. It is concluded and recommended that improvement in the isolation of the G signal from the F signal will lead to even better performance of the radar system in the future.

REFERENCES

1. Skolnik, M.I., Introduction to Radar Systems, McGraw-Hill Book Company, New York, N.Y., 1962.

2. McDonald, M.W., "Study of and Proposals for the Correction of Errors in a Radar Ranging Device Designed to Facilitate Docking of the Teleoperator Maneuvering System", in NASA Contractor Report - 1982 - NASA/ASEE Summer Faculty Fellowship Program, edited by B.F. Barfield, et al, NASA CR - 162051, August, 1982.

3. Johnson, H.C., R.W. Paglione, and J.P. Hoffman, "A Short Range Radar for Measuring Blast-Furnace Burden Height", RCA Laboratories Report PE - 714, David Sarnoff Research Center, Princeton, N.J., 1978.

1983

NASA/ASEE SUMMER FACULTY RESEARCH FELLOWSHIP PROGRAM

MARSHALL SPACE FLIGHT CENTER
THE UNIVERSITY OF ALABAMA

THE DEVELOPMENT OF A DIGITAL PROCESSING SYSTEM FOR ACCURATE RANGE DETERMINATIONS

Prepared By	Alfonso Pujol, Jr., Ph.D.
Academic Rank:	Associate Professor
University and Department:	University of Tennessee Space Institute Department of Electrical Engineering
NASA/MSFC: (Laboratory) (Division) (Branch)	 Information & Electronic Systems Computers and Communication Communications Systems
MSFC Counterpart:	B.R. Reed
Date:	August 12, 1983
Contract No:	NGT-01-008-021 (The University of Alabama in Huntsville)

THE DEVELOPMENT OF A DIGITAL PROCESSING SYSTEM FOR ACCURATE RANGE DETERMINATIONS

BY

Alfonso Pujol Jr., Ph.D.
Associate Professor Electrical Engineering
The University of Tennessee Space Institute
Tullahoma, Tennessee 37388

ABSTRACT

As a member of the NASA-ASEE Summer Faculty Fellowship Program it was my task to investigate, identify and develop a means of providing millimeter detection capabilities for a close range radar system. The system under investigation is a digital processor that converts incoming signals from the radar system into their related frequency spectra. Identification will be attempted by correlating spectral characteristics with accurate range determinations. The system will utilize an analog to digital converter for sampling and converting the signal from the radar system into 16-bit digital words (two bytes) for RAM storage, data manipulations, and computations. To remove unwanted frequency components the data will be retrieved from RAM and digitally filtered using Large Scale Integration (LSI) circuits. Filtering will be performed by a biquadratic routine within the chip which carries out the required filter algorithm. Prior conversion to a frequency spectrum the filtered data will be processed by a Fast Fourier Transform chip. Analysis and identification of spectral characteristics for accurate range determinations will be made by microcomputer computations. System operations and computations, including chip routines will be under the complete control of a 16-bit microcomputer. However, because of the limited time of the summer program and the long procurement time for necessary electronics and support items, the design and hardware development phases of the project were focused to the input portion of the digital processor.

ACKNOWLEDGMENTS

The writer wishes to express his appreciation to the NASA/ASEE Summer Faculty Fellowship program for the research opportunity it has provided. Sincere gratitude is extended to Dr. Gerald Karr, Dr. Jim Dozier and Mr. Leroy Osborn for their very capable administration of this program and to Mr. B.R. Reed, Mr. E.H. Gleason and Mr. G.C. Tucker who again provided many creative ideas, stimulating conversations, and a jovial atmosphere.

Credit is given to Donna Hall for her patience in typing this paper.

LIST OF FIGURES

Figure No.	Title	Page
1	Digital signal processing system	XXIV-3
2a	Sample and storage circuit	XXIV-5
2b	Sample and storage circuit	XXIV-6

INTRODUCTION

For the past few years research has been undertaken at the George C. Marshall Space Flight Center (MSFC) for the development of an accurate close range (from 0.0 meters to 30.0 meters) radar system for Teleoperator Maneuvering Systems (TMS). The TMS system will perform functions much like a harbor tug; the Frequency Modulated-Continuous Wave (FM-CW) close range radar system will provide accurate range measurements for precision alignment maneuvers for docking (for satellite towing or repair purposes) or other complex procedures with orbital objects. Initially, the TMS systems will operate from the space shuttle and move satellites between the shuttle and higher orbits. Later, the TMS systems will be based with space stations where basic repairs can be performed at distant orbital work sites.

As a member of the NASA-ASEE Summer Faculty Fellowship Program for 1982 and 1983 it was my task to investigate (1), identify (1) and develop a means of providing millimeter detection capabilities for the radar system. The procedure under investigation involves a digital signal processor that converts incoming analog waveforms (radar echoes) into their frequency spectra. From the spectrum attempts will be made to identify and correlate spectral characteristics such as, amplitude, phase or frequency shifts with accurate ($\pm$ 0.5 millimeters) range determinations. Because of the limited time of the fellowship program and the long procurement times for the necessary electronics and support items, attention was focused to only the design and hardware development of the input (sample and storage) circuitry to the digital processor. Thus, this paper will present a discussion on the overall digital signal processing system under study and on the input circuitry to that system.

OBJECTIVES

The objectives guiding the scope of this research effort are:

1. To investigate a digital signal processing system for accurate range determinations.

2. To develop the input circuitry to that system.

DIGITAL SIGNAL PROCESSING SYSTEM

The Proposed System

Referring to Figure 1, the proposed digital signal processing system will be interfaced to the short range radar system after the Automatic Gain Control (AGC) circuit. The system will utilize an Analog to Digital converter (ADC) for sampling and converting the analog signal from the AGC circuit (analog waveform of 0.0 volts to 5.0 volts) to 16-bit digital words (two bytes) for RAM storage, data manipulations, and computations. The freqneucy of the analog signal will be between 0.0 and 40 KH_Z for target distances from 0.0 to 30.0 meters, respectively. Thus, for a digital representation of the analog signal, the Nyquist frequency will be 80.0 KH_Z for a minimum ADC sampling rate of 12.5 μ sec. To remove unwanted high frequency components and enhance certain frequency bands the data will be retrieved from RAM storage and digitally filtered using Large Scale Integration (LSI) signal processing circuits. A biquadratic routine stored in RAM within the chip will perform the required filtering (2,3). Filter coefficients, cut off and reject frequencies, and other filter parameters will be input to the digital filter chip (DF) by the software control program of the 16-bit microcomputer. For conversion to a frequency spectrum, the filtered data will be processed by a Fast Fourier Transform chip (FFT). The chip, in conjunction with a microprocessor, will calculate up to a 1024 point complex FFT using internally generated coefficients in single or multiple passes. Analysis and identification of spectral characteristics for accurate range determinations will be made by microcomputer computations. System operations and computations, including chip routines, will also be under the control of a 16-bit microcomputer.

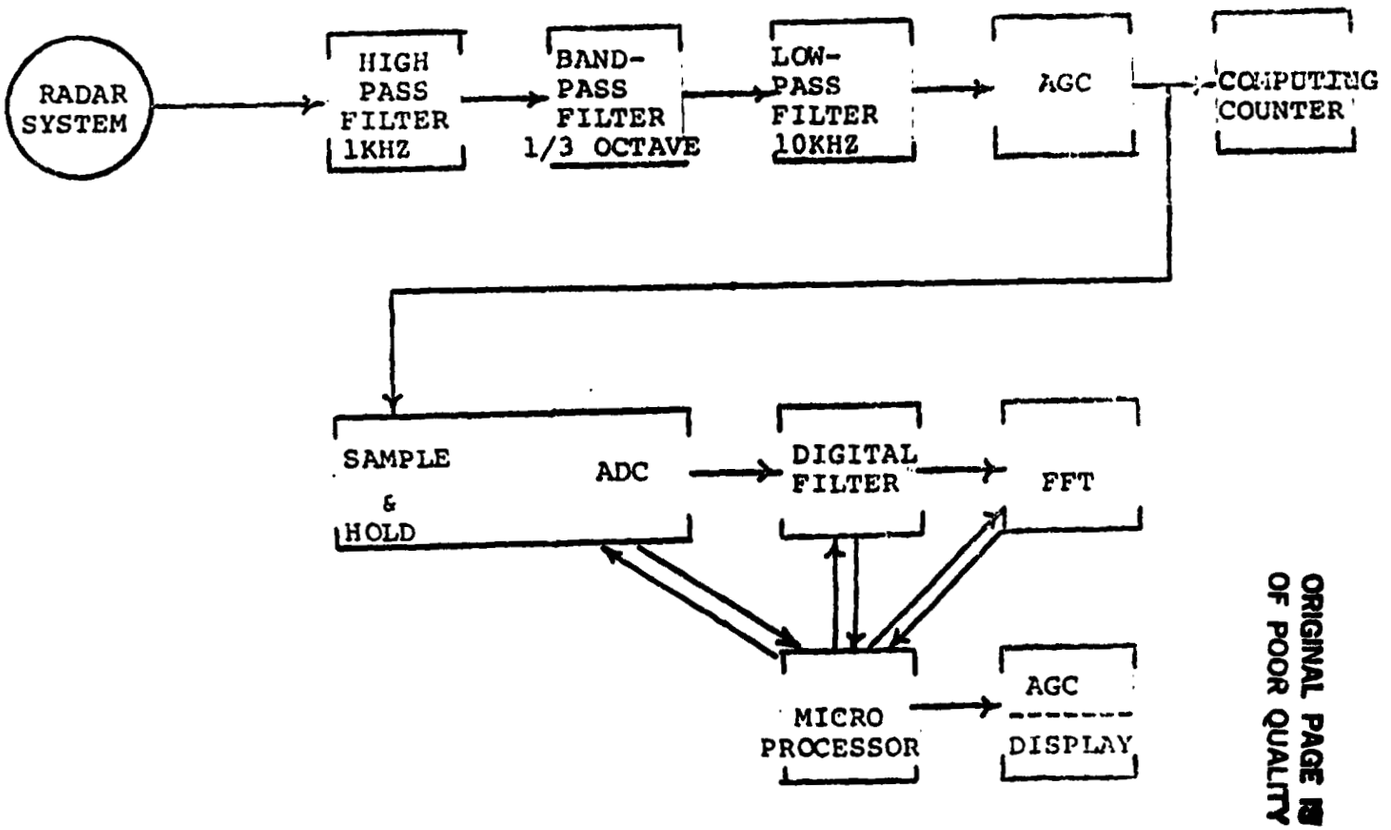

Figure 1. Digital signal processing system.

Input Circuitry to the System

Figures 2a and 2b illustrate the input (sampling and storage) circuitry to the digital signal processing system (Figure 1). The circuit utilizes twenty-one LSI chips and will operate as a stand-alone system in two modes: writing data to the RAM; sending data to the DAC (digital to analog converter). The stand-alone modes will allow other portions of the digital processing system (to be developed later) to perform functions independently of the input. The system will be activated by a positive signal (start pulse) or by a single-pole double-throw switch (SW) located within the "Start Conversion" portion (Figure 2b) of the circuit. Activation by a positive signal will be generated by a microprocessor. The following section will present a discussion at the chip level, on the operations of this circuit.

I. Writing Data to RAM

Referring to Figure 2b, to initiate sampling of the analog signal from the AGC circuit, the system will be activated by a start pulse from a microprocessor or by a switch within the "Start Conversion" portion of the circuit. Referring to Figures 2a and 2b, this pulse will not only activate all B nodes within the circuit, but also the A nodes and node 34 (the output line 34) to the ADC. Referring to the figures, the B and A will disable the LS 245 transmission dates, enable the LS 244 transmission gates (to the RAM) and the S 4016 RAM chips. The start pulse will also reset the CD4040 counting (address) chip (pin 11). The output of node 34 will be input to the ADC 1131 analog to digital converter (pin 34). This input signal will activate the sampling and converting action of the ADC. The ADC will sample the analog signal from the AGC and convert each sample into a 14-bit word. Each word will be transmitted to RAM and stored as a 16-bit word. The address for each word will be assigned by the CD4040 counting chip. After each address assignment, the CD4040 counter will be incremented by one (pin 10) by a signal generated by the ADC (pin 33). For repeating the sampling and storage process, this signal will also be input to the LS 123 one-shot chip (Figure 2b).

This process will be repeated until the CD4040 counter reaches 2000 (the 2k RAM is filled). At this time a signal will be sent from the CD4040 (pin 1) to the LS74 (pin 1) D-flip-flop. The LS74 will complement the input signal (pin 1). The complement will be sent through a NOR gate to another LS 123 one-shot which will disable line 34. The ADC is also

ORIGINAL PAGE IS
OF POOR QUALITY

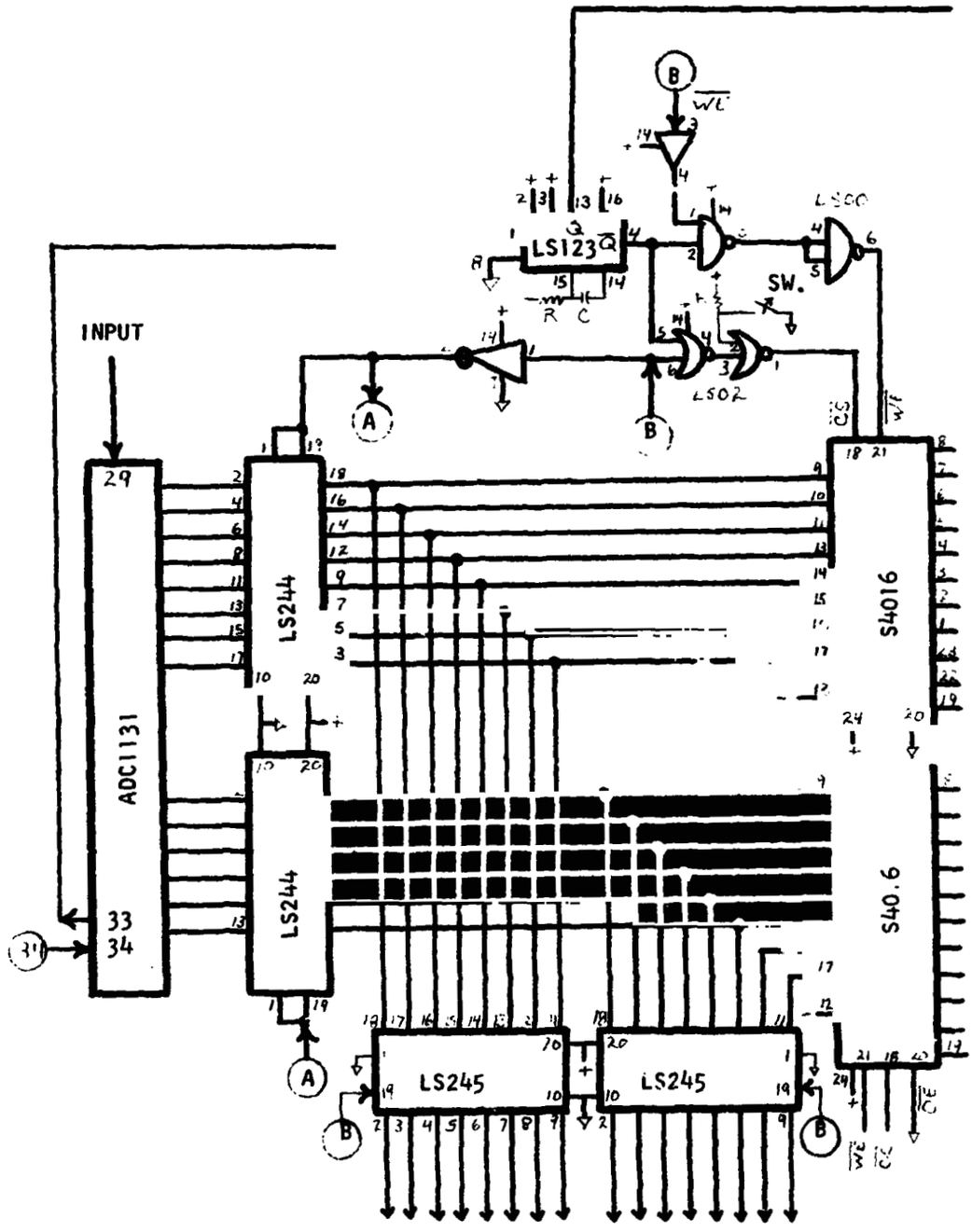

Figure 2a. Sample and storage circuit.

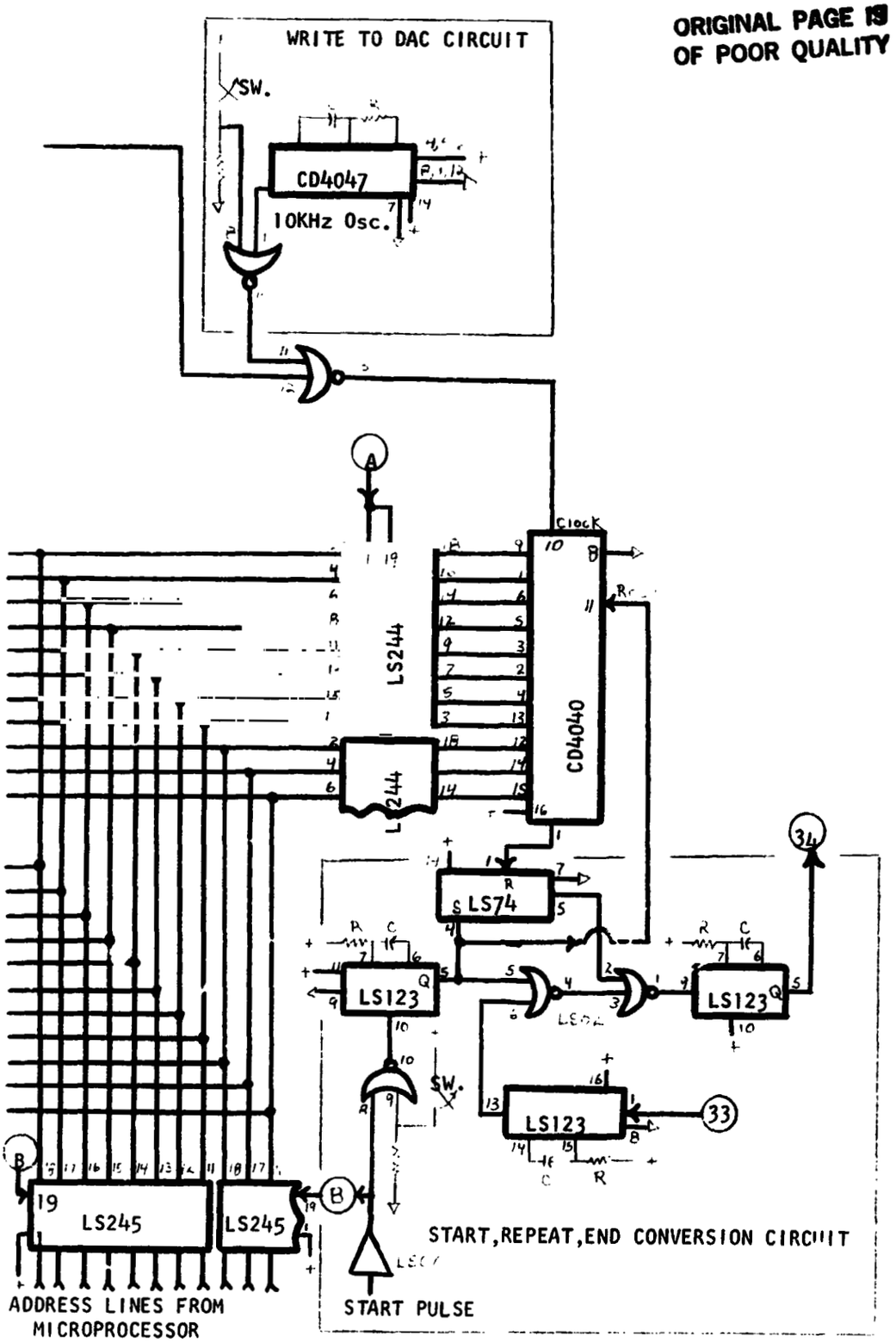

Figure 2b. Sample and storage circuit.

disabled and the process is completed. The data stored in RAM is ready to be read (by the microprocessor) for data manipulations, and computations.

II. Reading Data from RAM

Once the above procedure is completed, a microprocessor will address and read the stored data. To execute the read procedure, a low pulse is sent as a start pulse. The RAM is enabled by this low pulse to all B nodes. Referring to Figure 2a and 2b, in terms of disabling and enabling LSI chips, the reverse process of gating (Section I) will occur. With the LS 245's enabled, the microprocessor will address the S 4016 RAM chips for reading of the data. This process will be repeated as many times as necessary.

III. Writing to the DAC

This mode of operation will be used for debugging the system. In this mode the data stored in RAM will be written to the DAC (not shown) and compared to input signals from the AGC. If the circuit is functioning properly, both signals should compare almost identically. The activate writing to the DAC, the circuit will be activated by a positive start pulse. This will place the circuit chips in their proper mode of operations (similar to Section I above). Activating the switch located in the "Write to DAC" portion of the circuit will enable the CD4047, 10 KH_z oscillator and the CD4040 counter. The counter will address the S 4016 and write the data to the DAC at a continuous 10 KH_z rate.

The data will be displayed and compared as desired by the user. Opening the switch will disable the system.

SUMMARY AND CONCLUSION

This paper presented a discussion on the proposed digital signal processing system, and on the hardware associated with the input portion to that system. Because of the lack of time, the hardware and software development phases for the overall system was not completed. Because of the many technical areas involved (hardware, software, microcomputers, etc.), it is recommended that such a project be given a year around priority. It is also recommended that the systems software be developed in conjunction with the hardware. Once these phases are completed, then analysis for range determinations can begin.

REFERENCES

1. The Application of Digital Signal Processing Techniques to a Teleoperator Radar System. A. Pujol, NASA/ASEE Faculty Research Publication, Contract N.: NGT-01-002-099, Vol. I, No. XXXIII, pp. 1-16, 1982.

2. Oppenheim, A.V., Schafer, R.W., Digital Signal Processing, Prentice-Hall, Inc., 1975.

3. Rabiner, L.R. Gold, B., Theory and Applications of Digital Signal Processing, Prentice-Hall, Inc., 1975.

1983

NASA/ASEE SUMMER FACULTY RESEARCH FELLOWSHIP PROGRAM

MARSHALL SPACE FLIGHT CENTER
THE UNIVERSITY OF ALABAMA IN HUNTSVILLE

SENSOR CONTROL OF ROBOT ARC WELDING

Prepared by:	Fred R. Sias, Jr., Ph.D.
Academic Rank:	Associate Professor
University and Department:	Clemson University Electrical and Computer Engr.
NASA/MSFC:	
Division:	Process Engineering Division
Branch:	Metals Processing Branch, EH-42
MSFC Counterpart:	Arthur C. Nunes, Jr., Ph.D.
Date:	July 29, 1983
Contract No.:	NGT 01-008-021 The University of Alabama in Huntsville

SENSOR CONTROL OF ROBOT ARC WELDING

Abstract

Acknowledgements

1.0 Introduction
1.1 Robot Welding
1.2 Special Constraints of SSME Welding

2.0 Objectives
2.1 Problem Statement
2.2 Justification of Robot Arc Welding Control
2.3 Weld Quality Control

3.0 Controllable Parameters
3.1 Weld Axis Location
3.2 What the Human Welder Does
3.3 Torch Control

4.0 Use of Industrial Robots for Welding
4.1 Robot Types
4.2 Robot Controllability
4.3 Factors associated with Vendors
4.5 Constraints due to Production Procedures

5.0 Approaches to Sensor Control
5.1 Sensory Systems for Arc-welding Control
5.2 Limits to Sensor Capability
5.3 System Hardening
5.4 Future Possibilities

6.0 Robot Vision
6.1 Source Materials
6.2 General Terminology and Background
6.3 Visual Functions for Robotics
6.4 Image Processing Methods
6.5 State-of-the-Art

7.0 A Survey of Robot Vision Systems

8.0 A Survey of Robot GTAW Systems

9.0 Conclusions and Recommendations

10.0 References

APPENDIX

A. Vendors Marketing Computer Vision Systems

B. Vendors Offering Seam-welding Systems

ABSTRACT

SENSOR CONTROL OF ROBOT ARC WELDING

A basic problem in the application of robots for gas-tungsten arc welding (GTAW) is how to guide an arc-welding torch along a weld seam using sensory information. This study is an analysis of the potential for using computer vision as sensory feedback for robot arc welding. The primary motivation for this study is the proposal to automate some of the welds that are currently hand operations on the Space Shuttle Main Engine (SSME). Factors that complicate the automation of many of the welds that are currently performed manually include difficult access, poor fitup, material movement during the weld, complex shapes, and the fact that there are a large number of small welds.

This study examines the basic parameters that must be controlled while directing the movement of an arc-welding torch. The actions of a human welder are examined to aid in determining the sensory information that would permit a robot to make reproducible high-strength welds. Special constraints imposed by both robot hardware and software are considered.

Several sensory modalities that will potentially improve weld quality are examined Special emphasis is directed to the use of computer vision for controlling gas-tungsten arc welding. Vendors of available automated seam-tracking arc-welding systems and of computer vision systems are surveyed. An assessment is made of the state-of-the-art and the problems that must be solved in order to apply computer vision to robot-controlled arc welding on the Space Shuttle Main Engine.

ACKNOWLEDGEMENTS

My summer experience at the Marshall Space Flight Center has added greatly to my understanding of robotics and especially arc welding. Many persons have contributed to that understanding and have provided both background material and technical details that are included in this report. Among those most responsible for my education are Mr. Bill Wilson, Mr. Clyde Jones, III, Ms. Lisa Hawkins, Mr. Joe Sexton, Mr. Ernie Bayless, Mr. Sam Clark, Mr. Jeff Norris, and, of course, my NASA counterpart Dr. Arthur C. Nunes, Jr. Ms. Vanita Brown has been of great assistance in preparing this report.

While many persons have contributed to the factual material in this report, the opinions expressed are those of the author.

1.0 INTRODUCTION

1.1 ROBOT WELDING:

The use of robots for automated welding is a subject that has received much attention. Several manufacturers offer total or partial systems that are called "seam trackers" that locate a weld axis by mechanical or computer vision systems. Such systems are known as one or two-pass systems depending on whether the seam location is determined before or during the actual welding motion by the robot.

Currently existing systems vary in the ability to locate a weld axis; some systems require special joint preparation in order to reliably follow a joint that is to be welded. Mechanical seam trackers require that a seam has a mechanically discernible groove and two passes may be required to locate and then complete the weld. Scratches, oxidized or rusty work, pencil marks, stains, etc. all interfere with the ability of a visual curve tracker to follow a given weld seam. Other sensory modalities, such as ultrasonic seam detectors, are being studied.

This report addresses the basic problem of using sensory information to control arc welding by a robot. There are no inherent constraints on the sensory modality that may be considered. In particular, this report is to provide background information for selecting a robot welding system for use in automating welds that are currently made manually on the Space Shuttle Main Engine (SSME).

1.2 SPECIAL CONSTRAINTS OF SSME WELDING

A primary purpose of this study is to investigate the potential for automating some of the welds that are currently hand operations on the Space Shuttle Main Engine (SSME). Currently, about one third of the 10,000 inches of welding on the SSME are performed manually. Manual welding as opposed to automated welding, is performed due to several factors. These factors include the following:

1. Difficult access.
2. Poor fitup.
3. Material movement during weld.
4. Complex shapes.
5. Large number of small welds.

Robot control of welding on the SSME is proposed to automate at least some of the welds that are currently performed manually. To provide a significant increase in the number of welds that may be automated, a robotic welding system must be able to follow complex weld shapes in tight, almost inaccessible locations. This places a serious constraint on the following components of the robotic system:

1. Torch shape.
2. Torch size.
3. Feed mechanism for filler wire.
4. Hardware for the seam tracker.
5. Illumination system for imaging equipment.
6. Size of the AVC effector.
7. Controllability of the robot wrist assembly.

Each of the above constraints will be examined in more detail to illustrate the effect on overall system design.

Torch shape: Difficult access to components of the SSME suggests that TIG torch shape will be a factor in the design of a system automated with a general-purpose industrial robot. Manual torches are available with the head set at various angles to the torch body. In addition, flex-head torches may be used where the angle of the head can be set at any convenient position. Some of the welds on the SSME had to be performed using a mirror for visual control of the torch. The flexibility that is possible when using a manual torch will probably be limited in a robot-controlled environment. It is likely that a straight-line torch will not be usable in all weld locations on the SSME.

Torch size: Manual torches are often smaller than torches attached to automated welding equipment. Limited access to many of the welds on the SSME will place a severe constraint on the size of the torch that can be used.

Feed mechanism for filler wire: Automated welding systems require the use of a filler-wire feed mechanism. Usually the reel of filler wire is positioned remotely from the welding torch, a mechanism for advancing the wire is located closer to the torch head, and, finally, a wire guide is located very close to the torch head. The wire advancing mechanism can probably be located at a sufficiently remote position; however, the wire guide located close to the torch head may interfere with both mechanical and visual access to the weld. Visual access will be discussed further in the next paragraph. It is likely that standard wire guides will interfere; however, special wire guides can probably be constructed to route feedwire in such a way as to minimize mechanical and visual interference.

Hardware for seam tracker: Automated welding using a general- purpose industrial robot presupposes that some form

of seam-tracking control system will be used. Some welds can be accomplished using only the robot "teach" mode to program the weld path. However, most SSME welds will require some sort of seam tracking since fitup and warpage will prevent the utilization of a completely pre-programmed weld seam axis. In addition, SSME construction involves a large number of small discrete welds that would be very difficult to preprogram accurately. Any form of seam tracker will occupy physical space in the vicinity of the welding torch.

Optical access is required in order to use any form of optical seam tracker that utilizes a video camera to input data. The simplest optical arrangement is to use a coherent fiber-optic bundle to transmit an image from a location in close proximity to the welding torch head to the video camera. Conventional optics and fiberoptic bundles have been installed coaxially with torches to control seam tracking in systems developed at Ohio State University and the General Electric Company. This works well when installed within an in-line torch; however, the optical system will have to be reconsidered to permit a coaxial optical pathway if the torch head is installed at an angle to the torch body. An optical system installed external to the torch will have to be compact in order to not limit access to tight locations on the SSME.

Illumination system for imaging equipment: Optical seam trackers have been developed that function using both externally supplied illumination and inherent illumination provided by the welding arc itself. External illumination is usually "structured". That is, a high intensity collimated source such as a laser is configured to project a stripe on the weld joint. The use of structured light simplifies the image analysis problem when locating the seam axis. Structured light may also be used to determine the shape of the work and to measure distance. In these cases the light source is generally set up to project a stripe on the work at an angle. Under any circumstance, the use of a non-coaxial light source will increase the utilization of space immediately adjacent to the torch head and, in some cases, may require a clear view of the work from some specific angle. The use of fiber optics may provide a solution to many design configurations; however, the overall lack of space in the immediate vicinity of the torch head should be kept in mind.

Size of AVC effector: Automatic voltage control is generally achieved in arc welding by moving the torch head in and out relative to the work surface using a special feed mechanism. The drive mechanism is generally coaxial with an inline torch head. Such a configuration is probably not acceptable for many of the complicated welds on the SSME. Often there will be insufficient space for a conventional AVC drive system. Utilization of a welding torch with an angled head will preclude the use of any standard AVC drive mechanism designed to be used with a straight torch. It is likely that any AVC

drive mechanism designed to operate at an angle will be impractical and that AVC corrections must be applied by modifying the preprogrammed path of the robot.

Controllability of robot wrist assembly: Industrial robots capable of motion with six or more degrees of freedom are capable of "reaching" into tight areas if the welding torch and associated equipment are sufficiently compact. However, factors other than merely accessing the weld location are important. For example, it is necessary to hold the torch head at some controlled angle relative to the work surface and joint axis. This is complicated while tracking a complex joint. A simple "cross slide" to compensate for tracking error is probably not possible. Also a separate drive normal to the work surface for Automatic Voltage Control (AVC) is probably not acceptable due to the space limitation on the SSME. AVC and seam tracking adjustments will probably have to be made by modifying the preprogrammed path of the robot. The ease by which this can be done will vary with robots and software supplied by various vendors. In some cases it may be very difficult to obtain access tc proprietary software to permit input of AVC and seam tracking corrections.

2.0 OBJECTIVES

2.1 PROBLEM STATEMENT:

The primary purpose of this study is to investigate the use of sensory information to direct and control arc welding robots. Any sensory modality will be considered that potentially will aid in producing high-quality automated welds.

While not limited to computer vision, this study will concentrate on the use of visual information, in combination with other information such as arc voltage and current, to guide and regulate a robot arc welder used to weld large and small complex shapes and structures. The emphasis will be on techniques that will contribute to improving the consistency of welds that are currently made manually on the Space Shuttle Main Engine.

Primary consideration will be given to techniques that will function with Gas Shielded Tungsten Arc Welding systems manipulated by a general-purpose industrial robot.

The overall problem of controlling weld quality may be subdivided as follows:

1. How to orient and align the arc welding torch with the weld axis.

2. How to control the torch movement when following complex shapes.

3. How to control the height of the torch above the work.

4. How to contro. weld penetration.

5. How to direct a weld passing over a previously placed tack weld.

6. How to provide reliable control when the visual image of the weld seam is degraded by smoke.

7. How to provide reliable control when the seam is to be a butt weld with tight initial fitup.

8. How to couple additional sensory feedback with a robot control system.

9. How to insure that a system will operate in an electrically noisy environment.

Special considerations presented by application to the Space

Shuttle Main Engine include the following: thin materials, complicated and short radius shapes, difficult access, variable fitup, and movement of the metal during the welding operation. Most welds are Gas Tungsten Arc Welds (GTAW) on Inconel* 718 alloy.

2.2 JUSTIFICATION OF ROBOT ARC WELDING CONTROL:

Robots are often justified as a labor-saving device that is cost effective. Improved product consistency and improved quality are less often cited as a justification for robot aided manufacturing.

About 60 percent of 10,000 inches of welding are performed manually on the Space Shuttle Main Engine. A higher percentage of manual welds require rework than welds that are currently automated. Thus it is concluded that additional automatation using industrial robots will improve weld consistency and minimize reworking.

In an ideal situation, weld consistency may be improved to the extent that quality assurance using expensive and time-consuming radiographic methods can be reduced.

2.3 WELD QUALITY CONTROL:

The term weld quality could have a number of different meanings; however, most meanings are ultimately related to the strength of the weld. Since weld strength can only be determined by destructive testing, weld quality is usually related to non-destructive radiographic examination. This is the meaning that will be implied here.

Weld quality is a function of many factors ranging from material choice to welding technique. Welding technique is a factor that could be modified by the use of robots to minimize welding discontinuities that, in turn, may be sufficient to produce a weld defect that would cause weldment rejection or repair. Defective welds on the SSME must be reworked since the engine assembly is sufficiently expensive to not permit part rejection.

Weld defects have been classified by Cary (1979) as follows:

Series 100 Cracks
Series 200 Cavities
Series 300 Solid Inclusions
Series 400 Incomplete fusion or penetration
Series 500 Imperfect shape or unacceptable contour
Series 600 Miscellaneous defects not included above

*Inconel is a registered trademark of Huntington Alloys, Inc.

Series 100, 400, and 500 defects may be related to welding technique that could be improved by more consistent torch control using a robot and other forms of automatic feedback control.

Once appropriate welding schedules have been developed for arc welding, weld quality is related to the following factors:

1. Arc length.
2. Welding current.
3. Torch travel speed.
4. Torch angle.
5. Shielding-gas coverage.

Of these factors, shielding gas coverage is generally fixed for a given torch and cup size. However, the other factors may be variable and are important from the standpoint of robot controlled welding.

Theoretically, arc length is a constant for a given weld schedule and is maintained by an automatic voltage control system (AVC). From a practical standpoint, however, arc voltage may be adjusted somewhat to maintain proper torch distance above the work under conditions when penetration is incorrect. Once set with a given set of conditions, the AVC maintains a fixed voltage and consequently a fixed arc length within tolerance.

Torch angle related to the work and torch travel speed are likely to be fixed for a given weld schedule when using a robot-directed torch. Torch travel speed would not be simple to modify during a weld on most industrial robots; therefore, heat input to the work must be controlled by varying the welding current.

From this discussion it should be evident that a robot is basically a machine for producing a controlled movement. When used to direct an arc welding torch a robot must be able to precisely control arc length, travel speed and travel angle. These factors are easy to control when simple paths are under robot control since the usual industrial robot is programmed to move in straight lines, paths of constant radius, or in paths with constant tool orientation. These usual robot control modalities may not be adequate for many welds that are currently performed by hand on the SSME.

It is likely that the production of high strength weldments on the SSME will require special modification of robot-control software. Probably all of the above factors that determine weld quality or strength can be controlled using various forms of sensory feedback to a robot control system. For example, some sort of depth perception is necessary to maintain proper arc length. Automatic voltage control is usually used for this purpose, however, the torch-work standoff distance could

be measured directly using visual, ultrasonic, capacitative or tactile sensors. In order to control torch angle, the line perpendicular to the weld axis must be determined and similar sensors may be suitable. To control the weld path the joint position must be sensed. In addition, the weld axis direction must be determined to project the path of movement ahead of the torch when welding irregular shapes. Tactile and simple visual seam trackers have been used when special joint preparation is acceptable; however, seam tracking on unmodified butt joints will require exceptional visual processing. Visual perception may provide an optimum means of detecting tack welds and projecting the best path past the tack weld.

Heat input to the work must be properly controlled to maintain a correct weld penetration. Certain weld pool mechanical characteristics have been examined to determine proper penetration. However, the penetration is most likely to be a function of puddle diameter in the absence of any significant heat sinks along the weld path. Puddle diameter is controlled visually by the human welder and a robot welding system can use the same visual feedback information if torch stand-off distance is maintained constant using an independent AVC feedback controller. Infra-red viewers and scanners are theoretical alternatives to visible-light sensors.

3.0 CONTROLLABLE PARAMETERS

3.1 WELD AXIS LOCATION:

The ultimate purpose of any welding system is the production of high-quality welds. Since weld quality, per se, is not a measurable quantity at the time of the weld, all automatic welding systems must base control on correlated measurables. A single primary measurable parameter is always the position of the welding torch relative to the centerline or axis of the weld joint. Irrespective of all other possible control parameters, it is necessary to know the position of the joint centerline within some tolerance.

Determining a weld centerline seems like a simple problem; however, the introduction of automated machinery introduces additional complexity. First, some sort of machine perception is required to locate the weld axis. Then it is necessary to position a torch relative to the perceived weld axis. Both processes are subject to errors that we shall call positional error, Ep, and control error, Ec. The maximum error in locating a tool relative to the true weld centerline is therefore expressed as follows:

$$Emax = Ep + Ec \qquad 3.1$$

In other words, the final error in weld position is determined by the accuracy with which the actual weld centerline is known p'us or minus the error introduced by an automated positional control system. The maximum error in welding tool location is sum of the two individual errors.

Allowable positional error: The above discussion defines positional error in terms of the hardware used for automated welding. However, weld quality must be related to the weld displacement relative to the true weld axis. We will define this as allowable error, Ea, which, in turn, must always be less than or equal to Emax.

For any given weld, Ea, or allowable error, is a function of the weld geometry. If one assumes a butt weld such as shown in Figure 3.1, the allowable error may be specified in terms of root width. If one defines the butt weld gap as S, the maximum allowable displacement in the true position of the weld is one-half the root width minus S. Such a displacement will just match the edge of the weld seam with one edge of the original butt gap. This is expressed in the equation:

$$Ea = (RW/2) - S \qquad 3.2$$

The maximum error introduced by the automated welding system

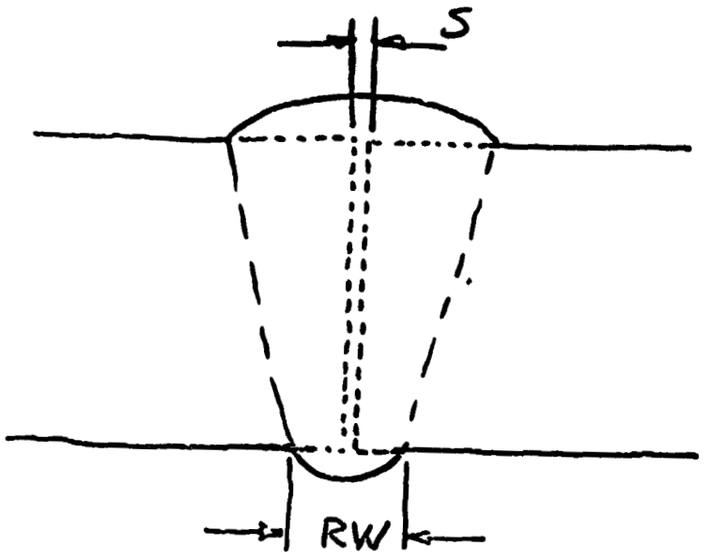

RW = root width

S = butt weld gap.

Figure 3.1 Parameters for calculating Allowable positional error.

must be equal to or less than the allowable error; therefore we may combine the above equations as follows:

$$Emax = Ep + Ec = (RW/2) - S \qquad 3.3$$

This equation defines the upper limit for errors introduced by an automated welding system in terms of the weld geometry. Normally, one might introduce an additional safety factor to allow for statistical variations in control parameters.

From the previous discussion it is evident that positional error is a function of any sensor that is used to locate a weld axis and control error is a function of a robot or weld tooling control system used to position a welding torch.

If one proposes any automated welding system, the centerline of the weld may be defined in one of two ways: either in a coordinate system relative to the torch position or in some absolute or global coordinate system (e.g., relative to the robot base). One could theoretically produce a weld knowing only the weld axis relative to any current torch position. One merely moves the torch to a new position corresponding to the true weld axis. Of course, this is a mode of operation of some seam trackers.

Absolute weld position may be expressed by the equation of a line in some global coordinate system such as rectangular coordinates referred to the base of a robot, for example. Relative weld position is theoretically the only information required by a seam-tracker welding control system; however, from a practical standpoint, at least a starting point in global coordinates is required to initially position a welding torch.

On the other hand, an accurate knowledge of the equation of a weld seam in some global coordinate system would be very effective in guiding a robot if the work is precisely fixed. However, warping or shifting of the work would effectively defeat any welding control system based on absolute weld position sensing only. Some combination of absolute and relative sensing of a weld axis would appear to be important for optimal control of an automated welding system.

On the basis of the discussion in this section, we may conclude that robotic control of arc welding requires a control system that is able to position a welding torch on a weld axis in both relative and absolute terms. The maximum positional error is the sum of the errors introduced by both the system for perceiving the weld axis and the control system that positions the welding torch. The maximum permissible error has been defined in terms of the weld geometry.

3.2 WHAT THE WELDING OPERATOR DOES:

A welding operator is readily able to provide both initial torch positioning and relative positional control in manual welding. Relative positional information is seldom provided alone. The human controller is able to track a weld more easily if the direction or curvature of a weld seam is known. We might assume a similar improvement in performance in an automated system where complex shapes and edges are to be welded.

If one watches a welding operator prior to the start of the weld, it becomes apparent that a number of processes are going on. First, the work piece is positioned at some convenient location. If the work cannot be moved, the operator must position himself relative to the work. We may observe a person adjust his position once or twice and wonder just what was wrong with the first position.

Analysis of the initial set-up process of a welding operator suggests several problems. Initially, he seems to position his hands and body in such a way that his movements are "natural" in some as yet undefined way. Hand movement, once the weld is started, must be in a direction that is comfortable for the human operator. He must not start a movement that will end up requiring an impossible range of motion for some bodily joint. He must position his arms and hands to avoid obstacles that could interfere with arm movement.

Exactly the same considerations must be addressed when initially positioning a welding robot as described above for the human operator. The weld torch must be oriented relative to the "direction" of the weld axis. If one is welding around the circumferance of a right-circular cylinder, knowledge of the axis of the cylinder will probably improve the robots ability to track the weld seam. Information of this sort must be provided a priori by a human being or some sort of global perception or scene analysis must take place. At a minimum, the torch must be placed normal to the work (or at a specific angle relative to normal). The direction of the weld axis must be perceived and obstacles in the work area must be located.

Global scene analysis can be visual, tactile, or a combination of visual and tactile information. For example, the line normal to the starting point of the weld might be determined with a tactile sensor. Starting coordinates and weld axis direction could be provided by a scene analysis computer vision system. Irregularly shaped seams would greatly increase the complexity of the scene analysis phase of robot welding.

Earlier it was suggested that a tactile sens might provide

an indication of the line normal to the plane of the weld. The human welder obtains this information visually to a major extent and one might expect computer vision sensors could provide this information as well.

As a first step, therefore, one might expect a robot arc welding system to visually survey a welding "scene" and extract information needed for initial orientation and guidance of the robot and welding torch. Once a weld is initiated, a seam tracker would take over control. The initial overall scene analysis phase might also be used to locate tack welds and obstacles much in the same way as done by a human welder. This information could over-ride or modify the seam-tracker control when necessary.

The last few paragraphs have been written to provide some overall guidance in selecting the types of sensory information that is required to successfully apply a robot-controlled arc welding system to the manufacture of the SSME. Current systems do not provide all of these capabilities and it is likely that deficiencies will become evident based on the type of problems outlined here.

3.3 TORCH CONTROL:

For convenience, we have classified all control parameters other than weld axis location as "torch control." Included are the following:

1. Torch attitude or torch angle.
2. Arc length.
3. Arc voltage.
4. Arc current including polarity and pulse control.
5. Travel speed.
6. Shielding and/or arc gas control.

Once an arc welding torch has been located over the axis of a weld, several process parameters affect the final weld strength. "Weld parameters" as used here has the same meaning as "weld variables" used in some handbooks (Cary, 1979). The power or heat input to the work is a function of voltage and current. Voltage is, in turn, a function of electrode work spacing and possibly shield gas flow. In addition, arc voltage, welding current, and travel speed all affect bead width, bead height, penetration and, consequently, weld strength. With several factors interacting to affect weld quality, most parameters are held constant during automated

welding as specified by a welding program or schedule. Current is regulated to produce a desired heat input. Travel speed, torch angle, and shield-gas flow are generally fixed for a given weld.

A welding operator may control power input by first setting an approximate current and then by adjusting arc length (voltage), torch movement speed, and/or torch angle to maintain puddle size visually. Puddle size is a measure of power input to the work; however, variable losses such as due to heat sinks along the weld path, may be compensated for by controlling puddle size and/or travel speed.

The choice of weld parameters to regulate therefore becomes the primary problem in designing a robot controlled arc-welding system. The whole problem of selecting the proper control variables will be examined in detail in Section 4 of this report.

4.0 USE OF INDUSTRIAL ROBOTS FOR WELDING

4.1 ROBOT TYPES:

The use of robots for arc welding is not new. In fact a number of systems are available on the market. Most are Gas-Metal Arc Welding (GMAW, sometimes called MIG) although examples of Gas-Tungsten Arc Welding (GTAW, sometimes called TIG) are reported in the literature. (Gutow and Richardson, 1983) Many characteristics of GMAW are similar to GTAW except that Tungsten Arc systems frequently use high-frequency arc-starting methods that interfere with robot control unless exceptional shielding precautions are taken. Plasma Arc and Variable Polarity Plasma Arc (VPPA) welding systems also place constraints on the robot control systems.

Industrial robots are hydraulically controlled or electrically controlled. Hydraulically controlled robots use a fluid for power transmission to actuators and are inherently somewhat more immune to interference from high-frequency arc starting noise than are electrically powered robots that utilize high-power electrical servo motors to drive robot elements. All robots, except for a few low-power stepper-motor driven teaching robots, utilize closed-loop servo systems to control motion in each degree of freedom.

Robots may be further classified relative to the type of motion that is inherent to the basic kinematics. Four types (shown in Figure 4.1) are commonly described:

1. Rectangular or Cartesian coordinate robots.
2. Cylindrical coordinate robots.
3. Spherical or Polar coordinate robots.
4. Articulated or Revolute coordinate robots.

Each axis of movement or joint is called a "degree of freedom." Only three degrees of freedom are required to locate a point in space; however, industrial robots typically have four or more degrees of freedom in order to control orientation of an end effector that is often called a hand or, more generally, a tool. Tool orientation is often very important in robot utilization, therefore, six degrees of freedom are common and research utilizing additional degrees of freedom has been reported (Hayafusa, 1981) using additional degrees of freedom for obstacle avoidance. Redundant degrees of freedom may be necessary for robot welding on the SSME due to the difficult accessability of some welds.

Figure 4.1

Basic Manipulator Geometries

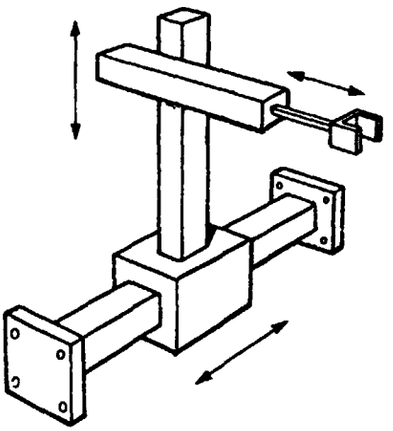

Rectangular
(Cartesian Coordinates)

a.

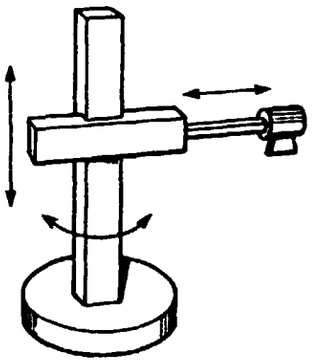

Cylindrical Coordinates

b.

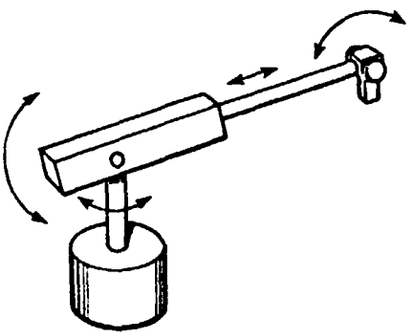

Spherical
(Polar Coordinates)

c.

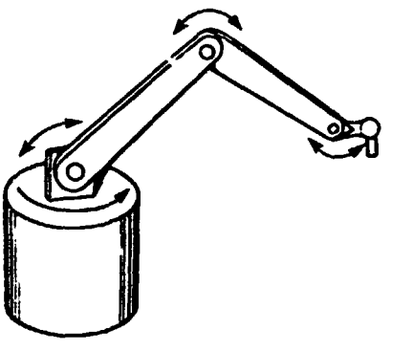

Articulated or Jointed Spherical
(Revolute Coordinates)

d.

From Gevarter, 1982.

Robots of each configuration have been used for welding. In particular, welding booms that have been used in the aerospace industry for many years have the basic cylindrical coordinate manipulator geometry. If each axis is automatically controlled using position-sensing feedback the system would meet the technical definition of a robot. In addition, welding systems may also include a separate work positioner that could be coordinated with the welding boom to provide the additional degrees of freedom that are required for weld orientation.

The choice of robot geometry may be influenced somewhat by the geometry of an object to be welded. Since weldments frequently are either rectangular or right-circular cylinders, it is not surprising that many special purpose and general purpose welding tools have geometries that correspond to the basic rectangular and cylindrical manipulator geometries. Welding tools that are specifically called robots may be constructed using commercially-available industrial robots with the appropriate manipulator geometry. Usually each axis of the robot would be placed to correspond to an axis of the work. A work positioner would be used to adjust the work for proper axis orientation. However, such systems would be somewhat special purpose in that a given system might not be able to accommodate all weldment geometries.

Robots with spherical or articulated manipulator geometries could be utilized for welding by controlling motion with appropriate computer software. Control software typically will move an articulated robot along straight or circular paths with controlled tool orientation irrespective of the natural axes of the system. Since the control software is more complicated and may be proprietary, coupling external control hardware to an articulated robot may be more difficult than using a rectangular or cylindrical coordinate robot. Varying dynamic loads makes the coordination of motion using an articulated robot a distinctly more complicated problem.

4.2 ROBOT CONTROLLABILITY:

The modern industrial robot is an outgrowth of two preceding technologies that evolved in the late 1940's: (1) numerically controlled machine tools and (2) teleoperators. The teleoperator was developed in the nuclear industry to enable an operator to remotely control a pair of tongs (or a gripper) used to manipulate radioactive objects. The numerically-controlled milling machine was developed to control the machining of aircraft parts. In both cases the control problem was to position an end effector or tool. The industrial robot does much the same thing except that various forms of automatic feedback must be incorporated to inable the robot to perform acceptably in a dynamic as well as positional sense.

Conceptually, the problem of controlling a robot is simple; however, as in many engineering problems, the practical application of theory is difficult and an analytical solution of actual robot control equations may be analytically impossible. Numerical solutions of robot control equations are unique for each robot design and are complicated.

The mathematics of robot control is presented in detail in "Robot Manipulators" by Richard P. Paul. (Paul, 1981) The following discussion is based on this work. The general-purpose in strial robot involves motion with at least six degrees of freedom. Three degrees of freedom or axes are used to position the tool in space while an additional three degrees of freedom are required to orient the tool.

Any robot consists of a number of linkages that are oriented relative to each other. The relationship between linkages differs depending on the manipulator geometry as discussed earlier. Matrix arithmetic is used to perform all robot control operations and the relationship between two adjacent linkages is represented by what is called the A matrix. Six A matrices are required to represent a robot with six linkages or six degrees of freedom. The equation representing the overall position of a tool relative to the base of a six-link manipulator is given by the following matrix equation:

$$T_6 = A_1 A_2 A_3 A_4 A_5 A_6 \qquad 4.1$$

The usual control problem, however, is to solve for the joint coordinates given T_6 as an input. According to Paul (p66): "We normally know where we want to move the manipulator in terms of T_6 and we need to obtain the joint coordinates in order to make the move. Obtaining a solution for the joint coordinates requires intuition and is the most difficult problem we will encounter."

To obtain a kinematic solution for each joint, equation 4.1 is expanded to 6 matrix transform equations representing the six degrees of freedom of the robot. For each transform equation twelve non-trivial equations are obtained that yield the required solutions. The solutions are different for each manipulator geometry.

The kinematic equations of a robot do not provide a sufficient representation for control. Robot manipulators are complicated dynamic systems that require describing equations that "relate forces and torques to positions, velocities, and accelerations; they are usually solved in order to obtain the equations of motion of the manipulator." (Paul, 1981, p157) In particular, gravitational and inertial forces must be considered.

Once the equations of motion for each joint have been solved (with appropriate simplifications and approximations)

operation is achieved by servo controlling each joint. Appropriate gain and damping along with compensation for coulomb friction and gravity are required. "A multi-link manipulator may be considered a series of inde endent servo systems which are only weakly coupled. ...the outer joints have greater servo bandwidth than the inner joints. ... The feedback gains, and hence the servo bandwidth, are determined by friction and gravity loading effects. ... In order to compensate for gravity loading and to calculate the effective intertia of the joints, the mass and moments of any load the manipulator is carrying must be known." (Paul, 1981, p214)

Most modern robots are computer-controlled sampled-data servos, sometimes with a separate microprocessor dedicated to each link. From the long discussion just presented, it should be evident that control of a robot is achieved by inputting desired positions and velocities to a multi-control-loop servo system. Many robot control systems have a "teach mode" whereby the direction and velocity of each movement is specified. Movement between points is servo controlled to follow a particular path with specified tool orientation. The dynamic profile of the whole path must be calculated in order to coordinate the movement of the several linkages to maintain proper tool orientation. If the specified path is altered by virtue o some dynamically changing process (such as work movement during a weld pass) then a new path must be calculated and all input for each joint servo must be updated.

In the general case, revision of a tool path involves changes in all linkages; however, if one axis of the manipulator is oriented in the plane of path distortion (e.g. the weld plane) and at right angles to the tool path, one might obtain path correction by merely modifying motion in only one coordinate. Seam tracking with a welding robot could thus be achieved by modifying error signals in one axis without recalculating all equations of motion. On the other hand, seam tracking or weave motion applied to a general-purpose six-degrees-of-freedom articulated robot would cause the whole robot arm to weave back and forth. In the case of vendor supplied control software, the appropriate options would have to be available to allow input of separate seam tracking error signals.

Computer simulation techniques may be of some benefit in applying robotic welding methods to SSME manufacture. In particular, simulation may be of aid in developing and proving methods of integrating sensory feedback with kinematic and dynamic equations of motion. This potential should receive further investigation.

4.3 FACTORS ASSOCIATED WITH VENDORS:

As expected, vendors that market robot systems tend

to consider their software proprietary. Therefore, it is usually not possible, without special arrangements, for a user to modify software to perform special tasks such as interacting with sensors. Any modifications that are requested of the robot vendor would, quite naturally, be considered a special option that the vendor may program and feel free to sell to other users. Of course, any other arrangement may be agreed to by contract -- for a price.

The usual industrial robot was developed to move a tool or gripper from point to point at a predetermined velocity. Once a path has been calculated the move usually takes place without interruption unless special features have been built into the software. For example, with one vendor a WEAVE function for welding or gluing is a special option that is provided with certain limited parameter-changing capability. Should it be desirable to modify the weave motion based on sensor input, the vendor would have to be consulted, and an additional special software option purchased.

The appropriate options needed for sensor control of welding are most likely to be available from vendors marketing sensor-based systems. There are several systems on the market that provide special user programming capability. Special robot control languages have been developed that ease the problem of user programming and aid in the ability to incorporate sensory feedback.

It is likely that several marketing approaches are available from different vendors. In addition, some vendors may prefer to market complete turn-key systems rather than pieces that can be put together by the user. With a growth industry like robots, it is likely that vendor marketing strategy will provide an additional variable to be considered in evaluating various proposals. A user with significant in house computer programming capability may wish to procure a system with as much flexibility as possible.

4.4 EFFECT OF WELD COMPLEXITY:

The complexity of a weld contour is an obvious factor controlling the ease with which a robot welding system can follow the proper seam. A straight joint in a single plane would be the easiest contour to follow; a straight joint on a surface of constant radius would also be relatively easy to weld. However, when the contour of a weld becomes complicated either by introducing sharp changes in seam direction or by introducing an irregular change in the weld surface, the ability of a robot to properly track the seam is compromised. A number of systems have been developed permit seam tracking using various sensors and these all function best on uncomplicated seams.

Two factors contribute to poor seam-tracking performance. First, tack welds are often present along a weld seam. In order to properly bypass a tack weld, the tracking system must project the seam direction beyond the tack weld. The human welder is able to visually choose the best path to meet the weld seam beyond the tack weld. Systems with limited optical or mechanical seam trackers would have difficulty following an irregular weld seam. A sophisticated visual seam tracking system capable of choosing the proper path past a tack weld is conceptually possible although further development may be necessary to enhance available systems.

Another factor contributing to poor seam tracking performance is the offset between the reference point for seam tracking and the actual weld puddle. Most seam trackers use either a mechanical probe or optical system to locate the desired weld track up to several centimeters ahead of the weld puddle. This produces a time delay between the sensing of control information and the actual torch control movement. A simple system might assume no sudden shift in seam direction while a system able to follow sharply curving seams would have to "remember" the seam track and guide the welding torch after an appropriate time delay.

The two complicating factors just considered suggest that a sophisticated vision-based seam tracker would have to view a seam well ahead of the actual weld puddle, store data on the shape of the weld seam, and then choose an optimum path around curves and across tack welds.

Still another factor contributing to seam tracking complexity when sharply curving surfaces are welded is the necessity of determining the line normal to the plane tangent to the work surface and seam axis. The normal line must be sensed in order for the torch to be held at a proper angle with the weld. Again, it is easier to develop sensors to determine a line normal to a large flat surface than to surfaces with short and varying radii. Tactile sensors and structured light have been used to provide surface orientation with varying degrees of success.

The presence of data in a Computer-aided Design (CAD) system could greatly simplify the design of a sensory system to aid in robot welding on the SSME. Much of the global information regarding the location of various weld seams could be obtained directly from the design data base and control of the actual welding could be limited to seam tracking to a large extent. This coupling of design and the actual manufacturing process should be investigated further.

4.5 CONSTRAINTS DUE TO PRODUCTION PROCEDURES:

Introduction of robotic welding procedures to replace manual

welding will inevitably impact SSME manufacture by requiring new manufacturing process specifications. The use of a robot could cause changes in fixtures, weld sequence, and possibly joint preparation. Fixtures may require changes in order to permit robot access to a weld since robots typically do not permit the degrees of freedom of motion that a human operator is capable of. For similar reasons it is conceivable that the use of a robot could also affect the weld production sequence.

Special joint preparation, however, is an engineering change that could cause even greater impact. Some weld seam trackers require special joint preparation. Tactile seam trackers require a groove deep enough to guide the tracker probe. Joint preparation of this sort would probably be too expensive to justify in some instances if the joint preparation costs exceed the cost savings due to automation. Of course, tactile sensors may be rejected for other reasons such as weld joint contamination.

Use of visual seam sensors would probably have less impact on production procedures but some possibilities are presented here. Many of the SSME welds are butt joints that vary in fitup. A very tight butt joint would be difficult to track. The ultimate limit would be the ability to detect a very fine line indicating the butt joint location on parts. Several solutions are possible. (1) The joint could be prepared with a beveled edge that would improve the visibility of the joint and thus improve tracking ability. (2) The joint could be fixtured and tack welded to maintain a minimum joint gap suitable for automated visual tracking. (3) Surface preparation of the work adjacent to the weld seam could be prepared by a process such as sandblasting since the quality of the surface finish adjacent to the weld location would affect the ability of the vision system to track the seam location. (4) A shim of filler material could be inserted in the seam to enhance the visual image. (5) The visual seam tracking system could be made more sophisticated to detect very tight joints. Any system for seam tracking must be able to differentiate between tight and wide seam fitup and choose the proper torch path. As the resolution of the visual system is increased, the sophistication of the visual image processing software must be improved with a concomitant increase in both cost and processing time.

Introduction of robot welding to replace manual welding must impact Process and/or Production Specifications. The cost of any joint or work-surface preparation would have to be balanced against the value of any improved weld quality or consistency due to use of a robot. A similar cost justification must be made if the sophistication of seam tracking equipment is increased to minimize the required seam preparation.

5.0 APPROACHES TO SENSOR CONTROL

5.1 SENSORY SYSTEMS FOR ARC-WELDING CONTROL:

Research has been underway for some time to develop control mechanisms suitable for producing high-quality welds. Quality, in this case primarily means high-strength. Since strength is not a quantity that is directly measurable during the time that the weld is being made, real-time control has been directed primarily at sensing and controlling parameters that are correlated with weld quality. Figure 5.1 is a diagram showing the interrelationship of several types of sensors used for controlling weld quality.

Two factors are of primary importance in the real-time control of an arc-weld. First, it is necessary to know whether the weld is accurately located on the seam. Any sensory system primarily designed to locate the proper weld axis is called "seam tracking." The second factor that must be controlled is the penetration of the weld once it is located on the proper seam axis. This will be called "penetration control." Penetration control and seam tracking do not necessarily result from information derived from a single sensor although visual sensors have the potential, at least, of acquiring both types of information.

As has been discussed in Section 2, penetration is a function of several weld parameters including heat input and weld speed. Penetration may be sensed directly by observing the reverse side of a bead during the weld or by observing one of several parameters from the front of the weld. Puddle size is thought by many to be the variable most directly related to weld penetration for any given work thickness. Research is underway at several laboratories to develop non-visual methods of controlling weld penetration and/or seam axis location. The following list shows several techniques under development along with the laboratories involved:

Mechanical Methods
- Tactile - Several locations
- Acoustic - Carnegie-Mellon
- Ultrasonic - Mass. Institute of Technology
- Puddle dynamics - MIT, Ohio State

Electrical/Electronic
- Eddy Current
- Voltage Waveform
- Magnetic - Carnegie-Mellon
- Capacitance - Carnegie-Mellon

Tactile seam trackers are commercially available but are not particularly suitable in many situations where special seam preparation is not feasible or where the mechanical contactor may contaminate the weld seam. The major thrust of several

Figure 5.1

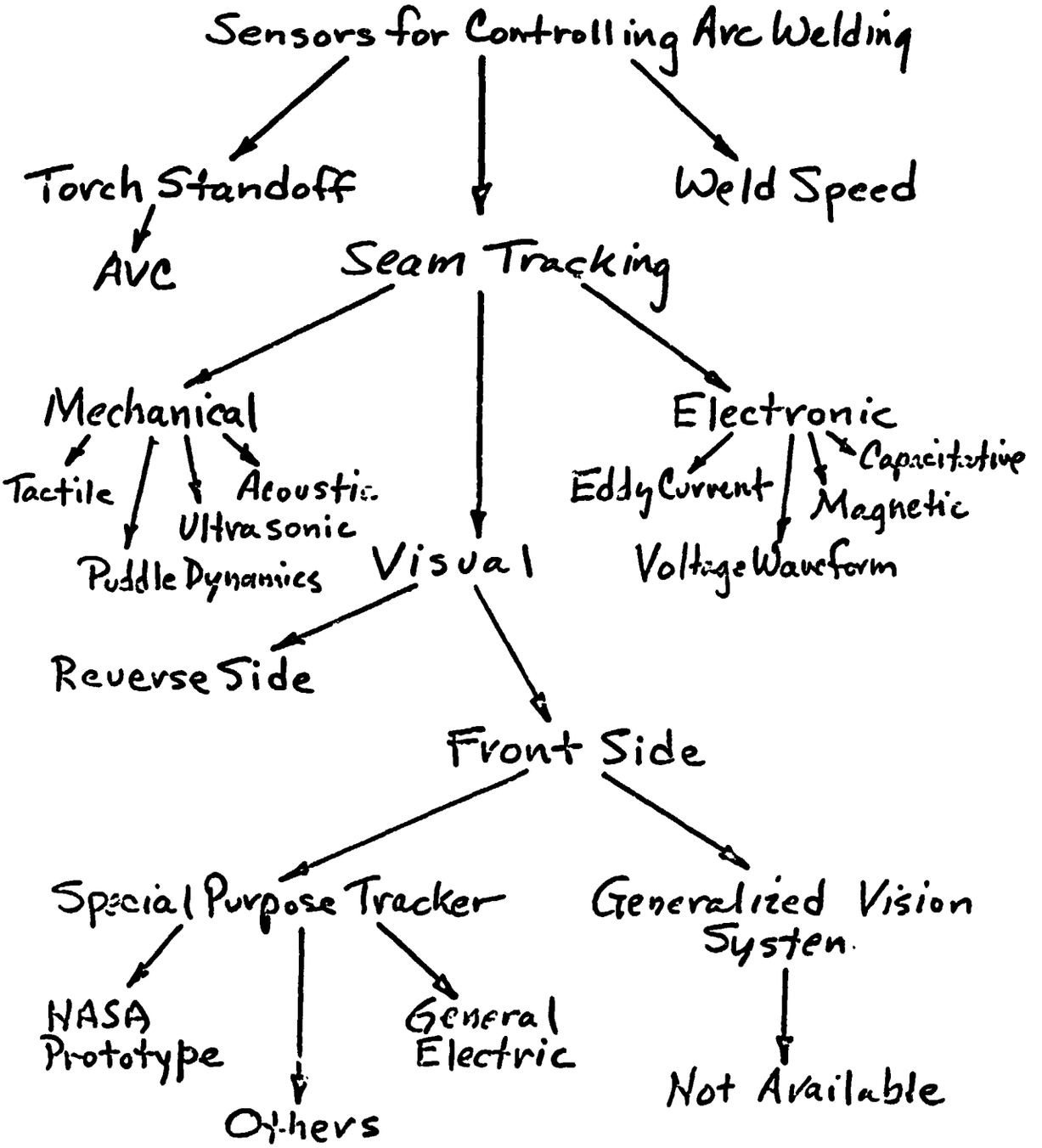

research projects as well as commercial offerings is to concentrate on visual seam-tracking methods. Commercial offerings now on the market will be reviewed in Section 6. The purpose here is to take a more general view of sensors.

5.2 LIMITS TO SENSOR CAPABILITY:

All measurements have a minimum resolution. In mechanical systems this may be constrained by such variables as friction. Various instruments may be limited by the ability to read a scale or by noise introduced by measuri methods or amplifiers. Repeatable errors introduced y improper calibration or imperfections in the measuring system are known as "systemic errors" while errors that may vary from time to time are known as "random errors". Random errors may be eliminated by averaging successive measurements while systemic errors must be minimized by better system design or better calibration. In the case of on-line control systems, averaging may not be possible and both types of error limit the minimum resolution possible with a given measurement.

In the case of visual sensing, a video camera is the most common sensor. Solid state cameras are often used and the resolution is determined by the number of detectors or picture elements (pixels) and the optical magnification of the visual image. It is usual to calculate the minimum resolution by measuring the center-to-center distance between pixels on the photoelectric detector and then divide that distance by the image magnification. Any image degradation introduced by the optical system obviously must be considered. In addition, image magnification and total visual field are inversely related, therefore, a limiting factor, in the case of a seam tracker, may be the overall field of view that must be spanned by the optical system. This is, in turn, a function of the size of the image of the seam width. Magnification cannot be increased to the point where the image of the seam covers all of the pixels of the sensor. It should be obvious that minimum resolution in a visual system is a function of several variable associated with the actual seam being tracked. From a practical standpoint, resolution of a few thousandths of an inch is readily feasible using simple optical systems.

5.3 SYSTEM HARDENING:

Any system designed to function in a "dirty" production environment must be protected against degradation by the environment. Electrical noise due to arc-welding equipment must be filtered out of the sensory systems. Especially troublesome is the radio-frequency arc-starting voltage used in TIG welding. In addition, optical degradation by the intense light of the arc, as well as smoke and splatter must be controlled. System hardening is a product of experiment

and experience and is only mentioned here to draw attention to the fact that sensor-system resolution may be affected by these very practical factors.

5.4 FUTURE POSSIBILITIES:

Existing seam tracking systems will be discussed in a later section of this report. No current seam tracking system utilizes a truly general-purpose visual system that may be used for all of the visual requirements of a robot. Several non-optical seam tracking systems are being developed in the laboratory but their utility remains to be proved. Robot vision appears to offer the best potential for general purpose control of a robot but the techniques are still in the research laboratory.

6.0 ROBOT VISION

6.1 SOURCE MATERIAL:

The terms "Robot Vision" and "Computer Vision" are often used interchangably. Most of the techniques are interchangable; however, since there are applications for computer vision that do not apply to robots, we will use the term robot vision to imply an application specifically relating to robots while computer vision will imply general concepts that are not particularly related to any given application.

Computer vision, in general, has been the subject of intense artificial intelligence research for many years. Recently the application to robotics has come to the forefront and many activities are related to this area even if the application is not specifically stated.

Within the last several years a number of state-of-the-art surveys have been published, some with NASA funding. Several textbooks have been recently published. The following references are particularly relevant:

Gevarter, William B., AN OVERVIEW OF COMPUTER VISION, NBSIR 82-2582, National Bureau of Standards, 1982.

Gennery, Donald, COMPUTER VISION, JPL Publ. 81-92, Jet Propulsion Laboratory, 1981.

Geo-Centers, Inc., A REVIEW OF THREE-DIMENSIONAL VISION FOR ROBOTICS, ARPA Order No. 3089, 1982.

Dodd, George G. and Lothar Rossol, COMPUTER VISION AND SENSOR-BASED ROBOTS, Plenum Press, 1979.

Ballard, Dana H. and Christopher M. Brown, COMPUTER VISION, Prentice-Hall, 1982.

This report will not attempt to re-evaluate the entire computer vision field, but will concentrate on a summary of robot vision and particularly an assessment of the techniques that could be applied to robot arc welding.

6.2 GENERAL TERMINOLOGY AND BACKGROUND:

An extensive terminology has been developed in the fields of Artificial Intelligence and in the sub field known as computer vision. The following definitions are taken from Gevarter (1982):

"Image processing is a signal processing task that transforms an input image into a more desirable output image through processes such as noise reduction, contrast enhancement and registration.

"Pattern recognition is a classification task that classifies images into predetermined categories.

"Computer vision is an image understanding task that automatically builds a description not only of the task itself, but of the three dimensional scene that it depicts."

Computer vision is primarily concerned with "scene analysis" which Gevarter defines as follows:

"Scene analysis is concerned with the transformation of simple features into abstract descriptions relating to objects that cannot be simply recognized based on pattern matching. ... To a large extent, the terms scene analysis, image understanding, and computer vision have become synonymous."

Marr and Nishihara (1978) offer the following definition:

"Artificial Intelligence is (or ought to be) the study of information processing problems that characteristically have their roots in some aspect of biological information processing."

The various tasks that make up image understanding are often broken down into subtasks called feature extraction, symbolic representation, and semantic interpretation.

Images are defined as "grey scale" or "binary" depending on whether an image is digitized into multi-levels of luminance or only two levels respectively.

6.3 VISUAL FUNCTIONS FOR ROBOTICS:

Any visual system, whether biological or robotic, has certain functional capabilities. These visual functions in the order of increasing complexity are range detection, feature extraction, object orientation, object recognition, and scene analysis. Low-level functions are little more than signal processing while the highest level function, scene analysis, is a complex artificial intelligence process that is still the object of intense research activity.

Range detection: The human visual system is able to determine the range of visual objects at a subconscious level. The mechanisms are not completely understood; however, we do know that most persons automatically superimpose the images detected by both eyes and also automatically recognize the

range of objects within a few feet distance. This process is known as steriopsis. Since we do not know how the human brain processes range information, various methods have been developed to provide this capability in robot or computer vision. These are called stereo ranging, triangulation, active ranging, and optical focusing.

Stereo ranging implies that two images viewed from different points in space are shifted until respective points in the two images coincide. The amount that one image must be shifted to "match" the other image is a function of range.

Triangulation implies that angles are calculated between two image locations and an object visible in both images. Simple trigonometry allows one to calculate the range. Triangulation and stereo ranging are somewhat similar concepts except that in the triangulation method a simplified "structured" light using a spot or line of illumination is used to create a unique "object" visible from two locations. Stereo ranging implies that whole images are shifted or superimposed to derive range information.

Active ranging implies that a beam of light or sound is projected upon an object and range is calculated from the "time of light."

Optical focusing implies that an object is placed in sharp focus by an optical system and the object range is calculated from the lens to image distance when the focal length of the optical system is known.

Object orientation: Information about the orientation of an object in space is often required to pick up the object. Human beings do this almost automatically but very specific orientation data is needed for a robot gripper to grasp an object. If object orientation is the primary objective of a robot visual system, a binary or silhouette image is often used to simplify the image-processing computer calculations. Special "back lighting" may be used to illuminate the object. Techniques for object orientation are fairly commonplace in current robot technology.

Feature extraction: Feature extraction is an intermediate processing step on the way to object recognition or scene analysis. An edge or sudden shift in image intensity is the most common form of feature that can be detected in a visual scene. Edges, of course, generally delimit some object or region within an object. Edges are very simple to detect in binary images and this is often exploited in robot vision. Edge detection in grey-scale images is computationally much more complex but is an essential step in some forms of object recognition or scene analysis.

Other features that may be extracted from an image include

regions of common luminosity, often called "blobs", and regions of common color. Research efforts are also directed to developing effective ways of detecting features such as surface orientation or surface texture.

Object recognition: Of course, feature extraction is seldom the purpose of artificial vision. Object recognition, such as in sorting different items in a production line, may be the total reason for a robot vision system. The general technique for object recognition is often called "template matching." Once a robot stores the template or image of an object, recognition is achieved when a second object "matches" the stored template to some acceptable mathematical precision. A more sophisticated form of object recognition may be used in quality control by storing a "good" template and rejecting any object that does not match within a certain measure of precision.

Scene analysis: The most sophisticated form of robot vision is generalized scene analysis. Based on some form of a priori information, a generalized vision system would be able to identify or recognize all the objects in any non-structure scene. The least complicated industrial application would be the identification and selection of various objects jumbled together in a bin. Such a scene would include overlapping object images in all sorts of orientation. Only a limited amount of progress has been made in generalized scene analysis by those engaged in artificial vision research.

6.4 IMAGE PROCESSING METHODS:

Binary vs. grey scale methods: A number of approaches are possible in the development of robot vision systems. Initial production of a binary image rather than an image consisting of continuous tones or grey scales greatly reduces the amount of information that must be processed. Of course, such an approach is only possible of the actual information that is desired is present in the binary image. The orientation of the profile of an object is an example mentioned earlier of an application suitable for binary image processing.

Grey scale images, on the other hand, are required when the information content of the scene, texture for example, would not be retained in a binary image.

Template matching: This image processing method implies that an object is viewed by the vision system to produce a stored version of a known object. This image becomes the "template" for later "recognition" of similar objects. Template matching is relatively simple using binary images; however, grey-scale scenes require much more complex object recognition methods that are still the subject of research.

Edge and region statistics: The proper collection of edge

and/or region statistics could be used to recognize an object. For example, in two-dimensional space four edges of equal length and each separated from the next by a right angle, would define a square. This, in turn, might be sufficient information for recognition of some type of object.

Regional statistics include the area, centroid, perimeter length, maximum and minimum dimensions of a blob of common regional characteristics. The region being statistically described might be of constant luminosity or color in a general image.

Transform methods: The general purpose of any vision system is to recognize objects or some feature of objects. The coefficients of the spatial fourier transform of a scene have been used for this purpose.

Parallel processing: The human visual system is known to process much visual information in a parallel fashion. Most computer algorithms are serial, consequently computer vision is relatively slow compared to natural vision. To speed up computer vision various forms of parallel computer processing are possible. In addition, parallel analog preprocessing is possible to reduce the computational load on a computer being used for a visual task. Considerable parallel preprocessing is done by the retina of the human eye before visual information is transmitted to the primary visual cortex for further processing. It is likely that similar artificial vision methods would be benificial and research into parallel methods is underway.

6.5 STATE-OF-THE-ART:

Intense research activity in computer and robotic vision is currently in process. Gevarter states: "It has been estimated that NASA spending on image processing and evaluation approaches one hundred million dollars a year. ... NASA spends roughly ($500,000 a year) to support research at JPL in vision systems to guide robot manipulation." NSF and NIH are other federal agencies that are annually spending one to two million dollars each in the area of computer vision.

A view of the current state of development of industrial computer vision has been stated by Kruger and Thompson (1981):

> "Dispite substantial research efforts, the study of computer vision is still in its infancy... Significant reductions in complexity are possible if automated perception is limited to an industrial environment. Even here, however, we still lack a clear understanding of the fundamental problems that must be addressed if computer vision is to have a major impact on manufacturing."

They further state that "The current state-of-the-art precludes the construction of one general-purpose computer vision system with applicability to all industrial vision tasks...."

Current computer vision systems for industrial use are generally limited to very simple tasks such as pattern matching using binary images and lighting structured to highlight a particular feature such as an object profile or a weld seam.

Gevarter quotes Gennery et. al. as stating: "...two tasks that are beyond the capability of any existing computer system are the recognition of parts in a jumble in a bin and operation of a robot vehicle in a complicated outdoor environment."

Tenenbaum and Barrow (1981) conclude:

> "While no such (general-purpose computer vision) system yet exists, most of the pieces have been experimentally demonstrated. Thus it would not be unreasonable to attempt to construct one within the current state-of-the-art. Of course, many details still remain unresolved, especially at the higher levels of processing."

Gevarter (1982) concludes his assessment of the state-of-the-art with the following statement:

> "Though quite a number of high-level research vision systems have been explored, no general vision system is available today or is imminent. Major current efforts in this area are ACRONYM at Stanford U. and VISIONS at the U. of Mass."

7.0 A SURVEY OF COMPUTER VISION SYSTEMS

7.1 SOURCE MATERIAL:

The recent literature in Robotics and Computer Vision is voluminous. Surveys have appeared in many publications concerned with manufacturing, industrial automation, and computers. Several state-of-the-art surveys have been prepared by various government and private agencies. Several of these are listed in the references. The most recent comprehensive overview of computer vision was published during the fall of 1982 by Gevarter (1982) at the Bureau of Standards. Much of the material presented here was collected by Gevarter.

7.2 VENDOR SURVEY:

Gevarter (1982, p74) stated "It has been estimated that more than 200 companies are now playing a role in the vision field." He listed about 35 developers of commercial vision systems. This report contains all those mentioned in Gevarter's report plus a number of other vendors that have been mentioned in other reports, magazine articles, directories and proceedings of conferences. An effort has been made in Appendix A to assemble all addresses and telephone numbers of the various vendors, however, some are not listed in the Thomas Register. The remark has been made that many of the companies in this rapidly growing field have been organized in the past few months. In addition, a number of large diversified manufacturers may be involved in the development of commercial vision systems for in-house use only. These are listed in Table 7.1 from Gevarter (1982, p48).

Vendors that are involved in computer vision-system development present a wide diversity of commercial offerings. These vary from simple visual sensors to complete hardware and software systems. A few companies are involved both in computer vision and robotics. Since the addition of sensors to robots is very much in vogue, it is expected that this trend will grow. An even smaller number of vendors are involved in both computer vision and robot welding. Notable are Automatix, Inc., Copperweld Robotics, the General Electric Co., and Unimation.

Table 7.2 is an effort to succinctly summarize the material about various vendors. In general, the companies with computer vision offerings fall into three categories: (1)

those offering sensors only, (2) those offering various components that may be combined to create a computer vision system, and (3) those offering complete systems including interface hardware, image processors, and computer systems for extracting and manipulating visual information. Commercial systems may be further classified as binary, grey-scale or combination systems. Vendors that offer complete systems differ in that some offer turn-key systems with little potential for user software development while others offer software development systems and software modules that the user is expected to combine into a final system. Several offer high-level programming languages specifically developed for computer vision and/or robotics applications.

Table 7.1 will ultimately be a complete summary of vision systems currently on the market. The table included in this report is from a survey in the magazine High Technology (1982). An updated version is not included in this report since a number of vendors have not responded to inquiries and other names were recently discovered and added to the list. Completion of this survey is suggested in the RECOMMENDATIONS section of this report.

TABLE 7.1

LARGE DIVERSIFIED MANUFACTURERS
WITH IN-HOUSE SYSTEMS*

General Electric Company
Chrysler Corporation
General Motors
International Business Machines
Texas Instruments
International Harvester
Westinghouse
Hughes
Lockheed - Palo Alto Research Lab.
Fairchild Camera and Instrument Corp.
Martin Marietta
McDonald-Douglas Automation Company
Cheesebrough Ponds

*Gevarter, 1982.

TABLE 7.2

Table of commercial machine vision systems

Company	Model	Gray-scale levels	Resolution (pixels)	Processing speed (per minute)	Camera type	Computer wordlength*	Typical system price	Comments
Applied Intelligent Systems Ann Arbor, MI	Pixie	64	256 x 256	600 parts	SS		$25 000	Must be programmed by vendor
Automatix Billerica, MA	Autovision II	16	256 x 256	360 parts	SS/Vid	32/16	$30 000	Supports 6 cameras
	Robovision II-V	64	512 x 512	900 parts	SS/Vid	32/16	$100 000	Includes arc welding robot
	Cybervision III-V	64	512 x 512	900 parts	SS/Vid	32/16	$100 000	Assembly robot system
	Autovision IV	256	512 x 512	1800 parts	SS/Vid	32/16	$37.000	Supports 16 cameras
Cognex Boston, MA	Dataman	64	640 x 480	3600 chars	SS/Vid	16	$30.000	Reads poorly lit or partially obscure labels
Control Automation Princeton, NJ	CAV-1000	2	128 x 128	120 parts	SS		$20 000	
Copperweld Troy, MI	Opto-Sense	256	244 x 248	16 msec	SS/Vid	16	$29 000	
	Mentor	256	244 x 248	16 msec	SS/Vid	8	$24 000	
EOIS, Inc. Santa Monica, CA	Series 1100	16	240 x 256	300 parts	SS/Vid	16/8	$14 000	
	Series 1400	256	240 x 512		SS/Vid	16/8	$17.000	
	Series 1800	256	480 x 512		SS/Vid	16/8	$19 400	
Everett/Charles Rancho Cucamonga, CA	ERMAC 2500	2	255 x 255	1800 parts	Vid	8	$23 000	
General Electric Syracuse, NY	Optomation II	2	244 x 248	900 parts	SC		$55 000	
	IPARS	>2			SS		$23 000	Optical character reader
Ham Industries Macedonia, OH	HS-1000	64	1% FOV	1/30 sec	SS	32/16	$5-7000	
	HS-2000	64	1% FOV	1/30 sec	SS	32/16	$5-7000	
	HS-3000	64		1/10 sec	Vid	32/16	$5-7000	
Penn Video, Inc. Akron, OH	Vidomet II	64	320 x 240	900 parts	SS		$30 000	Turnkey system adapts to existing conveyor
Intelledex, Inc. Corvallis, OR		64	256 x 256	60 parts	SS/Vid	16	$12 16 000	Available only as option on Intelledex robot
Machine Intelligence Corp Sunnyvale, CA	VS-100	2	256 x 256	900 parts	SS/Vid	16	$40 000	Programmable image digitizer
	VS-110	2	256 x 256	900 parts	SS/Vid	16	$40 000	
Object Recognition Systems Princeton, NJ	100	256	N/A	300 parts	Vid	8	$12 000	
	200	256	N/A	300 parts	Vid	8	$26 000	
	0	256	256 x 240	240 parts	Vid	8	$12-19 000	
	1000	256	256 x 240	120 parts	Vid		$80 000	
	i-bot 1	256	320 x 240	30 parts	SS		$25 000	Bin picking system for robots
Octek, Inc Burlington, MA	20/20 Vision Devel System	16	320 x 240	300 parts	SS/Vid	16	$50 000	Development system for Series 2000
	Series 2000	16	320 x 480	300 parts	SS/Vid	16	$8000	
Prothon Parsippany, NJ	Robotic Vision System	2	1% of FOV	1800 parts	Vid		$10.000	
Robotic Vision Systems Melville, NY	ACOMS 1100	N/A		57 600 points/sec	SS	16	$75,000	3-D scanning system
	Robo Sensor 200	N/A	001 inches	14 400 points/sec	SS		$75 000	3-D ranging sensor based on light stripe techniques
Unimation Danbury, CT	Univision I	2	256 x 256	<500 msec/frame	SS	16	$35,000	Robot vision system
	Univision II	2	256 x 240	56 msec/frame	SS	8	$20,000	Available for use in arc welding applications
View Engineering Chatsworth, CA	719	2	100 x 100		Vid		$20 000	
Vision Peripherals Anaheim, CA	Pixelcaster	16	1024	3000 chars	SS/Vid	8	$5-10 000	

*Indicates number of gray shades (including black and white) discriminated by system

†FOV = field of view

‡SS = solid state camera

*Indicates size of basic unit of information processed by the computer. Two sizes indicate data wordering hi machine

Note: This table is based in part from a report by Robotic Vision Systems, Inc. Numbers are

Reproduced from High Technology magazine.

8.0 A SURVEY OF ROBOT ARC-WELDING SYSTEMS

8.1 SOURCE MATERIAL:

A relatively small number of commercial firms and research organizations are engaged in the development of robot-controlled Gas-tungsten Arc Welding (GTAW) systems. NASA has been in contact with several of these organizations. An extensive list of vendors with some activity in any aspect of robot-controlled seam welding is included in Appendix B. Table 8.1, however, is a more limited list of vendors with GTAW experience who have offered systems to NASA, that are listed in various directories, or have published articles on sensor feedback controlled gas-tungsten robot arc welding.

8.2 VENDOR SURVEY:

Robot arc-welding systems may be categorized in several ways. First, a system may be classified as a vision or non-vision based system. As discussed elsewhere in this report, seam-tracking may be accomplished using mechanical or other non-visual sensors, however, most of the recent development has concentrated on visual seam-tracking. Next, a seam tracking system may be classified as a one-pass or two-pass system depending on whether or not the robot locates the seam axis prior to the actual welding pass. Finally, systems may be classified as Gas-metal Arc Welding or Gas-tungsten Arc Welding systems. The signficance here is that GTAW is more difficult since radio-frequency arc-starting signals interfere with the robot and vision systems.

Since this report is directed primarily to the application of robot vision to gas tungsten arc welding, the following discussion is limited to those organizations listed in Table 8.1 with demonstrated activity in this area.

Automatix, Inc.: This vendor is one of a very small number of organizations with experience in both robot vision and robot-controlled seam welding. At the present time delivered systems are Gas-metal Arc Welding systems although the company claims to have the capability of operating in the high-frequency arc starting environment of Gas-tungsten Arc Welding.

Automatix markets both stand-alone programmable vision systems, called Autovision, and Programmable Arc Welding systems, called Robovision. The company is also able to provide one and two-axis Welding positioners and is thus able to offer complete manufacturing systems. Linkages with

CAD/CAM systems are currently under development so that this vendor is able to offer a completely integrated design and manufacturing system.

The Automatix Autovision system is a sophisticated vision system that incorporates the Motorola 68000 32-bit microprocessor chip. The system is user-programmable in a special high-level robotics system language called RAIL. The system is highly flexible and the vendor offers expertise in robotics, robot vision, and welding.

Advanced Robotics Corporation: This vendor markets the Cyro series of robots. They have experience with seam-tracking welding applications based on the arc voltage sensing techniques developed by Dr. Cook at Vanderbilt University.

Cincinnati Milacron: This vendor has been marketing robots for many years. They offer arc welding sytems using the Miltrac Seam Tracking System. Currently, no GTAW systems have been delivered that use high-frequency arc starting and it appears that the electrically-driven robots are unable to function satisfactorily in the electrically noisy environment associated with GTAW welding.

General Electric Company: This company has an extensive line of robots and is also a primary supplier of solid-state video cameras that are used for computer vision systems offered by a number of vendors. General Electric has collaborated with Dr. Richardson at Ohio State University and currently markets a visually controlled seam tracker that uses an optical system that views the weld puddle through the torch.

The General Electric seam tracker is the only visual seam tracker now being offered commercially; however, the torch and vision system is only available as a complete welding system including the General Electric robot.

Ohio State University: The Department of Welding Engineering and the Center for Welding Research has been active at Ohio State University for some time. Both Gas Tungsten Arc Welding and Gas Metal Arc Welding methods have been under investigation. This university research center has been studying weld puddle motion, "puddle dynamics", with a view toward obtaining information for control of weld quality.

Dr. Richardson, Director of the Center for Welding Research, developed a prototype "coaxial through-the-torch visually controlled arc-welding system. He collaborated with the General Electric Company that now markets a modified version of this system.

TABLE 8.1

DEVELOPERS OF ROBOT ARC-WELDING SYSTEMS

Automatix, Inc.

Advanced Robotics

General Electric Company

Cincinnati Milacron

Ohio State University

9.0 CONCLUSIONS AND RECOMMENDATIONS

9.1 CONCLUSIONS:

The field of robot vision and visually-controlled arc welding is in a state of intense development. A number of vendors are active or are just entering the field. The next few years will see new systems being developed especially as the demand from such organizations as NASA foster further research and procurement.

At the present time, only a few organizations are willing to contract to deliver a robot welding system with visual seam-tracking capability, especially if a certain performance is called for in the contract. Other organizations are willing to enter into development contracts.

It is likely that the vendor reluctance to contract for a specific visually-controlled Gas Tungsten Arc Welding system is a realistic assessment of the state-of-the-art. Vision systems now on the market seem to have the capability of following a welding seam axis but both visual "noise" and electrical interference make the total system a developmental program.

The following conclusions, subdivided in several categories, are probably justified at this time:

9.2 GENERAL CONCLUSIONS:

1. Requirements for additional automation of Space Shuttle Main Engine welding is probably beyond the capability of commercially available seam-tracking systems.

2. Introduction of robot welding on SSME welds that are currently done manually will inevitably impact existing manufacturing process specifications.

3. Many computer and robot vision systems are available on the commercial market. (The total number is between 50 and over 200.)

4. The most sophisticated computer vision systems appear to be able to provide the information needed for seam tracking.

5. "Dispite substantial research efforts, the study of computer vision is still in its infancy.... Significant reductions in complexity are possible if automated perception is limited to an industrial environment. Even here, however, we still lack a clear understanding of the fundamental problems that must be addressed if computer vision is to have a major impact on manufacturing.... The current state of the art precludes the construction of one general-purpose vision

system with applicability to all industrial vision tasks." (Kruger and Thompson, 1981)

6. A number of suppliers are capable of providing the components needed for developing a visually controlled seam-tracking robot able to meet the needs of specialized SSME welding.

7. Probably it is possible, with substantial research and development, to build a seam tracking system suitable for use with robot torch control on welds that are currently performed by hand on the SSME.

9.3 CONCLUSION ABOUT ARC-WELDING TORCH:

8. Difficult access and complicated shapes will place severe constraints on the size of welding torches and associated hardware (such as AVC effectors and wire feeders) that must be placed near the torch cup.

9.4 CONCLUSIONS ABOUT WORK PIECE:

9. Special joint preparation to permit use of existing seam-tracking control systems is undesirable.

10. Special joint visibility enhancement preparation procedures will be necessary if research determines that tight butt welds cannot be tracked by available visual systems.

11. Required field size is determined by the poorest joint fit while required resolution is determined by the minimum seam gap.

9.5 CONCLUSIONS ABOUT MANIPULATOR (ROBOT):

12. Robot wrist motion will require special control and possibly redundant degrees of freedom will be required for robot SSME welding due to the difficult access to the welds.

13. All robot control electronics will have to be TIG hardened (i.e. protected against high-frequency arc-starting electrical noise).

14. To aid in specifying welding control system precision, a mathematical representation of maximum allowable positional error has been derived.

9.6 CONCLUSIONS ABOUT SENSORS:

15. All sensory electronics will have to be TIG hardened (i.e. protected against high-frequency arc-starting voltages).

16. A robot seam-tracking system must be able capable of

locating a welding seam both in global and relative coordinates (i.e. relative to the robot base and relative to the tool location).

17. The sensory system must be able to determine the line normal to the weld plane for proper torch attitude control.

18. Several non-optical seam tracking systems are being developed in various laboratories, however, their utility for improving weld consistancy on the SSME remains to be proved.

19. Weld seam tracking will have to be on-line, real-time rather than a two-pass system that is inherently unable to compensate for seam axis shifts due to warping of the work.

20. Although other sensory systems are being investigated, visual feedback based on weld puddle location and diameter may offer the best potential for providing the needed sensory information for robot welding control in the SSME.

21. Infra-red viewers and scanners are theoretical alternatives or supplements to visible-light sensors.

22. Additional research is needed to determine whether visual seam trackers can reliably follow very tight butt welds.

23. With increased sophistication, robot visual system may be able to track tight butt welds.

24. Any system for seam tracking must be able to differentiate between tight and wide seam fitup and choose the proper torch path for each.

25. Visual seam-tracking systems have a resolution limited to the spacing between adjacent picture elements (pixels).

26. The ultimate dimensional limit in visual resolution is determined by the number of picture elements in the primary sensor and the overall field size required by the control system.

27. Required sensor field size is determined by the poorest joint fit while required resolution is determined by the minimum seam gap.

29. Depth perception is an additional complexity required for torch attitude control; this may be provided by structured light systems.

30. Robot vision for seam tracking probably requires the capability for sophisticated "generalized scene analysis" rather than the simple binary, template-matching capability of the less expensive robot vision inspection systems.

9.7 CONCLUSIONS ABOUT VISION AND CONTROL PROCESSOR(S):

31. A significant simplification of the robot vision system for SSME welding may be possible if global seam information is transferred to a robot welding system from a computer-aided design (CAD) system.

32. A seam-tracking robot must be able to choose an optimum welding path past tack welds based on knowledge about the actual seam axis in complex geometries.

33. The robot welding system will have to integrate AVC feedback with weld path control.

34. Robot kinematic and dynamic calculations are complex and require appreciable computational power that is generally beyond the capabilities of 8-bit microprocessors.

35. Computations associated with visual sensory information are also complex and require additional significant computational power (e.g. 32-bit microprocessors or minicomputers).

36. Seam-tracking feedback information must be integrated into calculations of robot tool (torch) paths.

37. Computer simulation may aid in the integration of sensory feedback systems with a robot control system.

38. Vendors vary in the amount of software flexibility offered to the end user.

39. Some robot control systems may have insufficient inherent flexibility for the addition of on-line sensory feedback.

40. Some vendors offer special high-level programming languages rather than comparatively simple teach-mode programming methods; these may be more suitable for the incorporation of sensory feedback.

41. Three-dimensional calculation of the weld seam axis will be required for acceptable tracking of small radius and complex curves.

9.2 RECOMMENDATIONS:

Development of a visually-controlled seam-tracking GTAW system can be pursued in several ways. First, one can enter into a contract with a single vendor who will take on the systems integration function. Two or three organizations would do this. Second, one might procure separate computer-vision and robot systems and join these two in-house. To do this requires an understanding of both the robot and visual system limitations.

Finally, one might might continue with some in-house or sponsored university research to further define the requirements and constraints.

It is suggested that SSME robot welding be pursued on several pathways:

1. Proceed with further investigation into the details of the welds for which robot automation is desired. This includes (a) the radius of curving joint axes; (b) the nature of any obstacles that the robot arm must avoid; (c) maximum and minimum fitup expected in actual manufacturing; (d) the extent of any work movement due to heat for which on-line compensation is required; (e) the extent of any tack welds for which weld path projection is required.

2. Initiate research to determine the most suitable means of determining the axis normal to the weld plane for torch attitude control on sharply curving surfaces.

3. Initiate research to determine the minimum detectable weld gap using available visual image processing systems and optical magnification determined by the maximum fitup determined in (1) above.

4. Maintain an ongoing study of all the new computer vision systems being marketed. Develop a rating scale to indicate the relative value of various systems on the market.

5. Determine whether any seam visibility enhancement methods are possible to improve seam tracking when butt weld fitup is tight.

6. Investigate the potential for simplifying the global vision problem by coupling a robot welding system to a CAD data base.

7. Develop an overall systems design to determine an optimum seam-tracking system that is possible utilizing the present state-of-the-art in robotics and computer vision.

8. Utilize computer simulation, when possible, to demonstrate the feasibility of coupling vision systems to robot control systems.

9. Procure prototype hardware to test and develop methods using actual components from the SSME.

10.0 REFERENCES

Ballard, D.H. and C. M. Brown. Computer Vision, Prentice-Hall, Englewood Cliffs, N.J., 1982.

Barrow, H. G. and J. M. Tenenbaum. "Computational Vision", Proceedings of the IEEE, 69:5, 1981, pp. 572-595.

Cary, H. B. Modern Welding Technology, Prentice-Hall, Englewood Cliffs, N.J., 1982.

Dodd, G. G. and L. Rossol. Computer Vision and Sensor-Based Robots. Plenum Press, New York, 1979.

Gennery, D., R. Cunningham, E. Saund, J. High, and C Ruoff. Computer Vision, JPL Publication 81-92, Pasadena, CA., 1981.

Geo-Centers, Inc. A Review of Three-dimensional Vision for Robotics. ARPA Order No. 3089, May 1982.

Gevarter, W. B. An Overview of Computer Vision. National Bureau of Standards, NBSIR 82-2582, Washington, D.C., 1982.

Richardson, R. W., D. A. Gutow, and S. H. Rao. "A Vision Based System for Arc Weld Pool Size Control." from Measurement and Control for Batch Manufacturing. Ed. D. E. Hardt, The American Society of Mechanical Engineers, New York, 1981.

Hanafusa, H., T. Yoshikawa, and Y. Nakamura. "Analysis and Control of Articulated Arms with Redundancy," Reprints of the 8th Triennial World Congress of the International Federation of Automatic Control. Kyoto, Japan, August 1981.

Kruger, R. P. and W. B. Thompson. "A Technical and Economic Assessment of Computer Vision for Industrial Inspection and Robotic Assembly," Proceedings of the IEEE, 69:12, Dec. 1981, PP. 1524-1538.

Marr, D. and H. Nishihara. "Visual Information Processing: Artificial Intelligence and the Sensorium of Sight," Technology Review, October 1978, pp. 28-47.

Paul, R. P. Robot Manipulators: Mathematics, Programming, and Control. The MIT Press, Cambridge, Mass., 1981.

APPENDIX A

VENDORS MARKETING COMPUTER VISION SYSTEMS

Applied Intelligent Systems, Inc.
110 Parkland Plaza
Ann Arbor, MI 48103
(313) 995-2035

Automatix, Inc.
217 Middlesex Turnpike
Burlington, MA 01803
(617) 273-4340

Cognex Corporation
1505 Commonwealth Ave.
Boston, MA 02135
(617) 254-1231

Colorado Video, Inc.
Box 928-A
Boulder, Colorado 80306
(303) 444-3972

Control Automation, Inc.
P.O. Box 2304
Princeton, NJ 08540
(609) 799-6026

Copperweld Robotics
1401 East 14 Mile Rd.
Troy, MI 48084
(313) 585-5972

Cyberanimation, Inc.
4621 Granger
Akron, OH 44313
(216) 666-8293

Diffracto Ltd.
19640 Harper Avenue
Grosse Pte. Woods, Mich. 48236
(313) 965-0140

Digital Graphic Systems, Inc.
935 Industrial Ave.
Palo Alto, CA 94303
(415) 856-2500

E.G. & G. Reticon
345 Potrero Ave.
Sunnyvale, CA 94086
(408) 739-4266

Eigen Video
P.O. Box 848
Nevada City, CA 95959
(916) 272-3461

Electro-Optical Information Systems
710 Wilshire Blvd., Suite 501
Santa Monica, CA 90401
(213) 451-8566

Everett/Charles, Inc.
6101 Cherry Ave.
Fontana, CA 92335
(714) 899-2411

Fairchild CCD Imaging Division
3440 Hillview Ave.
Palo Alto, CA 94304
(415) 493-8001

General Electric Company
IVSO- Marketing
P.O. Box 17500
Orlando, FL 32860-7500
(305) 886-2200

Ham Industries, Inc.
835 East Highland Road
Macedonia, OH 44056
(218) 467-4256

Imaging Technology, Inc.
400 West Cummings Park, Suite 4350
Woburn, MA 01801
(617 938-8444

Intelledex, Inc.
33840 Eastgate Circle
Corvallis, OR 97333
(503) 758-4700

International Robomation/Intelligence
2281 Las Palmas Dr.
Carlsbad, CA 92008
(619) 438-4424

Loge/Spatial Data Systems
500 So. Fairview Ave.
Goleta, Ca. 93116
(805) 967-2383

Machine Intelligence Corp.
330 Potrero Ave.
Sunnyvale, CA 94086
(408) 737-7960

Object Recognition Systems, Inc.
1101-B State Road
Princeton, NJ 08540
(609) 924-1667

Octek, Inc.
7-T Corporate Place, S. Bedford St.
Burlington, MA 01803
(617) 273-0851

Opcon
720 80th St. S.W.
Everett, WA 98203
(800) 426-9184
(206) 353-0900

Penn Video, Inc.
929 Sweitzer Ave., Dept. 14
Akron, OH 44311
(216) 762-4840

Perception Electronics
1445-T Koll Circle
San Jose, CA 95112
(408) 297-7464

Periphicon
P.O. Box 324
Beaverton, OR 97075
(503) 222-4966

Prothon

Parsippany, NJ

Robotic Vision Systems
536 Broadhollow Road
Melville, NY 11747
(516) 694-8910

Spectron Engineering, Inc.
800 West 9th Avenue
Denver, Colorado 80204
(303) 623-8987

SRI International
333-T Ravenswood Ave.
Menlo Park, CA 94025
(415) 326-6200

Synthetic Vision Systems, Inc.
2311 Green Road
Ann Arbor, MI 48105
(313) 995-9580

Unimation, Inc.
Shelter Rock Lane
Danbury, Conn. 06810
(203) 744-1800

Vanzetti Systems, Inc.
111 Island St.
Stoughton, MA 02072
(617) 828-4650

Vicon Industries, Inc.
125-T E. Bethpage Rd.
Plainview, NY 11803
(516) 293-2200

Videometrix
9421 Winnetka Ave./Bldg. F
Chatsworth, CA 91311
(213) 701-6972

View Engineering
9736 Eton Ave.
Chatsworth, CA 91311
(213) 998-4230

Vision Peripherals
P. O. Box 6888
Buena Park, CA 90622
(714) 952-1176

APPENDIX B

VENDORS OFFERING ROBOT SEAM-WELDING SYSTEMS

Advarced Robotics Corp
777 Manor Park Dr
Columbus, OH 43228
(614) 870-7778

American Can Co
American Lane
Greenwich, Conn. 06830
(203) 552-2000

Armax Robotics Inc.
38700 Grand River Ave.
Farmington Hills, MI 48018
(313) 478-9330

ASEA Inc.
1176 East Big Beaver Road
Troy, Mich. 48084
(313) 528-3630

Automatix, Inc.
217 Middlesex Turnpike
Burlington, MA 01803
(617) 273-4340

Bendix Robotics Div.
21238 Bridge Street
Southfield, MI 48034
(313) 352-7700

Cincinnati Milicron Inc.
215 South West Street
Lebanon, OH 45036
(513) 932-4400

Cybotech Corp (Ransburg Corp)
P.O. Box 88514
Indianapolis, IN 46208
(317) 298-5890

Cyclomatic Industries Inc.
7520 Convoy Court
San Diego, CA 92111
(714) 292-7440

DeVilbiss Co.
300 Phillips Ave/P.O. Box 913
Toledo, OH 43692
(419) 470-2169

Fared Robot System Inc.
3860-T Revere
Denver, Colorado 80239
(303) 371-5865

GCA Corp.
Industrial System Group
One Energy Center
Neperville, IL 60566
(312) 369-2110

General Electric Automation Systems
1285 Boston Ave.
Bridgeport, CT 06602
(203) 382-2876

Hitachi American Ltd
59 Route 17-S
Allendale, NJ 07401
(201) 825-8000

Hodges Robotics Intl.
3710 N. Grand River Ave.
Lansing, MI 48906
(517) 323-7427

Marline Intelligence Corp.
330 Potrero Ave.
Sunnyvale, CA 94086
(408) 737-7960

Pickomatic Systems Inc.
37950 Commere Drive
Sterling Heights, MI 48077
(313) 939-9320

REIS Machines
1426 Doris Road
Elgin, IL 60120
(312) 741-9500

Robotic Vision System
536 Broadhallow Road
Melville, NY 11747
(516) 694-8910

Thermwood Machines Mfg.Co.Inc.
P.O. Box 436
Dale, IN 47523
(812) 937-4476

Unimation Inc.(Condec Corp)
Shelter Rock Lane
Danburg, CT 06810
(103) 744-1800

United Technologies Corp.

(203) 728-7000

Westinghouse Electric CE
Industry Automation Drive
400 High-Tower Office Bldg
400 Media Drive
Pittsburg, PA 15205

1983

NASA/ASEE SUMMER FACULTY RESEARCH FELLOWSHIP PROGRAM

MARSHALL SPACE FLIGHT CENTER
THE UNIVERSITY OF ALABAMA IN HUNTSVILLE

STATISTICAL ANALYSIS OF A DEBUGGING MODEL

Prepared By:	Kyle Siegrist, Ph.D.
Academic Rank:	Assistant Professor
University and Department:	The University of Alabama in Huntsville Department of Mathematics
NASA/MSFC: Division:	Systems Dynamics
MSFC Counterpart:	Mario H. Rheinfurth
Date:	August 12, 1983
Contract No.:	NGT 01-008-021 The University of Alabama in Huntsville

STATISTICAL ANALYSIS OF A DEBUGGING MODEL

Kyle Siegrist
Assistant Professor of Mathematics
The University of Alabama in Huntsville
Huntsville, Alabama

ABSTRACT

Suppose that a system is undergoing a sequence of trials and design changes in an effort to find and eliminate design flaws in the system. Specifically, suppose that each trial is classified as an assignable-cause failure (if the failure is due to one or more design flaws), an inherent failure (if the failure is not due to a design flaw), or a success. After each assignable-cause failure, the design flaws that caused the failure are removed. In the case of statistically independent and identical design flaws, a probabilistic model is developed to describe this debugging process. Explicit expressions are obtained for the distributions of the important random variables and for the important measures of reliability. Statistical methods are developed for estimating the parameters of the model from accumulated test data.

ACKNOWLEDGEMENTS

I am grateful to have had the opportunity to participate in the NASA/ASEE Summer Faculty Fellowship Program. I would like to thank Dr. Gerald Karr for his excellent administration of the program.

I would especially like to thank my NASA counterpart, Mario H. Rheinfurth for his guidance and friendship.

INTRODUCTION

When a new system is being developed, it usually has a number of well-defined design flaws. Typical design flaws in a newly-developed areospace system, for example, are overstressed parts, improper materials, design configurations that give rise to damaging vibrational modes, "hot spots," improper operating procedures, etc. Such a system usually undergoes a sequence of tests in an effort to find and eliminate these design flaws. Specifically, suppose that each design flaw in the system may (or may not) cause the system to fail, in some sense, when a trial is conducted, and that after each trial an effort is made to redesign the system to eliminate all design flaws that were discovered on that trial. In addition, the system can fail when a trial is conducted for "inherent" reasons (such as "normal" failure of components, acts of God, etc.) which are not due to any specific design flaw. Note that it is assumed that a test failure can have more than one cause; this assumption is appropriate for systems in which the failure caused by a design flaw does not destroy the system or otherwise stop the test.

It is usually impossible to model the testing and design change of a complex system deterministically. Therefore it is important to develop good probabilistic models. After a probabilistic model has been developed, it is important to find statistical methods of estimating the parameters of the model from accumulated test data. Then the model can be used to estimate the reliability or quality of the system at some point during the testing or at some point in the future. For systems of the type described above, important measures of reliability and quality are the probability of success, the expected number of design flaws remaining in the system, the probability that all design flaws have been eliminated, and the expected number of trials necessary to eliminate all design flaws.

The debugging problem studied in this project falls in the domain of

mathematical reliability theory. An excellent general reference for this theory is the book by Barlow and Proschan [1]. Reference [4] is a survey of reliability growth models. Several authors have considered "failure source" or "design flaw" debugging models;see [2], [3], [6], [7], [8], [9], and [10].

OBJECTIVES

The objectives of this project were to develop a probabilistic model for a system undergoing a sequence of trials and design changes and then to develop statistical methods of estimating the parameters from accumulated test data.

These objectives were met for a system satisfying two simplifying assumptions, namely that the design flaws are statistically independent and identical and that the redesign attempts are always successful. Precise assumptions and definitions are given in the next section. In the following section, the distributions of the important random variables and explicit expressions for the reliability and quality functions are obtained. Next the fundamental parameters of the model are estimated using the method of maximum likelihood and substitution principle. Maximum likelihood and uniformly minimum variance unbiased estimators are obtained. The last section is devoted to a Bayesian analysis of the parameters.

ASSUMPTIONS AND DEFINITIONS

Suppose that a system undergoes a sequence of trials and design changes. We make the following assumptions:

(a) The system has one irremovable failure source. The system has some number (perhaps unknown, perhaps random) of removable failure sources. More than one failure source may cause failure when a trial is conducted.

(b) When a trial is conducted, the irremovable failure source causes failure with probability q_0 $(0 \leq q_0 < 1)$. Each removable failure causes failure with probability q $(0 < q < 1)$. All failure sources act independently.

(c) If one or more removable failure sources leads to failure on a trial, the trial is classified as an assignable-cause (or type 1) failure (regardless of whether or not the irremovable failure source led to failure). If no removable failure source leads to failure, but the irremovable failure source does, the trial is classified as an inherent (or type 0) failure. If no failure source leads to failure, the trial is classified as a success.

(d) After each type 1 failure, all removable failure sources that led to the failure are permanently removed from the system.

Basic definitions and notation for the model will now be given. First we assume that there is an underlying probability space (Ω,F,P) relative to which all events and random variables are defined.

Let M denote the initial number of removable failure sources in the

system. M takes values in $\{0, 1, \cdots\}$. We will usually assume that either M takes on a fixed value, $M = m$, or that M has a Poisson distribution with parameter λ. Thus, the fundamental parameters of the model are q, q_0, and m (or λ).

For $n = 1, 2, \cdots$, let X_n denote the number of removable failure sources that led to failure on trial n (and hence were removed from the system before trial $n + 1$). X_n takes values in $\{0, 1, \cdots\}$.

For $n = 1, 2, \cdots$, let Y_n denote the outcome of trial n as follows: $Y_n = 0$ if trial n was an inherent failure, $Y_n = 1$ if trial n was an assignable-cause failure, and $Y_n = 2$ if trial n was a success.

Note that $X_1, Y_1, \cdots, X_n, Y_n$ are the observable data after n trials. Next, a number of important statistics will be defined in terms of the observable data.

For $n = 1, 2, \cdots$, let $S_n = X_1 + \cdots + X_n$. Note that S_n is the total number of removable failure sources that led to failure (and hence were removed) during the first n trials. S_n takes values in $\{0, 1, \cdots\}$.

For $n = 1, 2, \cdots$, let $T_n = \sum_{i=1}^{n} i \cdot X_i$. T_n takes values in $\{0, 1, \cdots\}$.

For $n = 1, 2, \cdots$, let $U_n = \#\{k: \ 1 \leq k \leq n, Y_k = 0\}$. Thus, U_n is the number of the first n trials that were classified as inherent failures. U_n takes values in $\{0, 1, \cdots, n\}$.

For $n = 1, 2, \cdots$, let $V_n = \#\{k: \ 1 \leq k \leq n, Y_k = 2\}$. Thus, V_n is the number of the first n trials that were classified as successes. V_n takes values in $\{0, 1, \cdots, n\}$.

Note that $n - (U_n + V_n)$ is the number of the first n trials that were classified as assignable-cause failures. In particular note that $U_n + V_n = \#\{k: \ 1 \leq k \leq n, X_k = 0\}$ and $n - (U_n + V_n) = \#\{k: \ 1 \leq k \leq n, X_k > 0\}$.

Let $N = \min\{n: S_n = M\}$. Note that N is the number of trials necessary to remove all removable failure sources from the system.

A number of important measures of the reliability of the system can now be defined in terms of these random variables.

For $n = 1, 2, \cdots$, $P[Y_n = 2]$ is the probability of success on trial n. The probability of success as a function of trial number n is called the reliability function.

For $n = 1, 2, \cdots$, $E[M] - E[S_n]$ is the expected number of removable failure sources remaining in the system after n trials.

For $n = 1, 2, \cdots$, $P[S_n = M]$ is the probability that the system is completely repaired (i.e., all removable failure sources have been eliminated) after n trials.

E[N] is the expected number of trials necessary to eliminate all removable failure sources.

Of course, these reliability measures depend on the basic parameters q, q_0, and m (or λ). Hence, statistical estimation of the basic parameters will allow statistical estimation of the important reliability measures.

Finally we mention some notational conventions which will be employed. For $m, x \in \{0, 1, \cdots\}$, $\binom{m}{x}$ denotes the usual binomial coefficient $m!/x!(m-x)!$. The expression $m!/(m-x)!$ (and hence also $\binom{m}{x}$) is to be interpreted as 0 if $x > m$. Sums over vacuous index sets are also to be interpreted as 0.

DISTRIBUTIONS

In this section, the distributions of the important random variables and explicit formulas for the reliability measures will be obtained. We start with the main result of the section, the distribution of the observable data after n trials.

Suppose that $M = m$ (where m is a fixed positive integer). The distribution of $(X_1, Y_1, \cdots, X_n, Y_n)$ is given by

$$P[X_1 = x_1, Y_1 = y_1, \cdots, X_n = x_n, Y_n = y_n] =$$

$$\frac{m!}{x_1! \cdots x_n!(m-s_n)!} q^{(s_n)}(1-q)^{n(m-s_n)+(t_n-s_n)} q_0^{(u_n)}(1-q_0)^{(v_n)} \cdot h_n(x_1, y_1, \cdots, x_n, y_n) \qquad (1)$$

for $x_1, \cdots, x_n \in \{0, 1, \cdots\}$ and $y_1, y_2, \cdots, y_n \in \{0, 1, 2\}$ where h_n is defined as follows:

$$h_n(x_1, y_1, \cdots, x_n, y_n) = \begin{cases} 0 \text{ if for some } i,\ x_i = 0 \text{ and } y_i = 1 \text{ or if} \\ \quad \text{for some } i,\ x_i > 0 \text{ and } y_i \in \{0, 2\}, \\ 1 \text{ otherwise.} \end{cases} \qquad (2)$$

For n = 1, this result follows from the assumptions that govern the system. For general n, the result can be proved by mathematical induction.

From (1) and the standard factorization theorem (see [4]), it follows that (S_n, T_n, U_n, V_n) is a sufficient statistic for (m, q, q_0); (S_n, T_n) is a sufficient statistic for (m, q); (U_n, V_n) is a sufficient statistic for η_0; and if q is known, S_n is a sufficient statistic for m.

Now suppose that M has a Poisson distribution with parameter $\lambda > 0$.

Then the distribution of $(X_1, Y_1, \cdots, X_n, Y_n)$ is given by

$$P[X_1 = x_1, Y_1 = y_1, \cdots, X_n = x_n, Y_n = y_n] =$$

$$\frac{e^{-\lambda[1-(1-q)^n]}}{x_1! \cdots x_n!} (\lambda q)^{(s_n)} (1 - q)^{(t_n - s_n)} q_0^{(u_n)} (1 - q_0)^{(v_n)} \cdot$$

$$\cdot h_n(x_1, y_1, \cdots, x_n, y_n) \qquad (3)$$

for $x_1, \cdots, x_n \in \{0, 1, \cdots\}$ and $y_1, \cdots, y_n \in \{0, 1, 2\}$, where h is given in (2).

This result can be proved using (1) and a standard conditioning argument.

The family of distributions in (3), indexed by the parameters λ, q, and q_0 is a 4 parameter exponential family with natural sufficient statistic (S_n, T_n, U_n, V_n) (see [4] for the definition of an exponential family of distributions). Also, from the factorization theorem, (S_n, T_n, U_n, V_n) is a sufficient statistic for (λ, q, q_0); (S_n, T_n) is a sufficient statistic for (λ, q); (U_n, V_n) is a sufficient statistic for q_0; and if q is known, S_n is a sufficient statistic for λ.

Suppose that M = m. Then for n = 1, 2, $\cdots$, S_n has the binomial distribution on {0, 1, $\cdots$, m} with parameters m and $1 - (1 - q)^n$, i.e.,

$$P[S_n = s] = \binom{m}{s} [1 - (1 - q)^n]^s [(1 - q)^n]^{m-s}, \quad s = 0, 1, \cdots, m. \qquad (4)$$

This result can be proved by induction on n, however we will give a simple probabilistic argument. The probability that a removable failure source will lead to failure on one of the first n trials is $1 - (1 - q)^n$. Since the failure sources act independently, S_n has the binomial distribution on {0, 1, $\cdots$, m} with parameters m and $1 - (1 - q)^n$.

From (4) and a standard conditioning argument it follows that if M has a Poisson distribution with parameter $\lambda > 0$ then S_n has a Poisson

distribution with parameter $\lambda[1 - (1 - q)^n]$, i.e.,

$$P[S_n = s] = e^{-\lambda[1-(1-q)^n]}\{\lambda[1 - (1 - q)^n]\}^s/s!, \quad s = 0, 1, \cdots. \tag{5}$$

Suppose that $M = m \in \{1, 2, \cdots\}$. Then for $n = 1, 2, \cdots$, X_n has the binomial distribution with parameters m and $(1 - q)^{n-1}q$, i.e.,

$$P[X_n = x] = \binom{m}{x}[(1 - q)^{n-1}q]^x[1 - (1 - q)^{n-1}q]^{m-x}, \quad x = 0, 1, \cdots, m. \tag{6}$$

As before, this result can be proved by induction on n, however we will give a simple probabilistic argument. The probability that a removable failure source does not lead to failure during the first $n - 1$ trials, but does lead to failure on trial n is $(1 - q)^{n-1}q$. Since the m removable failure sources are independent, X_n has the binomial distribution with parameters m and $(1 - q)^{n-1}q$.

From (6) and a standard conditioning argument it follows that if M has a Poisson distribution with parameter $\lambda > 0$ then X_n has a Poisson distribution with parameter $\lambda(1 - q)^{n-1}q$, i.e.,

$$P[X_n = x] = e^{-\lambda(1-q)^{n-1}q}[\lambda(1 - q)^{n-1}q]^x/x!, \quad x = 0, 1, \cdots. \tag{7}$$

From (6) and a standard conditioning argument it can be shown that if $M = m \in \{1, 2, \cdots\}$ then for $n = 1, 2, \cdots$, the distribution of $(X_1, \cdots, X_n)$ is given as follows:

$$P[X_1 = x_1, \cdots, X_n = x_n] =$$

$$\frac{m!}{x_1! \cdots x_n!(m-s_n)!}\, q^{(s_n)}(1 - q)^{n(m-s_n)+(t_n-s_n)} \tag{8}$$

for $x_1, \cdots, x_n \in \{0, 1, \cdots\}$. This result is also given in [10].

From (8) it follows easily that if $M = m \in \{1, 2, \cdots\}$ then for $n = 1, 2, \cdots$, the distribution of (S_n, T_n) is given as follows:

$$P[S_n = s, T_n = t] = k_n(s, t)\frac{m!}{(m - s)!} q^s(1 - q)^{n(m-s)+(t-s)} \tag{9}$$

for $s, t \in \{0, 1, \cdots\}$ where k is defined by

$$k_n(s, t) = \sum_{\substack{x_1, \cdots, x_n \\ s_n=s,\ t_n=t}} \left(\frac{1}{x_1! \cdots x_n!}\right). \tag{10}$$

Note that $P[N = n] = P[S_n = M] - P[S_{n-1} = M]$. Hence if $M = m \in \{1, 2, \cdots\}$, then by (4), the distribution of N is given by

$$P[N = n] = [1 - (1 - q)^n]^m - [1 - (1 - q)^{n-1}]^m, \quad n = 1, 2, \cdots. \tag{11}$$

If M has the Poisson distribution with parameter $\lambda > 0$, then by (5), the distribution of N is given by

$$P[N = n] = \begin{cases} e^{-\lambda}, & n = 0 \\ e^{-\lambda(1-q)^n} - e^{-\lambda(1-q)^{n-1}}, & n = 1, 2, \cdots \end{cases} \tag{12}$$

We will close this section by giving explicit formulas for the important reliability measures. Suppose first that $M = m \in \{1, 2, \cdots\}$. The probability of success on trial n is

$$P[Y_n = 2] = [1 - (1 - q)^{n-1}q]^m(1 - q_0), \quad n = 1, 2, \cdots. \tag{13}$$

The expected number of removable failure sources remaining in the system after n trials is

$$m - E[S_n] = m(1 - q)^n, \quad n = 1, 2, \cdots. \tag{14}$$

The probability that all removable failure sources have been eliminated after n trials is

$$P[S_n = m] = [1 - (1 - q)^n]^m, \quad n = 1, 2, \cdots. \tag{15}$$

The expected number of trials necessary to eliminate all removable failure sources is

$$E[N] = \sum_{k=0}^{\infty}\{1 - [1 - (1 - q)^k]^m\}. \tag{16}$$

Finally suppose that M has the Poisson distribution with parameter $\lambda > 0$. The probability of success on trial n is

$$P[Y_n = 2] = e^{-\lambda(1-q)^{n-1}}(1 - q_0), \quad n = 1, 2, \cdots. \tag{17}$$

The expected number of removable failure sources remaining in the system after n trials is

$$E[M] - E[S_n] = \lambda(1 - q)^n, \quad n = 1, 2, \cdots. \tag{18}$$

The probability that all removable failure sources have been eliminated after n trials is

$$P[S_n = M] = e^{-\lambda(1-q)^n}, \quad n = 1, 2, \cdots. \tag{19}$$

The expected number of trials necessary to eliminate all removable failure sources is

$$E[N] = \sum_{k=0}^{\infty}[1 - e^{-\lambda(1-q)^k}]. \tag{20}$$

Formulas (13) through (20) can be derived easily from the previous results of this section. Also, explicit proofs of some of the formulas can be found in [8].

ESTIMATION OF PARAMETERS

In this section we will use the method of maximum likelihood and the method of moments to obtain estimators of the basic parameters q, q_0 and m (or λ) from the observed data after n trials. Under certain conditions we will obtain maximum likelihood estimators (MLE's) and uniformly minimum variance unbiased estimators (UMVUE's).

Suppose first that $M = m \in \{1, 2, \cdots\}$ is known. The log likelihood function $L = L(q, q_0; x_1, y_1, \cdots, x_n, y_n, m)$ corresponding to the family of distributions in (1) is given by

$$L = \ln\left[\frac{m!}{x_1! \cdots x_n!(m-s_n)!}\right] + s_n \ln(q) + [n(m - s_n) + (t_n - s_n)]\ln(1 - q)$$

$$+ u_n \ln(q_0) + v_n \ln(1 - q_0) \tag{21}$$

where $x_1, \cdots, x_n \in \{0, 1, \cdots\}$ and $y_1, \cdots, y_n \in \{0, 1, 2\}$ are such that $h_n(x_1, y_1, \cdots, x_n, y_n) = 1$ and $s_n \leq m$. Maximizing L in (21) with respect to q gives the MLE $\hat{q}$ of q:

$$\hat{q} = \frac{S_n}{n(m - S_n) + T_n} . \tag{22}$$

Maximizing L in (21) with respect to q_0 gives the MLE $\hat{q}_0$ of q_0:

$$\hat{q}_0 = \frac{U_n}{U_n + V_n} . \tag{23}$$

Suppose now that M has the Poisson distribution with unknown mean $\lambda > 0$. Suppose also that q_0 is unknown but that q is known. The log likelihood function $L = L(\lambda, q_0; x_1, y_1, \cdots, x_n, y_n, q)$ corresponding to the family of distributions in (3) is given by

$$L = -\lambda[1 - (1 - q)^n] + s_n[\ln(\lambda) + \ln(q)] + (t_n - s_n)\ln(1 - q)$$
$$+ u_n \ln(q_0) + v_n \ln(1 - q_0) - \ln(x_1! \cdots x_n!) \tag{24}$$

where $x_1, \cdots, x_n \in \{0, 1, \cdots\}$ and $y_1, \cdots, y_n \in \{0, 1, 2\}$ are such that $h_n(x_1, y_1, \cdots, x_n, y_n) = 1$. Maximizing L in (24) with respect to λ gives the MLE $\hat{\lambda}$ of λ:

$$\hat{\lambda} = \frac{S_n}{1 - (1 - q)^n}. \tag{25}$$

By (5), $E[S_n] = \lambda[1 - (1 - q)^n]$ and therefore the estimator in (25) is unbiased. Since S_n is a complete sufficient statistic for λ if q is known, it follows from Theorem 4.2.3 of [4] that $\hat{\lambda}$ given in (25) is also the UMVUE of λ. Note that

$$\mathrm{Var}(\hat{\lambda}) = \frac{\lambda}{1 - (1 - q)^n}.$$

Maximizing L in (24) with respect to q_0 gives precisely the same estimator that was obtained previously, namely $\hat{q}_0 = U_n/(U_n + V_n)$.

Suppose now that $M = m \in \{1, 2, \cdots\}$ is unknown and that q is also unknown. The log likelihood function corresponding to the family of distributions in (1) can be used to obtain a pair of equations for the MLE's of m and q. However it is not clear how to solve these equations explicitly. Similarly, if M has the Poisson distribution with unknown mean $\lambda > 0$ and if q is unknown, the log likelihood function corresponding to the family of distributions in (3) can be used to obtain a pair of equations for the MLE's of λ and q, but again the equations probably cannot be solved explicitly. In either case however, numerical techniques can be used to obtain approximations to the MLE's.

Suppose now that $M = m \in \{1, 2, \cdots\}$. From (4) it follows that

$$E[S_n] = m[1 - (1 - q)^n]. \tag{26}$$

If q is known, the substitution principle applied to (26) yields the following estimator $\tilde{m}$ of m:

$$\tilde{m} = \frac{S_n}{1 - (1 - q)^n}. \tag{27}$$

Clearly this is an unbiased estimator of m. Since S_n is a complete, sufficient statistic for m when q is known, it follows from Theorem 4.2.3 of [4] that $\tilde{m}$ is the UMVUE of m. Note that (see (4))

$$\mathrm{Var}(\tilde{m}) = \frac{m(1 - q)^n}{1 - (1 - q)^n}.$$

Therefore $\mathrm{Var}(\tilde{m}) \to 0$ as $n \to \infty$ and $\tilde{m}$ is a consistent estimator of m. Notice also that the estimator in (27) is the same as the MLE and UMVUE estimator of λ given in (25).

Returning to (26), if m is known, the substitution principle yields the following estimator $\tilde{q}$ of q:

$$\tilde{q} = 1 - \left[\frac{m - S_n}{m}\right]^{1/n}. \tag{28}$$

Note that $\tilde{q}$ is not the same as the MLE $\hat{q}$ given in (22). An application of Jensen's inequality shows that $\tilde{q}$ is positively biased, that is, $\tilde{q}$ tends to overestimate q.

Suppose now that M has the Poisson distribution with parameter $\lambda > 0$. From (5) it follows that

$$E[S_n] = \lambda[1 - (1 - q)^n]. \tag{29}$$

If q is known, the substitution principle applied to (29) yields the estimate $S_n/[1 - (1 - q)^n]$ of λ. But this is simply the estimate $\hat{\lambda}$ given in (25) which we know is the MLE and the UMVUE of λ. If λ is known, the

substitution principle applied to (29) yields $1 - [(\lambda - S_n)/\lambda]^{1/n}$ as an estimator of q. This estimator is analagous to $\tilde{q}$ given in (28) with λ replacing m. As before, the estimator is positively biased and tends to overestimate q.

Recall from the previous section that the conditional distribution of X_n given M is the binomial distribution with parameters M and $(1 - q)^{n-1}q$. It follows that

$$(1 - q)E[X_{n-1}] = E[X_n]. \tag{30}$$

The substitution principle applied to (30) yields the following estimate q* of q:

$$q^* = 1 - \frac{X_n}{X_{n-1}} . \tag{31}$$

The advantage of this estimator is that it does not depend on M. Hence if both m (or λ) and q are unknown, q* can be used to estimate q and then the estimator in (27) can be used to estimate m (or the estimator in (25) can be used to estimate λ). The disadvantages of the estimator q* are that it may be unreasonable (if $X_n > X_{n-1}$) and that it does not use all of the sample information. These disadvantages may be offset somewhat by replacing q* with the estimator

$$q^* = \frac{1}{\#\{j:\ 1 \leq j \leq n-1,\ X_{j+1} \leq X_j\}} \sum_{\{j:\ 1 \leq j \leq n-1,\ X_{j+1} \leq X_j\}} [1 - \frac{X_{j+1}}{X_j}].$$

We will close this section by obtaining the UMVUE of q after n trials in the case in which $M = m \in \{1, 2, \cdots\}$ is known. First recall that X_1 has the binomial distribution with parameters m and q. Therefore X_1/m is an unbiased estimator of q. Since (S_n, T_n) is a complete, sufficient statistic for q, it follows from Theorem 4.2.2 of [4] that

$$E[X_1/m \mid S_n, T_n]$$

is the UMVUE of q. Using (9) and Bayes' theorem, we can show that

$$P[X_1 = x \mid S_n = s, T_n = t] = \frac{k_{n-1}(s - x, t - s)}{x!k_n(s, t)} .$$

Therefore the UMVUE of q is the estimator q' defined as follows:

$$q' = \frac{1}{m} \sum_{x=0}^{S_n} \frac{xk_{n-1}(S_n - x, T_n - S_n)}{x!k_n(S_n, T_n)}$$

(recall that k is defined in (10)).

The estimators of the basic parameters q, q_0, and m (or λ) obtained in this section can be used in formulas (13) through (20) to generate estimators of the reliability measures.

BAYESIAN ANALYSIS

In this section, it is assumed that each of the basic parameters is a random variable. The object of Bayesian analysis is to use the observed data to revise the probability distributions of the parameters.

Recall that the beta distribution with parameters $a > 0$ and $b > 0$ is the distribution with probability density function

$$f(z) = \frac{z^{a-1}(1 - z)^{b-1}}{B(a,b)}, \quad 0 < z < 1$$

where $B(a, b) = \Gamma(a)\Gamma(b)/\Gamma(a + b)$ (Γ of course denotes the standard gamma function). Recall also that the gamma distribution with parameters $\alpha > 0$ and $\beta > 0$ is the distribution with probability density function

$$g(z) = \frac{\beta^{\alpha}}{\Gamma(\alpha)} z^{\alpha-1}e^{-\beta z}, \quad z > 0 .$$

The results of this section are obtained by applying Bayes' theorem and other standard techniques to the distributions derived previously. Explicit proofs are omitted.

Suppose that $M = m \in \{1, 2, \cdots\}$ is known. Then the beta family of distributions forms a conjugate family of distributions for the removable failure source probability q. Specifically, if q has the beta distribution with parameters $a > 0$ and $b > 0$, then given $X_1 = x_1$, $Y_1 = y_1$, $\cdots$, $X_n = x_n$, $Y_n = y_n$ (or simply given $S_n = s_n$ and $T_n = t_n$), q has the beta distribution with parameters $a + s_n$ and $b + n(m - s_n) + (t_n - s_n)$. (We assume, of course, that $x_1, \cdots, x_n \in \{0, 1, \cdots\}$ and $y_1, \cdots, y_n \in \{0, 1, 2\}$ are such that $h_n(x_1, y_1, \cdots, x_n, y_n) = 1$ and $s_n \leq m$.)

The beta family of distributions forms a conjugate family of distributions for the irremovable failure source probability q_0. Specifically, if q_0 has the beta distribution with parameters $a > 0$ and $b > 0$, then given $X_1 = x_1$, $Y_1 = y_1$, $\cdots$, $X_n = x_n$, $Y_n = y_n$ (or simply given $U_n = u_n$ and $V_n = v_n$), q_0 has the beta distribution with parameters $a + u_n$, $b + v_n$. (We assume that $x_1, \cdots, x_n \in \{0, 1, \cdots\}$ and $y_1, \cdots, y_n \in \{0, 1, 2\}$ are such that $h_n(x_1, y_1, \cdots, x_n, y_n) = 1$.)

Suppose that q is known and that M has a Poisson distribution with unknown mean λ. The gamma family of distributions forms a conjugate family of distributions for λ. Specifically, if λ has the gamma distribution with parameters $\alpha > 0$ and $\beta > 0$, then given $X_1 = x_1$, $Y_1 = y_1$, $\cdots$, $X_n = x_n$, $Y_n = y_n$ (or simply given $S_n = s_n$), λ has the gamma distribution with parameters $\alpha + s_n$ and $\beta + 1 - (1 - q)^n$. (We assume again that x_1, $\cdots$, $x_n \in \{0, 1, \cdots\}$ and $y_1, \cdots, y_n \in \{0, 1, 2\}$ are such that $h_n(x_1, y_1, \cdots, x_n, y_n) = 1$.)

CONCLUSIONS AND RECOMMENDATIONS

A thorough probabilistic and statistical analysis has been carried out for a system undergoing testing and design change, subject to two simplifying assumptions--the failure sources are statistically independent and identical, and the redesign attempts are always successful. Explicit representations for the important distributions and measures of reliability have been obtained. Statistical methods have been developed for estimating the basic parameters of the model from accumulated test data.

Probabilistic models need to be developed for systems in which the simplifying assumptions are not satisfied, that is, for systems whose failure sources are not necessarily statistically independent and identical, and for which the redesign attempts may not be successful and may even be harmful. Although such models would be more realistic, it is doubtful that the analysis could be as complete as for the simpler model. In fact, it may be that only approximate or asymptotic results could be obtained. In any event, continuing work needs to be done in the important area of probabilistic modeling of reliability growth.

REFERENCES

1. Barlow, Richard E. and Proschan, Frank, Mathematical Theory of Reliability, Wiley & Sons, Inc., New York, 1965.

2. Barlow, Richard E. and Scheuer, Ernest M., "Reliability Growth During a Development Testing Program," Technometrics, Vol. 8, No. 1, 1966.

3. Barr, Donald R., "A Class of General Reliability Growth Prediction Models," Operations Research, Vol. 18, No. 1, 1970.

4. Bickel, Peter J. and Doksum, Kjell A., Mathematical Statistics, Holden-Day, Inc. , San Francisco, 1977.

5. Corcoran, W. J., Weingarten, H., and Zehna, P. W., "Estimating Reliability After Corrective Action," Management Science, Vol. 10, No. 4, 1964.

6. Crow, Larry H., "Reliability Growth Modeling," U. S. Army Materiel Systems Analysis Agency Technical Report No. 55, 1972.

7. Siegrist, Kyle, "Reliability Growth with an Arbitrary Number of Initial Failure Sources," submitted to Operations Research, 1983.

8. Siegrist, Kyle, "Reliability Growth With Independent Failure Sources and Random Masking," submitted to IEEE Transactions on Reliability, 1983.

9. Wolman, William, "Problems in System Reliability Analysis," Statistical Theory of Reliability, University of Wisconsin Press, 1963.

10. Yang, Mark C. C., Wackerly, Dennis D., and Rosalsky, Andrew, "Optimal Stopping Rules in Proofreading," Journal of Applied Probability, Vol. 19, 1982.

1983

NASA/ASEE SUMMER FACULTY RESEARCH FELLOWSHIP PROGRAM

MARSHALL SPACE FLIGHT CENTER
THE UNIVERSITY OF ALABAMA IN HUNTSVILLE

A NUMERICAL INVESTIGATION OF THE MULTIPLE VORTEX PHENOMENON: VORTEX NUMBER AND STRUCTURE AS A FUNCTION OF SWIRL RATIO

Prepared By:	David R. Smith, Ph.D.
Academic Rank:	Assistant Professor
University and Department:	Purdue University Department of Geosciences
NASA/MSFC Division: Branch:	Systems Dynamics Laboratory Atmospheric Sciences Division Fluid Dynamics Branch
MSFC Counterpart:	Fred W. Leslie, Ph.D.
Contract No.:	NGT 01-008-021 The University of Alabama in Huntsville
Date:	August 12, 1983

A Numerical Investigation of the Multiple Vortex Phenomenon: Vortex Number and Structure as a Function of Swirl Ratio

By

David R. Smith
Assistant Professor
Department of Geosciences
Purdue University
W. Layfayette, IN 47907

ABSTRACT

A numerical investigation of the multiple vortex phenomenon (MVP) for tornado-like flows is conducted to determine the conditions for when a vortex becomes unstable and divides into smaller subsidiary vortices, as well as to determine the structure of these vortices. This study utilizes a three-dimensional numerical model developed by Rotunno (1983) which has been demonstrated to successfully simulate MVP with properties observed both in natural as well as laboratory tornado-like vortices. In this study MVP is generated for several swirl ratio conditions in order to determine the number of vortices generated for those flow configurations. These results are then compared to experimental measurements (Church, et al., 1979; Pauley, et al., 1982, Diamond, 1982) to validate the numerical model. The number of vortices produced is consistent with observational results made in the Purdue tornado vortex chamber. Furthermore, horizontal and vertical cross-sections are taken through the vortices to determine the structure of MVP. Preliminary results indicate that tangential velocities within these smaller asymmetric vortices increase by 20% over values observed in a single axisymmetric vortex at the same swirl ratio.

LIST OF FIGURES

FIGURE	TITLE	PAGE
1	Comparison between measurements in tornado vortex simulators at Oklahoma and Purdue Universities for centr l pressure deficit versus swirl ratio.	XXVII-9
2	Vertical (r-z) cross sections of non-dimensionalized variables for axisymmetric model after steady state is reached at S=0.5: (a) radial velocity, (b) vertical velocity, (c) tangential velocity, (d) pressure.	XXVII-11
3	Horizontal (r-θ) cross sections at surface (z=0) for S=0.5 at T=10: (a) tangential velocity, (b) pressure.	XXVII-12
4	Same as Figure 3, except at T=20.	XXVII-12
5	Same as Figure 3, except at T=30.	XXVII-14
6	Same as Figure 3, except at T=40.	XXVII-14
7	Vertical (r-z) cross sections for S=0.5 at T=40: (a) azimuthally averaged tangential velocity, (b) tangential velocity through center of vortex core.	XXVII-15
8	Same as Figure 7b, except (a) for S=0.5 at T=20, (b) for S=1.0 at T=20.	XXVII-15
9	Same as Figure 3, except for S=1.0 at T=20.	XXVII-17
10	Same as Figure 3, except for S=1.0 at T=30.	XXVII-17
11	Same as Figure 3, except for S=1.0 at T=40.	XXVII-18
12	Same as Figure 7, except for S=1.0 at T=40.	XXVII-18
13	Same as Figure 3, except for S=1.5 at T=20.	XXVII-20

LIST OF FIGURES

FIGURE	TITLE	PAGE
14	Same as Figure 3, except for S=1.5 at T=40.	XXVII-20
15	Same as Figure 7, except for S=1.5 at T=40.	XXVII-21
16	Same as Figure 3, except for S=3.0 at T=12.	XXVII-21

Introduction

Tornadoes have been reported on some occurrences to contain smaller secondary vortices. These subsidiaries vortices, sometimes called the multiple vortex phenomenon, or MVP (Church, et al., 1979), revolve around and rotate in the same direction as the parent vortex. Their importance are of more than just academic interest since damage surveys indicate that some of the most violent and destructive tornado damage in terms of loss of lives and property has been associated with such multiple vortices (Fujita, 1970; Fujita, 1974; Agee, et al., 1976).

Since observational studies of tornadoes have produced somewhat limited insights into such matters as the causal factors and structure of MVP, experimental and theoretical approaches have been utilized to investigate this phenomenon. Ward (1972) constructed a chamber to simulate tornado-like vortex flows. This model has demonstrated that a single vortex can subdivide into two or more vortices (MVP) under certain flow configurations. Davies-Jones (1973) has shown that the critical non-dimensional parameter for the Ward-type simulator is the swirl ratio (defined later). Leslie (1977) has reported values of critical swirl ratios at which the transition occurs between single to multiple vortices, as well as the transition to progressively larger numbers of multiple vortices, for both a smooth as well as a rough lower boundary surface. Experiments also have been conducted at Purdue University (Church, et al., 1979), in which the critical values of swirl ratios at which transition occurs was somewhat larger than those reported by experiments at Oklahoma University (Diamond, 1982). More recently there have been attempts to quantify the structure of laboratory generated tornado-like vortices, especially the velocity and surface pressure profiles (Baker and Church, 1979; Pauley, et al., 1982). Such measurements provide information about the horizontal and vertical structure of simulated vortices which can be applied to their atmospheric counterparts for which measurements are sparse.

Numerical experimentation also has proven very fruitful. Early efforts involving axisymmetric models of the Ward-type simulator (Harlow and Stein, 1974; Rotunno, 1977, 1979; Wilson, 1981; Smith, 1982) demonstrated that single columnar vortices could be simulated very well, comparing quite favorably with observations made in the experimental vortex chambers. An obvious limitation of such models, however, is that many aspects of tornado-like vortices, such as MVP, are highly asymmetric and cannot be simulated with an axisymmetric model. Rotunno and Lilly (1981) describe a three-dimensional, time-dependent model capable of reproducing asymmetric vortex motions as observed in a Ward-type chamber. In particular they have demonstrated that the MVP is a result of the development of strong radial shear in tangential and vertical velocities in an axisymmetric

vortex, that is unstable to azimuthal perturbations. Furthermore, they found that asymmetric vortices have tangential velocities approximately 20-30% higher than those found in the parent axisymmetic vortex and that these vortices have an intertwining helical structure tilting clockwise in the vertical.

This current investigation involves experiments using the Rotunno model in order to determine the importance of swirl ratio as an indicator of when transition will occur for producing multiple vortices. Since there is some disagreement between the laboratory measurements made at Purdue and Oklahoma Universities, utilization of numerical results could be quite revealing. Furthermore, we wish to examine the structure of these multiple vortices under different swirl conditions, focusing particularly on the pressure and velocities found in the subsidiary vortices. Such observations also will be compared with measurements made in tornado-like vortices generated in a laboratory chamber.

Description of the Model

The numerical model used in this investigation is described thoroughly by Rotunno (1983). In this section I will briefly mention only the primary features of the model and refer the reader to the aforementioned paper for additional details. The mathematical model is designed to simulate flow in a Ward-type vortex chamber as described by Ward (1972) or Church, et al. (1977). (Diagrams of these tornado vortex chambers are illustrated in these papers.)

The equations governing the flow are the momentum equations for each velocity component (radial, tangential and vertical) expressed respectively by

$$\frac{du}{dt} - \frac{v^2}{r} = - \frac{\partial p}{\partial r} + \frac{1}{R_e} F(u) \qquad (1)$$

$$\frac{dv}{dt} + \frac{uv}{r} = - \frac{1}{r} \frac{\partial p}{\partial \theta} + \frac{1}{R_e} I(v) \qquad (2)$$

$$\frac{dw}{dt} = - \frac{\partial p}{\partial z} + \frac{1}{R_e} H(w) \qquad (3)$$

and the continuity equation

$$\frac{1}{r} \frac{\partial}{\partial r} (ru) + \frac{1}{r} \frac{\partial v}{\partial \theta} + \frac{\partial w}{\partial z} = 0. \qquad (4)$$

(See Nomenclature section for definition of the symbols.)

The equations are given in cylindical coordinates (r,θ,z) and are non-dimensionalized (length by R; velocity by u_R; pressure by ρu_R^2; time by R/u_R). These equations are solved by specifying an initial value of u, v, w, and p and then marching forward in time with eq. (1) - (3) to obtain new values of u, v, w. A diagnostic equation for p is derived by taking the divergence of eq. (1)-(3) to yield

$$\nabla^2 p = \nabla \cdot \underset{\sim}{G} + \frac{\partial}{\partial t} (\nabla \cdot \underset{\sim}{V}), \qquad (5)$$

which is solved using u, v and w to compute p at each time step.

The boundary conditions are given by

(a) Lower boundary (z=0):

$$w = 0 \qquad \text{(closed)}$$

$$\frac{\partial u}{\partial z} = \frac{\partial v}{\partial z} = 0 \qquad \text{(free-slip)}$$

$$\frac{\partial p}{\partial z} = 0$$

(b) Upper boundary (z=Z):

$$u = v = 0 \qquad \text{(no - slip)}$$

$$\frac{\partial w}{\partial z} = 0 \qquad \text{(open)}$$

$$p = p\Big|_{r=0} - \int_0^r \left\{ w \frac{\partial u}{\partial z} - \frac{1}{R_e} \frac{\partial^2 u}{\partial z^2} \right\} dr$$

(c) Outer boundary (r=R):

$$u = \begin{cases} u_R & 0 < z < h \qquad \text{(open)} \\ 0 & h < z < Z \qquad \text{(closed)} \end{cases}$$

$$\begin{cases} v = v_R & 0 < z < h \qquad \text{(constant input rotation rate)} \\ \dfrac{\partial (rv)}{\partial r} = 0 & h < z < Z \qquad \text{(zero shear stress)} \end{cases}$$

$$\frac{\partial w}{\partial r} = \frac{\partial u}{\partial z} = 0 \qquad \text{(zero shear stress)}$$

$$\frac{\partial p}{\partial r} = \frac{v^2}{r} + F(u) - \frac{du}{dt}$$

(d) Inner boundary (r=a)*

$u = 0$ (zero flow across inner cylinder)

$\frac{\partial}{\partial r}\left(\frac{v}{r}\right) = \frac{\partial w}{\partial r} = 0$ (zero shear stress)

$\frac{\partial p}{\partial r} = \frac{v^2}{r} + F(u)$

The initial condition for the model is a steady-state, axisymmetric "sink-type" flow. Rotation is added axisymmetrically through the lower portion (z=h) of the lateral boundary, using

$$v = v_R \exp(-2t)$$

to simulate spin-up of the rotating screen in the vortex chamber. This axisymmetrically rotating condition is then allowed to achieve a steady state, which then becomes the initialized state for the three-dimensional model.

Objectives

The primary purpose of this study is to determine the effect of swirl ratios on the development of the multiple vortex phenomenon. In particular, it is the intent of this investigation to determine the number of vortices produced at various values of swirl ratio and compare these results with experiments conducted within Ward-type simulators at both Oklahoma and Purdue Universities. Also it is desired to examine the structure of the multiple vortices, especially the horizontal and vertical profiles of the velocity components and pressure and compare them with azimuthally averaged fields. Such information can provide valuable insights into the dynamics of natural tornado-vortices, especially those which produce MVP that are often associated with the most destructive tornadic activity.

Methodology

The Rotunno three-dimensional vortex model will be run using the CRAY-1 computer at the National Center for Atmospheric Research. The model will be initialized with a variety of flow configurations as specified by the non-dimensionalized parameter called swirl ratio (S). S, very simply is a ratio of azimuthal momentum to inflow momentum at some specified location in the chamber. More precisely, it is defined by

*Not necessary, but to permit a larger time step for computional stability a cylinder (r=a) is used to prevent r from becoming too small.

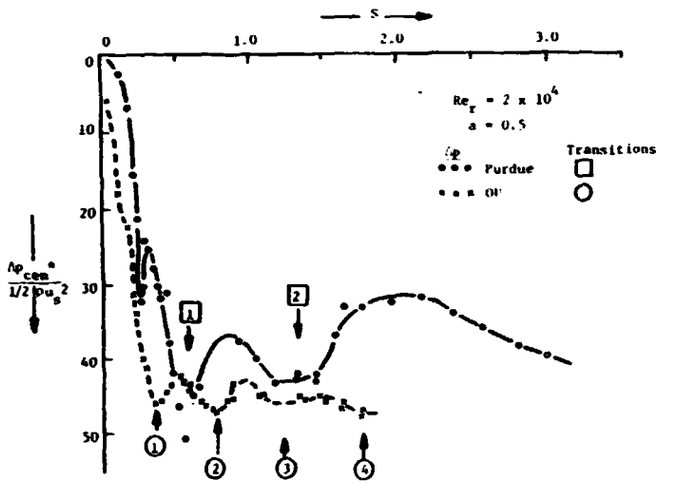

Figure 1. Comparison between measurements in tornado vortex simulators (Oklahoma and Purdue Universities) for central pressure deficit versus swirl ratio. For transition number markers, 1 indicates transition between one and two vortices. (Diagram taken from Diamond, 1982.)

$$S = \frac{R\Gamma_R}{2Q} = \frac{Rv_R}{2hu_R} \qquad (6)$$

where the variables, measured at the lateral boundary (r=R), are specified as constant. The swirl ratios utilized in this study are S=0.5, 1.0, 1.5, and 3.0. These values of swirl ratio are near the critical values at which transition occurs for producing multiple vortices in the Oklahoma and Purdue University vortex chambers. As mentioned previously the critical values cited for the Oklahoma simulator are somewhat higher than those of the Purdue chamber. These numerical experiments can shed light on the discrepancy and help determine the critical swirl ratios for transitions to progressively larger numbers of multiple vortices.

The structure of the multiple vortices will also be investigated. Both horizontal and vertical cross sections of the velocity components and pressure will be examined. In particular, we will focus on slices through the core of the vortices, as indicated by the values of maximum tangential velocity. The velocity and pressure profiles will be analyzed for several swirl ratios in order to determine structural variations as the intensity of the vortex is changed. These profiles will also be compared to the azimuthally averaged fields to determine the structural differences between the asymmetric vortex and the overall rotating environment from which they are generated. Such comparisons should provide valuable insights into the dynamics of tornado-like vortices.

Results

The model was run for four values of swirl ratio (S=0.5, 1.0, 1.5, 3.0). These values were chosen based upon a comparison of experimental results (Fig. 1) from the Oklahoma University and Purdue University simulators (Diamond, 1983). The value of S=0.5 lies near the point of transition occurrence (from one to two vortices) for the two tornado simulators (note the Oklahoma chamber has two vortices for this swirl ratio, while the Purdue chamber still has one). Similarly, S=1.0 is near the transition point for two to three vortices, and S=1.5 is near the next transition point. A case with S=3.0 was also run to determine if higher numbers of vortices (N=4,5 or 6) might be produced.

Case 1 (S=0.5):

At low swirl ratio one expects a single columnar vortex which is very nearly axisymmetric. Visual observations in Ward-type simulators indicate that as S approaches 0.5 the flow becomes increasingly complex and eventually the single vortex divides into two smaller vortices each rotating about the central vertical axis. This case simulates flow very near this critical transition point between one and two vortices.

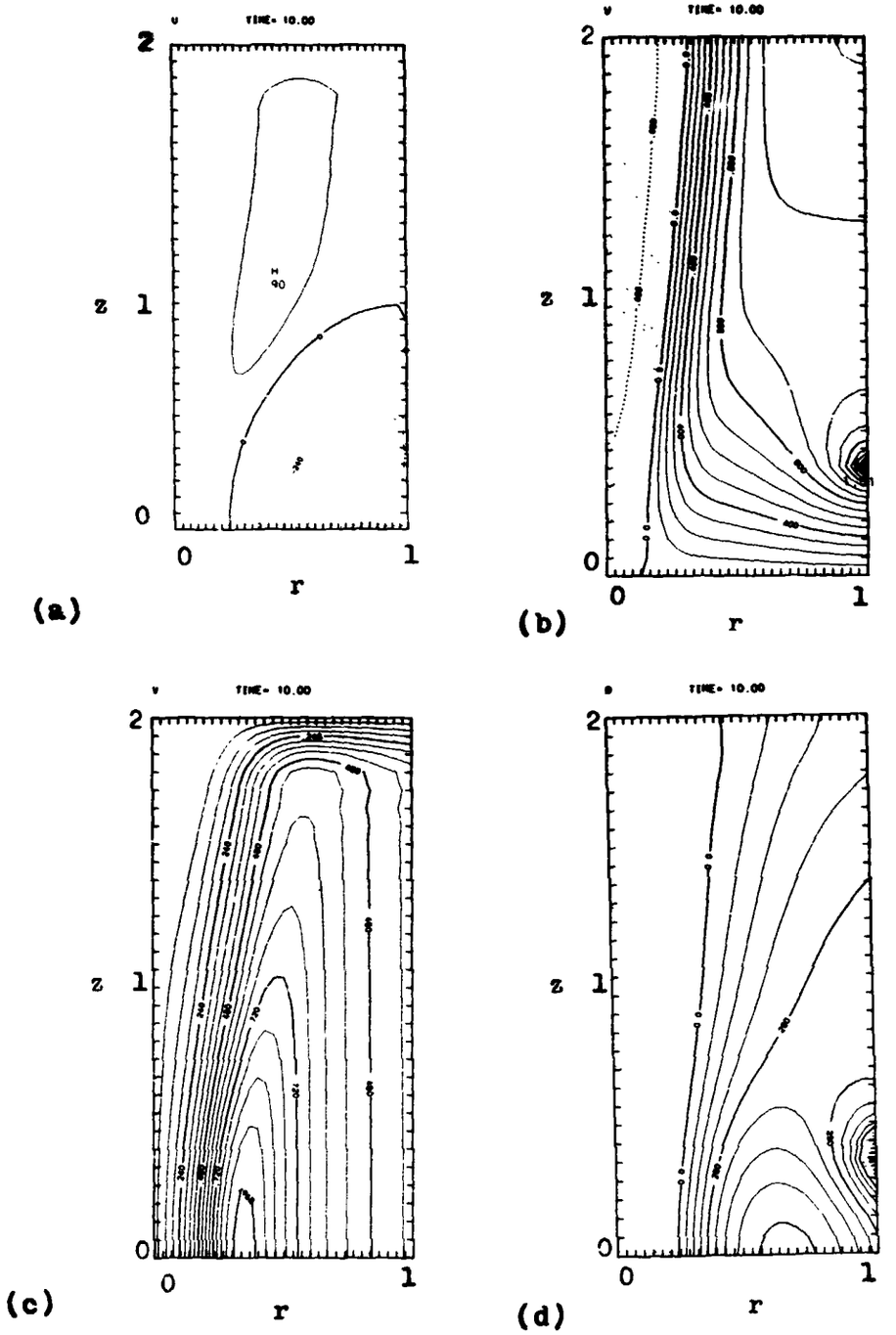

Figure 2. Vertical (r-z) cross-sections of non-dimensional variables for axisymmetric model after steady state is reached for S=0.5: (a) radial velocity (contour interval = 60, values scaled by 1000); (b) vertical velocity (contour interval = 0.1); (c) tangential velocity (contour interval = 0.06); (d) pressure (contour interval =0.07). Dashed lines indicate negative values.

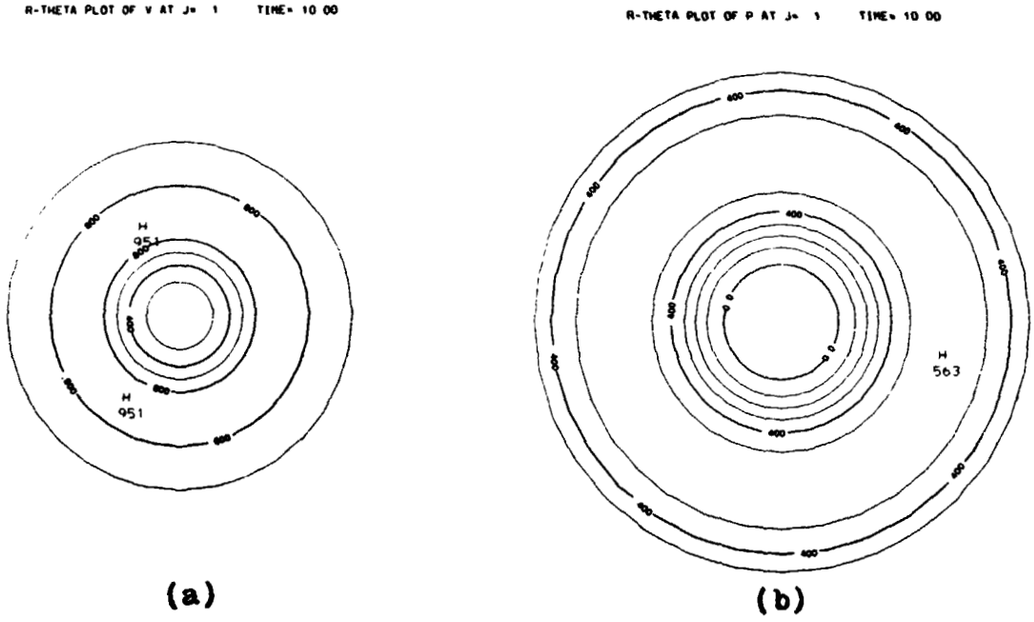

Figure 3. Horizontal (r-θ) cross-sections at surface (z=0) for S=0.5 at T=10: (a) tangential velocity (contour interval = 0.2); (b) pressure (contour interval = 0.1).

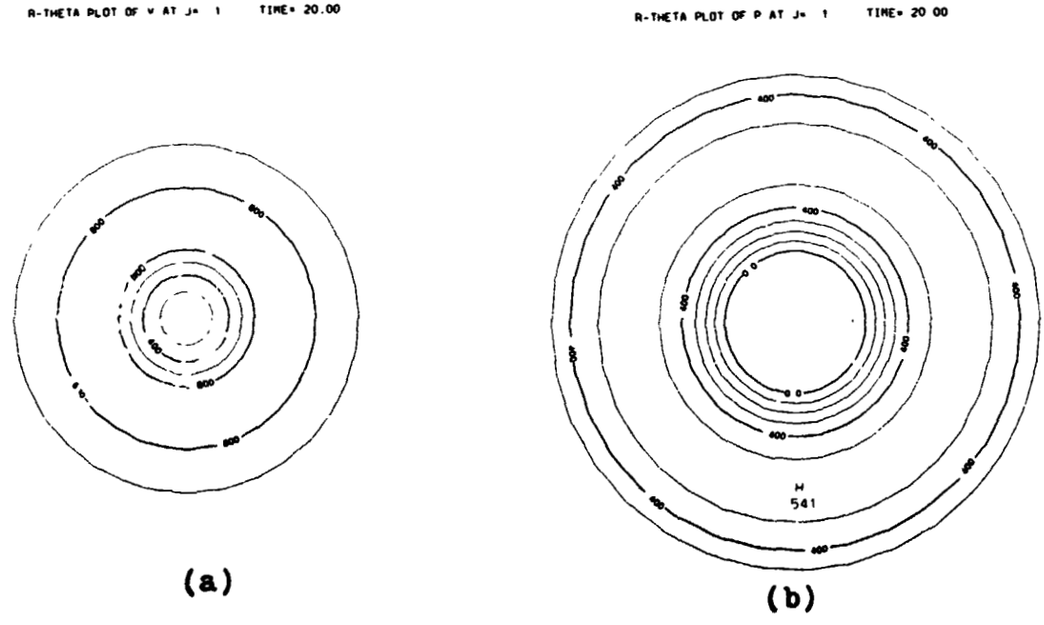

Figure 4. Same as Fig. 3, except at T=20.

As mentioned earlier the initial state of the model is generated by using an axisymmetric version of the code. A single axisymmetric vortex is allowed to reach a steady state condition, which in turn provides initial values of u, v, w, and p used by the three dimensional model.

Figure 2 shows vertical (r-z) cross sections of the pressure and velocity components from the axisymmetric model after steady state has been reached for S=0.5. This is a single columnar vortex with the two-cell structure. The maximum tangential velocity (v_{max}) is located along the lower boundary at approximately r=0.4R. (This position of maximum tangential velocity is referred to as the core radius, r_{max}.) Inside the vortex ($r<r_{max}$) the flow is directed radially outward (u>0) and downward (w<0), while outside the flow is inward (u<0) and upward (w>0), hence the two-celled structure. Within the vortex core there is a marked pressure deficit with the pressure minimum located on the lower boundary along the central axis of the vortex. Examination of the v-field reveals that this vortex satisfies the Rayleigh stability criteria

$$\frac{d\Gamma^2}{dr} > 0$$

and hence will remain stable to axisymmetric disturbances.

This axisymmetric vortex is allowed to continue undisturbed for a period of time. At T=6.0 (non-dimensional time units) however, a single, randomly-generated perturbation is introduced into the v-field. Figure 3 shows that shortly after the flow has been disturbed (T=10) the v- and p-fields are still essentially axisymmetric near the lower boundary. Even at T=20 (Fig. 4) there is little if any noticeable asymmetries in the vortex. The only observable change through this period is a gradual concentration of the vortex toward the central axis with an accompanying increase in tangential velocity and decrease of pressure within the vortex core.

However, by T=30 (Fig. 5) there is a distinctly asymmetric appearance to the vortex as the maximum tangential velocity contour (v=1.0) is cresent-shaped compared with previously concentric circles bounding the region of maximum rotation. The maximum v value of 1.05 is approximately 13% higher than that at its reflection point in this plot. Furthermore, this represents an increase of a factor of 2.65 over the input value (v_R=0.4) at the lateral boundary as the angular momentum of the intruding rotating air parcels is conserved. The pressure field has a similar asymmetry with a maximum presssure deficit (p=-0.3.88) located just off the central axis.

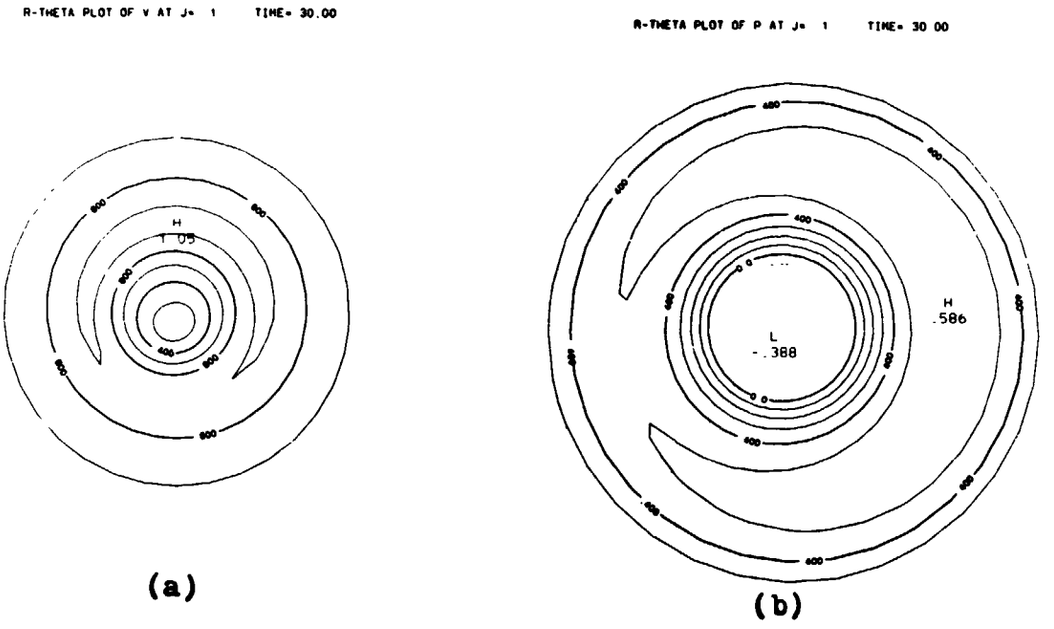

Figure 5. Same as Fig. 3, except at T=30.

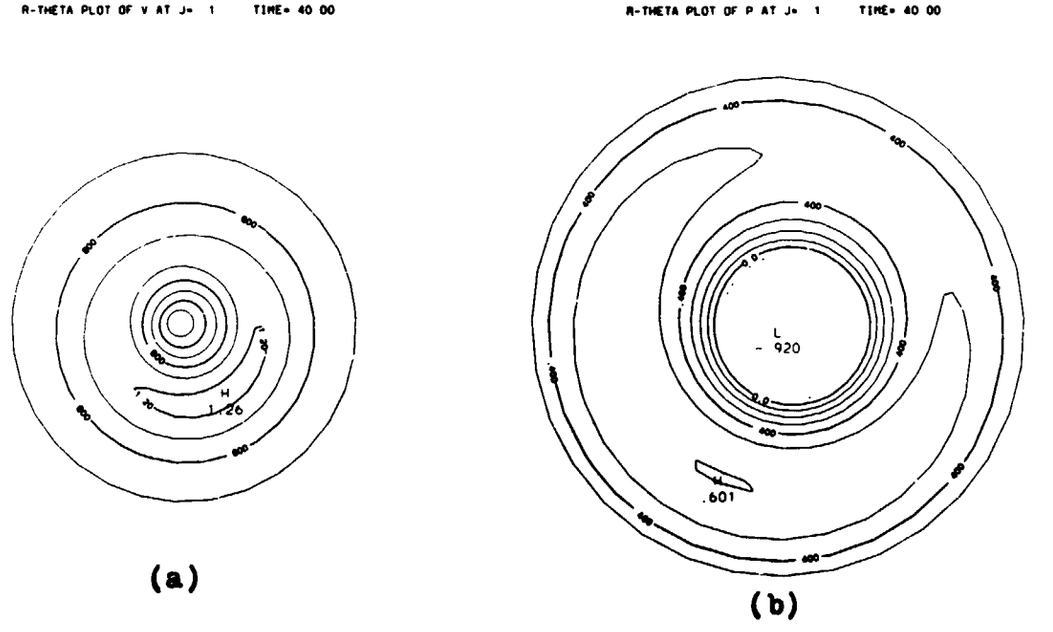

Figure 6. Same as Fig. 3, except at T=40.

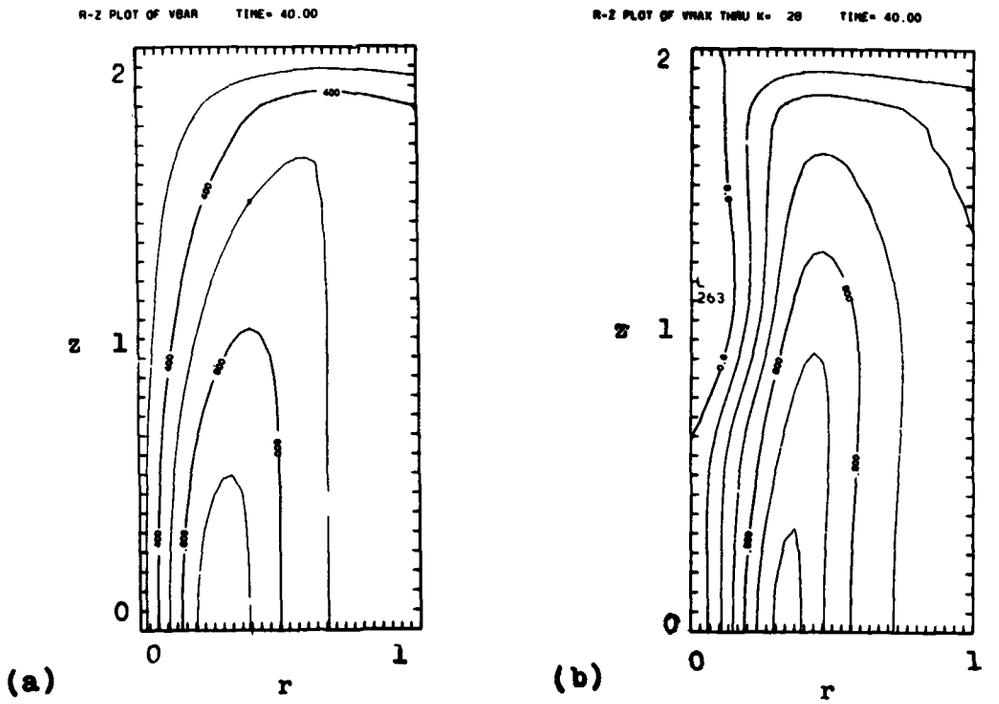

Figure 7. Vertical (r-z) cross-sections for S=0.5 at T=40: (a) azimuthally averaged tangential velocity (contour interval = 0.2); (b) tangential velocity through vortex core (contour interval = 0.2).

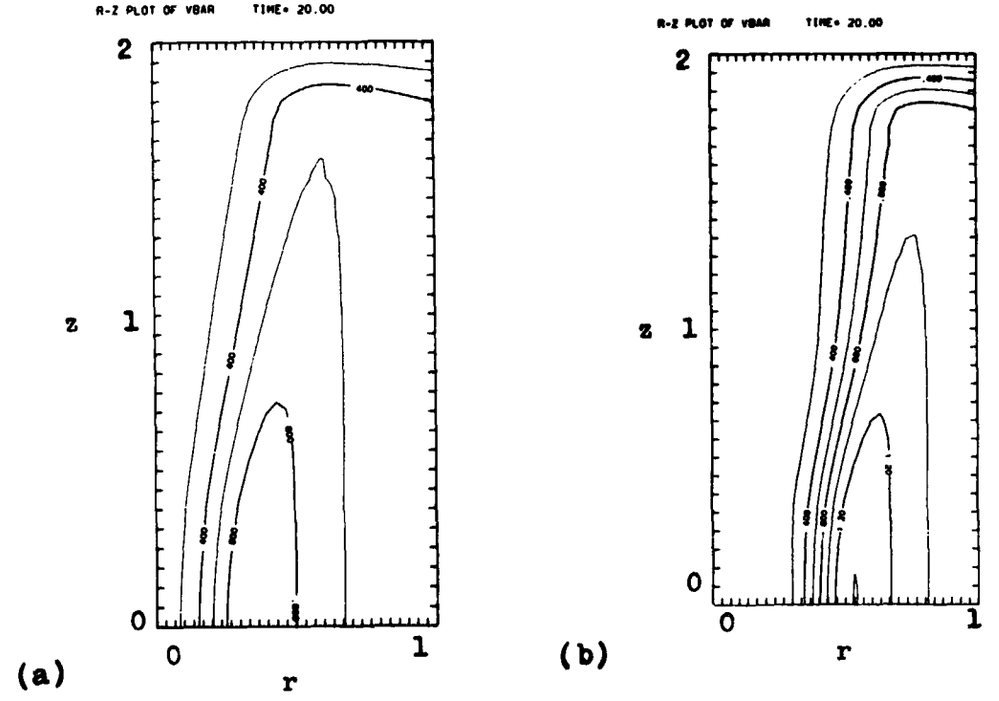

Figure 8. Same as Fig. 7b, except (a) for S=0.5 at T=20; (b) for S=1.0 at T=20.

At T=40 the vortex retains its asymmetric pattern (Fig. 6) with the maximum tangential velocity having increased to 1.26 and the pressure minimum having decreased to -0.920. Although the vortex is asymmetric, the radial shear of the tangential velocity is apparently not strong enough to produce MVP.

The vertical structure of the vortex is also quite interesting. Figure 7a gives a vertical cross-sectional view of the azimuthally averaged tangential velocity ($\bar{v}$). Such a plot strongly resembles the r-z distribution of v from an axisymmetric vortex model. Such a depiction of the tangential velocity field gives the impression of a smooth, laminar vortex whose core expands with height, not unlike the idealized stereotypical cone-shaped columnar tornado vortex. Figure 7b, on the other hand, gives the vertical cross section along the azimuth intersecting the point of maximum tangential velocity within the vortex. While the vortex continues to expand outward as one progresses upward, there is a definite tilt to its vertical axis as illustrated by the negative v-value along the upper central axis. This is consistent with the observations of actual tornadoes which often have a tilted appearance in their upper regions (near the ban of the parent thunderstorm). Rotunno (1983) has represented this conceptually and noted that vortex lines tilt clockwise with height. Another feature of note is v_{max} is approximately 20% higher than the maximum azimuthally averaged value ($\bar{v}_{max}$). Consequently, there is considerably more complexity to this asymmetric vortex.

There was little significant change in the vortex beyond this point, the vortex did not generate MVP during the period of integration.

Case 2: (S=1.0)

Observational studies (Leslie, 1977; Church et al., 1979) indicate that a higher swirl ratio the single vortex will become unstable due to the strong radial shear in the tangential and vertical velocity fields and generate MVP. A comparison of the azimuthally averaged tangential velocity fields at T=20 for S=0.5 (Fig. 8a) and S=1.0 (Fig. 8b) reveals a stronger radial gradient in v at the higher swirl ratio. This region (r=0.3R to 0.6R) of maximum radial gradient is where the multiple vortices should develop. Horizontal (r-θ) plots of tangential velocity (Fig. 9a) and pressure (Fig. 9b) verify that two vortices are well-established by T=20. Each subsidiary vortex is depicted by a high-low couplet in the tangential velocity field and is centered on the low in the pressure field. Each vortex revolves around the central axis with the mean flow velocity, but also rotates about its own axis, thereby contributing to the maximum value of v (to the outside) and the minimum value (to the inside) for each couplet in the v-field.

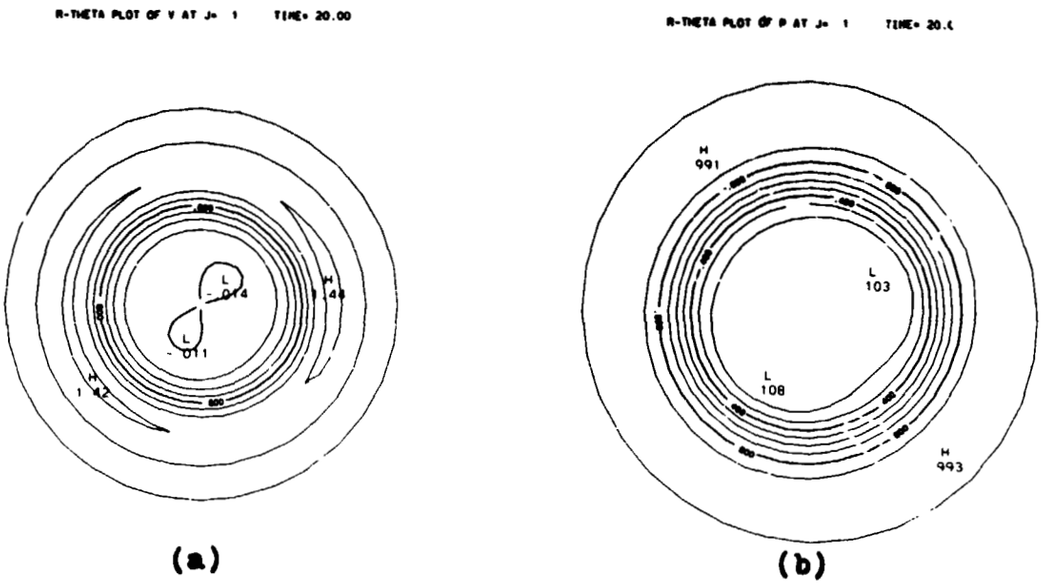

Figure 9. Same as Fig. 3, except for S=1.0 at T=20.

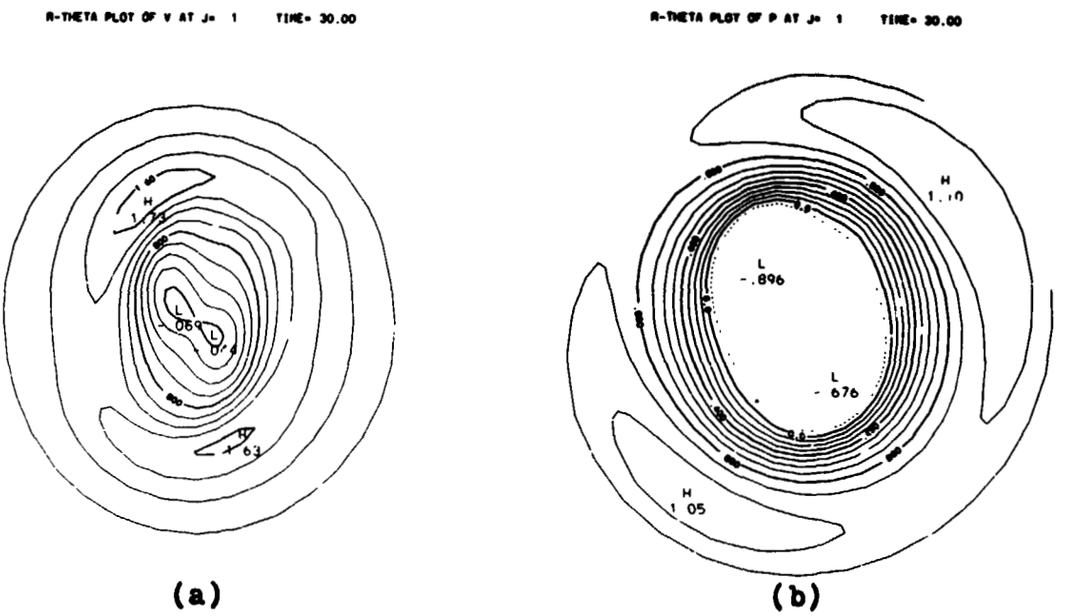

Figure 10. Same as Fig. 3, except for S=1.0 at T=30.

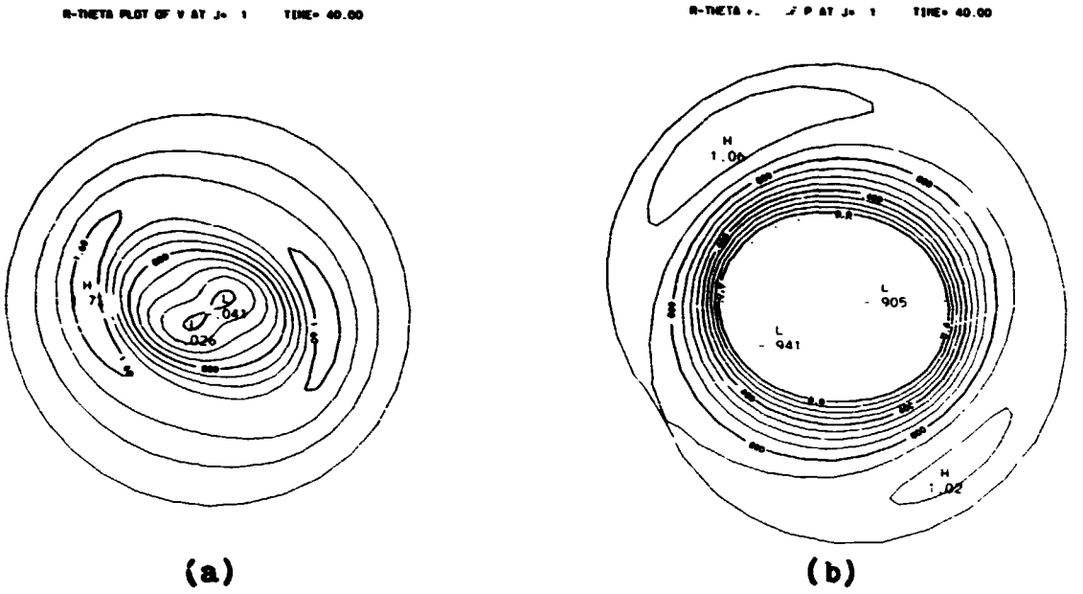

Figure 11. Same as Fig. 3, except for S=1.0 at T=40.

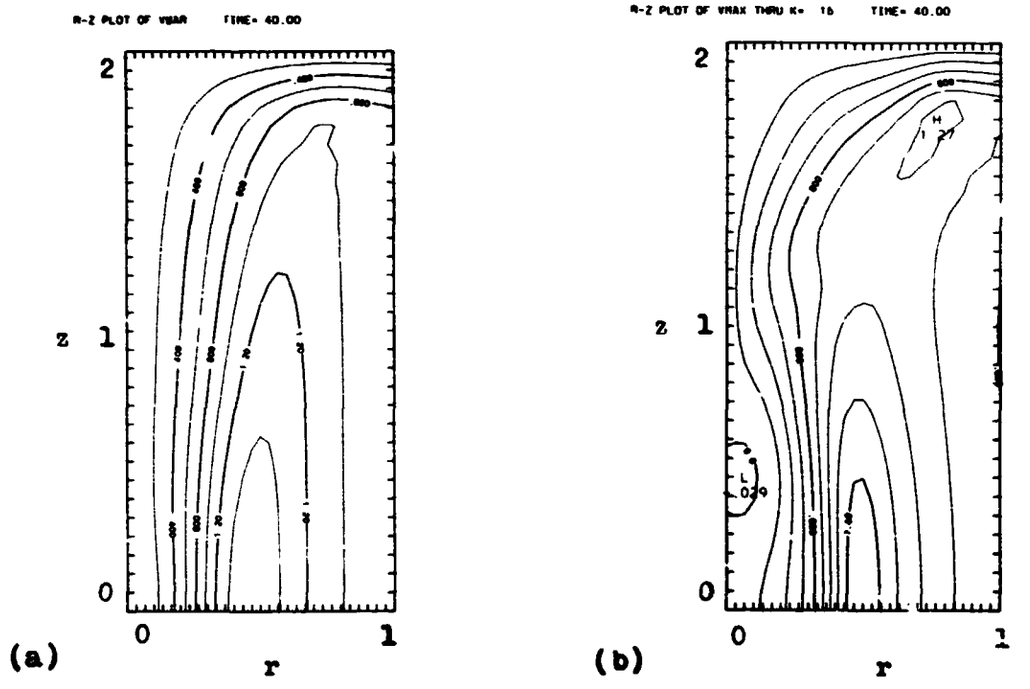

Figure 12. Same as Fig. 7, except for S=1.0 at T=40.

The vortices continue to intensify through T=30, with v_{max}=1.73 (Fig. 10a) having increased by about 20% during this period. It is interesting to note that the two vortices are not equal in intensity, not only for v_{max} but for the central pressure deficit as well. Both surface pressure minima (Fig. 10b) continue to fall as the vortices intensify.

The two vortices persist through the remainder of the integration period (T=40). The tangential velocities (Fig. 11a) are essentially unchanged in magnitude during this final time segment, as the vortices continue to rotate about the central axis. The pressure (Fig. 11b) within these vortices continue to fall with both minima less than -0.9 within the core. It is interesting to note that while the maximum tangential velocities in the subsidiary vortices are nearly 40% higher than those found in the single vortex at S=0.5, the surface pressure deficits are approximately equal for these two swirl cases. Surface pressure measurements made in the Purdue tornado simulator by Pauley, et al. (1982) show that the maximum pressure deficit occured at S=0.45 very near the transition point from a single vortex to a pair of subsidiary vortices. There is a notable drop in these surface pressure measurements associated with penetration of the vortex breakdown to the surface. There was no attempt to verify this phenomenon in this experiment.

The vertical cross-section of $\bar{v}$ (Fig.12a) strongly resembles its lower swirl counterpart (Fig. 7a), except for the obviously larger values of $\bar{v}$ throughout the domain and the stronger radial gradients, especially within the vortex core. The position of v_{max} is also displaced further outward in the radial direction than in the lower swirl case.

The vertical cross-section through v_{max} (Fig. 12b) has some interesting features. The negative v values are located lower along the central axis than for the lower swirl case. Furthermore, the positive contours above are bulging back toward the central axis (as opposed to a gradual spreading outward as seen in the $\bar{v}$ field). This indicates that the subsidiary vortices have a helical structure in the vertical, which tilt clockwise with height. Rotunno (1983) has explained this tilt as an result of the upper boundary (which reduces vertical vorticity to zero) interacting with the vortex lines in the domain.

Consequently, the subsidiary vortices have a more complicated structure with higher maximum tangential velocities located at a greater radial distance from the central axis than the single vortex. Furthermore the occurrence of two vortices is consistent with the observations in the Purdue simulator for S=1.0.

Case 3: (S=1.5)

As swirl ratio increased further one would expect continued intensification of the vortices, and perhaps transition to even larger number of vortices. Fig. 13 shows three distinct vortices in the tangential velocity and pressure fields at T=20. While v_{max} is nearly

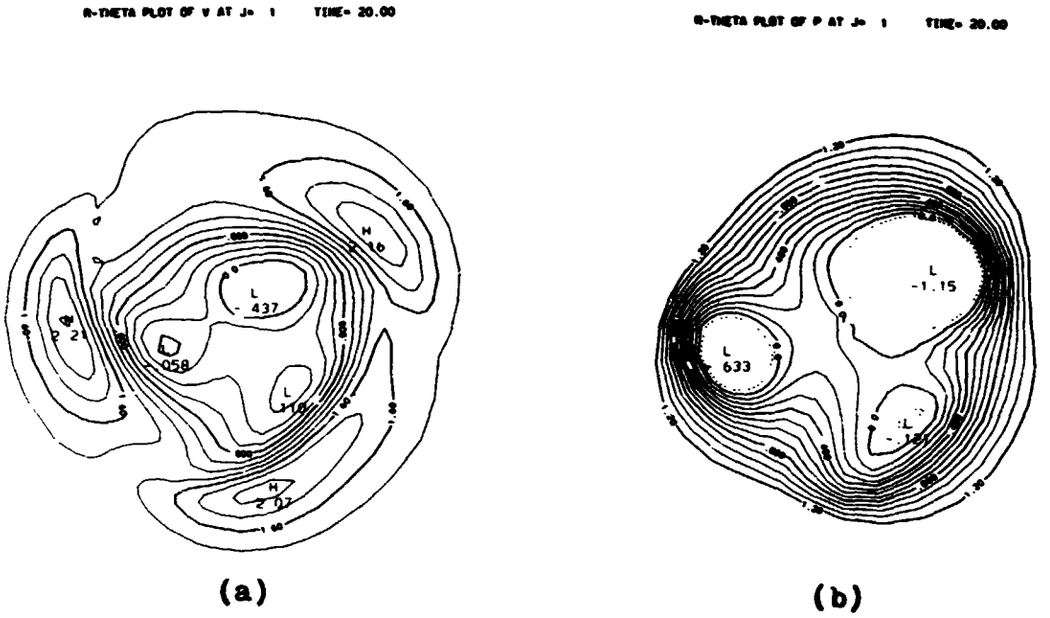

(a) (b)

Figure 13. Same as Fig. 3, except for S=1.5 at T=20.

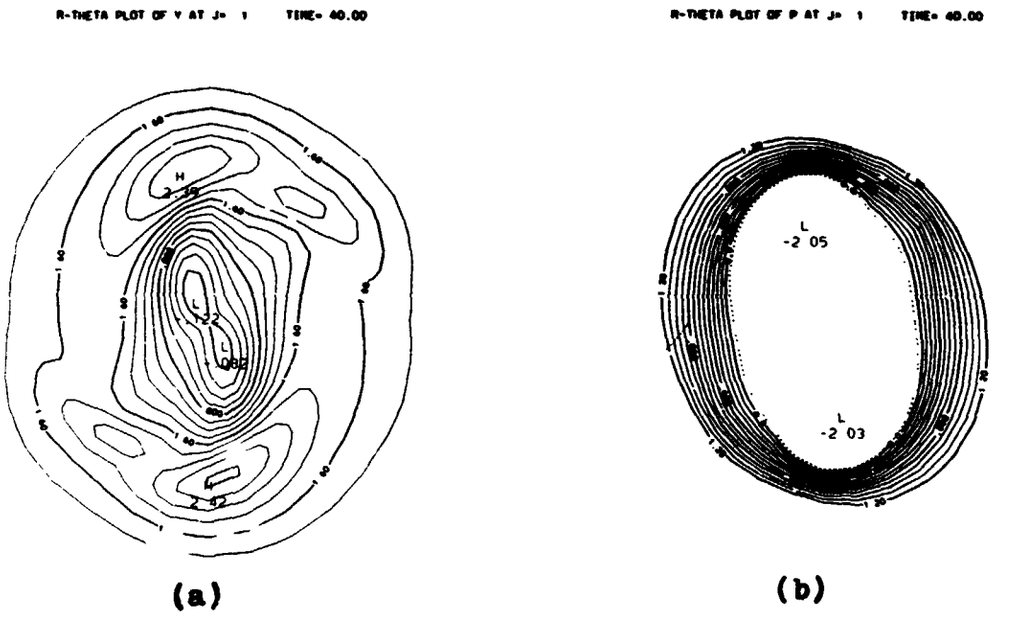

(a) (b)

Figure 14. Same as Fig. 3, except for S=1.5 at T=40.

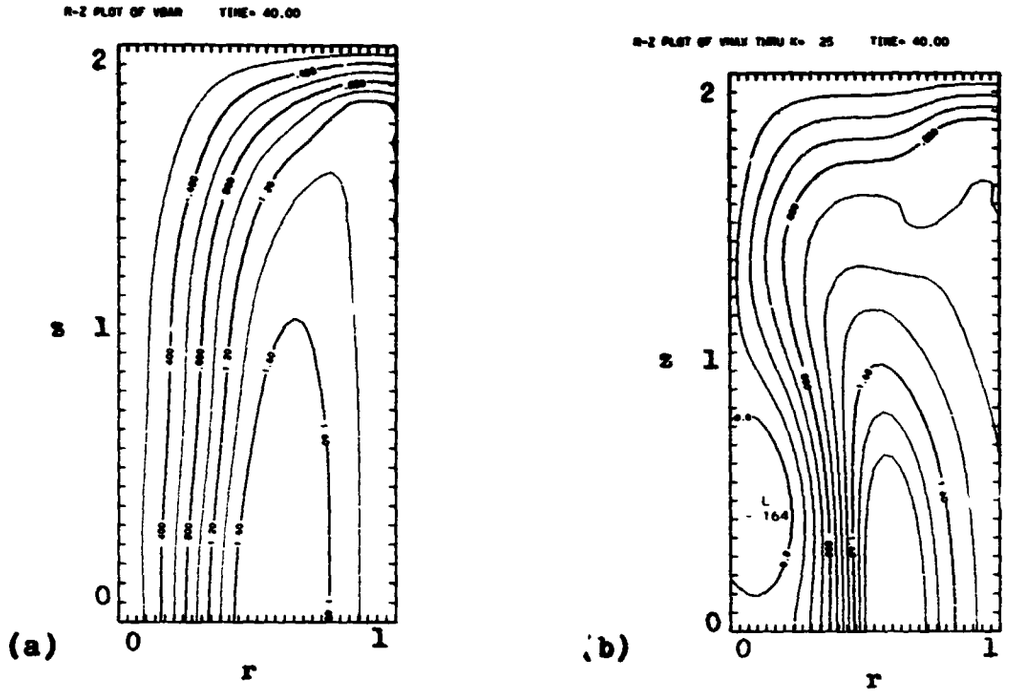

Figure 15. Same as Fig. 7, except for S=1.5 at T=40.

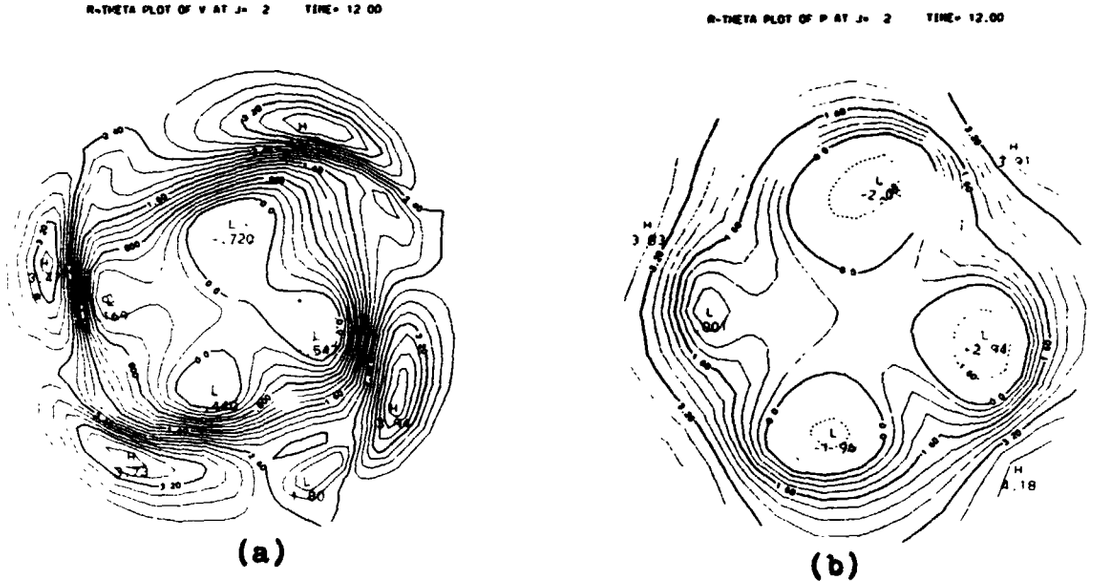

Figure 16. Same as Fig. 3, except for S=3.0 at T=12: (a) contour interval = 0.2; (b) contour interval = 0.4.

equal for all three vortices, there is marked variability in the pressure deficits. The vortex with the smallest pressure deficit suggests that it is weakening, and may not sustain itself for the duration of the integration period.

By T=40 the flow has been restored to a two vortex configuration. The maximum tangential velocity (Fig. 14a) has increased to approximately 2.4 in both vortices, located at a slightly larger radius (r=0.62R) than in the lower swirl case (e.g., r=0.56R for S=1.0). This is to be expected as Davies-Jones (1973) has shown for a single axisymmetric vortex, the core radius increases with swirl ratio. Since the subsidiary vortices form in the region of maximum radial gradient of tangential velcoity which is found just inside the core radius of the parent single vortex, one would expect the locations of the subsidiary vortices to expand outward with increasing swirl ratio as well.

The central pressure deficits (Fig. 14b) at T=40 are approximately -2.0 in each vortex, which is approximately twice the value found for S=1.0. The magnitude is somewhat surprising but Pauley, et al. (1982) found surface pressure deficit increasing with swirl ratio for S>1.6.

The r-z cross-section of v through the vortex (Fig. 15a) and $\bar{v}$ (Fig. 15b) are similar to their counterparts for S=1.0 except for larger magnitudes. Again the tangential velocity field suggests a tilted vortex and v_{max} is approximately 20% larger than the highest value in the averaged field.

The maximum number of vortices generated was three for S=1.5, as observed in the Purdue vortex chamber, although we see that during the integration one vortex dissipates. Rotunno and Lilly (1983) found similar results, whereas the laboratory vortices appear to be more stable. A probable explanation for the demise of the weaker vortex is that the viscosity used by the numerical model is larger than in the chamber (R_e = 150 is at least one order of magnitude less than that cited for the laboratory measurements). Consequently, frictional forces may be eroding the vortices.

Case 4: (S=3.0)

The primary purpose of this run was to determine the number of vortices generated at this swirl ratio. At T=12 there are four vortices clearly discernible in both the tangential velocity (Fig. 16a) and pressure (Fig. 16b) fields. The centers of v_{max} were located near the lateral boundary (r=0.81R). The pressure minimum clearly indicates that three of the vortices are much more intense than the fourth, and in a short time this vortex will dissipate. There is little of additional interest in this case that has not already been addressed in the other cases t lower swirl ratios.

Table 1 Summary of Experiments

S	N_{max}	r_{max}	V_{max}	V_{max}/V_R	P_{min}
0.5	1	0.38	1.26	3.16	-0.92
1.0	2	0.56	1.77	2.22	-0.94
1.5	3	0.62	2.61	2.18	-2.05
3.0	4	0.81	4.64	1.94	-3.40

(N.B. All experiments were run at R_e=150 with a free slip lower boundary condition. The inner cylinder had a radius r=0.02R, while the depth of the inflow layer h=0.4 Z, where R=1 and Z=2. Each case was run for 40,000 time steps with Δt=.001).

Summary and Conclusions

A three-dimensional numerical model for tornado-like vortices is run for four cases in which swirl ratio varies over the range of 0.5 to 3.0. The unique aspect of the model is that it is capable of producing asymmetric vortices and, at sufficiently large swirl ratio, can generate multiple vortices. The values of swirl ratio were chosen for these experiments based upon the transition points for single to multiple vortex occurences as well as for progressively higher numbers of vortices.

For comparative purposes Table 1 summarizes pertinent numerical results for each experiment. The principal findings of this investigation include:

(1) The maximum number of vortices increases as the swirl ratio increases. For the swirl ratios examined the number of vortices produced is consistent with laboratory results. Furthermore, there appeared to be closer correlation with the transition points of the Purdue tornado vortex chamber than the one at Oklahoma University. A note of caution is needed, however, since the value of radial Reynolds number (R_e) used in the numerical experiments was smaller than in the laboratory studies due to numerical stability considerations. Also the final number of vortices was less than the maximum number observed in the numerical experiments, probably due to erosion of weaker vortices by frictional forces.

(2) The maximum tangential velocity (v_{max}) observed within the computational domain increased with increasing swirl ratio. Part of this can be attributed to the larger input of tangential velocity at the lateral boundary. It is also due to the ability of the vortex to achieve a smaller radius of rotation. At higher swirl ratio the vortex becomes unstable due to the radial shear of tangential velocities, progressively generating increasing numbers of subsidiary vortices, each with a smaller radius of rotation than the present vortex. The maximum tangential velocity of the subsidiary vortices is approximately 20% higher than the azimuthally averaged tangential velocity within the domain.

(3) The location (r_{max}) of the maximum tangential velocity moves progressively outward at higher swirl ratio. This is consistent with findings of Davies-Jones who found that the core radius of single axisymmetric vortices increased with swirl ratio. Since the subsidiary vortices from in the region of maximum radial shear of v, which occurs just within the core radius, one would expect to find

the subsidiary vortices at progressively larger radii as S increases.

(4) P_{min} decreases as S increases. Since vortices tend to approach cyclostrophic balance, as v_{max} increases, one expects P_{min} to decrease. Experimental measurements have shown that for S>1.6, P_{min} decreases in the subsidiary vortices. However, observations also show the lowest central surface pressure was found at the swirl ratio associated with the penetration of vortex breakdown to the surface of the chamber. This phenomenon was not verified by these numerical experiments.

(5) Comparisons of vertical (r-z) cross-sections of v through the center of the vortex and azimuthally averaged v indicate marked asymmetry of the structure of the vortices. The $\bar{v}$ plots show a smooth cone-shaped vortex structure which gradually widens with height. The plot show regions of negative values especially along the central axis indicating a tilting of the axis of the subsidiary vortices. Rotunno has shown this vertical structure to be a helical patterns, turning in a clockwise direction with height. These results show the helical angle to become sharper at higher swirl ratio.

Continued investigation of multiple vortices is still necessary to more fully understand their structure. Additional comparative studies between numerical and laboratory researchers will greatly enhance our knowledge about tornado dynamics. One area of future work that could prove beneficial would be to study trajectories in the fluid by inserting parcels as tracers into the flow field. Another suggestion would be to improve treatment of the boundary layer. However, to do this would require more computationally efficient numerical techniques to reduce runtime. For example, implicit schemes which are absolutely stable could be used to permit use of a longer time step. This would allow more calculations devoted to the physics of the problem rather than to just the time marching process at small time steps.

NOMENCLATURE

Symbols	Definition
a	Non-dimensional radius of a fictitious inner cylinder
$F(u)$	Diffusion term for u-velocity component
$\underset{\sim}{G}$	Vector expression for advection and diffusion of velocity
$H(w)$	Diffusion term for w-velocity component
h	Height of top of inflow layer
$I(v)$	Diffusion term for v-velocity component
N_{max}	Maximum number of vortices produced at S
P	Pressure (non-dimensionalized by ρu_R^2)
P_{min}	Pressure minimum in center of vortex
Q	Volume flow rate through chamber
R	Radius at lateral boundary (R=1)
r	Radial coordinate (non-dimensionalized by R)
r_{max}	Radius at which v_{max} occurs
R_e	Radial Reynolds number
S	Swirl ratio
T	Time (non-dimensionalized by R/u_R)
t	Time coordinate (non-dimensionalized by R/u_R)
u	Radial velocity (non-dimensionalized by u_R)
u_R	Inflow velocity at r=R
$\underset{\sim}{V}$	Total velocity vector
v	Tangential velocity (non-dimensionalized by u_R)
$\bar{v}$	Azimuthally averaged value of v
v_{max}	Maximum value of v within vortex
$\bar{v}$	Maximum value of $\bar{v}$
v_R	Tangential velocity at r=R
w	Vertical velocity (non-dimensionalized by u_R)
Z	Height at top boundary (Z=2)
Γ	Circulation
θ	Azimuthal coordiante
ρ	Fluid density

REFERENCES

1. Agee, E.M., J.T. Snow and P.R. Clare, 1976: Multiple Vortex Features in the Tornado Cyclone and the Occurrence of Tornado Families. Mon. Wea. Rev., 104, 552-563.

2. Baker, G.L. and C.R. Church, 1979: Measurements of Core Radii and Peak Velocities in modeled Atmospheric Vortices. J. Atmos. Sci., 36, 2413-2424.

3. Church, C.R., J.T. Snow and E.M. Agee, 1977: Tornado Vortex Simulation at Purdue University. Bull. Amer. Meteor. Soc., 58, 900-908.

4. Church, C.R., J.R. Snow, G.L. Baker and E.M. Agee, 1979: Characteristics of Tornado-Like Vortices as a Function of Swirl Ratio: a Laboratory Investigation. J. Atmos. Sci., 36, 1755-1776.

5. Davies-Jones, R.P., 1973: The Dependence of Core Radius on Swirl Ratio in a Tornado Simulator. J. Atmos. Sci., 30, 1427-1430.

6. Diamond, C., 1982: Laboratory Simulation of Tornado-like Vortices under the Effects of Translation. M.S. Thesis, Univ. of Okla., Norman, OK, 75pp.

7. Fujita, T.T., 1970: The Lubbock Tornadoes: A Study of Suction Spots. Weatherwise, 23, 161-173.

8. Fujita, T.T., 1976: History of suction vortices. Proc. of the Symposium on Tornadoes, Texas Tech Univ., Lubbock, TX, 28-88.

9. Harlow, F.H. and L.R. Stein, 1974: Structural Analysis of Tornado-like Vortices. J. Atmos. Sci., 31, 2081-2098.

10. Leslie, F.W., 1977: Surface Roughness Effects on Suction Vortex Formation: A laboratory simulation. J. Atmos. Sci., 34, 1022-1027.

11. Pauley, R.L., C.R. Church and J.T. Snow, 1982: Measurements of Maximum Surface Pressure Deficits in Modeled Atmospheric Vortices. J. Atmos. Sci., 39, 369-377.

12. Rotunno, R., 1977: Numerical Simulation of a Laboratory Vortex J. Atmos. Sci., 34, 1942-1956.

13. Rotunno, R., 1979: A Study in Tornado-like Vortex Dynamics. J. Atmos. Sci., 36, 140-155.

14. Rotunno, R., 1983: An Investigation of a Three-Dimensional Asymmetric Vortex. (Submitted for publication to J. Atmos. Sci.).

15. Rotunno, R. and D.K. Lilly, 1981: A Numerical Model Pertaining to the Multiple Vortex Phenomenon. Final Report to U.S. Nuclear Regulatory Commission, NTIS#NUREG/CR-1840, 51 pp.

16. Smith, D.R., 1982: Comparative Studies of Tornado-like Vortices. Proceedings of the International Conf. on Computational Methods and Experimental Measurements, Washington, D.C., 141-150.

17. Ward, N.B., 1972: The explanation of Certain Features of Tornado Dynamics using a Laboratory Model. J. Atmos. Sci., 49, 1194-1204.

18. Wilson, T.L., 1981: Vortex Boundary Layer Dynamics. M.S. Thesis, Univ. of California, Davis, 139pp.

ACKNOWLEDGEMENT

I wish to extend my gratitude to Dr. Richard Rotunno, National Center for Atmospheric Research for allowing me to use this numerical model and securing the computer resources to perform the experiments. Also, I would like to extend my sincerest appreciation to Dr. Fred W. Leslie for his support and collaboration throughout this summer program.

1983

NASA/ASEE SUMMER FACULTY RESEARCH FELLOWSHIP PROGRAM

Marshall Space Flight Center
The University of Alabama in Huntsville

DETERMINATION OF SYSTEMS SUITABLE FOR STUDY AS MONOTECTIC BINARY METALLIC ALLOY SOLIDIFICATION MODELS

Prepared By: James E. Smith, Jr., PhD

Academic Rank: Assistant Professor

University & Department: University of Alabama in Huntsville
Department of Mechanical Engineering/
Chemical Engineering Program

NASA/MSFC
Laboratory: Space Science Laboratory
Division: Space Processing Division
Branch: Solid State Branch

MSFC Counterpart: Donald O. Frazier, PhD

Date: August 8, 1983

Contract No: NGT 01-008-021
The University of Alabama in Huntsville

DETERMINATION OF SYSTEMS SUITABLE FOR STUDY AS MONOTECTIC BINARY METALLIC ALLOY SOLIDIFICATION MODELS

By

James E. Smith, Jr.
Assistant Professor of Chemical Engineering
The University of Alabama in Huntsville
Huntsville, Alabama 35899

ABSTRACT

Succinonitrile-water and diethylene glycol-ethyl salicylate are two transparent systems which have been studied as monotectic binary metallic alloy solidification models. Being transparent, these systems allow for the direct observations of phase transformations and solidification reactions. There is a need to expand the number of these transparent binary models to distinguish both the unique and general phenomena for generalization to metallic systems. The objective of this work was to develop a screening technique to find systems of interest and then experimentally measure those systems. The succinonitrile-water system was used to check the procedures.

To simulate the phase diagram of the system, two computer programs which determine solid-liquid and liquid-liquid equilibria were obtained. These programs use the UNIFAC method to determine activity coefficients and together with several other programs were used to predict the phase diagram. An experimental apparatus was developed and the succinonitrile-water phase diagram measured. The diagram was compared to both the simulation and literature data. Substantial differences were found in the comparisons which serve to demonstrate the need for this procedure. The work also produced a new phase diagram for this system.

Introduction

Succinonitrile-water and diethylene glycol-ethyl salicylate are two "well known" transparent systems which have been studied as monotectic binary metallic alloy solidification models. These transparent models are important because they permit the direct observation of phase transformations and solidification reactions which are impossible in metallic systems. Many interesting phenomena have been observed using these and a few other systems but there is a need to expand the available number of these transparent binary models. The additional systems will be used to determine both the unique and generalizable phenomena to develop a better understanding of metallic systems. A greater understanding of metallic systems will permit the consistently reproducible manufacturing of tougher and stronger alloys.

A model material must be transparent, have a low heat of fusion, form a plastic crystal and contain the desired solidification reaction (monotectic, eutectic, etc.). A partial list of material adhering to these criteria was given by Jackson[1]. The main problem is that phase diagrams of these materials, when combined with any of the many thousands of possible chemicals to form binary alloys, have never been experimentally measured.

Objective

The objective of this work was to develop a set of procedures to expand the number of available transparent binary systems for use as monotectic metallic alloy solidification models. The developed procedures first required the prediction of the phase diagram using established estimation methods (UNIFAC-UNIQUAC). If the phase diagram contained a monotectic reaction, then a careful experimental measurement of the phase diagram was deemed necessary. Both objectives were accomplished. However, the prediction procedures should be refined to make them easier to use and to yield a better prediction of known phase diagrams. The experimental portion resulted in the development of a new apparatus for phase equilibria determinations.

Phase Diagram Prediction

Theoretical Background

One of the objectives of this work was to predict unknown phase diagrams of chemical systems for which limited physical property data were available or which had not previously been experimentally measured. The major questions to be answered by the predicted phase diagram were, did the system form;

1. a monotectic composition?
2. a eutectic composition?
3. an immiscible solution (miscibility gap)?

The predicted phase diagram did not have to exactly fit the system's phase diagram but was to be used as a screening device to prevent the random experimental measurement of systems which might have the above phenomena.

As previously mentioned in the objective section, an established estimation method (UNIFAC-UNIQUAC) was used to predict the activity coefficients and compositions associated with the solid-liquid[2] and liquid-liquid[3] portions of the phase diagram. A brief review of the thermodynamic and the UNIFAC-UNIQUAC method will now be given to aid those not totally familiar with the approach. Additional information on the thermodynamic development may be obtained from many chemical thermodynamic references[4,5], while a detailed treatment of the UNIFAC-UNIQUAC method may be obtained from references 6 and 7.

Liquid-Liquid Equilibria

The basic thermodynamic equation governing liquid-liquid phase equilibria using an integral approach to generate the phase equilibrium relationship is given by the following expression;

$$f_i^I = f_i^{II} \qquad (1.1)$$

where the superscripts I and II refer to the different partially miscible liquid phases and f_i is the fugacity of the component. If a standard state is chosen such that it is the same for each liquid phase, equation (1.1) can be rewritten as:

$$x_i^I \gamma_i^I = x_i^{II} \gamma_i^{II} \qquad (1.2)$$

In order to generate the miscibility gap, all that is required is a knowledge of the isothermal variation of the activity coefficients of each component as a function of composition. With this information, it is possible to generate the spinodal curve[4]. If the solution forms a miscibility gap, than a local maxima and minima will exist on the spinodal which lie just inside the true binodal curve (see Figure 1). To determine the molar concentrations in the two partially miscible liquid phase, equation (1.2) is used along with a trial and error procedure to find the points on the spinodal curve that satisfy the equality. A line connecting these two points is the tie line for that temperature. This procedure is repeated at different temperatures to generate additional points on the binodal curve.

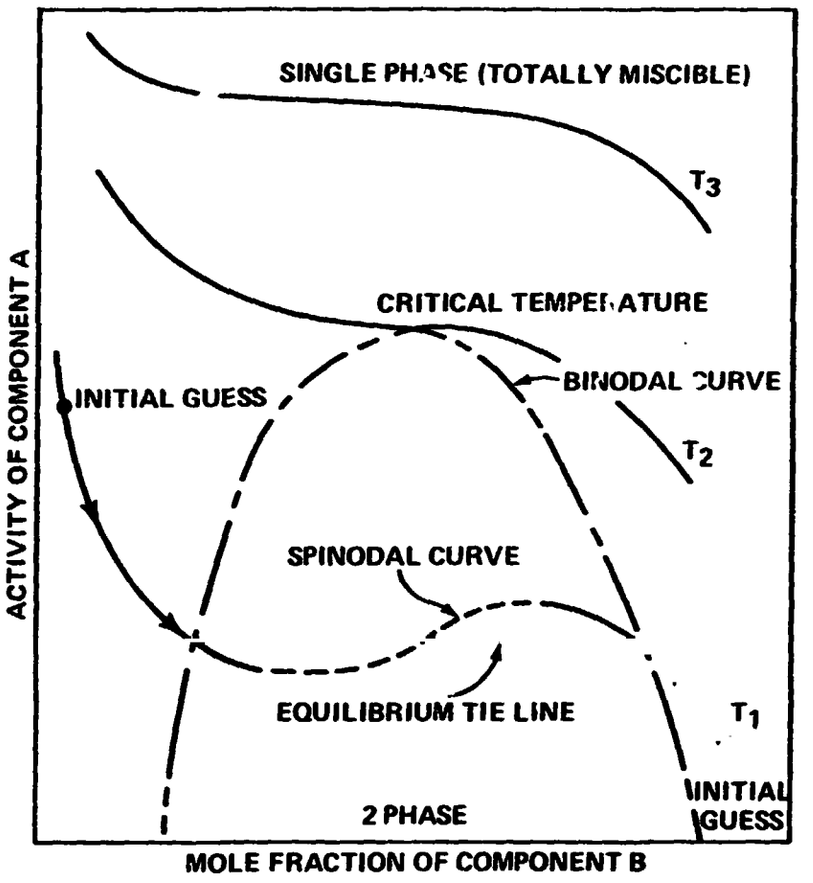

Figure 1. Spinodal and Binodal Curves Interrelationship

Solid-Liquid Equilibria

The basic integral thermodynamic equation governing the solid-liquid phase equilibria is given by the following equation:

$$f_i^S = f_i^L \tag{2.1}$$

where f_i^S is the fugacity of the pure solid and f_i^L is the fugacity of the solute in the liquid solution.[5] The fugacity in the liquid phase may be rewritten as

$$f_i^L = X_i^L \gamma_i^L f_i^{L,0} \tag{2.2}$$

where X_i^L is the mole fraction of component i, γ_i^L is the activity coefficient of component i, and $f_i^{L,0}$ is the standard reference state for the liquid phase. Substitution of equation (2.2) into (2.1) yields

$$X_i = \frac{f_i^S}{\gamma_i^L f_i^{L,0}} \tag{2.3}$$

The molar Gibbs free energy change which characterizes the solid-liquid phase transformation is given by

$$\Delta G_{S\to L} = RT \ln\left(\frac{f^L}{f^S}\right) = \Delta H_{S\to L} - T\Delta S_{S\to L} \tag{2.4}$$

The right side of this equation may be expanded using standard thermodynamic relationships to become 5;

$$\ln\left(\frac{f^L}{f^S}\right) = \frac{\Delta H_{ft}}{RT}\left[1 - \frac{T}{T_t}\right] - \frac{\Delta C_p}{R}\left[\frac{T_t - T}{T}\right] + \frac{\Delta C_p}{R}\left[\ln\frac{T_t}{T}\right] \tag{2.5}$$

where T_t is the triple point temperature of the pure component and the H_{ft} is the heat of fusion measured at the triple point. For most materials, there is only a small difference between the triple point and normal melting point temperature so T_m will be substituted for T_t. There is also little difference between the heat of fusion at the triple point and the heat of fusion at the normal melting point so ΔH_{fm} is substituted for ΔH_{ft}. Finally, the heat capacity terms, being of opposite signs, have a cancelling effect with the difference adding only a small contribution to the overall equation and is therefore neglected. Substituting these assumptions into equation (2.5) yields the final equation for the equilibrium[5].

$$\ln\left(\frac{f^L}{f^S}\right) = \frac{\Delta H_{fm}}{RT}\left[1 - \frac{T}{T_m}\right] \tag{2.6}$$

UNIFAC Group-Contribution Method

The basic approach of this method is to utilize existing phase equilibrium data to predict the equilibria of unknown systems. The method requires the reduction of experimentally obtained activity coefficient data to obtain interaction parameters between structural or functional groups of interacting molecules. The reduction follows the solution-of-groups method[8,9] to determine the interactions of a given group.

The UNIQUAC model calculates the activity coefficients of a system using a combinational contribution based on the size and shape of the molecules and a residual contribution due to molecular interaction. The UNIQUAC equation is[7]

$$\ln\gamma_k = \ln\gamma_k^C + \ln\gamma_k^R \qquad 3.1$$

The UNIFAC method uses the UNIQUAC model but incorporates functional groups or molecular fragments and their group size and shape for the combinational contribution along with the residual contribution due to functional group interactions. This method "builds" molecules with unknown interactions from functional groups of predictable interactions. Fredenslund et al.[1] describes the method for obtaining the group interaction parameters from the experimental data and this reference should be consulted for further explanation.

The UNIFAC method is composed of the following procedural steps to determine the activity of the i^{th} component[7];

1. UNIQUAC Equation

$$\ln\gamma_i = \ln\gamma_i^C + \ln\gamma_i^R \qquad 3.2$$

2. Combination portion is calculated using the following series of equations;

$$\ln\gamma_i^C = \ln\left(\frac{\Phi_i}{X_i}\right) + 5q_i \ln\left(\frac{\theta_i}{\Phi_i}\right) + \ell_i - \frac{\theta_i}{X_i}\sum_{j=1}^{n} X_j \ell_j \qquad 3.3$$

where

$$\ell_i = 5(r_i - q_i) - (r_i - 1) \qquad 3.4$$

$$\theta_i = \frac{q_i X_i}{\sum_{j=1} q_j X_j} \text{ molecular surface area fraction} \qquad 3.5$$

$$\Phi = \frac{r_i X_i}{\sum_{j=1} r_j X_j} \text{ molecular volume fraction} \qquad 3.6$$

where

$$r_i = \sum_{k=1}^{n} \nu_k^{(i)} R \quad \text{volume component} \qquad 3.7; \quad q_i = \sum_{k=1}^{n} \nu_k^{(i)} Q_k \quad \text{surface area component} \qquad 3.8$$

$\nu_k^{(i)}$ = the number of groups of kind k in the molecule i.
n = the total number of groups in the molecule.
R_k = group volume constant.
Q_k = group area constant.

3. Residual portion is calculated using the following series;

$$\ell n \gamma_i^R = \sum_{k=1}^{n} \nu_k^{(i)} \left[\ell n(\Gamma_k) - \ell n (\Gamma_k^{(i)}) \right] \qquad 3.9$$

where

$$\ell n\, \Gamma_k = Q_k \left[1 - \ell n\left(\sum_{m=1}^{n} \theta_m \psi_{mk} \right) \right] - \sum_{m=1}^{n} \left(\theta_m \psi_{km} \Big/ \sum_{n=1}^{n} \theta_n \psi_{nm} \right) \qquad 3.10$$

$$\theta_m = \frac{Q_m x_m}{\sum_{n=1}^{n} Q_n x_n} \quad \text{surface area fraction} \qquad 3.11 \qquad x_m = \frac{\sum_{j=1}^{n} \nu_m^{(i)} X_j}{\sum_{j=1}^{n} \sum_{n=1}^{n} \nu_n^{(j)} X_j} \quad \text{group fraction} \qquad 3.12$$

$$\psi_{nm} = \exp(-A_{nm}/T) \qquad 3.13$$

$\ell n \Gamma_k^{(i)}$ uses the same equation as $\ell n\, \Gamma_k$

A_{nm} is the group interaction parameter (experimentally determined)

The adjustable parameter using the above method are R_k, Q_k and A_{nm}. The values assigned to R_k and Q_k are obtained from atomic and molecular structural data while the values of A_{nm} are experimentally derived interactions. For example, if there are 3 groups in a given molecule i then 3 sets of R_k and Q_k are required along with 9 sets of interaction parameters to characterize this molecule.

The UNIFAC group-contribution method used in this work contained 43 main groups with 38 subgroups. The subgroup uses the main group's interaction parameters but have different volume and surface area parameters but have different volume

and surface area parameters. In all, the data set was composed of 81 different sets of P_K and Q_K values along with a 43 element square matrix of interaction parameters. These values represent the best statistically obtained value for each group resulting from the reduction of 10,000 sets of vapor-liquid equilibrium data[10].

Computer Programs

The programs which accomplish the solid-liquid (1979) and liquid-liquid (1982) equilibria, briefly described above, were provided to NASA's MSFC by J. M. Prausnitz[11] and had to be adapted to operate on the IBM 4341 computer using the FORTRAN level H compiler. The liquid-liquid program had a greatly expanded data set as compared to the solid-liquid equilibrium, so the solid-liquid program was modified to accept the additional inputs. The liquid-liquid program was written in a more modern version of FORTRAN for use with the CDC-6400 computer and required substantial conversion to run on the IBM 4341 FORTRAN H compiler.

The program to predict the binodal curve was written in basic on a Commodore 64 computer. This program first uses a least squares matrix routine to fit the best exponential function through the isothermal activity coefficients generated as a function of composition by the liquid-liquid program for each component in the mixture. These functions are then used along with a trial gap[4,7]. This program was written in basic but will be incorporated into the overall FORTRAN liquid-liquid program at a later time.

Experimental Apparatus

As previously mentioned, a second objective of this work was to experimentally verify the simulation. The standard approach for the determination of a solid-liquid phase diagram is to visually monitor the phase transition with a microscope noting the temperature at which the last crystal melts or until the phase becomes homogeneous. This method may be prone to thermal and mass transfer gradients across the viewed area due to lack of adequate mixing. To overcome these problems the experimental apparatus depicted in Figure 2 was constructed.

The principle features that this apparatus has over the visual method is that a laser beam is passed through a well mixed solution which impinges on a photodiode. The photodiode creates an electronic output which is applied to a chart recorder. This method takes advantage of the fact that, as a material undergoes a phase transformation, a change in the index of refraction of both the majority and minority phases occurs in the system. The change in the index of refraction changes the angle of the beam relative to the detector. Since the photodiode detector used contained a concentrating lense,

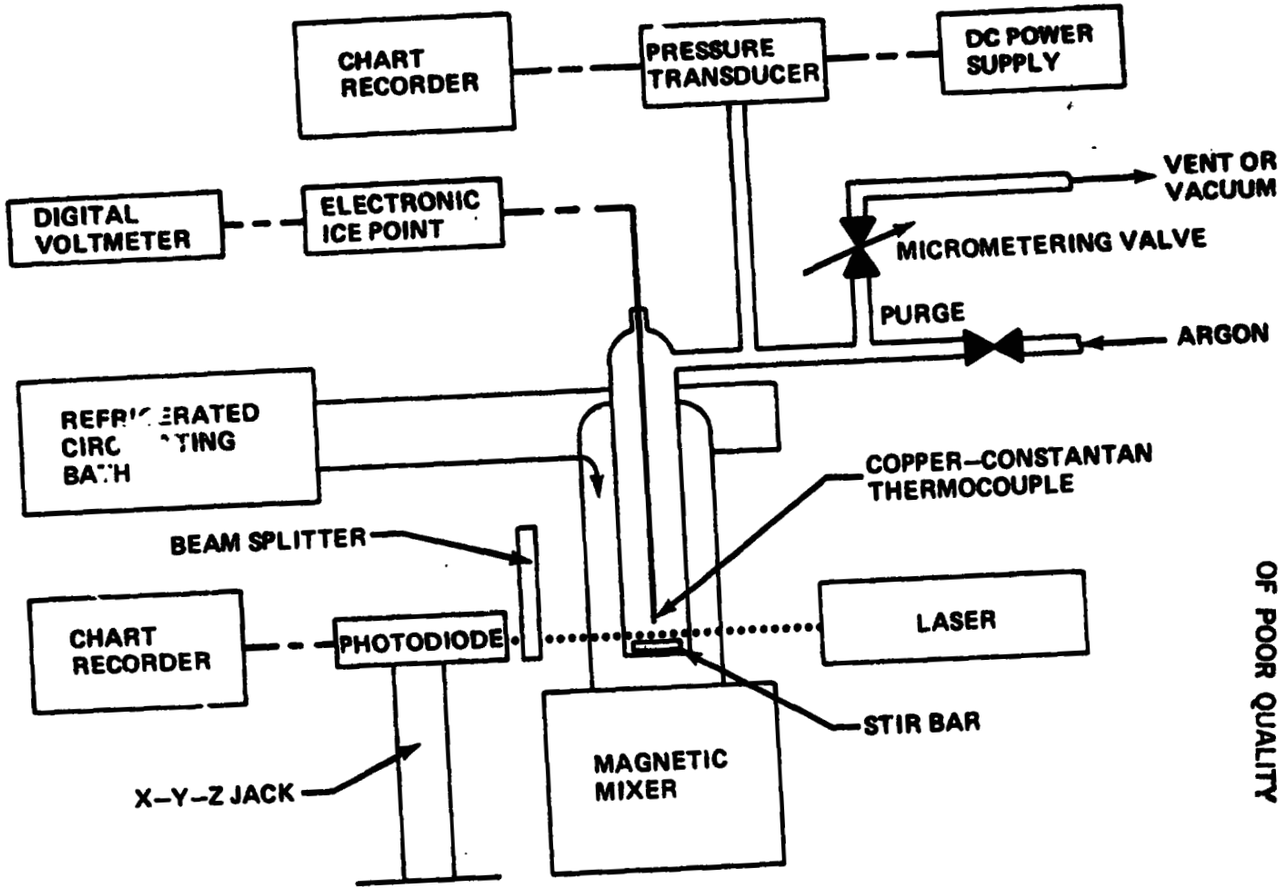

Figure 2. Experimental Apparatus

any change away from the true focal point produces a large change in the detectors output voltage. This method proved to be very effective in determining both the cloud point following the cooling curve and the melting point following the heating curve.

A second feature of this apparatus was the ability to operate under vacuum or any other type of atmosphere. The pressure transducer included in the system measured the system pressure to within 0.01 mm Hg which is useful in determining reproducible cooling curves since the rate of nucleation is a function of applied pressure.

The temperature was determined using a copper-constantan thermocouple connected to a voltmeter through the electronic ice point. The microvolt output was converted to temperature using the manufacturers published charts to overcome the error associated with the Seebeck effect. The bare junction was exposed directly to the mixture for greatest sensitivity. Since nucleation rate was not important to this study the exposed junction presented no problems. The experimental apparatus should be modified by shielding the thermocouple in a glass well if nucleation is to be considered.

A minor problem with this system is that the voltage produced by the thermocouple must be manually recorded as the transformation takes place. This problem can be easily overcome with a simple base-line comparator circuit, though this circuit has not yet been built.

The temperature in the vessel was controlled by circulating cooling water through the jacketed vessel. This bath was manually controlled during the experiment and adjusted carefully so that the rate of heating of the two-phase mixture was very gradual. This was confirmed by both the photodiode and thermal outputs.

Table 1 provides the make and model numbers of much of the equipment used in this apparatus.

Table 1.

Equipment List

1. Spectra-Physics Model 144 Laser with Model 246 Exciter
2. Photodiode (Pin 125 DP/L, MWO 4803) United Detector Technology, Inc.
3. Harrison G261A DC Power Supply
4. Hewlett Packard Model 3490A Digital Multimeter
5. Omega Copper - Constantan electronic ice point.

Table 1 (Continued)

6. Jodon VBN-200 Variable Beam Splitter

7. Newport Research Corp. Model 440 X-Y-Z Jack.

8. Spin-Mater Model 4803 Magnetic Mixer

9. Nupro B-4SG Micrometering Valve

10. Endocal Refrigerated Circulating Bath Model RTE-4

11. Hewlett Packard Model 17501A Pen Chart Recorder

Experimental Procedures

A sample of triply distilled and zone refined succinonitrile was tare weighted into the vessel which had been heated to about 60°C. The molten state was used to allow for placement of the temperature probe and stir bar. The system was outgassed to remove dissolved gases and the photodiode positioned to maximize the output voltage. The sample was next cooled until the phase transformation occurred. The melting point of the pure succinonitrile was then determined by following the heating curve until the photodiode's output voltage returned to its initial value. The complete cooling and heating process is depicted in Figure 3. The melting point of the pure succinonitrile was used as a check of the purity of the sample and was generally very close to the published value of 58.086[12].

The system was then placed under an argon blanket so that the phase diagram could be measured at one atmosphere and the melting point of pure succinonitrile redetermined. Argon was used because it is an inert gas larger in size to that of air. Air was found to lower the melting point of pure succinonitrile by as much as 0.7 to 0.8°C and should be avoided during the handling of this material.

Purified water, distilled and deionized to a resistance of 16MΩ was then tare weighted into the system and the cooling and heating procedures repeated. Using this procedure repeatedly permitted the determination of the entire phase diagram.

The monotectic and eutectic temperatures were determined by carefully cooling the system while observing the photodiode output. As one would expect, these reactions had a dramatic effect on the laser throughput which was observable by the photodiode's output voltage. The monotectic and eutectic temperatures remained constant as the large quantity of material in the vessel underwent these phase transformations.

The experiment was repeated a second time to confirm the

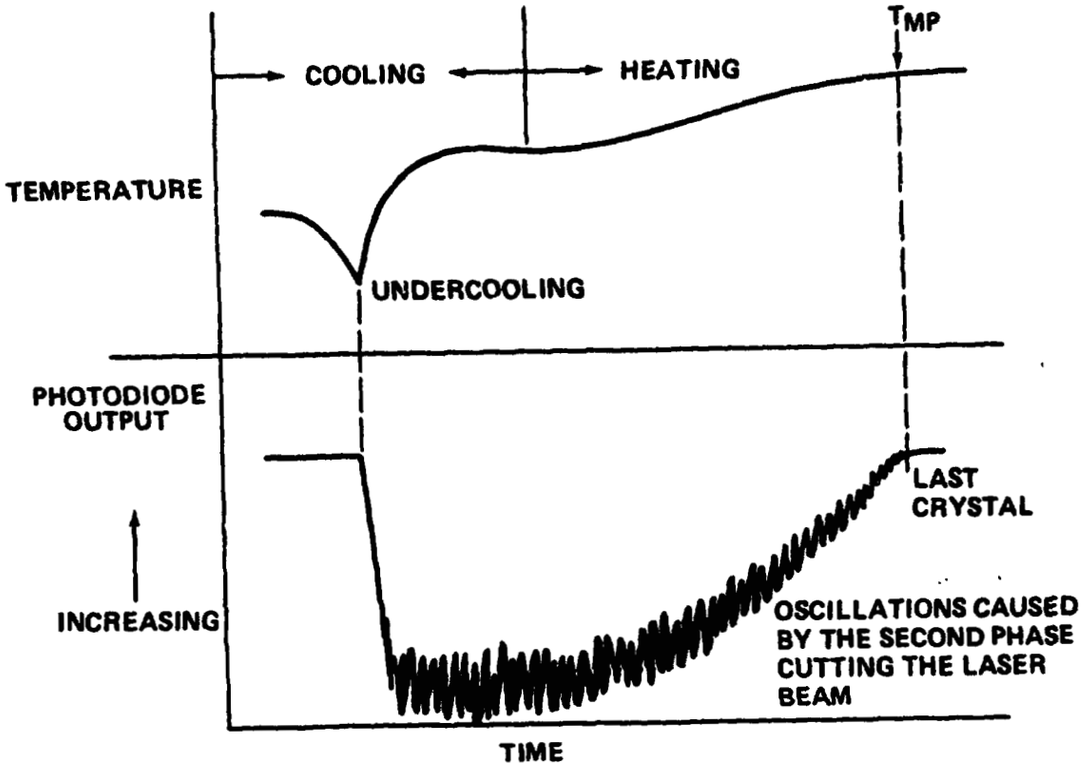

Figure 3. Photodiode Output Relative to the Sample Temperature for the Cooling and Heating Cycles (not actual data).

initial results. Additional points were added to the original two data sets in a third run by making up solutions in the zones which were devoid of experimental data from the first two runs.

Results and Discussion

This section will present the results of the computer simulation, briefly review the literature phase diagram and then present the experimental results of this study obtained on the succinonitrile-water system. Finally, a comparison of the various phase diagrams will be considered.

The computer simulation of succinonitrile-water system is shown in Figure 4. The simulation predicts a monotectic at 19.5 mole percent water at 21.5°C and a eutectic at 96 mole percent water at -1.5°C. The inputs to generate this phase diagram were the two components represented as functional groups for both the liquid-liquid and solid-liquid programs. Additionally, the solid-liquid program required both the normal melting point and heat of fusion for each component.

The phase diagram experimentally measured by F. Schreinemakers[13] is shown in Figure 5. As previously mentioned, these diagrams contained at least one point of error, namely the normal melting point of pure succinonitrile found by Schreinemakers as 54.5°C. The currently accepted value[12] is 58.086 ± .001. A second point of interest centers around the limited amount of data used to generate the diagram. Many researchers have confirmed this diagram[14,15] but few have published the results. A point has been added to the diagram in the area of the critical point of the binodal curve from reference 15.

The experimental results obtained in this study are presented in Table 2 and plotted in Figure 6. The tolerance range for the temperatures presented in the table was ± .06°C which resulted from the truncation error associated with the digital voltmeter used to measure the thermocouple output voltages. The melting point of pure succinonitrile was measured at 58.04°C indicating that the material used was very pure. The monotectic temperature was measured at four different compositions with an average of 18.82°C while the eutectic temperature was measured twice and was found to be -1.26°C. These experimental points are shown in Figure 6 and listed in Table 3. The monotectic composition was determined as 31.60±.1 mole percent water using the average point determined from a least squares fit of the data on either side of the monotectic point and the monotectic temperature. The eutectic composition was determined from a least squares fit of the data on the left side of the eutectic point and the eutectic temperature and was found to be 98.96 mole percent water. The right side of the eutectic composition did not contain enough data elements to permit an evaluation of the

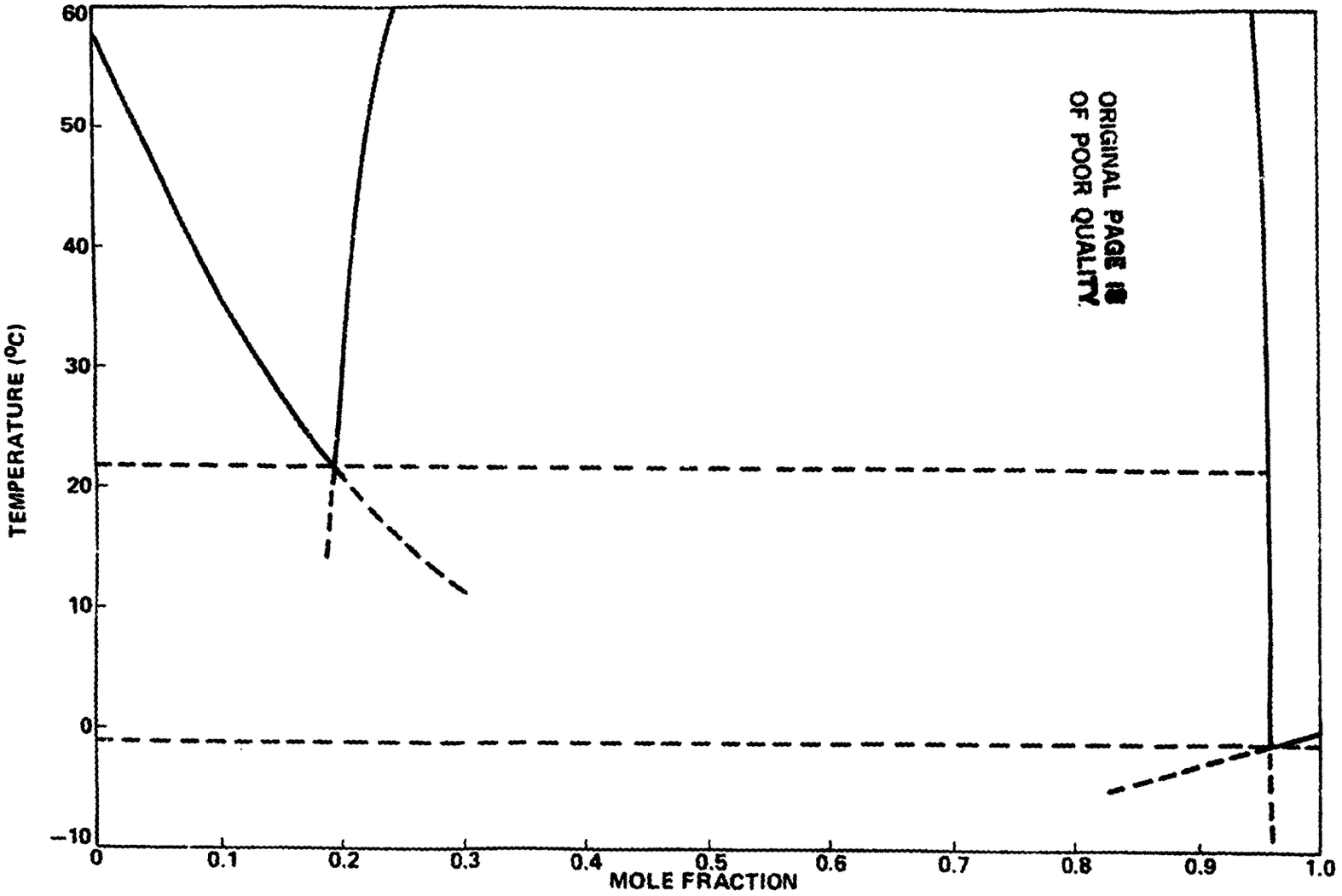

Figure 4. Computer Simulation of the Succinonitrile-Water Phase Diagram

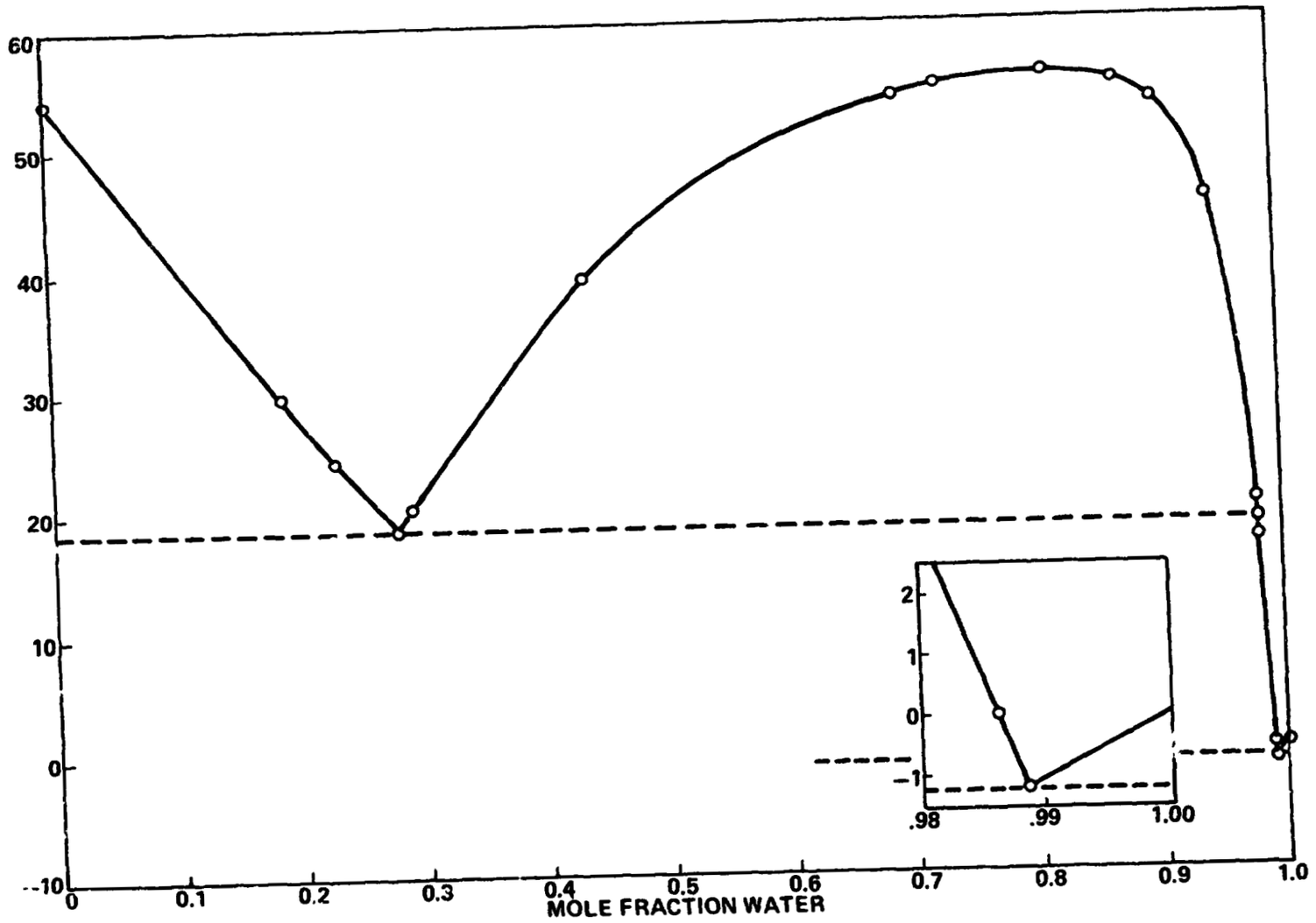

Figure 5. Succinonitrile-Water Phase Diagram (Schmemak [13])

Table 2

Succinonitrile-Water Experimental
Solid-Liquid Equilibria Data

Composition Mole Fraction Water	Temperature (°C)	Composition Mole Fraction Water	Temperature (°C)
0	58.04	.7670	55.95
.0695	46.86	.8068	56.14
.1128	40.26	.8270	56.17
.13[illegible]	38.06	.8712	55.17
.162[illegible]	32.88	.8955	54.57
.2052	27.00	.9162	52.06
.2421	23.86	.9339	47.49
.2491	22.85	.9368	46.96
.2366	20.20	.9581	35.54
.3202	19.91	.9589	35.29
.3519	26.01	.9720	21.10
.2633	27.51	.9780	14.06
.4452	38.46	.9836	6.49
.4498	39.02	.9862	2.15
.5075	44.07	.9890	-0.59
.5379	46.40	.9908	-0.72
.6306	52.26	.9924	-0.44
.6571	53 01	.9953	-0.31
.7201	55.34		

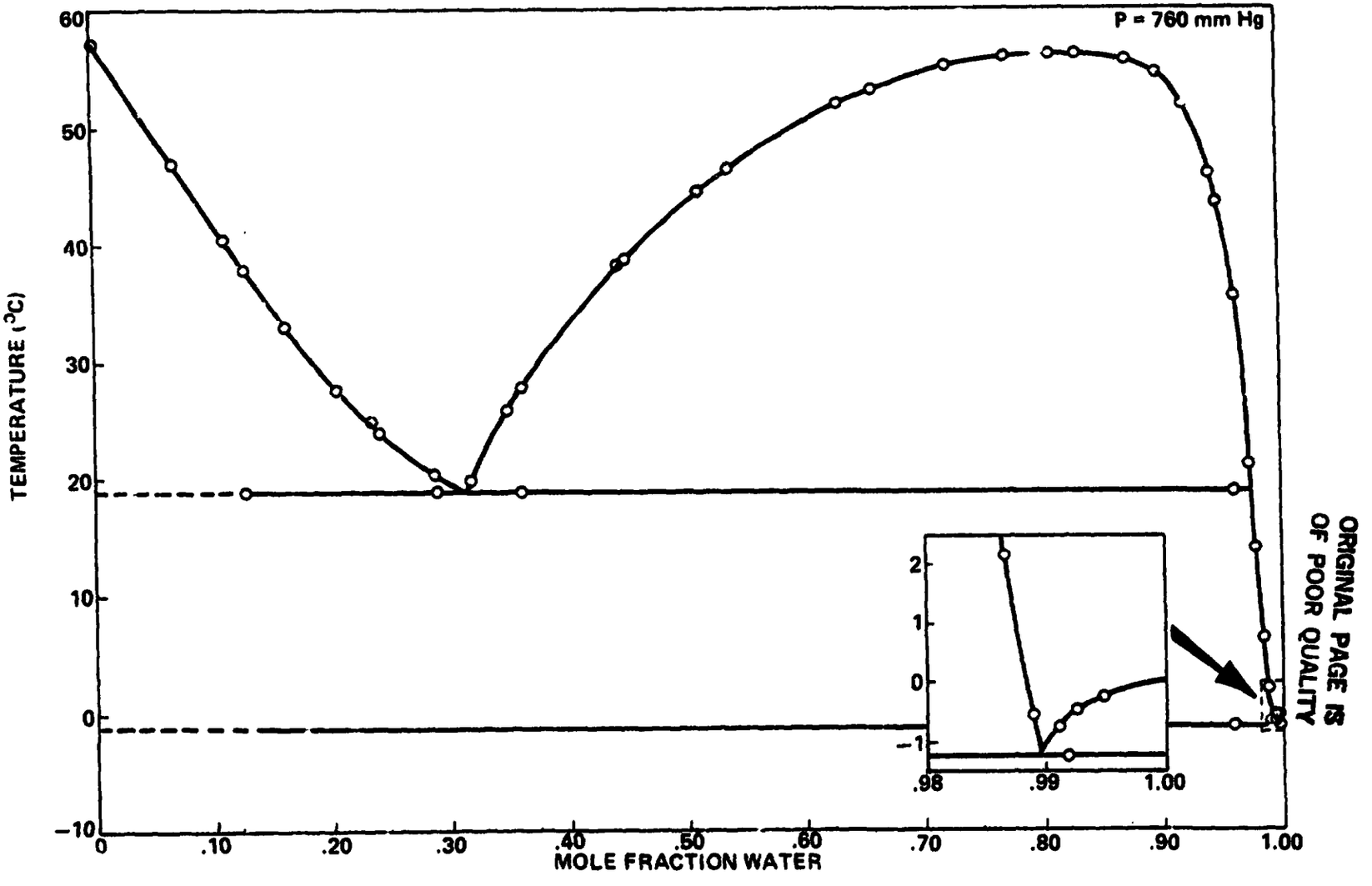

Figure 6. Succinonitrile-Water Phase Diagram (Smith & Frazier)

Table 3

Monotectic and Eutectic Temperatures

Monotectic Composition Mole Fraction Water	Temperature (°C)	Eutectic Composition Mole Fraction Water	Temperature (°C)
.1304	18.80	.9656	-1.263
.2866	18.83	.9919	-1.263
.3633	18.83		
.9656	18.80		

higher order function necessary to obtain a fit of these data. The critical composition and temperature were determined graphically since a function could not be found which would adequately fit the upper portion of the binodal curve. This point was found to be 82.7 mole percent water at 56.17°C. This phase diagram was very reproducible as indicated by the lack of scatter of the data points. The experimental method virtually eliminated the errors associated with the operator's interpretation of the point at which the phase transformation takes place.

Figure 7 presents a comparison of the computer simulation with the experimental data. It is quite apparent from this figure that the simulation's binodal curve does a poor prediction of the true shape and size of the experimental curve. It does estimate the range of compositions over which the system forms two liquid phases. This indicates that the system's true activity is a stronger function of composition and temperature than the UNIFAC method predicts. The solid-liquid portion of the phase diagram is a much better predictor of the true shape of the experimental curve but one must remember that additional experimental values must be used in the prediction.

Figure 8 presents a comparison of Schreinemakers' work with that of this study. The differences between the two phase diagrams was most likely due to impurities observed by Schreinemakers[12] who wrote, "It is also difficult to work continuously with completely pure (succino)nitrile, since a solution after longer use turns somewhat brown...". The difference associated with the monotectic composition may help to explain the many different observed phenomena observed in the hypermonotectic region of Schreinemakers' diagram which would be hypomonotectic or monotectic using the results of this study.

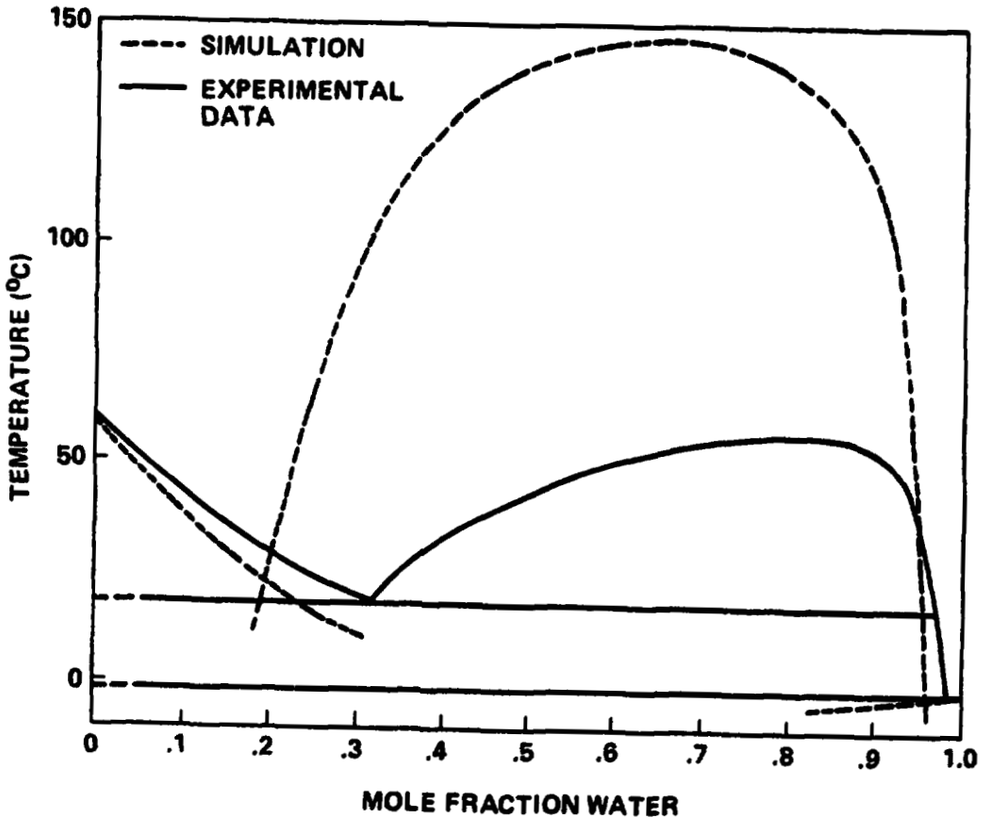

Figure 7. A Comparison of the Experimental Data and the Computer Simulation

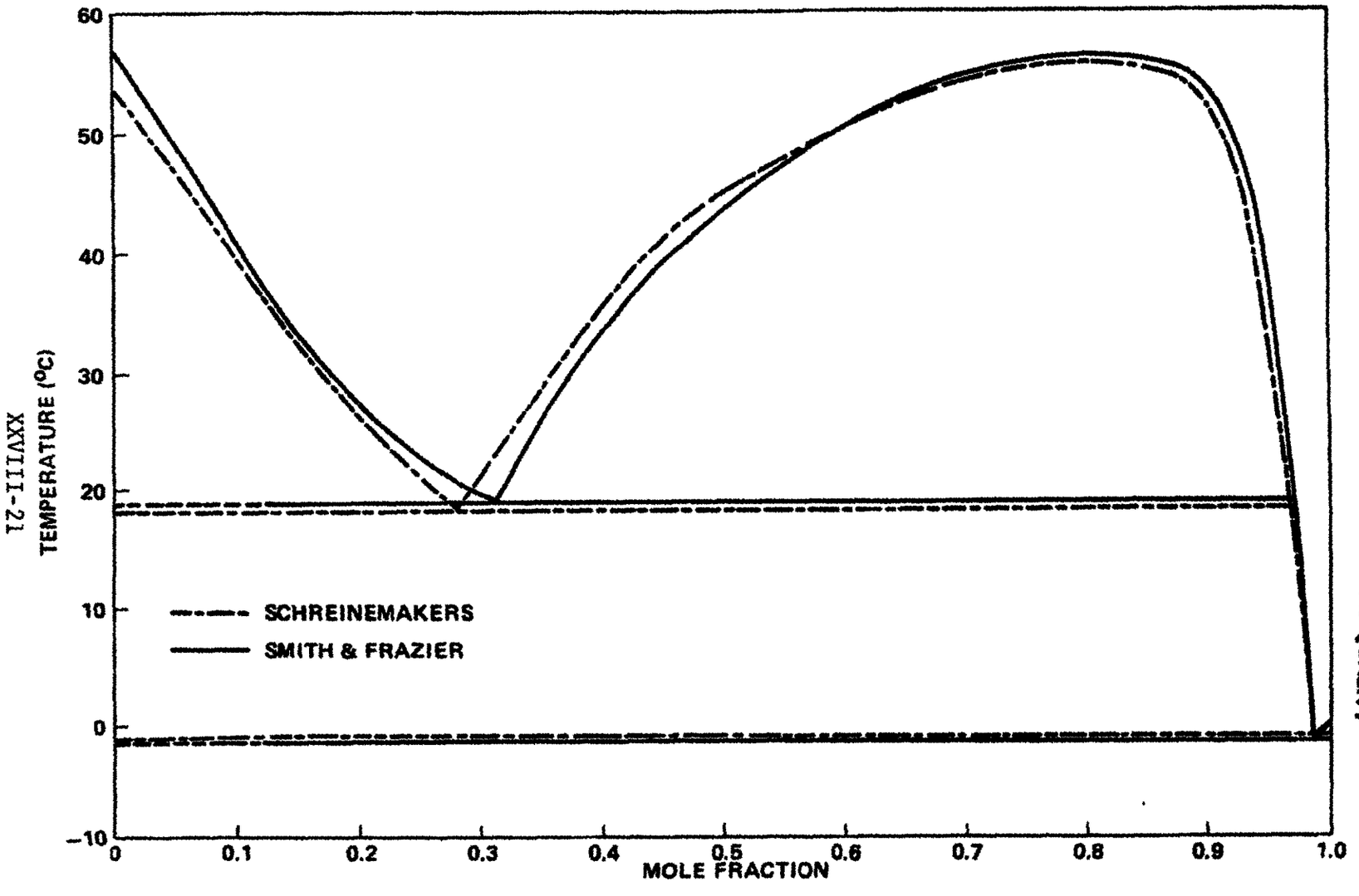

Figure 8. A Comparison of Schrein makers with Smith and Frazier's.

Conclusions and Recommendations

The computer programs used in this work will require additional modifications to make them more compact, faster and easier to use. They currently require extensive operator manipulations of the output to obtain the desired results. Additionally, the systems succinonitrile-acetone and succinonitrile-ethanol have been simulated but these results were not available for inclusion in this report.

This work has achieved its primary objective which was to develop a method to screen potential systems for monotectic study while developing a rapid and reproducible method for experimentally determining those systems which show this potential.

References

1. K. A. Jackson and J. D. Hunt, Acta Met. 13, 1212(1965).

2. J. G. Gmehling, T. F. Anderson and J. M. Prausnitz, "Solid-Liquid Equilibria using UNIFAC," Documentation for the Computer Program MTSLE, University of California, Berkley, CA 94720 (1972).

3. A Fredenslund, R. L. Jones and J. M. Parusnitz, "Group-Contribution Estimations of Activity Coefficients in Nonideal Liquid Mixtures," University of California, Berkley, CA 94720 (1982).

4. M. Modell and R. C. Reid, "Thermodynamics and Its Applications," 2nd edition, Prentice-Hall Inc., Englewood Cliffs, NJ (1974).

5. J. M. Prausnitz, "Molecular Thermodynamics of Fluid-Phase Equilibria," Prentice-Hall Inc., NJ (1969).

6. J. M. Prausnitz, et al., "Computer Calculations for Multicomponent Vapor-Liquid and Liquid-Liquid Equilibria," Prentice-Hall, NJ (1980).

7. A. Fredenslund, J. Gmehling and P. Rasmussen, "Vapor-liquid equilibria using UNIFAC," Elsevier Scientific Publishing Company, NY (1977).

8. E. L. Derr and M. Papadopoulos, J. Am. Chem. Soc., 81, 2285 (1959).

9. G. M. Wilson and C. H. Deal, Ind. Eng. Chem. Fund., 1, 20 (1962).

10. J. Gmehling, P. Rasmussen and A. Fredenslund, Ind. Eng. Chem. Proc. Des. Dev. 21, 118 (1982).

11. J. M. Prausnitz, Private communications (1983).

12. M. E. Glicksman, R. J. Schaefer, and J. D. Ayess, Met. Trans. 7A, 1747 (1976).

13. F. A. H. Schreinemakers, Z. Phys. Chem., 23, 417 (1897).

14. I. K. Zhuravleva and G. M. Mikryukova Ahurnal Obshchei Khimii, 45, 1417 (1975).

15. I. K. Mel´Nikova and E. F. Zhur. lev, Ahurnal Obshchei Khimii, 34, 3527 (1964).

1983

NASA/ASEE SUMMER FACULTY RESEARCH FELLOWSHIP PROGRAM

MARSHALL SPACE FLIGHT CENTER
THE UNIVERSITY OF ALABAMA IN HUNTSVILLE

COMPUTER CONTROL OF A SEVEN DEGREE OF FREEDOM MANIPULATOR ARM

Prepared By:	John Stensby
Academic Rank:	Assistant Professor
University and Department:	University of Kansas Department of Electrical Engineering
NASA/MSFC: Division: Branch:	 Guidance, Control & Optical Systems Control Electronics
MSFC Counterpart:	E. C. Smith
Date:	August 12, 1983
Contract No.:	NGT 01-008-021 The Univeristy of Alabama in Huntsville

COMPUTER CONTROL OF A SEVEN DEGREE OF FREEDOM MANIPULATOR ARM

BY

John L. Stensby
Assistant Professor of Electrical Engineering
The University of Kansas
Lawerence, Kansas

ABSTRACT

An algorithm for the computer control of a seven degree of freedom manipulator arm is described. The algorithm is segmented into two distinct parts. One part controls the extension, azimuth, and elevation of the wrist joint. The second part controls the attitude of the terminal device. The two segments interact to achieve decoupling of wrist joint translation and terminal device rotation.

I. INTRODUCTION

An algorithm for the computer control of an 2.4 meter (8 foot), seven degree of freedom (DOF), manipulator arm is described below. Six of the degrees of freedom are controlled by the algorithm; the seventh DOF is controlled directly by the operator and is not influenced by the algorithm. The algorithm has been termed the Hawk Control Mode and the manipulator arm is referred to as the Proto-Flight Manipulator Arm (P-FMA).

The P-FMA contains two segments and a terminal device (TD). An upper segment is connected to the manipulator's base through a shoulder joint; the upper segment's other end is connected to a lower segment through an elbow joint. A terminal device is connected through a wrist joint to the remaining end of the lower segment. The arm controller consists of a PDP 11/34 minicomputer. The arm's hardware was originally developed by the Denver division of Martin Marietta. Current efforts are coordinated with Essex Corporation of Huntsville, Alabama.

The Hawk control algorithm is segmented into two distinct parts. One part receives three operator-derived inputs and controls the extension, azimuth, and elevation, as seen from the manipulator's base coordinate system, of the wrist joint. The second part receives three more operator derived inputs and controls the attitude (rotation as described by pitch, yaw, and roll angles) of the terminal device relative to a coordinate system embedded in the terminal device. Segmentation of the control algorithm in this manner reduces its complexity and reduces requirements placed on the host computer used in the control loop.

The two segments of Hawk interact to achieve decoupling of wrist joint translation and terminal device rotation. These two types of motion are inherently coupled in that a change in the wrist's position relative to the manipulator's base coordinate system produces a rotation of the terminal device in its coordinate system. Hawk serves to decouple these motions; the algorithm computes terminal device rotational commands which, when applied to the wrist's joint, will negate terminal device rotation caused by a translation of the wrist joint. Decoupling translational and rotational motions greatly simplifies use of the arm for many tasks such as the insertion of objects into holes.

II. OBJECTIVE

Derivation of the Hawk control algorithm represents the main objective of this effort. This objective has been accomplished; the derivation appears in Section IV.

Section V and Appendix A describes a numerical simulation of the Hawk algorithm.

III. P-FMA MODEL

Figure 1 depicts the P-FMA. Shoulder pitch and yaw, elbow pitch, and wrist pitch, yaw, and roll are controlled by Hawk. Upper arm roll is controlled independently of the algorithm by an operator.

Figure 2 depicts both angular quantities and coordinate systems which are relevant to the analysis which follows. The quantities θs and Ψs are shoulder pitch and yaw; they represent elementary rotations about the Y_1, and Z_1, axes, respectively. Elbow pitch, given by θe, represents an elementary rotation about Y_2. The quantities θw, Ψw, and ϕw are wrist pitch, yaw, and roll; they represent elementary rotations about the Y_3, Z_3, and X_3 axes, respectively.

IV. HAWK CONTROL ALGORITHM

The Hawk mode allows the operator to control the TD's position with respect to the manipulator's base coordinate system without changing the attitude of the TD. The TD's position is controlled through use of the shoulder and elbow angles (θs, Ψs, θe). The TD's attitude can be controlled through use of the wrist angles (θw, Ψw, ϕw).

The Hawk algorithm is segmented into two distinct parts. One part receives translational rate information as input and controls translation of the TD. The second part receives rotational rate information as input and controls the attitude of the TD. The two parts interact to achieve decoupling of TD translation and rotational motions.

TD Translation Control

Denote the position of the wrist point in the Cartesian base coordinate frame as X, Y, Z. The wrist point range, denote by R on Figure 2, is expressible as

$$R = \{X^2 + Y^2 + Z^2\}^{\frac{1}{2}} \qquad \text{(IV-1)}$$

The derivative of R with respect to time can be written as

$$\dot{R} = \tfrac{1}{2}\{X^2 + Y^2 + Z^2\}^{-\frac{1}{2}} \quad (2X\dot{X} + 2Y\dot{Y} + 2Z\dot{Z})$$

$$= \{(X/R)\dot{X} + (Y/R)\dot{Y} + (Z/R)\dot{Z}\} \qquad \text{(IV-2)}$$

Now, the quantities X/R, Y/R, and Z/R are expressible in terms of the angles shown on Figure 2 as

$$X/R = \text{COSE COS } \Psi s$$

$$Y/R = \text{COSE SIN } \Psi s$$

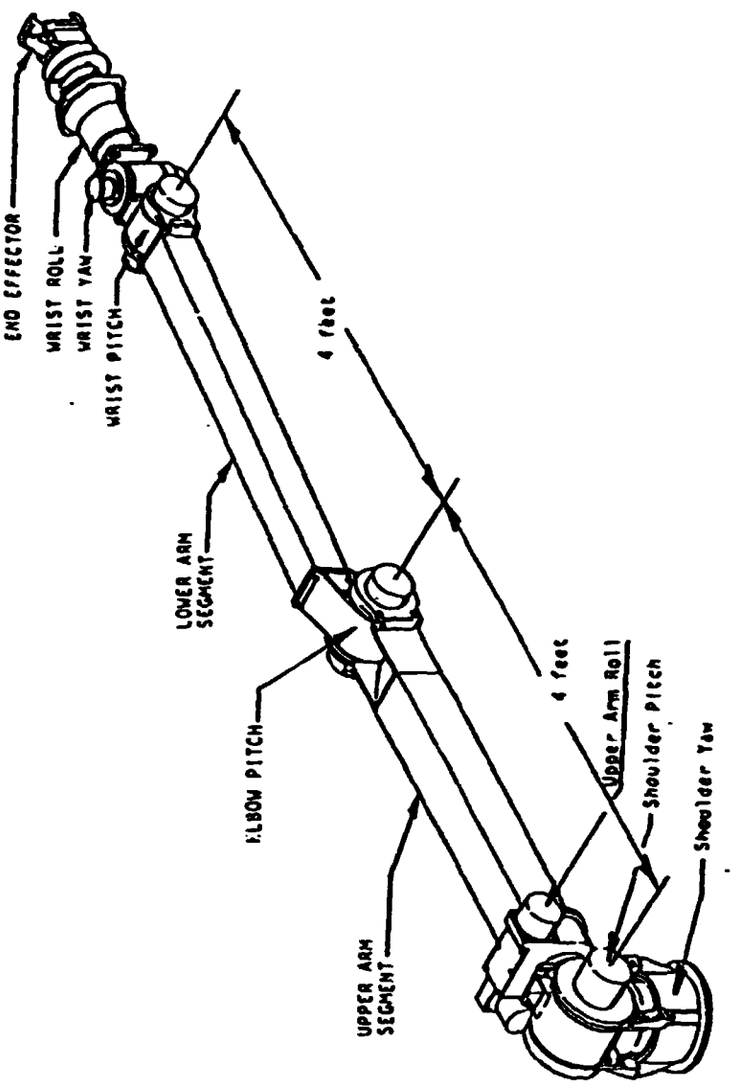

Figure 1: P-FMA

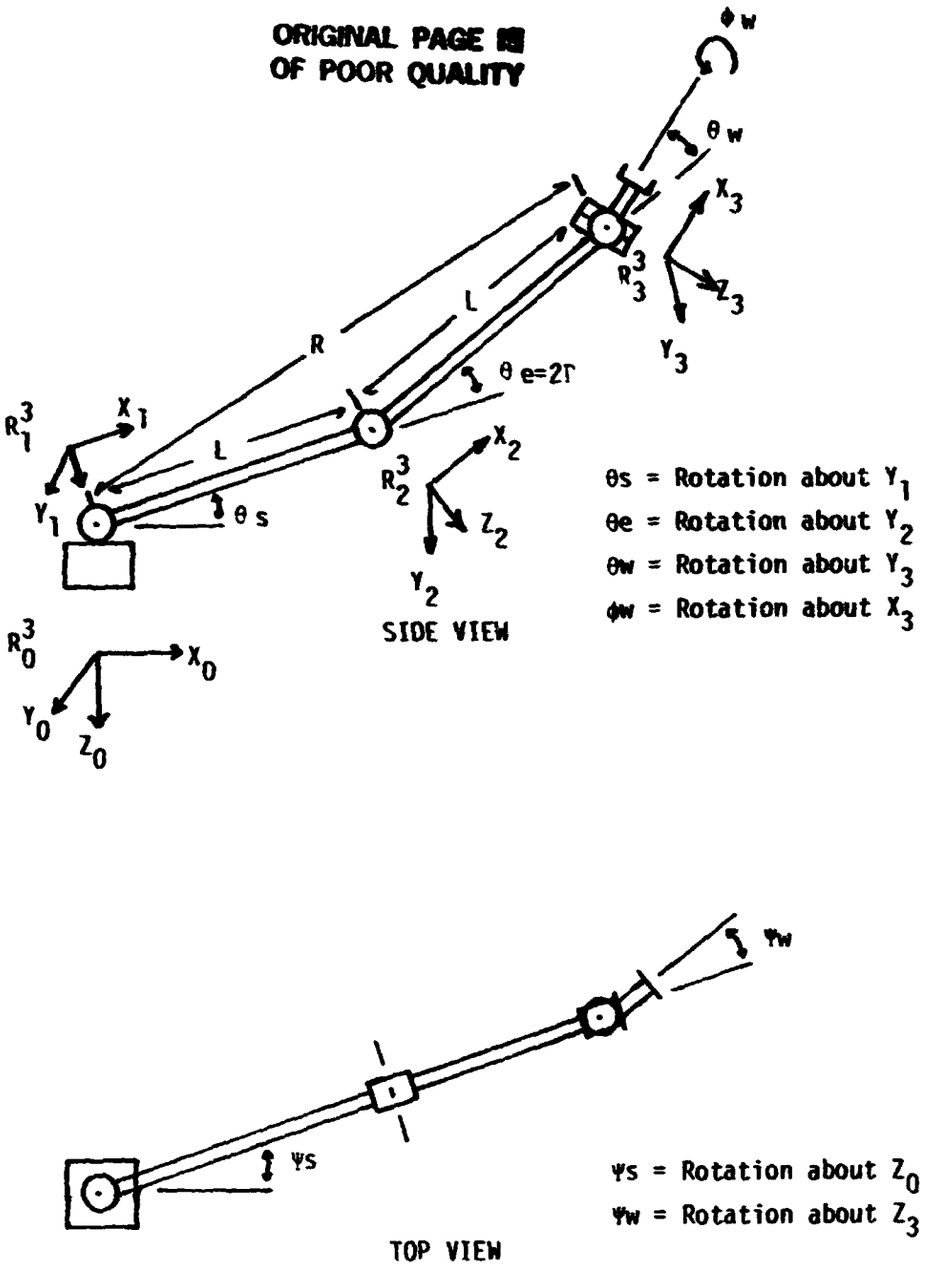

Figure 2 : P-FMA coordinate systems and angles.

$$Z/R = -\sin E \qquad \text{(IV-3)}$$

$$E \triangleq \theta s + \tfrac{1}{2}\theta e \ .$$

Equation (IV-2) can be expressed as the inner product

$$\dot{R} = \begin{bmatrix} \text{COSE COS}\Psi s & \text{COSE SIN}\Psi s & -\text{SIN E} \end{bmatrix} \begin{bmatrix} \dot{X} \\ \dot{Y} \\ \dot{Z} \end{bmatrix} \qquad \text{(IV-4)}$$

with the use of (IV-3). Equation (IV-2) expresses the simple relationship between wrist point range-rate and input rate information referenced to the base Cartesian coordinate system.

The shoulder yaw angle Ψs can be expressed in terms of the base coordinate system as

$$\Psi s = \text{Tan}^{-1}\,(Y/X). \qquad \text{(IV-5)}$$

The derivative of Ψs with respect to time is

$$\dot{\Psi}s = \{\, 1 + (Y/X)^2 \}^{-1} \{\, (X\dot{Y} - Y\dot{X})/X^2 \,\}$$

$$= \{\, X^2 + Y^2 \}^{-1} \{\, X\dot{Y} - Y\dot{X} \,\} \ . \qquad \text{(IV-6)}$$

The quantity $X^2 + Y^2$ can be expressed as

$$X^2 + Y^2 = (\text{RCOSE})^2 \qquad \text{(IV-7)}$$

by using Pythagorean's Theorem.

Equations (IV-6) and (IV-7) produce

$$\dot{\Psi}s = -\{\, (Y/\text{RCOSE})/(\text{RCOSE}) \}\, \dot{X} \qquad \text{(IV-8)}$$

$$+ \{\, (X/\text{RCOSE})/(\text{RCOSE}) \}\, \dot{Y}$$

Equation (IV-8) can be simplified by use of (IV-3) to produce

$$\dot{\Psi}s = -\{\, \text{Sin}\,\Psi s/(\text{RCOSE}) \}\, \dot{X} + \{\, \text{COS}\,\Psi s/(\text{RCOSE}) \}\, \dot{Y} \ . \qquad \text{(IV-9)}$$

Equation (IV-9) can be expressed as the inner product

$$\dot{\Psi}sR = \begin{bmatrix} -(\text{Sin}\,\Psi s/\text{COSE}) & (\text{COS}\Psi s/\text{COSE}) & 0 \end{bmatrix} \begin{bmatrix} \dot{X} \\ \dot{Y} \\ \dot{Z} \end{bmatrix} \qquad \text{(IV-10)}$$

Equation (IV-10) expresses the simple relationship between shoulder yaw angular rate and input rate information referenced to the base Cartesian coordinate system.

The angle E can be expressed in terms of Z and R as

$$E = \sin^{-1}(-Z/R) \qquad \text{(IV-11)}$$

The derivative of E with respect to time can be written as

$$\dot{E} = -\{1 - (Z/R)^2\}^{-\frac{1}{2}} \{(R\dot{Z} - \dot{Z}R)/R^2\}$$

which, after some simple algebra involving (IV-7), becomes

$$\dot{E}R = -\{R\cos E\}^{-1} \{R\dot{Z} - \dot{R}\} \qquad \text{(IV-12)}$$

The quantity $\dot{R}$ expressed by (IV-4) can be substituted into (IV-12) to obtain

$$\dot{E}R = \frac{-\dot{Z}}{\cos E} + \frac{+Z}{R\cos E}\left[(\cos E \cos\Psi s)\dot{X} + (\cos E \sin\Psi s)\dot{Y} - (\sin E)\dot{Z}\right] . \qquad \text{(IV-13)}$$

After some simple algebra involving (IV-3), (IV-13) becomes

$$\dot{E}_r = -(\sin E \cos\Psi s)\dot{X} - (\sin E \sin\Psi s)\dot{Y} - (\cos E)\dot{Z}$$

$$= -\begin{bmatrix}\sin E \cos\Psi s & \sin E \sin\Psi s & \cos E\end{bmatrix}\begin{bmatrix}\dot{X}\\ \dot{Y}\\ \dot{Z}\end{bmatrix} . \qquad \text{(IV-14)}$$

The rates $\dot{R}$, $\dot{\Psi}s$, and $\dot{E}$ were computed above. These quantities are used below to compute output angular rates $\dot{\theta}s$ and $\dot{\theta}e$ which control rate servos in the arm's shoulder and elbow ($\dot{\Psi}s$ is given by (IV-9)).

The angle Γ can be expressed as

$$\Gamma = \cos^{-1}(\ 2L)$$

which can be differentiated to produce

$$\dot{\Gamma} = -\{1 - (R/2L)^2\}^{-\frac{1}{2}} (2L)^{-1}\dot{R} .$$

However, note that

$$\text{Sin}\,\Gamma = \{1 - \text{Cos}^2\Gamma\}^{\frac{1}{2}}$$
$$= \{1 - (R/2L)^2\}^{\frac{1}{2}}$$

so that

$$\dot{\Gamma} = -\{2L\,\text{Sin}\Gamma\}^{-1}\,\dot{R}\,. \qquad \text{(IV-15)}$$

Equation (IV-15) can be used with (IV-4) and (IV-14) to produce output angular rates

$$\dot{\theta}e = 2\,\dot{\Gamma} \qquad \text{(IV-16)}$$
$$\dot{\theta}s = \dot{E} - 2\,\dot{\Gamma}\,.$$

TD Attitude Control

The segment of Hawk which is responsible for TD attitude control is described below. This segment calculates rotational components which are coupled into the TD axis when the TD undergoes translational motion. These rotational components are combined with inputs representing desired TD rotation rates to form outputs which are fed to the wrist joint servos. This process serves to 1) decouple TD translational and rotational motion, and 2) control the attitude of the TD.

Coordinate system R_3^3 can always be described in terms of a translation and rotation of the system R_0^3. The rotational transformation relating R_3^3 and R_0^3 is of interest here. This rotational transformation, denoted T_3, can be expressed as

$$T_3 = \text{Rot}(Z_1;\Psi s)\text{Rot}(Y_1;\theta s)\text{Rot}(Y_2;\theta e)\text{Rot}(Y_3;\theta w)\text{Rot}(Z_3;\Psi w) \quad \text{(IV-17)}$$

where, for example, $\text{Rot}(z_1;\Psi s)$ denotes an elementary rotation by an angle of Ψs around axis Z_1. Note that T_3 does not involve rolls of R_1^3 (elementary rotation about X_1) or R_3^3 (elementary rotation about X_3). A roll of R_1^3 cannot be produced by Hawk and is rarely accomplished(by external indexing) in practice. It is assumed here that system R_3^3 has not been subjected to an initial roll so

that Z_3 lies in the plane formed by the two arm segments.

The rotational transformations comprising T_3 are available from Paul (1). An elementary rotation by an arbitrary angle θ about an arbitrary Y axis can be produced by

$$\text{Rot}(Y;\theta) = \begin{bmatrix} \text{Cos}\theta & 0 & \text{Sin}\theta \\ 0 & 1 & 0 \\ -\text{Sin}\theta & 0 & \text{Cos}\theta \end{bmatrix} . \qquad \text{(IV-18)}$$

An elementary rotation by an arbitrary angle ϕ about an arbitrary Z axis can be produced by

$$\text{Rot}(z;\phi) = \begin{bmatrix} \text{Cos}\phi & -\text{Sin}\phi & 0 \\ \text{Sin}\phi & \text{Cos}\phi & 0 \\ 0 & 0 & 1 \end{bmatrix} . \qquad \text{(IV-19)}$$

Equations (IV-18) and (IV-19) can be used to write

$$T_3 = \begin{bmatrix} C\Psi s & -S\Psi s & 0 \\ S\Psi s & C\Psi s & 0 \\ 0 & 0 & 1 \end{bmatrix} \begin{bmatrix} C\theta T & 0 & S\theta T \\ 0 & 1 & 0 \\ -S\theta T & 0 & C\theta T \end{bmatrix} \begin{bmatrix} C\Psi w & -S\Psi w & 0 \\ S\Psi w & C\Psi w & 0 \\ 0 & 0 & 1 \end{bmatrix}$$

$$= \{t_{ij}\} \quad ij = 1,2,3 \qquad \text{(IV-20)}$$

where

t_{11} = CθT CΨw CΨs - SΨs SΨw

t_{12} = -CθT CΨs SΨw - SΨs CΨw

t_{13} = CΨs SθT

t_{21} = CθT SΨs CΨw + CΨs SΨw

t_{22} = -CθT SΨs SΨw + CΨs CΨw

t_{23} = SΨs SθT

$$t_{31} = -S\theta T\ C\Psi w$$

$$t_{32} = S\theta T\ S\Psi w$$

$$t_{33} = C\theta T$$

$$\theta T \overset{\Delta}{=} \theta s + \theta e + \theta w\ .$$

The abbreviations $C\theta = \text{Cos}\theta$ and $S\theta = \text{Sin}\theta$ are used in (IV-20). Also, note that the three successive pitch transformations in T_3 were combined into one transformation involving θT.

The relationship between incremental angles $d\theta s$, $d\Psi s$, and $d\theta e$ and an incremental change in T_3, denoted by dT_3, is developed below. This relationship is given by

$$dT_3 = \left[\frac{\delta T_3}{\delta \theta T}\frac{\delta \theta T}{\delta \theta s}\right] d\theta s + \left[\frac{\delta T_3}{\delta \Psi s}\right] d\Psi s + \left[\frac{\delta T_3}{\delta \theta T}\ \frac{\delta \theta T}{\delta \theta e}\right] d\theta e \qquad \text{(IV-21)}$$

where T_3 is given by (IV-20). If (IV-20) is substituted into (IV-21) one obtains

$$dT_3 = \{dt_{ij}\}\ ij=1,2,3 \qquad \text{(IV-22)}$$

where

$$dt_{11} = -S\theta T\ C\Psi w\ C\Psi s \left[d\theta s + d\theta e\right] - \left[C\theta T\ C\Psi w\ S\Psi s + C\Psi s\ S\Psi w\right] d\Psi s$$

$$dt_{12} = S\theta T\ C\Psi s\ S\Psi w \left[d\theta s + d\theta e\right] + \left[C\theta T\ S\Psi s\ S\Psi w - C\Psi s\ C\Psi w\right] d\Psi s$$

$$dt_{13} = C\Psi s\ C\theta T \left[d\theta s + d\theta e\right] - \left[S\Psi s\ S\theta T\right] d\Psi s$$

$$dt_{21} = -S\theta T\ S\Psi s\ C\Psi w \left[d\theta s + d\theta e\right] + \left[C\theta T\ C\Psi s\ C\Psi w - S\Psi s\ S\Psi w\right] d\Psi s$$

$$dt_{22} = S\theta T\ S\Psi s\ S\Psi w \left[d\theta s + d\theta e\right] - \left[C\theta T\ C\Psi s\ S\Psi w + S\Psi s\ C\Psi w\right] d\Psi s$$

$$dt_{23} = S\Psi s\ C\theta T \left[d\theta s + d\theta e\right] + \left[C\Psi s\ S\theta T\right] d\Psi s$$

$$dt_{31} = -C\theta T\ C\Psi w \left[d\theta s + d\theta e\right]$$

$$dt_{32} = C\theta T\ S\Psi w \left[d\theta s + d\theta e\right]\ .$$

$$dt_{33} = -S\theta T \left[d\theta s + d\theta e\right]\ .$$

Equation (IV-22) demonstrates how infinitesimal changes in angles ψs, θs, and θe produce infinitesimal changes in T_3. Equivalently, Equation (IV-22) shows how infinitesimal changes in the attitude of system R_3^3 (containing the TD) can be produced by infinitesimal changes in the shoulder and elbow angles.

The above mentioned infinitesimal change in the attitude of system R_3^3 can be produced by rotating R_3^3 through infinitesimal pitch, yaw, and roll angles, denoted by $d\theta w$, $d\psi w$, and $d\phi w$, respectively, referenced to R_3^3 (for example, $d\theta w$ represents a rotation about Y_3). This fact is used below to obtain a relationship between the wrist angles $d\theta w$, $d\psi w$, and $d\phi w$ and the shoulder/elbow angles $d\theta s$, $d\psi s$, and $d\theta e$; both sets of angles produce the same infinitesimal change in the attitude of R_3^3.

An infinitesimal change in the attitude of system R_3^3 due to a rotation, as described above, of this system through angles $d\theta w$, $d\psi w$, and $d\phi w$ is given in Paul [1] by

$$T_3 \left[ROTE - I\right] \qquad \text{(IV-23)}$$

where T_3 is given by (IV-20) and

$$ROTE = \begin{bmatrix} 1 & -d\psi w & d\theta w \\ d\psi w & 1 & -d\phi w \\ -d\theta w & d\phi w & 1 \end{bmatrix} . \qquad \text{(IV-24)}$$

Transformation ROTE is a first - order approximation of ROT $(X_3; d\phi w)$ ROT $(Y_3; d\theta w)$ ROT $(Z_3; d\psi w)$.

The desired relationship between wrist angles and shoulder/elbow angles is obtained by equating (IV-22)and (IV-23)to obtain

$$T_3 \left[ROTE - I\right] = dT_3$$

or

$$ROTE - I = T_3^{-1} dT_3 . \qquad \text{(IV-25)}$$

Computing the matrix product on the right hand side of (IV-25)can best be accomplished in three parts by realizing that (see (IV- 20))

$$T_3^{-1} = M_1 M_2 M_3$$

where

$$M_1 = \begin{bmatrix} C\psi w & -S\psi w & 0 \\ S\psi w & C\psi w & 0 \\ 0 & 0 & 1 \end{bmatrix}^{-1} = \begin{bmatrix} C\psi w & S\psi w & 0 \\ -S\psi w & C\psi w & 0 \\ 0 & 0 & 1 \end{bmatrix}$$

$$M_2 = \begin{bmatrix} C\theta T & 0 & S\theta T \\ 0 & 1 & 0 \\ -S\theta T & 0 & C\theta T \end{bmatrix}^{-1} = \begin{bmatrix} C\theta T & 0 & -S\theta T \\ 0 & 1 & 0 \\ S\theta T & 0 & C\theta T \end{bmatrix}$$

$$M_3 = \begin{bmatrix} C\Psi s & -S\Psi s & 0 \\ S\Psi s & C\Psi s & 0 \\ 0 & 0 & 1 \end{bmatrix}^{-1} = \begin{bmatrix} C\Psi s & S\Psi s & 0 \\ -S\Psi s & C\Psi s & 0 \\ 0 & 0 & 1 \end{bmatrix}$$

The quantity $T_3^{-1}\, dT_3$ is most easily computed by first computing $M_3\, dT_3$ followed by $M_2\,(M_3\, dT_3)$ and finally by $M_1\,(M_2\,(M_3\, dT_3))$.

Equation (IV-25) produces

$$\begin{bmatrix} 0 & -d\Psi w & d\theta w \\ d\Psi w & 0 & -d\phi w \\ -d\theta w & d\phi w & 0 \end{bmatrix} = \begin{bmatrix} 0 & 0 & C\Psi w \\ 0 & 0 & -S\Psi w \\ -C\Psi w & S\Psi w & 0 \end{bmatrix} (d\theta s + d\theta e) + \begin{bmatrix} 0 & -C\theta T & S\Psi w\, S\theta T \\ C\theta T & 0 & S\theta T\, C\Psi w \\ -S\theta T\, S\Psi w & -S\theta T\, C\Psi w & 0 \end{bmatrix} d\Psi s \qquad \text{(IV-26)}$$

Equation (IV-26) produces

$$\begin{aligned} d\Psi w &= (\text{Cos } \theta T)\, d\Psi s \\ d\theta w &= \text{Cos } \Psi w\, (d\theta s + d\theta e) + (\text{Sin } \Psi w\, \text{Sin } \theta T)\, d\Psi s \\ &= \text{Cos } \Psi w\, \{d\theta s + d\theta e + (\text{Tan } \Psi w\, \text{Sin } \theta T)\, d\Psi s\} \\ d\phi w &= \text{Sin } \Psi w\, (d\theta s + d\theta e) - (\text{Sin } \theta T\, \text{Cos } \Psi w)\, d\Psi s \\ &= \text{Sin } \Psi w\, \{d\theta s + d\theta e - (\text{Sin } \theta T/\text{Tan } \Psi w)\, d\Psi s\} \end{aligned} \qquad \text{(IV-27)}$$

which are the desired relationships between shoulder, elbow and wrist infinitesimal angles. The relationship between shoulder, elbow, and wrist angular rates can be obtained from (IV-27) by replacing differentials of angles by derivatives of angles.

Let $\dot{P}w$, $\dot{Y}w$, and $\dot{R}w$ denote the desired R_3^3 - based TD pitch, yaw, and roll rates obtained as input data. Output rate information which must be fed to wrist rate servos to obtain the above-mentioned TD rates is given by

$$\begin{aligned}
\dot{\theta}w &= \dot{P}w - \mathrm{Cos}\Psi w \{\dot{\theta}s + \dot{\theta}e + \{\mathrm{Tan}\Psi w\ \mathrm{Sin}\theta T\}\ \dot{\Psi}s\ \} \\
\dot{\Psi}w &= \dot{Y}w - \{\mathrm{Cos}\theta T\}\ \dot{\Psi}s \qquad \text{(IV-28)} \\
\dot{\phi}w &= \dot{R}w - \mathrm{Sin}\Psi w \{\dot{\theta}s + \dot{\theta}e - \{\mathrm{Sin}\theta T/\mathrm{Tan}\Psi w\}\ \dot{\Psi}s\ \}
\end{aligned}$$

where θw, Ψw, and ϕw denote wrist pitch, yaw, and roll, respectively.

V. NUMERICAL SIMULATION

The Hawk Control Algorithm developed in Section IV was numerically simulated on the computer. The Fortran program listed below receives rates $\dot{X}$, $\dot{Y}$, $\dot{Z}$, $\dot{P}w$, $\dot{Y}w$, and $\dot{R}w$ as input. The arm segment length(see Figure 2), L, is arbitrary and was selected as unity. The program computes X, Y, Z, θs, Ψs, θe, θw, Ψw, ϕw, θT, and $\Psi s + \Psi w$ as functions of time. These quantities are printed out periodically as instructed by the user. The program is listed in Appendix A.

The first simulation run to be described involves the initial angles (describing the initial position of the arm)

$$\begin{aligned} \theta s &= 0 \\ \Psi s &= 0 \\ \theta e &= \pi/4 \\ \theta w &= -\pi/4 \\ \Psi w &= 0 \\ \phi w &= 0. \end{aligned} \qquad \text{(V-1)}$$

The input rates selected were

$$\begin{aligned} \dot{X} &= -.2 \text{ meters/second} \\ \dot{Y} &= 0 \\ \dot{Z} &= 0 \\ \dot{P}w &= 0 \\ \dot{Y}w &= 0 \\ \dot{R}w &= 0. \end{aligned} \qquad \text{(V-2)}$$

The output is presented in Table I. The time units are seconds. The correspondence

$$\begin{aligned} EL &= \theta s + \theta e + \theta w \\ AZ &= \Psi s + \Psi w \\ ROLL &= \phi w \\ TS &= \theta s \end{aligned}$$

```
TIME=.000000
EL=.000000 AZ=.000000 ROLL=.000000
X=1.70711  Y=.000000  Z=-.707106

TS=.000000  PSIS=.000000
TE=.785398
TU=-.785398  PSIU=.000000  PHIU=.000000
&
$TIME=.000000
 EL=-.143081E-04 AZ=.000000 ROLL=.000000

X=1.50883  Y=.000000  Z=-.706876

TS=-.149103  PSIS=.000000
TE=1.17547
TU=-1.02639  PSIU=.000000  PHIU=.000000

TIME=1.99993
EL=-.133514E-04 AZ=.000000 ROLL=.000000
X=1.30874  Y=.000000  Z=-.706682

TS=-.237813  PSIS=.000000
TE=1.46712
TU=-1.22932  PSIU=.000000  PHIU=.000000

TIME=2.99985
EL=-.762939E-05 AZ=.000000 ROLL=.000000
X=1.10873  Y=.000000  Z=-.706496

TS=-.286472  PSIS=.000000
TE=1.70925
TU=-1.42278  PSIU=.000000  PHIU=.000000

TIME=3.99978
EL=-.667572E-05 AZ=.000000 ROLL=.000000
X=.908765  Y=.000000  Z=-.706302

TS=-.296812  PSIS=.000000
TE=1.91714
TU=-1.62033  PSIU=.000000  PHIU=.000000

TIME=4.99971
EL=-.190735E-05 AZ=.000000 ROLL=.000000
X=.708838  Y=.000000  Z=-.706091

TS=-.262854  PSIS=.000000
TE=2.09544
TU=-1.83259  PSIU=.000000  PHIU=.000000

TIME=5.99964
EL=.381470E-05 AZ=.000000 ROLL=.000000
X=.508945  Y=.000000  Z=-.705861

TS=-.173330  PSIS=.000000
TE=2.24268
TU=-2.06935  PSIU=.000000  PHIU=.000000
$EXITS
$$$$EO TERMINATED$$$
```

Table 1: Arm movement in one second intervals.
First simulation run.

TE = θe

TW = θw

PSIS = Ψs

PSIW = Ψw

PHIW = ϕw

should be made. The quantities X, Y, Z denote the wrist point's position relative to R_0^3(see Figure 2). Observe that the values of X given in Table I descrease with time while the values for Y and Z remain essentially unchanged(as they should). The very small changes observed in Z (see Table I) are due, primarily, to program and algorithm truncation errors as discussed below.

Observe that the attitude of the TD remains unchanged under the above wrist point translation. The total wrist elevation angle θT remains essentially unchanged with time. The wrist point translational and TD rotational motions described in Table I are decoupled.

The second simulation run to be described involves arm movement in the X and Y directions simultaneously. The initial position of the arm is described by the angles (V-1). The input rates are

$\dot{X}$ = -.2 meters/second

$\dot{Y}$ = .2 meters/second

$\dot{Z}$ = 0

$\dot{P}w$ = 0

$\dot{Y}w$ = 0

$\dot{R}w$ = 0

The output is presented in Table 2. Observe the movement of the arm in the X and Y directions while essentially no movement in the Z direction occurs. Observe that the attitude of the TD remains essentially unchanged under the above wrist point translation. The total wrist elevation angle $\theta T = \theta s + \theta e + \theta w$ remains essentially unchanged with time. The total wrist yaw, $\Psi s + \Psi w$, also remains constant.

The angular output obtained from the second simulation run described above was used to drive a computer graphics model of the arm developed by Fernandez (2). The results are shown in Figures 3 through 9.

```
TIME=.000000
EL=.000000 AZ=.000000 ROLL=.000000
X=1.70711  Y=.000000  Z=-.707106

TS=.000000  PSIS=.000000
TE=.700288
TU=-.700288  PSIU=.000000  PHIU=.000000

TIME=.000000
EL=.6300408E-03 AZ=.8000408E-07 ROLL=.1300408E-01
X=1.00044  Y=.100007  Z=-.700001


TS=-.141617  PSIS=.131791
TE=1.15289
TU=-1.01175  PSIU=-.131791  PHIU=.1320408E-01

TIME=1.00003
EL=.4111987E-02 AZ=.5364428E-06 ROLL=.4588418E-01
X=1.30783  Y=.300004  Z=-.706773

TS=-.215940  PSIS=.296690
TE=1.38668
TU=-1.16682  PSIU=-.296690  PHIU=.4588418E-01

TIME=2.00005
EL=.1284198E-01 AZ=.7152568E-06 ROLL=.8698238E-01
X=1.10712  Y=.599520  Z=-.706710

TS=-.252993  PSIS=.496303
TE=1.52951
TU=-1.26388  PSIU=-.496296  PHIU=.8698238E-01

TIME=3.00078
EL=.2310008E-01 AZ=.4500158E-04 ROLL=.1169278
X=.906386  Y=.798000  Z=-.706687

TS=-.268385  PSIS=.722513
TE=1.69114
TU=-1.30.86  PSIU=-.722468  PHIU=.1169288

TIME=4.00071
EL=.2158408E-01 AZ=.1137268E-03 ROLL=.1692018
X=.705757  Y=.898298  Z=-.706677

TS=-.252651  PSIS=.955414
TE=1.57317
TU=-1.28894  PSIU=-.955300  PHIU=.1692018

TIME=5.00054
EL=-.1607068E-01 AZ=.1277928E-03 ROLL=.4372268E-01
X=.905391  Y=1.19763  Z=-.706842

TS=-.239812  PSIS=1.17144
TE=1.47485
TU=-1.25201  PSIU=-1.17132  PHIU=.4372888E-01
$EXITS
$$$
```

Table 2: Arm movement in one s nd intervals.
Second simulation run.

Figure 3 shows the initial position of the arm at T = 0. The arm's position in one second increments is shown by the remaining figures. Note that the arm moves in the X and Y directions but has no movement in the Z direction. Note that the attitude of the TD remains essentially unchanged under this wrist point translation.

VI. CONCLUSION

An algorithm for the computer control of a seven degree of freedom manipulator arm has been developed. The algorithm has been segmented into two parts. The first part receives input translational rate information and controls translation of the terminal device. The second segment receives rotational rate information and controls the attitude of the terminal device. The two segments interact to achieve decoupling of terminal device translational and rotational motions. The algorithm is summarized in Table 3 below. The relevant angles are shown on Figure 2.

The Hawk control algorithm does not represent an exact solution to the arm's Kinematic equations. Instead, Hawk represents a simple first order approximation to the exact solution (see (IV-24) and the sentence following this equation). Hence, small errors (due to truncation) should be expected. However, these truncation errors can be made insignificant by using a sufficiently small integration step size (Double precision arithmetic maybe required to control round-off errors when the step size is made small).

TD Translation Motion

$$\begin{bmatrix} \dot{R} \\ \dot{\Psi}sR \\ \dot{E}R \end{bmatrix} = \begin{bmatrix} \text{Cos E Cos } \Psi s & \text{Cos E Sin } \Psi s & -\text{Sin E} \\ -\text{Sin } \Psi s/\text{Cos E} & \text{Cos } \Psi s/\text{Cos E} & 0 \\ -\text{Sin E Cos } \Psi s & -\text{Sin E Sin } \Psi s & -\text{Cos E} \end{bmatrix} \begin{bmatrix} \dot{X} \\ \dot{Y} \\ \dot{Z} \end{bmatrix}$$

$$E = \theta s + \tfrac{1}{2}\,\theta e$$

$$R = 2L\,\text{Cos}(\tfrac{1}{2}\theta e)$$

$$\Gamma = \tfrac{1}{2}\,\theta e$$

$$\dot{\Gamma} = -\left[2L\,\text{Sin}\Gamma\right]^{-1}\dot{R}$$

$$\dot{\theta}e = 2\,\dot{\Gamma}$$

$$\dot{\theta}s = \dot{E} - \dot{\Gamma}$$

$\dot{X}, \dot{Y}, \dot{Z}$ Represent Input Data

$\dot{\Psi}s, \dot{\theta}s, \dot{\theta}e$ Represent Output Data

TD Rotational Motion

$$\dot{\Psi}w = \dot{Y}w - [(\text{Cos } \theta T)\,\dot{\Psi}s]$$

$$\dot{\theta}w = \dot{P}w - [\text{Cos } \Psi w\,(\dot{\theta}s + \dot{\theta}e) + (\text{Sin } \Psi w \text{ Sin } \theta T)\,\dot{\Psi}s]$$

$$= \dot{P}w - \text{Cos } \Psi w\,[\dot{\theta}s + \dot{\theta}e + \{\text{Tan } \Psi w \text{ Sin } \theta T\}\,\dot{\Psi}s]$$

$$\dot{\phi}w = \dot{R}w - [\text{Sin } \Psi w\,(\dot{\theta}s + \dot{\theta}e) - (\text{Sin } \theta T \text{ Cos } \Psi w)\,\dot{\Psi}s]$$

$$= \dot{R}w - \text{Sin } \Psi w\,[\dot{\theta}s + \dot{\theta}e - \{\text{Sin } \theta T/\text{Tan } \Psi w\}\,\dot{\Psi}s]$$

$$\theta T = \theta s + \theta e + \theta w$$

$\dot{P}w, \dot{Y}w, \dot{R}w$ Represent Input Data

$\dot{\theta}w, \dot{\Psi}w, \dot{\phi}w$ Represent Output Data

Table 3: Hawk Control Algorithm

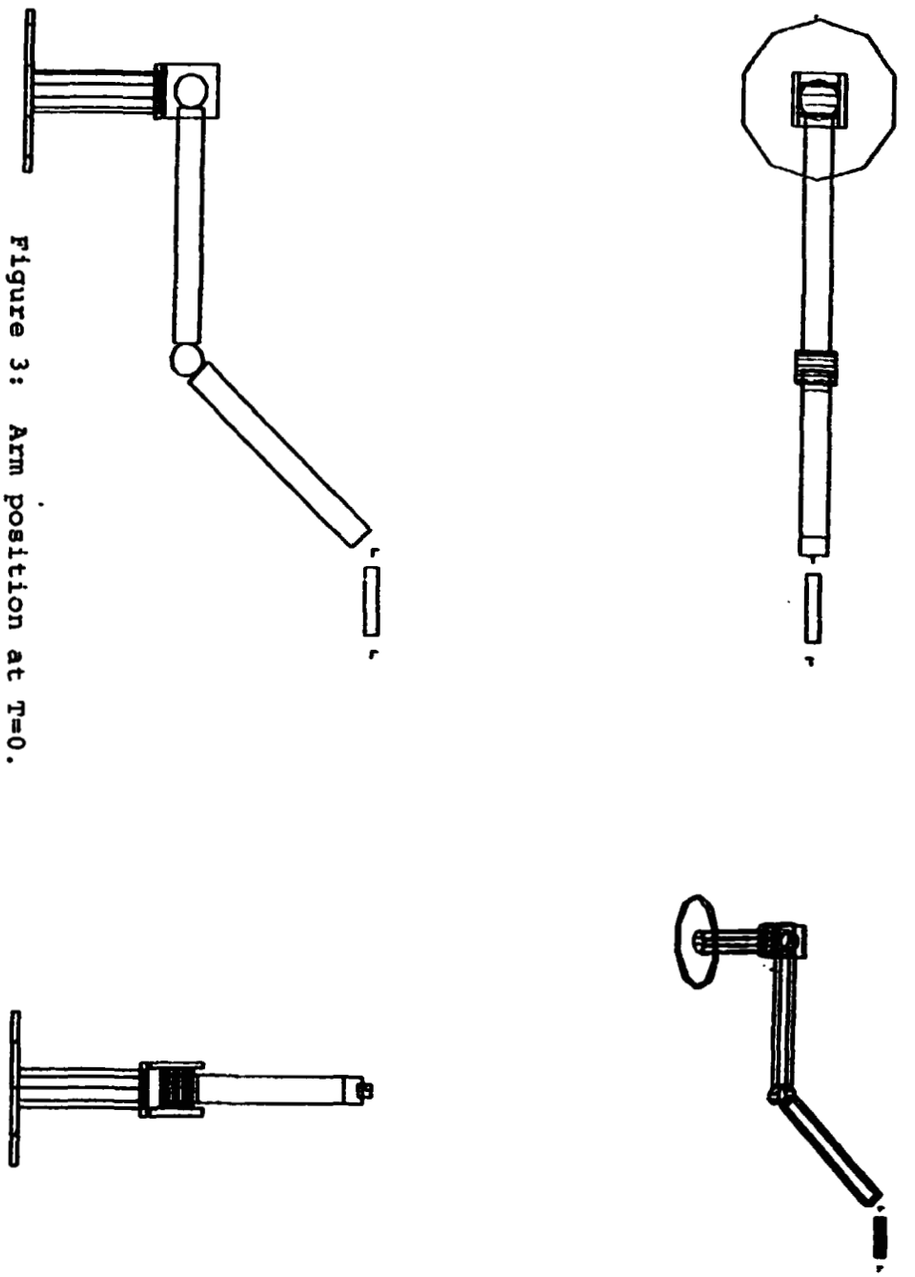

Figure 3: Arm position at T=0.

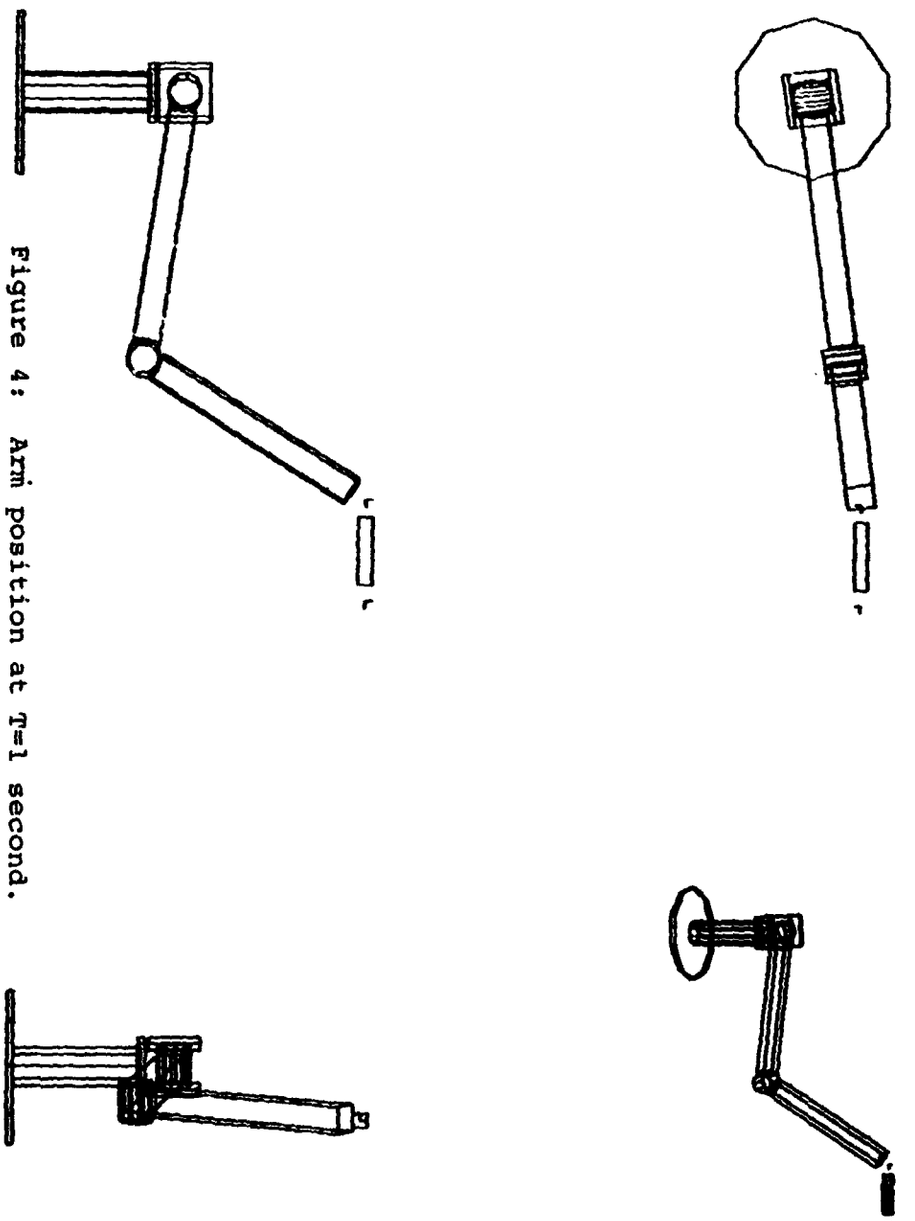

Figure 4: Arm position at T=1 second.

Figure 5: Arm position at T=2 seconds.

Figure 6: Arm position at T=3 seconds.

Figure 7: Arm position at T=4 seconds.

Figure 8: Arm position at T=5 seconds

?

Figure 9: Arm position at T=6 seconds.

APPENDIX A

The computer program used to simulate Hawk in Section V is described below. The main program, which implements the equations listed in Table 1, is written in Fortran. This program accepts initial (T=0) values for the angles θs, Ψs, θe, θw, Ψw, ϕw, as well as the desired rates $\dot{X}$, $\dot{Y}$, $\dot{Z}$, $\dot{P}w$, $\dot{Y}w$, and $\dot{R}w$ (the initial roll angle ϕw should always be input as zero).

The program computes θs, Ψs, θe, θw, Ψw, and ϕw as functions of time. These output rates are integrated and periodically (period determined by user) printed out and (simultaneously) written to a file for use by a graphics routine that plots the arm.

PROGRAM FLOWCHART

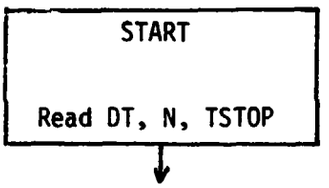

DT represents a time increment used in the numerical integration (trapezoidal rule). All angles are computed every DT seconds.

N represents the output interval. Output is printed every N DT seconds.

The program terminates when T = TSTOP.

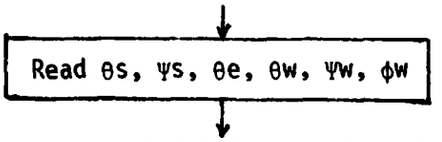

These quantities represent initial conditions for the joint angles. The algorithm was developed by assuming that ϕw is initially zero.

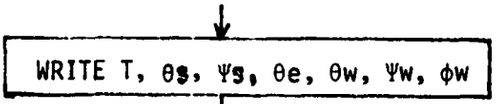

The initial conditions(T=0) are printed out.

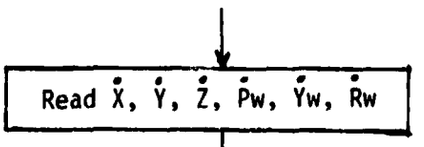

$\dot{X}$, $\dot{Y}$, $\dot{Z}$ represent desired wrist point translation rates.

$\dot{P}w$, $\dot{Y}w$, $\dot{R}w$, represent desired TD rotational rates

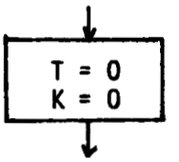

Initialize time and loop counter.

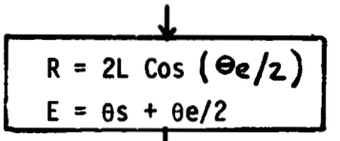

R represents length of wrist point vector

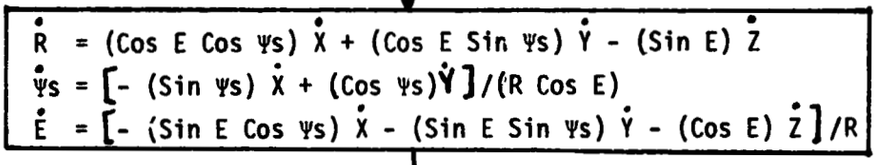

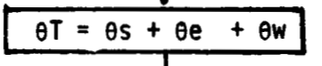

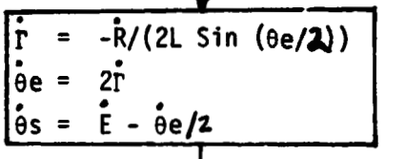

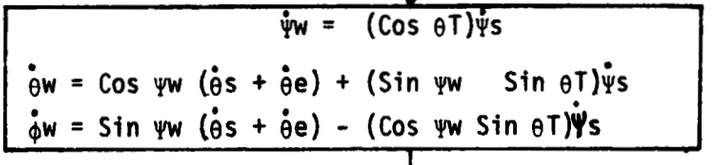

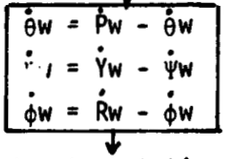

Last block shows how wrist rate rotation commands are calculated as the difference between desired values and those resulting from wrist point translation motion.

ORIGINAL PAGE IS
OF POOR QUALITY

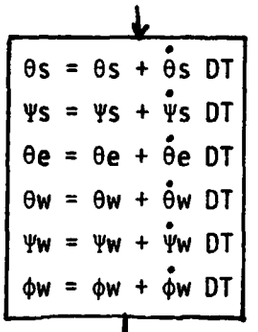

Update angles by integration using trapezoidal rule

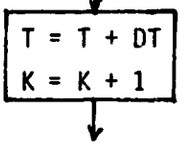

Increment time and loop counter

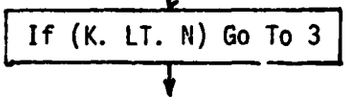

K < N ⇒ Do not plot arm; go back and compute

K = N ⇒ It's time to print output.

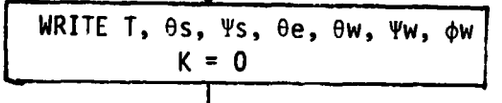

Plot arm and set loop counter to zero

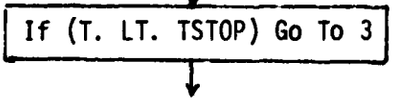

T < TSTOP Not through; go back and compute

T > TSTOP End program

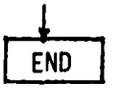

```
TV
  1.000 C THIS PROGRAM IS A GRAPHIC SIMULATION OF THE HAUK
  1.500 C CONTROL MODE IMPLEMENTED ON THE PFMA
  1.700       REAL L
  2.100       READ(10,1)DT
  2.500       READ(10,2)N
  2.500       READ(10,1)TSTOP
  2.700  1    FORMAT(G)
  2.800  2    FORMAT(G)
  3.000 C SHOULDER PITCH IS TS
  4.000 C SHOULDER YAW IS PSIS
  5.000 C ELBOW PITCH IS TE
  6.000 C WRIST PITCH IS TW
  7.000 C WRIST YAW IS PSIW
  8.000 C WRIST ROLL IS PHIW
  9.000 C
 10.000 C READ INITIAL ANGLES
 11.000       READ(10,1)TS
 11.100       READ(10,1)PSIS
 11.200       READ(10,1)TE
 11.300       READ(10,1)TW
 11.400       READ(10,1)PSIW
 11.500       READ(10,1)PHIW
 14.000 C READ DESIRED WRIST COORDINATE RATES
 15.000 C XDOT IS X-AXIS WRIST VELOCITY COMPONENT
 16.000 C YDOT IS Y-AXIS WRIST VELOCITY COMPONENT
 17.000 C ZDOT IS Z-AXIS WRIST VELOCITY COMPONENT
 18.000       READ(10,1)XDOT
 18.100       READ(10,1)YDOT
 18.200       READ(10,1)ZDOT
 19.000 C READ DESIRED WRIST ANGLE RATES
 20.000 C PWDOT IS WRIST PITCH RATE
 21.000 C YWDOT IS WRIST YAW RATE
 26.000 C RWDOT IS WRIST ROLL RATE
 31.000       READ(10,1)PWDOT
 36.000       READ(10,1)YWDOT
 41.000       READ(10,1)RWDOT
 42.000       T=0.
 43.000       K=0
 46.000       L=4.
 46.600       EL=TS+TE+TW
 46.700       AZ=PSIS+PSIW
 46.800       ROLL=PHIW
 46.805       R=2.*L*COS(TE/2.)
 46.810       X=R*COS(TS+TE/2.)*COS(PSIS)
 46.820       Y=R*COS(TS+TE/2.)*SIN(PSIS)
 46.830       Z=-R*SIN(TS+TE/2.)
 46.900       WRITE(1,55)T
 47.000       WRITE(1,50)EL,AZ,ROLL
 48.000       WRITE(1,51)X,Y,Z
 48.100       WRITE(1,61)TS,PSIS
 48.200  61   FORMAT('0','TS=',G,1X,'PSIS=',G)
 48.300       WRITE(1,62)TE
 48.400  62   FORMAT(' ','TE=',G)
 48.500       WRITE(1,63)TW,PSIW,PHIW
 49.500  63   FORMAT(' ','TW=',G,1X,'PSIW=',G,1X,'PHIW=',G)
 49.510       WRITE(13,77)PSIS,TS,TE,TW,PSIW,PHIW
 49.520  77   FORMAT(6G)
 51.000   3   CONTINUE
 56.000       R=2.*L*COS(TE/2.)
 57.000       E=TS+TE/2.
 58.000 C COMPUTE RANGE RATE FOR WRIST VECTOR
 59.000       RDOT=COS(E)*COS(PSIS)*XDOT
 60.000       RDOT=RDOT+COS(E)*SIN(PSIS)*YDOT
 60.500       RDOT=RDOT-SIN(E)*ZDOT
 61.000 C COMPUTE SHOULDER YAW RATE
 62.000       ADOT=-SIN(PSIS)*XDOT+COS(PSIS)*YDOT
 67.000       ADOT=ADOT/(R*COS(E))
 72.000 C COMPUTE E RATE
 77.000       EDOT=-SIN(E)*COS(PSIS)*XDOT
 82.000       EDOT=EDOT-SIN(E)*SIN(PSIS)*YDOT
 87.000       EDOT=(EDOT-COS(E)*ZDOT)/R
 92.000 C COMPUTE TOTAL ELEVATION ANGLE
 97.000       TT=TS+TE+TW
102.000 C COMPUTE GAMMA RATE AND ELBOW ANGLE RA
107.000       GDOT=-RDOT/(2.*L*SIN(TE/2.))
108.000       TEDOT=2.*GDOT
109.000 C COMPUTE SHOULDER PITCH RATE
110.000       TSDOT=EDOT-TEDOT/2.
111.000 C COMPUTE WRIST YAW RATE DUE TO SHOULDER
112.000 C AND ELBOW MOTION
117.000       PSIWDOT=COS(TT)*ADOT
122.000 C COMPUTE WRIST PITCH RATE DUE TO SHOULDER
127.000 C AND ELBOW MOTION
132.000       PWDOT=COS(PSIW)*(TSDOT+TEDOT)
137.000       TWDOT=TWDOT+SIN(PSIW)*SIN(TT)*ADOT
138.000 C COMPUTE WRIST ROLL RATE DUE TO SHOULDER AND
139.000 C ELBOW MOTION
140.000       PHIWDOT=SIN(PSIW)*(TSDOT+TEDOT)
141.100       PHIWDOT=PHIWDOT-COS(PSIW)*SIN(TT)*ADOT
142.000 C COMPUTE DIFFERENCE BETWEEN DESIRED WRIST
143.000 C ANGLE RATES AND WRIST ANGLE RATES DUE TO
144.000 C SHOULDER AND ELBOW MOTION
145.000       PSIWDOT=YWDOT-PSIWDOT
146.000       TWDOT=PWDOT-TWDOT
147.000       PHIWDOT=RWDOT-PHIWDOT
152.000 C COMPUTE UPDATED ANGLES
157.000       TS=TS+TSDOT*DT
162.000       PSIS=PSIS+ADOT*DT
167.000       TE=TE+TEDOT*DT
172.000       TW=TW+TWDOT*DT
177.000       PSIW=PSIW+PSIWDOT*DT
182.000       PHIW=PHIW+PHIWDOT*DT
183.000       T=T+DT
187.000       K=K+1
192.000       IF(K.LT.N)GO TO 3
197.000       EL=TS+TE+TW
197.100       AZ=PSIS+PSIW
197.150       ROLL=PHIW
197.200       X=R*COS(E)*COS(PSIS)
197.300       Y=R*COS(E)*SIN(PSIS)
197.400       Z=-R*SIN(E)
197.500       WRITE(1,55)T
197.600  55   FORMAT('0','TIME=',G)
198.000       WRITE(1,50)EL,AZ,ROLL
199.000  50   FORMAT(' ','EL=',G,'AZ=',G,'ROLL=',G)
200.000       WRITE(1,51)X,Y,Z
201.000  51   FORMAT(' ','X=',G,1X,'Y=',G,1X,'Z=',G)
201.100       WRITE(1,61)TS,PSIS
201.200       WRITE(1,62)TE
201.300       WRITE(1,63)TW,PSIW,PHIW
202.000       K=0
202.100       WRITE(13,77)PSIS,TS,TE,TW,PSIW,PHIW
207.000       IF(T.LT.TSTOP)GO TO 3
208.000       CALL EXIT
212.000       END
```

REFERENCES

1. Paul, Richard P., Robot Manipulators, The MIT Press, Cambridge, Mass, 1982.

2. Fernandez, Ken, Unpublished Work, Mail Code EB44, MSFC, Al 35812,1983.

3. Tewell, J. R., et al.: Configuration and Design Study of Manipulator Systems Applicable to the Free-Flying Teleoperator, Final Report. Contract NAS8-30266, Martin Marietta Corp., July 1974.

1983

NASA/ASEE SUMMER FACULTY RESEARCH FELLOWSHIP PROGRAM

MARSHALL SPACE FLIGHT CENTER
UNIVERSITY OF ALABAMA IN HUNTSVILLE

ORBITAL MANEUVERING VEHICLE SIMULATION SYSTEM ON-BOARD PROCESSING LOGIC

Prepared by:	William Teoh, Ph.D.
Academic Rank:	Research Scientist
University & Department:	University of Alabama in Huntsville Kenneth Johnson Center
NASA/MSFC Division:	Guidance, Control and Optical Systems Div.
Branch:	Control Electronics
MSFC Counterpart:	E. C. Smith
Date:	August 12, 1983
Contract No:	NGT 01-008-021 UAH

ABSTRACT

The control logic for an Orbital Maneuvering Vehicle (OMV) Simulation system is developed. In order that better control over the vehicle can be exercised, several modifications to the vehicle are suggested. The need of better position feedback leads to the development of an alternative simpler but more reliable navigation system which is also discussed. The control logic is presented in pseudocode form, and can be implemented in FORTRAN and/or MACRO II.

INTRODUCTION

Orbital Maneuvering System (OMV) is a concept being investigated here at NASA in which a free-flying space module is put under the remote control of a human operator. Such a system is of great importance in space explorations as such a module can perform tasks in an environment that is too hostile for humans. Mission capabilities of the OMV module could include tasks such as placement, retrieval, inspection and orbit-boosting of space vehicles or satellites. When fitted with a remote-control manipulator arm, such a module can service and perhaps repair satellites, thereby drastically reducing an astronaut's need for extra-vehicular activities (EVA). An interesting possibility would be in debris collection; in this process, an OMV module could dock with a spent satellite or any man-made object no longer operational, and boost it into a "junk" orbit.

The operator controlling the OMV module is physically remote from the module, and exercises control over the module based on video feedback from the module, using some form of a hand controller. Realistically, this system is not very suitable when the distance between the operator and the module is too large, as the long time delay would make meaningful control impossible. Actual studies have shown that a time delay of up to 1/4 seconds is imperceptible to humans. Thus, when the OMV module is in a low orbit, the operator could be on the ground. When the module is at a higher orbit, the operator could be in the space shuttle or a space station.

Orbital Maneuvering Vehicle Simulation System

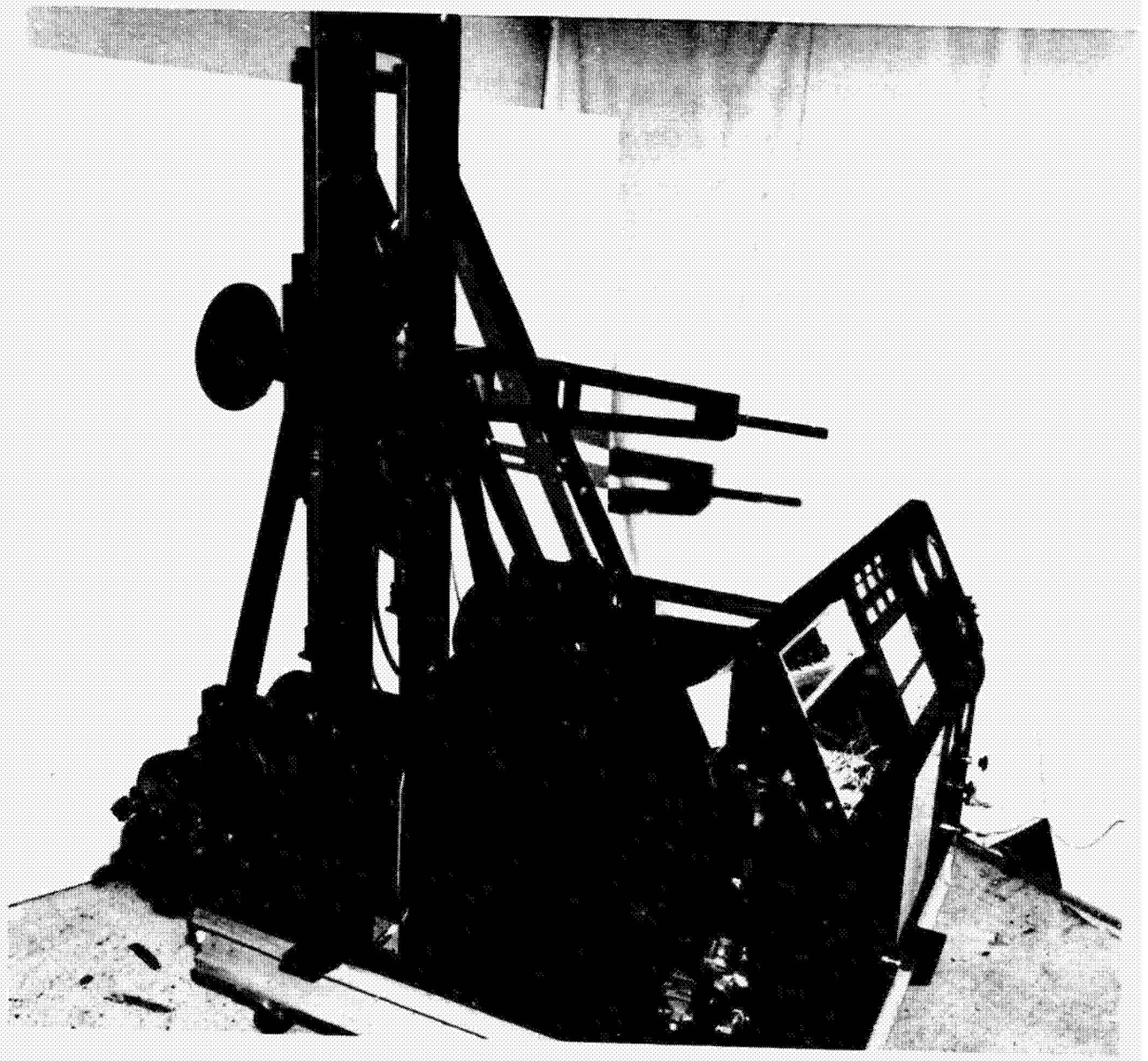

Figure 2. TOM-B

OMV SIMULATION SYSTEM

A simulation of the OMV system has been constructed here at Marshall Space Flight Center, Huntsville, Alabama. The hardware of this system consists of a vehicle (called TOM-B) which floats on air bearings on a flat floor measuring 80 by 40 feet. TOM-B has 6 degrees of freedom. A mock-up of the OMV module can be mounted on TOM-B. By executing appropriate motions of this vehicle one can simulate the motion of the OMV module. An artist's perception of the hardware system is shown in Figure 1. In this figure, an operator in a separate room controls the OMV mock-up using a hand controller. A computer examines constantly the status of the hand controller, and feeds the information into a mathematical model in the computer. The output of this model is translated into a sequence of commands to be transmitted to TOM-B to be executed. It is important to realize that the motion of TOM-B is not necessarily that of the mock-up module. For example, if the mock-up module were to execute a yaw about its Z axis, the output of the model would generate a sequence of commands to TOM-B to execute a translation plus a rotation.

This report concerns a project that involves developing suitable control logic and software for the on-board computer on TOM-B in such a manner that commands transmitted by the mainframe computer will be intercepted and executed. The command sequence consists of a set of 6 numbers from which one can deduce the absolute positions of the 6 axes of motion, and the command sequence is updated ten times per second.

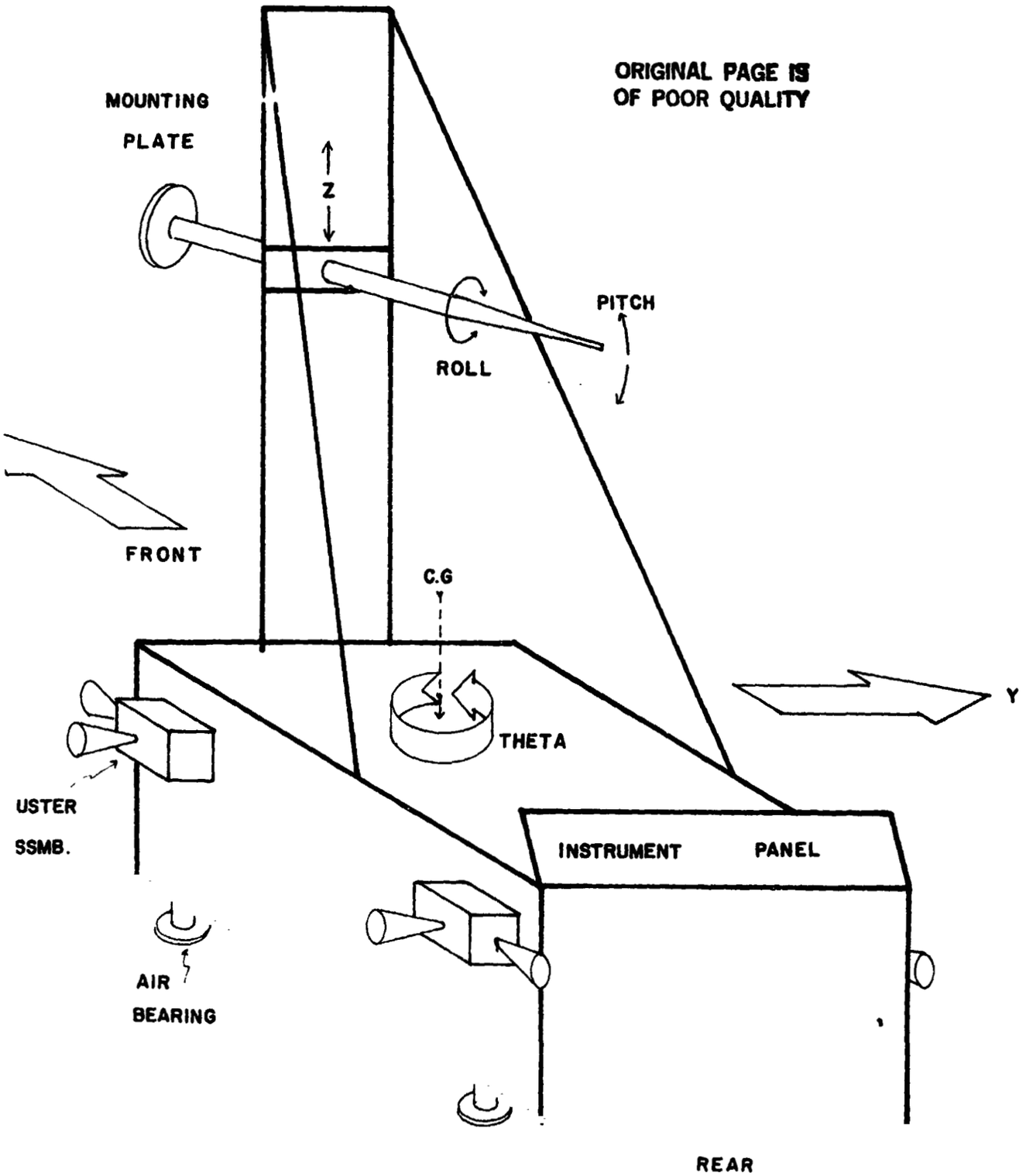

Figure 3. TOM-B Showing the Six Degrees of Freedom and Thruster Assembly.

Thus, the on-board logic must be capable of executing a command sequence within 100 milli-seconds, which shall be referred to as a major period. A PDP 11/23 micro-computer will be used to interpret and execute this control logic.

Figure 2 shows a picture of the almost completed TOM-B while Table 1 lists some of the specifications of the vehicle:

Table 1

TOM-B Characteristics

Approximate mass	:	55.9 slugs
Moment of inertia	:	240.6 slug-ft-ft
Mass of fuel	:	9.4 slugs
Number of thrusters	:	8
Thrust developed	:	3 lbs/thruster

A pair of thrusters, each of which is capable of delivering 3 lbs of thrust, is mounted at each corner of the vehicle. Cold compressed air at 3500 psi is used as a propellant. Six air cylinders are used to store this compressed air, which is also used to power the air bearings, as shown in Figure 3. The on-board processor, associated electronics and sensors will be mounted near the control panel. Two accelerometers and a gyroscope are used to monitor the position and orientation of the vehicle. Note that translation in X and Y direction, as well as yaw motion of the vehicle are obtained by firing the appropriate thrusters, while translation along the Z axis, as well as

Figure 4.

TOM-B

Control Hardware Organization

ORIGINAL PAGE IS
OF POOR QUALITY

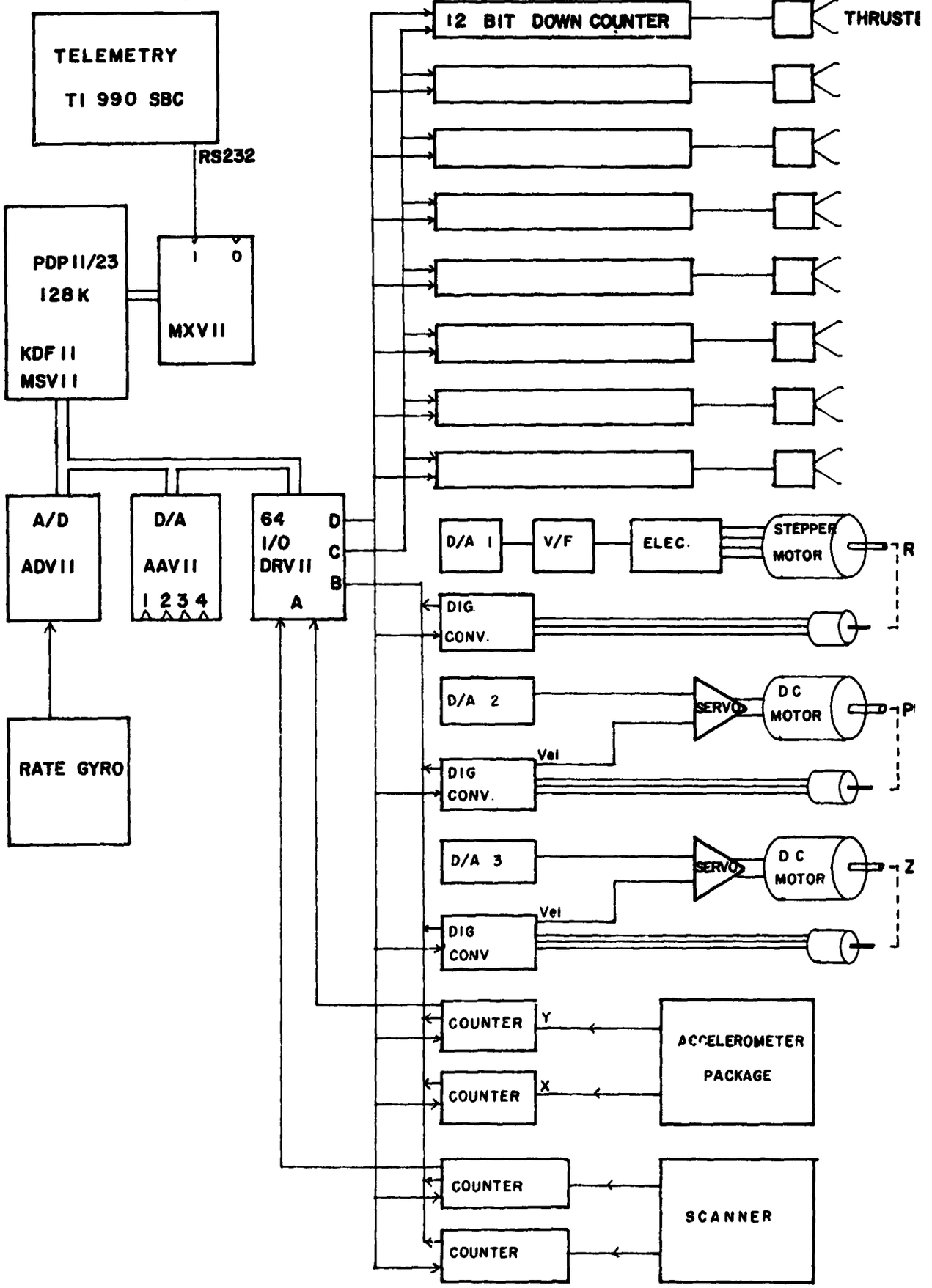

pitch and roll (of the mock-up module) is carried out using stepping motors fitted with optical decoders. A hardware organization diagram is shown in Figure 4. In addition, a radar is used to determine distance between the module and target module during docking maneuvers.

It is important to note that this is only a simulator and is not the actual OMV module. In an actual OMV module, the thrusters would be mounted on the OMV itself.

The control logic for the stepping motors is quite straightforward. It involves calculating the number of pulses needed, sending this information to the appropriate motor controller, and subsequently examining the decoder feedback to determine if the desired position has been reached. The control logic for the thrusters is much more complicated, and the rest of the report concerns the development of appropriate thruster control logic.

RECOMMENDED MODIFICATIONS

A closer examination of Figure 3 reveals that the thrusters along the long axis of the vehicle are not symmetrical with respect to the center of mass (CG) of the long axis of the vehicle. Furthermore, the CG is not coplanar with CG's of the 6 air cylinders. A direct consequence of the second observation is that the center of mass will shift towards the front end of the vehicle as fuel is being depleted. A digital simulation study shows that the center of mass can shift by as much as an inch when the cylinders are nearly empty. This is

deemed unsatisfactory. Further, the same simulation study reveals that since the thrusters cannot be throttled to vary the thrust, the vehicle cannot move in a straight line perpendicular to the long axis, and that the attitude of the vehicle will be changed, unless corrective burns are made every major cycle. The amount of fuel wasted can be as much as 30%.

A simple modification is therefore proposed (Please see Appendix 1) that would significantly reduce fuel wastage. In addition, the control laws should be drastically simplified. Counter weights can be added to the rear of the vehicle so as to shift the center of mass of TOM-B to be coplanar with that of the air cylinders. In this manner, the shift of center of mass due to depletion of fuel is eliminated. Further, the rear pair of thrusters can be moved towards the front of the vehicle such that all the thrusters are symmetric with respect to the new center of mass. A quick calculation shows that the counter weight needed to accomplish this is given by the formula:

$$M_B = (14\ M_m + 3\ m) / 17 - M_{Bat}$$

where m is the mass of the empty vehicle, M_m is the weight of the mock-up module and counter weights, and M_{Bat} is the weight of the battery pack and associated electronics. Using available data for TOM-B, M_B worked out to be 300 to 600 pounds, depending on the mass of the mock-up assembly. The various advantages for such a modification is presented in Appendix 1. From this point onwards, work is carried out

on the assumption that the above modification will be carried out.

A question that arose naturally is that, given such modification, what sort of performance one can expect from TOM-B. Specifically, a figure of merit for positional accuracy is needed. A detailed analysis shows that the positional accuracy of TOM-B is dictated by the following factors:

a) Center of mass off-set

b) Thruster off-set

c) Thruster differential

d) sensor off-set and

e) sensor drift.

The first three sources of error are related to construction of the vehicle, and can be minimized. It can be shown that the positional accuracy D along either the X or Y direction can be given by the formula:

$$D = \frac{1}{2m} \left[(\epsilon_1 + \epsilon_2)F + (\epsilon_1 - \epsilon_2)\,\Delta F + \frac{\Delta\ddot{\theta}}{6}\, Ft^2 \right] t^2$$

where m is the mass of the vehicle, F is the thrust of a single thruster, ΔF is the thruster differential, ϵ_1, ϵ_2 are the thruster off-set in radians, t is the firing time, and

$$\Delta\ddot{\theta} = \left[5\,\Delta F + \frac{\Delta L}{2} + 5\,(3 + \Delta F)\varepsilon_1 + 5(3 - \Delta F)\varepsilon_2 \right] \Big/ J_{zz}$$

ΔL is the center of mass off-set. Worst case calculation shows that D is about 3 inches after 5 seconds of continuous firing. By worst case we assume a center of mass off-set of 0.2 inches, a thruster off-set of 9 degrees, and a thruster differential of 10%. This result shows that corrective burns must be made after 5 seconds of firing if a positional accuracy of three inches were to be maintained. However, since the commands will be updated every 100 milli-seconds, so will the position. Further, in practice, one can with care align the thrusters to better than 9 degrees from the normal, and that thruster differential may be less than 10%. Thus a positional accuracy much better than 3 inches is expected.

The errors arising from the sensors (accelerometers and rate gyro) are a bit more complicated to analyze. In the present system, it is intended that a pair of accelerometers be used for measuring position, and that a gyro will be used to measure the orientation (or attitude) of the vehicle. The gyro to be installed in TOM-B has a total error rate of 5×10^{-6} degree/sec, which is more than adequate to provide feedback information on angular velocity and displacement. The same cannot be said for the accelerometers. Mr. Tom Bryan has estimated that the drift rate of each accelerometer is of the order of 1 kilometer per hour which far exceeds the accuracy requirement of the present system. This incredibly large error arises from:

1) the high drift rate of the sensor,

2) the signals from the sensors must be integrated numerically to obtain the translational displacement, and

3) the errors are cumulative and propagate with time.

It is important to realize that accelerometers and gyros are really designed to measure acceleration and velocities. When the signals must be integrated to get displacement, the following steps must be carried out:

a) they must be sampled frequently within every major cycle,

b) the signals must be conditioned and corrected for bias, scaling, off-set and drift before they can be used, and

c) to provide reliable displacement, sophisticated integrating algorithms must be used

All these factors contribute to a large computational overhead. In addition, there is no meaningful method of correcting for the drift other than by the use of an external reference, as in spacecrafts. In the case of spacecrafts, ground-based stations or distant stars whose positions are known are frequently used.

Since position control will be used in the present system, it is mandatory to have an accurate navigation system. This effectively rules out the use of accelerometers to provide positional feedback. An alternative, simpler navigational system is needed. It is important to realize that this new nagivation system does not replace the

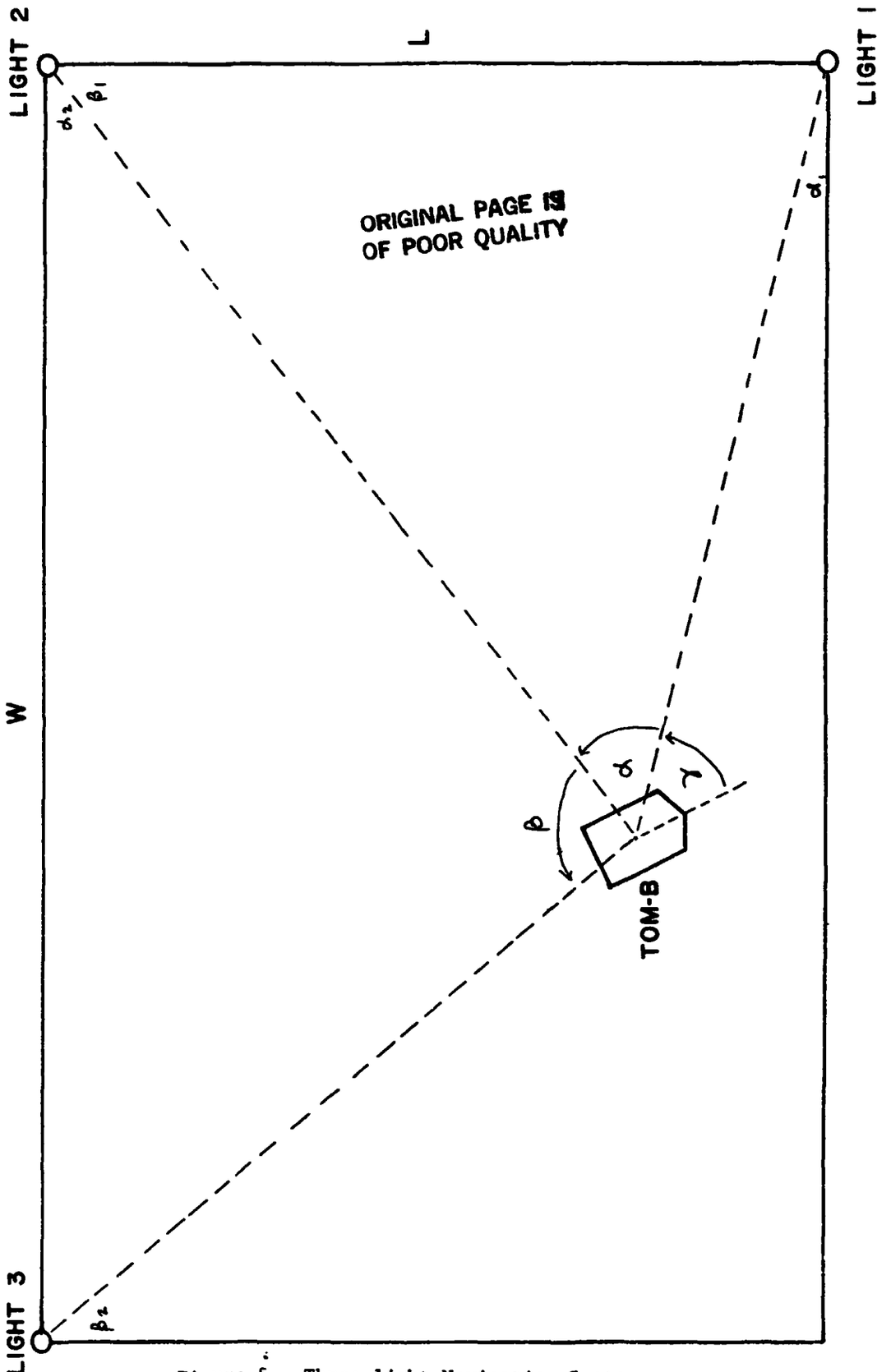

Figure 5. Three-light Navigation System

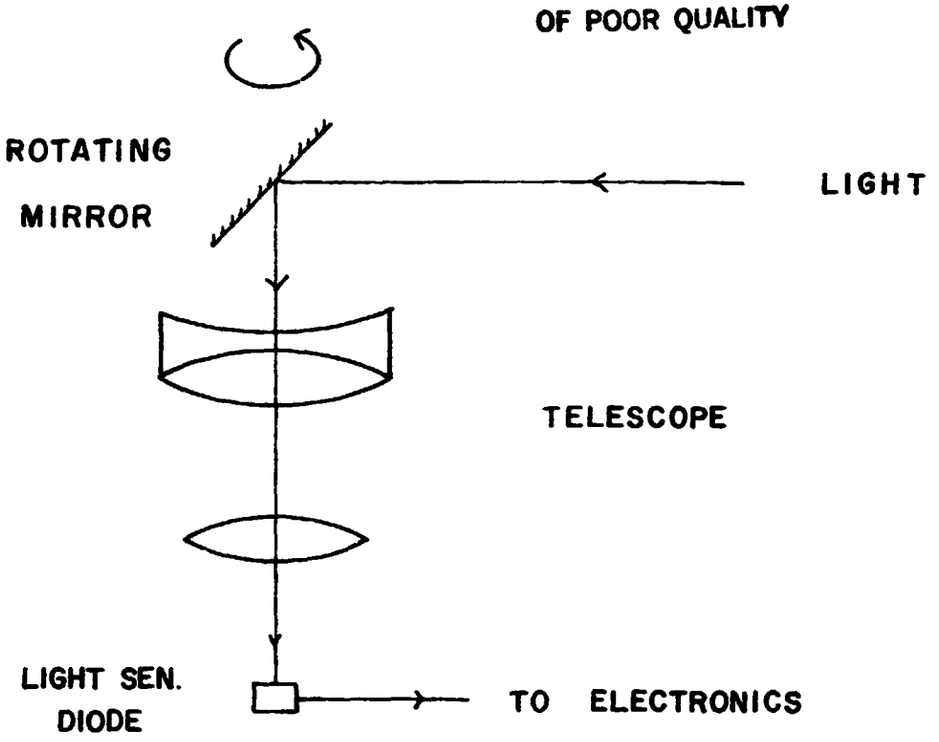

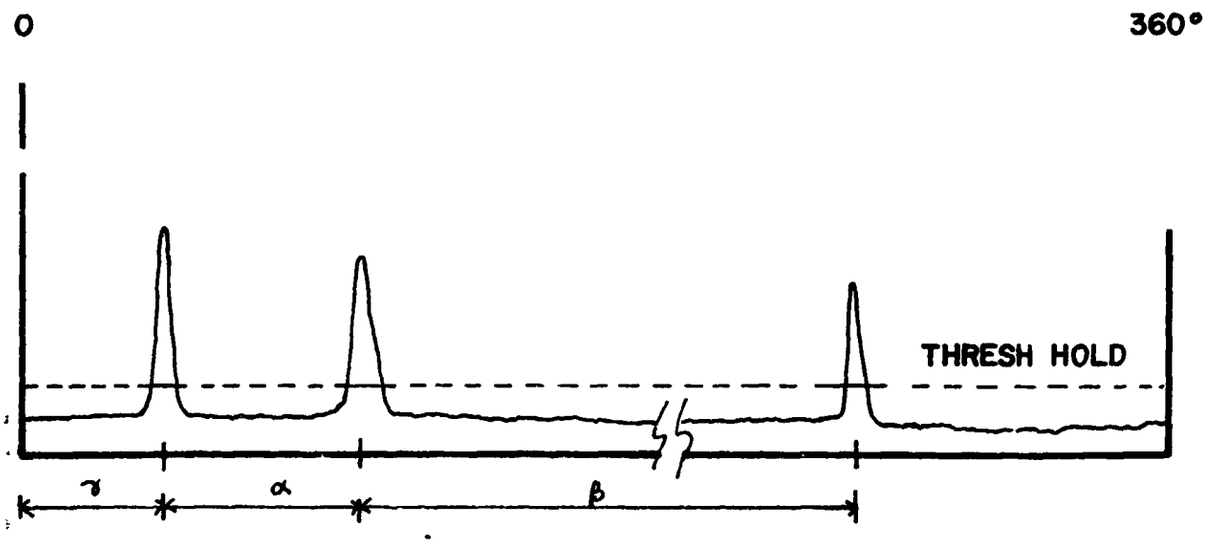

Figure 6. Three-light Navigation System - Rotating Mirror Scanner

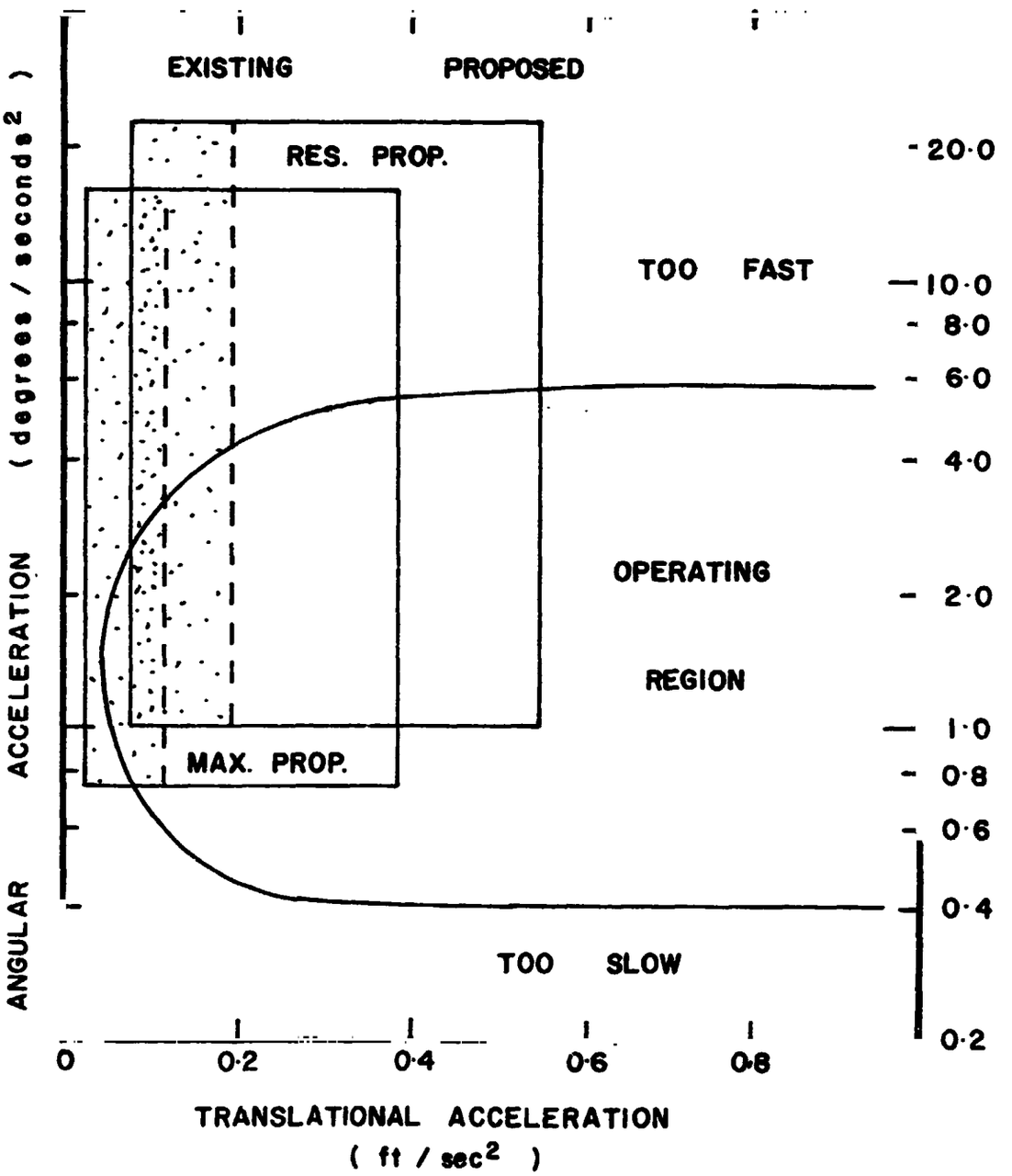

Figure 7. TOM-B Handling Quantities - Translational Acceleration versus Angular Acceleration

accelerometers; they are still needed to provide the rate feedback. The proposed navigation works on the principle that if three lights are erected at three corners of the floor, as shown in Figure 5, then a rotating mirror arrangement as depicted in Figure 6 can be used to detect these three lights. The three angles γ, α and β can be measured with precision. From these three angles, and knowing the length (80 feet) and width (40 feet) of the floor, one can determine the absolute position and orientation of TOM-B. The mathematics for this mode of navigation is quite straightforward, and is derived in detail in Appendix 2, and does not involve any numerical integration. It is estimated that a positional accuracy of one inch can be accomplished easily this way. More importantly, the computation is straightfoward and fast, and the error does not propagate with time. It is emphasized again that this navigation system does not replace those used of accelerometers or gyros.

It is noted that since the mass of the vehicle is quite large, and that each thruster can only provide 3 pounds of thrust, TOM-B would be quite sluggish. A question that arose during the course of this summer is that can additional thrusters be added to TOM-B so that it is capable of achieving a translational acceleration of 0.4 ft/sec/sec ?. A detailed analysis shows that if there were 4 pairs of thrusters instead of 1 pair at each corner, such an acceleration can be attained. The handling qualities of TOM-B is given in Figure 7, which depicts the translational versus rotational acceleration when

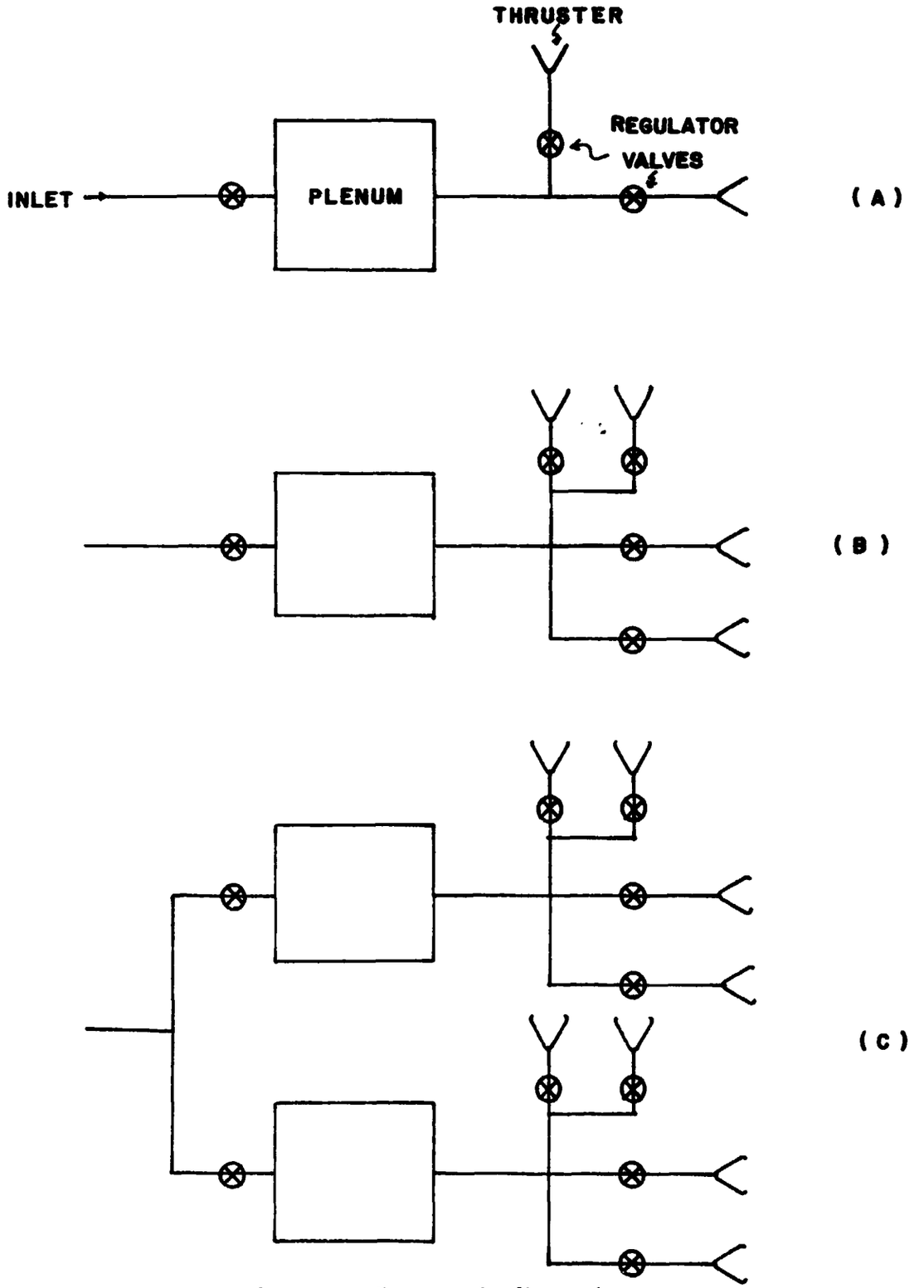

Figure 8. TOM-B Thruster Configuration

the vehicle is full (maximum propellant) and when the vehicle is nearly empty (residue propellant). It is clear from this diagram that TOM-B can rotate about its Z-axis much better than it can translate along the X or Y axis.

From a technical standpoint, it does not seem impossible to install additional thrusters. At present, a pair of thrusters are mounted at right angles on a plenum as shown in a) part of Figure 8. Calculation shows that each plenum is capable of supporting an additional pair, as shown in the b) part of the same figure. Thus, to have four pairs of thrusters at each corner, a configuration as shown in c) part can be used. This involves some plumbing and an additional plenum, but otherwise the implementation is straightforward. From the operational standpoint, the only penalty is a higher rate of fuel consumption, and does not further complicate the control software. In fact, a provision to control up to four individually controllable thruster pairs at each corner is included in the control software.

OMV SIMULATION SYSTEM -- CONTROL LAWS

The modification to be made on TOM-B means that the control laws for the vehicle can be drastically simplified. If the three-light navigation system is also implemented, then the position and orientation (attitude) of the vehicle can be determined rapidly with precision. Since position control will be used, the command structure is expected to consist of a sequence of 6 numbers, each of which specifies the desired position and orientation of the vehicle when the com-

mand is executed. As it turns out, only a limited amount of information can be transmitted over the radio link in 0.1 seconds. Consequently, it is decided that the command string will consist of positional increment (which must be added to the current position to yield the desired position). Further, the most efficient mode of transmission is in integer format and this format will be adopted here. Thus, it is understood that for positional quantities (such as X, Y and Z), the unit used will be 0.001 inch, while for the remaining quantities (angular), a unit of 0.1 degree will be used. By way of example, the command string:

10 0 20 0 0 0

would be interpreted that TOM-B be moved along X axis by 0.01 inches from the current position, and rotate by 2 degrees about its Z axis, all other axes remain unchanged. If we can use symbolic names to represent each of these quantities in the command string, then the command transmitted to TOM-B would look like:

CMD_X, CMD_Y, CMD_THETA, CMD_Z, CMD_P, and CMD_R

that specifies the incremental position and orientation. Appendix 3 shows the detail thruster logic which must be executed by the on-board processor in TOM-B.

Essentially, based on the desired position/orientation and the current position/orientation, one can calculate the required impulses f_x and f_y. This is the required impulse that would move TOM-B from the present position to the desired position, and is expressed most

conveniently in floor coordinates. This impulse must be translated into the corresponding impulses FX and FY which are impulses that must be exerted by TOM-B. This is necessary because at any particular moment, the body-centered coordinate system defined with respect to TOM-B may not be lined up with the floor coordinates. Once FX and FY are known, the individual impulses FX1, FX2, FY1 and FY2 to be exerted by the appropriate thrusters must be determined. From these impulses, one can calculate the firing times of these thrusters since they cannot be throttled. The firing times are then suitably scaled, and the appropriate numbers loaded into the corresponding one-shot down counter. A control signal can then be sent to fire the thrusters, as shown in Figure 4.

Appendix 3 shows the detail derivation of the thruster control logic. Qualitatively, one can see that these control laws make sense. Take the simplest case in which CMD_X = CMD_Y = CMD_THETA = THETA = 0. This portion of the command string corresponds to a no move command. If, at this particular instant, TOM-B happens to be moving with a velocity V_{OX} which is not zero in X direction, then equation [A-3-3] would cause a reverse thrust to be developed to brake the vehicle. On the other hand, if the velocity of the vehicle is also zero, then the same equation dictates that none of the thrusters is to be fired in order to remain at rest. For the situation in which CMD_X = X and CMD_Y = Y but CMD_THETA is not equal to THETA, and the vehicle is currently standing still, such a command demands a pure rotation about

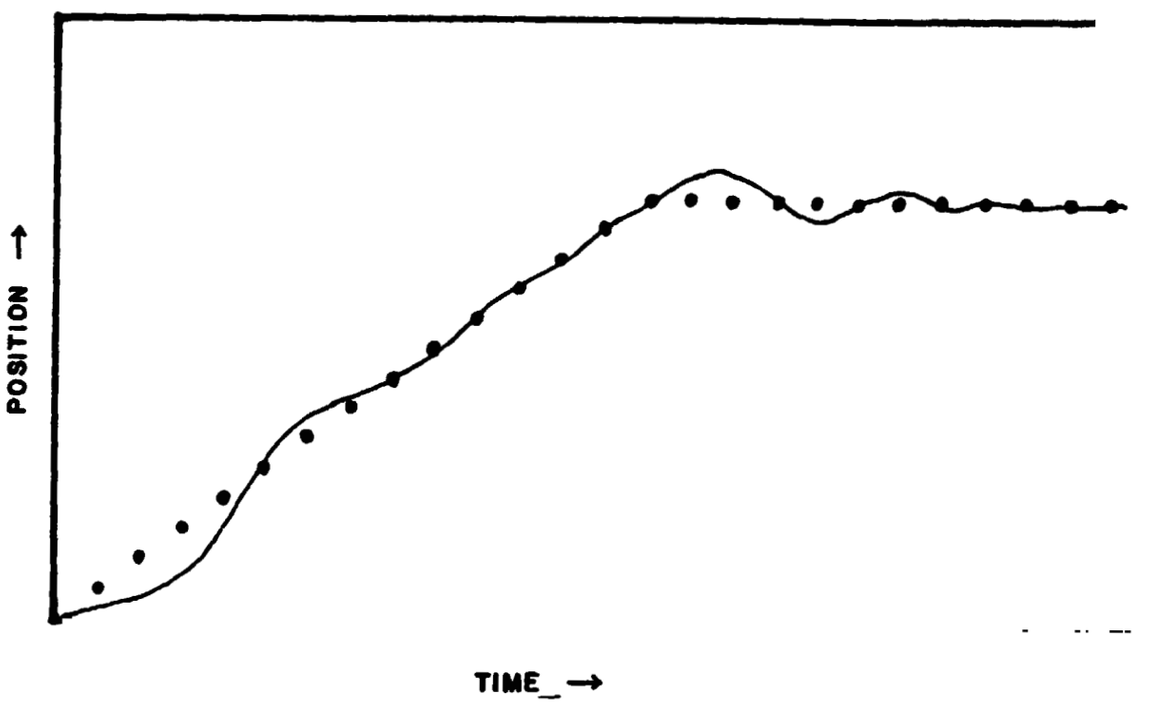

Figure 9. TOM-B Position - Time Curve

Z axis without translation. In this case, equations [A-3-3] and [A-3-4] yield FX = FY = 0 which is exactly what we want. In addition, it is noted that T_θ is now non-zero quantity, and from equation [S-3-6] we get:

$$FY1 = T_\theta/(2Ly) \quad ; \quad FY2 = -FY1$$

$$FX1 = 0 \quad ; \quad FX2 = 0$$

It is easy to see that the couple produced by FX1 and FY2 would be needed to produce the required rotation without causing any translation.

An interesting property of position control as used in the present system is that the on-board control logic is forever behind the command. If we plot the position versus time, the curve may resemble Figure 9. In this figure, the points represent the position and orientation as specified by the command strings, while the solid curve represents the corresponding position and orientation of the vehicle. In most cases, the vehicle attempts to "catch up" with the command. When the desired position is finally reached, the vehicle may overshoot and would try to correct itself in the next cycle. This "oscillating" effect is expected because when the vehicle reaches a desired position, its momentum causes it to overshoot. The control laws contains sufficient logics to critically damp out this oscillating effect, but one should not be surprised when it occurs. Since the vehicle is quite massive, and the thrusters can deliver a

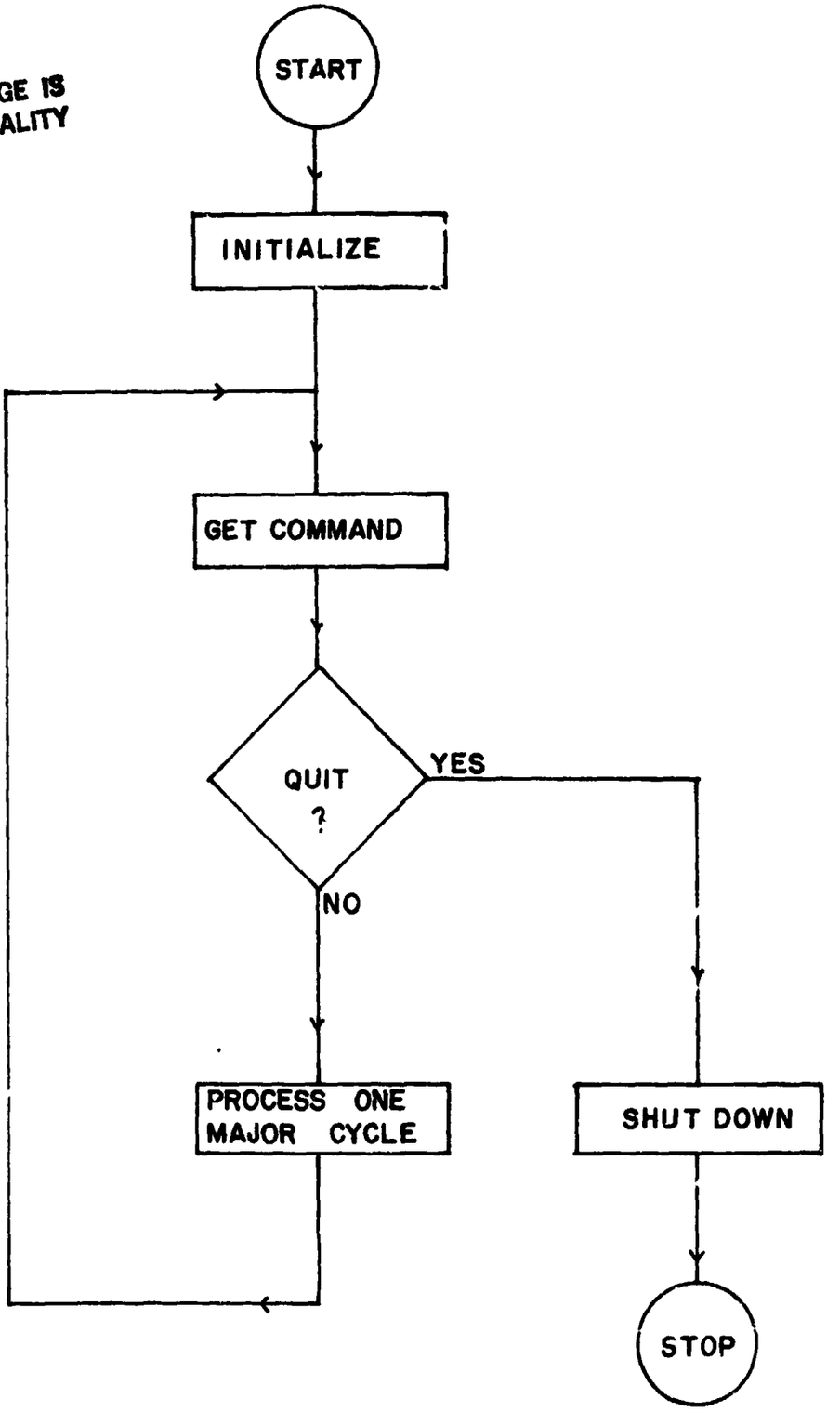

Figure 10. Control Software - Main Program

relatively small impulse, the oscillatory effect may be so small that it may not be perceptible to the operator in the control room. A person standing by the flat floor may hear the thrusters being turned on and off a number of times before the vehicle comes to a standstill.

OMV SIMULATION SYSTEM -- ALGORITHM

Since the on-board computer hardware is not yet implemented in TOM-B, the control algorithm will be discussed in rather general terms. Minor modifications are expected, depending on the final hardware logic. In this section, high level control logic will be discussed using flow diagrams, while the detailed logic written in pseudocode will be presented in Appendix 4. It is anticipated that a combination of FORTRAN and MACRO-II will be used to translate the algorithm into the final program. Top down design will be used throughout.

The "main" program of the control logic is shown in Figure 10. The initialization procedure consists of the following steps:

a) a routine is used to set up a schedule to interrupt the system ten times every second. The interrupt service routine must:

    1) intercept the incoming command string,
    2) determine the present position and orientation of TOM-B using the three-light navigation system,
    3) get the buffers containing the accelerometer and gyro reading. Note that the positions for the

other three axes (Z, pitch and roll) will also be determined by this service routine.

Thus, updated information is always available in any given major cycle.

b) Static quantities (such as physical dimensions of the vehicle which are not expected to change) are initialized.

c) A data file is open and accessed so that dynamic quantities (such as mass of fuel, number of thruster pairs per side, thrust that will be developed by each thruster, calibration data, scale factors and so forth) will be read. It is decided that this a more efficient design, as the system may be subject to further modifications, or that the experimental set up may change (e.g. a different module maybe mounted), so that the mass of the vehicle maybe different). Under this circumstance, one needs only to modify the data file off-line, without having to modify and re-compile the entire software.

After the initialization phase, the balance of the main program involves intercepting the command string once every 0.1 second, and executing this command string until a command to stop is encountered. When this happens, some housecleaning chores (such as turning off all thrusters and the like) maybe carried out before the system shuts down.

The processing of a major cycle is carried out in a procedure

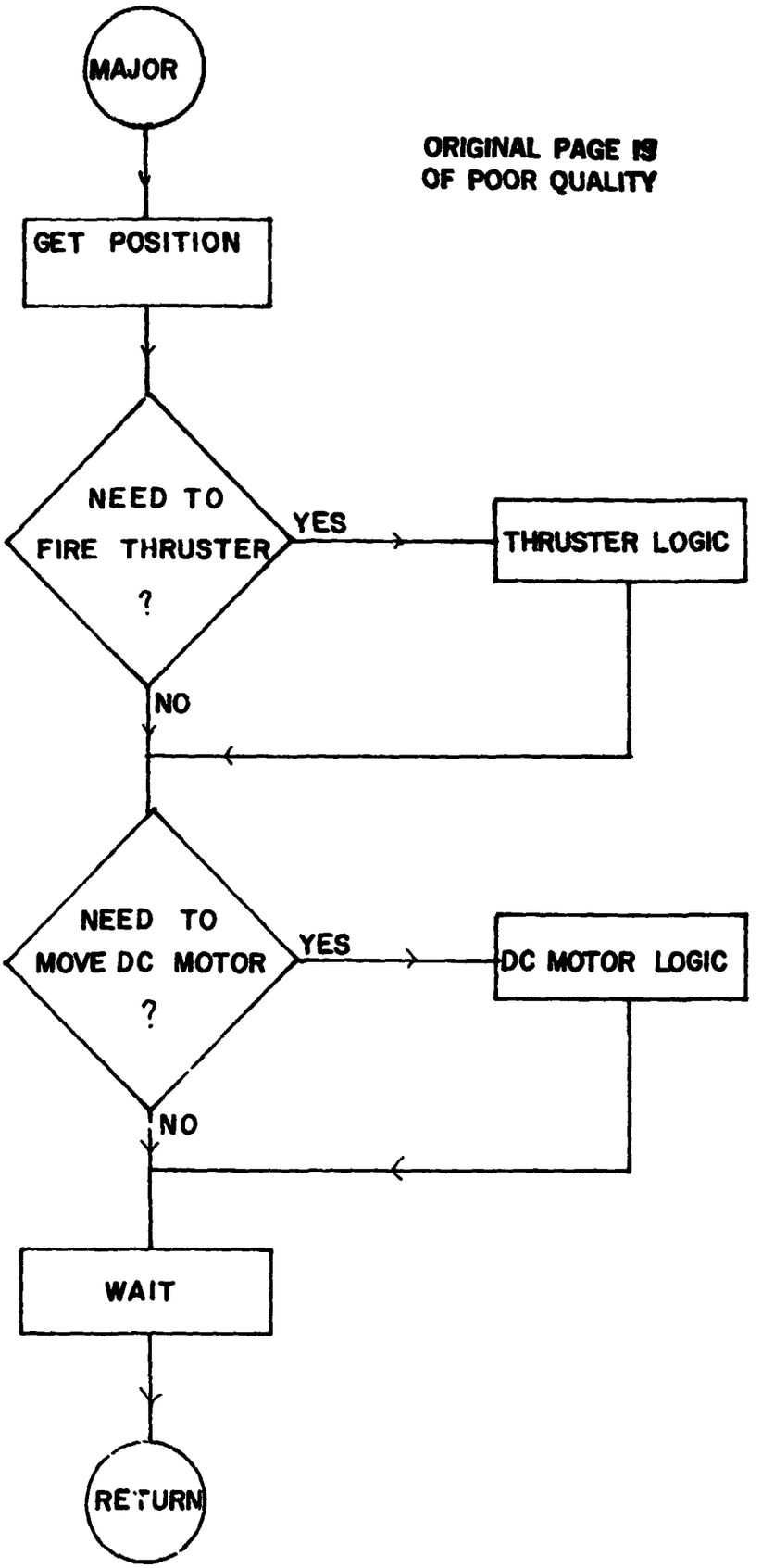

Figure 11. Control Software - Major Cycle

Figure 12

Software Organization

called MAJOR, as shown in Figure 11. On entering this procedure, appropriate memory locations are accessed and the current position and orientation of TOM-B are determined. The command string is examined to see first if any thrusters need to be activated. A separate routine called THRUSTER performs the necessary thruster logic. When this sub-task is completed, the balance of the command string is then examined to see if it is necessary to move any of the stepping motors which control the remaining axes (Z, pitch and roll). The procedure MOTOR performs the necessary stepping motor control logic. A waiting procedure is implemented to place the processor in a dormant state until the next command string is intercepted.

It is obvious to a shrewd reader that a higher priority is assigned to thruster logic. This is deliberately done because of the nature of the thruster hardware logic. As an appropriate number is placed in the corresponding down counter and a control signal is issued to fire a thruster, the hardware would commence firing the thrust and decrement the counter until its content is zero, at which point the thruster shuts down. During this interval, the processor can perform other tasks, and need not wait until the firing cycle is completed. For this reason alone, thruster logic is processed first in procedure MAJOR.

Figure 12 shows the system flow diagram of the entire logic. It noted that the name of the control program will be called TOMB. It is not anticipated that any confusion with the vehicle will arise since

in one case, the name TOMB refers to the control software, while in the other instance, the name TOM-B refers to the vehicle (hardware). It is noted that the procedure SETUP, BANGX and MVMOTOR are not defined in the pseudocode. These are machine language routines that cannot be completed until the hardware logic is finished.

It would be very useful to verify the above algorithm using simulation techniques. Unfortunately, the shortage of time does not permit this to be carried out.

LIST OF REFERENCES

1) Teleoperator Maneuvering System - Technical Report. NAS8-33903. Vaught Corporation, 1983.

2) Teleoperator Maneuvering System Mark II Propulsion Module Study. NAS8-34581. Martin Marietta Aerospace, December 1982.

3) Redundant Strapdown Navigation Project Requirements Document. NAS8-31335, IBM, 1976.

4) Three Axis Low-G Accelerometer Package. NASA TM-78211, 1978.

5) Skylab Thruster Altitude Control System. NASA TMX-64852, 1974.

Appendix 1

Preliminary Report

NASA UAH-ASEE SUMMER FACULTY PROGRAM

Preliminary Report

by

William Teoh

June 28, 1983

ABSTRACT

The results of a digital simulation studies (from June 6 to June 24, 1983) of the TMS system are presented. It is concluded from the studies that the thruster control law is more complex than necessary. This stems from that fact that :

a. the unsatisfactory location of the center of mass, and
b. the gradual shift of center of mass as fuel is being depleted.

A minor modification can be made to the basic design that would circumvent the above mentioned problems, thereby drastically improving the performance of the vehicle.

ORIGINAL PAGE IS
OF POOR QUALITY

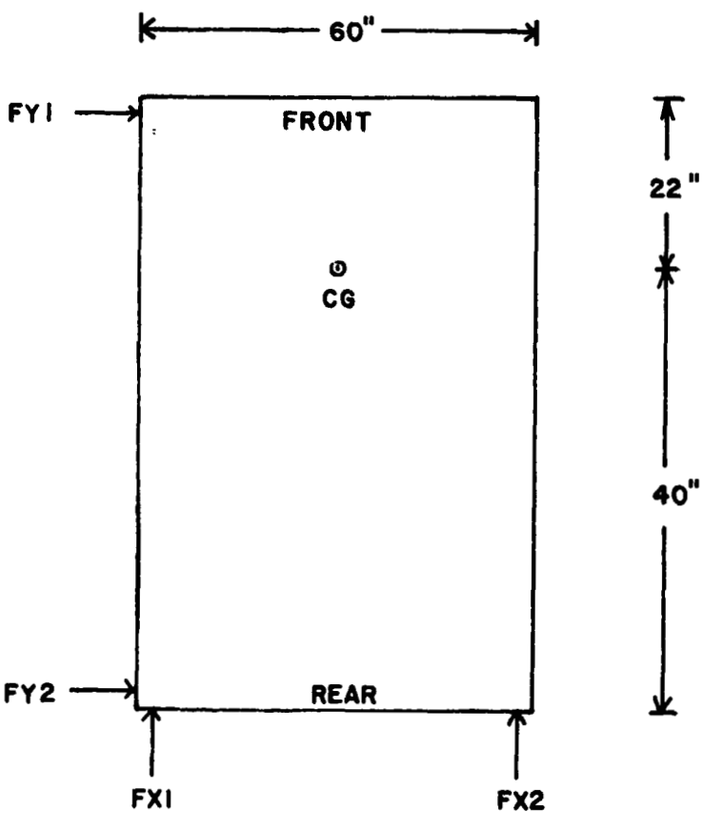

FIGURE 1.

INTRODUCTION :

The TMS physical simulation system consists of a vehicle fitted with air bearings that enable it to move with very little friction on a flat floor. A mock-up module can be mounted on this vehicle. As this vehicle has six degrees of freedom, one can simulate the various maneuvers of the module in space.

Radio telemetry provides the only physical link between the vehicle and a host computer. High level commands can be issued bythe host computer, and these commands are executed by an on-board microprocessor (PDP 11/23) The present project involves the development of the needed control software.

Motion along the X and Y directions turns out to be the more involved portion of the project due to the fact that thrusters are used to effectuate such motion. Thus, the first portion of this work concerns the development of appropriate thruster control logic.

As the hardware is not yet ready, the only practical way to study vehicle dynamics is digital simulation. A mathematical model of the system is constructed. This program is written in PASCAL and the simulation is carried out on an IBM Personal Computer. The present preliminary report summarises the result of this simulation.

THRUSTER CONTROL LOGIC :

Figure 1 shows the top view of the TMS vehicle. As can be seen, the center of mass (CG) is at a point 22 inches from the

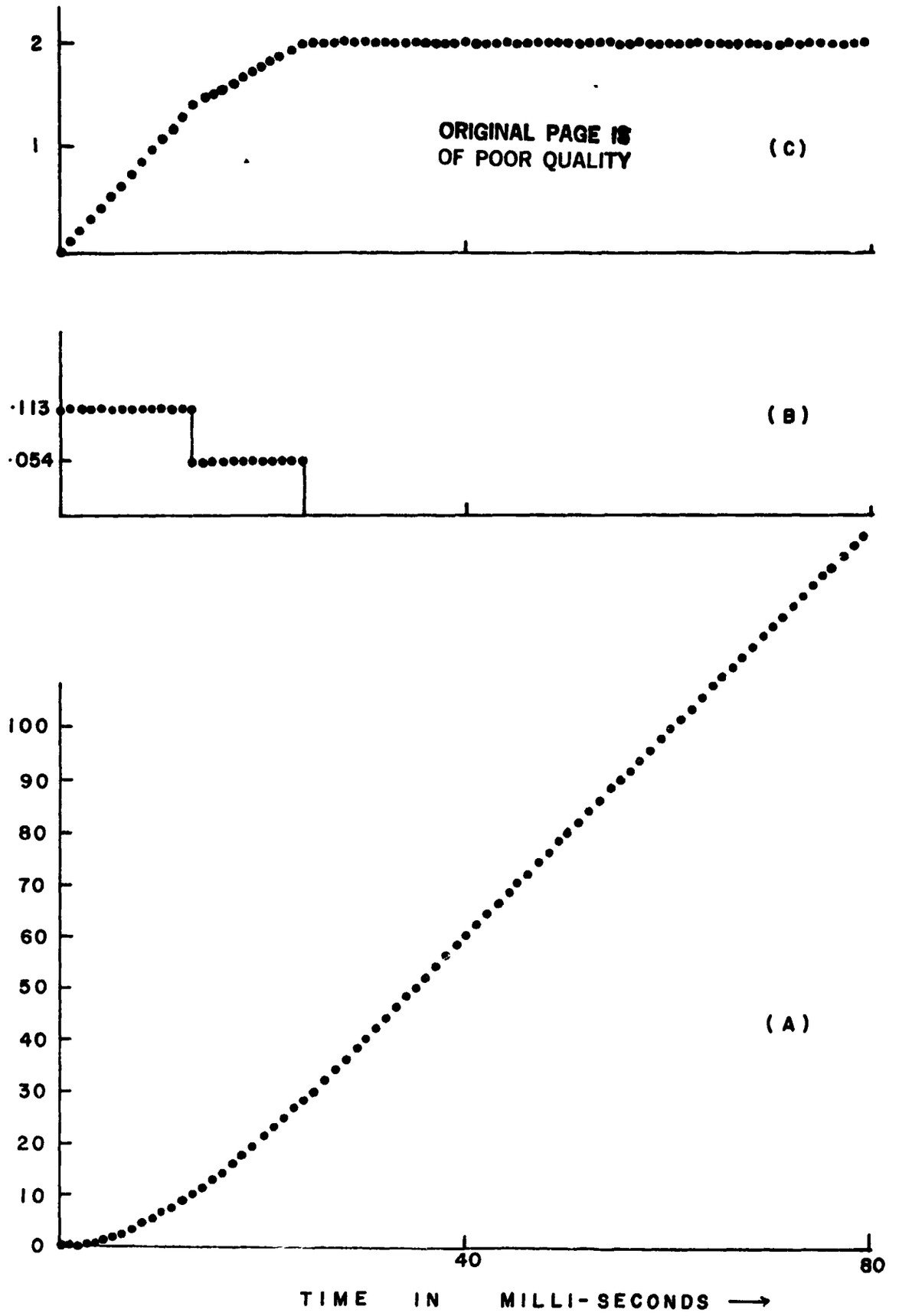
2
1
ORIGINAL PAGE IS
OF POOR QUALITY
(C)
·113
·054
(B)
100
90
80
70
60
50
40
30
20
10
0
(A)
40
80
TIME IN MILLI-SECONDS ⟶

FIGURE 2

front of the vehicle along the long axis, and is not equidistant from the thrusters.

Detail thruster control logic has been derived, and the mathematics will be presented here. Suffice it here to say that when high level commands ($\dot{X}_{CMD}$, $\dot{Y}_{CMD}$, $\dot{\theta}_{CMD}$) are intercepted, the corresponding thrust FX1, FX2, FY1 and FY2 are calculated to cause such a desired motion. However, the thrusters on the TMS vehicle are not throttlable (I hope there is such a word !), as each can exert a constant thrust of 3 pounds. Thus, the force information must be translated into firing times TX1, TX2, TY1 and TY2, respectively. From Figure 1, one can see that motion along the X direction is straightforward. Thus, the rest of the discussion pertains to motion along the Y direction.

Consider the simple case where the high level command $\dot{X}_{CMD}=0$ $\dot{Y}_{CMD}$ = 2 and $\dot{\theta}_{CMD}$ = 0 is received from the host computer. In simple terms, this means that a pure translation along the Y direction without rotation is required. Since the thrusters are not throttlable, the engine FY1 must be fired longer than FY2 in order to cause a null $\dot{\theta}_{CMD}$. Figure 2 shows the position (Y), velocity ($\dot{Y}$) and acceleration ($\ddot{Y}$) of the vehicle during a period of 80 milli seconds, from rest. Note that the engine FY1 is fired for a period of 24 milli seconds while FY2 is fired for 13 milli-seconds to achieve a velocity of 2.0 ft/sec. Otherwise, the behaviour of the vehicle is as expected.

However, when both engines are on, an unbalanced torque is produced (because of the position of the CG), causing a net

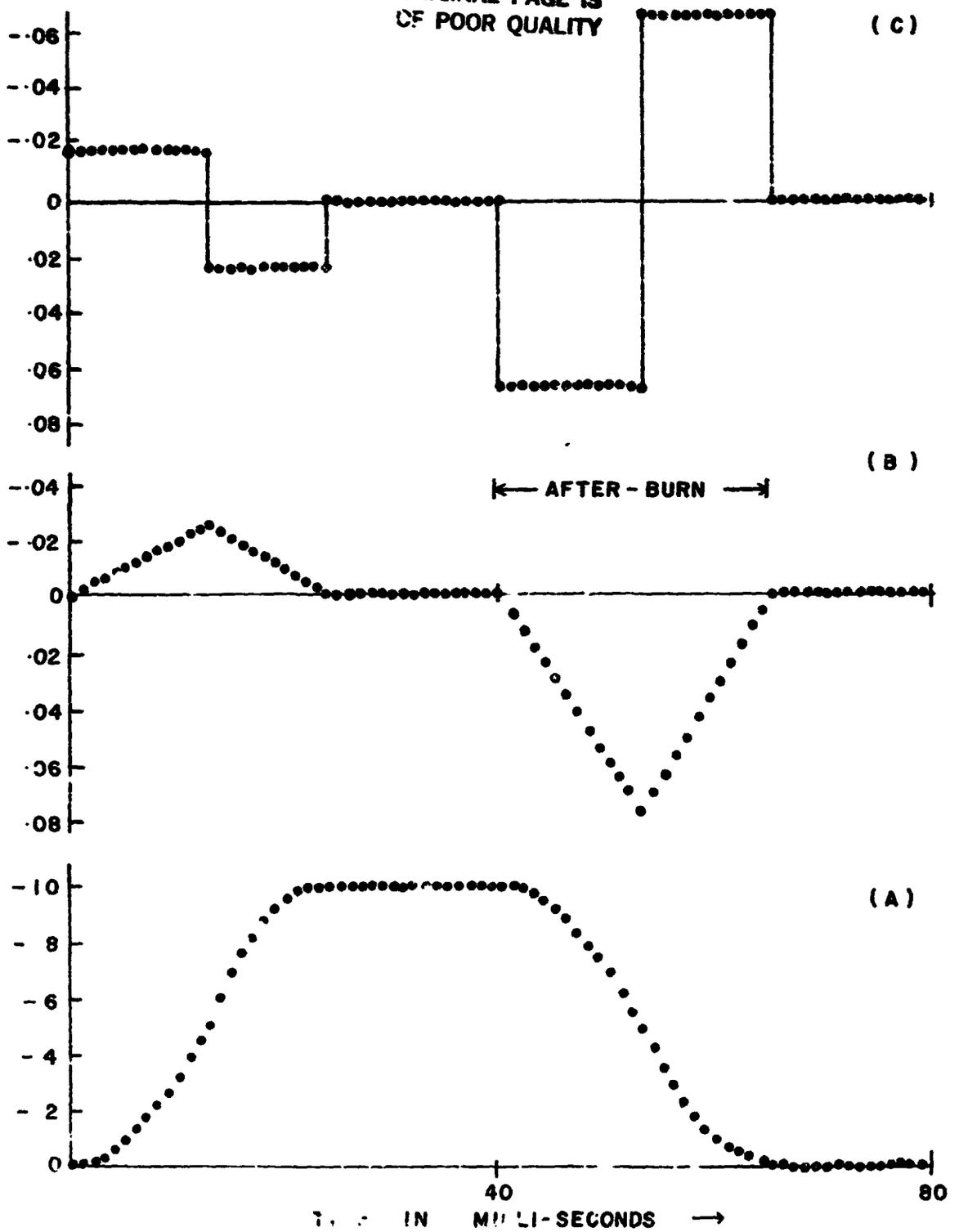

FIGURE 3

angular acceleration. In this work, we shall take on the notation that clockwise rotation is positive. When FY2 stops, the remaining engine are able to reduce this angular velocity to zero, as demanded by the incoming command. This is demonstrated in Figure 3 b) in the time interval 0 to 40 milli-seconds. It is noted, however, that during this period, the vehicle would have attained a non-zero angular displacement, as shown in a) of the same figure. At the end of 40 milli-seconds, although the vehicle is moving with speeds as specified by the incoming command, the attitude of the vehicle has been changed by an amount equal to the angular displacement. To maintain the same attitude, it is necessary to implement an after-burn.

The after-burn to correct for the rotation is done by firing FX1 and FX2 in opposite directions to create a couple. Because of the position of the CG, this configuration can cause a rotation without translation. This after-burn is carried out after t = 40 milli-seconds. Here, we have arbitrarily chosen the system response time to be 40 milli-seconds, so that the on-board processor can examine the state of the vehicle, as well as communicate with the host computer 25 times per second. As can be seen from the other half of Figure 3, such after-burns are necessary to restore the original attitude.

It must be pointed out that such complex control logic is needed solely because of the fact that the CG does not lie at the mid point between the corresponding thrusters. It must be pointed out that more fuel is spent in correcting the angular displacement than that needed to propel the vehicle. The ratio turns out

ORIGINAL PAGE IS
OF POOR QUALITY

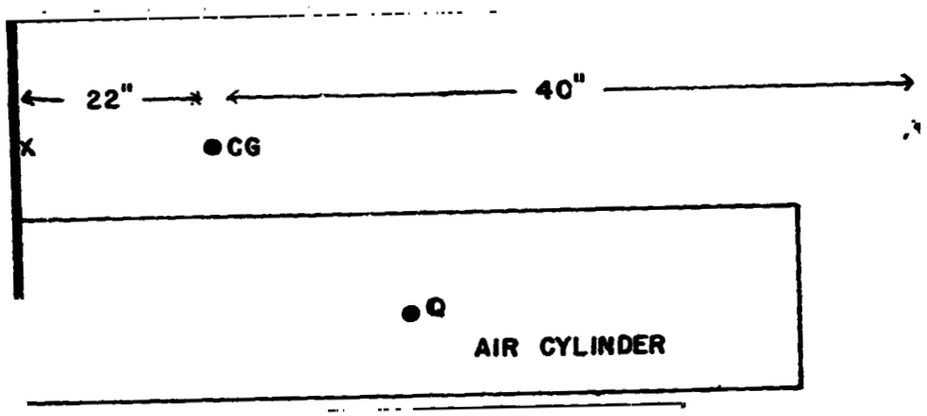

FIGURE 4

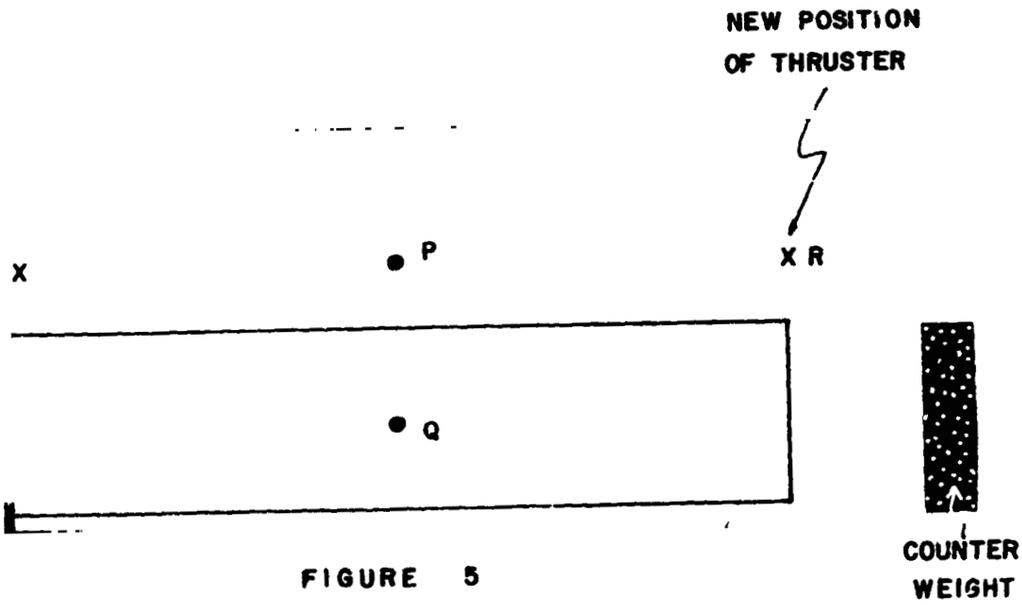

FIGURE 5

to be approximately 25/24. This extra expenditure of fuel should be regarded as unacceptable, considering the fact that such after-burns can be totally eliminated.

A further flaw in the current design gives rise to a second complication. Referring to Figure 4, it can be seen that the CG of the fuel reservoir (air tanks) [point Q] are not conplanar with the CG of the vehicle. This means that as fuel is continuously depleted, there is gradual shift in the CG of the vehicle. A quick calculation shows that if the half-length of the cylinder is 28 inches, and that it holds about 300 pounds of compressed air, then the CG of the vehicle can shift by as much as 1 inch. Without compensating for such a shift, the current control laws would cause an average angular acceleration of 0.002 rad/sec/sec. This may seem insignificant. But consider the following hypothetical situation in which the vehicle moves on an infinite floor, and further suppose that the fuel is totally depleted in 10 minutes. We can also assume that the engines FY1 and FY2 have been on for 5 minutes. The vehicle would have rotated 43 complete revolutions during this period due to the shift of center of mass alone! This calculation is probably unrealistic in that we do not have an infinite floor, but it does hit home the fact that we cannot ignore the shift in the center of mass.

In summary, the offset of the center of mass gives rise to:

- rotation when pure translation is needed in the Y direction
- after-burns are needed

- shift in center of mass also cause rotation which must also be compensated for
- drastic waste in fuel
- complex control logic, and
- if $\dot{\theta}_{CMD} \neq 0$ then complicated calculation is needed to determine the amount of after-burn.

RECOMMENDATION :

The following simple modification would solve both problems mentioned above :

1) Sufficient counter weight can be placed at the rear end of the vehicle such that the center of mass of the vehicle, with the module mounted, is shifted to a point P as shown in Figure 5. Point P is directly 'above' point Q, the center of mass of the air cylinder. Using the dimensions available, this counter weight M_B is given by:

$$M_B = (14 M_m + 3m) / 17 - M_{bat}$$

where m is the weight of the empty vehicle,

M_m is the weight of the module, and

M_{bat} is the weight of the battery pack.

Using reasonable figures of m = 1500 lbs, M_m = 200 lbs and the weight of the battery pack = 100 lbs, the counter weights works out to be 380 lbs which is not unreasonable.

2) move one pair of thrusters to point r so that they are symmetric about the new center of mass P.

The advantages of such minor modifications are many:

- drastic savings in fuel
- much simpler control logic

- flexibility

The last point is an important one. One should note that since the CG at P no longer shifts due to fuel depletion, one can easily re-calculate the counter weights whenever a different module is mounted on the vehicle without having to modify the control logic. This makes the vehicle much more flexible in that it can be easily adapted to handle various modules. The control logic will be so simple that intricate maneuver of the modules (such as docking) can be executed with ease.

Appendix 2

Equations for the Three-light Navigation System

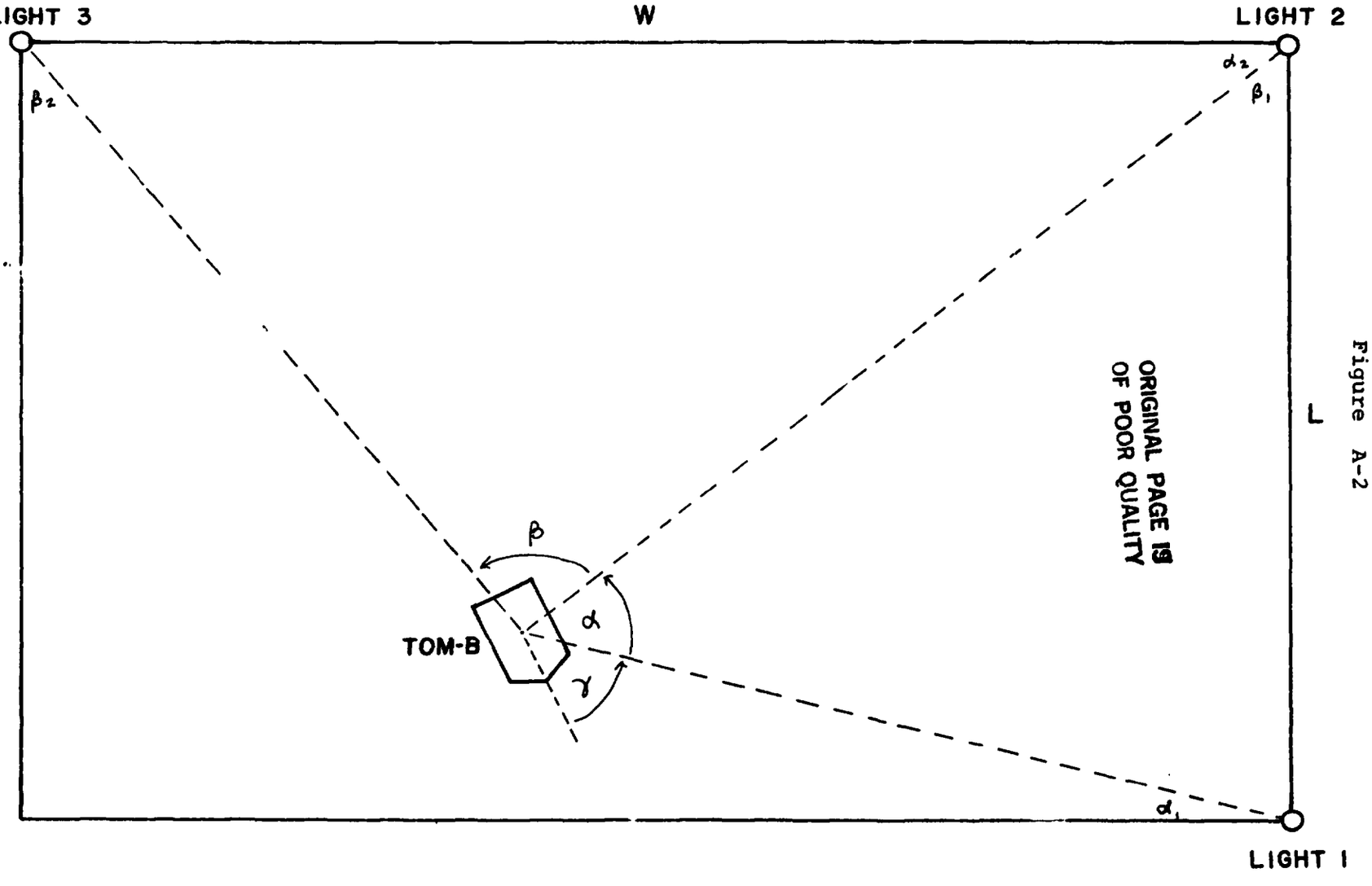
LIGHT 3
W
LIGHT 2
β_2
α_2
β_1
β
α
γ
TOM-B
α_1
LIGHT 1
L
ORIGINAL PAGE IS
OF POOR QUALITY

Figure A-2

Referring to diagram A-2, the following relations held:

$$\alpha = \alpha_1 + \alpha_2$$

$$\beta = \beta_1 + \beta_2 \qquad \text{A-2-1}$$

$$\alpha_2 + \beta_1 = 90^\circ$$

$$\psi = \tan^{-1}\frac{\omega}{\ell} = \tan^{-1}\tfrac{1}{2}$$

$$= 26{\cdot}565051^\circ \qquad \text{A-2-2}$$

$$D = \sqrt{\ell^2 + \omega^2}$$

and

$$\cos\psi = \frac{\ell}{D}$$

$$\sin\psi = \frac{\omega}{D} \qquad \text{A-2-3}$$

From sine rule,

$$\frac{\ell}{\sin\beta} = \frac{c}{\sin\alpha_2}$$

and

$$\frac{D}{\sin(\alpha+\beta)} = \frac{c}{\sin(\psi-\alpha_1)}$$

Therefore, eliminating c, we have:

$$\ell\,\frac{\sin(\alpha - \alpha_1)}{\sin\beta} = \frac{D}{\sin(\alpha+\beta)}\sin(\psi - \alpha_1)$$

therefore

$$\sin(\alpha - \alpha_1) = \frac{D}{\ell}\,\frac{\sin\beta}{\sin(\alpha+\beta)}\sin(\psi - \alpha_1)$$

$$= \frac{1}{\mu}\sin(\psi - \alpha_1)$$

where

$$\mu = \frac{\ell}{D}\,\frac{\sin(\alpha+\beta)}{\sin\beta} \quad .$$

Expanding both sides, we have:

$$\sin\alpha\cos\alpha_1 - \cos\alpha\sin\alpha_1 = \frac{1}{\mu}\left(\sin\psi\cos\alpha_1 - \cos\psi\sin\alpha_1\right)$$

therefore

$$\cos\alpha_1(\mu\sin\alpha - \sin\psi) = \sin\alpha_1(\mu\cos\alpha - \cos\psi)$$

therefore

$$\cot\alpha_1 = \frac{\mu\cos\alpha - \cos\psi}{\mu\sin\alpha - \sin\psi}$$

Squaring both sides and invert:

$$\frac{1}{\sin^2\alpha_1} = 1 + \left(\frac{\mu\cos\alpha - \cos\psi}{\mu\sin\alpha - \sin\psi}\right)^2$$

$$= \frac{1+\mu^2 - 2\mu\cos(\alpha+\psi)}{(\mu\sin\alpha - \sin\psi)^2}$$

therefore

$$\sin\alpha_1 = \frac{\mu\sin\alpha - \sin\psi}{\sqrt{1+\mu^2 - 2\mu\cos(\alpha+\psi)}}$$

where

$$\mu = \frac{\ell}{D}\,\frac{\sin(\alpha+\beta)}{\sin\beta}$$

therefore

$$\alpha_1 = \sin^{-1}\frac{\mu\sin\alpha - \sin\psi}{\sqrt{1+\mu^2 - 2\mu\cos(\alpha+\psi)}} \qquad \text{A-2-4}$$

We can now calculate the rest of the partial angles using equations A-2-1 through A-2-3 .

Appendix 3

Derivation of the Control Laws of TOM-B

Figure A-3 shows the hypothetical position and orientation of TOM-B when the current command string X_{CMD}, Y_{CMD}, θ_{CMD} is about to be executed.

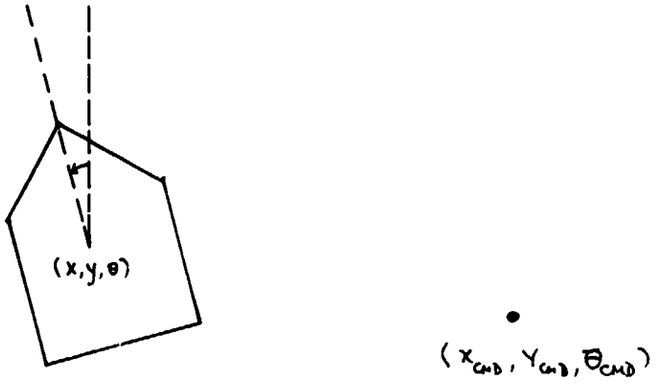

Figure A-3

The position and orientation of TOM-B is given by the vector (x, y, θ) determined from the tri-light navigation system. Here θ is the orientation of the vehicle. The desired position and orientation is dictated by the command string (X_{CMD}, Y_{CMD}, θ_{CMD}) such that the vehicle will be at this now position at the end of the current major cycle. The required impulse to accomplish this is given by

$$f_x = \text{mag}(X, X_{CMD}, V_{ox})$$
$$f_y = \text{mag}(Y, Y_{CMD}, V_{oy}) \qquad (A-3-1)$$

where f_x, f_y are the required impulses along X and Y direction in floor coordinates. V is the velocity of the vehicle, also expressed in floor coordinates. It is noted that V_{ox} and V_{oy} are obtained from the accelerometer readings V'_x and V'_y using the transformation:

$$\begin{bmatrix} V_{ox} \\ V_{oy} \end{bmatrix} = \begin{bmatrix} -\sin\theta & \cos\theta \\ \cos\theta & \sin\theta \end{bmatrix} \begin{bmatrix} V'_x \\ V'_y \end{bmatrix} \qquad \text{(A-3-2)}$$

and the function g is given by:

$$g(X, X_{CMD}, V_{ox}) = \begin{cases} T - \lambda & \text{if } \lambda^2 \text{ is non-negative} \\ \dfrac{-V_{ox} + \sqrt{V_{ox}^2 + 2a(X_{CMD} - X)}}{a} & \text{otherwise} \end{cases} \qquad \text{(A-3-3)}$$

where $$\lambda^2 = T^2 - \frac{2\,(X_{CMD} - X - V_{ox}T)}{a}$$

Here, a is the magnitude of the acceleration produced when one pair of thrusters is fired simultaneously in the same direction, and is approximately equal to 0.1 ft/sec^2. T = 0.1 is the major period. Note that the impulses f_x and f_y are defined relative to the floor coordinates. To determine the actual impulses F_x, F_y that TOM-B must exert to produce the same displacement, we can use the transformation:

$$\begin{bmatrix} F_x \\ F_y \end{bmatrix} = \begin{bmatrix} -\sin\theta & \cos\theta \\ \cos\theta & \sin\theta \end{bmatrix} \begin{bmatrix} f_x \\ f_y \end{bmatrix} \qquad \text{(A-3-4)}$$

where θ is the orientation of the vehicle as determined by the tri-light navigation system. Once the impulses F_x and F_y

are known, then the individual impulses F_{x1}, F_{x2}, F_{y1} and F_{y2} that each thruster must produce can be calculated. We shall use the notation as shown in the following figure :

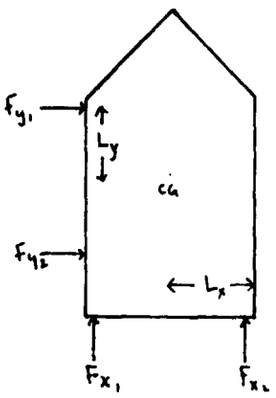

wherever a negative quantity is encountered, the directly opposite thruster will be used instead. Obviously, we must have the relation:

$$F_x = F_{x1} + F_{x2}$$

$$F_y = F_{y1} + F_{y2}$$

Note that the impulses must be such that not only must they produce the required displacement, but must also produce the necessary angular displacement. We can define the required torque T_θ by the relation:

$$T_\theta = 2 J_{zz} (\theta_{CMD} \quad \theta) / T^2 \qquad \text{(A-3-5)}$$

where T is the major period and J_{zz} is the principal moment

of inertia about Z - axis of TOM-B. It is prudent to consider the following two cases :

case 1. $F_x \leq F_y$

In this case, we have:

$$F_{y1} = F_y/2 + T_\theta/(2L_y)$$

$$F_{y2} = F_y - F_{y1}$$

if we define a quantity ΔF_x to be

$$\Delta F_x = (T_\theta + (F_{y2} - F_{y1})\, L_y) / (2L_x)$$

then

$$F_{x1} = F_x / 2 + \Delta F_x$$

$$F_{x2} = F_x - F_{x1}$$

(A-3-6)

Case 2. $F_x > F_y$

in this case, we can have

$$F_{x1} = F_x / 2 + T_\theta / (2L_x)$$

$$F_{x2} = F_x - F_{x1}$$

if we define another quantity T'_θ such that:

$$T'_\theta = T_\theta + (F_{x2} - F_{x1})\, L_x$$

then,

$$F_{y1} = F_y / 2 + T'_\theta / (2\, L_y)$$

$$F_{y2} = F_y - F_{y1} \qquad \text{(A-3-7)}$$

Remember, however, that these impulses must be converted into the corresponding firing times T_{x1}, T_{x2}, T_{y1} and T_{y2}, respectively because the thrusters are not throttlable. These can be accomplished using the formulae :

$$T_{xj} = F_{xj} / ma$$

$$T_{yj} = F_{yj} / ma \qquad \text{(A-3-8)}$$

for j = 1, 2. Here, ma (mass times acceleration) is the thrust developed by each thrusters. It is remembered that a negative T_{xj} means that the opposite thrusters will be used.

Appendix 4

Control Algorithm

(First Version)

Appendix C

For the algorithm listed in this appendix, the following common storage are used:

Block label	Variables
PHYS	MASS, JZZ, LX, LY, NUMTHR, THRUST, PIRAD, ACC MAJOR
SNRC	SNRSCAL (3), SNRBIAS (3)
SNRBF	SENSR (3)
NVGC	NVGSCAL
NVGBF	BANG (3)
DCC	DSCAL (3)
DCBF	DCDR (3)
COMMAND	DCMD (6), CMD (6), FLAG
POSTN	POT (3), OPOT (3)
ORIEN	POM (3), OPOM (3)
VEL	VPOT (3), OVPOT (3
ENGINES	FTABL (16), SCALE
JET	COUNTER (16), STATUS

Functional description of the four machine level routines:

1. Procedure SETUP
   This procedure must set up a schedule to interrupt the system once every 0.1 seconds. The interrupt service routine must:
   a) move command string from TI 990 into a buffer called DCMD.
   b) must read the two accelerator and gyro reading and places them into SENSR.
   c) collect reading from the tri-light navigation system, and place the three angles in BANG (1-3)
   d) read optical encoder reading and place them in DCDR, and
   e) place a zero in FLAG in block COMMAND to show that a command has been intercepted.

2. Procedure BANGX must send out a control signal to all thrusters to fire.

3. Procedure MVMOTR writes DCRD(1-3) to channels 1-3 of D/A converter.

4. Procedure XMIT (X, Y, THETA, Z, PITCH, ROLL) transmits the current position and orientation to TI 990 so that they may be broadcast to the control room.

```
start (TOM_B)

{main program}

call  INIT
call  FIRETHM (0, 0, 0, 0)
while  CMD(1)  >  -999.0 do

     {process one major cycle}

     call  MAJOR
     call  WAIT
end while
call  FIRETHM (0, 0, 0, 0)
stop
end  (TOM_B)


start  (INIT)

{this procedure initializes the system}

global  PHYS, SNRC, NVGC, DCC, COMMAND
open  (DATA)
read  (DATA)  MASS, JZZ, LX, LY
LX  <--  LX / 12
LY  <--  LY / 12
read  (DATA)  NUMTHR, THRUST
do  K  =  1  to  3
     read  (DATA)  SNRSCAL(K), SNRBIAS(K)
end do
read  (DATA)  NVGSCAL
do  K  =  1  to  3
     read  (DATA)  DSCAL(K)
     SENR(K)  <--  0
     BANG(K)  <--  0
     DCDR(K)  <--  0
     POT(K)   <--  0
     OPOT(K)  <--  0
     POM(K)   <--  0
     CMD(K)   <--  0
     CMD(K+3) <--  0
     DCMD(K)  <--  0
     DCMD(K+3)<--  0
end do
close  (DATA)
PIRAD  <--  180.0 * 113.0 / 355.0
call  SETUP
return
end  (INIT)
```

```
start  (WAIT)

{transmit current position and orientation to TI 990}

call  XMIT (X, Y, THETA, Z, P, R)
while FLAG  <>  0  do
     {wait until next command string is intercepted}
end while
return
end  (WAIT)



start  (MAJOR)

{this procedure processes a major cycle}

call  CMDFIX
call  POSITION
FLAG  <-- 1

{find out if we have to move anything}

call  DECISION (FIRE)
if  FIRE  -  FIRE/10  =  1
     then  call  THRUSTER
end if
if  FIRE  -  10 * (FIRE / 10)  =  1
     then  call  MOTOR
end if
return
end  (MAJOR)


start  (CMDFIX)

{this procedure interprets the command string}

global  PHYS, COMMAND
do  K  =  1  to  6
     if  K = 1 or K = 2 or K = 4
          then
               CMD(K)  <-- CMD(K) + FLOAT(DCMD(K)) / 12000.0
          else
               CMD(K)  <-- CMD(K) + FLOAT(DCMD(K)) / PIRAD / 10
     end if
end do
return
end  (CMDFIX)
```

```
start  (POSITION)

{this procedure saves the old position and orientation
then calls other procedures to find the new position
orientation and velocity}

global  POSTN, ORIEN, VEL
do K  =  1  to  3
     OPOT(K)  <-- POT(K)
     OPOM(K)  <-- POM(K)
     OVPOT(K) <-- VPOT(K)
end do
call  POST
call  POSM
call  SPEEDT
return
end  (POSITION)



start  (POST)

{this procedure determines the vehicle position
and orientation, and places the information in
POT(1-3) using the three light navigation system}

global  NVGC, NVGBF, POSTN
call  CONVG
PI    <--  355.0 / 113.0
PSI   <--  ATAN (0.5)
L   <--  80.0
W   <--  40.0
ALPHA  <--  BANG(2)
BETA   <--  BANG(3)
GAMMA  <--  BANG(1)
D   <--  SQRT(L*L + W*W)
RHO    <--  L * SIN(ALPHA + BETA) / (D * SIN(BETA))
DNO    <--  SQRT(1 + RHO * RHO - 2.0 * RHO * COS*ALPHA - PSI))
ALPHA1 <--  ASIN (( RHO * SIN(ALPHA) - SIN (PSI)) / DENO)
A   <--  W * (RHO - COS(ALPHA + PSI))/(DENO * SIN(ALPHA))
POT(1) <--  L - A * COS(ALPHA1)
POT(2) <--  A * SIN(ALPHA1)
TH     <--  GAMMA + ALPHA1 + PI/2.0
POT(3) <--  2.0 * PI - TH
return
end  (POST)
```

```
start  (POSM)

{this procedure determines the position of
A, PITCH and ROLL and place them in POM(1-3)}

global  DCC. DCBF, ORIEN
do  K  =  1  to  3
     POM(K)  <-- DCDR(K) * DSCAL
end do
return
end  (POSM)


start  (SPEEDT)

{this procedure reads the accelerometers and gyro,
calculates the current velocity and rate of rotation
and places the information in VPOT(1-3)}

global  SNRC, SNRBF, VEL
do  K  =  1  to 3
     VPOT(K)  <--  (SENSOR(K) - SNRBIAS(K)) * SNRSCALE(K)
end do
return
end  (SPEEDT)


start  (DECISION)  (FIRE)

{this procedure compares the current position and
orientation with the desired position and orientation
and determine if any thrusters or motors need to
be activated}

global  COMMAND. POSTN. ORIEN
FIRE  <--  0
GALF  <--  0
EPSLN <--  0.001
do  K  =  1  to  3
     if ABS(POT(K) - CMD(K)) > EPSLN
          then  FIRE  <--  1
     end if
end do
EPSLN <-  EPSLN / 10
do  K  =  1  to  3
     if  ABS(POM(K) - CMD(K+3)) > EPSLN
          then  GALF  <--  10
     end if
end do
FIRE  <--  FIRE  +  GALF
return
end  (DECISION)
```

```
start  (THRUSTER)

{this procedure handles thruster logic}

global  COMMAND, POSTN, VEL, PHYS
THETA  <--  POT(3)
C      <--  COS(THETA)
S      <--  SIN(THETA)

{tranform velocity vector to floor coordinates}

VX  <--  VPOT(2) * C  -  VPOT(1) * S
VY  <--  VPOT(2) * S  +  VPOT(1) * C

{calculate required impulses}

T1  <--  G (VX, POT(1), CMD(1))
T2  <--  G (VY, POT(2), CMD(2))
TT  <--  AMAX (T1, T2)
if  TT  =  0
     then  TT  <--  MAJOR
end if
FFX  <--  T1 * THRUST
FFY  <--  T2 * THRUST

{transform impulses to TOM-B coordinates}

FX   <--  FFY * C  -  FFX * S
FY   <--  FFY * S  +  FFX * C

{calculate individual thruster impulses}

TORQ <--  2 * JZZ * (CMD(3) - POT(3)) / (TT * TT)
if  FX  <=  FY
     then
          FY1  <--  FY / 2  +  TORQ / (2 * LY)
          call  LCHK (FY1)
          FY2  <--  FY  -  FY1
          call  LCHK (FY2)
          DF   <--  (TORQ + (FY2 - FY1) * LY) / (2 * LX)
          FX1  <--  FX / 2 + DF
          call  LCHK (FX1)
          FX2  <--  FX - FX1
          call  LCHK (FX2)
     else
          FX1  <--  FX / 2 + TORQ / (2 * LX)
          call  LCHK (FX1)
          FX2  <--  FX - FX1
          call  LCHK (FX2)
          DTQ  <--  TORQ + (FX2 - FX1) * LX
          FY1  <--  FY / 2 + DT / (2 * LY)
          call  LCHK (FY1)
          FY2  <--  FY - FY1
          call  LCHK (FY2)
end if
```

```
{select and fire the thrusters}

call  FIRETHM (FX1, FX2, FY1, FY2)
return
end  (THRUSTER)
```



```
start  (LCHK)  (F)

{this procedure makes sure that the required impulse
do not exceed the maximum thrust that can be developed}

global  PHYS
LIMIT  <--  NUMTHR * THRUST
if  F  >  LIMIT
     then
          F  <--  LIMIT
end if
return
end  (LCHK)


start  G (VO, XO, CMDX)

{this procedure evaluates the optimum impulse
without causing overshoot}

global  PHYS
RAD  <--  MAJOR * MAJOR - 2 * (CMDX - XO - VO * MAJOR) / ACC
if  RAD  >=  0
     then  P  <--  SQRT (RAD)
     else  RAD  <--  VO * VO + 2 * ACC * (CMDX - XO)
           RAD  <--  AMAX (RAD, 0.0)
           P  <--  (SQRT(RAD) - VO) / ACC
end if
G  <--  P
return  (G)
end  (G)

start  (FIRETHM)  (FX1, FX2, FY1, FY2)

{this procedure calculates the required firing times
and number of thrusters to be used and which thrusters
to be used, and stores the firing time in the firing
table FTBL}

globals  ENGINES, PHYS
arrays   TEMP(4)
call  SYM(FX1, FX2)
call  SYM(FY1, FY2)
TEMP(1)  <--  FX1
TEMP(2)  <--  FX2
TEMP(3)  <--  FY1
TEMP(4)  <--  FY2
```

```
do  K  =  1  to  16
     FTBL(K)  <--  0
end do

{determine which thruster to fire}

do K  =  1  to  4
     TIME  <--  TEMP(K) / THRUST
     JDX   <--  K
     if  TIME  <  0
          then  JDX  <--  K + 4
                TIME  <-- ABS(TIME)
     end if
     if  TIME  >  MAJOR
          then
               NN  <--  TIME / MAJOR
               N   <--  MIN (NN, NUMTHR)
     end if
     TIME  <--  ABS(TIME / N)
     do  J  =  1  to  N
          FTBL( JDX + (J-1) * 8)  <-- TIME * SCALE
     end do
end do
call  BANG(NUMTHR)
return
end  (FIRETHM)



start  (SYM)  (X, Y)

{this procedure makes sure that the firing times
are identical if the thrusts are the same}

PREC  <--  0.001
if  ABS0(X - Y)  <  PREC
     then  Y  <--  X
end if
return
end  (SYM)


start (BANG) (MAXENG)

{this procedure takes the information from the firing table
and converts them into absolute counts to be loaded into
the down counters of each thruster}

global  ENGINES
NN  <--  MAXENG * 2
do  K  =  1  to NN
     COUNTER(K)  <--  FTBL(K)
end do

{send control signal to fire them}
```

```
call  BANGX
return
end(BANG)
```



```
start  (MOTOR)

{this procedure moves the individual DC motors}

global  COMMAND, DCC, DCBF, ORIEN
do  K  =  1  to  3
     D  <--  CMD(K+3) - POM(K)
     if  ABS(D)  >  0.00001
          then  DCRD(K)  <--  D * DSCALE(K)
          else  DCRD(K)  <--  0.0
     end if
end do
call  MVMOTR
return
end  (MOTOR)
```

N84 16053

1983 NASA/ASEE SUMMER RESEARCH FACULTY FELLOWSHIP PROGRAM

MARSHALL SPACE FLIGHT CENTER
THE UNIVERSITY OF ALABAMA IN HUNTSVILLE

LABORATORY AUTOMATION OF A QUADRUPOLE MASS SPECTROMETER

Prepared by:	James M. Thompson, Ph. D
Academic Rank:	Associate Professor
University and Department:	Alabama A & M University Normal, Alabama
NASA/MSFC:	
Laboratory:	Materials and Processing
Division:	Nonmetallic Materials
Branch:	Analytical and Physical Chemistry
MSFC counterpart:	Dr. John G. Austin Jr.
Date:	August 4, 1983
Contract No.:	NGT 01-008-021 The University of Alabama in Huntsville

LABORATORY AUTOMATION OF A QUADRUPOLE MASS SPECTROMETER

By

James M. Thompson
Associate Professor of Chemistry
Alabama A & M University
Normal, Alabama 35762

ABSTRACT

Studies involving the thermal decomposition of materials related to the National Space Exploration Program is of major concern in this laboratory. Thus, our efforts have been directed toward interfacing an LSI 11 bus of a PDP 11/23 desktop computer with a quadrupole mass spectrometer for the purpose of providing a convenient system whereby mass spectral data, of the products of thermal decomposition, may be rapidly acquired and processed under programmed conditions.

The versatility and operations of the quadrupole mass spectrometer are described as well as the procedure for configurating the LSI 11 bus of the PDP 11/23 desktop computer for interfacing with the quadrupole mass spectrometer system.

Data from the mass filter and other units of the spectrometer are digitally transferred to the computer whereupon mass spectral data and related data are generated.

ACKNOWLEDGEMENTS

My summer stay at NASA has been pleasant and intellectually fullfilling, mainly because of the hospitality and assistance extended to me by my counterpart, John G. Austin, Jr.

I also extend special thanks to Cortes L. Perry for his assistance in the resolution of software problems and for his tolerance in light of the numerous questions that were asked.

Appreciation is also extended to Professor Gerald Karr and others involved in selecting me as a participant in this excellent program.

LIST OF ILLUSTRATIONS

Figure	Title	Page
1	Schematic of The Quadrupole Mass Filter	XXXI - 4
2	Schematic of the QMG 511 Quadrupole Mass Spectrometer	XXXI - 8
3	Block Diagram of the QMG 511 Quadrupole Mass Spectrometer	XXXI - 9
4	Diagrams of the Priority Jumpers for the LSI 11 and Unibus	XXXI - 16
5	Connections Between the LT 511 Transceiver and the DRV 11	XXXI - 17
6	The Configurated LSI 11 Bus of the PDP 11/23 Computer	XXXI - 18

LIST OF TABLES

Table		Page
1	The Parameters of the QMG 511 That are Automaticall Set and Read	XXXI - 13
2	An Example of the Mass Number and Intensity Printout, Obtained From the QMG 511/Computer System	XXXI - 14

INTRODUCTION

The use of interactive microcomputers to facilitate instrument control, data acquisition and processing has become commonplace in the last several years. The computer/instrument relationship extends the capability of the scientific instrument, making it possible to perform experimental operations that would be difficult or time consuming under manual control.

While the quadrupole mass spectrometer/computer relationship is not as common as similar relationships among more conventional mass spectrometers, there are many instances where computer control of quadrupole mass spectrometers have been successfully accomplished, some of which are listed in the reference section (1-3).

In this study is discussed the interfacing of an LSI-11 bus of a PDP 11/23 desktop computer with a Balzer quadrupole mass spectrometer (QMG 511) and the advantages derived therefrom. Initially the QMG 511 was adapted for interfacing with the unibus of the PDP 11 minicomputer. Thus it was necessary to change the configuration of the line transceiver (LT 511) so that transistor-transistor logic (TTL) could be converted to the proper output current to the buffer of the spectrometer.

Problems were also encountered with some incompatibilities between the FORTRAN IV and the extended version of FORTRAN IV, written especially for the the QMG 511 system. These problems dealt mainly with missing modules and the need for reconstructing the FORTRAN libraries.

Even without computer control, the quadrupole system offers certain advantages, not normally found in conventional mass spectrometers. For instance, mass scans are much faster, ranging on the order of milliseconds; quadrupole systems are usually more stable at higher pressures and the nature of the quadrupole mass filter makes it easy to moniter ions of a desired m/e value.

The longer range goal of coupling the QMG 511/computer system to a thermalanalyzer will make possible the rapid acquisition and processing of mass spectral data relating to thermalanalytical decomposition of nonmetallic materials involved in the National Space Exploration Program. Such a system would also provide a means of automatically setting and reading the parameter of the spectrometer for optimization and measurement in a "closed loop" operation. In addition the system should provide ancillary data such as ion intensities, concentration measurements, mass scans, accurate isotopic abundances and ion monitoring capabilities.

OBJECTIVES

The objective of this project is to provide a mass spectrometer/computer system wherby mass spectral data can be readily acquired and processed and the parameters of the instrument automatically set and read under programmed conditions. This objective is a precusor to longer range intentions which involve coupling the spectrometer/computer system to a thermalanalyzer in order to investigate the products of thermal decomposition of materials related to the National Space Exploration Program.

THE QUADRUPOLE MASS SPECTROMETER

Operating Principle

The quadrupole mass spectrometer is characterized by a nonmagnetic mass filter, which is composed of four solid rods, arranged symmetrically along the direction of ion flow (Figure 1). To the quadrupole rods are applied both a radiofrequency (RF) and a direct current voltage (DC).

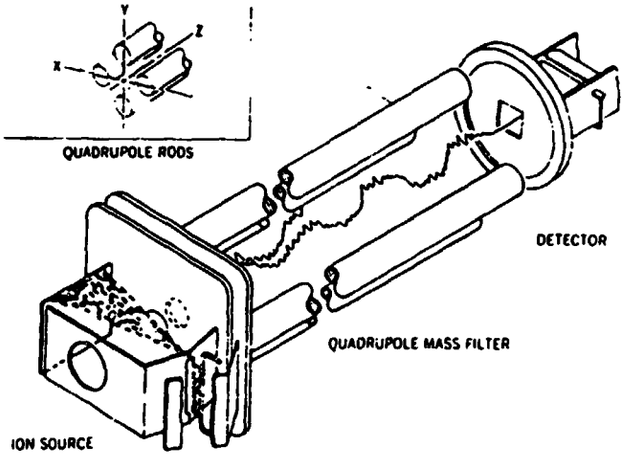

Figure 1. Schematic of the Quadrupole Mass Filter, Showing the Oscillations of the Positive Ions. From: Waller, G.R. (Editor) Biochemical Applications of Mass Spectrometry, Wiley Interscience, New York, 1972.

Once the positive ions are accelerated into the quadrupole field, they experience the influence of the applied radiofrequency and direct current. Depending upon the RF/DC ratio and the *m/e* values, the ions will acquire either a stable or unstable oscillation as they attempt to transverse the quadrupole field. Ions having a stable oscillation will successfully transverse the field and strike the detector,

while ions with unstable oscillations will collide with the quadrupole rods and go undetected. Thus by changing the RF/DC ratio, it is possible to prevent certain ions from passing through the quadrupole field, making selective ion monitering and single peak monitering (fragmentography) possible.

Quadrupole mass spectral data are produced on a linear scale with equal spacing between ion masses. This feature facilitates recognition of the mass scale, even without a mass marker.

The mass range achieved with the quadrupole mass spectrometer depends upon the energy of the radiofrequency applied to the quadrupole rods. In some of the newer instruments, the output of the RF-generator is sufficient to allow scans up to 10,000 mass units.

In most quadrupole mass spectrometers, the DC voltage and the radiofrequency can be rapidly changed while maintaining stable conditions throughout the mass region, a feature ideally suited for computer interfacing.

SOFTWARE DESCRIPTION

The software used to control, moniter and collect data from the QMG 511 is an extension of FORTRAN IV, appropriately called QMG FORTRAN. It consists of a number of controlling, monitering, utility and data acquisition subroutines and source programs, which completely support the QMG 511. All subroutines are integrated within a library module (called QFLIB) to be accessed when required by the user program. Access to the appropriate subroutine is initiated by call statements, with subsequent return to the calling program. The sequence of operations necessary to control, monitor and collect data is acheived by joining the appropriate subroutine call. Data is transferred to and from a subroutine by arguments. Some of the features of QMG FORTRAN may be summarized as follows:

1. All parameters of the mass spectrometer are completely set and read by computer. This allows for optimization and measurement in a "closed loop" operation.

2. The console of the QMG 511 may be set manually or by computer.

3. QMG FORTRAN call and statements are easy to understand, even by persons lacking FORTRAN programming experience.

4. The QMG FORTRAN library modules may be extended by adding new assembler or FORTRAN routines.

5. FORTRAN IV supports a number of DEC peripherals such as LPS-11 (laboratory peripheral system with A/D converter, real time clock and digital I/O interface) and the graphic display processor (GT 44).

6. Time division multiplexing offers for the simultaneous operation of as many as eight similar quadrupole mass spectrometers.

DESCRIPTION OF THE QMG 511 SYSTEM

The Balzer QMG 511 system consists of a combination of several intergrated units, including an analyzer, a control unit, an electrometer amplifier, a radiofrequency generator and a data recording device*. A general description of the system is shown in Figures 2 and 3.

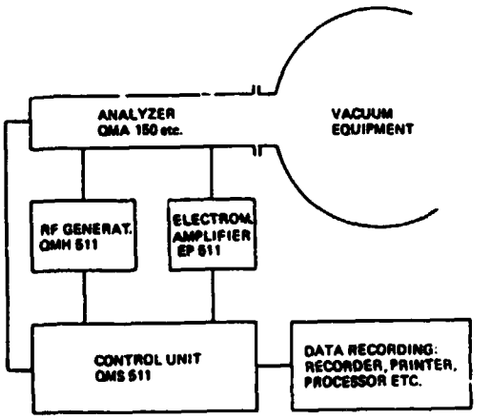

Figure 2. Schematic of the QMG 511 Quadrupole Mass Spectrometer System.

The mass analyzer itself consists of an ion source, the quadrupole mass filter and a secondary electron multiplier (SEM) as the ion detector.

The combined units in Figure 3, comprise the QMG 511 system (computer not included). A short description of some of the major units follows:

*The QMG 511 quadrupole mass spectrometer system is manufactured by Balzer Aktiengesellschaft fur Hochvakuumtechnik und Dunne Schichten FL-9496 Balzer, Principality of Liechtenstein. The USA Sales office is located in Hudson, New Hampshire.

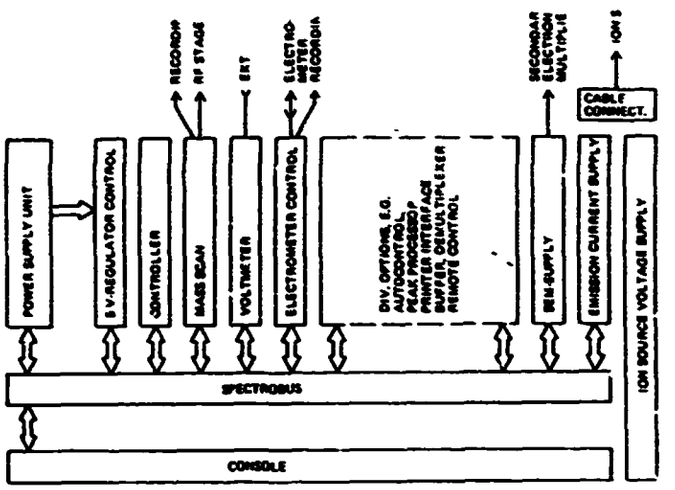

Figure 3. Block Diagram of the Quadrupole Mass Spectrometer System (QMG 511)

The Spectrobus

This is the information channel shared by all plug-in units. Assigment of supply voltage to the other units is determined by the spectrobus.

The Power Supply Unit

This unit generates and supplies stablized voltage to all other units requiring this need.

The 5 V-Regulator

This unit converts unstablized voltage into stablized +5V for all digital circuits.

The Controller

The unit controls the transfer of information between the other units. It also furnishes the programmable "clock" for mass scans and the mass marker.

Mass Scan

This unit controls the mass scan as well as the resolution of the RF-stage. The working conditions of the mass scan, and RF-stage are determined by messages to this unit.

Voltmeter

This is an analog-digital converter that measures electrometer output, emission current and ion source voltage. The respective values from this unit are furnished to the spectrobus.

Electrometer Controller

This unit automatically selects the range of the electrometer amplifier and picks up its output signal for transfer to the voltmeter via the spectrobus.

Ion Source

The ion sources consists of the emisssion current which feeds the filament.

Console

Through the console, it is possible to adjust all functional parameters which are digitized and transmitted to the other units via the spectrobus. Data such as voltmeter output, mass numbers, etc., are received by the console and displayed in a digital fashion.

SEM Supply

In this unit, the high voltage requirements necessary for the secondary electron multipler (SEM) is generated and controlled.

The Electrometer Amplifier (EP 511)

This unit converts the small current from the SEM or Faraday detector into analog voltage.

The RF-Generator

Here the RF and DC voltage necessary for the quadrupole mass filter is generated. This unit draws its voltage from the control unit.

Buffer (BF 511)

The buffer BF 511 is the interface between the the spectrometer and the computer. Information is digitally transferred to the buffer from the various units of the spectrometer. This information is provided to the computer and vice versa through an asynchronous dialogue. All controls and settings of the QMG 511 are accessible through the buffer.

Peak Processor

This is a fast digital processor. It takes information on intensities and mass numbers and evaluates it for peak maxima and corresponding mass numbers.

THE PDP 11/23 SYSTEM CONTROLLER

A PDP 11/23 desktop computer using the RT 11 operating system serves as the main controller for the quadrupole system. The computer, which is manufactured by Digital Equipment Company (DEC), has 256 k bytes of random access memory (RAM), dual 8 1/4 inch floppy disk drives, a high resolution VT 103 video display, a display terminal controller and a detachable keyboard.

All real time operations are initiated by keyboard entries, which in turn initiates operating commands to the data system of the spectrometers. This results in the necessary output for instrument control and data transfer.

The FORTRAN IV and QMG FORTRAN software control the I/O operations using print and write statements. These statements transfer alphanumeric output to the VT 103 or to the printer through a standard EIA RS 232C interface. Through keyboard operations, the user is able to access various FORTRAN source programs and subroutines that will perform the following operations.

1. Automatically read the first mass and prints its value to the printer and also subsequent masses under the same or different operating conditions.

2. Start mass scans at a mass number and mass range predetermined by the user.

3. Automatically command the digital voltmeter and ion source voltage to transfer its data to the buffer for later retrieval and processing.

4. Automatically initializes the BF buffer and set the console parameters.

5. Automatically send incrementing mass numbers to the QMG 511.

6. Automatically set and read twenty two variable parameters of the QMG 511 for optimum operating conditions. These parameters are listed in Table 1.

Table 1. The Parameters of the QMG 511 Automatically Set and Read.

ParameterCode	Parameters
1	Mass Numbers
2	Fraction
3	Scan Width
4	Resolution
5	SEM Voltage
6	Scan speed
7	Single/Manual/Repeat
8	Integral/Spectrum
9	RF On/Off
10	Electrometer Range
11	Polarity
12	Magnifier
13	Filter
14	SEM Switch
15	Filameter Switch On/Off
16	Normal/Degas
17	Electron Energy
18	Display
19	Auto Control Channnel
20	Auto Control/Operation
21	Autocontrol On/Off
22	Autocontrol Set/Not Set

7. Mass scans may be obtained between a set mass range and hard copies provided as shown in Table 2.

Table 2. An Example of the Mass Number and Intensity Printout From the QMG 511/Computer System. Note: These results were obtained using a "clean" mass filter, as a result, they do not represent an actual sample.

NR	MASS NUMBER	INTENSITY
1	0.00	-0.216E-08
2	0.08	-0.224E-08
3	0.20	-0.228E-08
4	0.33	-0.232E-08
5	0.39	-0.240E-08
6	0.52	-0.240E-08
7	0.64	-0.240E-08
8	0.77	-0.240E-08
9	0.89	-0.232E-08
10	1.02	-0.228E-08
11	1.14	-0.224E-08
12	1.27	-0.224E-08
13	1.39	-0.220E-08
14	1.45	-0.220E-08
15	1.58	-0.220E-08
16	1.70	-0.224E-08
17	1.83	-0.232E-08
18	1.95	-0.232E-08
19	2.08	-0.236E-08
20	2.20	-0.240E-08
21	2.33	-0.236E-08
22	2.39	-0.236E-08
23	2.52	-0.236E-08
24	2.64	-0.228E-08
25	2.77	-0.224E-08
26	2.89	-0.224E-08
27	3.02	-0.220E-08
28	3.14	-0.220E-08
29	3.27	-0.220E-08
30	3.33	-0.224E-08
31	3.45	-0.228E-08
32	3.58	-0.232E-08
33	3.70	-0.236E-08
34	3.83	-0.240E-08
35	3.95	-0.240E-08
36	4.08	-0.240E-08
37	4.20	-0.232E-08
38	4.33	-0.228E-08
39	4.45	-0.224E-08
40	4.58	-0.224E-08

In general, the PDP 11/23 is capable of initializing all variable parameters. It also stores and transmits data at rates up to 44 k words per second.

With the spectrometer off line, the user may bypass computer automation fully and use the manual mode.

Computer control of the spectrometer enables the user to acquire spectral data by two modes: (1) data acquisition with buffering, and (2) intermediate mode. In the intermediate mode, data from the QMG buffer are converted directly from the internal data format into floating point notation. This data is available to the user in the FORTRAN program immediately for additional processing. In the "data acquisition with buffering mode", the data is stored directly in a predefined data field without conversion. An appropriate processing routine belongs to each data acquisition mode which provides data readout and floating point conversion.

EXPERIMENTAL

As previously indicated, the design of the BF buffer permits interfacing with the PDP 11/23 computer; the buffer provides for an easy asynchronous dialogue between the the QMG 511 over a defined data path. All operations of the spectrometer (except power) are accessible through the buffer. Data produced by the spectrometer are stored in the buffer and available as output. This concept permits a "closed loop" operation which is unique in mass spectrometry.

Data transfer between the buffer and the computer occurs on a high speed balanced line transmission system which consists of a general purpose 16 bit parallel line interface (DRV-11) and an LT 511 line transceiver. The latter is a pc board containing the electrical circuits necessary for converting transistor-transistor logic signals (TTL) to constant output current on the twisted pair lines leading to the buffer and vica versa.

The hardware of the LT 511 was initially designed for the unibus of the PDP 11 minicomputer. Thus, it became necessary to adapt the pin assignment on the LT 511 board so that compatability with the PDP 11/23 could be acheived. This involved disconnecting the priority jumper for the unibus and connecting the jumpers for the LSI 11 bus. Examples of the jumpers for the LSI 11 and unibus is shown in Figure 4.

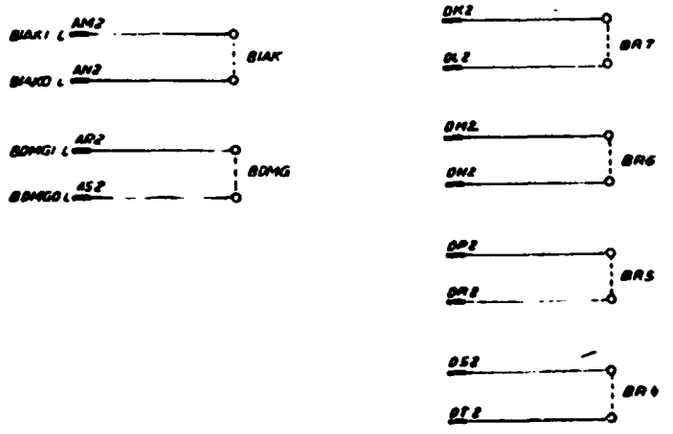

LSI 11 Bus Unibus

Figure 4. Diagram of the Priority Jumpers for the LSI 11 and Unibus.

INTERFACING THE DRV 11 AND THE LT 511 LINE TRANSCEIVER

Once the appropriate jumper had been set, it became necessary to interface the DRV 11 (manufactured by Digital Equipment) and the LT 511 (manufactured by Balzer). The DRV 11 is a necessary interface component for connecting parallel TTL logic devices to the LSI 11 bus. It also permits program controlled data transfer at rates up to 44 k words per second, and also provides for LSI 11 bus interface and control logic for interrupt processing and vector generation. Data is handled by a 16 diode-clamped input lines and 16 latched output lines. Device address is user-assigned and control/status registers (CRS) and data registers are compatible with PDP 11 software routines. Interfacing of the two components proceeded as described by Figure 5.

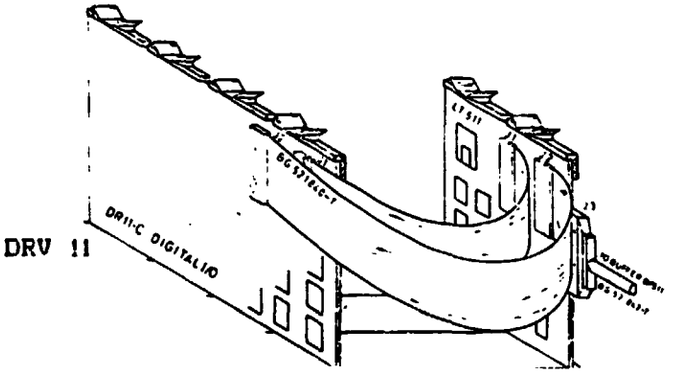

Figure 5. Interface Connections Between the LT 511 and the DRV 11

The cable connecting the LT 511 and the DRV 11 took up one slot in the LSI 11 bus cage. Therefore, it was necessary to insert an extender board in the slot reserved for the LT 511 and then insert the LT 511 into the extender board. This arrangement resulted in the LT 511 protruding beyond the backplane of the computer; however, the arrangement resulted in no apparent operating problems. With the LT 511 and DRV 11 in place and connecting made to the BF 511 buffer (Figure 5), configuration of the LSI bus was completed with all bus slots occupied as shown in Figure 6.

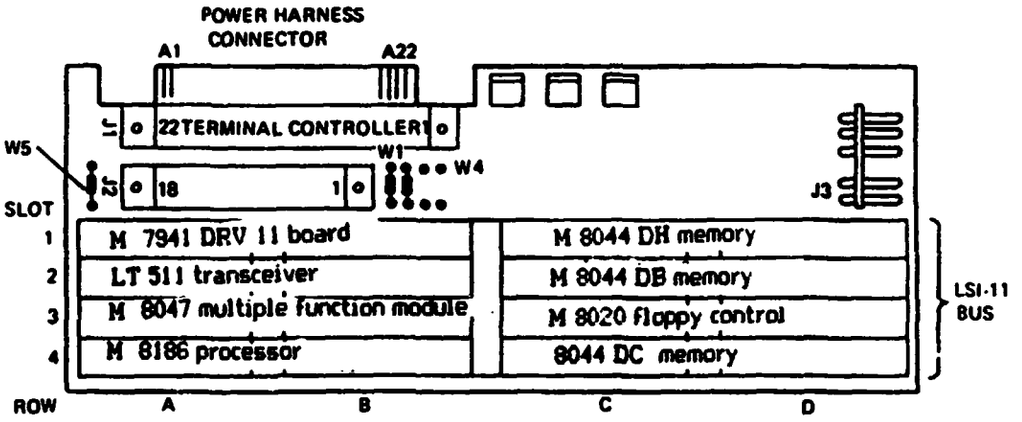

Figure 6. The Configurated LSI Bus of the PDP 11/23 Computer

RESOLUTION OF SOFTWARE PROBLEMS

The case of the missing global

In an attempt to compile and link certain of the QMG FORTRAN source programs, the following error message was consistly displayed on the CRT:

Link-W-undefined global
SAI $ IP

This message indicated that the SAI $ IP global (value) was missing from the FORTRAN library module provided with the RT 11 operating system furnished by DEC. The global was found in the library module of a newer version ot the RT 11 system. Several attempts to extract the missing global and place it in the " orginal library module" proved unsuccessful. As a result, it was decided to approach the problem in a circuitous manner by taking the library module containing the missing global and constructing another library module, called XLIB. It was necessary to give the library a name different from the one it was created from. Otherwise, there would have been two library modules with the same name, with only one containing the missing module. This would have made linking of the source program unpredictable.

As a result of the additional library module, it became necessary to link the source programs and subroutines with four library modules in order to obtain a runnable program: the QMG FORTRAN library (called QFLIB); the newly created library (called XLIB), and the standard SYSLIB and FORLIB FORTRAN IV libraries.

CONCLUSIONS AND RECOMMENDATIONS

Configuration of the LSI 11 bus of the PDP 11/23 desktop computer has been completed. Computer/spectrometer interfacing has been accomplished and computer dialogue is now possible.

The versatility of the system enables the user to rapidly acquire and process mass spectral data under programming conditions and under a "closed loop" operation, unique to mass spectrometry. Specifically, the buffer of the QMG 511 can now be initialized automatically and twenty two variable parameters of the spectrometer set and read in less that a second.

Mass scans over a desired range is also made possible and the mass numbers and corresponding intensities obtained as hard copies.

Selected ion monitering is also possible and standard console functions can automatically set and read. In the off line position, the spectrometer may be operated under complete manual control.

It remains for the spectrometer/computer system to be coupled to the thermal analyzer. It is recommended that this final operation be undertaken and possibly, a recorder should also be connected to the system so that a visual picture of the data (a bar chart of mass numbers verses % abundances) could be obtained.

REFERENCES

1. Bonelli, E. J., M. S. Story and J. B. Knight, Computerized Gas Chromatography and-Quadrupole Mass Spectrometry, Dynamic Mass Spectrometry, vol. 2, pp. 177-202, Heyden and Sons Ltd., Great Britan, 1971.

2. Karasek, F. W., GC/MS/Computer, Anal. Chem., 44(4) 32A - 42A (1972).

3. Lums, F. W., A Microcomputer for Laboratory Automation, Personal Computer in Chemistry, Peter Lykos (Editor), pp. 26 - 37, Wiley Interscience, New York (1981).

1983

NASA/ASEE SUMMER FACULITY RESEARCH FELLOWSHIP PROGRAM

MARSHALL SPACE FLIGHT CENTER
THE UNIVERSITY OF ALABAMA IN HUNTSVILLE

STIFFNESS PROPERTIES FOR DYNAMIC MODELING OF COMPOSITE GRAPHITE-EPOXY CYLINDRICAL ORTHOTROPIC SHELLS

Prepared By: R. Noel Tolbert, Ph.D., P.E.

Academic Rank: Associate Professor

University and Department: Tennessee Technological University
Civil Engineering Department

NASA/MSFC:
Division: Structural Dynamics
Branch: Systems Analysis

MSFC Counterpart: Robert S. Ryan

Date: August 12, 1983

Contract No.: NGT 01-008-021
The University of Alabama in Huntsville

STIFFNESS PROPERTIES FOR DYNAMIC MODELING OF COMPOSITE GRAPHITE-EPOXY CYLINDRICAL ORTHOTROPIC SHELLS

BY

R. Noel Tolbert
Associate Professor of Civil Engineering
Tennessee Technological University
Cookeville, Tennnessee

ABSTRACT

Traditional composite lamination theory was used to predict composite graphite-epoxy laminate stiffnesses for comparison to quasi-experimental stiffnesses developed from cylindrical bottle pressure testing.

Stiffness sensitivities were examined for variations in constituent materials and geometric properties. The material component interactions examined were the fiber longitudinal and transverse Young's modulus, the fiber shear modulus and primary Poisson's ratio, the resin Young's modulus, shear modulus, and Poisson's ratio. The geometric variation of the helical winding angle was also examined.

Two computer programs were written to generate the data used to demonstrate the stiffness variations.

ACKNOWLEDGEMENTS

There were several NASA employees who contributed to the work in this report and to the author's NASA/ASEE program. A few are singled out for their especially valuable contributions. Dr. John Admire, Mr. Sam Jones, and Mr. Gale Ernsberger provided training for using the NASA computer and associated terminals. Mr. Frank Bugg assisted with project meetings and laboratory testing. Ms. Carol Lee cordially and competently typed the report. Mr. Dennis Kross graciously shared his office and general supplies. Mr. Robert Ryan provided excellent program support and project leadership. Finally, Mr. Vince Verderaime provided research guidance, publications, suggestions, and encouragement. The author extends his appreciation to all of these.

INTRODUCTION

Experimental testing of a reduced-scale test article is often used to predict behavior for the full-scale structure for obvious reasons of economy, speed, and availability of adequate test facilities. The need for mathematical models to accurately predict structural behavior is an integral part of such a test program. NASA is currently conducting such a program for epoxy-graphite, filament-wound, solid rocket motor cases. A lack of agreement when comparing dynamic responses as measured in experimental testing to values calculated from computer analysis suggested the need for a thorough examination of methods used to predict laminate stiffness properties. Additionally, a study was needed to determine the sensitivity of both the micromechanical and macromechanical properties as related to the laminated cylinder extensional and bending properties.

OBJECTIVES

The objectives of this study were as follows: (1) to select appropriate mathematical, micromechanical models for calculating the plane stress elastic constants for a graphite-epoxy lamina, (2) to develop a mathematical macromechanical model for a filament-wound cylinder that would calculate the extensional, coupling, and bending stiffness matrices, and finally (3) to determine the sensitivity of both the micromechanical and macromechanical properties as related to the laminated cylinder extensional and bending stiffness properties.

MICROMECHANICS

Introduction

Based on Hooke's law for an orthotropic material subjected to a general state of stress, nine nonzero elastic constants are required for analysis. For the simplified case of plane stress, only four nonzero elastic constants are required. The four constants are (1) the longitudinal Young's modulus, E_1, (2) the transverse Young's modulus, E_2, (3) the primary Poisson's ratio, ν_{12}, and (4) the shear modulus, G_{12}. Experimentally, these properties can be determined from ASTM standard laboratory tests as performed by Smith and Huang[1] or from a combination of micromechanics theory and tube pressure testing as attempted by Hercules[2]. Analytically, these properties can be determined by substituting fiber and matrix properties into the appropriate micromechanical equations. In this latter method, it is imperative to have accurate fiber and matrix properties in both the longitudinal and transverse direction. The micromechanical model for each of the four elastic constants follows.

(1) Model for E_1

The mathematical model used to determine E_1, referred to as the rule of mixtures, is expressed in terms of the fiber Young's modulus, E_f, the fiber volume fraction, V_f, the matrix Young's modulus, E_m, and the matrix volume fraction, V_m, and is written as follows:

$$E_1 = V_f E_f + V_m E_m \tag{1}$$

While this equation yields reasonably accurate values when compared to experimental data, Jones[3] demonstrated this equation to be an upper bound for E_1 under certain conditions and thus presented the following modified equation as recommended by Tsai[4] to account for imperfections in fiber alignment.

$$E_1 = K (V_f E_f + V_m E_m) \tag{2}$$

The fiber misalignment factor, K, ordinarily varies from 0.9 to 1. The value is experimentally determined and is highly dependent on the manufacturing process. In an absence of testing to determine the proper value of K, a minimum reduction in E_1 of 2% or K = 0.98 would be appropriate. To assure adequate stiffness in stiffness dominated design criteria, a lower value of K would be justified.

(2) Model for ν_{12}

Corresponding to the development of E_1, ν_{12} can be approximated by the rule of mixtures as follows:

$$\nu_{12} = \nu_f V_f + \nu_m V_m \tag{3}$$

where ν_f and ν_m are the major Poisson's ratio of the fiber and matrix, respectively. Moderate variations in ν_{12} have little impact on laminate properties and additional refinement of this equation is of less importance. Rather, emphasis should be placed on the proper determination of ν_f and ν_m. All too often "industry values" are used that may be significantly in error.

(3) Model for E_2

Halpin and Tsai[5] developed empirical equations that accurately predicted the transverse stiffness for lamina fabricated using isotropic constituent materials. Whitney[6] later extended these equations to anisotropic fibers by substituting the anisotropic fiber transverse stiffness, E_{f_T}, for the general isotropic stiffness, E_f. A general procedure would permit a transverse modulus for both the fiber and matrix as given by Whitney[7] and written as follows:

$$E_2 = E_{m_T} \left(\frac{1 + \eta_1 V_f}{1 - \eta_1 V_f}\right) \tag{4}$$

where

$$\eta_1 = \frac{(E_{f_T}/E_{m_T} - 1)}{(E_{f_T}/E_{m_T} + \xi)} \tag{5}$$

in which ξ is a measure of the fiber's configuration and packing geometry. A value of $\xi = 2$ has been used with experimental verification for both circular and square fibers. For anisotropic fibers, such as graphite, the difficulty lies in the determination of the fiber transverse modulus. Whitney[6] estimated the value of the graphite fiber (Thornel 25) to be 1/12 of its longitudinal stiffness. Ultrasonic studies by Smith[8], when testing the same fiber, produced a similar ratio for the "ultrasonic moduli." However, other fiber types reported by Smith had varying ratios. The range of ratios by Smith is shown in Table 1 along with the results reported by other investigators[9-11]. From the table, one could deduct that a decrease in the transverse modulus may accompany an increase in its longitudinal modulus.

Finally, as taken from McCullough[12] and shown in Figure 1, a lower bound value for E_2 can be determined. The equation for this lower bound with E_{f_T} and E_{m_T} substituted for E_f and E_m, respectively, and the terms rearranged would be

$$E_2 \text{ (lower bound)} = \frac{E_{m_T} \; E_{f_T}}{V_m \; E_{f_T} + V_f \; E_{m_T}} \tag{6}$$

(4) Model for G_{12}

Following the general form of the Halpin-Tsai equation for E_2, the equation for the shear modulus, G_{12}, would be

$$G_{12} = G_m \; \frac{(1 + \eta_2 \; V_f)}{(1 - \eta_2 \; V_f)} \tag{7}$$

where

$$\eta_2 = \frac{(G_f/G_m - 1)}{(G_f/G_m + \mathfrak{J})} \tag{8}$$

in which a value of $\mathfrak{J} = 1$ has been used with experimental verification for both circular and square fibers. However, for volume fractions greater than 0.5, a Hewitt and deMalherbe equation given in Jones[3], suggested $\mathfrak{J}$ be determined from

$$\mathfrak{J} = 1 + 40 \; V_f^{10} \tag{9}$$

Again, the critical factor is accurately determining the shear modulus of the fiber. Table 1 gives a summary of shear modulus values for graphite fibers as reported by several researchers[6, 8-11].

Summary of Micromechanical Models

The micromechanical models chosen for the four required elastic constants are as follows:

E_1 will be determined using the rule of mixtures equation (2) as modified by fiber misalignment. A misalignment value of K = 0.96 will be used.

ν_{12} will be determined from the general rule of mixtures using equation (3) with special emphasis placed on properly determining ν_f and ν_m.

E_2 will be determined using the Halpin-Tsai equations (4) and (5) with a value of $\xi = 2$ being used for the coefficient. Also, in the absence of specific fiber test data, the fiber transverse modulus, E_{f_T}, will be taken as 2.0×10^6 psi.

G_{12} will likewise be calculated using the corresponding equations (7) and (8) with a value of $\xi = 1$ being used for the coefficient. Again, in the absence of specific fiber shear modulus test data, the fiber shear modulus will be set equal to 2.5×10^6 psi. The shear modulus of the matrix will be calculated from its isotropic relationship to Young's modulus and Poisson's ratio.

MACROMECHANICS

Introduction

Plane stress laminate theory is typically used for thin cylinder analysis. Pagano[13, 14] in two reports examined this "thin-walled cylinder" assumption for anisotropic materials. His study examined the three basic loadings of axial, torsion, and internal pressure and showed that for helical wound cylinders, the cylinder wall stress field approaches uniformity as the wall thickness approaches zero. Then examining nonzero small wall thickness, Pagano showed the stress gradient to be more severe for anisotropic materials such as graphite systems than for isotropic materials such as glass systems. His work indicates that for the cylinders of this study ($R/H > 40$), classical lamination theory can be used without serious error.

Macromechanical Model

Developed from classical lamination theory as shown by Agarwal and Broutman[15], the cylinder wall constitutive equation can be written as follows:

$$\begin{Bmatrix} N \\ M \end{Bmatrix} = \begin{bmatrix} A & B \\ B & D \end{bmatrix} \begin{Bmatrix} \epsilon_o \\ K \end{Bmatrix} \tag{10}$$

where N represents the resultant forces and M represents the resultant moments. The A, B, and D matrices are called the extensional stiffness matrix, coupling stiffness matrix, and bending matrix, respectively. The final column matrix contains the midplane strains, ϵ_o, and plate curvatures, K.

Equation (10) can be expanded as follows:

$$\begin{Bmatrix} N_x \\ N_y \\ N_{xy} \end{Bmatrix} = \begin{bmatrix} A_{11} & A_{12} & A_{16} \\ A_{12} & A_{22} & A_{26} \\ A_{16} & A_{26} & A_{66} \end{bmatrix} \begin{Bmatrix} \epsilon_{x_o} \\ \epsilon_{y_o} \\ \gamma_{xy_o} \end{Bmatrix} + \begin{bmatrix} B_{11} & B_{12} & B_{16} \\ B_{12} & B_{22} & B_{26} \\ B_{16} & B_{26} & B_{66} \end{bmatrix} \begin{Bmatrix} K_x \\ K_y \\ K_{xy} \end{Bmatrix} \tag{11}$$

$$\begin{Bmatrix} M_x \\ M_y \\ M_{xy} \end{Bmatrix} = \begin{bmatrix} B_{11} & B_{12} & B_{16} \\ B_{12} & B_{22} & B_{26} \\ B_{16} & B_{26} & B_{66} \end{bmatrix} \begin{Bmatrix} \epsilon_{x_o} \\ \epsilon_{y_o} \\ \gamma_{xy} \end{Bmatrix} + \begin{bmatrix} D_{11} & D_{12} & D_{16} \\ D_{12} & D_{22} & D_{26} \\ D_{16} & D_{26} & D_{66} \end{bmatrix} \begin{Bmatrix} K_x \\ K_y \\ K_{xy} \end{Bmatrix} \tag{12}$$

where the terms A_{ij}, B_{ij}, and D_{ij} can be written in terms of the summation of the transformed axes properties of the lamina and its corresponding layer thickness. These equations are generally developed in texts[15] on lamination theory.

In addition to the A, B, and D matrices, it is generally desirable to obtain the laminate extensional and bending stiffness properties which can be expressed in terms of the A and D matrix, respectively, First, the equations for the extensional stiffnesses and Poisson's ratio are

$$E_x = A_{11} - \frac{A_{12}^2}{A_{22}} \tag{13}$$

$$E_y = A_{22} - \frac{A_{12}^2}{A_{11}} \tag{14}$$

$$\gamma_{xy} = \frac{A_{12}}{A_{22}} \tag{15}$$

$$G_{xy} = A_{66} \tag{16}$$

and the bending stiffnesses are

$$E_x = D_{11} - \frac{D_{12}^2}{D_{22}} \tag{17}$$

$$E_y = D_{22} - \frac{D_{12}^2}{D_{11}} \tag{18}$$

Computer Programs

Two computer programs were written in Fortran IV and are listed along with a sample solution output in Appendices A and B. By making substitutions for the control statements and the general read format, the programs can be easily adapted to any computer with a Fortran compiler.

The first computer program called "LAM" and listed in Appendix A was specifically written to test the sensitivity of fiber and resin properties as related to both the lamina and the cylinder laminate. The program has an iteration option for

that express purpose. The program was structured for interactive use and input of data is explained and requested item by item during program execution. The program has several options and is particularly useful for symmetrical lay-ups of regularly alternating helical-hoop plys since the program will generate the layer data with a minimum of input. A "quarter scale" test winding was used in the sample solution listing. Additional information is given in the comment cards at the beginning of the program listing.

The second program was named "COMP" and is listed in Appendix B. This program was written specifically to generate cylinder laminate stiffness properties using general lamina data. This proved to be more satisfactory than adding a cumbersome modification to the first program. COMP permits each ply to have different lamina properties and the size is only restricted by the dimension statements. A simple change in dimension size will permit user expansion to accommodate problem requirements. No other changes are necessary. COMP is not written to be interactive due to the large number of laminations required for many practical applications. For example, the full-scale SRMC had 49 layers, was unsymmetric, and had a mixture of lamina properties. The use of a data file for this type of problem is recommended. Specific instructions on data input are given in the comment cards at the beginning of the program listing.

SENSITIVITY STUDIES

Introduction

The sensitivity studies were conducted on an epoxy-graphite laminated cylinder taken from the "STA Baseline Design" as described by Hercules[16]. The graphite fibers were Hercules AS4W-12K as manufactured from a Polyacrylonitrile precursor. The fiber longitudinal Young's modulus was extensively tested by Hercules and reported to be 33-34 x 10^6 psi. The Poisson's ratio of the fiber was given as 0 2, but this value was not supported with test data. The matrix used was HBRF-55A epoxy resin, with 24 parts Tonox to 100 parts resin. The Young's modulus of the resin was reported to be 0.489 x 10^6 psi, ±25 percent,[16] and the resin Poisson's ratio was listed as 0.35. The cylinder was manufactured using alternating helical-hoop windings, with layer geometry conforming to the sample output of LAM as given in Appendix B.

Micromechanical Sensitivity

The longitudinal Young's modulus of the fiber is known to be the dominant contributor to laminate stiffness. In this study, a small change in the fiber modulus generated a proportional change of 82 percent in the general laminate stiffness properties, with the exception of Poisson's ratio. The Poisson's ratio had a proportional change of 14 percent. Expressed differently, this would imply a 10 percent change in the longitudinal fiber modulus would cause an 8.2 percent change in laminate stiffness properties and a 1.4 percent change in Poisson's ratio. The laminate properties varied almost linearly with changes in fiber modulus. Thus, the effect of moderate variations in fiber modulus can be easily estimated. Even though the longitudinal fiber modulus is the dominant contributor to laminate stiffness, it is the better understood constituent property and of probable, less importance to this study. Properties with less Hercules test support and probable wider variations follows.

Hercules[16] provided a value of 0.2 for the primary Poisson's ratio of the ASW-12K graphite fiber. As indicated in Table 1, other studies suggest the ratio may be higher. If the fiber Poisson's ratio is increased 50 percent from 0.2 to 0.3, laminate properties are only slightly affected. The largest change takes place in the laminate Poisson's ratios but the difference is still less than 1 percent. For this same 50 percent change in fiber value, the lamina Poisson's ratio changes 21 percent. However, as alluded to during the discussion of the micromechanical model for ν_{12}, the laminate properties are insensitive to changes in the lamina Poisson's ratio.

Turning to the transverse Young's modulus of the graphite-fiber, other studies, as shown in Table 1, indicate its transverse value to be only a small fraction of its longitudinal value. If the fiber's transverse modulus is estimated to be 1.5×10^6 psi and then driven to zero, the lamina transverse stiffness is reduced 81 percent. However, the most sensitive matrix stiffness values, A_{12}-D_{12}, were reduced only 8.7 percent. If reasonably accurate values (±33 percent) of the transverse fiber modulus are initially used in stiffness analysis, the error due to its variations should be less than 3 percent in any laminate elastic stiffness constant.

The next property examined was the fiber's shear modulus. Values from other studies are shown in Table 1. Its value is only a small fraction of that if treated as an isotropic material. Using an estimated fiber shear modulus of 2.5×10^6 psi and then setting its value equal to zero, produces a correspondingly large reduction in the lamina shear modulus. In fact, the lamina shear modulus is reduced by 88 percent. While the reduction in fiber shear modulus produces similar effects as a reduction in fiber transverse Young's modulus, the A_{12}-D_{12} matrix terms and the lamina Poisson's ratio vary inversely. That is, a reduction in the fiber shear modulus produces an increase in these terms. For this case, a reduction in the fiber shear modulus produced an increase of 9.8 percent for the A_{12}-D_{12} laminate terms and a 15-percent increase in the laminate Poisson's ratio. Other laminate terms were reduced from 4 to 11 percent. Although deviations in the value of the fiber shear modulus from its true value should not be of the order tested in this report, the errors generated can be significant and, of most importance, can be additive.

Next, the sensitivity of the resin Young's modulus was examined by using ±25 percent variation as given by Hercules[16]. A reduction of 25 percent in the resin modulus produced a very small change (0.2 percent) in the lamina longitudinal modulus. However, the lamina transverse modulus was reduced 12 percent. When considered in terms of the laminate values, the effect was slight. The largest reduction in the laminate stiffness property was 3 percent while the corresponding largest reduction in the stiffness matrix coefficients was less than 2 percent.

Finally, the sensitivity of the resin Poisson's ratio can be examined by recalling the sensitivity of the laminate to changes in the fiber Poisson's ratio. While the resin makes a slightly larger contribution to the lamina Poisson's ratio, the effect is insignificant. Likewise, the shear modulus contribution of the resin is minimal.

Macromechanical Sensitivity

The sensitivity of the lamina properties (E_1, E_2, ν_{12}, and G_{12}) as related to the laminate was covered in adequate detail when discussing micromechanics sensitivity. From these discussions, it was noted that the laminate properties are very sensitive in changes in E_1 and relatively insensitive to changes in ν_{12}. The sensitivity of the remaining two terms, G_{12} and E_2, was low. However, should the effect of variations in G_{12} and E_2 be additive, the results can be significant.

Now, turning to the helical wind angles of the cylinder, Figure 2 was constructed to give representative values of the laminate stiffness constants. Normalized plots with respect to baseline values are plotted for the laminate terms A_{11}, A_{22}, A_{66}, and ν_{xy}. Graphs for D_{11} and E_x, D_{22} and E_y, as well as D_{66} and G_{xy} would closely follow those drawn for A_{11}, A_{22}, and A_{66}, respectively. The specific layer thicknesses and lay-up configuration for the cylinder are given in the solution listing of COMP in Appendix 2.

CONCLUSIONS AND RECOMMENDATIONS

The effect of small changes in fiber and resin mechanical properties on the composite laminated cylinder of this report, although not necessarily linear, can be reasonably estimated by linear proportion. While some laminate variations are, in fact, linear, the change in slope of the curves for the nonlinear terms is very small. The dominant constituent property, the fiber longitudinal Young's modulus, generated an 82 percent carryover response to the laminate. On the other hand, the laminate was insensitive to large changes in either the fiber or resin Poisson's ratio even though these fiber and resin ratios cause the lamina Poisson's ratio to vary widely. Thus, the lamina Poisson's ratio is such a small contributor to laminate properties, the accuracy of the fiber and resin Poisson's ratio is of lesser importance.

The interesting properties of this study were the fiber shear modulus and the fiber transverse Young's modulus. While these properties are very difficult to measure using traditionally experimental techniques, ultrasonic studies (8-11) and values "backed out" of laminate tests[6] agree in relative magnitudes and equally identify the graphite fiber as being highly anisotropic. Both moduli values are only small fractions of their magnitudes if incorrectly treated as isotropic. Neither value appears to have a definable relationship to the more easily measured longitudinal modulus. In fact, a constant value for each could be used without generating serious errors. For this study, the fiber shear modulus was estimated to be 2.5×10^6 psi, and the fiber transverse Young's modulus was estimated to be 1.5×10^6 psi. Both fiber properties, E_{f_T} and $G_{f_{LT}}$, dominate their related lamina values contributing 81 percent and 88 percent to E_2 and G_{12}, respectively. However, the largest contribution of the fiber's transverse modulus to any laminate stiffness term was 8.7 percent. Similarly, the fiber's shear modulus contributed a maximum of 10 percent. In addition, the fiber's shear modulus contributed 15 percent to the laminate Poisson's ratio while the fiber's transverse modulus contributed only 3.4 percent. Lamina values, E_2 and G_{12}, were computed to be 21% percent higher and 28.5 percent lower, respectively, than Hercules'[16] reported values. The Hercules reported value of E_2 was 33 percent less than the theoretical lower bound as given by equation (6). This Hercules value, while not correct for low and moderate stress levels, could be possible for high stress levels where the resin had partially failed. This difference between the Hercules values and the author's values reduced the laminate A_{12}, D_{12} terms 11.7 percent and reduced the laminate Poisson's ratio 9.4 percent. Unquestionably, these differences need to be resolved.

The author recommends several items for further study to permit better agreement of the dynamic response experimental data with analytical models. The recommendations are listed in the order of importance as viewed by the author.

(1) Adapt the current composite laminate computer code to calculate the four lamina elastic constants using the Hercules pressure bottle test data. The approach would be to iterate a solution of the applicable constitutive equations beginning with a micromechanics solution set and incrementing each value by its appropriate deviation adjustment. The analysis would be stress dependent to account for the high nonlinearity of the shear modulus as reported by Jones[17, 18] and Smith[1]. The Hercules approach of a direct solution by using micromechanics theory for the two lamina terms, E_1 and ν_{12}, and placing all deviations in the two other lamina values, E_2 and G_{12}, is unacceptable.

(2) Continue the numerical sensitivity study beyond the laminate properties to the affected dynamic responses. That is, determine the effect of a change in the fiber transverse modulus, as well as other constituent properties, on the dynamic frequencies and modal shapes.

(3) Examine the effect of nonsymmetric laminations on dynamic response. Whitney[19] indicates the coupling results in significantly-decreased vibration frequencies. This coupling effect is reported to reduce with increasing layers. However, Jones[20] showed, for a laminate with as many as 40 layers, the effect on the fundamental vibration frequency was about 10 percent. Each laminate must be examined independently because general results cannot be presented for an infinite variety of laminates.

(4) Examine the effect of the anisotropic constituent materials on the assumption of "thin-wall cylinder" analysis for the "STA Baseline Design"[16]. Anisotropic materials, such as graphite fibers, require a much larger radius to thickness ratio (r/h) than glass fiber composites[13, 14].

(5) Examine the Hercules composite for different moduli in tension and compression. Jones[21, 22] addresses this topic and indicates the compression modulus to be lower than its tensile value. The stiffness discontinuity at zero stress generates questions as to the proper modulus for free stress state dynamic testing. Residual curing stress may produce a compressive modulus for very low and zero stress states. Furthermore, Jones[23] shows the composite flexural modulus to be closer to the smaller of either the tensile or compressive modulus.

Table 1. Elastic Constants of Graphite Fibers

Reference	Fiber Young's Modulus (10^6 psi) E_L	Fiber Poisson's Ratio ν_{LT}	Ratio of Transverse to Longitudinal Young's Modulus E_T/E_L	Fiber Shear Modulus (10^6 psi)
Smith (8)	22	0.23	0.08	2.0
	51	0.41	0.02	2.2
	81	0.39	0.01	2.5
Uemura (11)	23	0.3	0.07	2.0
	38	0.4	0.04	2.0
Dean (9)	38	0.35	0.07	3.8
	58	0.35	0.02	1.9
Ishikawa (10)	23	0.30	0.09	-
Whitney (6)	17	0.30	0.08	2.0

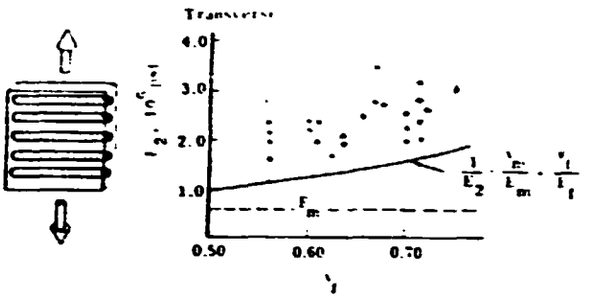

Figure 1. Comparison of Theory and Experiment for Transverse Modulus (reproduced from McCullough[12])

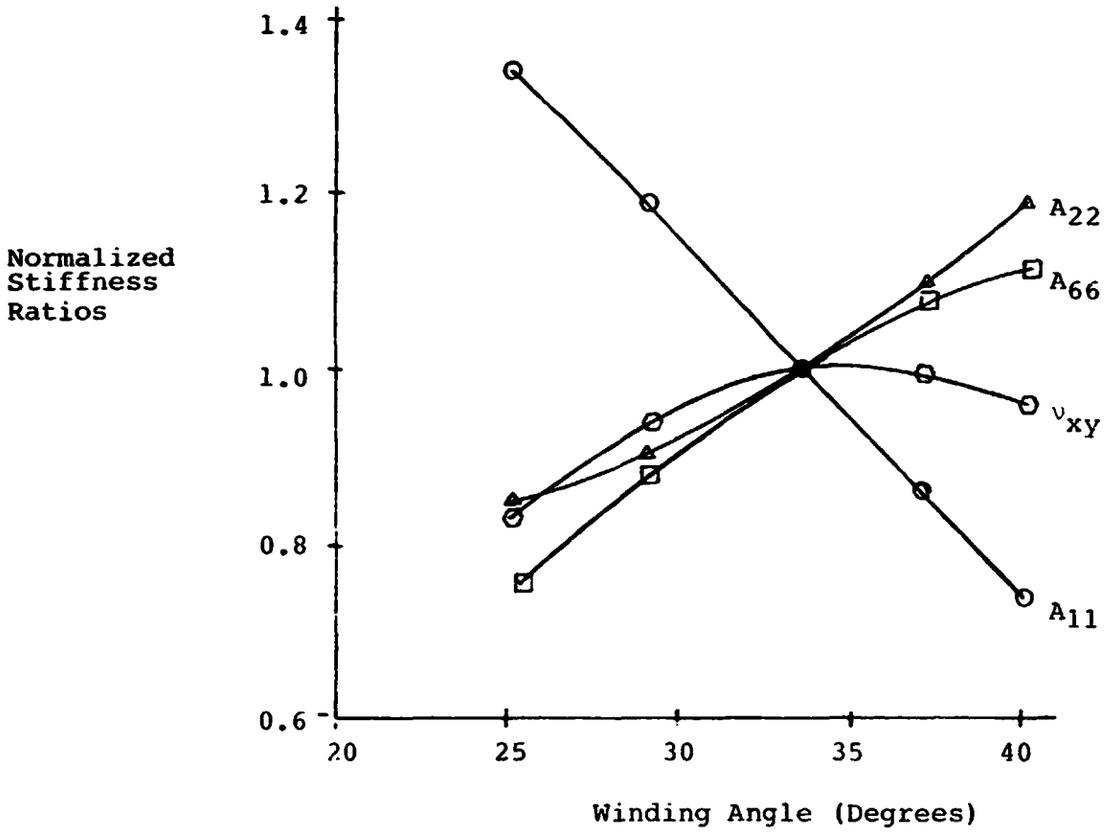

Figure 2. The Effect of Winding Angle on Stiffness Properties for the Hercules "STA Baseline Design"(16)

REFERENCES

1. Smith, Dallas G. and Huang, Ju-Chin: Post-Crazing Stress Analysis of Glass-Epoxy Laminates, Final Report. Contract DAAK40-78-C-0165, Tennessee Technological University, May 1979.

2. Hercules, Inc., Bacchus Works: Evolutionary History of FWC Lamina Properties, Report. Magna, Utah, May 24, 1983.

3. Jones, Robert M.: Mechanics of Composite Materials. Scripta Book Company, Washington, D.C., 1975.

4. Tsai, Stephen W.: Structural Behavior of Composite Materials. NASA CR-71, July 1964.

5. Halpin, J. C. and Tsai, S. W.: Effects of Environmental Factors on Composite Materials. AFML-TR 67-423, June 1969.

6. Whitney, J. M.: Elastic Moduli of Unidirectional Composites with Anisotropic Filaments. J. Composite Materials, Vol. 1, 1967, pp. 188-193.

7. Whitney, J. M., et al.: Experimental Mechanics of Fiber Reinforced Composite Materials. Society for Experimental Stress Analysis, Brookfield Center, CT, 1982.

8. Smith, Robert E.: Ultrasonic Elastic Constants of Carbon Fibers and Their Composites. J. Appl. Phys., Vol. 43, No. 6, June 1972, pp. 2555-2561.

9. Dean, G. D. and Turner, P.: The Elastic Properties of Carbon Fibers and Their Composites. Composites, July 1973, pp. 174-180.

10. Ishikawa, Takashi, et al.: Elastic Moduli of Carbon-Epoxy Composites and Carbon Fibers. J. Composite Materials, Vol. 11, July 1977, pp. 332-344.

11. Uemura, M. and Uamada, N.: Elastic Constants of Carbon Fiber Reinforced Plastic Material. Journal of the Society of Materials Science, Japan, Vol. 24, No. 257, 1975, p. 156.

12. McCullough, R. L.: Concepts of Fiber-Resin Composites. Marcel Dekker, Inc., New York, NY, 1971.

13. Pagano, N. J. and Whitney, J. M.: Geometric Design of Composite Cylindrical Characterization Specimens. Journal Composite Materials, Vol. 4, July 1970, pp. 360-378.

14. Pagano, N. J.: Stress Gradients in Laminated Composite Cylinders. Journal Composite Materials, Vol. 5, April 1971, pp. 260-265.

15. Agarwal, Bhagwan D. and Broutman, Lawrence J.: Analysis and Performance of Fiber Composites. Wiley and Sons, New York, NY, 1980.

16. Hercules, Inc.: Technical Working Group Report at NASA/MSFC, FWC Development Program, June 29, 1983.

17. Jones, Robert M. and Nelson, Dudley: Theoretical-Experimental Correlation of Material Models for Nonlinear Deformation of Graphite. AIAA Journal, October 1976, pp. 1427-1435.

18. Jones, Robert M. and Morgan, Harold S.: Analysis of Nonlinear Stress-Strain Behavior of Fiber-Reinforced Composite Materials. AIAA Journal, December 1977, pp. 1669-1676.

19. Whitney, J. M. and Lessa, A. W.: Analysis of Heterogeneous Anisotropic Plates. ASME Transactions, Journal of Applied Mechanics, June 1969, pp. 261-266.

20. Jones, Robert M. and Morgan, Harold S.: Buckling and Vibration of Cross-Ply Laminated Circular Cylindrical Shells. AIAA Journal, May 1975, pp. 664-671.

21. Jones, Robert M.: Stress-Strain Relations for Materials with Different Moduli in Tension and Compression. AIAA Journal, January 1977, pp. 16-23.

22. Jones, Robert M.: A Nonsymmetric Compliance Matrix Approach to Nonlinear Multimodulus Orthotropic Materials. AIAA Journal, October 1977, pp. 1436-1443.

23. Jones, Robert M.: Apparent Flexural Modulus and Strength of Multimodulus Materials. Journal of Composite Materials, September 1976, pp. 342-351.

APPENDIX A

"LAM"

```
1:@USE F,SYS$:MSFCFOR$
2:@F.FOR,IS MAIN,MAIN
3:C ********************************* LAM ************************************
4:C ************************** DATA INSTRUCTIONS ******************************
5:C INPUT DATA AS REQUESTED DURING PROGRAM EXECUTION.  SEPERATE EACH ITEM
6:C OF DATA WITH A COMMA.  USING MICROMECHANICS DATA, THE FOLLOWING FIBER
7:C AND MATRIX PROPERTIES ARE NEEDED:  THE FIBER LONGITUDINAL MODULUS AND
8:C THE POISSON'S RATIO, THE MATRIX YOUNG'S MODULUS AND ITS POISSON'S RATIO,
9:C THE VOLUME FRACTION OF THE FIBERS AND VOIDS, THE FIBER SHEAR MODULUS
10:C AND TRANSVERSE MODULUS IF KNOWN, AND FINALLY THE LAMINATE PLY GEOMETRY.
11:C ***************************************************************************
12:      DIMENSION TK(50),AN(50),Q11B(50),Q12B(50),Q16B(50),Q22B(50)
13:      DIMENSION Q66B(50),Z(51),Q26B(50),T(9,3),TD(9,3)
14: 9     WRITE(6,50)
15: 50    FORMAT(' TO READ IN LAMINA PROPERTIES, TYPE 1')
16:       WRITE(6,51)
17: 51    FORMAT(' FOR USING FIBER AND RESIN PROPERTIES, TYPE 2 ')
18:       READ(5,52)ITYPE
19:      WRITE(6,98)
20:      WRITE(6,97)
21: 98    FORMAT(' INPUT ALL LAMINA, FIBER, OR RESIN STIFFNESS VALUES')
22: 97    FORMAT(' DIVIDED BY 10 TO THE SIXTH WITH UNITS IN PSI')
23: 52     FORMAT()
24:        IF(ITYPE .EQ. 1) GO TO 10
25:      WRITE(6,54)
26: 54    FORMAT(' TYPE IN FIBER STIFFNESS MODULUS, EX, AND POISSONS RATIO')
27:       READ(5,52)EF,UF
28:       WRITE(6,199)
29: 199   FORMAT(' IF KNOWN, TYPE IN FIBER ALIGNMENT VALUE, OTHERWISE  0')
30:       READ(5,52)FAV
31:       ILOOP=0
32:       WRITE(6,55)
33: 55    FORMAT(' TYPE IN RESIN STIFFNESS MODULUS AND POISSON RATIO')
34:       READ(5,52)ER,UR
35:       WRITE(6,53)
36: 53    FORMAT(' VOLUME FRACTION OF FIBER AND VOLUME FRACTION OF VOIDS')
37:       READ(5,52)VF,VV
38:       WRITE(6,90)
39:       WRITE(6,91)
40:       WRITE(6,102)
41: 102   FORMAT(' FIBER SHEAR MODULUS, OTHERWISE TYPE 0 FOR EACH.')
42: 90    FORMAT(' IF FIBER IS ANISOTROPIC AS PER GRAPHITE FIBERS,')
43: 91    FORMAT(' TYPE IN EF2, FIBER TRANSVERSE MODULUS, AND GF2,')
44:       READ(5,52)EFT,GFT
45:       IF(EFT .EQ. 0)EFT=EF
46:       VR=1-VF-VV
47:       WRITE(6,56)
48: 56    FORMAT(' DO YOU HAVE SPECIAL HALPIN-TSAI COEFFICIENTS?')
49:       WRITE(6,57)
50: 57    FORMAT(' IF NOT, TYPE 0 FOR EACH, OTHERWISE INPUT FACTOR FOR E2 AN
51:     1D G12 RESPECTIVELY.')
52:       WRITE(6,58)
53: 58    FORMAT(' DEFAULT FACTORS ARE 2 FOR E2 AND 1 FOR G12.')
54:       READ(5,52)HTE1,HTG12
55:       IF(HTE1 .EQ. 0)HTE1=2.
```

```
      IF (HTG12 .EQ. 0)HTG12=1.
      GO TO 29
10    WRITE(6,106)
106   FORMAT(' INPUT STANDARD LAYER PROPERTIES.  IF HOOP AND HELICAL ARE
     1 DIFFERENT, INPUT HELICAL VALUES')
      WRITE(6,60)
60    FORMAT(' INPUT E1,U12,E2, AND G12 RESPECTIVELY')
      READ(5,52)ES1,US12,ES2,GS12
      WRITE(6,107)
107   FORMAT(' IF HOOP LAYER PROPERTIES ARE NOT EQUAL TO HELICAL, TYPE 1
     1, IF EQUAL TYPE 0.')
      READ(5,52)IH
      IF(IH .EQ. 0)GO TO 29
      WRITE(6,108)
108   FORMAT(' NOW TYPE IN HOOP VALUES, E1,U12,E2 AND G12 RESPECTIVELY')
      READ(5,52)EH1,UH12,EH2,GH12
29    WRITE(6,61)
61    FORMAT(' INPUT LAMINATE LAYER INFORMATION.  CONSECTIVE HOOP PLYS C
     1AN BE GROUPED.')
      WRITE(6,62)
62    FORMAT(' INPUT TOTAL NUMBER OF LAMINATE PLYS.')
      READ(5,52)NL
      WRITE(6,84)
      WRITE(6,85)
84    FORMAT(' IF THE LAMINATE IS SYMMETRIC AND REPEATING WITH +HELICAL,
     1 -HELICAL,')
85    FORMAT(' THEN HOOP WITH CONSTANT HELICAL WRAP ANGLE, TYPE 1, OTHER
     1WISE, TYPE 0.')
      READ(5,52)ILAM
      IF(ILAM .EQ. 0) GO TO 34
      WRITE(6,92)
92    FORMAT(' INPUT HELICAL TK, HOOP TK, AND HELICAL WRAP ANGLE ')
      READ(5,52)HETK,HPTK,AL
      NL1=(NL+1)/2
      DO 32 I=1,NL1,3
      TK(I)=HETK
      TK(I+1)=HETK
      TK(I+2)=HPTK
      AN(I)=AL
      AN(I+1)=-AL
32    AN(I+2)=90
      NF=NL-2
      NL1=NL1+1
      DO 33 I=NL1,NF,3
      TK(I)=HETK
      TK(I+1)=HETK
      TK(I+2)=HPTK
      AN(I)=-AL
      AN(I+1)=AL
33    AN(I+2)=90
      TK(NL-1)=HETK
      TK(NL)=HETK
      AN(NL-1)=-AL
      AN(NL)=AL
      GO TO 35
```

```
111:  34   WRITE(6,64)
112:       WRITE(6,65)
113:  64   FORMAT(' FOR EACH PLY, INPUT THICKNESS AND PLY ORIENTATION ANGLE')
114:  65   FORMAT(' USE + FOR CLOCKWISE ANGLE & MEASURE FROM LONGITUDINAL')
115:       DO 11 I=1,NL
116        WRITE(6,66)I
117:  66   FORMAT(' ENTER THICKNESS AND ANGLE FOR PLY',I3)
118:  11   READ(5,52)TK(I),AN(I)
119:       IF(ITYPE .EQ. 1)IH=0
120:  35   IF (ITYPE .EQ. 1) GO TO 30
121:       IF (FAV .EQ. 0) FAV=0.96
122:  16   E1=FAV*(EF*VF+ER*VR)
123:C     E1 IS MULTIPLIED BY A FIBER MISALIGNMENT FACTOR K=.96
124:       U12=UF*VF+UR*(1-VF)
125:       GF=EF/(2*(1+UF))
126:       IF(GFT .EQ. 0)GFT=GF
127:       GR=ER/(2*(1+UR))
128:       UNE=(EFT/ER-1)/(EFT/ER+HTE1)
129:       E2=ER*(1+UNE*HTE1*VF)/(1-UNE*VF)
130:       UNG=(GFT/GR-1)/(GFT/GR+HTG12)
131:       G12=GR*(1+HTG12*UNG*VF)/(1-UNG*VF)
132:       IH=0
133:       TKT=0
134:  30   DO 17 I=1,NL
135:       IF(IH .EQ. 0)GO TO 59
136:       IF(AN(I) .LT. 89) GO TO 59
137:       E1=EH1
138:       U12=UH12
139:       E2=EH2
140:       G12=GH12
141:       GO TO 120
142:  59   IF(ITYPE .EQ. 2) GO TO 120
143:       E1=ES1
144:       U12=US12
145:       E2=ES2
146:       G12=GS12
147: 120   AM=1/(E1-E2*U12**2)
148:       Q11=AM*E1**2
149:       Q22=AM*E1*E2
150:       Q12=U12*Q22
151:       Q66=G12
152:       A=AN(I)/57.29578
153:       CX=COS(A)
154:       CX2=CX**2
155:       CX3=CX**3
156:       CX4=CX**4
157:       CY=SIN(A)
158:       CY2=CY**2
159:       CY3=CY**3
160:       CY4=CY**4
161:       Q11B(I)=Q11*CX4+2*(Q12+2*Q66)*CY2*CX2+Q22*CY4
162:       Q12B(I)=CY2*CX2*(Q11+Q22-4*Q66)+Q12*(CX4+CY4)
163:       Q16B(I)=CY*CX3*(Q11-Q12-2*Q66)+CX*CY3*(Q12-Q22+2*Q66)
164:       Q22B(I)=Q11*CY4+2*(Q12+2*Q66)*CX2*CY2+Q22*CX4
165:       Q26B(I)=(Q11-Q12-2*Q66)*CY3*CX+(Q12-Q22+2*Q66)*CY*CX3
```

```
166:      Q66B(I)=(Q11+Q22-2*Q12-2*Q66)*CX2*CY2+Q66*(CX4+CY4)
167: 17   TKT=TKT+TK(I)
168:      NS=NL+1
169:      Z(1)=TKT/2.
170:      DO 12 I=2,NS
171: 12   Z(I)=Z(I-1)-TK(I-1)
172:      DO 36 IC=1,9
173:      DO 36 IR=1,3
174:      TD(IC,IR)=0.
175: 36   T(IC,IR)=0.
176:      DO 13 I=1,NL
177:      ZZ=Z(I)-Z(I+1)
178:      T(1,1)=T(1,1)+Q11B(I)*ZZ
179:      T(1,2)=T(1,2)+Q12B(I)*ZZ
180:      T(1,3)=T(1,3)+Q16B(I)*ZZ
181:      T(2,2)=T(2,2)+Q22B(I)*ZZ
182:      T(2,3)=T(2,3)+Q26B(I)*ZZ
183:      T(3,3)=T(3,3)+Q66B(I)*ZZ
184:      ZZ=Z(I)**2-Z(I+1)**2
185:      T(4,1)=T(4,1)+0.5*Q11B(I)*ZZ
186:      T(4,2)=T(4,2)+0.5*Q12B(I)*ZZ
187:      T(4,3)=T(4,3)+0.5*Q16B(I)*ZZ
188:      T(5,2)=T(5,2)+0.5*Q22B(I)*ZZ
189:      T(5,3)=T(5,3)+0.5*Q26B(I)*ZZ
190:      T(6,3)=T(6,3)+0.5*Q66B(I)*ZZ
191:      ZZ=Z(I)**3-Z(I+1)**3
192:      T(7,1)=T(7,1)+(Q11B(I)*ZZ)/3.
193:      T(7,2)=T(7,2)+(Q12B(I)*ZZ)/3.
194:      T(7,3)=T(7,3)+(Q16B(I)*ZZ)/3.
195:      T(8,2)=T(8,2)+(Q22B(I)*ZZ)/3.
196:      T(8,3)=T(8,3)+(Q26B(I)*ZZ)/3.
197: 13   T(9,3)=T(9,3)+(Q66B(I)*ZZ)/3.
198:      T(2,1)=T(1,2)
199:      T(3,1)=T(1,3)
200:      T(3,2)=T(2,3)
201:      T(5,1)=T(4,2)
202:      T(6,1)=T(4,3)
203:      T(6,2)=T(5,3)
204:      T(8,1)=T(7,2)
205:      T(9,1)=T(7,3)
206:      T(9,2)=T(8,3)
207:      X=1/TKT**2
208:      XX=12/TKT**3
209:      DO 38 IR=1,3
210:      DO 38 IC=1,3
211: 38   TD(IR,IC)=T(IR,IC)/TKT
212:      DO 39 IR=4,6
213:      DO 39 IC=1,3
214: 39   TD(IR,IC)=T(IR,IC)*X
215:      DO 40 IR=7,9
216:      DO 40 IC=1,3
217: 40   TD(IR,IC)=T(IR,IC)*XX
218:      IF(ILOOP .GT. 0) GO TO 37
219:      WRITE(6,70)
220: 70   FORMAT(' LAMINATE LAYER DESCRIPTION')
```

```
      WRITE(6,71)NL,TKT
71    FORMAT(' NO. OF LAYERS=',I3,5X,'LAMINATE THICKNESS=',F6.3,' IN.')
      WRITE(6,72)
      WRITE(6,73)
72    FORMAT(//' LAYER     THICKNESS     ANGLE OF PLY')
73    FORMAT(' COUNT     (INCHES)       (DEGREES)')
      DO 14 I=1,NL
14    WRITE(6,74)I,TK(I),AN(I)
74    FORMAT(I4,F13.4,F15.2)
37    CONTINUE
      IF(ILOOP .EQ. 0) WRITE(6,104)
      WRITE(6,105)
104   FORMAT(1H1)
105   FORMAT(' **********************************************************
     1**************************')
      IF (ITYPE .EQ. 1) GO TO 1
      WRITE(6,131)EF,UF
131   FORMAT(' LONGITUDINAL FIBER MODULUS=',F8.3,'  FIBER POISSON RATIO=
     1',F7.4)
      WRITE(6,132)ER,UR
132   FORMAT('  RESIN STIFFNESS MODULUS=',F8.3,'  RESIN POISSON RATIO='F7
     1.4)
      WRITE(6,133)VF,VV
133   FORMAT('  VOLUME FRACTION OF FIBERS=',F7.4,'  VOLUME FRACTION OF VO
     1IDS= ,F7.4)
      WRITE(6,134)EFT,GFT
134   FORMAT('  FIBER TRANSVERSE MODULUS=',F7.4,'  FIBER SHEAR MODULUS= ,
     1F7.4)
      WRITE(6,125)HTE1,HTG12
125   FORMAT(' HALPIN-TSAI FACTORS FOR E2=',F6.4,'  FOR G12=',F6.4)
1     WRITE(6,67)
67    FORMAT(///' STANDARD OR HELICAL LAMINA PROPERTIES')
      IF(ITYPE .EQ. 2)WRITE(6,68)E1,U12,E2,G12
      IF(ITYPE .EQ. 2)GO TO 119
      WRITE(6,68)ES1,US12,ES2,GS12
68    FORMAT(' E1=',F8.4,4X,'U12=',F7.4,4X,'E2=',F7.4,4X,'G12=',F7.4)
      IF(IH .EQ. 1)WRITE(6,109)
      IF(IH .EQ. 1)WRITE(6,68)EH1,UH12,EH2,GH12
109   FORMAT(/' HOOP LAMINA PROPERTIES ARE')
119   WRITE(6,69)
69    FORMAT(' E1,E2, AND G12 ARE TIMES 10**6 POWER PSI'//)
      WRITE(6,75)
75    FORMAT(//' THE FOLLOWING MATRIX VALUES ARE TO BE MULTIPLIED BY '
      WRITE(6,76)
76    FORMAT(' 10 TO THE SIXTH, UNITS ARE PSI'/)
      WRITE(6,80)
      DO 41 IR=1,9
      WRITE(6,77)T(IR,1),T(IR,2),T(IR,3),TD(IR,1),TD(IR,2),TD(IR,3)
      IF (IR .EQ. 3) WRITE (6,78)
41    IF(IR .EQ. 6) WRITE(6,79)
      EX=TD(1,1)-TD(1,2)**2/TD(2,2)
      EY=TD(2,2)-TD(1,2)**2/TD(1,1)
      UNXY=TD(1,2)/TD(2,2)
      EXF=TD(7,1)-TD(7,2)**2/TD(8,2)
      EYF=TD(8,2)-TD(7,2)**2/TD(7,1)
```

```
276:       WRITE(6,93)
277:       WRITE(6,94)
278:       WRITE(6,95)
279:  93   FORMAT(//1X,'LAMINATE STIFFNESS PROPERTIES')
280:  94   FORMAT(' AVERAGE AXIAL',40X,'FLEXURAL')
281:  95   FORMAT(5X,'EX',11X,'EY',11X,'GXY',10X,'NUXY',9X,'EX',11X,'EY')
282:       WRITE(6,96)EX,EY,TD(3,3),UNXY,EXF,EYF
283:  96   FORMAT(6F13.5//)
284:  80   FORMAT(/' THE A MATRIX',29X,'THE A DIVIDED BY TK MATRIX'/)
285:  77   FORMAT(3F12.6,8X,3F12.6)
286:  78   FORMAT(//' THE B MATRIX',29X,'THE B/(TK**2) MATRIX'/)
287:  79   FORMAT(//' THE D MATRIX',29X,'THE 12*D/(TK**3) MATRIX'/)
288:       IF(ILOOP .GT. 0) GO TO 31
289:       IF(ITYPE .EQ. 1) GO TO 26
290:       WRITE(6,82)
291:       WRITE(6,83)
292:  82   FORMAT('/' TYPE 1 FOR ITERATION OF MATERIAL PROPERTIES, OTHERWISE
293:      : TYPE 0 )
294:  83   FORMAT(  THIS OPTION CAN BE USED ONLY IF YOU READ IN FIBER AND RES
295:      1IN PROPERTIES'//)
296:       READ(5,52)IT
297:       IF(IT .EQ. 0)GO TO 26
298:  31   IF(ILOOP .EQ. 1) GO TO 28
299:       IF(ILOOP .EQ. 2) GO TO 19
300:       IF(ILOOP .EQ. 3) GO TO 21
301:       IF(ILOOP .EQ. 4) GO TO 23
302:       IF(ILOOP .EQ. 5) GO TO 25
303:       J=0
304:       ILOOP=1
305:       EFS=EF
306:       EF=EF-6
307:  28   IF(J .EQ. 11)GO TO 18
308:       EF=EF+1
309:       J=J+1
310:       WRITE(6,104)
311:       WRITE(6,105)
312:       WRITE(6,81)J,EF
313:  81   FORMAT(/' THIS IS LOOP',I3,'  LONGITUDINAL FIBER MODULUS=',F7.4/)
314:       GO TO 16
315:  18   EF=EFS
316:       J=0
317:       ILOOP=2
318:       EFTS=EFT
319:       EFT=EFT-1.2
320:  19   EFT=EFT+.2
321:       IF(J .EQ. 11)GO TO 20
322:       J=J+1
323:       WRITE(6,104)
324:       WRITE(6,105)
325:       WRITE(6,86)J,EFT
326:  86   FORMAT(/' THIS IS LOOP',I3,'  TRANSVERSE FIBER MODULUS =',F8.4/
327:       GO TO 16
328:  20   EFT=EFTS
329:       J=0
330:       ILOOP=3
```

```
331:       ERS=ER
332:       ER=ER-.3
333: 21    IF(J .EQ. 11) GO TO 22
334:       J=J+1
335:       ER=ER+.05
336:       WRITE(6,104)
337:       WRITE(6,105)
338:       WRITE(6,87)J,ER
339: 87    FORMAT(/' THIS IS LOOP',I3,'    RESIN TENSILE MODULUS =',F6.4/)
340:       GO TO 16
341: 22    ER=ERS
342:       J=0
343:       ILOOP=4
344:       URS=UR
345:       UR=UR-.06
346: 23    IF(J .EQ. 11) GO TO 24
347:       J=J+1
348:       UR=UR+.01
349:       WRITE(6,104)
350:       WRITE(6,105)
351:       WRITE(6,88)J,UR
352: 88    FORMAT(/' THIS IS LOOP',I3,'  WITH RESIN POISSON RATIO =',F6.4/)
353:       GO TO 16
354: 24    UR=URS
355:       J=0
356:       ILOOP=5
357:       UFS=UF
358:       UF=UF-.04
359: 25    IF(J .EQ. 11) GO TO 26
360:       UF=UF+.02
361:       J=J+1
362:       WRITE(6,104)
363:       WRITE(6,105)
364:       WRITE(6,89)J,UF
365: 89    FORMAT(/' THIS IS LOOP',I3,' WITH FIBER POISSON RATIO =',F6.4/)
366:       GO TO 16
367: 26    CONTINUE
368:       END
369:@MAP,IS SYM,ABS
370:LIB F.
371:@XQT ABS
```

Sample Solution Listing for "Quarter Scale Winding"

```
 TO READ IN LAMINA PROPERTIES, TYPE 1
 FOR USING FIBER AND RESIN PROPERTIES, TYPE 2
>2
 INPUT ALL LAMINA, FIBER, OR RESIN STIFFNESS VALUES
 DIVIDED BY 10 TO THE SIXTH WITH UNITS IN PSI
 TYPE IN FIBER STIFFNESS MODULUS, EX, AND POISSONS RATIO
>34.,.2
 IF KNOWN, TYPE IN FIBER ALIGNMENT VALUE, OTHERWISE  0
>0
 TYPE IN RESIN STIFFNESS MODULUS AND POISSON RATIO
>.489,.35
 VOLUME FRACTION OF FIBERS AND VOLUME FRACTION OF VOIDS
>.54,.05
 IF FIBER IS ANISOTROPIC AS PER GRAPHITE FIBERS,
 TYPE IN EF2, FIBER TRANSVERSE MODULUS, AND GF2,
 FIBER SHEAR MODULUS, OTHERWISE TYPE 0 FOR EACH.
>2,2.5
 DO YOU HAVE SPECIAL HALPIN-TSAI COEFFICIENTS?
 IF NOT, TYPE 0 FOR EACH, OTHERWISE INPUT FACTOR FOR E2 AND G12 RESPECTIVELY.
 DEFAULT FACTORS ARE 2 FOR E2 AND 1 FOR G12.
>0,0
 INPUT LAMINATE LAYER INFORMATION.  CONSECTIVE HOOP PLYS CAN BE GROUPED.
 INPUT TOTAL NUMBER OF LAMINATE PLYS.
>11
 IF THE LAMINATE IS SYMMETRIC AND REPEATING WITH +HELICAL, -HELICAL,
 THEN HOOP WITH CONSTANT HELICAL WRAP ANGLE, TYPE 1, OTHERWISE, TYPE 0.

>1
 INPUT HELICAL TK, HOOP TK, AND HELICAL WRAP ANGLE
>.0236,.0273,29
 LAMINATE LAYER DESCRIPTION
 NO. OF LAYERS= 11      LAMINATE THICKNESS=  .271 IN.


 LAYER     THICKNESS     ANGLE OF PLY
 COUNT     (INCHES)       (DEGREES)
   1         .0236           29.00
   2         .0236          -29.00
   3         .0273           90.00
   4         .0236           29.00
   5         .0236          -29.00
   6         .0273           90.00
   7         .0236          -29.00
   8         .0236           29.00
   9         .0273           90.00
  10         .0236          -29.00
  11         .0236           29.00

 **********************************************************************
 LONGITUDINAL FIBER MODULUS=  34.000  FIBER POISSON RATIO=  .2000
 RESIN STIFFNESS MODULUS=     .489  RESIN POISSON RATIO=  .3500
$OUTPUT INTERRUPT$
```

VOLUME FRACTION OF FIBERS= .5400 VOLUME FRACTION OF VOIDS= .0500
FIBER TRANSVERSE MODULUS= 2.0000 FIBER SHEAR MODULUS= 2.5000
HALPIN-TSAI FACTORS FOR E2=2.0000 FOR G12=1.0000

STANDARD OR HELICAL LAMINA PROPERTIES
E1= 17.8181 U12= .2690 U2= 1.0426 2= .4985
E1,E2, AND G12 ARE TIMES 10**6 POWER PSI

THE FOLLOWING MATRIX VALUES ARE TO BE MULTIPLIED BY
10 TO THE SIXTH. UNITS ARE PSI

THE A MATRIX

2.160380	.632390	-.000000
.632390	1.854632	.000000
-.000000	.000000	.691099

THE A DIVIDED BY TK MATRIX

7.980717	2.336129	-.000000
2.336129	6.851246	.000000
-.000000	.000000	2.553006

B MATRIX

-.000000	-.000000	.000000
-.000000	-.000000	.000000
.000000	.000000	-.000000

THE B/(TK**2) MATRIX

-.000000	-.000000	.000000
-.000000	-.000000	.000000
.000000	000000	-.000000

THE D MATRIX

.015181	.004427	.001797
.004427	.008286	.000575
.001797	.000575	.004786

THE 12*D/(TK**3) MATRIX

9.135382	2.678260	1.086864
2.678260	5.012318	.34761
1.086864	.347614	2.895138

LAMINATE STIFFNESS PROPERTIES

AVERAGE AXIAL				FLEXURAL	
EX	EY	GXY	NUXY	EX	EY
7.18415	6.16741	2.55301	.34098	7.70429	4.22712

TYPE 1 FOR ITERATION OF MATERIAL PROPERTIES, OTHERWISE TYPE 0
THIS OPTION CAN BE USED ONLY IF YOU READ IN FIBER AND RESIN PROPERTIES

XXXII-26

APPENDIX B

"COMP"

```
1:@ASG,UP PF.
2:@FREE PF.
3:@EXTEND PF.8
4:@ASG,A PF.
5:@BRKPT PRINT$/PF
6:@USE F,SYS$:MSFCFOP$
7:@F.FOR,IS MAIN,MAIN
8:C ************************** INPUT OF DATA **************************
9:C THIS PROGRAM CAN ACCEPT 25 LAMINA TYPES AND 100 LAYERS.  A CHANGE
10:C IN THE DIMENSION STATEMENTS WOULD PERMIT LARGER LAMINATES
11:C 1ST LINE....NUMBER OF LAMINA LAYER TYPES?
12:C NEXT.......ONE LINE OF DATA FOR EACH TYPE OF LAMINA.  GIVE E1,
13:C                E2,G12, AND U12, RESPECTIVELY.
14:C NEXT.......NUMBER OF LAYERS?
15:C THEN.......ONE LINE OF DATA FOR EACH LAYER GIVING THE THICKNESS,
16:C                WINDING ANGLE, AND LAMINA TYPE.  THE LAMINA TYPE FOR
17:C                EACH LAYER MUST MATCH THE PREVIOUS DATA.
18:C ***********************************************************************
19:C
20:      DIMENSION TK(100),AN(100),Q11B(100),Q12B(100),Q16B(100),Q22B(100)
21:      DIMENSION Q66B(100),Z(101),Q26B(100),T(9,3),TD(9,3)
22:      DIMENSION IE(100),EL(25),ET(25),GLT(25),ULT(25)
23:      READ(5,52)NLT
24: 52   FORMAT()
25:      DO 5 I=1,NLT
26: 5    READ(5,52)EL(I),ET(I),GLT(I),ULT(I)
27:      READ(5,52)NL
28:      DO 4 I=1,NL
29: 4    READ(5,52)TK(I),AN(I),IE(I
30: 30   DO 17 I=1,NL
31:      J=IE(I)
32:      AM=1/(EL(J)-ET(J)*ULT(J)**2)
33:      Q11=AM*EL(J)**2
34:      Q22=AM*EL(J)*ET(J)
35:      Q12=ULT(J)*Q22
36:      Q66=GLT(J)
37:      A=AN(I)/57.29578
38:      CX=COS(A)
39:      CX2=CX**2
40:      CX3=CX**3
41:      CX4=CX**4
42:      CY=SIN(A)
43:      CY2=CY**2
44:      CY3=CY**3
45:      CY4=CY**4
46:      Q11B(I)=Q11*CX4+2*(Q12+2*Q66)*CY2*CX2+Q22*CY4
47:      Q12B(I)=CY2*CX2*(Q11+Q22-4*Q66)+Q12*(CX4+CY4)
48:      Q16B(I)=CY*CX3*(Q11-Q12-2*Q66)+CX*CY3*(Q12-Q22+2*Q66)
49:      Q22B(I)=Q11*CY4+2*(Q12+2*Q66)*CX2*CY2+Q22*CX4
50:      Q26B(I)=(Q11-Q12-2*Q66)*CY3*CX+(Q12-Q22+2*Q66)*CY*CX3
51:      Q66B(I)=(Q11+Q22-2*Q12-2*Q66)*CX2*CY2+Q66*(CX4+CY4)
52: 17   TKT=TKT+TK(I)
53:      NS=NL+1
54:      Z(1)=TKT/2.
55:      DO 12 I=2,NS
56: 12   Z(I)=Z(I-1)-TK(I-1)
```

```
      DO 36 IC=1,9
      DO 36 IR=1,3
      TD(IC,IR)=0.
36    T(IC,IR)=0.
      DO 13 I=1,NL
      ZZ=Z(I)-Z(I+1)
      T(1,1)=T(1,1)+Q11B(I)*ZZ
      T(1,2)=T(1,2)+Q12B(I)*ZZ
      T(1,3)=T(1,3)+Q16B(I)*ZZ
      T(2,2)=T(2,2)+Q22B(I)*ZZ
      T(2,3)=T(2,3)+Q26B(I)*ZZ
      T(3,3)=T(3,3)+Q66B(I)*ZZ
      ZZ=Z(I)**2-Z(I+1)**2
      T(4,1)=T(4,1)+0.5*Q11B(I)*ZZ
      T(4,2)=T(4,2)+0.5*Q12B(I)*ZZ
      T(4,3)=T(4,3)+0.5*Q16B(I)*ZZ
      T(5,2)=T(5,2)+0.5*Q22B(I)*ZZ
      T(5,3)=T(5,3)+0.5*Q26B(I)*ZZ
      T(6,3)=T(6,3)+0.5*Q66B(I)*ZZ
      ZZ=Z(I)**3-Z(I+1)**3
      T(7,1)=T(7,1)+(Q11B(I)*ZZ)/3.
      T(7,2)=T(7,2)+(Q12B(I)*ZZ)/3.
      T(7,3)=T(7,3)+(Q16B(I)*ZZ)/3.
      T(8,2)=T(8,2)+(Q22B(I)*ZZ)/3.
      T(8,3)=T(8,3)+(Q26B(I)*ZZ)/3.
13    T(9,3)=T(9,3)+(Q66B(I)*ZZ)/3.
      T(2,1)=T(1,2)
      T(3,1)=T(1,3)
      T(3,2)=T(2,3)
      T(5,1)=T(4,2)
      T(6,1)=T(4,3)
      T(6,2)=T(5,3)
      T(8,1)=T(7,2)
      T(9,1)=T(7,3)
      T(9,2)=T(8,3)
      X=1/TKT**2
      XX=12/TKT**3
      DO 38 IR=1,3
      DO 38 IC=1,3
38    TD(IR,IC)=T(IR,IC)/TKT
      DO 39 IR=4,6
      DO 39 IC=1,3
39    TD(IR,IC)=T(IR,IC)*X
      DO 40 IR=7,9
      DO 40 IC=1,3
40    TD(IR,IC)=T(IR,IC)*XX
      WRITE(6,51)
51    FORMAT(//' ***** DATA FOR EACH LAYER *****')
      WRITE(6,72)
      WRITE(6,73)
72    FORMAT(//' LAYER     THICKNESS     ANGLE OF PLY      LAYER')
73    FORMAT(' COUNT     (INCHES)       (DEGREES)        TYPE')
      DO 9 I=1,NL
9     WRITE(6,74)I,TK(I),AN(I),IE(I)
      WRITE(6,70)NL,TKT
70    FORMAT(//' ** NUMBER OF LAYERS=',I3,5X,'LAMINATE THICKNESS='
     1,F6.3,' IN. **')
```

```
114: 74   FORMAT(I4,F13.4,F15.2,I10)
115:      WRITE(6,67)
116: 67   FORMAT(/' ** LAMINA PROPERTIES FOR LAYER TYPES **')
117:      WRITE(6,68)
118: 68   FORMAT(5X,'TYPE',8X,'E1',10X,'E2',10X,'G12',9X,'U12'/)
119:      DO 8 I=1,NLT
120: 8    WRITE(6,50)I,EL(I),ET(I),GLT(I),ULT(I)
121: 50   FORMAT(I8,4X,4F12.4)
122: 37   WRITE(6,75)
123: 75   FORMAT(//' THE FOLLOWING MATRIX VALUES ARE TO BE MULTIPLIED BY')
124:      WRITE(6,76)
125: 76   FORMAT(' 10 TO THE SIXTH, UNITS ARE PSI'/)
126:      WRITE(6,80)
127:      DO 41 IR=1,9
128:      WRITE(6,77)T(IR,1),T(IR,2),T(IR,3),TD(IR,1),TD(IR,2),TD(IR,3)
129:      IF (IR .EQ. 3) WRITE (6,78)
130: 41   IF(IR .EQ. 6) WRITE(6,79)
131:      EX=TD(1,1)-TD(1,2)**2/TD(2,2)
132:      EY=TD(2,2)-TD(1,2)**2/TD(1,1)
133:      UNXY=TD(1,2)/TD(2,2)
134:      EXF=TD(7,1)-TD(7,2)**2/TD(8,2)
135:      EYF=TD(8,2)-TD(7,2)**2/TD(7,1)
136:      WRITE(6,93)
137:      WRITE(6,94)
138:      WRITE(6,95)
139: 93   FORMAT(/,1X, LAMINATE STIFFNESS PROPERTIES')
140: 94   FORMAT(' AVERAGE AXIAL',40X,'FLEXURAL')
141: 95   FORMAT(5X,'EX',11X,'EY',11X,'GXY',10X,'NUXY',9X,'EX',11X,'EY')
142:      WRITE(6,96)EX,EY,TD(3,3),UNXY,EXF,EYF
143: 96   FORMAT(6F13.5/)
144: 80   FORMAT(/' THE A MATRIX',29X,'THE A DIVIDED BY TK MATRIX'/)
145: 77   FORMAT(3F12.6,8X,3F12.6)
146: 78   FORMAT(//' THE B MATRIX',29X, THE B/(TK**2) MATRIX'/)
147: 79   FORMAT(//' THE D MATRIX',29X,'THE 12*D/(TK**3) MATRIX'/)
148:      END
149:@MAP,IS SYM,ABS
150:LIB F.
151:@XQT ABS
```

Sample Solution Listing for
"STA Baseline Design"

***** DATA FOR EACH LAYER *****

LAYER COUNT	THICKNESS (INCHES)	ANGLE OF PLY (DEGREES)	LAYER TYPE
1	.0100	90.00	3
2	.0100	.00	3
3	.0313	33.55	1
4	.0313	-33.55	1
5	.0304	90.00	2
6	.0157	33.55	1
7	.0157	-33.55	1
8	.0304	90.00	2
9	.0157	33.55	1
10	.0157	-33.55	1
11	.0304	90.00	2
12	.0157	33.55	1
13	.0157	-33.55	1
14	.0304	90.00	2
15	.0157	33.55	1
16	.0157	-33.55	1
17	.0304	90.00	2
18	.0313	33.55	1
19	.0313	-33.55	1
20	.0152	90.00	2
21	.0313	33.55	1
22	.0313	-33.55	1
23	.0152	90.00	2
24	.0313	33.55	1
25	.0313	-33.55	1
26	.0152	90.00	2
27	.0313	33.55	1
28	.0313	-33.55	1
29	.0152	90.00	2
30	.0313	33.55	1
31	.0313	-33.55	1
32	.0152	90.00	2
33	.0313	33.55	1
34	.0313	-33.55	1
35	.0152	90.00	2
36	.0313	33.55	1
37	.0313	-33.55	1
38	.0152	90.00	2
39	.0522	33.55	1
40	.0522	-33.55	1
41	.0152	90.00	2
42	.0522	33.55	1
43	.0522	-33.55	1
44	.0152	90.00	2
45	.0522	33.55	1
46	.0522	-33.55	1
47	.0152	90.00	2
48	.0313	33.55	1
49	.0313	-33.55	1

```
288:
289: ** NUMBER OF LAYERS= 49     LAMINATE THICKNESS= 1.326 IN. **
290:
291: ** LAMINA PROPERTIES FOR LAYER TYPES **
292:     TYPE        E1          E2          G12         U12
293:
294:       1       18.6800       .2623       .6938       .2673
295:       2       19.4500       .2625       .6952       .2673
296:       3       17.4000      1.5900       .7110       .2750
297:
298:
299: THE FOLLOWING MATRIX VALUES ARE TO BE MULTIPLIED BY
300: 10 TO THE SIXTH, UNITS ARE PSI
301:
302:
303: THE A MATRIX                              THE A DIVIDED BY TK MATRIX
304:
305:    9.955963    3.512020     .000000          7.507137    2.648183     .000000
306:    3.512020    8.604845     .000000          2.648183    6.488347     .000000
307:     .000000     .000000    4.332412           .000000     .000000    3.266787
308:
309:
310: THE B MATRIX                              THE B/(TK**2) MATRIX
311:
312:    -.429700    -.194448     .102180          -.244314    -.110557     .058096
313:    -.194448     .865398     .050479          -.110557     .492037     .028701
314:     .102180     .050479    -.198996           .058096     .028701    -.113143
315:
316:
317: THE D MATRIX                              THE 12*D/(TK**3) MATRIX
318:
319:    1.462302     .499458    -.030718          7.523005    2.569526    -.158033
320:     .499453    1.293343    -.015175          2.569526    6.653776    -.078072
321:    -.030718    -.015175     .617723          -.158033    -.078072    3.177959
322:
323:
324: LAMINATE STIFFNESS PROPERTIES
325: AVERAGE AXIAL                                        FLEXURAL
326:     EX          EY          GXY         NUXY        EX          EY
327:    6.42830     5.55419     3.26679      .40814     6.53072     5.77614
328:
329:
```

N84 16055

1983

NASA/ASEE SUMMER FACULTY RESEARCH FELLOWSHIP PROGRAM

MARSHALL SPACE FLIGHT CENTER

THE UNIVERSITY OF ALABAMA

COMPOSITIONAL SEGREGATION IN UNIDIRECTIONALLY SOLIDIFIED SOLID SOLUTION CRYSTALS

Prepared By:	Jai-Ching Wang
Academic Rank:	Associate Professor
University and Department:	Alabama A&M University Department of Physics
NASA/MSFC:	
(Laboratory)	Space Science Laboratory
(Division)	Space Processing
(Branch)	Solid State Devices
MSFC Counterparts:	S. L. Lehoczky, F. R. Szofran
Date:	August 12, 1983
Contract No.:	NGT-01-008-021 The University of Alabama in Huntsville

Compositional Segregation in Unidirectionally Solidified Solid Solution Crystals

By

Jai-Ching Wang, Ph.D.
Associate Professor of Physics
Alabama A&M University
Normal, Alabama

ABSTRACT

A computer program has been developed to model compositional segregation in unidirectionally solidified solid-solution-semiconducting crystals. The program takes into account the variations of the interface segregation constant and solidification rate with composition. Calculations are being performed for the HgCdTe solid solution system that will be compared with experimental data.

ACKNOWLEDGEMENTS

I would like to express my sincere appreciation to the NASA/ASEE Summer Faculty Program Administrators Drs. Gerald R. Karr, J. D. Dozier, Mr. L. Osborn for providing me the opporutnity to participate in this activity. The seminars and the tours are very helpful. Special thanks goes to my NASA counterparts: Drs. S. L. Lehoczky, and F. R. Szofran for their valuable time, suggestions and guidance. I would also like to extend my sincere appreciation to Ernestine Cothran, Ronald Harris, Alice Dorries, Elizabeth A. Pentecost and Dr. Lawrence Holland for their valuable information and discussions. The hospitality and friendships of all the members in the Space Processing Division has made this summer very enjoyable for me. Appreciation also goes to Ms. Shirley Buford for typing this report.

LIST OF FIGURES

FIGURE	TITLE	PAGE
1	Coordinate system used in this model	XXXIII-17
2	Pseudo-binary phase diagram of $Hg_{1-x}Cd_xTe$	XXXIII-18
3	A comparison between the calculated and measured composition for Co = 0.202, Rl = 0.1116 cm/hr, G = 100°C/cm with D = 4.5×10^{-5} cm^2/sec.	XXXIII-19
4	A comparison between the calculated and measured composition for Co = 0.202, Rl = 0.1116 cm/hr, G = 100°C/cm with D = 3.0×10^{-5} cm^2/sec.	XXXIII-20
5	A comparison between the calculated and measured composition for Co = 0.202, Rl = 0.02466 cm/hr, G = 50°C/cm with D = 5.5×10^{-5} cm^2/sec.	XXXIII-21
6	A comparison between the calculated and measured composition for Co = 0.202, Rl = 0.02466 cm/hr, G = 100°C/cm with D = 5.5×10^{-5} cm^2/sec.	XXXIII-22
7	The variation of segregation constant and growth velocity along the growth axis for Co = 0.202, Rl = 0.1116 cm/hr, G = 100°C/cm with D = 4.5×10^{-5} cm^2/sec.	XXXIII-23

NOMENCLATURE

Symbols	Definition
Co (I)	Liquid compositon at step I from the interface at previous time.
Cn (I)	Liquid composition at step I from the interface at current time.
T (I)	Time (sec) taken for liquid to solidfied to time step I from the tp of the sample.
Z (I)	Interface location for time step I measured from furnace reference plane (first-free-position).
X (I)	Interface location for time step I measured from the tip of ampoule.
Sc (I)	Solid composition at interfce for time step I.
X$ (I)	Graphic output values.
XK (I)	Segregation constant for time step I.
V (I)	Interface valocity relative to furnace frames at time step I.
To (I)	Interface temperature at time step I.
P$, Q$	Graphic output symbols.
Ids$	Specimen identification.
D	Diffusion coefficient cm^2/sec.
Ls	Length of sample in cm.
Rl	Pull rate in cm/hr.
Ti	Time interval in sec.
Zi	Space interval in cm.
CO	Alloy composition
G	Temperature gradient °C/cm.
An$, An2$	Variables for checking rate change
Tst	Starting time in sec. for first rate change
Tend	Ending time in sec. for first rate change.
R2	Second pull rate in cm/hr.

NOMENCLATURE (CONT)

Tst2	Starting time for second rate change.
Tend2	Ending time for second rate change.
R22	Third pull rate in cm/hr.
Ep	Value for testing converging
TO	First freeze interface temperature.
Cu	Upper bound gussing composition.
Cd	Lower bound gussing composition.
Cs	Gussing composition.
R	Pull rate in cm/sec.
Xt	Distance from furnace reference position to the tip of sample.
Xs	Distance from interface to the tip of sample.
P, I, J	Counters
Temp	Interface temperature.
Im	Number of spacial steps.
Dt	Time rate of change of composition.
D1, B1	First spacial rate of change of composition.
D2, B2	Second special rate of change of composition.
En	Number of spacial steps moving forward in time interval Ti.
Sk, Kc	Segregation constant.
Sc	Solid composition.
ZO	Interface position from the furnace frame at time zero.
E1, E2, E3, E4	Coefficients of emparical expression for liquidus curve of HgCdTe phase diagram.
C1, C2 C3, C4	Coefficients of empirical expression for solidus curve of HgCdTe phase diagram.
X1	Liquid composition.
Xsc	Solid composition.

1. INTRODUCTION

Solid solution semiconducting alloys such as $Hg_{1-x}Cd_xTe$, produced under unidirectional solidified technique shows compositional segregation in both axial and radial directions[1-3]. Since Material Properties such as energy band gap depend on alloy composition, it is important to understand the growing parameters which influence the uniformity of the alloys.

In this work we modified the computer program developed by J. C. Clayton, etc.[4,5] to model compositional segregation in unidirectionally solidified solid-solution-semiconducting alloys with emphasis on the $Hg_{1-x}Cd_xTe$ systems in an effort to understand the effect of diffusion constant and ampule pulling rate on alloy axial compositional uniformity. The model is applied to the $Hg_{1-x}Cd_xTe$ system and takes into account the variations of the interface segregation constant and solidification rate with composition. We have used the empirical expressions for the liquidus and solidus curve of HgCdTe pseudobinary phase diagram developed by S. L. Lehoczky and F. R. Szofran[2] to calculate segregation constants, and used a binary search method to solve the diffusion equation for a finite ampule which solidified from its liquid state unidirectionally without source of solute added to the ampule. We have obtained solutions for the initial and final transient regions as well as steady state region for both fast and slow growing rate. The results for both cases agree very well with the experimental results[2-3] which show that the axial solute segregation in unidirectionally solidified HgCdTe systems is dominated by diffusion. Comparison of the model to experiments in the final transient regions gives values for the effective diffusion constant of 4.5×10^{-5} cm^2/sec for fast growing HgCdTe sample, 5.5×10^{-5} cm^2/sec for slow growing HgCdTe sample.

In Section 2, we gave the objective of this study. The theory used in this study is given in Section 3. Section 4 will compare the results obtained by using the model with the experimental data. In Section 5 we gave the conclusions and recommendations.

2. OBJECTIVE

The objective of this study is to develop a computer program to model the compositional segregation in unidirectionally solidified solid-solution-semiconducting alloys in its initial transient, final transient, and steady state growth regions. The variation in interface temperature, segregation constant and growth velocity with composition are taken into consideration. This should provide a understanding of the effect of growth parameters on the compositional uniformity in its axial direction. The model will be expanded for modeling two-dimensional diffusion problems to understand the effect of growth parameters on compositional segregation in its radial direction in the future.

3. THEORY

In this model, we have assumed the temperature gradient in the furnace is constant, and choose a coordinate system such that the coordinate is measured from a fixed laboratory frame (the position in the furnace where the sample first-to-freeze), x is measured in the sample from the ampule tip. The variable y is the distance into the liquid measured from the solid-liquid interface (figure 1).

Let us assume the ampule is being pulled downward at a rate R with R taken as a positive number, and the z coordinate of the ampule tip at t=0 as Z0 which is usually zero. The various coordinates at time t are related by

$$x = Z + Rt - Z0 \tag{1}$$

$$y = Z - Zs \tag{2}$$

where Zs is the interface position relative to the furnace frame. Let Ls be the length of the sample, Xs be the distance from the interface to the tip of the ampule, then

$$Ls' = Ls - Xs \tag{3}$$

will denote the distance from the interface to the top end portion of the molten alloy.

Let us assume the "thermal gradient" G is constant. Then the thermal field will have the form

$$T(z, t) = T0 + G\,Zs \tag{4}$$

where T0 is the first-to-freeze interface temperature. Let C(y, t) denote the liquid composition at the solid-liquid interface. Then by using iteration procedures we can obtain the interface temperature from the following empirical expression for the liquidus curve of the phase diagram (figure 2).

$$X\ell\,(T) = E_1 T^* + E_2 T^{*2} + E_3 T^{*3} + E_4 T^{*4} \tag{5}$$

where $T^* = (T - 670°C)/412°C$ and

$E_1 = 0.607640$ $\quad E_2 = 0.077209$

$E_3 = 0.696167$ $\quad E_4 = -0.381683.$

Substitute interface temperature into eq. (4) we will find the interface position Zs. By substituting the interface temperature into the following empirical expression for solidus curve of the phase diagram, we will be able to obtain the solid composition at the interface from

$$X_{sc}(T) = C_1 \mathrm{Sin}\left(\frac{\pi}{2}T^*\right) + C_2 \mathrm{Sin}\left(\frac{\pi}{2}T^{*\frac{1}{2}}\right) \qquad (6)$$

$$+ C_3 \mathrm{Log}_{10}(9T^* + 1) + C_4 T^{*\frac{1}{2}} \quad (T>690°C)$$

$$X_{sc}(T) = X_{sc}(690°C)\ (T - 670°C)/20°C \quad (670°C<T<690°C)$$

where

$C_1 = 0.502804$ $\qquad$ $C_2 = 0.165390$

$C_3 = 0.746318$ $\qquad$ $C_4 = -0.413546.$

We can then obtain segregation constant Xk from

$$Xk = Xsc/X\ell.$$

The liquid composition C satisfies

$$D\frac{\partial 2c}{\partial y2} + (R + V(t))\frac{\partial c}{\partial y} = \frac{\partial c}{\partial t} \qquad (7)$$

where D is the effective diffusion constant and (R + V(t)) is the growth velocity with

$$V(t) = \frac{dz}{dt} \qquad (8)$$

The boundary conditions are

$$C(y, t) = C0 \qquad t = o \qquad (9)$$

$$\frac{\partial c}{\partial y}(y,t) = 0 \text{ at } y = Ls' \text{ for all } t \qquad (10)$$

$$(R + V(t))\ (X k - 1)\ C(0, t) = D\frac{\partial c}{\partial y}(y,t) \qquad t>o \qquad (11)$$

The boundary condition eq.(10) is required to satisfy the condition that there is no source of solute at the ampule end.

The numerical procedure used to solve eq. (9) to eq. (11) is similar to that given reference 5. We give it here for self-completeness.

Let the time steps and spacial steps be Ti and Zi respectively. Assume at time t the value of C (y, t) have been determined for all $t \leq$ to and all y. The goal is to compute C (y,t´) for ail y, where t´ = to + Ti.

We assume a trial value Cs for the liquid composition at the interface at $t_o = t$, say

$$C(0,t') = Cs \tag{12}$$

we then compute

$$\frac{\partial C(0,t')}{t} = \frac{Cs - C(0,t)}{Ti} \tag{13}$$

The first spacial derivative Dl is calculated from the boundary condition eq. (11)

$$Dl = \frac{\partial C(0,t')}{\partial y} = \left(\frac{1}{D}\right)(R = V(t'))\ (Xk - 1)\ C(0,t') \tag{14}$$

The second spacial derivative D2 is calculated from the diffusion equation eq. (7)

$$D2 = \frac{\partial^2 C(0,t')}{\partial y^2} = \left(\frac{1}{D}\right)\left(\frac{\partial C(0,t')}{\partial t} - (R + V(t))\ \frac{\partial C}{\partial y}(0,t')\right) \tag{15}$$

We then obtain the liquid composition a distance Zi away from the interface by the expansion

$$C(Zi,t') = Cs + \frac{\partial C(0,t')}{\partial y}\ Zi + \frac{\partial^2 C(0,t')}{\partial y}\ \frac{Zi^2}{2} \tag{16}$$

We then propagate C(y,t) out in y until the end of the ampule is reached (y = Ls') and see if the boundary condition eq. (10) is met.

The solution may be propagated to y = Yi, the next spacial step by first calculate

$$\frac{\partial C(Zi,t')}{\partial y} = \frac{C(Zi,t') - C(Zi,t)}{Ti} \tag{17}$$

we then use a Tayor series expansion and the diffusion equation to obtain

$$\frac{\partial C(Zi,t')}{\partial y} = \frac{\partial C(0,t')}{\partial y} + \frac{\partial^2 C(0,t')}{\partial y^2}\ Zi \tag{18}$$

and

$$\frac{\partial^2 C(Zi,t')}{\partial y^2} = \frac{1}{D}\left(\frac{\partial C(0,t')}{\partial t} - (R+V(t'))\ \frac{\partial C(ti,t')}{\partial y}\right) \qquad (19)$$

A second expansion leads to

$$C\ (2Zi,t') = C\ (Zi,t') + \frac{\partial C\ (Zi,t')}{\partial y}\ Zi + \frac{\partial^2 C\ (Zi,t')}{\partial y^2}\ \frac{Zi^2}{2} \qquad (20)$$

The same process is used for the rest of spacial steps until $y = Ls'$, the end of ampule at this time step. We then test whether boundary condition eq. (10) is met, if it is not, a new trial solution obtained from binary search method is used and the entire process is repeated until the boundary conditions is met.

The initial boundary condition

$$C\ (y,\ 0) = C0 \qquad (21)$$

allows one to take $t_o = 0$ and calculate C (y, t) for any t and calculate the solid composition for the entire ampule.

4. RESULTS

The model has been applied to two HgCdTe systems with ampule pulling rate of 0.1116 cm/hr and 0.02466 cm/hr, respectively. The compositional segregation along axial direction depends on ampule pulling rate and the diffusion constant. From figure 7, we see that the solidification rate and the interface segr ation constant are not constant along the growing axis which we have taken into consideration in this model. In HgCdTe system, for fast ampule pulling rate case (0.1116 cm/hr) the solid composition is expected to exhibit an initial transient region with gradually decreasing solute composition, following by a steady region with solid composition equal to alloy composition C0 which is 0.202. Finally there is a fast decreasing solute composition final transient region. The analytical expression for all these three regions have been obtained by Smith, Tiller, and Rutter[6] for constant growth rate and constant interface segregation constant. In our model we have taken into account the variations of growth rate and interface segregation constant with composition. The calculations indicated that except the initial transient region, an effective diffusion constant of $4.5 \times 10^{-5} cm^2/sec$ gives very good fit to the experimental data which is shown in figure 3. The discrepancy in the initial transient region is believed to be due to undercooling of the sample. Figure 4 compares the calculated results with experimental data for effective diffusion constant of $3.0 \times 10^{-5} cm^2/sec$. The comparison indicates that the effective diffusion constant has a very strong effect on the final transient region.

For the case of very slow ampule pulling rate (0.02466 cm/sec), the diffusion layer is quite long. The diffusion layer will reach the end of the sample before the growth has reached its steady state. Therefore it is expected that the solid composition should gradually decrease until all the solute is consumed. Figure 5 compare the model result with experimental data for ampule pulling rate of 0.02466 cm/hr for an alloy

composition of 0.202 and a constant thermal gradient of 50°C/cm when sample undercooling is taking into consideration.

Figure 6 compares the calculated result with experimental data with thermal gradient is taken to be 100°C/cm. The effective diffusion constant of $5.5 \times 10^{-5} cm^2/sec$ and thermal gradient of 50°C/cm gives the best fit with the experimental data. The discrepancy is believed to be due to the fact that the furnace thermal gradient is not constant which shows much larger effect for fast ampule pulling rate case than slow ampule pulling rate case. The fact that the effective diffusion constant is larger for fast ampule pulling rate case is not quite understood at this time.

5. RECOMMENDATION

The model should be further modified to take into account the variation of thermal gradient along the furnace axis. Then the model should be expanded to model two-dimensional diffusion problems to understand the effect of growth parameters on compositional segregation in the radial direction.

REFERENCES

1. Lehoczky, S. L. and F. R. Szofran, "Directional Solidification and Characterization of $Hg_{1-x}Cd_xTe$ Alloys", in Materials Research Society Symposium Proceedings---Material Processing in the Reduced Gravity Environment of Space, ed., Guy E. Rindone (Elsevier, New York), 407, 1983.

2. Lehoczky, S. L. and F. R. Szofran, "Advanced Methods for preparation and characterization of Infrared Detector Materials", NASA, NAS8-33107 (September 1981).

3. Lehoczky, S. L., F. R. Szofran, and B. G. Martin, "Advanced Methods for preparation and characterization of Infrared Detector Materials", NASA, NAS8-33107 (July 1980).

4. Clayton, J. C., "Transient and Diffusion Analysis of HgCdTe" NASA Annual Report (Dec. 80 - May 82).

5. Clayton, J. C., M. C. Davidson, D. C. Gillies, and S. L. Lehoczky, "One Dimensional Analysis of Segregation in Unidirectionally Solidified HgCdTe", submitted to Journal of Crystal Growth.

6. Smith, V. G., W. A. Tiller, and J. W. Rutter, "A Mathematical Analysis of Solute Redistribution During Solidification", Can. J. Phys. 33, 723, 1953.

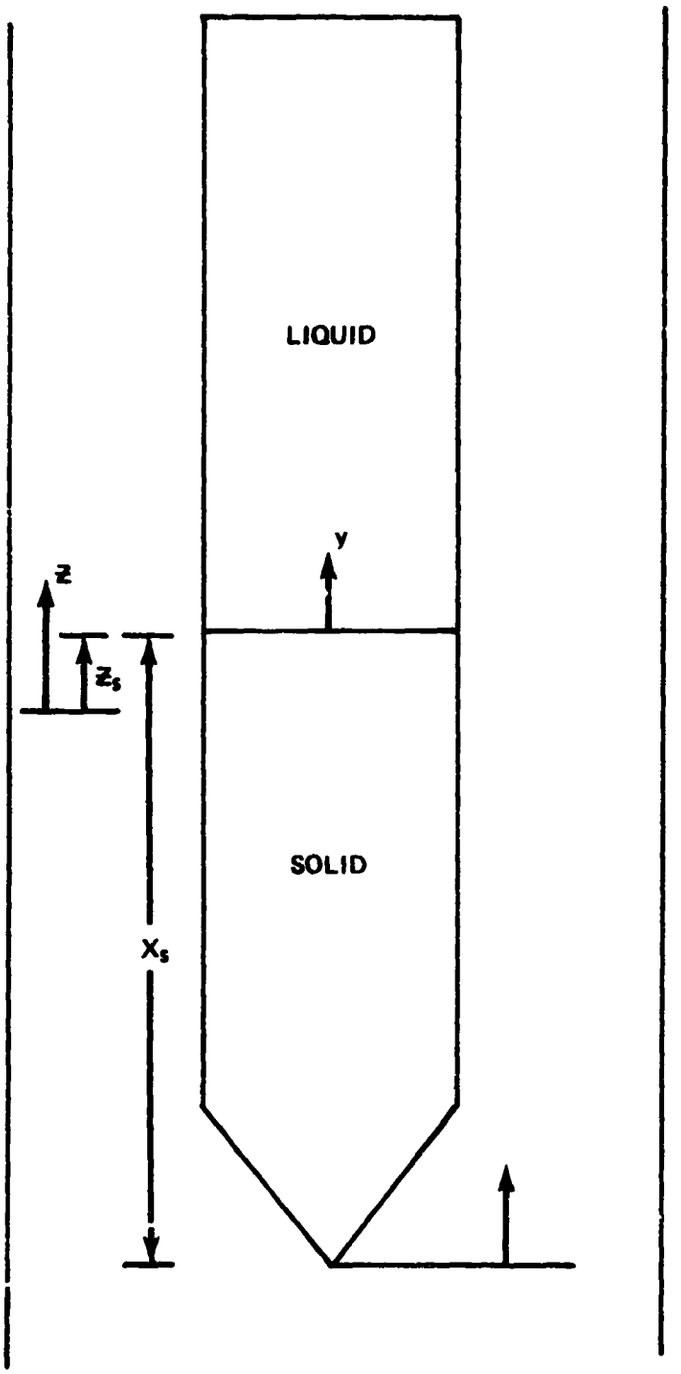

FIGURE 1. COORDINATE SYSTEM USED IN THIS MODEL

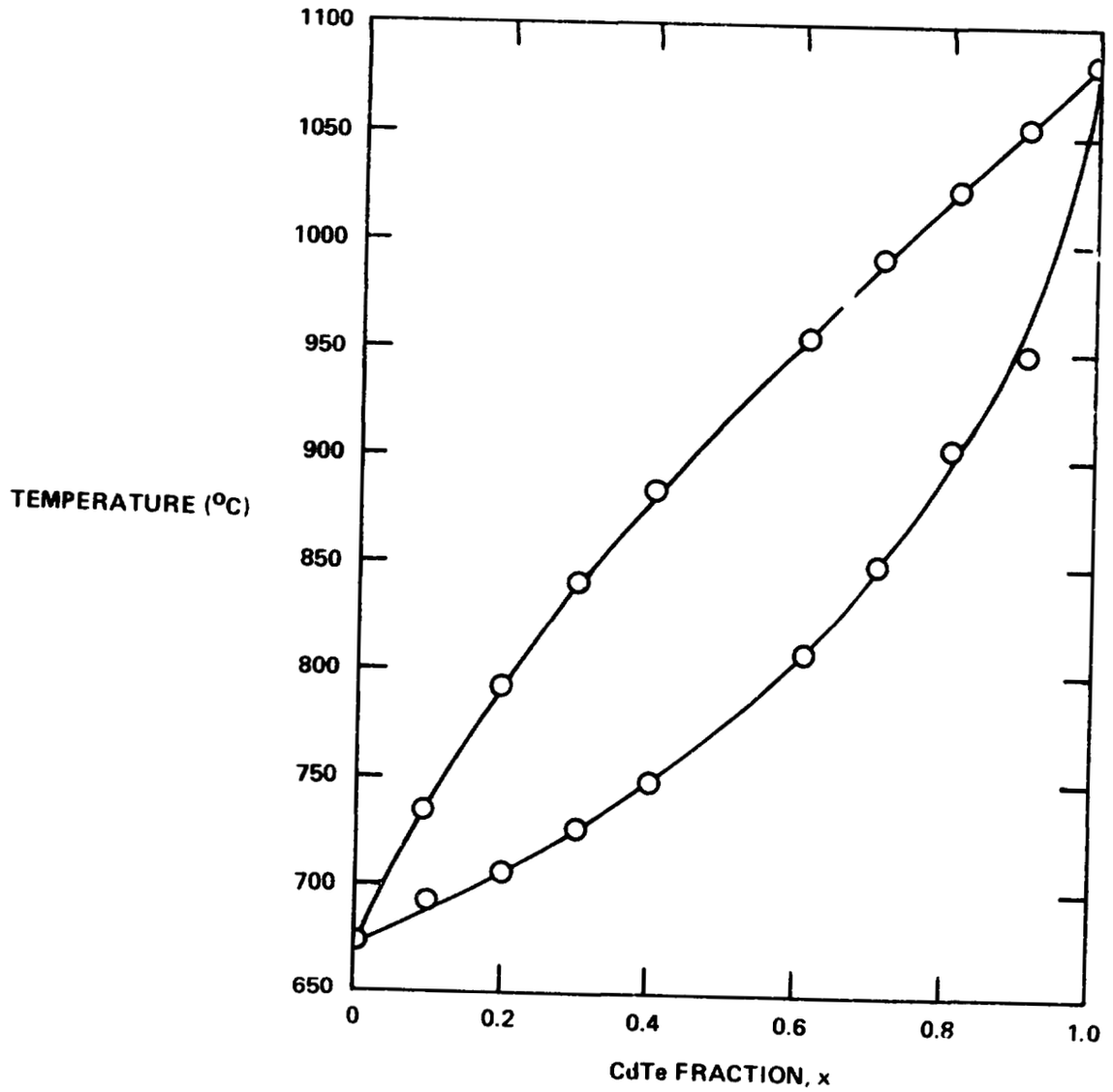

PSEUDO-BINARY PHASE DIAGRAM OF $Hg_{1-x}Cd_xTe$

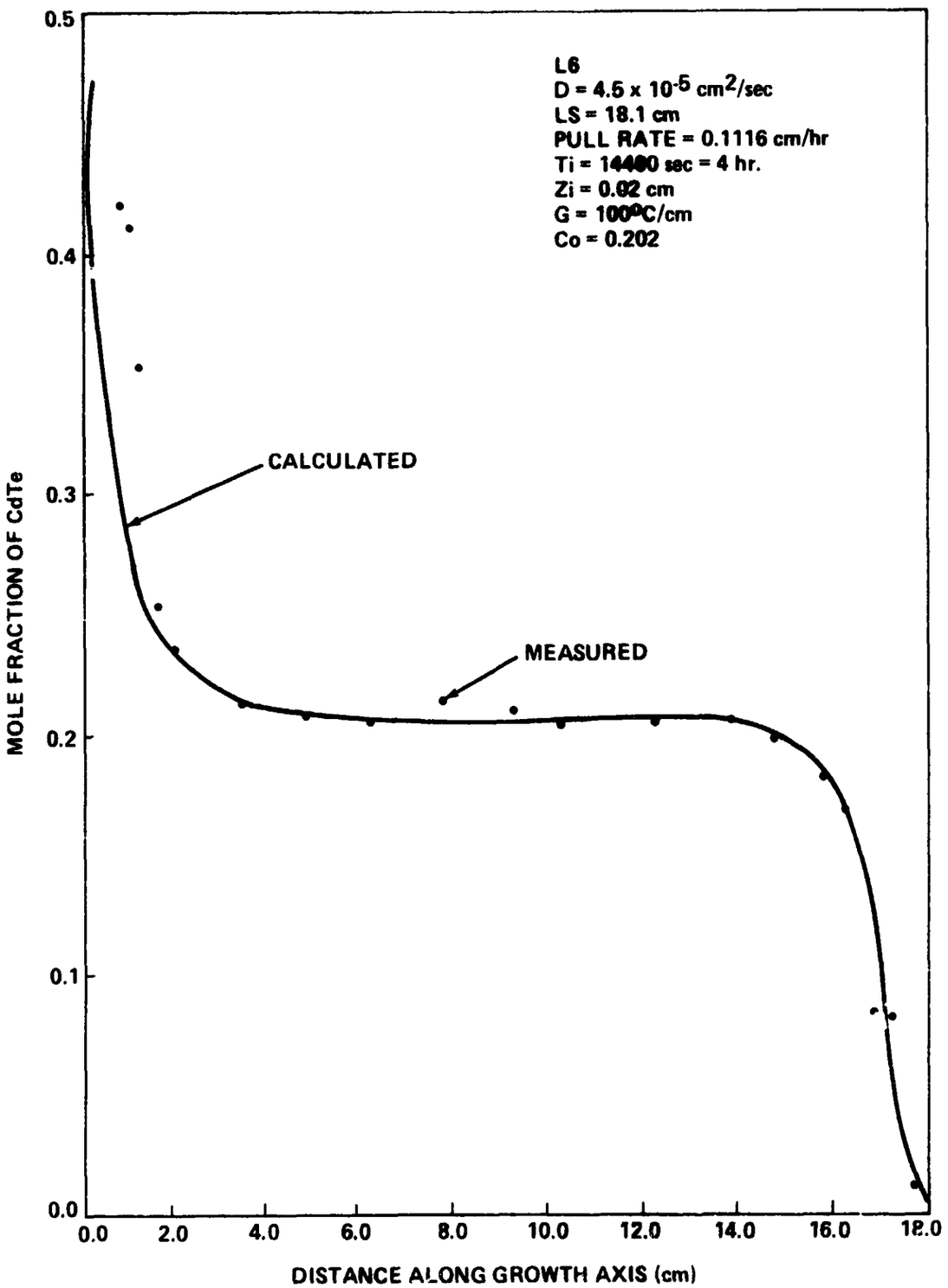

IGURE 3 A COMPARISON BETWEEN THE CALCULATED AND MEASURED COMPOSITION FOR Co = 0.202, R = 0.1116 cm/hr, G = 100°C/cm WITH D = 4.5 x 10^{-5} cm^2/sec.

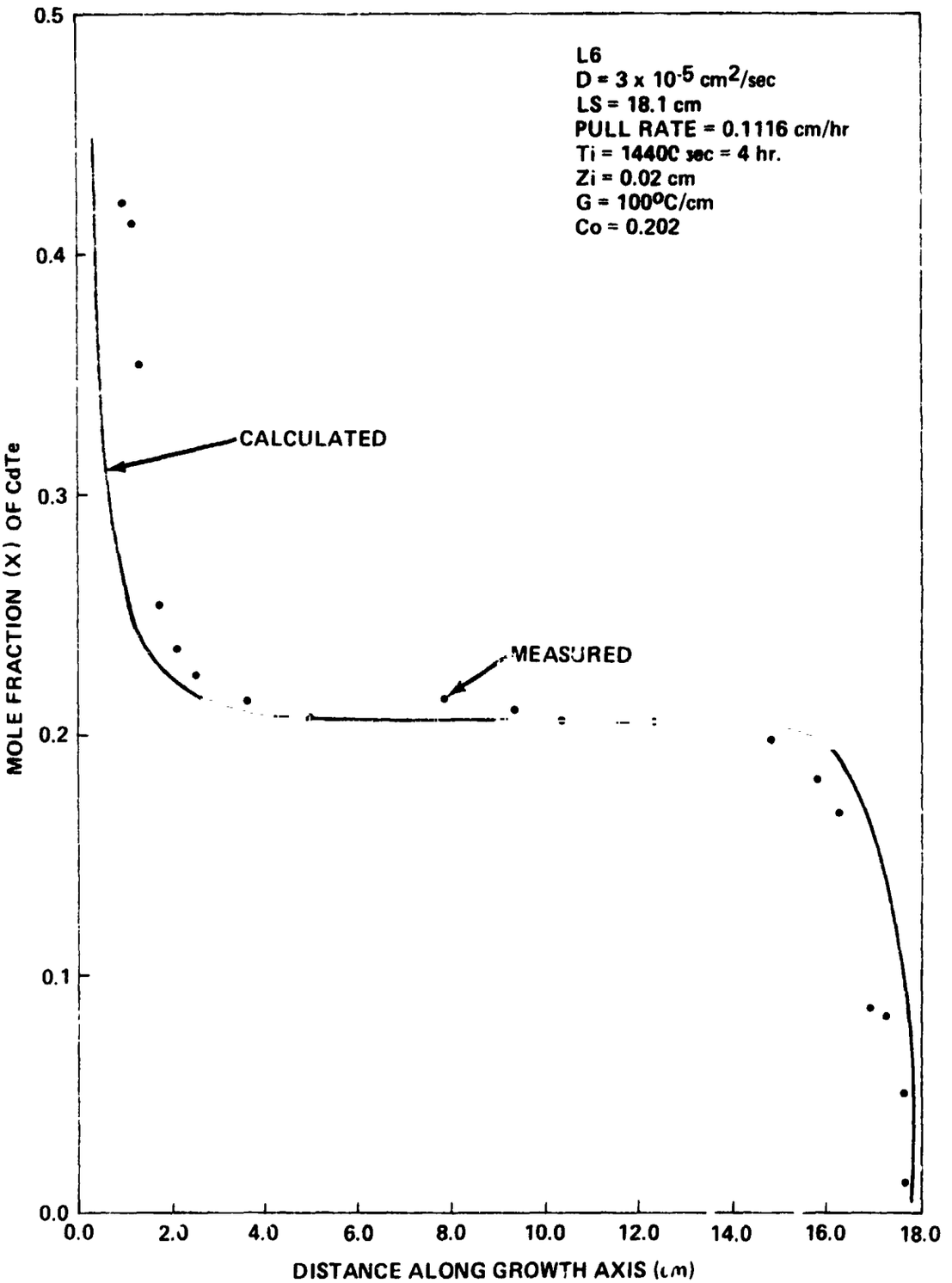

FIGURE 4. A COMPARISON BETWEEN THE CALCULATED AND MEASURED COMPOSITION FC Co = 0.202, R = 0.1116 cm/hr, G = 100°C/cm WITH D = 3.0 x 10^{-5} cm^2/sec.

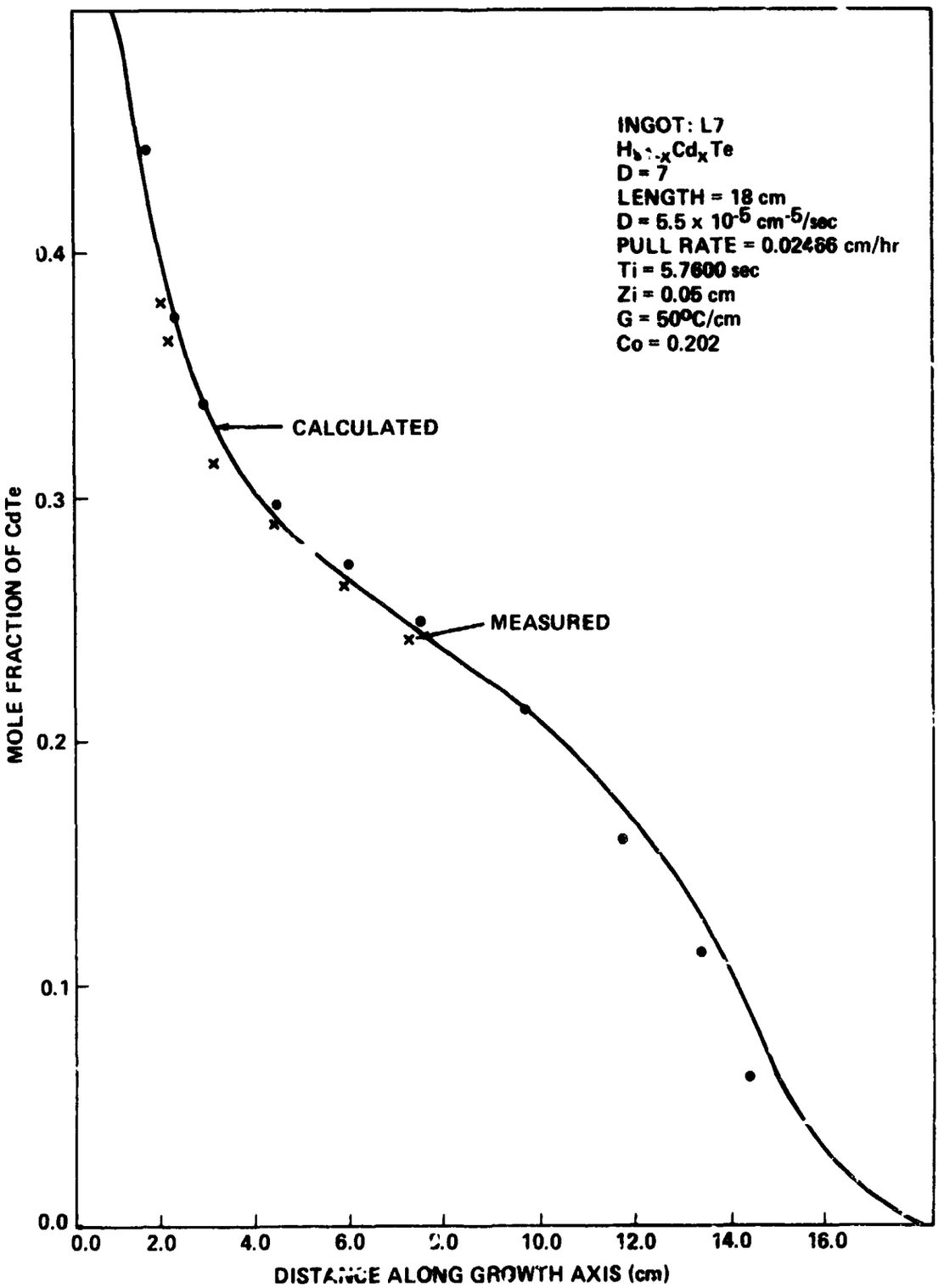

IGURE 5. A COMPARISON BETWEEN THE CALCULATED AND MEASURED COMPOSITION FOR Co = 0.202, R = 0.02466 cm/hr, G = 50°C/cm WITH D = 5.5 x 10^{-5} cm^2/sec.

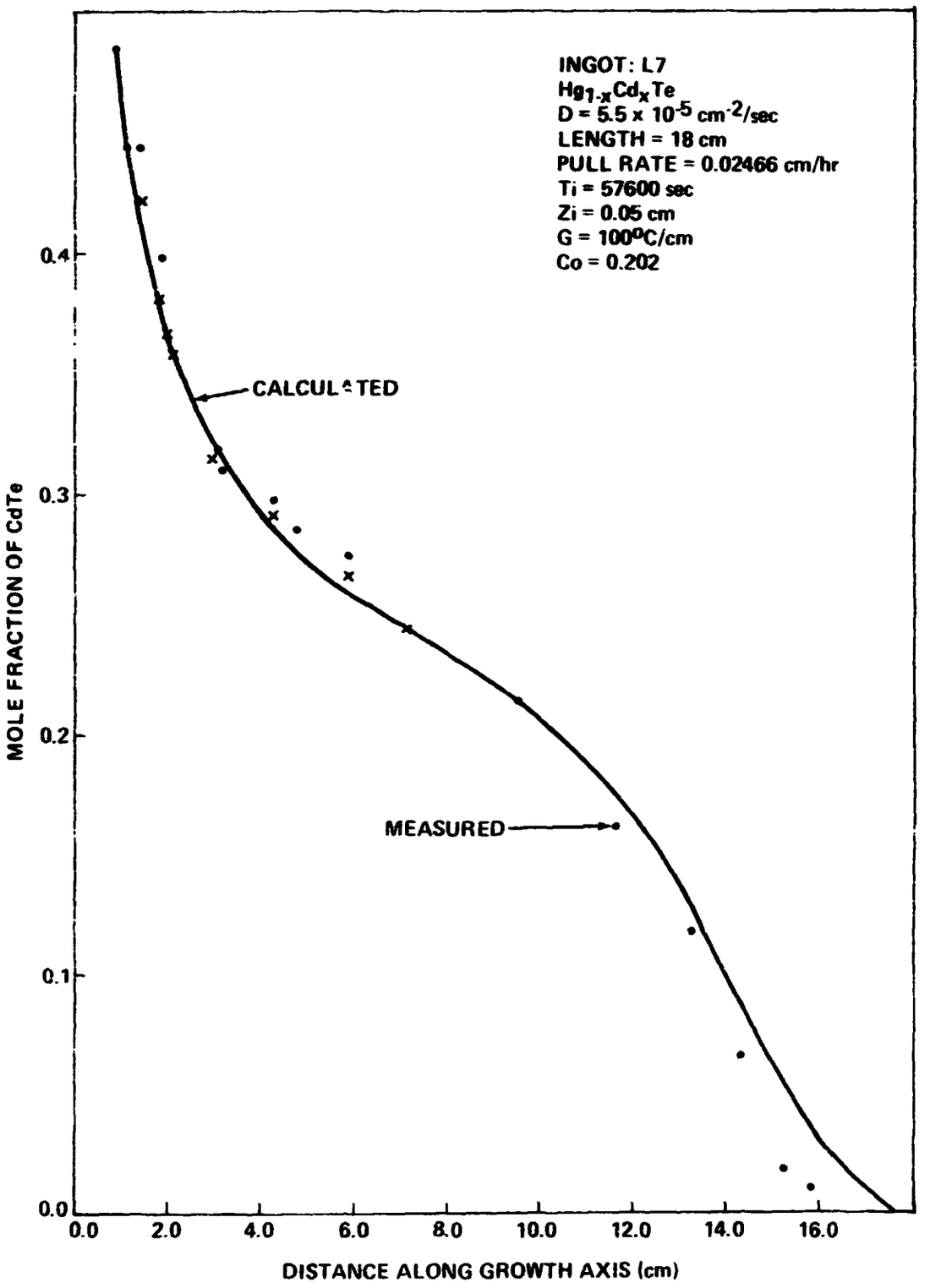

FIGURE 6. A COMPARISON BETWEEN THE CALCULATED AND MEASURED COMPOSITION F
$C_o = 0.202$, R = 0.02466 cm/hr, G = 100°C/cm WITH $D = 5.5 \times 10^{-5}$ cm^2/sec.

C-10

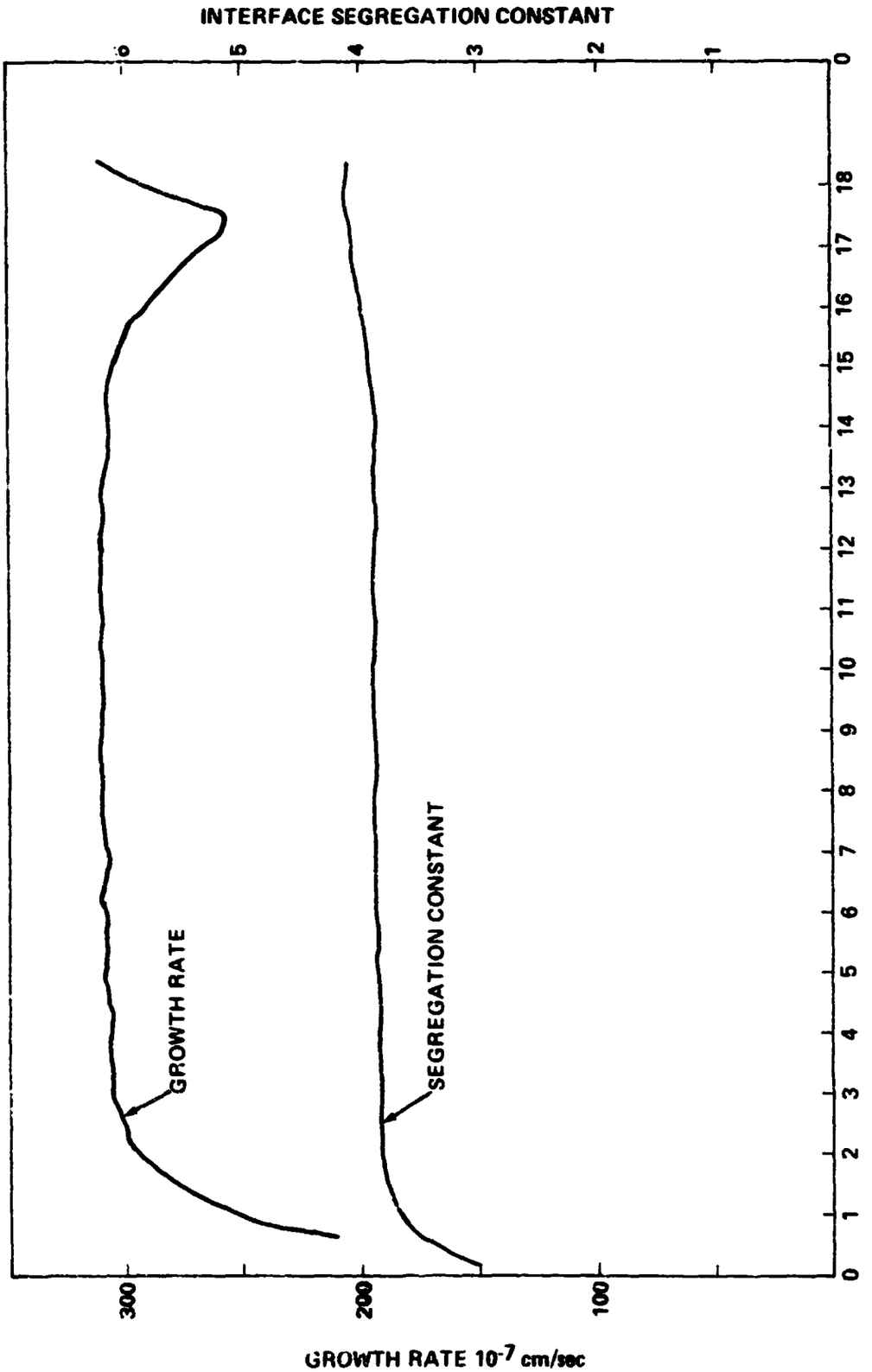

FIGURE 7 THE VARIATION OF SEGREGATION CONSTANT AND GROWTH VELOCITY ALONG THE GROWTH AXIS FOR Co = 0.202, R = 0.1116 cm/hr, G = 100°C/cm WITH D = 4.5×10^{-5} cm^2/sec.

```
10   ! PROGRAM NAME "BINSEG", THIS PROGRAM IS USED TO CALCULATE
20   ! ONE DUMENSUONAL SEGREGATIUN.
30   DIM Co(1000),Cn(1000),T(1000),Z(1000),X(1000),Sc(1000)
40   DIM X$(80),Xk(1000),V(1000),To(1000)
50   P$=" "       ! REM SYMBOL FOR GRAPHIC OUTPUT
60   Q$="O"
70   GOTO 100
80   ASSIGN "DATA1" TO #1
90   READ #1;Ids$,D,Ls,R1,Ti,Zi,Co,G,An$
100  Co=.202
110  Zi=.05
120  Ids$="L6"
130  D=4.5E-5
140  Ls=18.1
150  R1=.1116
160  Ti=21600
170  An$="N"
180  G=100
190  ! !  Kk=0
200  K=0
210  ! REM INPUT FROM FILE ENTITLED "DATA1"
220  R2=R1
230  R22=R1
240  IF D>1 THEN GOTO 1560
250  Xt=0
260  Im=INT(Ls/Zi)
270  PRINTER IS 7,6
280  PRINT "SPECIMEN IDENTIFICATION ";Ids$
290  PRINT "DIFFUSION COEFFICIENT IS (CM^2/SEC) ";D
300  PRINT "LENGTH OF SAMPLE IS (CM) ";Ls
310  PRINT "PULL RATE (CM/HR) ";R1
320  PRINT "TIME INTERVAL (SEC) ";Ti
330  PRINT "ZI (CM)";Zi
340  PRINT "ALLOY COMPOSITION CO ";Co
350  PRINT "TEMPERATURE GRADIENT (DEGC/CM)";G
360  PRINT "RATE CHANGE ? ";An$
370  IF An$="N" THEN 480
380  READ #1;Tst,Tend,R2,An2$
390  PRINT "STARTING TIME (SEC)";Tst
400  PRINT "ENDING TIME (SEC) ";Tend
410  PRINT "NEW RATE (CM/HR) ";R2
420  PRINT "SECOND RATE CHANGE ? ";An2$
430  IF An2$="N" THEN 480
440  READ #1;Tst2,Tend2,R22
450  Time=Tst2/3600
460  PRINT "STARTING TIME FOR SECOND RATE CHANGE (HR) ";Time
470  PRINT "NEW RATE (CM/HR) ";R22
480  Ep=.00009
490    FOR I=1 TO Im
500    Co(I)=Co
510    NEXT I
520  T0=FNK(Co)
530  GOSUB 1770
540  J=1
550    Cu=Co(1)*2
560    Cd=0
570    Cs=(Cu+Cd)*.5
580    IF T(J-1)>Tst THEN 610
590    R=R1/3600
600    GOTO 630
610    IF T(J-1)>Tend THEN R=R22/3600
620    IF (T(J-1)<Tend) OR (T(J-1)=Tend) THEN R=R2/3600
```

ORIGINAL PAGE IS
OF POOR QUALITY

```
630     Xt=Xt+R*T1
640     P=0
650       P=P+1
660         I=1
670         Cb=Co(I)
680         Cn(I)=Cs
690         Temp=FNK(Cn(1))
700         Zs=(Temp-T0)/G
710         Xs=Xt+Zs
720         Im=INT((Ls-Xs)/Z1)
730         To(J)=Temp
740         Dt=(Cs-Cb)/T1
750         IF J=1 THEN V(2)=(Zs-Z0)/T1
760         IF J>1 THEN V(J+1)=(Zs-Z(J-1))/T1
770         GOSUB 1930
780         D1=(R+V(J+1))/D*(Sk-1)*Cs
790         D2=(Dt-(R+V(J+1))*D1)/D
800         Cn(I+1)=Cs+D1*Z1+D2*Z1*Z1/2
810           I=I+1
820           Dt=(Cn(I)-Co(I))/T1
830           B1=D1+D2*Z1
840           B2=(Dt-(R+V(J+1))*B1)/D
850           D1=B1
860           D2=B2
870           Cn(I+1)=Cn(I)+D1*Z1+D2*Z1*Z1/2
880           IF Cn(I+1)<Co+Ep*10 THEN GOTO 940
890           IF ABS(Cu-Cs)<1.0E-11 THEN 980
900           IF Cn(I-1)<0 THEN Cd=Cs
910           IF Cn(I-1)>0 THEN Cu=Cs
920           Cs=(Cu+Cd)*.5
930         GOTO 660
940           ! '
950           IF (ABS(Cn(I)-Co)>Ep) OR (ABS(Cn(I)-Co)=Ep) THEN GOTO 1020
960           IF (ABS(Cn(I-1)-Co)<Ep) AND (ABS(Cn(I-2)-Co)<Ep) THEN 980
970           GOTO 1020
980             FOR L=I TO Im
990             Cn(L)=Co
1000            NEXT L
1010          GOTO 1200
1020          ! ''
1030          IF Cn(I+1)<0 THEN 1050
1040          IF I<Im THEN 810
1050      IF ABS(D1)<Ep*10 THEN 1200
1060      En=INT((R+V(J+1))*T1/Z1)
1070      IF (En>Im) AND (P>30) THEN 1200
1080      IF Im<1 THEN 1140
1090      IF En>Im THEN 1110
1100      IF (ABS(Cu-Cs)<1.0E-11) AND (Co(Im-En)<Co) THEN 1200
1110      IF (ABS(Cu-Cs)<1.0E-11) AND (En>Im) THEN 1200
1120      IF (D1>0) AND (Co(Im-1)=Co) THEN Cd=Cs
1130      IF (D1>0) AND (Co(Im-1)<Co) THEN Cu=Cs
1140      IF D1<0 THEN Cd=Cs
1150      Cs=(Cu+Cd)*.5+1E-12
1160      IF P>1000 THEN STOP
1170      GOTO 650
1180    '
1190    !
1200    GOSUB 1570
1210    J=J+1
1220    IF Xs<Ls THEN 550
1230      FOR L1=1 TO J STEP 1
1240      Sc(L1)=Sc(L1)/.6*80
1250      PRINT "SC(";L1;"):",Sc(L1)
```

```
1260      NEXT L1
1270        FOR M=1 TO J
1280        A=INT(Sc(M))
1290          FOR L=1 TO 80
1300          X$(L)=P$
1310          IF L=A THEN 1330
1320          GOTO 1350
1330          X$(L)=Q$
1340          PRINTER IS 7,6
1350          PRINT X$(L);
1360          NEXT L
1370        NEXT M
1380        PRINT CHR$(12)
1390        K=K+1
1400        IF K=1 THEN D=4.0E-5
1410        IF K=1 THEN GOTO 210
1420        IF (K=2) AND (Kk=2) THEN GOTO 100
1430       IF K=2 THEN D=3.5E-5
1440       IF K=2 THEN GOTO 1470
1450       IF K=3 THEN D=5.0E-5
1460       IF K=3 THEN GOTO 210
1470      IF K=4 THEN Ti=14400
1480      IF K=4 THEN Kk=Kk+1
1490      IF (K=4) AND (Kk=1) THEN 200
1500      Ids$="L7"
1510      G=50
1520      R1=.2466
1530      Ti=57600
1540      Ls=17.1
1550      GOTO 190
1560 STOP
1570 !
1580 Cs=Cn(1)
1590 GOSUB 1930
1600 Kc=Sk
1610 Sc=Kc*Cn(1)
1620 T(J)=Ti*J
1630 Z(J)=Zs
1640 X(J)=Xs
1650 Sc(J)=Sc
1660 Xk(J)=Kc
1670 PRINTER IS 7,6
1680 IMAGE DDDD.DD,3X,DD.DDD,3X,DD.DDD,3X,DD.DDD,3X,D.DDDD,3X,DD.DDDDDDD,3X,DDDD
DDDD,3X,D.DDDDDDDDDDD
1690 PRINT USING 1680;To(J),Z(J),Xk(J),X(J),Sc(J),R+V(J+1),T(J),Cs
1700 PRINT
1710   FOR L=1 TO Im
1720   Co(L)=Cn(L)
1730   NEXT L
1740 RETURN
1750   ! !
1760   ! !
1770 ! REM PRINTS AT T=0 ONLY
1780 Z0=0
1790 ! Z0=0 FOR CONSTANT R
1800 Xs=0
1810 Cs=Co
1820 GOSUB 1930
1830 Kc=Sk
1840 Sc=Kc*Co
1850 PRINT "   T          Z        K          X          CS          V(CM/S)"
1860 PRINT
1870 IMAGE DDDD.DD,3X,DDD.DD,4X,D.DDD,4X,D.DDD    ,D.DDDD
```

ORIGINAL PAGE IS
OF POOR QUALITY

```
1880 PRINT USING 1870;T0,Z0,Kc,Xs,Sc
1890 PRINT CHR$(13)   !!! CR
1900 RETURN
1910 !
1920 !
1930 E1=.607640
1940 E2=.077209
1950 E3=.696167
1960 E4=-.381683
1970 Tmi=671
1980 IF Cs>.1 THEN Tmi=730
1990 IF Cs>.2 THEN Tmi=790
2000 IF Cs>.3 THEN Tmi=835
2010 IF Cs>.35 THEN Tmi=855
2020 IF Cs>.4 THEN Tmi=875
2030 IF Cs>.45 THEN Tmi=895
2040   FOR Temp=Tmi TO 1075 STEP .1
2050   Tp=(Temp-670)/412
2060   X1=E1*Tp+E2*Tp^2+E3*Tp^3+E4*Tp^4
2070   IF ABS(X1-Cs)>.002 THEN GOTO 2090
2080   GOTO 2110
2090   NEXT Temp
2100 !
2110 C1=.502804
2120 C2=.165390
2130 C3=.746318
2140 C4=-.412546
2150 IF Temp<690 THEN 2180
2160 Xsc=C1*SIN(1.57*Tp)+C2*SIN(1.57*Tp^.5)+C3*LGT(9*Tp+1)+C4*Tp^.5
2170 GOTO 2210
2180 Tp=(690-670)/412
2190 Xsc=C1*SIN(1.57*Tp)+C2*SIN(1.57*Tp^.5)+C3*LGT(9*Tp+1)+C4*Tp^.5
2200 Xsc=Xsc*(Temp-670)/20
2210 Sk=Xsc/X1
2220 RETURN
2230 ! !
2240 ! !
2250 DEF FNK(Cs)
2260 E1=.607640
2270 E2=.077209
2280 E3=.696167
2290 E4=-.381683
2300 Tmi=671
2310 IF Cs<0 THEN 2470
2320 IF Cs>.1 THEN Tmi=730
2330 IF Cs>.2 THEN Tmi=790
2340 IF Cs>.3 THEN Tmi=835
2350 IF Cs>.35 THEN Tmi=855
2360 IF Cs>.4 THEN Tmi=875
2370 IF Cs>.45 THEN Tmi=895
2380   FOR Temp=Tmi TO 1075 STEP .1
2390   Tp=(Temp-670)/412
2400   X1=E1*Tp+E2*Tp^2+E3*Tp^3+E4*Tp^4
2410   IF ABS(X1-Cs)<.002 THEN RETURN Temp
2420   NEXT Temp
2430 IF ABS(X1-Cs)<.002 THEN 2480
2440 IF Cs<.038 THEN Temp=695
2450 IF Cs<.028 THEN Temp=689
2460     s<.018 THEN Temp=682
2470       <.008 THEN Temp=675
2480 ~   .<N Temp
2490 FNEND
2500   END
```

ORIGINAL PAGE IS
OF POOR QUALITY

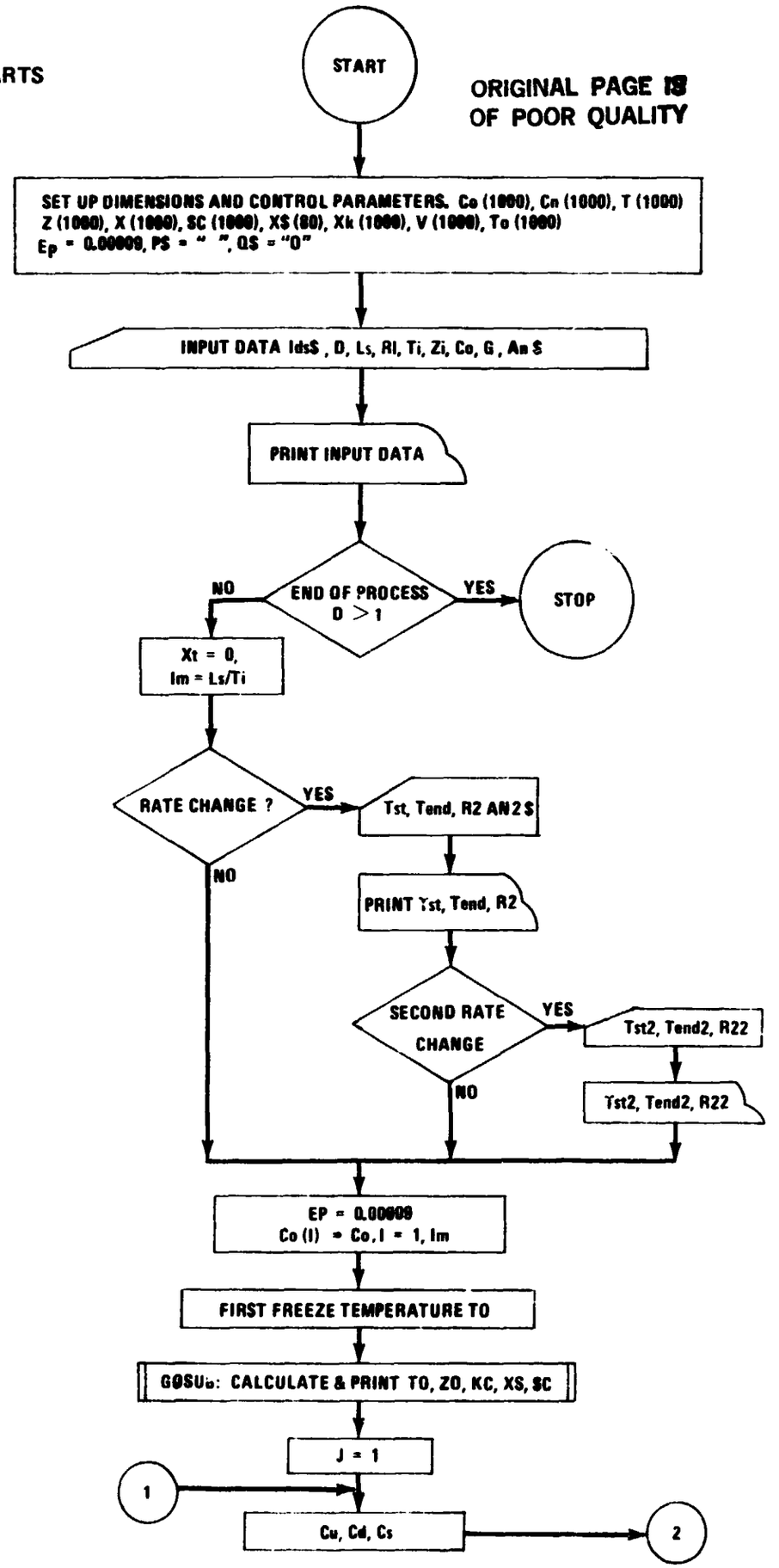

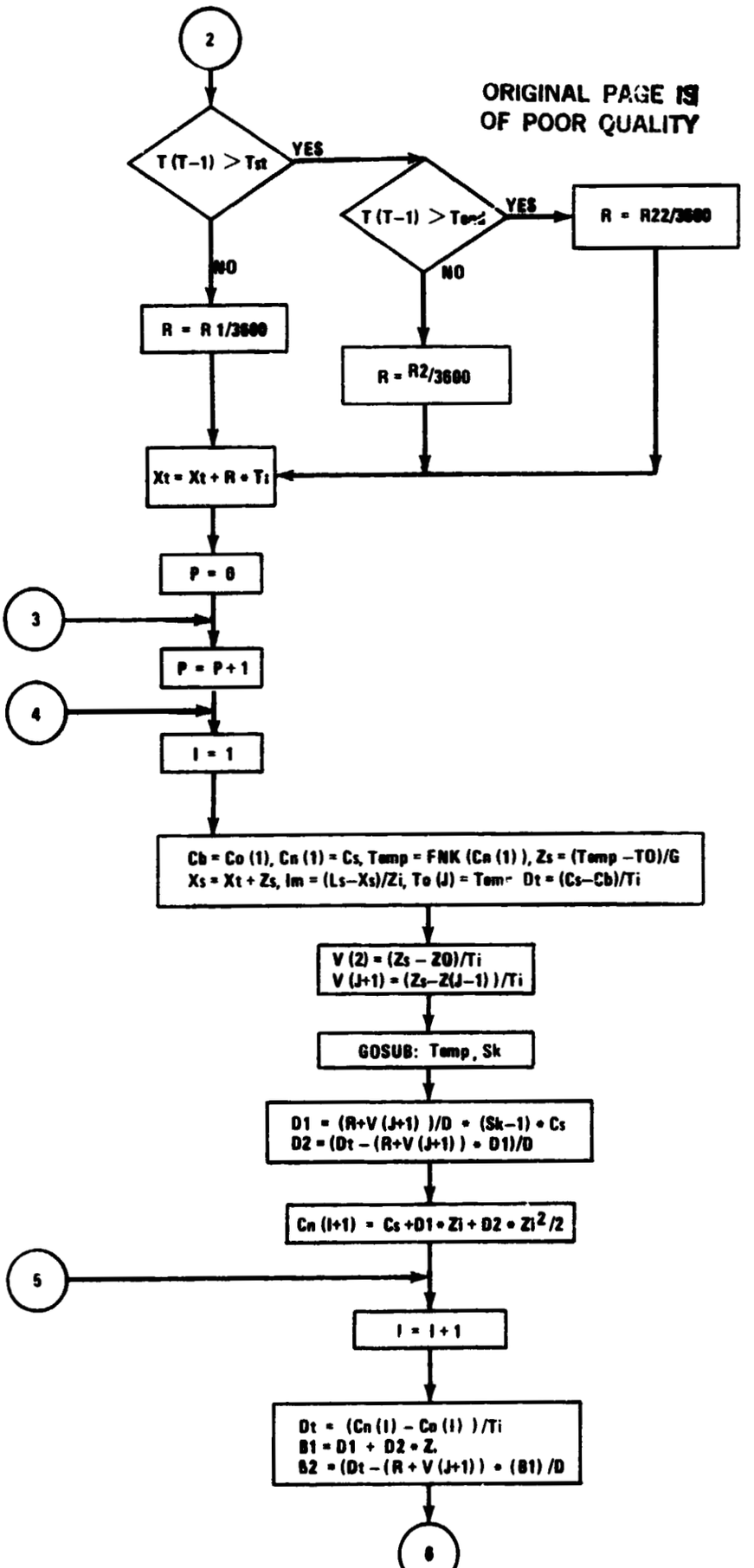

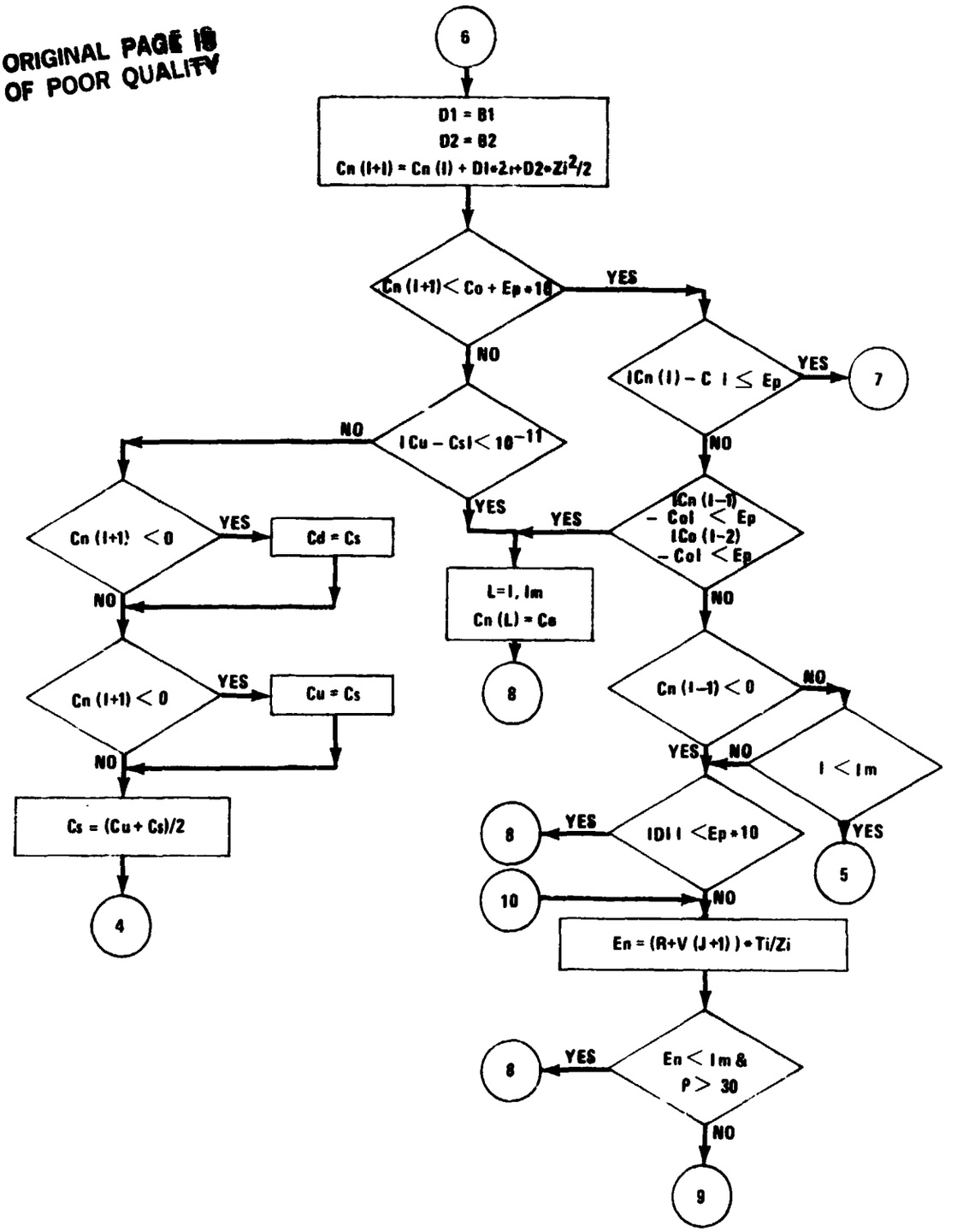

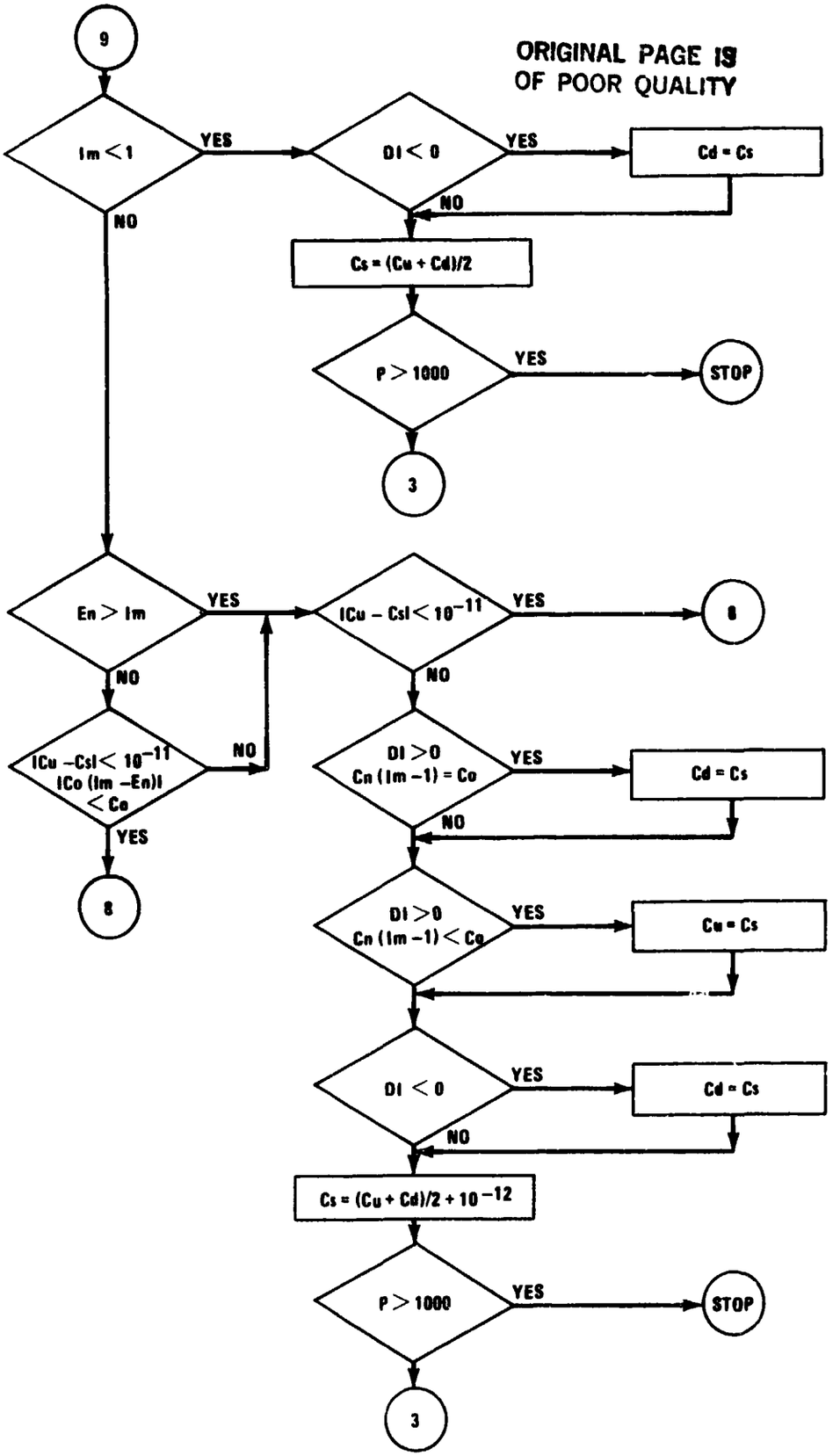

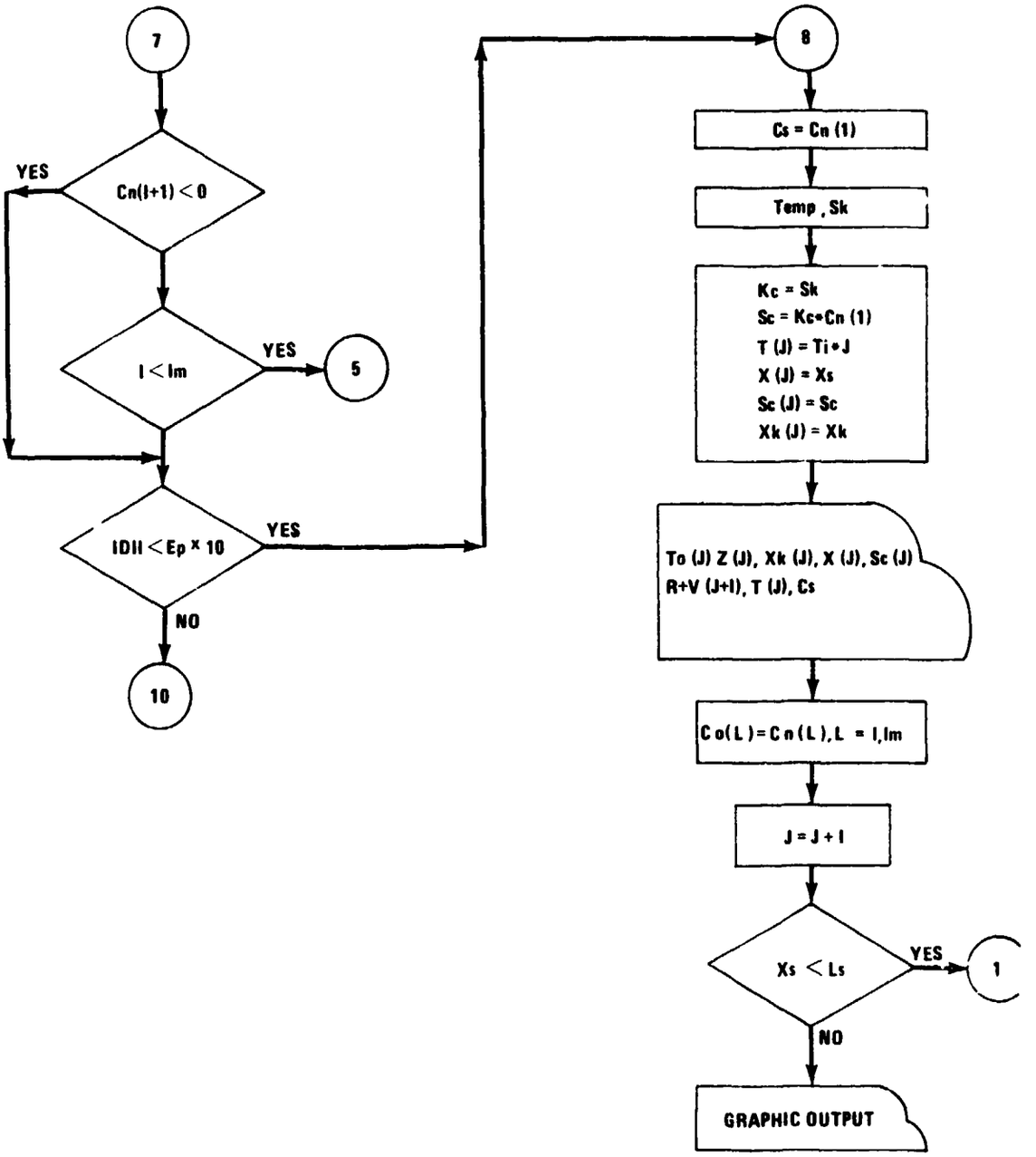

1983

NASA/ASEE SUMMER FACULTY RESEARCH FELLOWSHIP PROGRAM

MARSHALL SPACE FLIGHT CENTER
THE UNIVERSITY OF ALABAMA

FINITE ELEMENT ANALYSIS OF A DEPLOYABLE SPACE STRUCTURE

PREPARED BY:	GEORGE E. WEEKS
ACADEMIC RANK:	PROFESSOR
UNIVERSITY AND DEPARTMENT:	UNIVERSITY OF ALABAMA AEROSPACE ENGINEERING
NASA/MSFC:	
(LABORATORY)	SYSTEMS DYNAMICS
(DIVISION)	STRUCTURAL DYNAMICS
(BRANCH)	SYSTEMS ANALYSIS
MSFC COUNTERPART:	R. S. RYAN
DATE:	AUGUST 1, 1983
CONTRACT NUMBER:	NGT 01-008-021
	The University of Alabama in Huntsville

FINITE ELEMENT ANALYSIS OF A DEPLOYABLE SPACE STRUCTURE

by

George E. Weeks, Ph.D.
Professor of Aerospace Engineering
University of Alabama
Tuscaloosa, Alabama

ABSTRACT

This investigation is concerned with evaluating the dynamic characteristics of the SAFE structure during deployment and retraction. The SAFE structure consists of a deployable mast (EI = $18*10^6$ lb-in^2, GJ = $0.36*10^6$ lb-in^2, L = 0-1260") with an attached solar "blanket" (158" x 0-1260") designed with accordion-type folds to permit packaging in a small volume (158" x 15" x 10"). The planar form of the blanket geometry during deployment is maintained by a blanket tension/guidewire system.

Structurally, the mast is modeled as an Euler beam column with inplane and out-of-plane bending and finite torsional stiffness. For out-of-plane motion, the blanket is modeled as a distributed mass uniformly supported by the three guidewires. For inplane motion the blanket displacements are assumed to vary linearly from the mast base to the mast tip.

The mathematical model uses a virtual work formulation, required because the axial loading on the mast is nonconservative, combined with assumed beam modes to derive the differential equations of motion. Consideration of the time-dependent boundary conditions results in an infinite set of ODE with time-dependent coefficients. These equations are solved for the a) eigenvalues of the structure during deployment and b) the system dynamic response for evaluation of dynamic stability characteristics. Finally, correlation of mast tip accelerations to mast base bending moments for specified modal motions are indicated.

LIST OF FIGURES

FIGURE	TITLE	PAGE
1	SAFE Structure (Partial Extension)	XXXIV-7
2	Array Extension Mast	XXXIV-8
3	SAFE (Fully Deployed)	XXXIV-9
4	Containment Box Structure	XXXIV-10
5	SAFE Extension Sequence	XXXIV-11
6	Guidewire and Blanket Tension-Longeron Loads	XXXIV-12
7	SAFE Mast Tip Assembly	XXXIV-13

NOMENCLATURE

Symbols	Definition
e_1	Mast tip eccentricity
e_2	Mast tip to blanket tip distance
EI	Mast bending stiffness
Iy	Mast tip mass moment of inertia
K_T	Mast compliance
L	Instantaneous length of mast
M	Mast tip mass
T	Mast compressive force
T_b	Blanket tension
ω	Blanket normal displacement
y	Mast normal displacement
ρ	Mass per unit length
ζ	Mast base motion

INTRODUCTION

The Solar Array Flight Experiment (SAFE) structure is a deployable three-dimensional structure designed to demonstrate the shuttle capability to deploy one type of a large space structure on-orbit, maneuver, and retract the structure to the original stowed position. Vibration angles using the finite element method have been performed for this structure at 70% and 100% deployment [1,2]. However, analysis of the dynamic stability characteristics of the structure during the deployable modes of extension and retraction has not been investigated. Accordingly, this report describes such an analysis of the SAFE structure including determination of the eigenvalues of the system during deployment as well as the dynamic stability characteristics resulting from the time-dependent boundary conditions of the system.

The solution of problems with nonstationary boundaries present considerable mathematical difficulties, principally because they result in partial differential equations of motion with (time) variable coefficients. Although problems of this type are encountered in heat conduction and ablating boundary configurations, subject areas most closely associated with the topic considered herein are those in the textile industry concerned with moving threadlines [3] and the machine tool industries typically concerned with vibration and response characteristics of belt-pully, bandsaw type configurations [4].

While these problems have all been concerned with nonstationary boundaries, apparently the only investigation to date concerning the transverse vibrations of beams with a moving boundary was presented by Worley (5). Here the 2-D motion of a uniform Euler beam whose length is varying with a constant rate was studied using an asymtotic (perturbation) method of analysis. The basic formulation of the equations of motion was the same as presented herein. However, the asymtotic method of analysis is not applicable for a study of the dynamic characteristics of the SAFE structure.

THE SAFE STRUCTURE*

A summary view of the SAFE structure during deployment is shown in Figure 1. Deployability is made possible by the array extension mast (Figure 2) which consists of a coilable longeron, lattice structure of triangular cross-section nested in an aluminum cylinder cannister with a mast-cannister interface compliance of 300,000 in-lb/rad. The longerons are 0.25 in. diameter 5-glass epoxy with triangular batten frames located at 9 in. intervals along the mast length. The remaining detailed construction is such that the overall mast can be considered to have a uniform bending stiffness in the two planes parallel and perpendicular to the blanket of EI = $18*10^6$ lb-in^2, torsional stiffness GJ = $0.36*10^6$ lb-in^2, and a total weight of 41.6 lb when deployed to the maximum length of 105 feet.

The array blanket is composed of 84 stiffened substrate panels (Figure 3) 15 in. by 158 in. in size connected to each other with a piano type hinge composed of Kapton hinge loops and a 158 in. long fiberglass epoxy hinge pin (0.032 in dia.). Total weight of the blanket is 303 lb and when packaged, fits into a containment box structure (Figure 4) with volume approximately 10 in. by 15 in. by 158 in. During deployment the blanket is untensioned until it is 70% extended and the bottom 30% of the blanket is untensioned until it is fully extended. Guide wires running through grommets attached to every other panel hinge pin keeps the blanket in the plane between the containment box cover and base and prevents it from billowing out if it were to leave the box during extension. This guide wire system also aids the zero-gravity fold of the blanket when blanket tension is removed. Nominal constant tension values in the guide wires are maintained by negator powered storage reels on the underside of the container floor. Details of the array extension sequence is shown in Figure 5 with specific values of guide wire, blanket, and mast loads shown in Figure 6.

Finally, the blanket is offset from the mast centroid 10.6 in (Figure 6) by a relatively rigid cover assembly, tip fitting, and mast to blanket connection assembly as shown in Figure 1 with detail geometry and mass properties as indicated in Figure 7. For this investigation, this entire mast tip assembly is considered rigid.

*All structural descriptions and Figures indicated are taken from Refs. [1] and [2].

WING ASSEMBLY (PARTIALLY DEPLOYED)

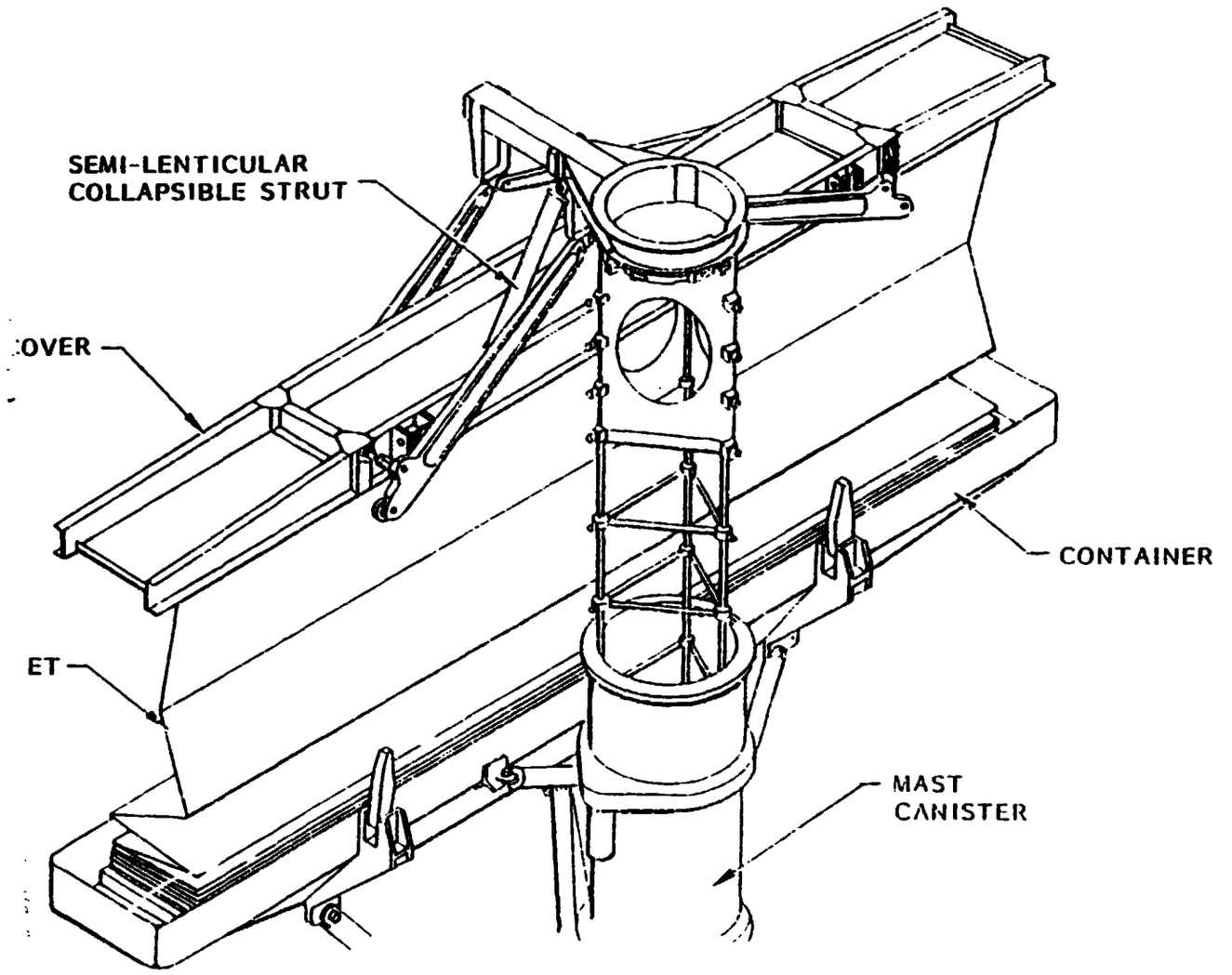

Figure 1. Summary View SAFE Structure

SOLAR ARRAY EXTENTION MAST

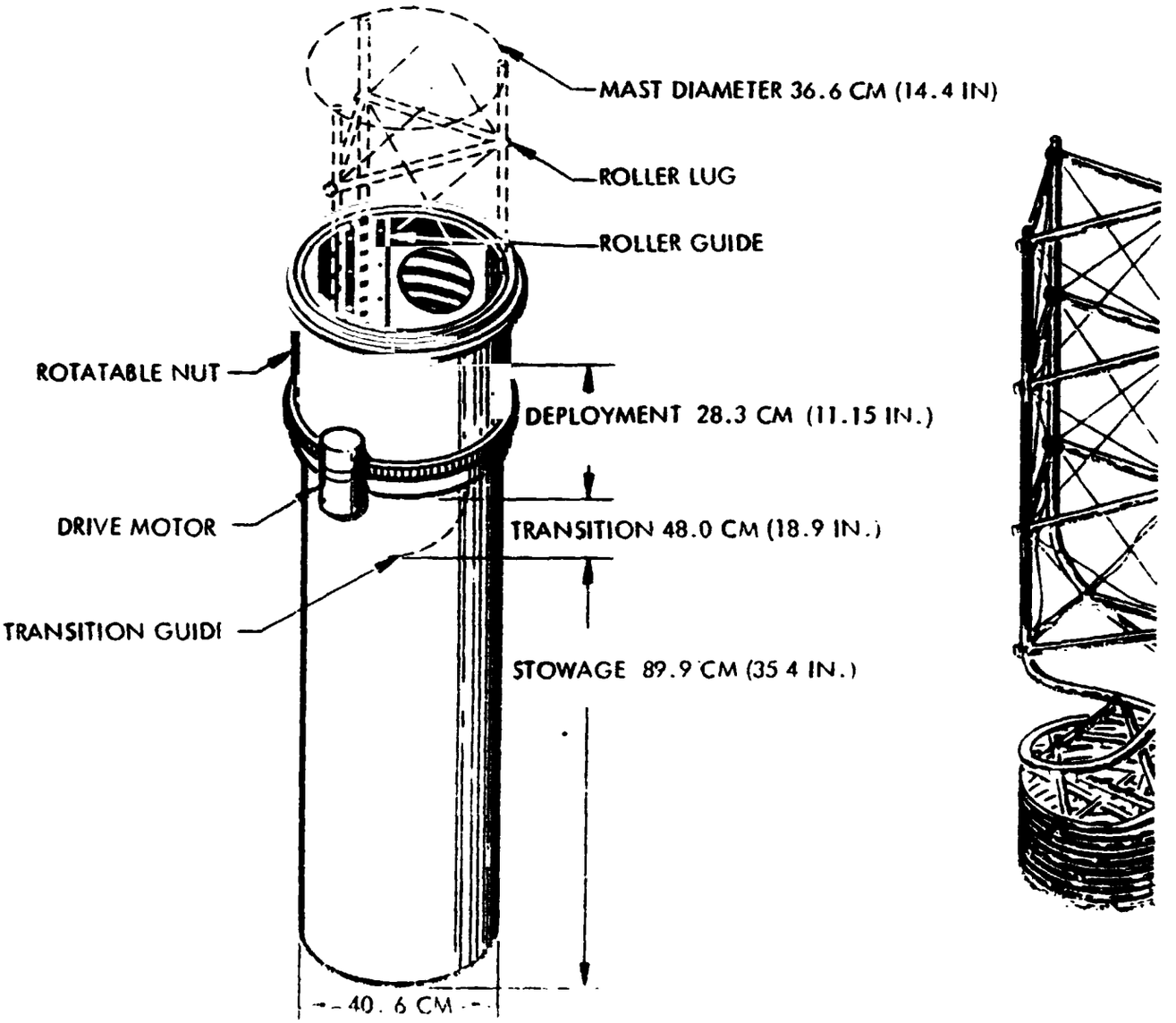

Figure 2. Solar Array Extension Mast

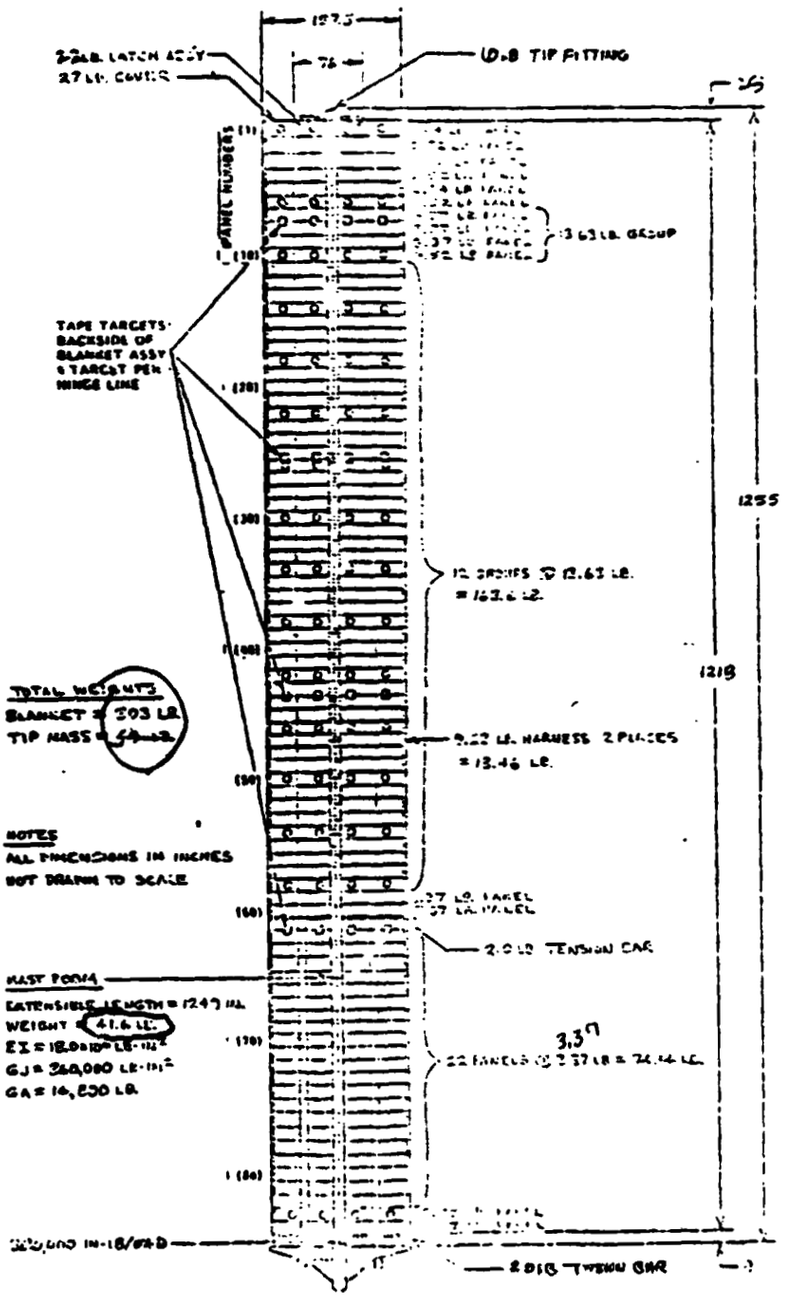

Figure 3. Array Blanket-Detail

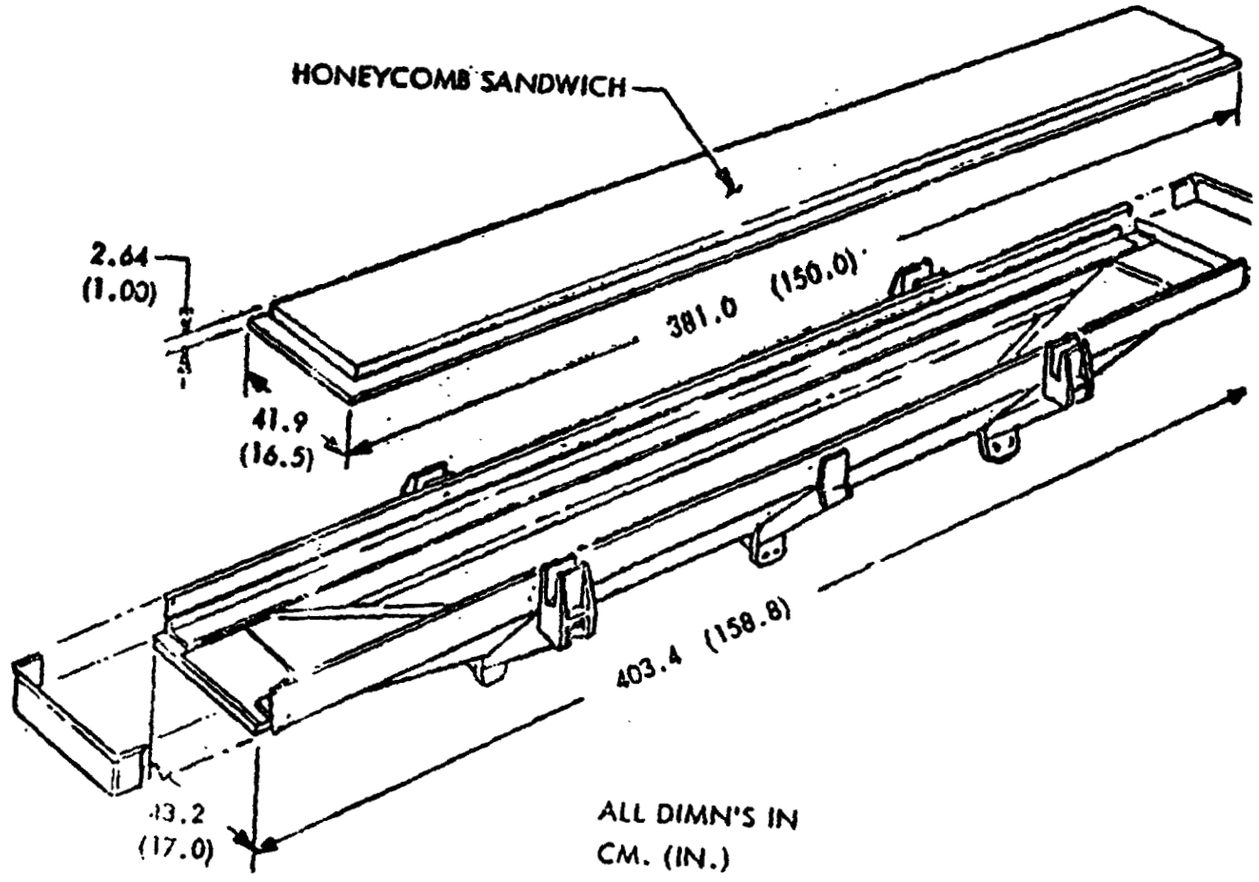

Figure 4. Array Containment Box

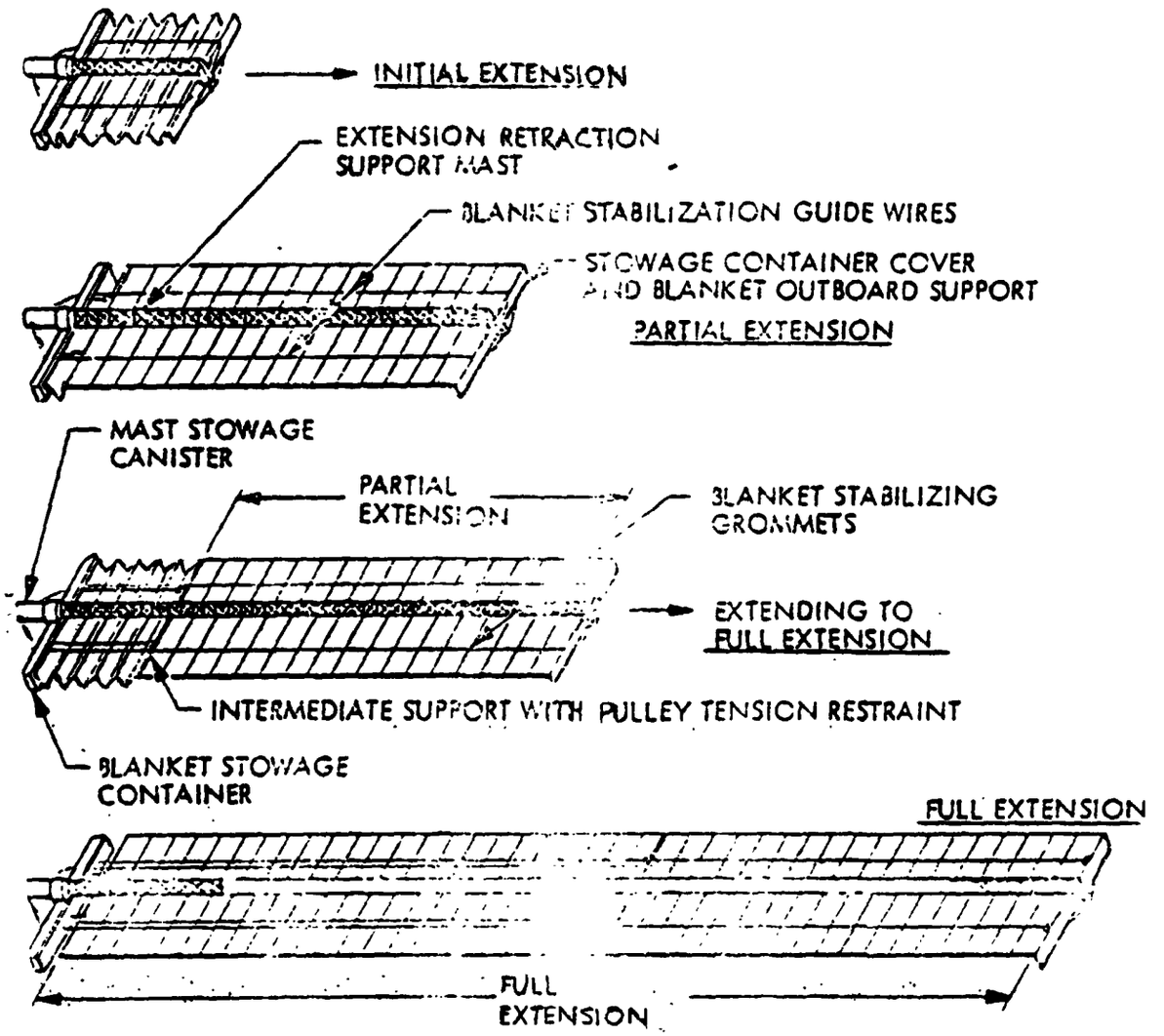

Figure 5. SAFE Extension Sequence

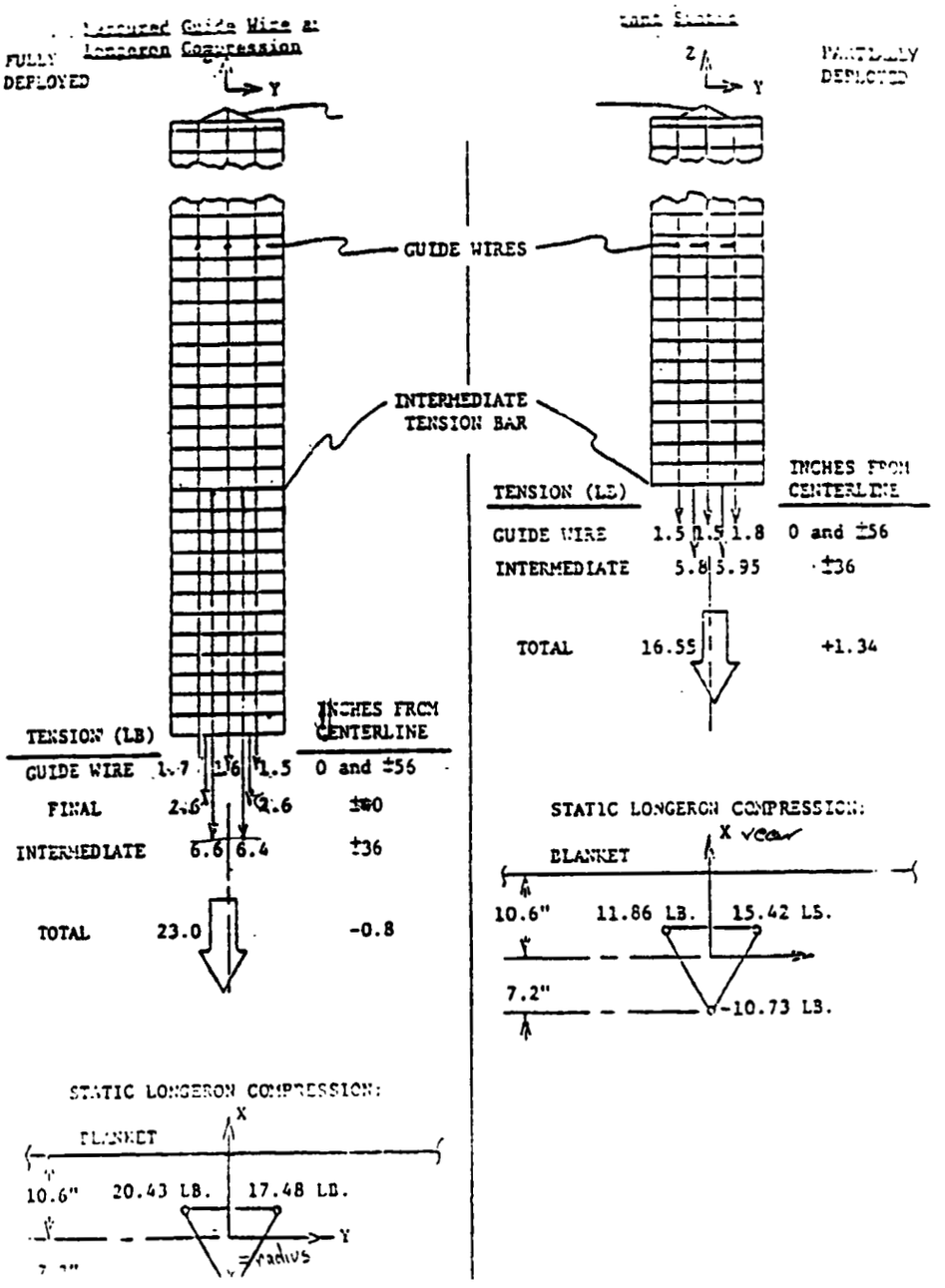

Figure 6. Detail Loads-SAFE 70% & 100% Deployment

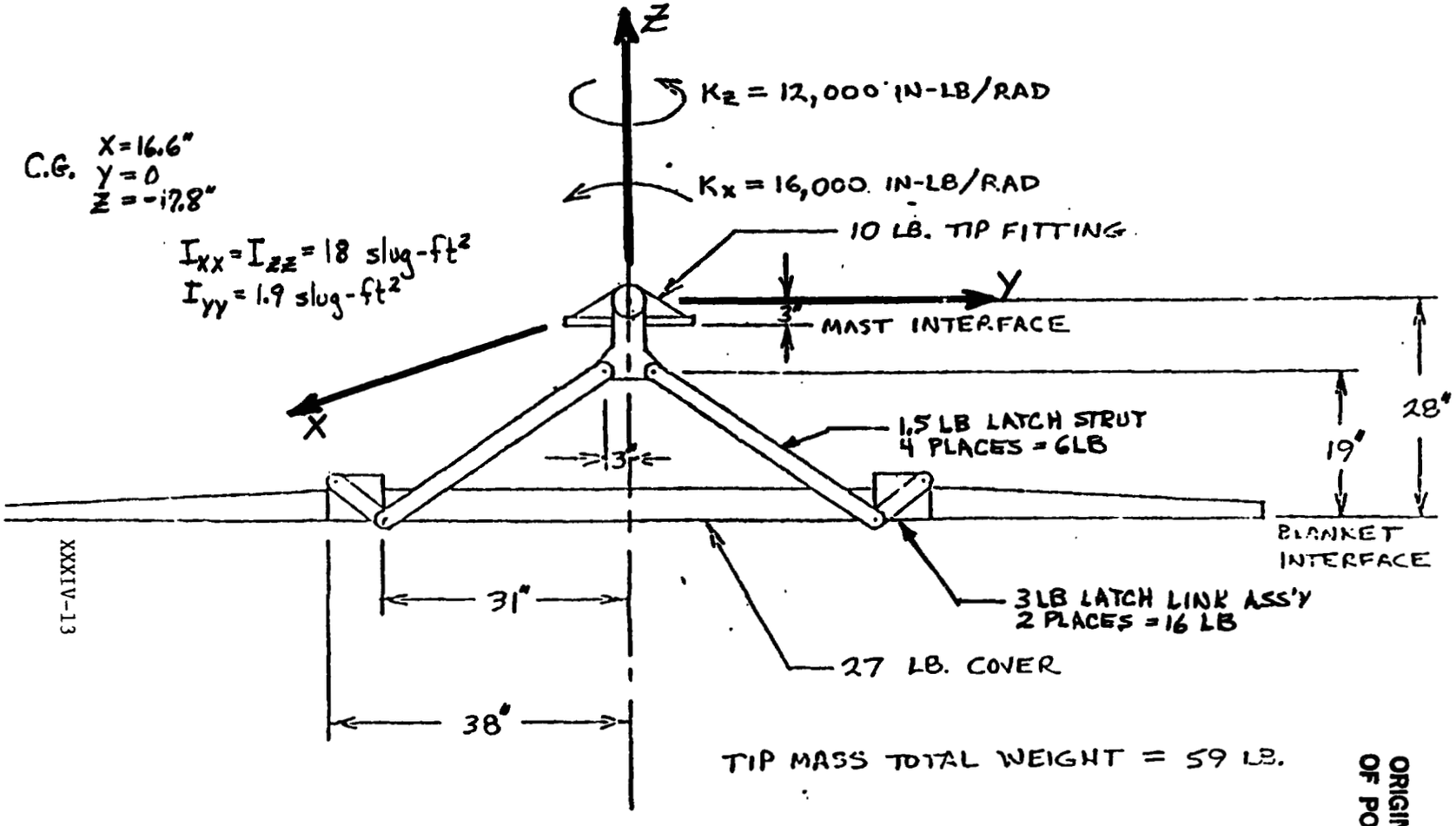

Figure 7. Mast Tip Fitting

MATHEMATICAL MODEL

Justification

The SAFE structure has been analyzed to determine its natural frequencies and mode shapes at 70% and 100% deployment [2] using the Structural Performance Analysis and Redesign (SPAR) code [6] This code was written for general structural analysis using the finite element method. Although this code could conceptually be used for the dynamic stability study presented here, it would require the solution of several hundred sets of algebraic equations (corresponding to the required several hundred DOF necessary to accurately the SAFE) at each time step-requiring prodigious amounts of comp time for simulating complete mast extension and retraction histo for the multitude of parameters that need to be investigated. In addition, consideration of the time-dependent length of the mast and blanket during deployment would require, at least, the reformulation of the mass, stiffness, and psuedo damping matrices at each time step.

In view of these considerations, and with the hindsight of the previously performed finite element frequency analysis in hand [2], it was felt that the most efficient method for the dynamic response analysis would be to use assumed beam modes for the mast and assumed membrane modes for the blanket. The accuracy (and convergence) characteristics of these assumed modes can be evaluated by calculating the corresponding natural frequencies and comparing with the finite element results. If good agreement is obtained, these modes could be used with confidence in the dynamic response (stability) analysis.

Virtual Work Formulation

The coupled in-plane and out-of-plane response behavior of the mast-blanket system is a complex motion requiring detailed three-dimensional sketches to accurately comprehend, and lengthy explanations for each of the required terms in the virtual work formulation. Thus, for clarity of presentation, and since the primary goal of this effort was to develop a model that accounts for the deployable dynamics of the SAFE, only the equations and results corresponding to the two-dimensional out-of-plane blanket motion will be presented here. The corresponding development for the three dimensional problem is shown in the Appendix.

A virtual work formulation is required because the compressive force in the mast during deployment is nonconservative. A 2-D sketch of the idealized SAFE mode used is shown below in the undeformed and deformed configuration. The corresponding virtual work statement for this model is given by the following expression

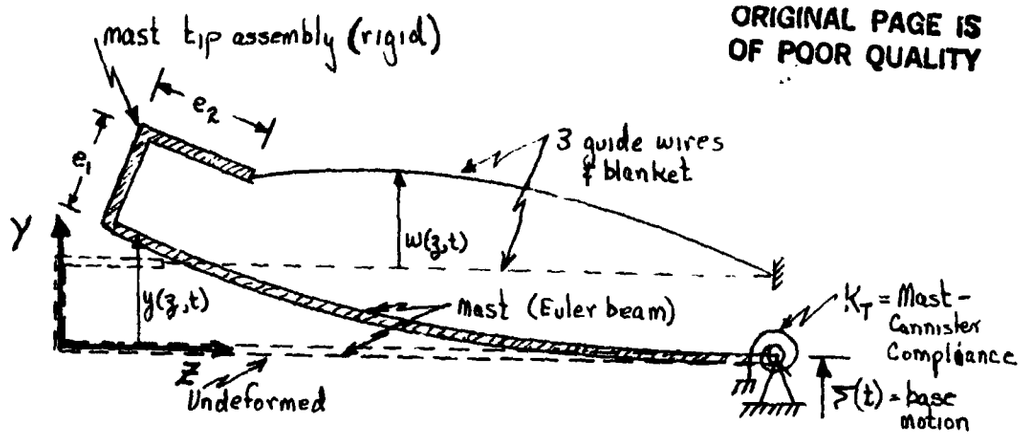

Sketch - Idealized Model For Blanket And Mast Configuration

$$\delta W^{total} = \delta W^{I} + \delta W^{II} + \delta W^{III} + \delta W^{IV} + \delta W^{V} + \delta W^{VI} + \delta W^{VII} + \delta W^{VIII} \tag{1}$$

where

δW^{I} = Virtual work mast bending

$$= -\int_0^L EI\, y''(z,t)\, \delta y''(z,t)\, dz \tag{2}$$

δW^{II} = Virtual work mast compressive force

$$= T\left\{\int_0^L y'(z,t)\,\delta y'(z,t)\,dz + \left[-e_1 - \frac{e_2}{L}\left(y(0,t) + e_2 y'(0,t)\right)\right]\delta y'(0,t) - \frac{1}{L}\left[y(0,t) + e_2 y'(0,t)\right]\delta y(0,t)\right\} \tag{3}$$

δW^{III} = Virtual work mast compliance

$$= -K_T\, y'(L,t)\,\delta y'(L,t) \tag{4}$$

δW^{IV} = Virtual work blanket and guide wire tension

$$= -T_b \int_0^L w'(z,t)\,\delta w'(z,t)\,dz \tag{5}$$

δW^{V} = Virtual work mast translational inertia including base motion

$$= -\rho_c \int_0^L \left[\ddot{y}(z,t) + \ddot{\bar{s}}(t)\right]\delta y(z,t)\,dz \tag{6}$$

δW^{VI} = Virtual work blanket and guide wire translational inertia including base motion

$$= -\rho_b \int_0^L \left[\ddot{w}(z,t) + \ddot{\bar{s}}(t)\right]\delta w(z,t)\,dz \tag{7}$$

δW^{VII} = Virtual work rigid mast tip cover assembly translational and rotational inertia

$$= -M\left[\ddot{y}(0,t) + \ddot{\bar{s}}(t)\right]\delta y(0,t) - I_g \ddot{y}'(0,t)\,\delta y'(0,t) \tag{8}$$

δW^{VIII} = Virtual work longitudinal (extensional) acceleration of SAFE

$$= -\int_0^L \left(M\ddot{L} + \rho_c L_4 \ddot{L} + \rho_b L_4 \ddot{L}\right) y'(z,t)\,\delta y'(z,t)\,dz \tag{9}$$

In these equations, dots denote differentiation with time and primes denote differentiation wrt z. Note that the coordinate z denotes the distance to a fixed point on the mast (and blanket).

For this analysis, it is convenient (and also efficient from a computational viewpoint) to transform these equations into a form such that the boundary conditions are not a function of time. This is accomplished by the transformation

$$x = z/L$$

where L is the time dependent length of mast (and blanket). The mast and blanket boundaries are then transformed from z = 0, L to x = 0,1. The derivatives with respect to z and t in Eqns. 2-8 now become

$$(\quad)' = \frac{1}{L}\frac{\partial(\quad)}{\partial x} \qquad (\quad)'' = \frac{1}{L^2}\frac{\partial^2(\quad)}{\partial x^2}$$

$$(\quad)^{\cdot\cdot} = \frac{\partial^2(\quad)}{\partial t^2} - 2\frac{\dot{L}}{L}x\frac{\partial^2(\quad)}{\partial x\,\partial t} + \left(-\frac{\ddot{L}}{L} + 2\frac{\dot{L}^2}{L^2}\right)x\frac{\partial(\quad)}{\partial x} + x^2\frac{\dot{L}^2}{L^2}\frac{\partial^2(\quad)}{\partial x^2} \tag{10}$$

where $\dot{L}$ and $\ddot{L}$ on the right hand side of Eqn. 10 indicates the velocity and acceleration respectively, of mast and blanket during deployment.

The final equations of motion are now derived by assuming that the mast deflections y(x,t) and blanket deflections z(x,t) can be expressed in the form

$$y(x,t) = \sum_{n=0}^{\infty} A_n(t)\,Y_n(x) \tag{11}$$

$$w(x,t) = \sum_{n=0}^{\infty} B_n(t)\,W_n(x) + \sum_{n=0}^{\infty} A_n(t)\,Y_n(0)\,(1-x) \tag{12}$$

$$W_n(x) = \sin n\pi x$$

The $Y_n(x)$ in Eqn. 11 is the nth eigenfunction of a free-rotationally restrained fixed length beam of length 1. (The eigenfunctions and corresponding eigenvalues for this beam with a compliance K_T=300,000 in-lb/rad is presented in the Appendix. Use of these eigenfunctions result in approximately 50% less number of assumed modes than required for similar accuracy when using the classical free-free beam modes. This results in considerable savings in computer time and storage required when performing the eigenvalue and dynamic response analysis of the SAFE structure).

Substituting Eqns. 11-12 into Eqns. 2-9, and using Eqn. 10 results in the equations of motion

$$\begin{bmatrix} K^c_{mn} & K^b_{mn} \\ k^c_{mn} & k^b_{mn} \end{bmatrix} \begin{Bmatrix} A_n \\ B_n \end{Bmatrix} + \begin{bmatrix} D^c_{mn} & D^b_{mn} \\ d^c_{mn} & d^b_{mn} \end{bmatrix} \begin{Bmatrix} \dot{A}_n \\ \dot{B}_n \end{Bmatrix} + \begin{bmatrix} S^c_{mn} & S^b_{mn} \\ s^c_{mn} & s^b_{mn} \end{bmatrix} \begin{Bmatrix} \ddot{A}_n \\ \ddot{B}_n \end{Bmatrix} = \begin{Bmatrix} F_m \\ R_m \end{Bmatrix} \quad (13)$$

where

$$K^c_{mn} = -\frac{EI}{L^3}\int_0^1 Y_n''(x) Y_m''(x)\,dx - \frac{K_T}{L^2} Y_n'(1) Y_m'(1) + \frac{I}{L}\int_0^1 Y_n'(x) Y_m'(x)\,dx - \frac{Ie_2}{L^2}\left(Y_n(0) Y_m'(0) + \frac{e_2}{L}\left(Y_n'(0) Y_m'(0)\right) - \frac{I}{L}\left(Y_n(0) Y_m(0) + \frac{e_2}{L} Y_n'(0) Y_m'(0)\right) + \rho_c L \int_0^1 \left[x^2 \frac{\dot{L}^2}{L^2} Y_n''(x) Y_m(x) + \left(2\frac{\dot{L}^2}{L^2} x - \frac{\ddot{L}}{L} x\right) Y_n'(x) Y_m(x)\right] dx + \rho_b L \int_0^1 \left(2\frac{\dot{L}^2}{L^2} x - \frac{\ddot{L}}{L} x\right) Y_n(0) Y_m(0)(1-x)\,dx - \frac{I_b}{L}\int_0^1 Y_n(0) Y_m(0)\,dx - \int_0^1 \left(m\ddot{L} + \rho_c L x \ddot{L} + \rho_b L x \ddot{L}\right) Y_n(x) Y_m(x)/L\,dx$$

$$D^c_{mn} = -\rho_c L \int_0^1 \left(-2\frac{\dot{L}}{L} x\right) Y_n'(x) Y_m'(x)\,dx - \rho_b L \int_0^1 2\frac{\dot{L}}{L} x\, Y_n(0) Y_m(0)(1-x)\,dx + \frac{I}{L} W_n'(0)\left[Y_m(0) + e_2 Y_m'(0)\right]$$

$$S^c_{mn} = -\rho_c L \int_0^1 Y_n(x) Y_m(x)\,dx - M Y_n(0) Y_m(0) - \frac{I_y}{L^2} Y_n'(0) Y_m'(0) - \rho_b L \int_0^1 Y_n(0) Y_m(0)(1-x)^2\,dx \quad (14)$$

$$K^b_{mn} = -\rho_b L \int_0^1 \left(x^2 \frac{\dot{L}^2}{L^2} W_n''(x) + \left(2\frac{\dot{L}^2}{L^2} x - \frac{\ddot{L}}{L} x\right) W_n'(x)\right) Y_m(0)(1-x)\,dx + \frac{I_b}{L}\int_0^1 W_n'(x) Y_m(0)\,dx$$

$$D^b_{mn} = -\rho_b L \int_0^1 -2\frac{\dot{L}}{L} x\, W_n'(x) Y_m(0)(1-x)\,dx$$

$$S^b_{mn} = -\rho_b L \int_0^1 W_n(x) Y_m(0)(1-x)\,dx$$

$$k^c_{mn} = \rho_b L \int_0^1 \left(2\frac{\dot{L}^2}{L^2} x - \frac{\ddot{L}}{L} x\right) Y_n(0)\, W_m(x)\,dx + \frac{I_b}{L}\int_0^1 Y_n(0) W_m'(x)\,dx$$

$$d^c_{mn} = -\rho_s L \int_0^1 2\frac{\dot{L}}{L}\eta\, Y_n(0) W_m(\eta)\, d\eta$$

$$k^b_{mn} = -\rho_b L \int_0^1 \left[\eta^2 \frac{\dot{L}^2}{L^2} W_n''(\eta) + \left(2\frac{\dot{L}^2}{L^2}\eta - \frac{\ddot{L}}{L}\eta\right) W_n'(\eta)\right] W_m(\eta)\, d\eta - \frac{I_b}{L}\int_0^1 W_n'(\eta) W_m'(\eta)\, d\eta$$

$$d^b_{mn} = \rho_b L \int_0^1 2\frac{\dot{L}}{L}\eta\, W_n'(\eta)\, W_m(\eta)\, d\eta$$

$$s^b_{mn} = -\rho_b L \int_0^1 W_n(\eta)\, W_m(\eta)\, d\eta \qquad \text{(14 Cont'd)}$$

$$s^c_{mn} = -\rho_b L \int_0^1 Y_n(0) W_m(\eta)(1-\eta)\, d\eta$$

$$F_m = T\frac{e_i}{L} Y_m'(0) + \left[\rho_c L \int_0^1 Y_m(\eta)\, d\eta + \rho_b L \int_0^1 Y_m(0)(1-\eta)\, d\eta - M Y_m(0)\right]\ddot{S}(t)$$

$$R_m = \rho_b L \ddot{S}(t) \int_0^1 W_m(\eta)\, d\eta$$

The time history of the response of the SAFE can now be obtained by integrating Eqn. 13 to determine the time-dependent amplitude coefficients (A and B) and using these results in Eqns. 11-12 to evaluate the mast and blanket deflections, velocities, and accelerations as functions of space and time. By setting the right hand side of Eqn. 13 equal to zero and assuming A and B to vary as exp(αt), the (complex) eigenvalues α of the structure may be determined. Finally, it is of interest to note, from Eqns. 13-14, that consideration of the moving boundary results in a psuedo damping matrix as well as an unsymmetric stiffness matrix. The damping matrix permits the possibility of complex eigenvalues and hence, dynamic instability of the SAFE structure during extension and retraction.

RESULTS AND DISCUSSION

The accuracy of the SAFE model used can be partially assessed by comparing the eigenvalues at 70% and 100% (static) deployment with those obtained from Ref. 2. Results of this comparison using five beam modes and five blanket modes are shown below for the first three out-of-plane natural frequencies of the SAFE structure. The agreement between the

		Natural Frequency (Hz)		
		1	2	3
Present Investigation	70%	.058	.108	.179
	100%	.036	.092	.145
Ref. 2	70%	.059	.119	.196
	100%	.034	.096	.153

ten DOF system of the current investigation is seen to be in excellent agreement with the several hundred DOF finite element analysis of Ref. 2. As a consequence, it is felt that a dynamic analysis of the SAFE structure using the 10 DOF model herein should yield accurate results.

A typical response of the mast tip deflection and acceleration is shown in the sketch below. These results were obtained using a constant deployment speed of 1.5 in/sec. Tension forces on the guide wires and blanket, and compressive forces on the mast during extension and retraction were as presented in Fig. 6.

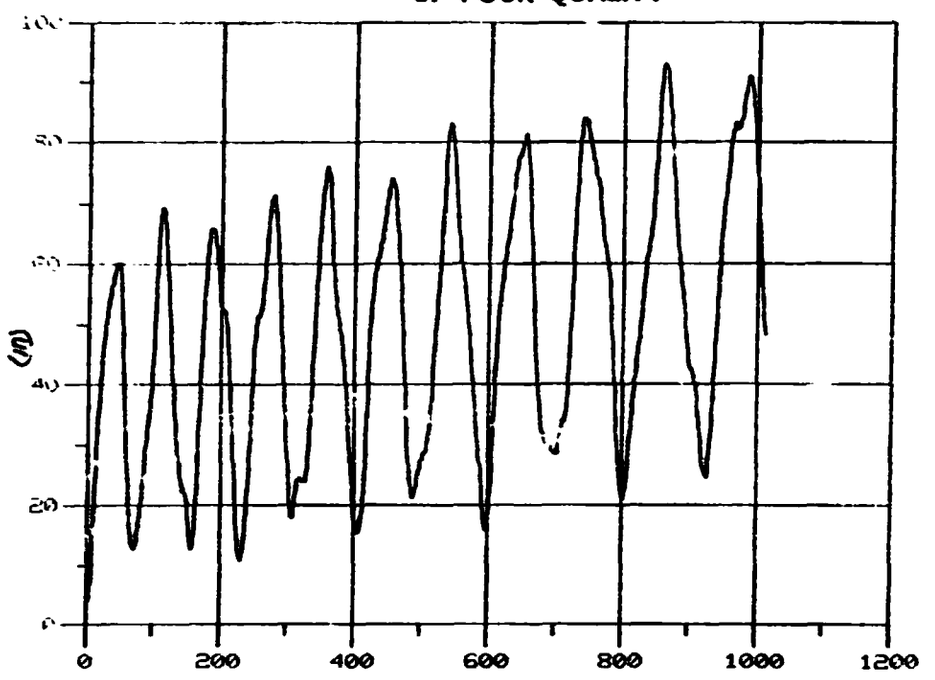

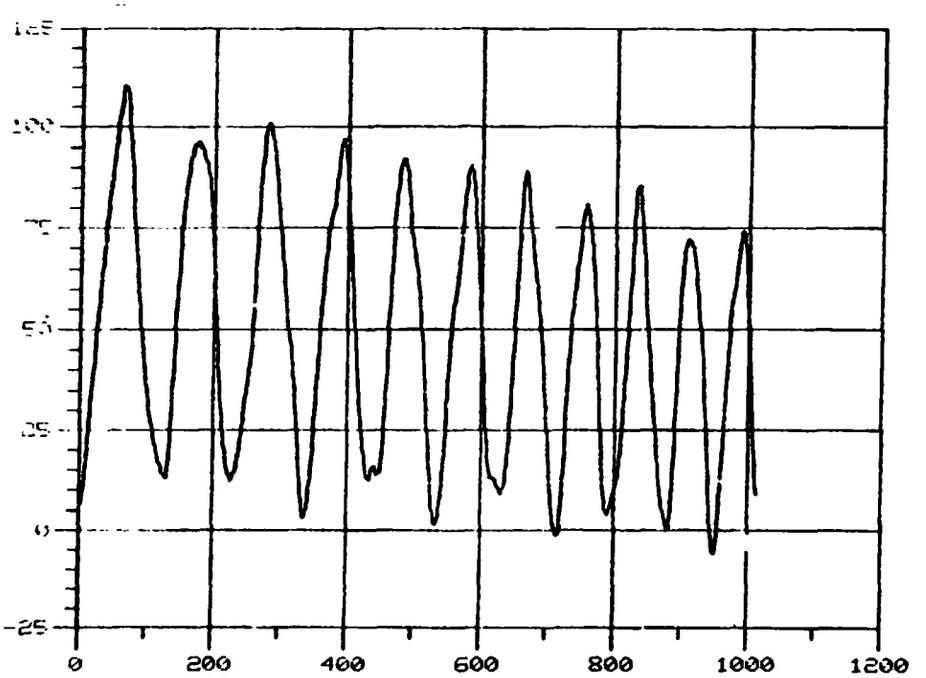

MAST TIP DEFLECTION

CONCLUSIONS AND RECOMMENDATIONS

An efficient algorithm for investigating the deployable dynamics of the SAFE type structure has been presented. The accuracy of the model for a 2-D analysis of natural frequencies has been verified by comparing with a detailed finite element analysis at 70% and 100% deployment. Time did not permit coding and debugging of the equations for 3-D motion. However, results obtained for the 2-D case indicate significant variations in dynamic response with rather small changes in certain parameters such as mast base motion, variation in mast axial load with deployed length, and variation in deployment velocities and accelerations. As a result, it is suggested that the complete 3-D analysis be coded and an extensive parameter study be carried out on the dynamic stability characteristics of the SAFE structure. Finally, while a psuedo-damping matrix is present in this analysis, due to the time-dependent length, it is suggested that the analysis presented here be extended to determine the modal mass and stiffness matrices of the structure and solve the resulting equations of motion including realistic modal damping values of 1/4%, 1/2%, etc. as judged appropriate for this configuration.

REFERENCES

1. Elms, R. V., "SEP Solar Array Shuttle Flight Experiment," Spec. No. 9000602, Lockheed Missiles and Space Co., Sunnyvale, Cal., Contract No. NA58-31352, Oct. 13, 1981.

2. Venator, T., "Updated Solar Array Flight Experiment Modesl," Engineering Memorandum No. SD/R-536, April 5, 1983.

3. Swope, R. D., Ames, W. F., "Vibrations of a Moving Threadline," Journal of the Franklin Institute, Vol. 275, 1963, pgs. 36-55.

4. Mote, C. D., Naguleswaran, S., "Theoretical and Experimental Band Saw Vibrations," Journal of Engineering for Industry, Vol. 88, Series B, 1966, pgs. 151-156.

5. Worley, H. E., "Dynamic Response of Beams to Time-Varying Length," Dessertation, University of Alabama, 1969.

6. SPAR Structural Analysis System Reference Manual, NASA CR 158970-2, 1978.

APPENDIX

Eigenfunctions and eigenvalues. The beam modes used in this analysis (Eqn. 11) correspond to those of a beam free at the left end and rotationally restrained at the right end ($K_T/EI = 0.01667$). For this case the eigenfunctions for free vibration are

$$Y_n(x) = \cosh \lambda_n x + \cos \lambda_n x - k_n(\sinh \lambda_n x + \sin \lambda_n x) \quad \text{(A1)}$$

where

$$k_n = (\cosh \lambda_n + \cos \lambda_n)/(\sinh \lambda_n + \sin \lambda_n) \quad \text{(A2)}$$

and the first ten eigenvalues are

$$\begin{aligned} \lambda_1 &= 1.7947724 & \lambda_6 &= 16.859803 \\ \lambda_2 &= 4.5194452 & \lambda_7 &= 19.966843 \\ \lambda_3 &= 7.5950817 & \lambda_8 &= 23.079604 \\ \lambda_4 &= 10.670567 & \lambda_9 &= 26.196822 \\ \lambda_5 &= 13.760235 & \lambda_{10} &= 29.317565 \end{aligned} \quad \text{(A3)}$$

Three-dimensional virtual work formulation. A sketch of the 3-D deformation is shown below as well as the additional virtual work terms (Eqn. 1) necessary for a 3-D formulation of the equations of motion.

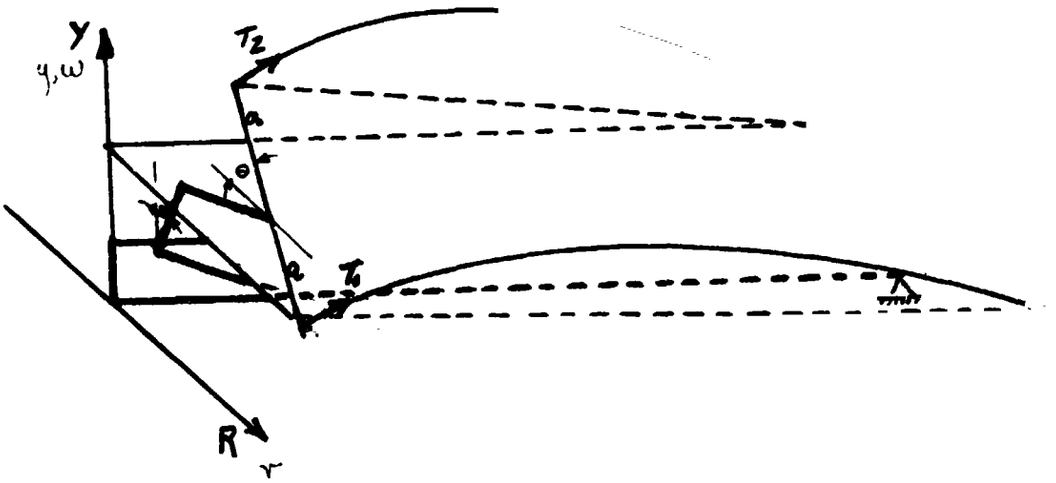

$$\delta W_{3\text{-}D} = -EI\int_0^L v''(z,t)\delta v''(z,t)dz - I_z\ddot{\theta}(0)\delta\varphi(0) - \rho_b\int \ddot{v}(z,t)\delta v(z,t)dz$$
$$-T_1\int_0^L p'(z,t)\delta p'(z,t)dz - T_2\int_0^L q'(z,t),\delta q'(z,t)dz$$
$$-\int_0^a T_b(\omega'(z,t)-\beta)z\,\delta\varphi + [(T_2-T_1)y(0) - (T_2+T_1)a\varphi]_L\delta\varphi(L)$$

where

$$p(z,t) = y(z,t) + a\varphi(z)$$

$$q(z,t) = y(z,t) - a\varphi(z)$$

and now

$$\omega(x,t) = A_n\sum \sin n\pi x + [y(0,t) + \theta(0,t)z + V(0)(1-x)]$$

ORIGINAL PAGE IS
OF POOR QUALITY

1983

NASA/ASEE SUMMER FACULTY RESEARCH FELLOWSHIP PROGRAM

MARSHALL SPACE FLIGHT CENTER
THE UNIVERSITY OF ALABAMA IN HUNTSVILLE

EVALUATION OF THE SEPARABILITY OF MONODISPERSE POLYSTYRENE LATEX MICROSPHERES IN A CONTINUOUS FLOW ELECTROPHORESIS SYSTEM

Prepared By:	Mr. George Williams, Jr.
Academic Rank:	Chairman, Dept. of Science
Academic Institution:	Calhoun State Community College Decatur, AL 35602
NASA/MSFC:	
(Laboratory)	Space Science Laboratory
(Division)	Space Processing
(Branch)	Separation Processes
MSFC Counterpart:	Dr. Robert S. Snyder
Date:	August 12, 1983
Contract No.:	NGT 01-008-021 The University of Alabama in Huntsville

EVALUATION OF THE SEPARABILITY OF MONODISPERSE POLYSTYRENE LATEX MICROSPHERES IN A CONTINUOUS FLOW ELECTROPHORESIS SYSTEM

By

George Williams, Jr.
Department of Natural Science
Calhoun State Community College
Decatur, AL

Abstract

The continuous flow electrophoresis system makes electrophoresis possible in a free-flowing film of aqueous electrolyte medium. The sample is introduced at one end of the chamber and is subjected to a lateral DC field. This process separates the sample into fractions since each component has a distinctive electrophoretic mobility. Evaluations were made of sample conductivity and buffer conductivity as they affect sample band spread and separation using the Continuous Particle Electrophoresis (CPE) system. Samples were prepared from mixtures of 5 percent and 1 percent PSL microspheres which were .4, .56 and .7 microns in diameter. These were prepared in electrolyte media 1x and 3x the conductivity of the curtain buffer, approximately 150 and 450 micro mhos/cm. Samples with matched conductivities produced greater resolution and less band spread than those with 3x the conductivity of the curtain buffer.

ACKNOWLEDGEMENTS

I wish to express appreciation to the following individuals who have provided assistance in this research. Dr. Robert Snyder, Chief, Separation Processes Branch, Space Processing Division, who served as my NASA counterpart and co-investigator in these studies. Ms. Teresa Miller for providing the experimental design, expertise with the CPE system and serving as co-investigator. Mr. Fred Herrmann who designed the computer software for data treatment and presentation. Ms. Jewell Reynolds for typing the final report.

Appreciation is also expressed to Dr. Gerald Karr, Mr. Leroy Osborn and Dr James Dozier for their support and the administration of the Summer Faculty Fellowship Program.

LIST OF FIGURES

Figure No.	Title	Page
1	1% RWB PSL in 1x conductivity	XXXV-7
2	1% RWB PSL in 1x conductivity	XXXV-8
3	1% RWB PSL in 3x conductivity	XXXV-9
4	1% RWB PSL in 3x conductivity	XXXV-10
5	5% RWB PSL in 1x conductivity	XXXV-11
6	1% and 1.6% Blue PSL in 1x conductivity	XXXV-12
7	1.6% and 5% Blue PSL in 1x conductivity	XXXV-13

I. Introduction

In the Space Science Laboratory, Separation Processes Branch, electrophoresis investigations have been conducted using a variety of particles, cells, instrumentation, buffers, measurements, collection techniques and procedures. Snyder discussed in detail several phases of the ground-based studies which have been conducted at MSFC.[1] NASA has included electrophoresis experiments on the two most recent Space Shuttle flights. Ground-based studies of several parameters using continuous flow electrophoresis have been the thrust of the work included in this report.

II. Objectives

1. To evaluate the separability of PSL microspheres at various concentrations within the sample medium.

2. To evaluate the separability of PSL microspheres relative to the conductivity of sample vs. that of the aqueous curtain.

3. To enhance treatment of data by modification of existing computer software.

4. To provide photographic documentation of particle stream characteristics in the lateral DC field.

III. Methods and Materials

In order to evaluate the separability of selected monodisperse polystyrene latex (PSL) microspheres, a Beckman Continuous Particle Electrophoresis (CPE) system was used. The CPE system makes electrophoresis possible in a free-flowing film of aqueous electrolyte medium. The chamber is 1.5 mm thick, 45 mm wide and 500 mm long. The electrodes are 300 mm long and are housed on each side of the chamber within cellulose acetate membranes in order to separate the electrode chamber from the electrophoresis chamber. The sample, which continuously enters the electrolyte at the top of the chamber, is subjected to the action of a lateral DC field. This divides the sample into fractions since each has a distinctive electrophoretic mobility based upon differences in surface charge density or zeta potential.[2]

Samples were prepared from mixtures of 5, 1.6, and 1 percent PSL microspheres which were .4, .56 and .7 microns in diameter. Since identical samples were flown on STS-6 and STS-7, the suspension medium was a propionate buffer (designed by MDAC; chemical composition classified) and polyoxyethylene lauryl ether, a wetting agent (Fisher Scientific).

The conductivities of the samples were matched as closely as

possible to those of the curtain buffer for tests at 1x the conductivity. Tests were also made using samples 3x the conductivity of the curtain buffer. Conductivities were measured with an Electro Mark analyzer by Markson. Deflection of the PSL particles was measured with the metric scale at the CPE viewing chamber.

Sample insertion rates were studied extensively by the author and T. Miller in the summer of 1982.[3] Optimum flow rates were determined to be 25 µl/min. A syringe pump (Sage Instruments) was used to introduce the sample by syringe into the sample injection tip. Curtain buffer temperatures were maintained at approximately 22°C. Two different curtain flow rates were used (9.5 cc/min and 15 cc/min) in order to study resolution, bandwidth and degree of separation. Samples were studied at zero field, 20 V/cm, 40 V/cm and 60 V/cm.

Photographs of the particle streams were made using a Nikon F camera body with a 55 mm micro lens and 2x extension tube. The light source was a cross-section illuminator (CSI) mounted in the back of the CPE at the rear of the viewing chamber.[4] The camera was mounted on a tripod for support and elimination of vibrations from the peristaltic buffer pumps. All laboratory lights were turned off in order to achieve high resolution photographs. A medium F-stop of 5.6 provided adequate depth of field. Tri-X film by Kodak was used and push-processed at ASA 800.

Exposures were made at 1/8 sec and 1/15 sec. A shutter-release cable was also used since the micro lens, extension tube and camera body is a relatively heavy system for a small tripod.

IV. Results

Good quality photos were made and cataloged by the Separation Processes Branch staff. None of the photos will be included in this paper. The technique given in the preceding section is for future reference. Extensive results and discussion of the photographic documentation of particle streams was included in the ASEE report for 1982 by this author.[3]

The results of the PSL conductivity and concentration studies are included in Figures 1-7. Thses graphs show compilations of several runs in the CPE system.

Figures 1 and 2 show a comparison of mixtures of red, white and blue samples at 1x the conductivity using 9.5 cc/min and 15 cc/min flow rates. Overall resolution of the samples at both flow rates was excellent. Bandwidths are also included in the graphs. At zero field the samples at both these flow rates were 0.25 mm wide. At 60 V/cm the blue PSL sample particle streams were generally more unstable than red or white. In

ORIGINAL PAGE IS
OF POOR QUALITY

FIG 1. 1% RWB PSL IN 1 X CONDUCTIVITY

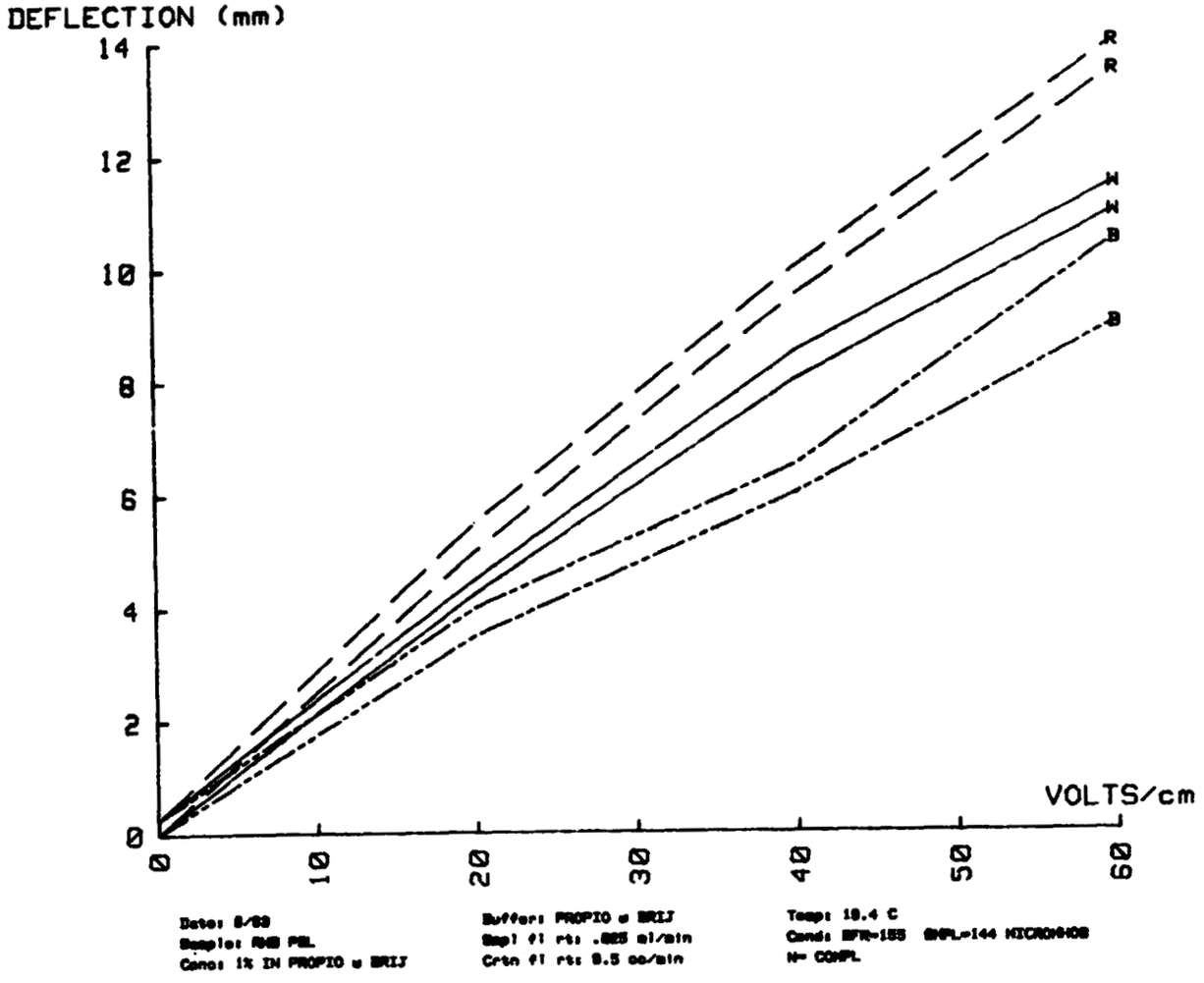

FIG 2. 1% RWB PSL IN 1 X CONDUCTIVITY

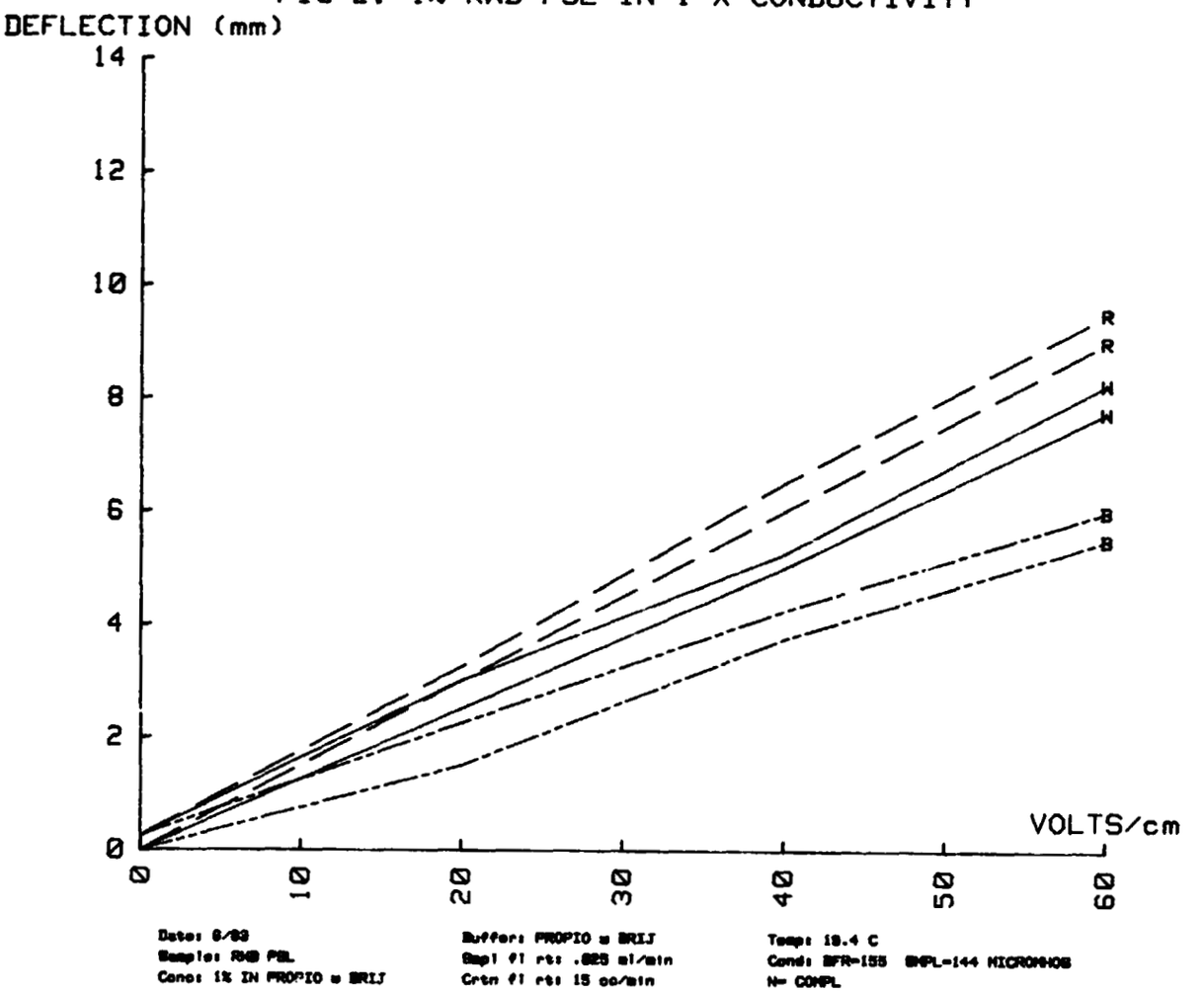

ORIGINAL PAGE IS
OF POOR QUALITY

FIG 3. 1% RWB PSL IN 3 X CONDUCTIVITY

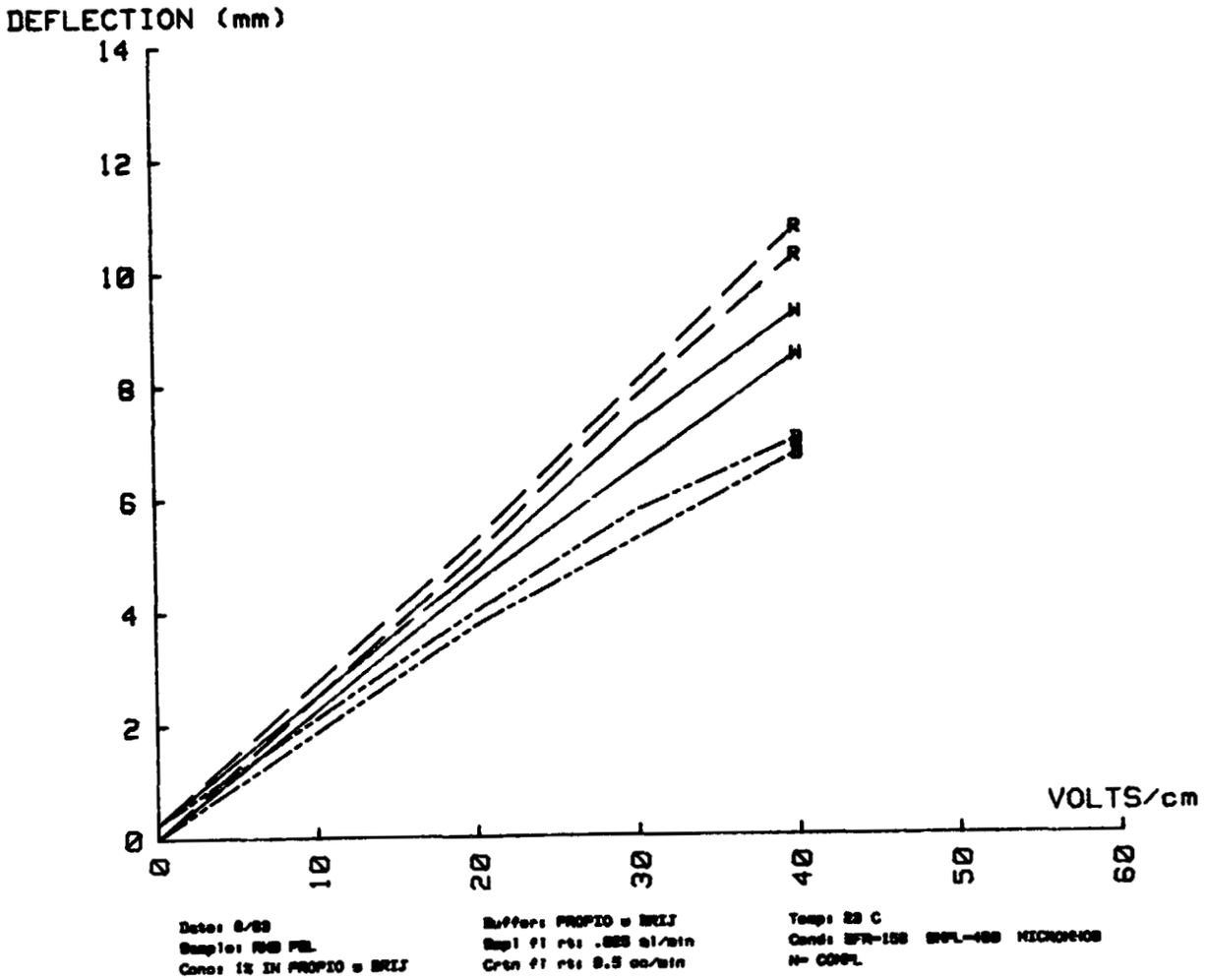

ORIGINAL PAGE IS
OF POOR QUALITY

FIG 4. 1% RWB PSL IN 3 X CONDUCTIVITY

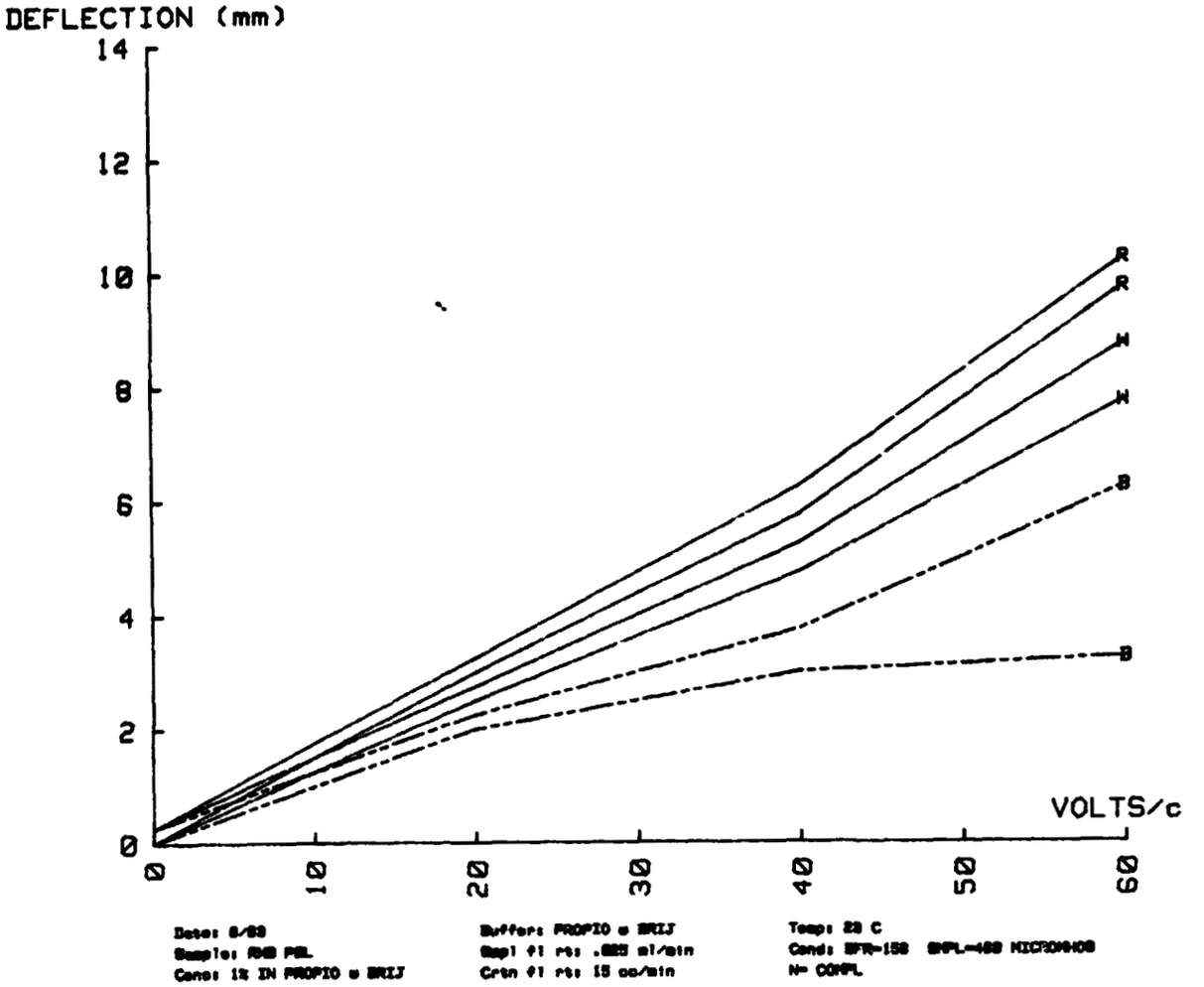

FIG 5. 5% RWB PSL IN 1 X CONDUCTIVITY

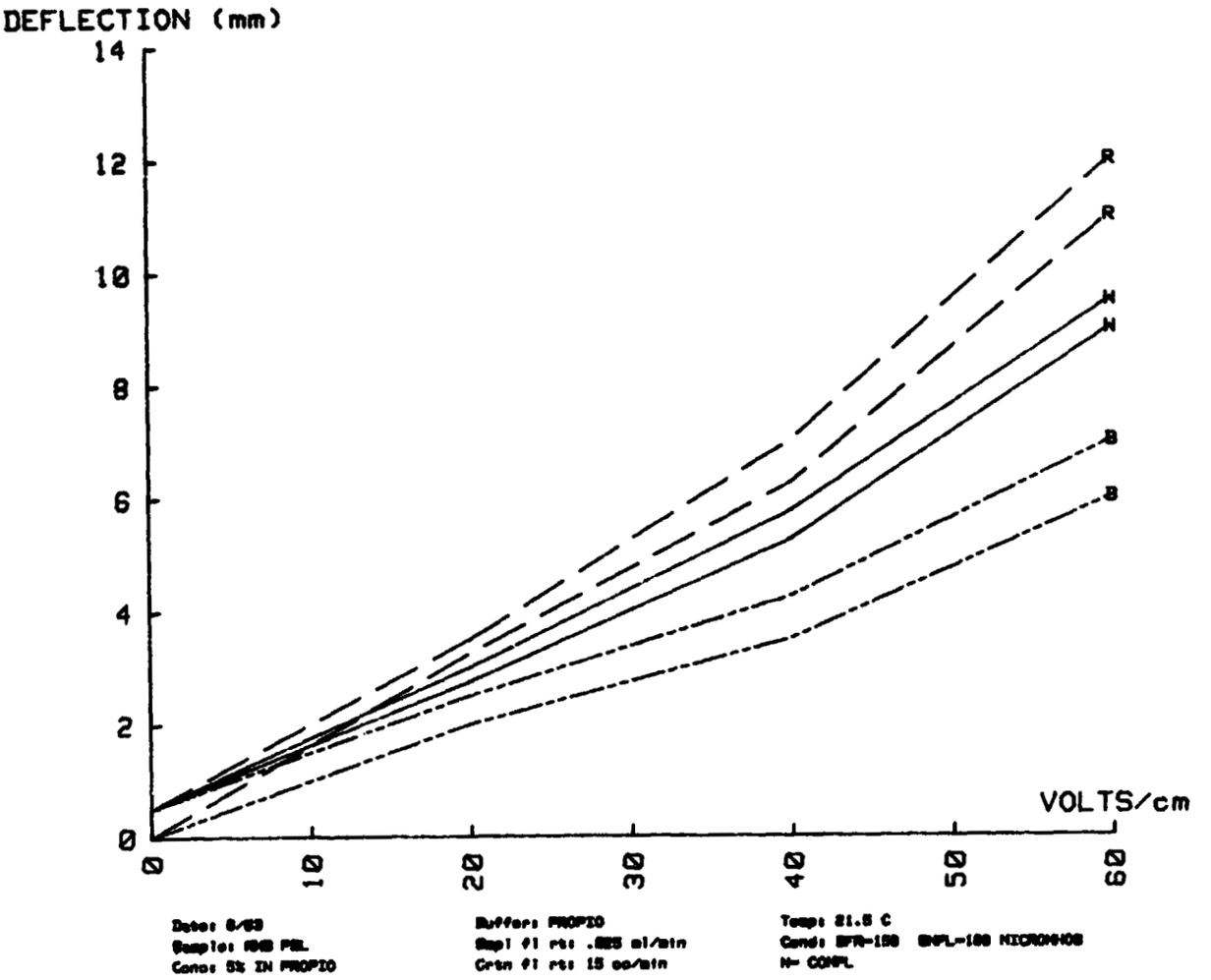

ORIGINAL PAGE IS
OF POOR QUALITY

FIG 6. 1% AND 1.6% BLUE PSL IN 1 X CONDUCTIVITY

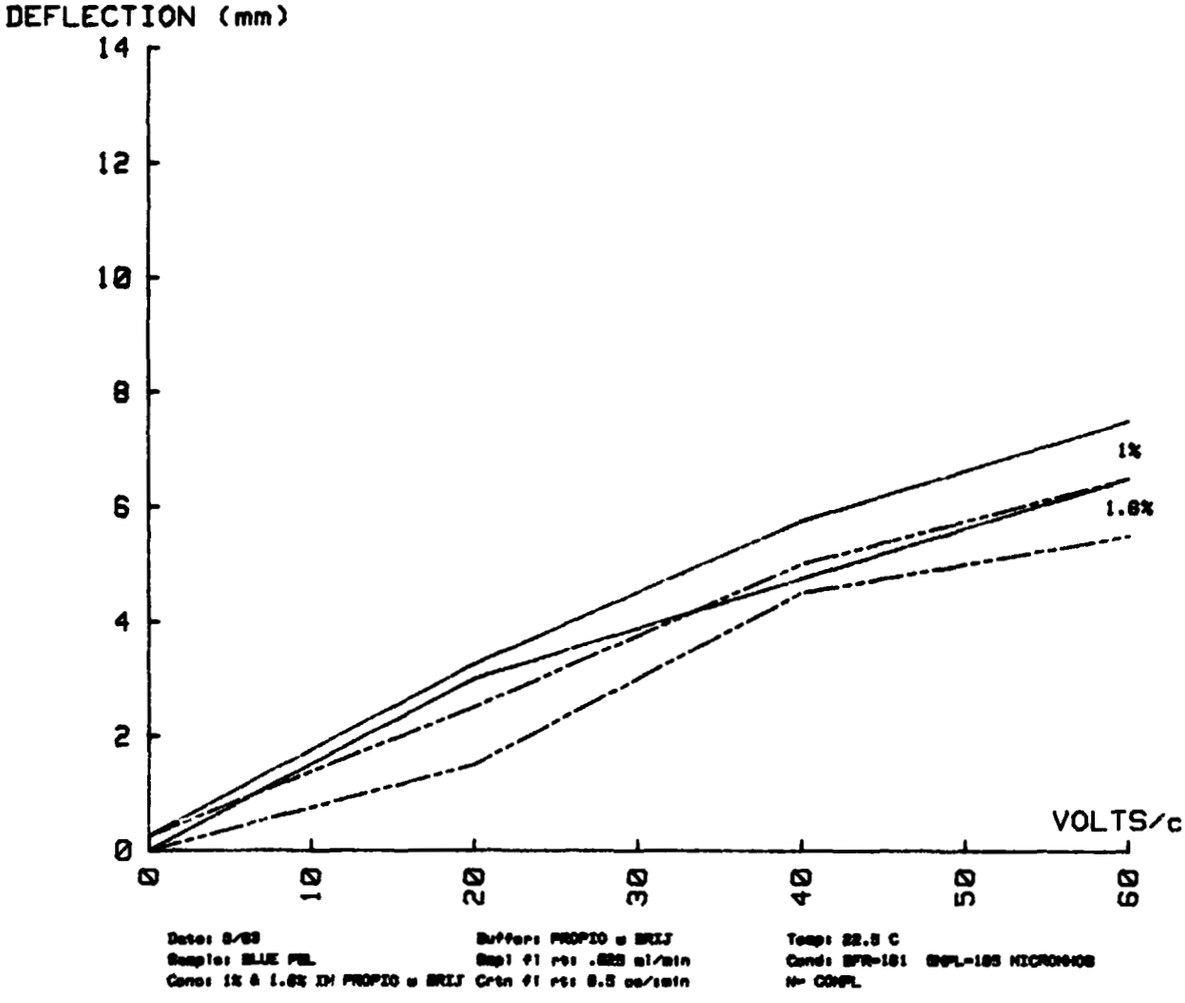

ORIGINAL PAGE IS
OF POOR QUALITY

FIG 7. 1.6 % AND 5% BLUE PSL IN 1 X CONDUCTIVITY

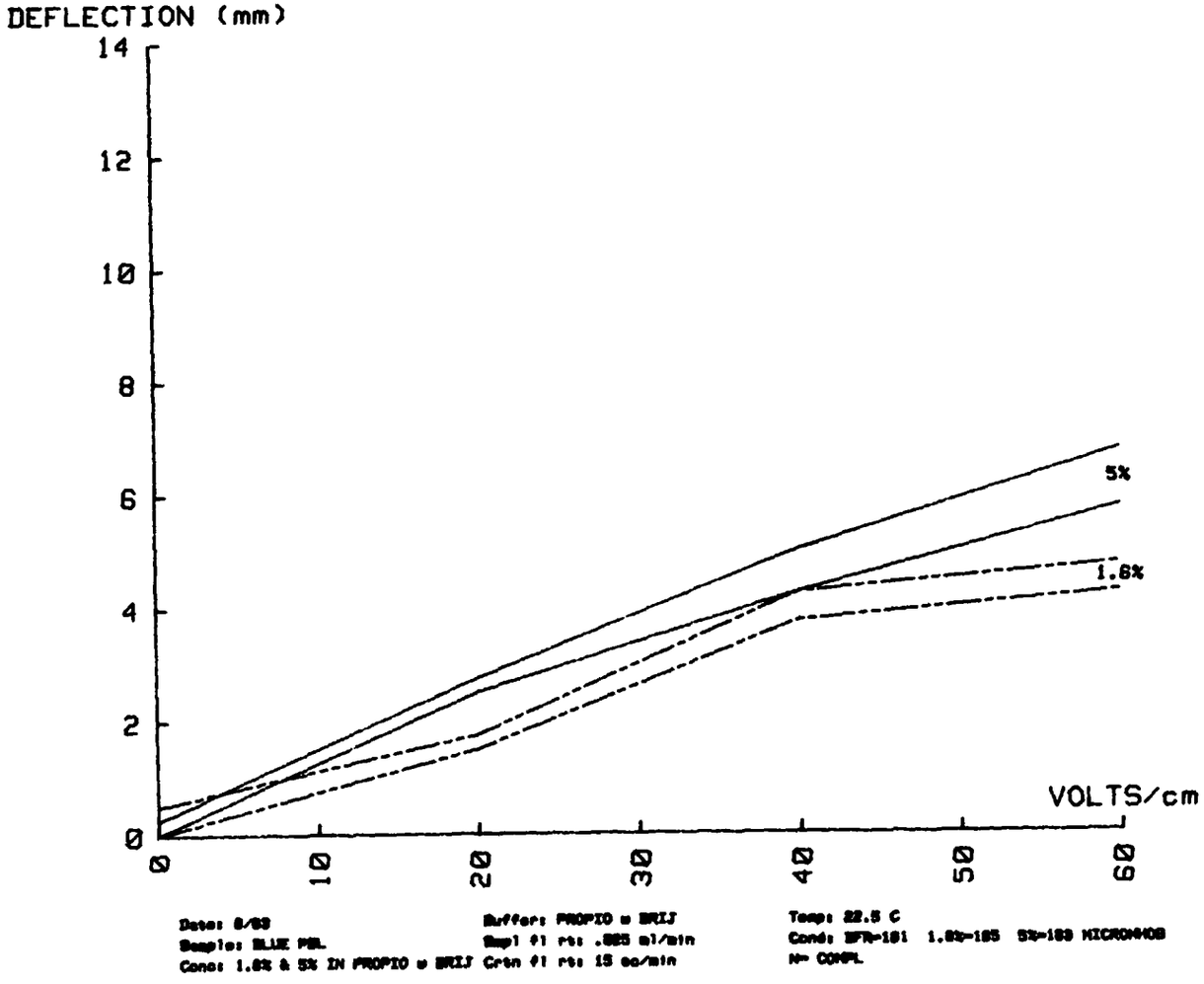

Fig. 1, the bandwidth of 1.5 mm for the blue (from 9.0 to 10.5) represents the largest of each of the samples. It may also be noted that the blue particles were observed from left, white in the center and red to the right of the chamber. The best results from these studies are shown in Fig. 2. Bandwidth at 60 V/cm were only 0.5 mm with separation of the colored particles averaging 0.75 mm. When the 15 cc/min flow rate is considered, these are optimum results.

Figure 3 shows the results of tests with red, white and blue sample at 3x the conductivity of the curtain buffer. Voltages of 20 V/cm and 40 V/cm were applied. Bandwidths of .25 mm at zero field were increased to .75 mm in the white and .5 mm in the red at 40 V/cm. Separations of at least 1 mm were recorded. These results were much more consistent with the ones in matched conductivities than the ones recorded in the faster flow rate (15 cc/min) when higher voltages were applied. Figure 4 gives the results of the red, white and blue sample at 3x the conductivity of the curtain buffer when the curtain flow rate was 15 cc/min. Band spreads in these tests were relatively insignificant at the lower voltages. At 60 V/cm good separation of red, white and blue microspheres occurred. The blue sample had an average of 3.0 mm. The white sample averaged 1.0 mm and the red .5 mm in width.

In Figure 5 the results of the studies with 5 percent solids in propionate and matched conductivities are given. Band spreads ranged from .5 mm to 1.0 mm for the components of the sample stream. At zero field the entire stream was .5 mm in width. Good sample separation was achieved during these CPE runs.

Figure 6 gives a comparison of two concentrations of the blue PSL. Concentrations of 1 and 1.6 percent solids in the propionate buffer at matched conductivities and the same curtain flow rates yielded similar results. At zero field the band spread for both samples (run separately) was .25 mm with both particle streams increasing in width to 1 mm at 60 V/cm.

Figure 7 is a composite graph showing studies with 1.6 and 5 percent blue PSL in propionate. These CPE runs were made in a curtain flow rate of 15 cc/min with matched conductivities. The 1.6 percent sample bandwidth was .5 mm at zero field, narrowed to .25 mm, then spread to .5 mm at the higher voltages. The 5 percent blue PSL bandwidth was .25 mm at zero field and 1.0 mm at 60 V/cm. Differences in particle deflection measurements were insignificant.

V. Conclusions and Recommendations

Results of these studies show that samples with conductivities matched to those of the curtain buffer yield greater resolution and less bandspread than those of three times the

conductivity. Moderate flow rates (15 cc/min) produced good sample resolution in the red, white and blue mixtures. Slower rates (9.5 cc/min) provide greater separation and more consistent bandwidths at the viewing chamber. We recommend matched conductivities at either flow rate for CPE studies with red, white and blue PSL mixtures. Some additional runs at each of the applied voltages with the 1% solids using curtain buffer with 3x the conductivity of the sample would be helpful.

Five percent samples produced consistent results with greater bandspread. These tests were made with samples having conductivities equal to those of the curtain buffer. Some additional runs with 5 percent solids in the 3x conductivity buffer are necessary; however, the very limited sample did not allow us to complete these tests.

Samples of blue PSL microspheres at 1.0, 1.6 and 5% solids produced results which were almost identical in particle deflection and bandspread (Figures 6 and 7). Therefore, either concentration may be used for future studies with blue samples.

During the two summers our objectives have been met. Photographic techniques have been satisfactorily determined. We have also determined optimum sample flow rates, conductivities and concentrations for research with PSL samples in the continuous particle electrophoresis system.

REFERENCES

1. Snyder, R. S., 1981. Review of the NASA Electrophoresis Program. Publ in Electrophoresis '81. Walter de Gruyter and Co., New York, p. 883-897.

2. Beckman Instruments, 1967. CPE System for Continuous Particle Electrophoresis. Bulletin 7096-B.

3. Williams, G., 1983. Studies With Sample Conductivity, Insertion Rates, and Particle Deflection in a Continuous Flow Electrophoresis System. NASA Contractor Report, CR-162051, XLII.

4. Strickler, A., 1970. Optimizing CPE Performance: Crescents, Artifacts, and Conductivity Effects. CPE Exchange No. 4.

☆ U.S. GOVERNMENT PRINTING OFFICE 1984 - 746-070/108